Advances in Delays and Dynamics 7

Tamás Insperger
Tulga Ersal
Gábor Orosz *Editors*

Time Delay Systems

Theory, Numerics, Applications, and Experiments

Springer

Advances in Delays and Dynamics

Volume 7

Series editor

Silviu-Iulian Niculescu, Paris-Sud, CNRS—CentraleSupèlec—Universitè, Gif-sur-Yvette, France
e-mail: Silviu.NICULESCU@l2s.centralesupelec.fr

About this Series

Delay systems are largely encountered in modeling propagation and transportation phenomena, population dynamics, and representing interactions between interconnected dynamics through material, energy, and communication flows. Thought as an open library on delays and dynamics, this series is devoted to publish basic and advanced textbooks, explorative research monographs as well as proceedings volumes focusing on delays from modeling to analysis, optimization, control with a particular emphasis on applications spanning biology, ecology, economy, and engineering. Topics covering interactions between delays and modeling (from engineering to biology and economic sciences), control strategies (including also control structure and robustness issues), optimization, and computation (including also numerical approaches and related algorithms) by creating links and bridges between fields and areas in a delay setting are particularly encouraged.

More information about this series at http://www.springer.com/series/11914

Tamás Insperger · Tulga Ersal · Gábor Orosz
Editors

Time Delay Systems

Theory, Numerics, Applications, and Experiments

Springer

Editors
Tamás Insperger
Department of Applied Mechanics
Budapest University of Technology
and Economics
Budapest
Hungary

Gábor Orosz
Department of Mechanical Engineering
University of Michigan
Ann Arbor, MI
USA

Tulga Ersal
Department of Mechanical Engineering
University of Michigan
Ann Arbor, MI
USA

ISSN 2197-117X ISSN 2197-1161 (electronic)
Advances in Delays and Dynamics
ISBN 978-3-319-53425-1 ISBN 978-3-319-53426-8 (eBook)
DOI 10.1007/978-3-319-53426-8

Library of Congress Control Number: 2017931054

Printed on acid-free paper

This Springer imprint is published by Springer Nature
The registered company is Springer International Publishing AG
The registered company address is: Gewerbestrasse 11, 6330 Cham, Switzerland

Preface

This volume of the series Advances in Delays and Dynamics collects contributions related to selected presentations from the 12th IFAC Workshop on Time Delay Systems, Ann Arbor, June 28–30, 2015. The great success of the workshop is reflected by the high number of presented papers (81), which is the highest number recorded to date in the history of IFAC TDS. This collection contains 23 papers, all of them presenting novel techniques and new results in the field of delayed dynamical systems. The topics cover different fields of control theory, numerical analysis, engineering and biological applications, and experiments.

We thank the authors for their high-quality contributions to this volume. We also acknowledge the encouragement of Prof. Silviu-Iulian Niculescu, the editor of the series Advances in Delays and Dynamics.

Budapest, Hungary — Tamás Insperger
Ann Arbor, USA — Tulga Ersal
Ann Arbor, USA — Gábor Orosz

Contents

Sampled-Data Stabilization of Nonlinear Delay Systems with a Compact Absorbing Set and State Measurement

Iasson Karafyllis and Miroslav Krstic

Abstract We present a methodology for the global sampled-data stabilization of systems with a compact absorbing set and input/measurement delays. The methodology is based on a numerical prediction scheme, which is combined with a projection of the state measurement on an appropriate sphere. The stabilization is robust to perturbations of the sampling schedule and is robust with respect to measurement noise. The obtained results are novel even for the delay-free case.

1 Introduction

Achieving global stabilization by Sampled-Data Feedback (SDF) and ensuring robustness to measurement noise and perturbations in the sampling schedule are challenges in nonlinear control over networks. In real networks, the presence of asynchrony and delays creates problems (see [7–9, 21, 22]). Almost all results rely on delay-dependent conditions for the existence of stabilizing feedback and the stability domain depends on the sampling interval/delay. Predictive feedback seems to be the only systematic way for handling large delays (see [3–5, 11–16, 18, 19, 23]). However, global stabilization of control systems with large delays by means of SDF remains a challenging problem. In general, global results for SDF control of delayed systems are limited; see [2, 6, 11, 12, 20].

The recent works [13, 16] provided global stabilization results for nonlinear delay systems with a compact absorbing set (see also [1, 10]). More specifically, the Inter-Sample-Predictor, Observer, Predictor, Delay-Free Controller (ISP-O-P-DFC)

I. Karafyllis (✉)
Department of Mathematics, National Technical University of Athens, Zografou Campus, 15780 Athens, Greece
e-mail: iasonkar@central.ntua.gr

M. Krstic
Department of Mechanical and Aerospace Engineering, University of California, San Diego, La Jolla, CA 92093-0411, USA
e-mail: krstic@ucsd.edu

T. Insperger et al. (eds.), *Time Delay Systems*,
Advances in Delays and Dynamics 7, DOI 10.1007/978-3-319-53426-8_1

control scheme was utilized in [13, 16] for the robust global stabilization of the nonlinear delay system. The recent work [16] used the numerical prediction scheme proposed in [14, 15] which can be easily implemented in computer software (since it was proved that the applied time step is constant). The present work extends the results in [16] for the case of state measurement. We consider systems of the form

$$\dot{x}(t) = f(x(t), u(t-\tau)),\ x \in \Re^n, u \in U \tag{1.1}$$

where $U \subseteq \Re^m$ is a nonempty compact set with $0 \in U$, $\tau \geq 0$ is the input delay and $f: \Re^n \times \Re^m \to \Re^n$ is a smooth vector field with $f(0,0) = 0$. The measurements are sampled and the output is given by

$$y(\tau_i) = x(\tau_i - r) + \xi(\tau_i) \tag{1.2}$$

where τ_i, $i = 0, 1, 2, \ldots$ are the sampling times, $\xi \in \Re^k$ is the measurement noise and $r \geq 0$ is the measurement delay. In this case, we apply the numerical prediction scheme proposed in [14] with an important difference: the measurement is projected on specific set. The projection guarantees robustness with respect to measurement errors (not guaranteed by the results in [14]) and stabilization for sampling schedules of arbitrary sampling period (not guaranteed by the results in [16]). Therefore, the results in this work cannot be guaranteed by other results in the literature. Moreover, it should be emphasized that the proof of the main results in the present work differs from the proofs of the main results in [16], due to the projection operator.

Our main result (Theorem 2.2) provides explicit formulas for global stabilizers, which are robust with respect to perturbations of the sampling schedule. Moreover, Theorem 2.2 can be also applied to the case where the sampling times do not necessarily coincide with the times that the input changes. This feature is important for network systems and is rare in the sampled-data control literature. The state is driven to the equilibrium at an exponential rate in the absence of measurement noise. The result of Theorem 2.2 is novel even for the delay-free case $r = \tau = 0$. Corollary 2.3 presents a specialization of the result to the delay-free case.

Notation. Throughout this paper, we adopt the following notation.

- $\Re_+ := [0, +\infty)$. A partition of $\Re_+$ is an increasing sequence $\{\tau_i\}_{i=0}^{\infty}$ with $\tau_0 = 0$, $\lim_{i \to \infty} \tau_i = +\infty$. For $x \in \Re^n$, x' is its transpose and $|x|$ is its Euclidean norm.
- Let $I \subseteq \Re_+ := [0, +\infty)$ be an interval. By $B(I; U)$, we denote the space of locally bounded functions $u(\cdot)$ defined on I and taking values in $U \subseteq \Re^m$. By $L^\infty(I; U)$, we denote the space of measurable and essentially bounded functions $u(\cdot)$ defined on I and taking values in $U \subseteq \Re^m$. Let $A \subseteq \Re^n$ be an open set. By $C^0(A\ ;\ \Omega)$, we denote the class of continuous functions on A, which take values in $\Omega \subseteq \Re^m$. By $C^k(A\ ;\ \Omega)$, where $k \geq 1$ is an integer, we denote the class of functions on $A \subseteq \Re^n$ with continuous derivatives of order k, which take values in

$\Omega \subseteq \mathfrak{R}^m$. For a function $V \in C^1(A\,;\,\mathfrak{R})$, the gradient of V at $x \in A \subseteq \mathfrak{R}^n$ is denoted by $\nabla V(x)$.

- $V: \mathfrak{R}^n \to \mathfrak{R}_+$ is positive definite if $V(0) = 0$ and $V(x) > 0$ for all $x \neq 0$. $V: \mathfrak{R}^n \to \mathfrak{R}_+$ is radially unbounded if the sets $\{x \in \mathfrak{R}^n : V(x) \leq M\}$ are either empty or bounded for all $M \geq 0$. K_∞ is the class of increasing, continuous, unbounded functions $a: \mathfrak{R}_+ \to \mathfrak{R}_+$ with $a(0) = 0$. $[x]$ denotes the integer part of $x \in \mathfrak{R}$.
- For $u: [a-r, b) \to U$, where $U \subseteq \mathfrak{R}^m$, $b > a$ and $r > 0$, $u_t: [-r, 0] \to U$ for $t \in [a, b)$ denotes the function defined by $(u_t)(\theta) = u(t+\theta)$ for $\theta \in [-r, 0]$ and $\breve{u}_t: [-r, 0) \to U$ for $t \in [a, b]$ denotes the function defined by $(\breve{u}_t)(\theta) = u(t+\theta)$ for $\theta \in [-r, 0)$. For a bounded function $u: [-r, 0] \to U$ (or $u: [-r, 0) \to U$), $\|u\|$ denotes the norm $\|u\| = \sup_{-r \leq \theta \leq 0} (|u(\theta)|)$ (or $\|u\| = \sup_{-r \leq \theta < 0} (|u(\theta)|)$).

2 Problem Description and Main Result

Our first assumption for system (1.1) guarantees that there exists a compact set which is robustly globally asymptotically stable. We call the compact set "absorbing" because the solution "is absorbed" in the set after an initial transient period.

(H1) *There exist a radially unbounded (but not necessarily positive definite) function $V \in C^2(\mathfrak{R}^n; \mathfrak{R}_+)$, a positive definite function $W \in C^1(\mathfrak{R}^n; \mathfrak{R}_+)$ and a constant $R > 0$ such that the following inequality holds for all $(x, u) \in \mathfrak{R}^n \times U$ with $V(x) \geq R$*

$$\nabla V(x) f(x, u) \leq -W(x) \tag{2.1}$$

Moreover, the set

$$S_1 = \{x \in \mathfrak{R}^n : V(x) \leq R\} \tag{2.2}$$

contains a neighborhood of $0 \in \mathfrak{R}^n$.

Assumption (H1) guarantees that for every $x(0) \in \mathfrak{R}^n$ and for every $u: \mathfrak{R}_+ \to U$ the solution $x(t)$ of (1.1) enters the compact set $S_1 = \{x \in \mathfrak{R}^n : V(x) \leq R\}$ after a finite transient period. This fact is guaranteed by the following lemma, which is an extension of Theorem 5.1 in [17]. The proof of Lemma 2.1 can be found in [10].

Lemma 2.1 *Consider system (1.1) under assumption (H1). There exists $T \in C^0(\mathfrak{R}^n; \mathfrak{R}_+)$ such that for every $x_0 \in \mathfrak{R}^n$ and for every measurable and essentially bounded input $u: [-\tau, +\infty) \to U$ the solution $x(t) \in \mathfrak{R}^n$ of (1.1) with initial condition $x(0) = x_0$ and corresponding to input $u: [-\tau, +\infty) \to U$ satisfies $V(x(t)) \leq \max(V(x_0), R)$ for all $t \geq 0$ and $V(x(t)) \leq R$ for all $t \geq T(x_0)$.*

The second assumption guarantees the existence of an appropriate local stabilizer $u = k(x)$ for the delay-free version of system (1.1), i.e., system (1.1) with $\tau = 0$.

(H2) *There exist a positive definite function $P \in C^2(\Re^n; \Re_+)$, constants $\mu, K_1 > 0$ with $K_1|x|^2 \leq P(x)$ for all $x \in S_1$ and a locally Lipschitz mapping $k: \Re^n \to U$ with $k(0) = 0$ such that the following inequality holds*

$$\nabla P(x) f(x, k(x)) \leq -2\mu |x|^2, \text{ for all } x \in S_1 \tag{2.3}$$

Let $\rho \geq \max\{ |x| : x \in S_1 \}$ be a constant and define $Q: \Re^n \to \Re^n$ by the formula:

$$Q(x) := x \text{ if } |x| \leq \rho, \; Q(x) = \rho x/|x| \text{ if } |x| > \rho \tag{2.4}$$

Clearly, $Q: \Re^n \to \Re^n$ is the projection on the closed ball of radius ρ centered at $0 \in \Re^n$. Since $Q: \Re^n \to \Re^n$ is a projection on a closed convex set, it follows that

$$|Q(x) - Q(y)| \leq |x - y| \text{ for all } x, y \in \Re^n \tag{2.5}$$

Next, the reader is introduced to the approximate predictor mapping, which uses a numerical scheme for the prediction of the state value $r + \tau$ time units ahead. Let $N > 0$ be an integer and define the mapping:

$$\Phi_N: \Re^n \times L^\infty([-r-\tau, 0); U) \to \Re^n \tag{2.6}$$

which maps $(x_0, u) \in \Re^n \times L^\infty([-r-\tau, 0); U)$ to the vector $\Phi_N(x_0, u) := x_N \in \Re^n$, where $x_i \in \Re^n$ $i = 1, \ldots, N$ are vectors given by the recursive formula:

$$x_{i+1} = x_i + \int_{ih}^{(i+1)h} f(x_i, u(s - r - \tau)) ds, \text{ for } i = 0, \ldots, N-1 \tag{2.7}$$

and $h := (\tau + r)/N$. The prediction is performed by the auxiliary variables $z(t) \in \Re^n$, which approximate $x(t + \tau)$ and satisfy the following equations:

$$\dot{z}(t) = f(z(t), u(t)), \text{ for } t \in [\tau_i, \tau_{i+1}) \text{ and for all integers } i \geq 0 \tag{2.8}$$

$$z(\tau_i) = \Phi_N\left(Q(x(\tau_i - r) + \xi(\tau_i)), \breve{u}_{\tau_i}\right), \text{ for all integers } i \geq 0 \tag{2.9}$$

$$u(t) = k(z(jT_H)), \text{ for all } t \in [jT_H, (j+1)T_H) \text{ and for all integers } j \geq 0 \tag{2.10}$$

We are now in a position to state the main result of this work.

Theorem 2.2 *Consider system (1.1), (1.2) under assumptions (H1–2). Then for every $T_s > 0$, there exist a sufficiently small constant $T_H > 0$, a sufficiently large integer $N > 0$, a locally Lipschitz function $C \in K_\infty$ and constants $\sigma, \gamma > 0$ such that for every partition $\{\tau_i\}_{i=0}^\infty$ of $\Re_+$ with $\sup_{i \geq 0}(\tau_{i+1} - \tau_i) \leq T_s$, $x_0 \in C^0([-r, 0]; \Re^n)$ $\breve{u}_0 \in L^\infty([-r-\tau, 0); U)$, $\xi \in B(\Re_+; \Re^k)$, the solution of (1.1), (1.2) with (2.8),*

(2.9), (2.10), initial condition $x(\theta)=x_0(\theta)$ *for* $\theta\in[-r,0]$, $u(\theta)=\breve{u}_0(\theta)$ *for* $\theta\in[-r-\tau,0)$ *corresponding to input* $\xi\in B(\Re_+;\Re^k)$, *exists for all* $t\geq 0$ *and satisfies the following estimate:*

$$\|x_t\|+\left\|\breve{u}_t\right\|\leq \exp(-\sigma t)C\left(\|x_0\|+\left\|\breve{u}_0\right\|+\sup_{0\leq s\leq t}(|\xi(s)|)\right)+\gamma\sup_{0\leq s\leq t}(|\xi(s)|),\ \forall t\geq 0 \tag{2.11}$$

The result of Theorem 2.2 is novel even for the delay-free case $r=\tau=0$. Indeed, one can repeat the proof of Theorem 2.2 and obtain the following corollary (its proof is omitted due to the similarity with the proof of Theorem 2.2).

Corollary 2.3 *Consider system (1.1), (1.2) under assumptions (H1–2) with* $r=\tau=0$. *Then for every* $T_s>0$ *and for sufficiently small constant* $T_H>0$ *there exist a locally Lipschitz function* $C\in K_\infty$ *and constants* $\sigma,\gamma>0$ *such that for every partition* $\{\tau_i\}_{i=0}^{\infty}$ *of* $\Re_+$ *with* $\sup_{i\geq 0}(\tau_{i+1}-\tau_i)\leq T_s$, $x_0\in\Re^n$, $\xi\in B(\Re_+;\Re^k)$ *the solution of (1.1), (1.2) with*

$$\dot{z}(t)=f(z(t),u(t)),\ \text{for}\ t\in[\tau_i,\tau_{i+1})\ \text{and for all integers}\ i\geq 0 \tag{2.12}$$

$$z(\tau_i)=Q(x(\tau_i)+\xi(\tau_i)),\ \text{for all integers}\ i\geq 0 \tag{2.13}$$

$$u(t)=k(z(jT_H)),\ \text{for all},\ t\in[jT_H,(j+1)T_H)\ \text{and for all integers}\ j\geq 0 \tag{2.14}$$

initial condition $x(0)=x_0$ *corresponding to input* $\xi\in B(\Re_+;\Re^k)$, *exists for all* $t\geq 0$ *and satisfies the following estimate:*

$$|x(t)|\leq \exp(-\sigma t)C\left(|x_0|+\sup_{0\leq s\leq t}(|\xi(s)|)\right)+\gamma\sup_{0\leq s\leq t}(|\xi(s)|),\ \forall t\geq 0 \tag{2.15}$$

Remark 2.4 **(a)** The approximate predictor mapping given in (2.6), (2.7) is the repeated explicit Euler numerical scheme for the control system (1.1). The integer $N>0$ is the grid size of the numerical scheme and in contrast to the results in [14, 15] (where the grid size was state-dependent), Theorem 2.2 guarantees that the grid size can be selected to be constant. This is an important feature of Theorem 2.2, because the implementation of the prediction scheme is simplified considerably. However, there is a major difference between the proposed scheme used in [14, 15] and the present prediction scheme: notice that (2.9) does not provide a prediction based on the current measurement but rather provides a prediction based on the projection of the measurement on the closed ball of radius ρ centered at $0\in\Re^n$.

(b) Estimate (2.11) guarantees robustness with respect to measurement noise. Indeed, using estimate (2.11), we are in a position to prove an Input-to-State Stability (ISS) estimate with respect to the measurement noise $\xi\in\Re^k$; here we are referring to a direct extension of the well-known ISS notions introduced by E. D. Sontag for systems described by ODEs (see [24–26]). However, estimate (2.11)

shows an additional property: the fact that for every initial condition and for every bounded input $\xi \in B(\Re_+; \Re^k)$ the corresponding solution of the closed-loop system (1.1), (1.2) with (2.8), (2.9), (2.10) satisfies $\limsup_{t \to +\infty} \left(\|x_t\| + |z(t)| + \left\| \widetilde{u}_t \right\| \right) \leq \gamma \sup_{0 \leq s} (|\xi(s)|)$. This inequality shows that the asymptotic gain property holds for the closed-loop system (1.1), (1.2) with (2.8), (2.9), (2.10) with linear gain. The asymptotic gain property was first introduced in [25] for systems described by Ordinary Differential Equations (ODEs), where it was shown that a system is ISS if and only if $0 \in \Re^n$ is Globally Asymptotically Stable for the input-free system and satisfies the asymptotic gain property (see also [26]).

3 Proof of Main Result

Define the set:

$$S_2 := \{x \in \Re^n : V(x) \leq b\} \tag{3.1}$$

where $b > 0$ is an arbitrary constant that satisfies

$$b > \max\{ V(x) : |x| \leq \rho \} \tag{3.2}$$

with $\rho \geq \max\{ |x| : x \in S_1 \}$ being the constant involved in definition (2.4). Notice that since $V \in C^2(\Re^n; \Re_+)$ is radially unbounded, it follows that the sets defined in (2.2) and (3.1) are compact sets. The following technical lemmas are proved in [16] and provide estimates for the state and the prediction error.

Lemma 3.1 *Let $\sigma > 0$, $T_H > 0$ be sufficiently small constants. Then there exist constants $M_2, M_3 > 0$ such that every solution of (1.1) corresponding to (arbitrary) input $u \in L^\infty([-\tau, +\infty); U)$ and satisfying $x(t) \in S_1$ for all $t \geq \tau + jT_H$, where $j \geq 0$ is an integer, also satisfies the following inequality for all $t \geq jT_H$:*

$$\begin{aligned} &\sup_{jT_H \leq s \leq t} (|x(s+\tau)| \exp(\sigma s)) \leq M_2 \exp(\sigma j T_H) |x(jT_H + \tau)| \\ &+ M_3 \sup_{jT_H \leq s \leq t} \left(\left| u(s) - k\left(x\left(\tau + \left[\frac{s}{T_H} \right] T_H \right) \right) \right| \exp(\sigma s) \right) \end{aligned} \tag{3.3}$$

Lemma 3.2 *There exists an integer $N^* > 0$ and a constant $M_4 > 0$ such that for every $N \geq N^*$ for every $x_0 \in S_2$ and for every measurable and essentially bounded input $u \in L^\infty([-r-\tau, 0); U)$ the following estimates hold for the solution $x(t)$ of (1.1) with initial condition $x(-r) = x_0$, corresponding to (arbitrary) input $u \in L^\infty([-r-\tau, 0); U)$:*

$$|x(\tau) - \Phi_N(x_0, u)| \leq M_4(|x_0| + \|u\|)/N \tag{3.4}$$

$$x_i \in S_2, \text{ for all } i = 0, 1, \ldots, N \tag{3.5}$$

where $\|u\| = \sup_{-r-\tau \leq s < 0} (|u(s)|)$ *and* $x_i \in \Re^n$ $(i = 1, \ldots, N)$ *are vectors given by the recursive formula (2.7).*

The following technical lemma uses the two previous lemmas and provides an estimate for the norm of the solution of the closed-loop system (1.1), (1.2), (2.8), (2.9), (2.10). Its proof is provided at the Appendix.

Lemma 3.3 *For every* $T_s > 0$ *there exist sufficiently small constants* $\sigma > 0$, $T_H > 0$ *a sufficiently large integer* $N \geq 1$ *and constants* $G, \gamma_2 > 0$ *with the following property: for every partition of* $\Re_+$, $\{\tau_i\}_{i=0}^{\infty}$ *with* $\sup_{i \geq 0}(\tau_{i+1} - \tau_i) \leq T_s$, *for every* $\xi \in B(\Re_+; \Re^k)$ *and for every solution of (1.1), (1.2), (2.8), (2.9), (2.10) defined for all* $t \geq 0$ *and satisfying* $x(t) \in S_1$ *for all* $t \geq T$ *for some* $T \geq 0$, *the following inequality holds for all* $t \geq 0$:

$$\begin{aligned} &\left(\left\|\breve{u}_t\right\| + \|x_t\|\right) \exp(\sigma t) \leq \gamma_2 \exp(\sigma t) \sup_{0 \leq s \leq t} (|\xi(s)|) \\ &+ G \exp(\sigma j T_H) \left(\sup_{-r-\tau \leq s \leq jT_H} (|u(s)|) + \sup_{-r \leq s \leq jT_H + \tau} (|x(s)|) \right) \end{aligned} \tag{3.6}$$

where $j \geq 0$ *is any integer with* $jT_H \geq r + T + T_s$.

We are now ready to provide the proof of Theorem 2.2

Proof of Theorem 2.2 Let $T_s > 0$ be given and let $\sigma > 0$, $T_H > 0$ be sufficiently small constants and let $N \geq 1$ be a sufficiently large integer so that Lemma 3.4 holds. Let $\{\tau_i\}_{i=0}^{\infty}$ be a partition of $\Re_+$ with $\sup_{i \geq 0}(\tau_{i+1} - \tau_i) \leq T_s$ and let $x_0 \in C^0([-r, 0]; \Re^n)$, $z_0 \in \Re^n$, $\breve{u}_0 \in L^\infty([-r-\tau, 0); U)$, $\xi \in B(\Re_+; \Re^k)$ be given. We will show first that the solution of (1.1), (1.2), (2.11), (2.12), (2.13), (2.14), with initial condition $x(\theta) = x_0(\theta)$ for $\theta \in [-r, 0]$, $u(\theta) = \breve{u}_0(\theta)$ for $\theta \in [-r-\tau, 0)$ corresponding to input $\xi \in B(\Re_+; \Re^k)$, exists for all $t \geq 0$ and is unique. This is a direct consequence of the following claim and an application of the method of steps.

Claim 1: $\breve{u}_t$, x_t, $z(t)$ are uniquely determined for all $t \in [0, jT_H]$, where $j \in Z_+$.

Claim 1 is proved by induction. First we notice that the claim holds for $j = 0$. Next, we show that if the claim holds for some $j \in Z_+$ then the claim holds for $j + 1$. Indeed, (2.10) guarantees that $\breve{u}_t$ is uniquely determined for all $t \in (jT_H, (j+1)T_H]$. It follows from Lemma 2.1 that x_t is uniquely determined for all $t \in (jT_H, (j+1)T_H]$. Since the set $(jT_H, (j+1)T_H] \cap \{\tau_i\}_{i=0}^{\infty}$ is either empty or finite, we are in a position to determine uniquely $z(t)$ for all $t \in (jT_H, (j+1)T_H]$. Thus $\breve{u}_t$, x_t, $z(t)$ are uniquely determined for all $t \in [0, (j+1)T_H]$, where $j \in Z_+$.

Lemma 2.1 implies there exists $T \in C^0(\Re^n; \Re_+)$ such that

$$V(x(t)) \leq \max(V(x_0(0)), R), \text{ for all } t \geq 0 \tag{3.7}$$

$$V(x(t)) \leq R, \text{ for all } t \geq T(x_0(0)) \tag{3.8}$$

Indeed, the above conclusions for $V(x(t))$ are direct consequences of Lemma 2.1. Inequality (3.8) and definition (2.2) show that

$$x(t) \in S_1, \text{ for all } t \geq T(x_0(0)) \tag{3.9}$$

Let $j \geq 0$ be the smallest integer so that $jT_H \geq r + T_s + T(x_0(0))$. Then (3.9) in conjunction with Lemma 3.3 implies the existence of constants $G, \gamma_2 > 0$ such that (3.6) holds. Since $f: \Re^n \times \Re^m \to \Re^n$, $k: \Re^n \to U$ are locally Lipschitz mappings with $f(0,0) = 0$, $k(0) = 0$ and since $U \subset \Re^m$ is compact, there exists a continuous, nondecreasing function $L: \Re_+ \to [1, +\infty)$ such that:

$$|f(x,u)| + |k(x)| \leq L(|x|)(|x| + |u|), \text{ for all } x \in \Re^n,\ u \in U \tag{3.10}$$

Furthermore, using induction, (3.10), definitions (2.6), (2.7) and the fact that $U \subset \Re^m$ is compact, we are in a position to guarantee that there exists a continuous, nondecreasing function $\tilde{L}: \Re_+ \to [1, +\infty)$ such that:

$$|\Phi_N(x,u)| \leq \tilde{L}(|x|)(|x| + \|u\|), \text{ for all } (x,u) \in \Re^n \times L^\infty([-r-\tau, 0); U) \tag{3.11}$$

Using (2.4), (2.5), (2.9) and (3.11) we obtain for all integers $i \geq 0$:

$$|z(\tau_i)| \leq \tilde{L}(\rho)\left(|x(\tau_i - r)| + |\xi(\tau_i)| + \left\|\breve{u}_{\tau_i}\right\|\right) \tag{3.12}$$

Applying Lemma 2.1 to (2.8) we can guarantee that

$$V(z(t)) \leq \max(V(z(\tau_i)), R), \text{for all } t \in [\tau_i, \tau_{i+1})\ i \geq 0 \text{ and for all integers} \tag{3.13}$$

Next, define the following family of sets for all $p \geq 0$:

$$S(p) := \{x \in \Re^n : V(x) \leq \max(\max\{V(\xi) : \xi \in \Re^n,\ |\xi| \leq p\},\ R)\} \tag{3.14}$$

Notice that by virtue of assumption (H1) the above sets are compact for each $p \geq 0$ and that $S(p_1) \subseteq S(p_2)$ for every $p_1, p_2 \geq 0$ with $p_1 \leq p_2$. Define the nondecreasing function for all $p \geq 0$:

$$\phi(p) := \max_{x \in S(p)} (|x|). \tag{3.15}$$

It follows from (3.7), (3.10), (3.13) and definitions (3.14), (3.15) that the following inequalities hold:

$$|f(x(t),u(t-\tau))| \le L(\phi(|x_0(0)|))(|x(t)|+|u(t-\tau)|), \text{ for } t \ge 0 \tag{3.16}$$

$$|f(z(t),u(t))| \le L(\phi(|z(\tau_i)|))(|z(t)|+|u(t)|), \text{ for } t \in [\tau_i,\tau_{i+1}) \tag{3.17}$$

We next show the following claim.

Claim 2: There exists a sequence of nondecreasing functions $\Gamma_i: \Re_+ \to \Re_+$ with $\Gamma_i(s) \le \Gamma_{i+1}(s)$ for all $s \ge 0$ and for all integers $i \ge 0$ such that the following inequality holds for every integer $i \ge 0$:

$$\sup_{0\le t\le iT_H}\left(\left\|\breve{u}_t\right\|+\|x_t\|+|z(t)|\right) \le \left(\left\|\breve{u}_0\right\|+\|x_0\|+\sup_{0\le t\le iT_H}(|\xi(t)|)\right)\Gamma_i\left(\|x_0\|+\sup_{0\le t\le iT_H}(|\xi(t)|)\right) \tag{3.18}$$

We prove Claim 2 by constructing the sequence $\Gamma_i: \Re_+ \to \Re_+$ inductively. Inequality (3.18) for $i=0$ with the function $\Gamma_0(s) \equiv 1+\tilde{L}(\rho)$ is a direct consequence of (3.12). In order to show Claim 2, we assume that there exists an integer $i \ge 0$ and a nondecreasing function $\Gamma_i: \Re_+ \to \Re_+$ such that (3.18) holds. We next show that there exists a nondecreasing function $\Gamma_{i+1}: \Re_+ \to \Re_+$ with $\Gamma_i(s) \le \Gamma_{i+1}(s)$ for all $s \ge 0$ such that (3.18) holds with $i \ge 0$ replaced by $i+1$.

Using (2.10), (3.10), and (3.18), we get for $t \in [iT_H,(i+1)T_H)$:

$$|u(t)| \le L(|z(iT_H)|)|z(iT_H)| \le L\left(\left(\left\|\breve{u}_0\right\|+R\right)\Gamma_i(R)\right)\Gamma_i(R)\left(\left\|\breve{u}_0\right\|+R\right)$$

where $R := \|x_0\| + \sup_{0\le t\le iT_H}(|\xi(t)|)$. Using (3.18), the above inequality and the fact that $U \subset \Re^m$ is compact, we obtain the existence of a nondecreasing function $Z_i: \Re_+ \to \Re_+$ such that:

$$\sup_{0\le t\le (i+1)T_H}\left(\left\|\breve{u}_t\right\|\right) \le \left(\left\|\breve{u}_0\right\|+\|x_0\|+\sup_{0\le t\le (i+1)T_H}(|\xi(t)|)\right)Z_i\left(\|x_0\|+\sup_{0\le t\le (i+1)T_H}(|\xi(t)|)\right) \tag{3.19}$$

Using (3.16), (3.19) and (1.1) we obtain the inequality $|x(t)| \le |x(iT_H)| + L(\varphi(|x_0(0)|))\int_{iT_H}^t |x(s)|ds + L(\varphi(|x_0(0)|))T_H \sup_{0\le s\le (i+1)T_H}\left(\left\|\breve{u}_s\right\|\right)$ for all $t \in [iT_H, (i+1)T_H]$. A direct application of the Gronwall–Bellman Lemma in conjunction with the fact that $|x_0(0)| \le \|x_0\|$, implies that $|x(t)| \le \exp(L(\phi(\|x_0\|))T_H)\left(|x(iT_H)| + L(\phi(\|x_0\|))T_H \sup_{0\le s\le (i+1)T_H}\left(\left\|\breve{u}_s\right\|\right)\right)$ for all $t \in [iT_H,(i+1)T_H]$. The previous inequality in conjunction with (3.18), (3.19) implies the existence of a nondecreasing function $\tilde{Z}_i: \Re_+ \to [1,+\infty)$ such that:

$$\sup_{0\le t\le (i+1)T_H}\left(\left\|\breve{u}_t\right\|+\|x_t\|\right)\le\left(\left\|\breve{u}_0\right\|+\|x_0\|+\sup_{0\le t\le (i+1)T_H}(|\xi(t)|)\right)\tilde{Z}_i\left(\|x_0\|+\sup_{0\le t\le (i+1)T_H}(|\xi(t)|)\right) \tag{3.20}$$

Using (3.12), (3.18), (3.20) and the fact that $\tilde{Z}_i(s)\ge 1$ for all $s\ge 0$, we obtain that $|z(\tau_j)|\le\tilde{L}(\rho)\left(\left\|\breve{u}_0\right\|+\|x_0\|+\sup_{0\le t\le (i+1)T_H}(|\xi(t)|)\right)\ 2\tilde{Z}_i\left(\|x_0\|+\sup_{0\le t\le (i+1)T_H}(|\xi(t)|)\right)$ for all integers $j\ge 0$ with $[iT_H,(i+1)T_H]\cap[\tau_j,\tau_{j+1})$. Using (2.8), (3.17), (3.20) and the previous inequality we get $|z(t)|\le Q+|z(iT_H)|+L(\phi(Q))\int_{iT_H}^{t}|z(s)|ds+L(\phi(Q))T_HB$ for all $t\in[iT_H,(i+1)T_H]$, where $Q:=\tilde{L}(\rho)\left(\left\|\breve{u}_0\right\|+\|x_0\|+\sup_{0\le t\le (i+1)T_H}(|\xi(t)|)\right)$ $2\tilde{Z}_i\left(\|x_0\|+\sup_{0\le t\le (i+1)T_H}(|\xi(t)|)\right)$, $B:=\left(\left\|\breve{u}_0\right\|+\|x_0\|+\sup_{0\le t\le (i+1)T_H}(|\xi(t)|)\right)$ $\tilde{Z}_i\left(\|x_0\|+\sup_{0\le t\le (i+1)T_H}(|\xi(t)|)\right)$. We next apply the Gronwall–Bellman Lemma (although the function $t\to|z(t)|$ is piecewise continuous and not continuous –in general- on the interval $[iT_H,(i+1)T_H]$, the reader should realize that the Gronwall–Bellman Lemma holds for piecewise continuous functions as well) and obtain the inequality $|z(t)|\le\exp(L(\phi(Q))T_H)(Q+|z(iT_H)|+L(\phi(Q))T_HB)$ for all $t\in[iT_H,(i+1)T_H]$. Using (3.18), (3.20), the previous inequality and the fact that $U\subset\mathfrak{R}^m$ is compact, we obtain the existence of a nondecreasing function $\Gamma_{i+1}:\mathfrak{R}_+\to\mathfrak{R}_+$ with $\Gamma_i(s)\le\Gamma_{i+1}(s)$ for all $s\ge 0$ such that (3.18) holds with $i\ge 0$ replaced by $i+1$.

Since $T\in C^0(\mathfrak{R}^n;\mathfrak{R}_+)$ is continuous, there exists a constant Ω and a function $\kappa\in K_\infty$ such that $T(x)\le\Omega+\kappa(|x|)$ for all $x\in\mathfrak{R}^n$. Since $j\ge 0$ is the smallest integer so that $jT_H\ge r+T_s+T(x_0(0))$, it follows that $iT_H\ge\tau+jT_H$ for $i=\psi(\|x_0\|)=1+\left[\frac{r+\tau+T_H+T_s+\Omega+\kappa(\|x_0\|)}{T_H}\right]$. Combining (3.6) with (3.18) and using a standard causality argument, we obtain the following estimate for all $t\ge 0$:

$$\|x_t\|+\left\|\breve{u}_t\right\|\le\gamma_2\sup_{0\le s\le t}(|\xi(s)|)+\exp(-\sigma t)\left(\|x_0\|+\left\|\breve{u}_0\right\|+\sup_{0\le s\le t}(|\xi(s)|)\right)\tilde{C}\left(\|x_0\|+\sup_{0\le s\le t}(|\xi(s)|)\right) \tag{3.21}$$

where $\tilde{C}(s)=G\Gamma_{\psi(s)}(s)\exp(\sigma T_H\psi(s))$ for all $s\ge 0$. Since $\tilde{C}:\mathfrak{R}_+\to\mathfrak{R}_+$ is a nondecreasing function, there exists a C^1 nondecreasing function $\hat{C}:\mathfrak{R}_+\to\mathfrak{R}_+$ such that $\hat{C}(s)\ge\tilde{C}(s)$ for all $s\ge 0$. Inequality (2.11) is a direct consequence of (3.21) and the definition $C(s):=s\hat{C}(s)$ for all $s\ge 0$. The proof is complete. ◁

Appendix: Proof of Lemma 3.3

Let $\sigma > 0$, $T_H > 0$ be sufficiently small constants so that Lemma 3.1 holds. Let $N \geq N^*$ be an integer, where N^* is the integer constant in Lemma 3.2. Let a partition of $\Re_+$ $\{\tau_i\}_{i=0}^{\infty}$ with $\sup_{i\geq 0}(\tau_{i+1}-\tau_i) \leq T_s$, $\xi \in B(\Re_+; \Re^k)$ and consider a solution of (1.1), (1.2), (2.8), (2.9), (2.10) defined for all $t \geq 0$ and satisfying $x(t) \in S_1$ for $t \geq T$ for some $T \geq 0$. Since $\{\tau_i\}_{i=0}^{\infty}$ is a partition of $\Re_+$, there exists an integer $l \geq 0$ such that $\tau_l \geq r + T$. It follows that $x(t) \in S_1$ for $t \geq \tau_l - r$.

Definition (3.1) and inequality (3.2) in conjunction with (2.9) imply that $z(\tau_i) \in S_2$ for all integers $i \geq 0$. Therefore, Lemma 2.1 in conjunction with (2.8) implies that $z(t) \in S_2$ for all $t \in [\tau_i, \tau_{i+1})$. Define:

$$L_X := \sup\{|f(x,u)-f(z,u)|/|x-z| : x, z \in S_2,\ x \neq z,\ u \in U\} \tag{A.1}$$

Equations (1.1), (2.8), the fact that $x(t+\tau) \in S_1$ for all $t \geq \tau_i$ with $i \geq l$, in conjunction with definition (A.1) imply that the following inequality holds for all $t \in [\tau_i, \tau_{i+1})$ and for all integers $i \geq l$:

$$|z(t)-x(t+\tau)| \leq |z(\tau_i)-x(\tau_i+\tau)| + L_X \int_{\tau_i}^{t} |z(s)-x(s+\tau)|ds \tag{A.2}$$

A direct application of the Gronwall–Bellman inequality to (A.2) gives the following inequality for all $t \in [\tau_i, \tau_{i+1})$ and for all integers $i \geq l$:

$$|z(t)-x(t+\tau)| \leq \exp(L_X T_s)|z(\tau_i)-x(\tau_i+\tau)| \tag{A.3}$$

Let $\tilde{x}(t)$ denote the solution of (1.1) with initial condition $\tilde{x}(\tau_i - r) = Q(x(\tau_i - r) + \xi(\tau_i))$ corresponding to the same input u. Lemma 3.2 implies the existence of a constant $M_4 > 0$ such that:

$$|z(\tau_i)-\tilde{x}(\tau_i+\tau)| \leq M_4\left(|Q(x(\tau_i-r)+\xi(\tau_i))| + \left\|\widetilde{u}_{\tau_i}\right\|\right)/N \tag{A.4}$$

By virtue of the fact that $x(t) \in S_1$ for all $t \geq \tau_i - r$ with $i \geq l$, in conjunction with definition (A.1), Eq. (1.1), inequality (2.5) and Lemma 2.1 (which implies that $\tilde{x}(t) \in S_2$ for all $t \geq \tau_i - r$ with $i \geq l$), we obtain the following inequality for all $t \geq \tau_i - r$ with $i \geq l$:

$$|\tilde{x}(t)-x(t)| \leq |\xi(\tau_i)| + L_X \int_{\tau_i - r}^{t} |\tilde{x}(s)-x(s)|ds \tag{A.5}$$

A direct application of the Gronwall–Bellman inequality to (A.2) gives the following inequality for all integers $i \geq l$:

$$|\tilde{x}(\tau_i+\tau)-x(\tau_i+\tau)| \leq \exp(L_X(r+\tau))|\xi(\tau_i)| \tag{A.6}$$

Using (A.4), (A.6), (2.5) and the triangle inequality, we obtain the following inequality for all integers $i \geq l$:

$$\begin{aligned} |z(\tau_i)-x(\tau_i+\tau)|N &\leq M_4\left(|Q(x(\tau_i-r)+\xi(\tau_i))| + \left\| \breve{u}_{\tau_i} \right\| \right) + N \exp(L_X(r+\tau))|\xi(\tau_i)| \\ &\leq M_4\left(|x(\tau_i-r)| + \left\| \breve{u}_{\tau_i} \right\| \right) + (N \exp(L_X(r+\tau)) + M_4)|\xi(\tau_i)| \end{aligned} \tag{A.7}$$

Using (A.3), (A.7) we get for $t \in [\tau_i, \tau_{i+1})$ and for all integers $i \geq l$:

$$\begin{aligned} N|z(t)-x(t+\tau)| \leq\ & \exp(L_X T_s) M_4\left(|x(\tau_i-r)| + \left\| \breve{u}_{\tau_i} \right\| \right) \\ &+ \exp(L_X T_s)(N \exp(L_X(r+\tau)) + M_4)|\xi(\tau_i)| \end{aligned} \tag{A.8}$$

Define:

$$K := \sup\{|k(x)-k(z)|/|x-z| : x, z \in S_2\,,\ x \neq z\} \tag{A.9}$$

Definition (A.9) combined with (A.8), the fact that $\sup_{i\geq 0}(\tau_{i+1}-\tau_i) \leq T_s$ and the fact $x(t+\tau) \in S_1$ for all $t \geq \tau_i$ with $i \geq l$, directly implies the following estimate for all $t \in [\tau_i, \tau_{i+1})$ and for all integers $i \geq l$:

$$\begin{aligned} &|k(z(t))-k(x(t+\tau))| \exp(\sigma t) N \leq K \exp(L_X T_s)(N \exp(L_X(r+\tau)) + M_4) \\ &\quad \exp(\sigma t) \sup_{\tau_l \leq s \leq t} (|\xi(s)|) + K M_4 \exp(L_X T_s)\ \exp(\sigma\,(T_s+r+\tau)) \\ &\quad \sup_{\tau_l - r - \tau \leq s \leq t} (|x(s+\tau)| \exp(\sigma s)) + K M_4 \exp(L_X T_s) \\ &\quad \exp(\sigma\,(T_s+r+\tau)) \sup_{\tau_i - r - \tau \leq s < t} (|u(s)| \exp(\sigma s)) \end{aligned} \tag{A.10}$$

Since the above inequality is independent of the integer $i \geq l$, it follows that inequality (A.10) holds for $t \geq \tau_l$. Define for all $t \geq 0$:

$$q(t) = [t/T_H] T_H \tag{A.11}$$

Combining (A.10) with definition (A.10) and definition (2.10), we obtain the following estimate for all $t \geq jT_H$, where j is any integer with $jT_H \geq \tau_l$:

$$\begin{aligned} &\sup_{jT_H \leq s \leq t} (|u(s)-k(x(q(s)+\tau))| \exp(\sigma s)) N \\ &\leq K M_4 \exp(L_X T_s)\ \exp(\sigma\,(T_H+T_s+r+\tau)) \sup_{\tau_l - r - \tau \leq s \leq t} (|x(s+\tau)| \exp(\sigma s)) \\ &\quad + K M_4 \exp(L_X T_s)\ \exp(\sigma\,(T_H+T_s+r+\tau)) \sup_{\tau_i - r - \tau \leq s < t} (|u(s)| \exp(\sigma s)) \\ &\quad + K\ \exp(L_X T_s)(N\ \exp(L_X(r+\tau)) + M_4) \exp(\sigma t) \sup_{\tau_l \leq s \leq t} (|\xi(s)|) \end{aligned} \tag{A.12}$$

Using (A.11), (A.12), the triangle inequality, (A.9) and the fact $x(t+\tau)\in S_1$ for all $t\geq\tau_i$, we obtain for $t\geq jT_H$, where j is any integer with $jT_H\geq\tau_l$:

$$\begin{aligned}
&\sup_{jT_H\leq s\leq t}(|u(s)-k(x(q(s)+\tau))|\exp(\sigma s))N\\
&\leq KM_4\exp(L_XT_s)\exp(\sigma(T_H+T_s+r+\tau))\sup_{\tau_i-r-\tau\leq s<jT_H}(|u(s)|\exp(\sigma s))\\
&+KM_4\exp(L_XT_s)\exp(\sigma(T_H+T_s+r+\tau))\sup_{jT_H\leq s<t}(|u(s)-k(x(q(s)+\tau))|\exp(\sigma s))\\
&+KM_4\exp(L_XT_s)\exp(\sigma(T_H+T_s+r+\tau))(1+K\exp(\sigma T_H))\sup_{\tau_l-r-\tau\leq s\leq t}(|x(s+\tau)|\exp(\sigma s))\\
&+K\exp(L_XT_s)(N\exp(L_X(r+\tau))+M_4)\exp(\sigma t)\sup_{\tau_l\leq s\leq t}(|\xi(s)|)
\end{aligned}$$

Selecting $N>K\exp(L_XT_s)M_4\exp(\sigma(T_H+T_s+r+\tau))$, we obtain from the above estimate for all $t\geq jT_H$, where j is any integer with $jT_H\geq\tau_l$:

$$\begin{aligned}
(N-\tilde{K})\sup_{jT_H\leq s\leq t}(|u(s)-k(x(q(s)+\tau))|\exp(\sigma s))&\leq\tilde{K}\sup_{\tau_i-r-\tau\leq s<jT_H}(|u(s)|\exp(\sigma s))\\
&+\tilde{K}(1+K\exp(\sigma T_H))\sup_{\tau_l-r-\tau\leq s\leq t}(|x(s+\tau)|\exp(\sigma s))\\
&+K\exp(L_XT_s)(N\exp(L_X(r+\tau))+M_4)\exp(\sigma t)\sup_{\tau_l\leq s\leq t}(|\xi(s)|)
\end{aligned}\tag{A.13}$$

where $\tilde{K}:=K\exp(L_XT_s)M_4\exp(\sigma(T_H+T_s+r+\tau))$. Using (A.13) and (3.3), we get the above estimate for all $t\geq jT_H$, where j is any integer with $jT_H\geq\tau_l$:

$$\begin{aligned}
(N-\tilde{K})\sup_{jT_H\leq s\leq t}(|x(s+\tau)|\exp(\sigma s))&\leq M_2(N-\tilde{K})\exp(\sigma jT_H)|x(jT_H+\tau)|\\
&+M_3\tilde{K}\sup_{\tau_i-r-\tau\leq s<jT_H}(|u(s)|\exp(\sigma s))+M_3\tilde{K}(1+K\exp(\sigma T_H))\sup_{\tau_l-r-\tau\leq s\leq t}(|x(s+\tau)|\exp(\sigma s))\\
&+M_3K\exp(L_XT_s)(N\exp(L_X(r+\tau))+M_4)\exp(\sigma t)\sup_{\tau_l\leq s\leq t}(|\xi(s)|)
\end{aligned}\tag{A.14}$$

Using (A.13) and selecting $N>\tilde{K}+\tilde{K}M_3(1+K\exp(\sigma T_H))$, we get the above estimate for all $t\geq jT_H$, where j is any integer with $jT_H\geq\tau_l$:

$$\begin{aligned}
(N-\tilde{K}-\tilde{K}M_3(1+K\exp(\sigma T_H)))\sup_{jT_H\leq s\leq t}(|x(s+\tau)|\exp(\sigma s))&\leq M_3\tilde{K}\sup_{-\tau\leq s<jT_H}(|u(s)|\exp(\sigma s))\\
M_2(N-\tilde{K})+\tilde{K}M_3(1+K\exp(\sigma T_H))\sup_{-\tau\leq s\leq jT_H}(|x(s+\tau)|\exp(\sigma s))&\\
+M_3K\exp(L_XT_s)(N\exp(L_X(r+\tau))+M_4)\exp(\sigma t)\sup_{r\leq s\leq t}(|\xi(s)|)&
\end{aligned}\tag{A.15}$$

Inequality (A.15) implies the existence of $\Lambda_1\geq 1$ (constant independent of j) for which the following inequality holds for $t\geq 0$ and for all integers j with $jT_H\geq\tau_l$:

$$\sup_{-r-\tau\le s\le t}(|x(s+\tau)|\exp(\sigma s))\le\Lambda_1\sup_{-r-\tau\le s\le jT_H}(|x(s+\tau)|\exp(\sigma s))+\Lambda_1\sup_{-r-\tau\le s<jT_H}(|u(s)|\exp(\sigma s))+\Lambda_1\exp(\sigma t)\sup_{0\le s\le t}(|\xi(s)|) \tag{A.16}$$

The definition of the norms $\|x_t\|$ and $\left\|\widetilde{u}_t\right\|$ give for all $t\ge 0$:

$$\sup_{0\le s\le t}(\|x_s\|\exp(\sigma s))\le\exp(\sigma(r+\tau))\sup_{-r-\tau\le s\le t}(|x(\tau+s)|\exp(\sigma s)) \tag{A.17}$$

$$\sup_{0\le s\le t}\left(\left\|\widetilde{u}_s\right\|\exp(\sigma s)\right)\le\exp(\sigma(r+\tau))\sup_{-r-\tau\le s\le t}(|u(s)|\exp(\sigma s)) \tag{A.18}$$

When $t\le jT_H$ we have from (A.18) that $\sup_{0\le s\le t}\left(\left\|\widetilde{u}_s\right\|\exp(\sigma s)\right)\le\exp(\sigma(r+\tau))\sup_{-r-\tau\le s\le jT_H}(|u(s)|\exp(\sigma s))$. When $t\ge jT_H$, we obtain from (A.9), (A.11), (A.13), (A.16), the facts that $k(0)=0$, $0\le s-q(s)\le T_H$, $x(t)\in S_1$ for all $t\ge jT_H$, the existence of a constant $\Lambda_2\ge 1$ (independent of j) for which the following inequalities hold for $t\ge jT_H$:

$$\sup_{0\le s\le t}\left(\left\|\widetilde{u}_s\right\|\exp(\sigma s)\right)\le\Lambda_2\exp(\sigma t)\sup_{0\le s\le t}(|\xi(s)|)+\Lambda_2\sup_{-r-\tau\le s\le jT_H}(|u(s)|\exp(\sigma s))+\Lambda_2\sup_{-r-\tau\le s\le jT_H}(|x(\tau+s)|\exp(\sigma s))$$

Combining the two cases ($t\le jT_H$ and $t\ge jT_H$) and using (A.17), (A.18), we obtain the existence of a constant $\Lambda_3\ge 1$ (independent of j) for which the following inequality holds for all $t\ge 0$ and for all integers j with $jT_H\ge\tau_l$:

$$\sup_{0\le s\le t}\left(\left\|\widetilde{u}_s\right\|\exp(\sigma s)\right)+\sup_{0\le s\le t}(\|x_s\|\exp(\sigma s))\le\Lambda_3\sup_{-r-\tau\le s\le jT_H}(|u(s)|\exp(\sigma s))+\Lambda_3\exp(\sigma t)\sup_{0\le s\le t}(|\xi(s)|)+\Lambda_3\sup_{-r-\tau\le s\le jT_H}(|x(\tau+s)|\exp(\sigma s)) \tag{A.19}$$

We notice that since $\sup_{i\ge 0}(\tau_{i+1}-\tau_i)\le T_s$, the smallest the integer $l\ge 0$ with $\tau_l\ge r+T$ also satisfies $\tau_l\le r+T+T_s$. Therefore, we conclude that inequality (A.19) holds for all $t\ge 0$ and for all integers j with $jT_H\ge r+T+T_s$. Inequality (3.6) is a direct consequence of estimate (A.19). The proof is complete. ◁

References

1. Ahmed-Ali, T., Karafyllis, I., Lamnabhi-Lagarrigue, F.: Global exponential sampled-data observers for nonlinear systems with delayed measurements. Syst. Control Lett. **62**(7), 539–549 (2013)
2. Ahmed-Ali, T., Karafyllis, I., Krstic, M., Lamnabhi-Lagarrigue, F.: Robust stabilization of nonlinear globally Lipschitz delay systems. In: Malisoff, M., Mazenc, F., Pepe, P., Karafyllis, I. (eds.) to appear in the edited book entitled Recent Results on Nonlinear Time Delayed Systems in the series Advances in Delays and Dynamics (ADD@S). Springer
3. Bekiaris-Liberis, N., Krstic, M.: Compensation of state-dependent input delay for nonlinear systems. IEEE TAC **58**, 275–289 (2013)
4. Bekiaris-Liberis, N., Krstic, M.: Nonlinear Control Under Nonconstant Delays, SIAM (2013)
5. Bekiaris-Liberis, N., Krstic, M.: Robustness of nonlinear predictor feedback laws to time- and state-dependent delay perturbations. Automatica **49**(6), 1576–1590 (2013)
6. Castillo-Toledo, B., Di Gennaro, S., Sandoval Castro, G.: Stability analysis for a class of sampled nonlinear systems with time-delay. In: Proceedings of the 49th CDC, GA, USA, pp. 1575–1580 (2010)
7. Fridman, E., Seuret, A., Richard, J.-P.: Robust sampled-data stabilization of linear systems: an input delay approach. Automatica **40**(8), 1441–1446 (2004)
8. Gao, H., Chen, T., Lam, J.: A new system approach to network-based control. Automatica **44** (1), 39–52 (2008)
9. Heemels, M., Teel, A.R., van de Wouw, N., Nešić, D.: Networked control systems with communication constraints: tradeoffs between transmission intervals, delays and performance. IEEE TAC **55**(8), 1781–1796 (2010)
10. Karafyllis, I., Kravaris, C.: Global exponential observers for two classes of nonlinear systems. Syst. Control Lett. **61**(7), 797–806 (2012)
11. Karafyllis, I., Krstic, M.: Nonlinear stabilization under sampled and delayed measurements, and with inputs subject to delay and zero-order hold. IEEE TAC **57**(5), 1141–1154 (2012)
12. Karafyllis, I., Krstic, M.: Stabilization of nonlinear delay systems using approximate predictors and high-gain observers. Automatica **49**(12), 3623–3631 (2013)
13. Karafyllis, I., Krstic, M., Ahmed-Ali, T., Lamnabhi-Lagarrigue, F.: Global stabilization of nonlinear delay systems with a compact absorbing set. Int. J. Control **87**(5), 1010–1027 (2014)
14. Karafyllis, I., Krstic, M.: Numerical schemes for nonlinear predictor feedback. Math. Control Signals Syst. **26**(4), 519–546 (2014)
15. Karafyllis, I., Malisoff, M., de Queiroz, M., Krstic, M., Yang, R.: Predictor-based tracking for neuromuscular electrical stimulation. Int. J. Robust Nonlinear Control **25**(14), 2391–2419 (2015)
16. Karafyllis, I., Krstic, M.: Sampled-data stabilization of nonlinear delay systems with a compact absorbing set. SIAM J. Control Optim. **54**(2), 790–818 (2016)
17. Khalil, H.K.: Nonlinear Systems, 2nd edn. Prentice-Hall (1996)
18. Krstic, M.: Delay Compensation for Nonlinear, Adaptive, and PDE Systems. Birkhäuser (2009)
19. Krstic, M.: Input delay compensation for forward complete and strict-feedforward nonlinear systems. IEEE TAC **55**(2), 287–303 (2010)
20. Lozano, R., Castillo, P., Garcia, P., Dzul, A.: Robust prediction-based control for unstable delay systems: application to the yaw control of a mini-helicopter. Automatica **40**(4), 603–612 (2004)
21. Nešić, D., Teel, A.: A framework for stabilization of nonlinear sampled-data systems based on their approximate discrete-time models. IEEE TAC **49**(7), 1103–1122 (2004)
22. Nešić, D., Teel, A.R., Carnevale, D.: Explicit computation of the sampling period in emulation of controllers for nonlinear sampled-data systems. IEEE TAC **54**(3), 619–624 (2009)

23. Polyakov, A., Efimov, D., Perruquetti, W., Richard, J.-P.: Output stabilization of time-varying input delay systems using interval observation technique. Automatica **49**(11), 3402–3410 (2013)
24. Sontag, E.D.: Smooth stabilization implies coprime factorization. IEEE TAC **34**, 435–443 (1989)
25. Sontag, E.D., Wang, Y.: New characterizations of input to state stability. IEEE TAC **41**, 1283–1294 (1996)
26. Sontag, E.D.: Input to state stability. In: Levine, W.S. (ed.) The Control Systems Handbook: Control System Advanced Methods, 2nd edn, pp. 1034–1054. CRC Press, Boca Raton (2011)

Parametric Transfer Matrices for Sampled-Data Control Systems with Linear Continuous Periodic Process and Control Delay

Bernhard P. Lampe and Efim N. Rosenwasser

Abstract For the class of multi-input multi-output systems being composed of a linear continuous periodic (LCP) process, pure delay, and a digital controller, the paper provides closed expressions for the parametric transfer matrix (PTM), even for the difficult, but practically important case, when the external excitations act on continuous system parts. In the same way as ordinary transfer matrices in the linear time-invariant (LTI) case, the PTM for LCP systems is a fundamental concept for analysis and design of those systems. The properties of the constructed parametric transfer matrices as functions of the real parameter and the complex variable are investigated. These properties are similar to those from ordinary transfer matrices, so that the PTM after some modifications, can be applied with similar tools. Moreover, formulae are derived that are appropriate for the practical computation of the PTM. An example demonstrates, how the formulae can be handled.

1 Introduction

The classical approach for analysis and design of sampled-data (SD) systems containing continuous LTI processes consists of the transfer to a discrete (-time) model [1, 2, 6, 28]. This approach only provides exact solutions in the case, when all continuous input signals are sampled before acting on the continuous system parts. Then it is sufficient to consider the problems from the viewpoint of the computer, i.e., computer-oriented models are adequate [2]. However, in most practical situations, this condition does not hold, because, e.g., continuous disturbances directly act on the continuous plant. In those cases, a rigorous solution needs the application of process-oriented models of the system, which are more complicated, because the closed loop establishes itself as linear continuous periodic (LCP) nonstationary system.

B.P. Lampe (✉)
Institute of Automation, University of Rostock, Rostock, Germany
e-mail: bernhard.lampe@uni-rostock.de

E.N. Rosenwasser
Stae Marine Technical University, Saint Petersburg, Russia

T. Insperger et al. (eds.), *Time Delay Systems*,
Advances in Delays and Dynamics 7, DOI 10.1007/978-3-319-53426-8_2

Hence the traditional approach by ordinary (continuous or discrete) transfer functions or state-space descriptions with matrices of finite size cannot be used. The exact description is ordinarily in the focus, when the concept of sampled-data (SD) systems (in a stricter sense) is addressed. As in the LTI case, two principle approaches have been established for the description of SD systems—one works in time domain and uses state-space representations, the other one works in frequency domain and applies input–output representations. The lifting method [4, 27] in state space and two methods in frequency domain, namely the frequency response (FR) operator [5], and the parametric transfer matrix (PTM) [23, 24] are most common. The PTM completely bases on a frequency domain description, so transformation to state space is not required. This fact makes PTM interesting for the solution of design problems for SD systems with delay [10, 11].

In the monographs [21, 22], it was already shown that the PTM $W(\lambda, t)$ is useful for analysis and design of linear continuous periodic (LCP) systems. In contrast to the ordinary transfer matrix $W(\lambda)$ for continuous LTI systems, the PTM does not only depend on the complex frequency variable λ, but also on real parameter time t. In numerous works, see, e.g., [7, 9, 16–18, 20, 25], the PTM was used to solve various kinds of control problems mainly for single-input single-output (SISO) SD systems with arbitrary delay, including stability and stabilization, modal control, advanced statistical analysis, $\mathscr{H}_2$, $\mathscr{H}_\infty$ or $\mathscr{L}_2$ optimization, see [12–15]. In [24], the PTM method was generalized for multi-input multi-output (MIMO) SD systems.

In [11] the PTM is constructed for SD systems containing an LCP process and delay, under the assumption that the input signal acts to the sampler. The present paper constructs the PTM in the practically more important case, when the input signal acts directly to the LCP element. Moreover, the properties of the PTM as function of the complex variable λ are investigated. The results open possibilities to solve for this class of systems important kinds of control problems, e.g., stability and stabilization, modal control, advanced statistical analysis, $\mathscr{H}_2$, $\mathscr{H}_\infty$ or $\mathscr{L}_2$ optimization with the help of methods and tools, which are elaborated by the authors and co-workers [3, 19].

2 Mathematical Description of LCP Processes

Below, it is supposed that the LCP process is described by the state equation

$$\frac{\mathrm{d}v(t)}{\mathrm{d}t} = A(t)v(t) + B(t)r(t) \tag{1}$$

and the output equation

$$y(t) = C(t)v(t). \tag{2}$$

Here, $v(t), r(t), y(t)$ are vectors of dimensions $\chi \times 1$, $m \times 1$, $n \times 1$, respectively, and $A(t) = A(t+T)$, $B(t) = B(t+T)$, $C(t) = C(t+T)$ are real periodic matrices of

appropriate size. Furthermore, we suppose that these matrices are continuous and of bounded variation in $[0, T]$.
Assume the matrix equation

$$\frac{\mathrm{d}v(t)}{\mathrm{d}t} = A(t)v(t), \tag{3}$$

where $v(t)$ is a $\chi \times \chi$ matrix. Under the initial condition $v(0) = I_\chi$, where I_χ is the $\chi \times \chi$ identity matrix, we obtain the solution $H(t)$. As is known, [26], the matrix $H(t)$ allows a representation of the form

$$H(t) = L(t)\mathrm{e}^{Nt}, \tag{4}$$

where $L(t) = L(t + T)$ is a nonsingular continuously differentiable $\chi \times \chi$ matrix, and N is a constant $\chi \times \chi$ matrix. Hereby, without loss of generality, the matrices $L(t)$ and N can be assumed to be real.
With the help of the Lyapunov transformation

$$v(t) = L(t)v_L(t), \tag{5}$$

state equation (1) appears as

$$\frac{\mathrm{d}v_L(t)}{\mathrm{d}t} = Nv_L(t) + L^{-1}(t)B(t)r(t), \tag{6}$$

and the output equation as

$$y(t) = C(t)L(t)v_L(t). \tag{7}$$

Indeed, differentiating (5) yields

$$\frac{\mathrm{d}v(t)}{\mathrm{d}t} = \frac{\mathrm{d}L(t)}{\mathrm{d}t}v_L(t) + L(t)\frac{\mathrm{d}v_L(t)}{\mathrm{d}t}. \tag{8}$$

Moreover, from (4) we find

$$L(t) = H(t)\mathrm{e}^{-Nt}, \tag{9}$$

and after differentiation

$$\begin{aligned}\frac{\mathrm{d}L(t)}{\mathrm{d}t} &= \frac{\mathrm{d}H(t)}{\mathrm{d}t}\mathrm{e}^{-Nt} - H(t)\mathrm{e}^{-Nt}N = A(t)H(t)\mathrm{e}^{-Nt} - L(t)N \\ &= A(t)L(t) - L(t)N.\end{aligned} \tag{10}$$

Inserting (10) into (8), we achieve

$$\frac{\mathrm{d}v(t)}{\mathrm{d}t} = A(t)L(t)v_L(t) - L(t)Nv_L(t) + L(t)\frac{\mathrm{d}v_L(t)}{\mathrm{d}t} \tag{11}$$

Formula (1) with the help of (5) can be written in the form

$$\frac{\mathrm{d}v(t)}{\mathrm{d}t} = A(t)L(t)v_L(t) + B(t)u(t) \tag{12}$$

Comparing (11) and (12), we achieve

$$L(t)Nv_L(t) + L(t)\frac{\mathrm{d}v_L(t)}{\mathrm{d}t} = B(t)u(t). \tag{13}$$

Since the matrix $L(t)$ for all t is nonsingular, so from (13) we directly derive (6). Moreover, inserting (5) into (2) yields (7).

Further on, the totality of equations (6), (7) is called the $\mathscr{L}$-equivalent LCP process.

The matrix

$$M = \mathrm{e}^{NT} \tag{14}$$

commonly is named the monodromy matrix of state equation (1), and the roots of equation

$$\det(I_\chi - \zeta M) = 0 \tag{15}$$

are its inverse multipliers.

3 PTM of Open SD System with LCP Process and Delay

In this section, we consider the open SD system with delay, as presented in Fig. 1.

In Fig. 1, DC stands for the digital controller, containing the analogue to digital converter (ADC), the control program (CP), and the digital to analogue converter (DAC), respectively described by the equations

$$\begin{aligned} \xi_k &= x(kT), \quad (k = 0, \pm 1, \ldots) \\ \alpha(\zeta)\psi_k &= \beta(\zeta)\xi_k, \\ u(t) &= h(t - kT)\psi_k, \quad kT + 0 \le t \le (k+1)T - 0. \end{aligned} \tag{16}$$

Here $x(t), \psi_k, u(t)$ are $n \times 1$, $q \times 1$, $m \times 1$ vectors, and ζ is the shift operator for one step backward, [2]. Further, $\alpha(\zeta), \beta(\zeta)$ are polynomial matrices of size $q \times q$ and

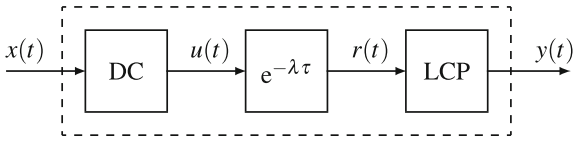

Fig. 1 Open SD system with LCP process and delay

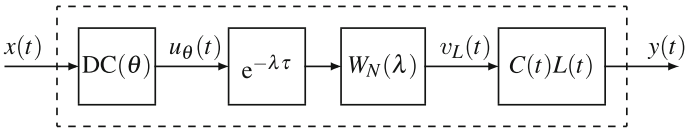

Fig. 2 Open SD system after Lyapunov transformation

$q \times n$, respectively, satisfying the causality condition $\det \alpha(0) \neq 0$. Moreover, $h(t)$ is an $m \times q$ matrix, where its elements are of bounded variation at the interval $0 < t < T$. Finally, in Fig. 1 τ is a real constant, for which we use the two decompositions

$$\tau = \mu T + \theta = (\mu + 1)T - \gamma, \tag{17}$$

where μ is a nonnegative integer, and $0 \leq \theta < T$, $0 < \gamma \leq T$.

Below, we will always suppose that the LCP process is given by its $\mathscr{L}$-equivalent model (6), (7). The open chain under investigation can be configured to the structure of Fig. 2, containing a dynamic time-invariant continuous element.
In Fig. 2 the block DC(θ) is the conventional digital controller, described by the equations

$$\begin{aligned} \xi_k &= x(kT), \quad (k = 0, \pm 1, ...), \\ \alpha(\zeta)\psi_k &= \beta(\zeta)\xi_k, \\ u_\theta(t) &= h_\theta(t - kT)\psi_k, \quad kT + 0 \leq t \leq (k+1)T - 0, \end{aligned} \tag{18}$$

where

$$h_\theta(t) = L^{-1}(t + \theta)B(t + \theta)h(t). \tag{19}$$

Moreover, in Fig. 2 $W_N(\lambda)$ is the rational matrix

$$W_N(\lambda) = (\lambda I_\chi - N)^{-1}. \tag{20}$$

As is seen from Fig. 2, a conventional DC and a continuous LTI block are acting between the input $x(t)$ and output $v_L(t)$. Therefore, formulae from [24] can be applied for the calculation of the PTM $W_{Lx}(\lambda, t)$ from the input $x(t)$ to the output $v_L(t)$ with the result

$$W_{Lx}(\lambda, t) = \mathrm{e}^{-\lambda t}\mathrm{e}^{-(\mu+1)\lambda T}\tilde{\mathscr{I}}_N(\lambda, t)\tilde{W}_d(\lambda). \tag{21}$$

Here

$$\begin{aligned} \tilde{\mathscr{I}}_N(\lambda, t) &\triangleq \int_0^T \tilde{D}_N(T, \lambda, t + \gamma - \nu)h_\theta(\nu)\,\mathrm{d}\nu, \\ \tilde{W}_d(\lambda) &= \alpha^{-1}(\zeta)\beta)\zeta)\Big|_{\zeta = \mathrm{e}^{-\lambda T}}, \end{aligned} \tag{22}$$

where

$$\tilde{D}_N(T,\lambda,t) = \frac{1}{T}\sum_{k=-\infty}^{\infty} W_N(\lambda + k\mathrm{j}\omega)\mathrm{e}^{(\lambda+k\mathrm{j}\omega)t}, \tag{23}$$

which is determined for $-\infty < t < \infty$ by the formulae [24]

$$\begin{aligned}\tilde{D}_N(T,\lambda,t) &= \tilde{\mathscr{D}}_N(T,\lambda,t) = \mathrm{e}^{Nt}(I_\chi - \mathrm{e}^{-\lambda T}M)^{-1}\\ &= (I_\chi - \mathrm{e}^{-\lambda T}M)^{-1}\mathrm{e}^{Nt}, \quad 0 < t < T,\\ \tilde{D}_N(T,\lambda,t+T) &= \tilde{D}_N(T,\lambda,t)\mathrm{e}^{\lambda T}.\end{aligned} \tag{24}$$

Using (24), (17) and (4), from (22), we obtain

$$\tilde{\mathscr{I}}_N(\lambda,t) = \mathrm{e}^{Nt}\tilde{F}(\lambda,t)\left[(I_\chi - e^{-\lambda T}M)^{-1}P(\theta) - R(t,\theta))\right], \tag{25}$$

where we denoted

$$\begin{aligned}\tilde{F}(\lambda,t) &= \begin{cases} M, & 0 < t < \theta,\\ \mathrm{e}^{\lambda T}I_\chi, & \theta < t < T,\end{cases}\\ P(\theta) &= \int_0^T H^{-1}(\nu+\theta)B(\nu+\theta)h(\nu)\,\mathrm{d}\nu,\\ R(t,\theta) &= \begin{cases} \int_{t+\gamma}^{T} H^{-1}(\nu+\theta)B(\nu+\theta)h(\nu)\,\mathrm{d}\nu, & 0 < t < \theta,\\ \int_{t-\theta}^{T} H^{-1}(\nu+\theta)B(\nu+\theta)h(\nu)\,\mathrm{d}\nu, & \theta < t < T.\end{cases}\end{aligned} \tag{26}$$

Formula (25) is extended onto the whole axis $-\infty < t < \infty$ with the help of the relation

$$\tilde{\mathscr{I}}_N(\lambda,t+T) = \tilde{\mathscr{I}}_N(\lambda,t)\mathrm{e}^{\lambda T}. \tag{27}$$

Regarding (21)–(27), it can be shown that the PTM $W_{Lx}(\lambda,t)$ is continuous with respect to t for all t.

Now, from Fig. 2, we easily derive an expression for the PTM $W_{yx}(\lambda,t)$ from the input $x(t)$ to the output $y(t)$

$$\begin{aligned}W_{yx}(\lambda,t) &= C(t)L(t)W_{Lx}(\lambda,t)\\ &= \mathrm{e}^{-\lambda t}\mathrm{e}^{-(\mu+1)\lambda T}C(t)L(t).\tilde{\mathscr{I}}_N(\lambda,t)\tilde{W}_d(\lambda).\end{aligned} \tag{28}$$

Under the taken propositions, the PTM $W_{yx}(\lambda,t)$ is continuous with respect to t.

4 PTM of Closed SD System with LCP Process and Delay

Consider the closed SD system $\mathscr{S}_\tau$, shown in Fig. 3 described by the equations

$$\begin{aligned}
\frac{\mathrm{d}v(t)}{\mathrm{d}t} &= A(t)v(t) + B_1(t)g(t) + B(t)u(t-\tau),\\
y(t) &= C(t)v(t),\\
\xi_k &= y(kT), \quad (k = 0, \pm 1, \ldots),\\
\alpha(\zeta)\psi_k &= \beta(\zeta)\xi_k,\\
u(t) &= h(t-kT)\psi_k, \quad kT + 0 \le t \le (k+1)T - 0,
\end{aligned} \tag{29}$$

where all propositions of the last section should still hold, and in addition $B_1(t) = B_1(t+T)$ is a $\chi \times \ell$ matrix, where its elements are continuous functions of bounded variation inside the period. When we apply in (29) Lyapunov transformation (5), then we achieve the equivalent system of equations, which is the starting point of the further investigations

$$\begin{aligned}
\frac{\mathrm{d}v_L(t)}{\mathrm{d}t} &= Nv_L(t) + L^{-1}(t)B_1(t)g(t) + u_\theta(t-\tau),\\
y(t) &= C(t)L(t)v_L(t),\\
\xi_k &= C(0)v_L(kT), \quad (k = 0, \pm 1, \ldots),\\
\alpha(\zeta)\psi_k &= \beta(\zeta)\xi_k,\\
u_\theta(t) &= h_\theta(t-kT)\psi_k, \quad kT + 0 \le t \le (k+1)T - 0,
\end{aligned} \tag{30}$$

where we used that $L(0) = I_\chi$.

Observing the structure of the open system in Fig. 2, the closed system $\mathscr{S}_\tau$ can be configured to the structure shown in Fig. 4.

According to the general approach, [23, 24], for the determination of the PTM for the system $\mathscr{S}_\tau$, we assume

$$g(t) = \mathrm{e}^{\lambda t} I_\ell \tag{31}$$

and find the solution of equation (30), where

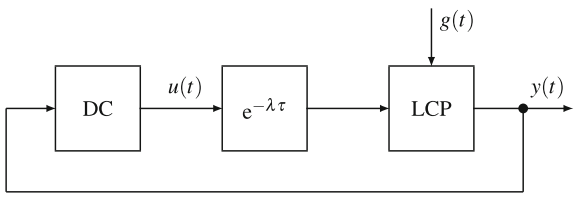

Fig. 3 Closed SD system $\mathscr{S}_\tau$

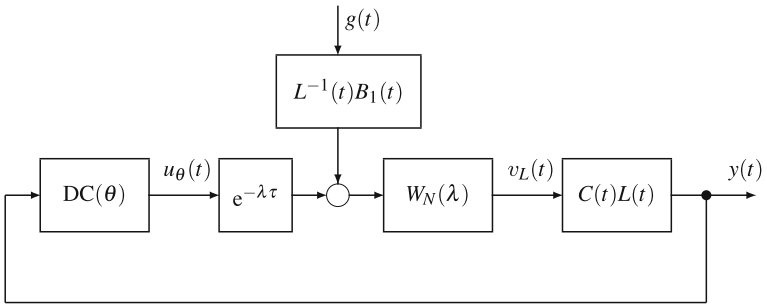

Fig. 4 Closed SD system $\mathscr{S}_\tau$ after Lyapunov transformation

$$\begin{aligned} v_L(\lambda,t) &= \mathrm{e}^{\lambda t} W_{Lg}(\lambda,t), \qquad & W_{Lg}(\lambda,t) &= W_{Lg}(\lambda,t+T), \\ y(\lambda,t) &= \mathrm{e}^{\lambda t} W_{yg}(\lambda,t), \qquad & W_{yg}(\lambda,t) &= W_{yg}(\lambda,t+T), \end{aligned} \tag{32}$$

where $W_{Lg}(\lambda,t)$ and $W_{yg}(\lambda,t)$ are the PTM from the input $g(t)$ to the outputs $v_L(t)$ and $y(t)$, respectively.

Theorem 1 *If (17) is valid, then the PTM $W_{Lg}(\lambda,t)$ and $W_{yg}(\lambda,t)$ are determined by the formulae*

$$\begin{aligned} W_{Lg}(\lambda,t) &= \mathrm{e}^{-\lambda t}\mathrm{e}^{-(\mu+1)\lambda T}\tilde{\mathscr{I}}_N(\lambda,t)\tilde{R}(\lambda)C(0)g_1(\lambda,0) + g_1(\lambda,t), \\ W_{yg}(\lambda,t) &= C(t)L(t)W_{Lg}(\lambda,t), \end{aligned} \tag{33}$$

where, in addition to the above notations

$$\begin{aligned} \tilde{R}(\lambda) &= \tilde{W}_d(\lambda)\left[I_n - \mathrm{e}^{-(\mu+1)\lambda T}C(0)\tilde{\mathscr{I}}_N(\lambda,0)\tilde{W}_d(\lambda)\right]^{-1}, \\ g_1(\lambda,t) &= \mathrm{e}^{-\lambda t}\int_0^T \tilde{D}_N(T,\lambda,t-\nu)L^{-1}(\nu)B_1(\nu)\mathrm{e}^{\lambda\nu}\,\mathrm{d}\nu. \end{aligned} \tag{34}$$

Proof Assume in system $\mathscr{S}_\tau$ the regime (31), (32). Then the closed system in Fig. 4, respecting the stroboscopic property of the digital controller [23], can be configured to the open system in Fig. 5.

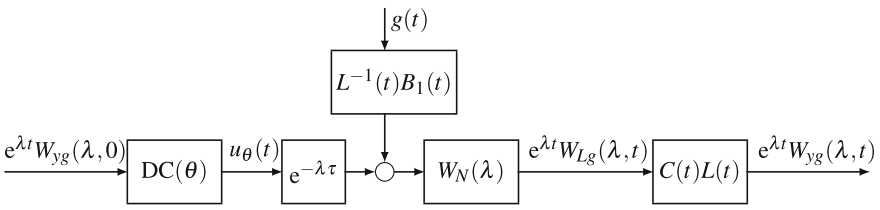

Fig. 5 Open loop equivalent of Fig. 4

Applying the formulae of Sect. 2, after reduction by $e^{\lambda t}$, we find

$$C(t)L(t)W_{Lx}(\lambda,t)W_{yg}(\lambda,0)+C(t)L(t)g_1(\lambda,t)=W_{yg}(\lambda,t), \tag{35}$$

where $g_1(\lambda,t)$ is the matrix in (34). Since the left and right side of the last equation are continuous according to t, so for $t=0$, we obtain

$$\begin{aligned} W_{yg}(\lambda,0) &= \left[I_n - C(0)W_{Lx}(\lambda,0)\right]^{-1} C(0)g_1(\lambda,0) \\ &= \left[I_n - e^{-(m+1)\lambda T}C(0)\tilde{\mathscr{F}}_N(\lambda,0)\tilde{W}_d(\lambda)\right]^{-1} C(0)g_1(\lambda,0). \end{aligned} \tag{36}$$

Substituting this expression on the left side of (35), we achieve the second formula in (33). The first formula in (33) directly follows from (36) and Fig. 5. □

5 PTM of System $\mathscr{S}_\tau$ as Function of the Argument λ

As was stated before, the PTM $W_{Lg}(\lambda,t)$ and $W_{yg}(\lambda,t)$ depend continuously on t for all λ, excluding a certain set of singular points. In this section we will show that these singular points are poles, and therefore, for all t the matrices $W_{Lg}(\lambda,t)$, $W_{yg}(\lambda,t)$, $W_{vg}(\lambda,t)$ are meromorphic functions of the argument λ.

Denote

$$\begin{aligned} \tilde{a}(\lambda) &= I_\chi - e^{-\lambda T}M, \\ \tilde{b}(\lambda) &= M\left[e^{-\lambda T}MA_3(\theta)+A_1(\theta)\right], \end{aligned} \tag{37}$$

where the matrices $A_1(\theta)$ and $A_3(\theta)$ are defined by the relations

$$\begin{aligned} A_1(\theta) &= \int_0^\gamma H^{-1}(\nu+\theta)B(\nu+\theta)h(\nu)\,d\nu, \\ A_3(\theta) &= \int_\gamma^T H^{-1}(\nu+\theta)B(\nu+\theta)h(\nu)\,d\nu. \end{aligned} \tag{38}$$

Further assume

$$\tilde{\alpha}(\lambda)=\alpha(\zeta)|_{\zeta=e^{-\lambda T}}, \quad \tilde{\beta}(\lambda)=\beta(\zeta)\big|_{\zeta=e^{-\lambda T}}. \tag{39}$$

Then, by using (37)–(39), we can construct the block matrix

$$\tilde{Q}_T(\lambda,\tilde{\alpha},\tilde{\beta})=\begin{bmatrix} I_\chi - e^{-\lambda T}M & 0_{\chi n} & -e^{-(\mu+1)\lambda T}\tilde{b}(\lambda) \\ -C(0) & I_n & 0_{nq} \\ 0_{q\chi} & -\tilde{\beta}(\lambda) & \tilde{\alpha}(\lambda) \end{bmatrix}, \tag{40}$$

where 0_{ik} stands for the $i\times k$ zero matrix.

Theorem 2 *The PTM $W_{vg}(\lambda,t)$ and $W_{yg}(\lambda,t)$ for all t are meromorphic functions of the argument λ, and they permit representations of the form*

$$W_{vg}(\lambda,t)=\frac{P_L(\lambda,t)}{\det\tilde{Q}_T(\lambda,\tilde{\alpha},\tilde{\beta})},$$
$$W_{yg}(\lambda,t)=\frac{P_y(\lambda,t)}{\det\tilde{Q}_T(\lambda,\tilde{\alpha},\tilde{\beta})}, \tag{41}$$

where the matrices $P_L(\lambda,t)$ and $P_y(\lambda,t)$ for all t are integral functions of the argument λ.

Proof Enhancing the first equation in (29) to matrix input, under (31), we obtain with the notation $v(\lambda,kT)=v_k(\lambda)$

$$v(\lambda,t)=H(t)M^{-k}v_k(\lambda)+\int_{kT}^{t}H(t)H^{-1}(\nu)B_1(\nu)\mathrm{e}^{\lambda\nu}\,\mathrm{d}\nu$$
$$+\int_{kT}^{t}H(t)H^{-1}(\nu)B(\nu)h(\nu-\tau)\,\mathrm{d}\nu. \tag{42}$$

When (17) is fulfilled, we find, as in [2]

$$u(t-\tau)=\begin{cases}h(t-kT+\gamma)\psi_{k-\mu-1}(\lambda), & kT<t<kT+\theta,\\ h(t-kT-\theta)\psi_{k-\mu}(\lambda), & kT+\theta<t<(k+1)T.\end{cases} \tag{43}$$

With the help of this equation, taking in (42) $t=(k+1)T$, we obtain a discrete model of the vector state for input (31), which after substituting k by $k-1$, takes the form

$$v_k(\lambda)=Mv_{k-1}(\lambda)+M^2A_3(\theta)\psi_{k-\mu-2}(\lambda)+MA_1(\theta)\psi_{k-\mu-1}+\mathrm{e}^{(k-1)\lambda T}G(\lambda), \tag{44}$$

where the $\chi\times\ell$ matrix

$$G(\lambda)=M\int_0^T H^{-1}(\nu)B_1(\nu)\mathrm{e}^{\lambda\nu}\,\mathrm{d}\nu \tag{45}$$

is an integral function of the argument λ. Combining (44) with the discrete model for the output $y(t)$ and the equations of the digital control program, we obtain a discrete model of the closed system $\mathscr{S}_\tau$ for the input (31)

$$\begin{aligned}&v_k(\lambda)=Mv_{k-1}(\lambda)+M^2A_3(\theta)\psi_{k-\mu-2}(\lambda)+MA_1(\theta)\psi_{k-\mu-1}(\lambda)+\mathrm{e}^{(k-1)\lambda T}G(\lambda),\\ &\xi_k(\lambda)=C(0)v_k(\lambda),\\ &\alpha_0\psi_k(\lambda)+\cdots+\alpha_\rho\psi_{k-\rho}(\lambda)=\beta_0\xi_k(\lambda)+\cdots+\beta_\rho\xi_{k-\rho}(\lambda),\end{aligned} \tag{46}$$

where $L(kT) = I_{\chi}$ has been used. In analogy to Theorem 7.4 in [24], it can be shown that matrix (42) takes the form

$$v(\lambda, t) = \mathrm{e}^{\lambda t} W_{vg}(\lambda, t), \quad W_{vg}(\lambda, t) = W_{vg}(\lambda, t + T) \tag{47}$$

if and only if the sequences $v_k(\lambda)$ and $\psi_k(\lambda)$ are chosen as solution of system of linear matrix equations (46), satisfying the conditions

$$\begin{aligned} &v_k(\lambda) = \mathrm{e}^{\lambda T} v_{k-1}(\lambda), \quad \psi_k(\lambda) = \mathrm{e}^{\lambda T} \psi_{k-1}(\lambda), \\ &\xi_k(\lambda) = \mathrm{e}^{\lambda T} \xi_{k-1}(\lambda). \end{aligned} \tag{48}$$

Due to these conditions, from (46), we find the linear system of matrix equations according to the matrices $v_0(\lambda)$, $\psi_0(\lambda)$, $\xi_0(\lambda)$

$$\begin{aligned} &(I_{\chi} - \mathrm{e}^{-\lambda T} M) v_0(\lambda) - \mathrm{e}^{-(\mu+1)\lambda T} \tilde{b}(\lambda) \psi_0(\lambda) = \mathrm{e}^{-\lambda T} G(\lambda), \\ &\xi_0(\lambda) = C(0) v_0(\lambda), \\ &\tilde{\alpha}(\lambda) \psi_0(\lambda) = \tilde{\beta}(\lambda) \xi_0(\lambda). \end{aligned} \tag{49}$$

Introduce the block matrices

$$Z(\lambda) = \begin{bmatrix} v_0(\lambda) \\ \xi_0(\lambda) \\ \psi_0(\lambda) \end{bmatrix}, \qquad \bar{G}(\lambda) = \begin{bmatrix} G(\lambda) \\ 0_{n\ell} \\ 0_{q\ell} \end{bmatrix}. \tag{50}$$

Then Eq. (48) can be written in the form

$$\tilde{Q}_T(\lambda, \tilde{\alpha}, \tilde{\beta}) Z(\lambda) = \mathrm{e}^{-\lambda T} \bar{G}(\lambda), \tag{51}$$

from which we directly find

$$Z(\lambda) = \tilde{Q}^{-1}(\lambda, \tilde{\alpha}, \tilde{\beta}) \bar{G}(\lambda) \mathrm{e}^{-\lambda T}. \tag{52}$$

Since $\bar{G}(\lambda)$ is an integral function of the argument λ, from (52) we obtain the expressions

$$v_0(\lambda) = \frac{M_v(\lambda)}{\det \tilde{Q}_T(\lambda, \tilde{\alpha}, \tilde{\beta})}, \quad \xi_0(\lambda) = \frac{M_{\xi}(\lambda)}{\det \tilde{Q}_T(\lambda, \tilde{\alpha}, \tilde{\beta})}, \quad \psi_0(\lambda) = \frac{M_{\psi}(\lambda)}{\det \tilde{Q}_T(\lambda, \tilde{\alpha}, \tilde{\beta})}, \tag{53}$$

in which the numerators are integral functions (matrices) of the argument λ. Further on, like in the proof of Theorem 7.4 in [24], it can be shown that the expression

$$W_{vg}(\lambda, t) = \mathrm{e}^{-\lambda t} v_0(\lambda, t), \tag{54}$$

where the matrix $v_0(\lambda, t)$ is determined by formulae (42), (43), (52) yields the PTM $W_{vg}(\lambda, t)$ in form (41). Analogously, the representation of the PTM $W_{yg}(\lambda, t)$ takes the form

$$W_{vg}(\lambda, t) = \mathrm{e}^{-\lambda t} C(t) L(t) v_0(\lambda, t), \tag{55}$$

so the proof is complete. □

Remark 1 A direct solution of equations (49) yields the relations

$$\begin{aligned} v_0(\lambda) &= \left[I_\chi - \mathrm{e}^{-\lambda T} M - \mathrm{e}^{-(\mu+1)\lambda T} \tilde{b}(\lambda) \tilde{W}_d(\lambda) C(0)\right]^{-1} G(\lambda) e^{-\lambda T}, \\ \xi_0(\lambda) &= C(0) v_0(\lambda), \\ \psi_0(\lambda) &= \tilde{W}_d(\lambda) \xi_0(\lambda), \end{aligned} \tag{56}$$

which can be used for the practical construction of the PTM for the system $\mathscr{S}_\tau$.

6 Numerical Example

Construct the PTM $W_{yg}(\lambda, t)$ for the system $\mathscr{S}_\tau$ with the LCP process of first order

$$\begin{aligned} \frac{\mathrm{d}v(t)}{\mathrm{d}t} &= (a - \frac{\sin t}{2 - \cos t}) v(t) + g(t) + u(t - \pi), \\ y(t) &= v(t), \\ \xi_k &= y(kT), \quad (k = 0, \pm 1, \ldots), \\ \alpha(\zeta)\psi_k &= \beta(\zeta)\xi_k, \\ u(t) &= \psi_k, \quad kT < t < (k+1)T, \end{aligned} \tag{57}$$

where $a \neq 0$ is a real constant. In the actual case, we have

$$\begin{aligned} A(t) &= a - \frac{\sin t}{2 - \cos t}, \quad B(t) = B_1(t) = C(t) = 1, \\ h(t) &= 1. \end{aligned} \tag{58}$$

Moreover,

$$T = 2\pi, \quad \theta = \gamma = \pi, \quad \mu = 0, \tag{59}$$

and $\alpha(\zeta), \beta(\zeta)$ are the polynomials of the digital controller. For analysis, the controller is assumed to be given, in case of controller design, these polynomials will be determined later, using expressions with them as parameters.
It is easy to verify that in the actual case

$$H(t) = \frac{\mathrm{e}^{at}}{2 - \cos t}, \quad L(t) = \frac{1}{2 - \cos t}, \quad N = a, \quad M = \mathrm{e}^{2\pi a}, \tag{60}$$

and, hence

$$H^{-1}(t) = \mathrm{e}^{-at}(2 - \cos t), \quad L^{-1}(t) = 2 - \cos t\,. \tag{61}$$

Therefore, formulae (38) and (45) yield

$$\begin{aligned} A_1(\theta) &= \mathrm{e}^{-\pi a}\int_0^{\pi} \mathrm{e}^{-a\nu}(2 + \cos\nu)\,\mathrm{d}\nu, \\ A_3(\theta) &= \mathrm{e}^{-\pi a}\int_{\pi}^{2\pi} \mathrm{e}^{-a\nu}(2 + \cos\nu)\,\mathrm{d}\nu, \\ G(\lambda) &= \mathrm{e}^{2\pi a}\int_0^{2\pi} \mathrm{e}^{-a\nu}(2 - \cos\nu)\mathrm{e}^{\lambda\nu}\,\mathrm{d}\nu \end{aligned} \tag{62}$$

and from (37), we find

$$\begin{aligned} I_{\chi} - \mathrm{e}^{-2\pi\lambda}M &= 1 - \mathrm{e}^{-2\pi\lambda}\mathrm{e}^{2\pi a}, \\ \tilde{b}(\lambda) &= \mathrm{e}^{2\pi a}\left[\mathrm{e}^{-2\pi\lambda}\mathrm{e}^{2\pi a}\tilde{A}_3(\theta) + A_1(\theta)\right]. \end{aligned} \tag{63}$$

With the help of (57)–(62), from (55) we obtain

$$v_0(\lambda) = \frac{\mathrm{e}^{-2\pi\lambda}\tilde{\alpha}(\lambda)G(\lambda)}{\det\tilde{Q}_T(\lambda,\tilde{\alpha},\tilde{\beta})}, \qquad \psi_0(\lambda) = \frac{\mathrm{e}^{-2\pi\lambda}\tilde{\beta}(\lambda)G(\lambda)}{\det\tilde{Q}_T(\tilde{\alpha},\tilde{\beta})}, \tag{64}$$

where

$$\det\tilde{Q}_T(\lambda,\tilde{\alpha},\tilde{\beta}) = (1 - \mathrm{e}^{-2\pi\lambda}\mathrm{e}^{2\pi a})\tilde{\alpha}(\lambda) - \mathrm{e}^{-2\pi\lambda}\tilde{b}(\lambda)\tilde{\beta}(\lambda). \tag{65}$$

Using (42), (43) and (63), we find from the equations of the LCP process, that for $0 \le t \le T$, the representation of $W_{yg}(\lambda,t)$ in form (41) apppears as

$$W_{yg}(\lambda,t) = \frac{\mathrm{e}^{(a-\lambda)t}\mathrm{e}^{-2\pi\lambda}}{(2-\cos t)\det\tilde{Q}_T(\lambda,\tilde{\alpha},\tilde{\beta})}G(\lambda)\tilde{H}_{yg}(\lambda,t) + \frac{\mathrm{e}^{(a-\lambda)t}}{2-\cos t}\int_0^t (2-\cos\nu)\mathrm{e}^{(\lambda-a)\nu}\,\mathrm{d}\nu \tag{66}$$

where

$$\tilde{H}_{yg}(\lambda,t) = \begin{cases} \tilde{\alpha}(\lambda) + \tilde{\beta}(\lambda)\mathrm{e}^{-2\pi\lambda}\displaystyle\int_0^t \mathrm{e}^{-a\nu}(2-\cos\nu)\,\mathrm{d}\nu, & 0 \le t \le \pi, \\ \tilde{\alpha}(\lambda) + \tilde{\beta}(\lambda)\left[\mathrm{e}^{-2\pi\lambda}\displaystyle\int_0^{\pi} \mathrm{e}^{-a\nu}(2-\cos\nu)\,\mathrm{d}\nu\right. & \\ \qquad\left. + \displaystyle\int_{\pi}^t \mathrm{e}^{-a\nu}(2-\cos\nu)\,\mathrm{d}\nu\right] & \pi \le t \le 2\pi. \end{cases} \tag{67}$$

7 Conclusions

The contribution provides closed expressions for the parametric transfer matrices (PTM) of sampled-data (SD) systems containing a periodic continuous process and delay, where the external excitation acts on the input to the process. It is shown that the PTM $W_{yx}(\lambda, t)$ for all t is a meromorphic function of the complex variable λ, the poles of it are among the set of eigenvalues of certain matrices, depending on λ, but not depending on the parameter t. An example is given. The achieved results open possibilities to solve, in analogy to that of previous works of the authors, various control problems, including stability and stabilzation, advanced statistical analysis, $\mathscr{H}_2$, $\mathscr{L}_2$ and $\mathscr{H}_\infty$ optimization for systems of the considered class. The development of computational tools for analysis and design of digital filters and controllers interacting with RLCP processes, will be a main task in future work.

References

1. Ackermann, J.: Sampled-Data Control Systems: Analysis and Synthesis, Robust System Design. Springer, Berlin (1985)
2. Åström, K.J., Wittenmark, B.: Computer Controlled Systems: Theory and Design, 3rd edn. Prentice-Hall, Englewood Cliffs, NJ (1997)
3. Cepeda Gomez, R., Lampe, B.P.: Towards a newer toolbox for computer aided, polynomial design of sampled-data systems. Simul. Notes Europe **25**, 79–84 (2015)
4. Chen, T., Francis, B.A.: Optimal Sampled-Data Control Systems. Springer, Berlin (1995)
5. Hagiwara, T., Araki, M.: FR-operator approach to the $\mathscr{H}_2$-analysis and synthesis of sampled-data systems. IEEE Trans. Autom. Contr. AC **40**(8), 1411–1421 (1995)
6. Jury, E.I.: Sampled-Data Control Systems. Wiley, New York (1958)
7. Lampe, B.P., Rosenwasser, E.N.: Statistical analysis and $\mathscr{H}_2$-norm of finite dimensional linear time-periodic systems. In: Proceedings. IFAC Workshop on Periodic Control Systems, Como, Italy, pp. 9–14 (2001)
8. Lampe, B.P., Rosenwasser, E.N.: Causal polynomial stabilization for forward models of linear discrete-time systems. PAMM: Proc. Appl. Math. Mech. **5**(1), 173–174 (2005)
9. Lampe, B.P., Rosenwasser, E.N.: Digital stabilization of linear continuous-time periodic processes with pure delay. In: Proceedings of PSYCO, Saint Petersburg, Russia, pp. FrM1–2, 1–6 (2007)
10. Lampe, B.P., Rosenwasser, E.N.: $\mathscr{H}_2$-optimization of time-delayed sampled-data systems on basis of the parametric transfer matrix method. Autom. Remote Control **71**(1), 49–69 (2010)
11. Lampe, B.P., Rosenwasser, E.N.: Transfer matrices and advanced statistical analysis of digital controlled continuous-time periodic processes with delay. Eur. J. Control **18**(4), 391–404 (2012)
12. Lampe, B.P., Rosenwasser, E.N.: Characteristic equation for MIMO linear continuous periodic systems with several delays. In: Proceedings of 5th PSYCO, Caen, F, pp. 160–165 (2013)
13. Lampe, B.P., Rosenwasser, E.N.: $\mathscr{H}_2$ optimization and fixed poles of sampled-data systems under colored noise. Eur. J. Control **19**(3), 222–234 (2013b)
14. Lampe, B.P., Rosenwasser, E.N.: $\mathscr{L}_2$-optimization and fixed poles of multivariable sampled-data systems with delay. Int. J. Control **88**(4), 815–831 (2015). Published online Dec 2014
15. Lampe, B.P., Rosenwasser, E.N., Kurowski, M.: Characteristic equation for linear periodic systems with distributed delay. In: Proceedings of 19th IFAC Triennial World Congress, Cape Town, ZA, pp. 6068–6073 (2014)

16. Polyakov, K.Y.: Polynomial design of sampled-data control systems. II. Robust optimization. Autom. Remote Control **59**(12), 1774–1785 (1998)
17. Polyakov, K.Y.: Polynomial design of optimal sampled-data tracking systems. II: Robust optimization. Autom. Remote Control **62**(3), 430–442 (2001)
18. Polyakov, K.Y., Rosenwasser, E.N., Lampe, B.P.: Associated $\mathscr{H}_\infty$-problem for sampled-data systems. In: Proceedings of 3rd IFAC Symposium on Robust Control Design, Pergamon, Prague, pp. 669–674 (2000)
19. Polyakov KY, Rosenwasser EN, Lampe BP (2006) `DirectSD` Polyakov, K.Y., Rosenwasser, E.N., Lampe, B.P.: 3.0 toolbox for MATLAB: further progress in polynomial design of sampled-data systems. In: Proceedings of IEEE International Symposium on Computer Aided Control Systems Design, Munich, Germany, pp. 1946–1951
20. Polyakov, K.Y., Rosenwasser, E.N., Lampe, B.P.: Optimal stochastic sampled-data control with preview. IEEE Trans. Autom. Control **AC-52**(8), 1532–1538 (2007)
21. Rosenwasser, E.N.: Periodically Nonstationary Control Systems. Nauka, Moscow (1973). (in Russian)
22. Rosenwasser, E.N.: Linear Theory of Digital Control in Continuous Time. Nauka, Moscow (1994). (in Russian)
23. Rosenwasser, E.N., Lampe, B.P.: Computer Controlled Systems—Analysis and Design with Process-orientated Models. Springer, London (2000)
24. Rosenwasser, E.N., Lampe, B.P.: Multivariable Computer-Controlled Systems—A Transfer Function Approach. Springer, London (2006)
25. Rybinskii, V.O., Rosenwasser, E.N., Lampe, B.P.: Advanced statistical analysis with guaranteed estimation of current performance for sampled-data systems with delay and generalized higher order hold. In: Proceedings of 9th IFAC Conference on Control Applications in Marine Systems, Osaka, pp. Fr.1A 1–6 (2013)
26. Yakubovich, V.A., Starzhinskii, V.M.: Linear Differential Equations with Periodic Coefficients, vol. 1. Wiley, New York (1975)
27. Yamamoto, Y.: A function space approach to sampled-data systems and tracking problems. IEEE Trans. Autom. Control **AC-39**(4), 703–713 (1994)
28. Zypkin, J.S.: Sampling Systems Theory. Pergamon Press, New York (1964)

An SL/QP Algorithm for Minimizing the Spectral Abscissa of Time Delay Systems

Vyacheslav Kungurtsev, Wim Michiels and Moritz Diehl

Abstract We consider a problem of eigenvalue optimization, in particular finding a local minimizer of the spectral abscissa—the value of a parameter that results in the smallest value of the largest real part of the spectrum of a system. This is an important problem for the stabilization of control systems, but it is difficult to solve because the underlying objective function is typically nonconvex, nonsmooth, and non-Lipschitz. We present an expanded sequential linear and quadratic programming algorithm that solves a series of linear or quadratic subproblems formed by linearizing, with respect to the parameters, a set of right-most eigenvalues at each point as well as historical information at nearby points. We present a comparison of the performance of this algorithm with the state of the art in the field.

Research Supported by the Czech Science Foundation Under Project No. 16-17398S.

V. Kungurtsev (✉)
Faculty of Electrical Engineering, Department of Computer Science,
Agent Technology Center, Czech Technical University in Prague, Prague, Czech Republic
e-mail: vyacheslav.kungurtsev@fel.cvut.cz

W. Michiels
Computer Science Department and Optimization in Engineering Center (OPTEC),
Kasteelpark Arenberg 10, 3001 KU Leuven, Leuven-Heverlee, Belgium
e-mail: wim.michiels@cs.kuleuven.be

M. Diehl
Department of Microsystems Engineering IMTEK, University of Freiburg,
Georges-Koehler-Allee 102, 79110 Freiburg, Germany
e-mail: moritz.diehl@imtek.uni-freiburg.de

T. Insperger et al. (eds.), *Time Delay Systems*,
Advances in Delays and Dynamics 7, DOI 10.1007/978-3-319-53426-8_3

1 Introduction

We are interested in optimizing the spectrum of continuous time systems. Recall that finding the spectrum of a time-delay system of the form,

$$v'(t) = \sum_{j=0}^{m} A_j(x)v(t - \tau_j).$$

presents a nonlinear eigenvalue problem. We will assume that $\tau_0 = 0$. To solve for the eigenvalues, we find the solutions $\lambda(x)$ of,

$$\det(\Lambda(\lambda; x)) = 0,$$

with,

$$\Lambda(\lambda; x) = \lambda I - A_0(x) - \sum_{j=1}^{m} A_j(x)e^{-\lambda\tau_j}.$$

The number of eigenvalues in this case is generally infinite, but within any right half-plane the number of eigenvalues is finite [17]. We let $F(x)$ be the infinitesimal generator corresponding to the solution operator of the delay system, and the spectrum as $\sigma(F(x))$.

As an illustrative special case, consider a simpler problem of optimizing the spectrum of a linear system controlled with static, undelayed output feedback, where the operator $F(x)$ reduces to the matrix,

$$F(x) = A + BXC,$$

where A is the open-loop matrix for the system, B the input matrix and C the output matrix, and X is formed by arranging the components of x into a matrix of the appropriate dimensions. This presents a linear eigenvalue problem, with a finite spectrum.

The problem of interest can be written in the form,

$$\min_{x\in\mathbb{R}^n} f(x) = \min_{x\in\mathbb{R}^n} \alpha(F(x)), \tag{1}$$

where the spectral abscissa α is defined to be,

$$\alpha(F(x)) = \max_{\lambda\in\sigma(F(x))} \mathfrak{Re}\lambda.$$

The spectral abscissa corresponds to the largest real part of the eigenvalues of $F(x)$.

The properties of the spectrum of a matrix subject to parameters is an involved topic, for an early work, see [1]. A more thorough analysis with respect to the spectral abscissa in particular was presented in [4]. For recent work see, for instance [5, 14]. An important fact that permits a lot of the subsequent analysis is that the spectrum

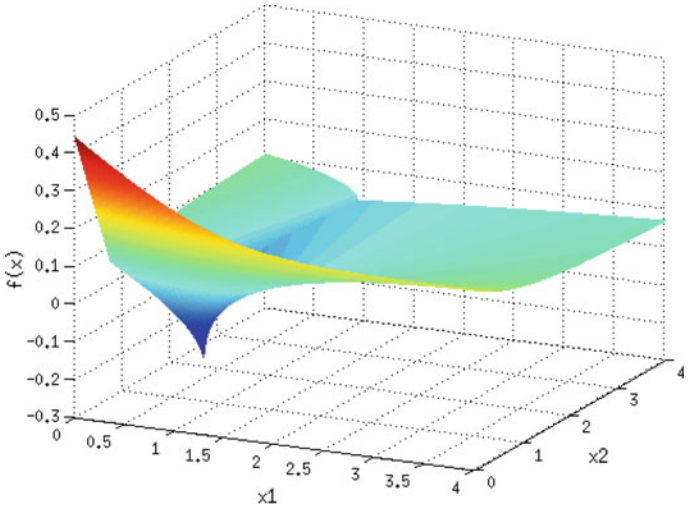

Fig. 1 $\alpha(F(x))$ for a two-dimensional eigenvalue optimization problem

$\{\lambda_0(x), \lambda_1(x), \ldots, \lambda_{N-1}(x)\}$ of a matrix $F(x)$ is a continuous function of x. Typically, local minimizers correspond to points x at which some of the eigenvalues coalesce, i.e., $\mathfrak{Re}(\lambda_0(x)) = \mathfrak{Re}(\lambda_1(x)) = \ldots$. In [22] it was shown, however, that although for symmetric $F(x)$, $f(x)$ is convex, in the nonsymmetric case $f(x)$ is not even Lipschitz. If for all x, all of the active eigenvalues (i.e., λ_i such that $\mathfrak{Re}(\lambda_0(x)) = \mathfrak{Re}(\lambda_i(x))$ were simple, then $f(x)$ would correspond to the maximum of a set of smooth surfaces. However, this is typically not the case. Thus, the optimization problem is difficult to solve because it is nonconvex, nonsmooth, and typically non-Lipschitz.

It can be observed, however, that the extensive variational analysis of the spectral abscissa has been performed for matrix eigenvalue optimization, rather than time delays. The main difference lies in the fact that in the generic case there are infinitely many eigenvalues. Thus, at this point, we can expect that optimizing the spectrum of a nonlinear eigenvalue problem should be *at least as difficult* as for matrices, and so all of the variational properties presenting challenges extend appropriately.

We present the plot of a two-dimensional problem in Fig. 1. In this example, first given in [23], $F(x) = A + BK$, with,

$$A = \begin{pmatrix} 0.1 & -0.03 & 0.2 \\ 0.2 & 0.05 & 0.01 \\ -0.06 & 0.2 & 0.07 \end{pmatrix}, \; B = \frac{1}{2}\begin{pmatrix} -1 \\ -2 \\ 1 \end{pmatrix}, \; K^T = \begin{pmatrix} x_1 \\ x_2 \\ 1.4 \end{pmatrix}$$

Notice that all of the features of $\alpha(F(x))$ we describe above, nonconvexity, nonsmoothness, and non-Lipchitz behavior are evident in the figure.

2 Algorithms for Eigenvalue Optimization

2.1 State of the Art

In sampling methods, a set of gradients is generated by sampling around the current point, which serves to approximate the Clarke subdifferential. At each iteration, a step in the convex hull of the sampled gradients is taken [2, 3]. The authors test the algorithm for non-delayed problems in eigenvalue optimization. In addition, variable metric methods, in particular of the Broyden-Fletcher-Goldfarb-Shanno (BFGS) form, have been shown to exhibit good convergence properties for nonsmooth problems, albeit without convergence theory [15]. A variant BFGS-gradient sampling hybrid, in which sampling is performed within the quasi-newton updates, has also been shown to globally converge [7] using a dual set of QPs to generate the step from a sample of gradients. It should be noted, however, that the proven convergence of gradient sampling relies on the objective function being locally Lipschitz, which is not the case for the spectral abscissa in particular.

In bundle methods, originally developed for convex nonsmooth optimization build gradient information by maintaining historically calculated subgradients during the course of the iterations, and at each point solve cutting-plane underapproximations of the function [11, 13]. In the case of non-convex problems, the formulation and analysis of bundle methods is more complicated, but various variations of bundle algorithms exist (see, e.g., [9], and a nice survey in the beginning of [8]).

In application to eigenvalue optimization, for non-delayed matrices, variations of the bundle method in [18, 19] consider a method wherein the ϵ Clarke-subdifferential is approximated by incorporating eigenvalues in the spectrum that are within ϵ of the abscissa and including their derivatives with respect to x in the subproblem. This includes thorough and interesting convergence theory, however, only symmetric matrices are considered.

In [24] gradient sampling is applied for optimizing the spectral abscissa of a time-delay system. The procedure was found to be robust in terms of generating a sequence of directions of decrease until a stationary point of the spectral abscissa function is found.

2.2 Sequential Linear and Quadratic Methods

2.2.1 Basic Algorithm

It is possible to formulate a sequential quadratic programming (SQP) method, as well as a more simplified Sequential Linear Programming (SLP) method for minimizing the spectral abscissa. First presented for symmetric matrices in [20, 21], this approach is based on the realization that the problem $\min_{x\in\mathbb{R}^n} \alpha(F(x))$ can be rewritten as,

$$\begin{aligned} &\min_{\gamma\in\mathbb{R},x\in\mathbb{R}^n}\ \gamma,\\ &\quad\text{subject to } \gamma \geq \mathfrak{Re}(\lambda_i(F(x))) \text{ for all } i. \end{aligned} \tag{2}$$

This is a standard formulation for max-min programming. However, if we are to consider this problem in its entirety, we would have a semi-infinite programming problem, because in general a time-delay system will have an infinite number of eigenvalues. However, in any right half plane, the number of eigenvalues is finite, and so since we are interested in minimizing the rightmost eigenvalue, it is natural to consider the problem, instead,

$$\begin{aligned} &\min_{\gamma\in\mathbb{R},x\in\mathbb{R}^n}\ \gamma,\\ &\quad\text{subject to } \gamma \geq \mathfrak{Re}(\lambda_i(F(x))) \text{ for all } i \text{ such that } \mathfrak{Re}\lambda_i(F(x)) > \lambda_c, \end{aligned}$$

where λ_c separated the plane that we restrict our attention to, and will depend on the number of eigenvalue surfaces we want/are able to incorporate and the location of these eigenvalues. We will order the spectrum as $\mathfrak{Re}(\lambda_0(F(x))) \geq \mathfrak{Re}(\lambda_1(F(x))) \geq \mathfrak{Re}(\lambda_2(F(x))) \geq \cdots \geq \mathfrak{Re}(\lambda_{N_c}(F(x)))$ where $N_c + 1$ is the number of eigenvalues that fall to the right of λ_c.

In the case that the eigenvalues of $F(x)$ are isolated and simple, the gradient and Hessian of $\lambda_i(F(x))$ with respect to x is well defined for all $\lambda_i(F(x)) \in \sigma(F(x))$. In this case, the objective function is the maximum of a set of smooth surfaces, and is thus piece-wise smooth. Solving the problem by successive approximation of each surface is standard, and the associated convergence theory in [20, 21] proves that the procedure outlined below converges to the solution.

Of course, in the general setting, eigenvalues need not be simple and isolated. The number of points at which the objective function $\alpha(F(x))$ in (1) is nonsmooth is of measure zero in the Lebesgue space $\mathbb{R}^n$. This implies that for a.e. x, the function $\alpha(F(x))$ is a locally smooth surface. This surface corresponds to the value of $\lambda_0(F(x))$ as a function of x. This implies that the algorithm (and computing linearizations) is well-defined at every point. However, as minimizers tend to be points of nonsmooth and non-Lipschitz behavior, such a scheme is no longer certifiably convergent. In practice, however, following some modifications, we will see that it still performs well.

For now, consider the simple case that all eigenvalues $\lambda_i(F(x))$ are simple and isolated. It can be shown that, in the case where each $A_i(x)$ depends smoothly on x and where the eigenvalue has multiplicity 1, the derivative of the surface corresponding to each eigenvalue as well as $\nabla^2_{xx}\lambda_i(F(x))$ can be calculated from the formulas [12, 16, 17].

$$\nabla_x \lambda_i = \frac{u_i^*\left(\frac{\partial A_0}{\partial x} + \sum_{j=1}^m \frac{\partial A_j}{\partial x} e^{-\lambda_i \tau_j}\right) v_i}{u_i^*\left(I + \sum_{j=1}^m \tau_j e^{-\lambda\tau_j} A_j\right) v_i},$$

where u_i and v_i are the left and right eigenvectors of $F(x)$ corresponding to eigenvalue i, u^* corresponds to the conjugate of u and the second-derivatives may be calculated explicitly by

$$\nabla^2_{xx}\lambda_i(x) = -\frac{u_i^*(\nabla^2_{x\lambda}\Lambda(\lambda_i,x)\otimes\nabla_x\lambda_i+\nabla^2_{xx}\Lambda(\lambda_i,x)+\nabla^2_{\lambda\lambda}\Lambda(\lambda_i,x)\otimes(\nabla_x\lambda_i)\otimes(\nabla_x\lambda_i))v_i}{u_i^*\nabla_\lambda\Lambda(\lambda_i,x)v_i} + \frac{u_i^*(2\nabla_x\Lambda(\lambda_i,x)+2\nabla_\lambda\Lambda(\lambda_i,x)\otimes\nabla_x\lambda_i)\nabla_x v_i}{u_i^*\nabla_\lambda\Lambda(\lambda_i,x)v_i},$$

where $\nabla_x v_i$ can be calculated (along with $\nabla_x\lambda_i$) by,

$$\begin{pmatrix}\Lambda(\lambda_i,x) & \nabla_\lambda\Lambda(\lambda_i,x)\\ 2v_i^* & 0\end{pmatrix}\begin{pmatrix}\nabla_x v_i\\ \nabla_x\lambda_i\end{pmatrix} = \begin{pmatrix}\nabla_x v_i\\ 0\end{pmatrix},$$

where the second set of equations comes from differentiating $v_i^* v_i = 1$.

The Lagrangian function for the problem (2) is defined as,

$$L(\gamma,x,y) = \gamma - \sum_{i=0}^{N_c} y_i(\gamma - \mathfrak{Re}\left(\lambda_i(F(x))\right)), \tag{3}$$

where y is the vector of Lagrange multipliers.

This naturally suggests the SQP method wherein a sequence of iterations $x_{k+1} = x_k + t\Delta x$ is calculated, with t a line-search scalar and Δx is determined by solving subproblems of the form,

$$\begin{aligned}&\min_{\Delta x,\Delta\gamma}\ \Delta\gamma + \tfrac{1}{2}\Delta x^T H_k \Delta x,\\ &\text{subject to } \Delta\gamma + \alpha(F(x_k)) \geq \mathfrak{Re}(\lambda_i(F(x_k))) + \mathfrak{Re}(\nabla_x\lambda_i(F(x_k)))^T\Delta x,\\ &\qquad\qquad\qquad\qquad\qquad\qquad\qquad\qquad \forall i\in\{0,\dots,N_c\},\end{aligned} \tag{4}$$

for Δx and $\Delta\gamma$, where H_k is a Lagrangian Hessian term at x_k.

The nonconvexity of the problem implies that at any local quadratic approximation of an eigenvalue surface, the Hessian could be indefinite or even negative definite. This implies that the approximating quadratic program (4) could be unbounded below. We constrain the problem with a trust-region to prevent this. Since we have linear constraints, making an l^2 norm constraint impractical, we use an infinity norm trust-region, which acts as a "box" limiting the magnitude of the maximal component of Δx.

$$\begin{aligned}&\min_{\Delta x,\Delta\gamma}\ \Delta\gamma + \tfrac{1}{2}\Delta x^T H_k \Delta x,\\ &\text{subject to } \Delta\gamma + \alpha(F(x_k)) \geq \mathfrak{Re}(\lambda_i(F(x_k))) + \mathfrak{Re}(\nabla_x\lambda_i(F(x_k)))^T\Delta x,\ \forall i,\\ &\qquad\qquad\qquad\qquad\qquad\qquad\qquad\qquad \forall i\in\{0,\dots,N_c\},\\ &\qquad ||\Delta x||_\infty \leq \Delta_k.\end{aligned} \tag{5}$$

Since the Hessian could be indefinite, the solution Δx could be a direction of ascent for the objective function. Hence, after computing Δx we first test if,

$$\alpha(F(x_k + \Delta x)) < \alpha(F(x_k)), \tag{6}$$

in which case we set $x_{k+1} = x_k + \Delta x$ and continue to the next iteration. Otherwise, we test for descent,

$$\mathfrak{Re}(\nabla_x \lambda_i(F(x_k)))^T \Delta x < 0, \tag{7}$$

and if this does not hold we set $\Delta_{k+1} = \gamma_1 \Delta_k$, where γ_1 is a constant satisfying $\gamma_1 \in (0, 1)$, and resolve the subproblem.

If (7) holds, we follow the mixed trust-region/line-search procedure presented by Gertz [10], in which a backtracking line search reduces the size of the step t until decrease is achieved ($\alpha(F(x_k + t\Delta x)) < \alpha(F(x_k))$), and the next trust-region radius corresponds to $t||\Delta x||$.

$$\Delta_{k+1} = \begin{cases} \gamma_2 \Delta_k & \text{if } \alpha(F((x_k + \Delta x)) < \alpha(F(x_k)) \\ t||\Delta x|| & \text{otherwise,} \end{cases} \tag{8}$$

where γ_2 is a constant satisfying $\gamma > 1$.

We update the trust-region simply by increasing it if we achieve descent, and decreasing it otherwise. For consistency with convergence theory [6], we would enforce sufficient decrease conditions with respect to predicted (from the quadratic approximation) and actual decrease. However, since lax criteria of acceptance (e.g., with a small constant multiplying the predicted-actual decrease ratio) of the step is practically equivalent to this condition, we proceed as in the line-search criteria for the gradient sampling method [3] to just enforce descent.

If we omit the second order term H_k, then the algorithm becomes a sequential linear programming (SLP) method. With the trust-region, the solution is always bounded.

2.2.2 Incorporating Historical Gradients

We found that in the nonsymmetric case, the basic SL/QP algorithm would frequently stall at nonoptimal points. Recall that the reliability of the algorithm depended on some strong assumptions on the problem. To give a generic geometric picture of the situation for which this occurs, consider a "valley," or $n - 1$ dimensional hypersurface in $\mathbb{R}^n$ at which $\nabla \lambda_i(F(x))$ is undefined. It can happen that across the $n - 1$ dimensional manifold of x on which this occurs, the derivatives of $\lambda_i(F(x))$ jump discontinuously.

Locally, the directional derivative of $\alpha(F(x))$ is steeper toward the valley than parallel along it, so a local approximation that regards only the eigenvalue surfaces at a point on one side of the valley will result in the step of steepest decrease being in this direction. Since the surface on the other side of the valley is not accounted for on the original side, this is not incorporated directly into the subproblem. We illustrate this scenario in Fig. 2.

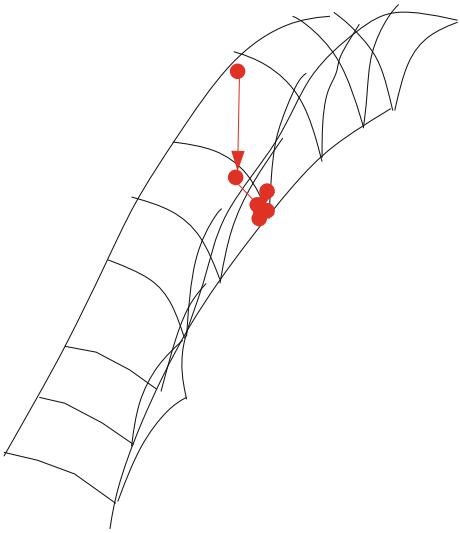

Fig. 2 Possible set of iterations of SQP without memory along a surface of $\alpha(F(x))$

To remedy this, we added "memory" to the SQP method with a set $\mathcal{M}$. Essentially this behaves as a bundle, whose elements (eigenvalue and derivative with respect to x) are included alongside the linearizations of the rightmost eigenvalues at the current point. When it occurs that $\alpha(F(x_k + \Delta x)) > \alpha(F(x_k))$, which we expect in the "jamming" scenario described above, the procedure stores the tuple $\{x_k + \Delta x_k, \mathfrak{Re}(\lambda_0(F(x_k + \Delta x_k))), \nabla_x \mathfrak{Re}(\lambda_0(F(x_k + \Delta x_k)))\}$ in $\mathcal{M}$. Then, if in a future iteration K, the current point x_K satisfies $||x_K - x^{(i)}||_\infty \leq \Delta_k$ for any $i \in \{1, \ldots, |\mathcal{M}|\}$, then we include this linearized surface in the QP subproblem. Thus at each iteration, subproblem (9) is solved to generate the trial point for the linar search.

$$\begin{aligned} &\min_{\Delta x, \Delta\gamma} \ \Delta\gamma + \tfrac{1}{2}\Delta x^T H_k \Delta x, \\ &\text{subject to } \Delta\gamma + \alpha(F(x_k)) \geq \mathfrak{Re}(\lambda_i(F(x_k))) + \mathfrak{Re}(\nabla_x \lambda_i(F(x_k)))^T \Delta x, \ \forall i \\ &\qquad \Delta\gamma + \alpha(F(x_k)) \geq \mathfrak{Re}(\lambda_{(i)}(F(x^{(i)}))) \\ &\qquad\qquad + \mathfrak{Re}(\nabla_x \lambda_{(i)}(F(x^{(i)})))^T (x_k + \Delta x - x^{(i)}), \ i \in M_k \\ &\qquad ||\Delta x||_\infty \leq \Delta_k, \end{aligned} \tag{9}$$

where $M_k \subset \mathcal{M}$ represents the points $x^{(i)}$ satisfying $||x^{(i)} - x_k|| \leq \Delta_k$.

We found in our experiments that this way of incorporating historical information proved to be the most effective. In genereal, on the smooth portions of the spectral abscissa function, the standard SLP/SQP produces iterates that quickly converge toward a region with a lower objective, then memory is needed to refine the solution to find a more precise local minimizer.

2.2.3 Algorithm Summary

We present a summary of the procedure, the SLP variation, in Algorithm 1. Note that we can select a subset of the eigenvalues N_k at each iteration k to evaluate and linearize. The stopping criterion corresponds to the step becoming small, without any new information (memory) being added at the current iteration.

Algorithm 1 SLP Algorithm for Eigenvalue Optimization

Define constants $0 < \gamma_1 < 1$, $\gamma_2 > 1$, $\delta_m > 0$, and $S \in \mathbb{N}$.
Determine N_0 or λ_c.
for S times **do**
  Randomly select starting point x_0.
  Set $\mathcal{M}_1 = \emptyset$. Set $k = 1$.
  Calculate initial $\{\lambda_i(F(x_0))\}$ and $\{\nabla_x \lambda_i(F(x_0))\}$ for $i \in \{0, \dots, N_0\}$.
  while $(||\Delta x|| > \delta_m$ or $\mathcal{M}_k \neq \mathcal{M}_{k-1})$ **do**
    Solve

$$
\begin{aligned}
&\min_{\Delta x, \Delta\gamma} \ \Delta\gamma, \\
&\text{subject to } \Delta\gamma + \alpha(F(x_k)) \geq \mathfrak{Re}(\lambda_i(F(x_k))) \\
&\qquad\qquad + \mathfrak{Re}(\nabla_x \lambda_i(F(x_k)))^T \Delta x, \ i \in \{0, \dots, N_k\} \\
&\qquad \Delta\gamma + \alpha(F(x_k)) \geq \mathfrak{Re}(\lambda_{(i)}(F(x^{(i)}))) \\
&\qquad\qquad + \mathfrak{Re}(\nabla_x \lambda_{(i)}(F(x^{(i)})))^T (x_k + \Delta x - x^{(i)}), \ i \in M_k \\
&\qquad ||\Delta x||_\infty \leq \Delta_k.
\end{aligned}
\tag{10}
$$

      for Δx_k.
    Calculate $\{\lambda_i(F(x_k + \Delta x_k))\}$ and $\{\nabla_x \lambda_i(F(x_k + \Delta x_k))\}$ for $i \in \{0, \dots, N_k\}$
    if $\alpha(F(x_k + \Delta x_k)) < \alpha(F(x_k))$ **then**
      Set $x_{k+1} \leftarrow x_k$
      Set $\Delta_{k+1} \leftarrow \gamma \Delta_k$.
    else
      Store $\{x_k + \Delta x_k, \mathfrak{Re}(\lambda_0(F(x_k + \Delta x_k))), \nabla_x \mathfrak{Re}(\lambda_0(F(x_k + \Delta x_k)))\}$
        in $\mathcal{M}_{k+1}$.
      Find t such that $\alpha(F(x_k + t\Delta x_k)) < \alpha(F(x_k))$.
      Set $x_{k+1} \leftarrow x_k + t\Delta x_k$.
      Set $\Delta_{k+1} \leftarrow t||\Delta x_k||$.
    end if
    Set $k \leftarrow k + 1$.
    Determine N_k. Typically, set $N_k = N$, the size of $F(x)$.
    Calculate all $\{\lambda_i(F(x_k))\}$ and $\{\nabla_x \lambda_i(F(x_k))\}$ for $i \in \{0, \dots, N_0\}$.
  end while
  Add the last point $(x_f, \alpha(F(x_f)))$ to $\mathcal{F}$.
end for
return $\{x_f, \alpha(F(x_f))\}$ corresponding to the lowest value of $\alpha(F(x_f))$ in $\mathcal{F}$.

Finally, we note that since this problem is nonconvex, there can be multiple local minima, possibly necessitating the use of global optimization strategies. In our experiments we have found this to be problem dependent, i.e., for some systems there are many local minima, but not others. Given that the objective function is not a closed form function, determinstic strategies for global optimization would be impossible to

implement. In our implementation, we use ten random starting points, initialized as a random normal variable centered at zero, and select the lowest minimizer out of the ten runs. In practice, for many problems, it is expected that the parameters should lie in some bounded region, permitting the use of more probabilistically sophisticated strategies [25]. In addition, in many applications, only a point at which the system is stable, e.g., the spectral abscissa is below zero, is needed rather than the absolute global minimizer, and so there would be some laxity in the treatment of the existence of multiple local minimizers.

3 Numerical Results

For all solvers, we used a stopping tolerance of 1e-4, indicating that the algorithms terminate when the (inf) norm of the previous step was smaller than 1e-4. The SL/QP algorithms were coded in MATLAB, with all tests run using MATLAB version 2013a and were performed on an Intel Core 2.2 GHz $\times 8$ running Ubuntu 14.04. For all algorithms we use the same procedure of using ten random starting points, specifically initializing a point by a normal distribution centered at zero, and then picking the best solution (the one with the lowest objective value) of ten runs.

We list the parameter and initial values we use in our implementations of SL/QP in Table 1 $0 < \gamma_1 < 1$, $\gamma_2 > 1$, $\Delta_m > 0$, $\delta_m > 0$, and $S \in \mathbb{N}$. We denote $k_{\max}$ the maximum number of iterations, $LSk_{\max}$ the maximum number of line-search steps, and η the backtracking contraction parameter.

We analyze the performance on two time-delay systems described in [24]. The first example is a third-order feedback controller system of the form,

$$v'(t) = Av(t) + B(x)v(t-5),$$

with A and $B(x)$ defined to be,

$$A = \begin{pmatrix} -0.08 & -0.03 & 0.2 \\ 0.2 & -0.04 & -0.005 \\ -0.06 & -0.2 & -0.07 \end{pmatrix}$$

Table 1 Control parameters and initial values required by algorithm 1

Parameter	Value	Parameter	Value	Parameter	Value
γ_1	`0.1`	S	`10`	$k_{\max}$	`20`
γ_2	`2.0`	N_0	N	$LSk_{\max}$	`20`
δ_m	`1.0e-r`	Δ_0	`1.0`	η	`0.5`

Table 2 Mean (standard deviation) for values and times for SLP and SQP (out of 500 sample runs). Value for each solver for each run is taken as the best of 10 random starting points. Time is the total clock time taken to perform the ten runs

	Value	Time
SLP	−0.081 (0.053)	4.6 (1.1)
SQP	−0.088 (0.055)	5.3 (1.6)

and

$$B(x) = \begin{pmatrix} -0.1 \\ -0.2 \\ 0.1 \end{pmatrix} \begin{pmatrix} x_1 & x_2 & x_3 \end{pmatrix}.$$

We present the sum of the results of the values and times in Table 2.

The best value was found to be −0.239, at $x = (-0.21, 0.074, 1.38)$ and −0.129 at $x = (-0.036, 0.67, 0.94)$ for SLP and SQP, respectively. For SLP, 16% of the initial random starting points corresponded to a stable (negative) value of the spectral abscissa, and 25% of the final iterations did, among all of the trials. For SQP these numbers were 10% and 23%, respectively.

The next example is given below,

$$\begin{aligned}
T_h \dot{x}_h(t) &= -x_h(t-\eta_h) + K_b x_a(t-\tau_b) + K_u x_{h,set}(t-\tau_u), \\
T_a \dot{x}_a(t) &= -x_a(t) + x_c(t-\tau_e) + K_a(x_h(t) - \tfrac{1+q}{2} x_a(t) - \tfrac{1-q}{2} x_c(t-\tau_e)), \\
T_d \dot{x}_d(t) &= -x_d(t) + K_d x_a(t-\tau_d), \\
T_c \dot{x}_c(t) &= -x_c(t-\eta_c) + K_c x_d(t-\tau_c), \\
\dot{x}_e(t) &= -x_c(t) + x_{c,set}(t),
\end{aligned}$$

with,

$$x_{h,set}(t) = \begin{pmatrix} K_1 & K_2 & K_3 & K_4 & K_5 \end{pmatrix} \begin{pmatrix} x_h(t) & x_a(t) & x_d(t) & x_c(t) & x_e(t) \end{pmatrix}^T.$$

The results comparing SLP and SQP, which are qualitatively similar as in the first example, are given in Table 3.

The best value was found to be −0.015, at $k = (2.2, -12, -7.5, -6.9, 0.35)$ and −0.016 at $k = (-0.77, -3.0, -3.6, -4.2, 1.4)$ for SLP and SQP, respectively. For SLP, 2% of the initial random starting points corresponded to a stable (negative) value of

Table 3 Mean (standard deviation) for values and times for BFGS with and without an additional gradient sampling phase, SLP, and SQP (out of 500 sample runs)

	Value	Time
SLP	−0.083 (0.0062)	83.5 (140)
SQP	−0.088 (0.0103)	75.5 (76)

the spectral abscissa, and 19% of the final iterations did, among all of the trials. For SQP these numbers were 5% and 11%, respectively.

It appears as though SQP and SLP perform similarly, both in terms of final objective value and time. In general it appears that, given enough random starting points, the algorithms are successful for a fair number of trials in obtaining a stable controller.

4 Conclusion

In this chapter we studied the eigenvalue optimization problem of minimizing the spectral abscissa for time delay systems. This problem is important for designing stabilizing controllers. We presented an algorithm that incorporated linear and quadratic models of eigenvalue surfaces corresponding to different eigenvalues in a sequential linear and sequential quadratic programming framework.

Our numerical results demonstrated the efficacy of the presented approach for minimizing the spectral abscissa of time-delay models, indicating that it appears to be competitive with the state of the art in terms of both finding a good local minimizer as well as in terms of computational speed. As such, the SL/QP algorithm is a promising approach for solving this class of problems.

Acknowledgements This research was supported by Research Council KUL: PFV/10/002 Optimization in Engineering Center OPTEC, GOA/10/09 MaNet, Belgian Federal Science Policy Office: IUAP P7 (DYSCO, Dynamical systems, control and optimization, 2012–2017); ERC ST HIGHWIND (259 166). V. Kungurtsev was also supported by the European social fund within the framework of realizing the project "Support of inter-sectoral mobility and quality enhancement of research teams at the Czech Technical University in Prague," CZ.1.07/2.3.00/30.0034 and the Czech Science Foundation under project No. 16-17398S.

References

1. Arnold, V.I.: On matrices depending on parameters. Russ. Math. Surv. **26**(2), 29–43 (1971)
2. Burke, J.V., Lewis, A.S., Overton, M.L.: Two numerical methods for optimizing matrix stability. Linear Algebra Appl. **351**, 117–145 (2002)
3. Burke, J.V., Lewis, A.S., Overton, M.L.: A robust gradient sampling algorithm for nonsmooth, nonconvex optimization. SIAM J. Optim. **15**(3), 751–779 (2005)
4. Burke, J.V., Overton, M.L.: Differential properties of the spectral abscissa and the spectral radius for analytic matrix-valued mappings. Nonlinear Anal. Theor. Methods Appl. **23**(4), 467–488 (1994)
5. Burke, J.V., Overton, M.L.: Variational analysis of non-lipschitz spectral functions. Math. Program. **90**(2), 317–351 (2001)
6. Conn, A.R., Gould, N.I., Toint, P.L.: Trust Region Methods, vol. 1. SIAM (2000)
7. Curtis, F.E., Que, X.: A Quasi-Newton Algorithm for Nonconvex, Nonsmooth Optimization with Global Convergence Guarantees. Technical report, Lehigh (2014)
8. Do, T.-M.-T., Artières, T.: Regularized bundle methods for convex and non-convex risks. J Mach. Learn. Res. **13**(1), 3539–3583 (2012)

9. Fuduli, A., Gaudioso, M., Giallombardo, G.: Minimizing nonconvex nonsmooth functions via cutting planes and proximity control. SIAM J. Optim. **14**(3), 743–756 (2004)
10. Gertz, E.M., et al.: Combination trust-region line-search methods for unconstrained optimization. Ph.D. thesis, University of California, San Diego (1999)
11. Kiwiel, K.: Methods of descent for nondifferentiable optimization. In: Lecture Notes in Mathematics, pp. 1133:1–360 (1985)
12. Lancaster, P.: On eigenvalues of matrices dependent on a parameter. Numerische Mathematik **6**(1), 377–387 (1964)
13. Lemaréchal, C.: Chapter vii nondifferentiable optimization. In: Handbooks in Operations Research and Management Science, vol. 1, pp. 529–572 (1989)
14. Lewis, A.S.: Nonsmooth optimization and robust control. Annu. Rev. Control **31**(2), 167–177 (2007)
15. Lewis, A.S., Overton, M.L.: Nonsmooth optimization via quasi-Newton methods. Math. Program. **141**(1–2), 135–163 (2013)
16. Magnus, J.R.: On differentiating eigenvalues and eigenvectors. Econ. Theor. **1**(2), 179–191 (1985)
17. Michiels, W., Niculescu, S.-I.: Stability and Stabilization of Time-Delay Systems: An Eigenvalue-Based Approach, vol. 12. SIAM (2007)
18. Noll, D., Apkarian, P.: Spectral bundle methods for non-convex maximum eigenvalue functions: first-order methods. Math. program. **104**(2–3), 701–727 (2005)
19. Oustry, F.: A second-order bundle method to minimize the maximum eigenvalue function. Math. Program. **89**(1), 1–33 (2000)
20. Overton, M.L.: On minimizing the maximum eigenvalue of a symmetric matrix. SIAM J. Matrix Anal. Appl. **9**(2), 256–268 (1988)
21. Overton, M.L.: Large-scale optimization of eigenvalues. SIAM J. Optim. **2**(1), 88–120 (1992)
22. Overton, M.L., Womersley, R.S.: On minimizing the special radius of a nonsymmetric matrix function: optimality conditions and duality theory. SIAM J. Matrix Anal. Appl. **9**(4), 473–498 (1988)
23. Vanbiervliet, J., Vandereycken, B., Michiels, W., Vandewalle, S., Diehl, M.: The smoothed spectral abscissa for robust stability optimization. SIAM J. Optim. **20**(1), 156–171 (2009)
24. Vanbiervliet, J., Verheyden, K., Michiels, W., Vandewalle, S.: A nonsmooth optimisation approach for the stabilisation of time-delay systems. ESAIM: Control Optim. Calc. Var. **14**(03), 478–493 (2008)
25. Zhigljavsky, A., Žilinskas, A.: Stochastic Global Optimization, vol. 9. Springer Science & Business Media (2007)

The Principle of "Borrowed Feedback" and Application to Control and Observation for Systems with Implicit State Dependent Delay

Erik I. Verriest

Abstract This chapter develops a general principle of "borrowed feedback" for linear systems with input delay, and in its dual form of observation with delayed measurements. This is of interest in problems where the external interaction with the system incurs a delay. We first focus on the simplest case of constant delay. This is then extended to the case where the delay may be varying. One application is the control of systems over a network. However, in this case the delay cannot be considered constant, but depends on a congestion state of the network. It is shown that if the causality constraint, which imposes an upper bound on the rate of change of the delay, does not hold the design method may fail to give consistent results.

1 Introduction

Recently, control strategies have been suggested for systems with delay in the control. We show that invariably these methods can be reduced to a notion of "borrowed state feedback," a kind of model reference control which is specific for systems with delay as for instance shown in [3, 5] among other. The dual problem involves observation from delayed information on outputs and perhaps inputs. One example of the latter that we analyzed before was the "soft landing" problem, first posed in [11]. The problem is one where the dynamics is linear and finite dimensional, but the observed quantity (either directly or indirectly) is a delay, which is itself dependent on the present and the delayed state.

A preliminary version of this paper was presented at the 12-th IFAC TDS workshop [10], where also the dual observation problem was explored. The paper is organized as follows: First we illustrate the problem for systems with a constant delay in the control in Sect. 2. In Sect. 3, we establish the stability of the system in closed loop when external inputs are present. Then we approach the dual problem of the observer

E.I. Verriest (✉)
School of Electrical and Computer Engineering, Georgia Institute of Technology, Atlanta, GA 30332-0250, USA
e-mail: erik.verriest@ece.gatech.edu

T. Insperger et al. (eds.), *Time Delay Systems*,
Advances in Delays and Dynamics 7, DOI 10.1007/978-3-319-53426-8_4

design for systems with delayed output in Sect. 4. Finally, Sect. 5 sketches problems that may exists if the delays are time varying, either with a known or predictable behavior, or when such delays depend on the system state.

2 The Control Problem

Let the dynamics be given by the finite dimensional

$$\dot{x} = Ax + Bu \tag{1}$$
$$y = Cx \tag{2}$$

where $x \in \mathbb{R}^n$ is the state and u and y are, respectively, a vector input and output signal. We shall assume that the system (A, B, C) is minimal. At time t, the actual input is $u(t) = u_{ext}(t) + v_s(t)$. Here $u_{ext}(t)$ is an external influence to the system, and $v_s(t) = u_s(t - \tau)$, for some fixed $\tau > 0$. Here, $u_s(t)$ is the synthesized feedback input, computed based on state information at time t. The delay may either originate from a slow computation time, or physical transmission delay if the feedback signal is connected to the plant via a link, which incurs coding/decoding delay or simple communication delay as in the deep space network.

Let us assume that the goal of the feedback was to assign the spectrum of the closed loop system, and that our design led the delay-free system to have a state feedback gain K, so that the delay-free closed loop system has characteristic equation $\det(sI - A + BK) = \alpha(s)$. However, implementing the gain K in the presence of the delay τ yields instead the characteristic equation

$$\det(sI - A + BK\mathrm{e}^{-s\tau}) = 0.$$

This equation has infinitely many roots, none of which equal the roots of the desired polynomial $\alpha(s)$ in general.

The design methodology of "borrowed feedback" starts by *assuming* that the closed loop behavior of the controlled delay system, for which now a gain K_τ is used, is such that the solution of the closed loop system

$$\dot{x}(t) = Ax(t) + B(u_{ext}(t) - K_\tau x(t - \tau))$$

has the same behavior as the delay-free closed loop system with gain K.

$$\dot{x}(t) = Ax(t) + B(u_{ext}(t) - Kx(t)).$$

The explicit solution of the latter is

$$x(t) = \mathrm{e}^{(A-BK)t}x_0 + \int_0^t \mathrm{e}^{(A-BK)(t-\theta)}Bu_{ext}(\theta)\,\mathrm{d}\theta.$$

In view of the delay in applying the control, let us keep the feedback signal $u_s(t)$ initially at 0 during the interval $[0, \tau)$, so that solution to the controlled delay system is found by solving the Cauchy problem from time 0 with initial value $x(0) = x_0$, and zero initial data in the interval $[-\tau, 0]$. Of course, this assumes that the delay is known to the controller. In the interval $[0, \tau]$, the controlled system has solution

$$x(t) = \mathrm{e}^{At}x_0 + \int_0^t \mathrm{e}^{A(t-\theta)}Bu_{ext}(\theta)\,\mathrm{d}\theta. \tag{3}$$

After that initial interval, the closed loop system solution is the solution to the Cauchy problem

$$\dot{x}(t) = Ax(t) + B(u_{ext}(t) - K_\tau x(t-\tau)), \tag{4}$$

started at $t = \tau$, with initial condition $x(\tau)$ given by (3) for $t = \tau$,

$$x(\tau) = \mathrm{e}^{A\tau}x_0 + \int_0^\tau \mathrm{e}^{A(\tau-\theta)}Bu_{ext}(\theta)\,\mathrm{d}\theta, \tag{5}$$

and initial data in the interval $[0, \tau]$:

$$\phi(t) = \mathrm{e}^{At}x_0 + \int_0^t \mathrm{e}^{A(t-\theta)}Bu_{ext}(\theta)\,\mathrm{d}\theta. \tag{6}$$

The solution to this Cauchy problem cannot be written explicitly in a simple analytic form (except using a series based on the method of steps). The "borrowed feedback" method postulates that a gain, K_τ, exists, so that the solution $x(t)$ for $t > \tau$ is "close to" the desired feedback controlled system with state $x_d(t)$ given by

$$x_d(t) = \mathrm{e}^{(A-BK)(t-\tau)}x(\tau) + \int_\tau^t \mathrm{e}^{(A-BK)(t-\theta)}Bu_{ext}(\theta)\,\mathrm{d}\theta. \tag{7}$$

Note that we assume that the applied control in this reference model is also zero before time τ in order to match the initial data for the delayed system, and initial condition $x_d(\tau) = x(\tau)$. Substituting (7) in Eq. (4), it was shown in [10] that if we set

$$K_\tau = K\mathrm{e}^{(A-BK)\tau}, \tag{8}$$

then for all initial conditions, $x(\tau)$, and therefore all x_0 and u_{ext} in $(0, \tau)$, we get an equation error

$$e(t) = BK\int_{t-\tau}^t \mathrm{e}^{(A-BK)(t-\theta)}Bu_{ext}(\theta)\,\mathrm{d}\theta. \tag{9}$$

Borrowing the feedback is in the sense that we assumed that a control exists achieving the goal, and then we use (borrow) that result to compute the necessary feedback signal. Note that this principle differs from the Smith-predictor in classical control theory.

2.1 Measure of Goodness

We note that in the absence of u_{ext}, the equation error is zero. Moreover, since the initial condition is also satisfied, the uniqueness theorem for the solution of the linear equation can be invoked to assert that $x(t) = x_d(t) = \mathrm{e}^{(A-BK)(t-\tau)}x(\tau)$, with $x(\tau)$ from (5) is indeed the solution for $t > \tau$. This was the solution given by [5].

The problem is that $x = x_d$ only holds for a system without external input (i.e., the entire input to the plant consists only of the feedback signal.). This is unrealistic from a practical point of view. Even if deterministic disturbances or set point changes are absent, there always is the ubiquitous noise entering the system. Obviously, one does have a system with delay, but the modeled end result of the controlled system is finite dimensional. This implies that the majority of the modes are not excited, and these modes may contain unstable modes.

The equation error (9) may be expressed as $e(t) = B\,u_{eq}(t)$, where $u_{eq}(t)$ is an equivalent input driving the system. In [10] we computed the maximal equation error norm, $\|e(t)\|$ as a measure of goodness. Here we compute an achievable upper bound on the L_2-norm of the equivalent input. Let $\mathscr{E}_u$ denote the energy in a signal u over an interval of length τ. Thus,

$$\mathscr{E}_u = \|u\|_\tau^2 \stackrel{\text{def}}{=} \int_{t-\tau}^{t} \|u(s)\|^2 \,\mathrm{d}s.$$

Let $\lambda_{\max}(M)$ denote the maximal eigenvalue of a symmetric matrix M.

Lemma 1 *The ratio between the energies in the equivalent input to the actual external input satisfies*

$$\frac{\mathscr{E}_{u_{eq}}}{\mathscr{E}_u} \leq \tau\ \lambda_{\max}(K\mathscr{R}_\tau K^\top),$$

where $\mathscr{R}_\tau$ is the finite interval reachability Gramian of the desired closed loop system $(A - BK, B)$.

$$\mathscr{R}_\tau(A - BK, B) = \int_0^\tau \mathrm{e}^{(A-BK)\theta} BB^\top \mathrm{e}^{(A-BK)^\top\theta}\,\mathrm{d}\theta.$$

Proof See Appendix. □

This ratio, $\mathscr{G} = \frac{\mathscr{E}_{u_{eq}}}{\mathscr{E}_u}$, is a measure of the goodness of the method of control by borrowed feedback.

3 Stability of the Closed Loop

Let us assume that the plant is unstable, i.e., the system matrix A is not Hurwitz. Stabilization with "borrowed feedback" with gain (8) yields for $t > \tau$ the closed loop system

$$\dot{x}(t) = Ax(t) - BK_\tau x(t-\tau) + Bu_{ext}(t). \tag{10}$$

The well-known Riccati-stability condition is not helpful since a necessary condition for the Riccati-stability of (10) is the Hurwitz-ness of A (See [7]). Here we propose a different method. Rewrite (10) as

$$\dot{x}(t) = (A - BK)x(t) + B[Kx(t) - K_\tau x(t-\tau)] + Bu_{ext}(t). \tag{11}$$

and note that with the choice of gain (8), it is of the form

$$\dot{x}(t) = Hx(t) + G[x(t) - \mathrm{e}^{H\tau}x(t-\tau)] + Bu_{ext}(t), \tag{12}$$

where $H = A - BK$ is Hurwitz, and (H, B) reachable by the minimality assumption on (A, B, C). It follows that also (H, G), with $G = BK$, is reachable. To illustrate the ideas, consider first the scalar case.

Theorem 1 *The state of the scalar system of form (12),*

$$\dot{x}(t) = hx(t) + g(x(t) - \mathrm{e}^{h\tau}x(t-\tau)) + bu_{ext}(t),$$

with $h < 0$ and initial condition x_0 and zero initial data has a bounded solution if u_{ext} is bounded and $|g| < \frac{|h|}{1-\mathrm{e}^{-|h|\tau}}$.

Proof Obviously, for $t < \tau$, the solution $x(t) = \mathrm{e}^{(g+h)t}x_0 + \int_0^t \mathrm{e}^{(g+h)(t-\theta)}bu_{ext}(\theta)\,\mathrm{d}\theta$ is bounded.
Let $\overline{U}$ be the bound on u_{ext}. Suppose that for $t > \tau$

$$\max_{\theta\in(t-\tau,t)} |x(\theta) - \mathrm{e}^{h\tau}x(\theta-\tau)| \le \overline{W}. \tag{13}$$

Then the solution to the scalar system satisfies

$$x(t) - \mathrm{e}^{h\tau}x(t-\tau) = \int_{t-\tau}^{t} \mathrm{e}^{h(t-\theta)}[g(x(\theta) - \mathrm{e}^{h\tau}x(t-\theta)) + bu_{ext}(\theta)]\,\mathrm{d}\theta$$

and it follows that

$$|x(t) - \mathrm{e}^{h\tau}x(t-\theta)| \leq \frac{(\mathrm{e}^{h\tau}-1)}{h}\left(|g|\overline{W} + |b|\overline{U}\right). \tag{14}$$

Hence, the assumption (13) is consistent for the autonomous system ($\overline{U} = 0$) if

$$|g|\frac{\mathrm{e}^{h\tau}-1}{h} < 1. \tag{15}$$

This implies in turn that

$$\mathrm{e}^{h\tau}x(t-\tau) - \overline{W} \leq x(t) \leq \mathrm{e}^{h\tau}x(t-\tau) + \overline{W}.$$

From this

$$|x(t)| \leq \mathrm{e}^{h\tau}|x(t-\tau)| + \overline{W}.$$

Thus, if in addition $h < 0$, the solution to the autonomous system must remain bounded. Note that we may set $\overline{W} = x_0$ if $h + g \leq 0$, and $\overline{W} = \mathrm{e}^{(h+g)\tau}x_0$ if $h + g > 0$. For the system with external input, let

$$x(t) - \mathrm{e}^{h\tau}x(t-\tau) = w(t) \tag{16}$$

and note the bound (14) gives now

$$|w(t)| \leq \frac{(\mathrm{e}^{h\tau}-1)}{h}\left[|g| \max_{\theta\in(t-\tau,t)} |w(\theta)| + |b|\overline{U}\right].$$

which implies that the bound on $w(t)$ is consistent if the right hand side of the above inequality is in turn bounded by $\overline{W}$. Since the factor $\frac{\mathrm{e}^{h\tau}-1}{h}$ is always positive, in view of (15), we may set

$$\overline{W} = \frac{|b|(1-\mathrm{e}^{h\tau})\overline{U}}{h + |g|(1-\mathrm{e}^{h\tau})}. \tag{17}$$

Finally, it follows from (16) that if w is bounded, then

$$|x(t)| \leq \mathrm{e}^{Nh\tau}|x(t-N\tau)| + \overline{W}\frac{1-\mathrm{e}^{Nh\tau}}{1-\mathrm{e}^{h\tau}},$$

or

$$|x(t+N\tau)| \leq \mathrm{e}^{Nh\tau}|x(t)| + \overline{W}\frac{1-\mathrm{e}^{Nh\tau}}{1-\mathrm{e}^{h\tau}}. \tag{18}$$

The right hand side converges for $N \to \infty$ to $\frac{\overline{W}}{1-\mathrm{e}^{h\tau}}$, and proves that the controlled system is BIBO stable if $h < 0$ in addition to (14). □

Remark 1 In view of (17), it follows that if the consistency condition (15) holds for some $h < 0$ (the pre-stability condition), the autonomous system is actually asymptotically stable.

Remark 2 We emphasize that the stability conditions are of the controlled finite dimensional system and not the actual delay system loaded with arbitrary initial data.

Similar results are obtained for higher order systems, (12). See [10].

Theorem 2 *Let H be Hurwitz. If u_{ext} is bounded, then the solution of (12) remains bounded if $\|\mathrm{e}^{H\tau}\| < 1$ and $\int_0^\tau \|\mathrm{e}^{Hs}G\|\,\mathrm{d}s \le \gamma$, where γ is the decay rate of the Hurwitz matrix, i.e., for all $t > 0$: $\|e^{Ht}\| \le C\mathrm{e}^{-\gamma t}$.*

Theorem 2 can be proven with Halanay's inequality. See for instance [6]. In [10], the contraction methodology reviewed in [2] was used.

The structure of the proof of Theorems 1 and 2 relates essentially to an implicit function inequality. Starting from an inequality of the form $|x(t)| \le f(|x(s)|, c)$, which depends on parameters c the existence of w such that

$$f(w; c) \le w$$

is shown using the implicit function theorem to establish

$$f(W; c) = W \quad \Longrightarrow \quad W = F(c).$$

Then find $C = \{c \mid F(c) > 0\}$. It follows that the bound $w < W$ holds under the condition $c \in C$.

3.1 New Sufficient Conditions for Lyapunov and BIBO Stability

At once the stability proof sketched above leads to new conditions for stability of a general delay system with fixed delay.

Theorem 3 *Given the general delay system*

$$\dot{x}(t) = Ax(t) + Bx(t - \tau).$$

If a Hurwitz matrix H can be found solving the matrix equation

$$A = H - B\,\mathrm{e}^{-H\tau} \tag{19}$$

and the pair $(G = A - H, H)$ *characterizing (11) satisfies the conditions of Theorem 2, then the given system is asymptotically stable.*

Proof Rewrite the given system in the form

$$\dot{x}(t) = Hx(t) + (A - H)x(t) - (B\,\mathrm{e}^{-H\tau})\mathrm{e}^{H\tau}x(t-\tau).$$

Then if $A - H = -B\mathrm{e}^{-H\tau} = G$, the new equation is of the form

$$\dot{x}(t) = Hx(t) + G[x(t) - \mathrm{e}^{H\tau}x(t-\tau)].$$

Now invoke the sufficient condition of Theorem 2. □

We present the explicit result for the scalar case. The transcendental equation (19) is

$$a = h - b\mathrm{e}^{-h\tau}.$$

If it has a solution $h_0(a,b) < 0$, set $g = -b\mathrm{e}^{-h_0\tau}$. We consider two cases:

(i) If $b > 0$, the function $h - b\mathrm{e}^{-h\tau}$ is monotonically increasing, and evaluates for $h = 0$ to $-b < 0$. This implies that $h \le 0$ iff $a \le -b$.

(ii) If $b < 0$, the function $h - b\mathrm{e}^{-h\tau}$ has a minimum at $h_m = \frac{\ln|b|\tau}{\tau}$. Note that $h_m > 0$ if $|b|\tau > 1$, and $h_m \le 0$ else. The minimum value is $a_m(b) = \frac{1+\ln|b|\tau}{\tau}$. Consequently, if $a < a_m(b)$, the transcendental equation does not possess a real solution. Consider now $a \ge a_m(b)$. If h is restricted to be negative, we have

$$\min_{h<0}(h - b\mathrm{e}^{-h\tau}) = \begin{cases} \frac{1+\ln|b|\tau}{\tau} & \text{if } -\frac{1}{\tau} < b < 0 \\ -b & \text{if } b < -\frac{1}{\tau}. \end{cases} \tag{20}$$

We conclude then that a unique $h < 0$ exists if $0 < b < -a$. If $b < 0$, then if $a > -b$, a unique solution exists, but for $\frac{1+\ln|b|\tau}{\tau} < a < -b$ two negative valued h's exist. By Theorem 1, the scalar delay system will then be stable if also $|g| = |b|\mathrm{e}^{|h|\tau} < \frac{|h|}{1-\mathrm{e}^{-|h|\tau}}$.

For instance, for $a = 0, \tau = 1$, we solve first

$$h - b\mathrm{e}^{-h} = 0.$$

This only has a real solution for h if $b > -\frac{1}{\mathrm{e}}$, and is expressible in terms of the (real) Lambert W-function.

$$h\mathrm{e}^{h} = b \Rightarrow h = W(b).$$

Note that $h < 0$ only if $b < 0$. Thus we limit $-\frac{1}{\mathrm{e}} < b < 0$. The additional stability condition is

$$|b|\mathrm{e}^{|h|} < \frac{|h|}{1-\mathrm{e}^{-|h|}} \Rightarrow |b| < \frac{|h|}{\mathrm{e}^{|h|}-1}.$$

Thus we require $b^2 < W(b)^2$, but that is always satisfied in the given region. Thus

$$\dot{x}(t) = bx(t-1)$$

is asymptotically stable for $-\frac{1}{\mathrm{e}} < b < 0$. The exact stability condition is known to be $-\pi/2 < b < 0$.

The following theorem on BIBO stability of the delayed closed loop complements the previous results:

Theorem 4 *Let $H = A - BK$ be Hurwitz. The closed loop system with τ-delayed control and gain $K_\tau = K\mathrm{e}^{(A-BK)\tau}$ is BIBO stable.*

Proof Represent the closed loop system by

$$\dot{x} = (A-BK)x + B\eta(t) \tag{21}$$

where

$$\eta(t) = u_{ext} + K(x(t) - \mathrm{e}^{(A-BK)\tau}x(t-\tau). \tag{22}$$

Integrate (21)

$$x(t) = \mathrm{e}^{(A-BK)\tau}x(t-\tau) + \int_{t-\tau}^{t} \mathrm{e}^{(A-BK)(t-s)}B\eta(s)\,\mathrm{d}s,$$

from which in turn

$$\eta(t) = u_{ext}(t) + K\int_{t-\tau}^{t} \mathrm{e}^{(A-BK)(t-s)}B\eta(s)\,\mathrm{d}s.$$

Taking norms

$$\|\eta(t)\| \le \|u_{ext}(t)\| + \int_{t-\tau}^{t} \|K\mathrm{e}^{(A-BK)(t-s)}B\|\|\eta(s)\|\,\mathrm{d}s.$$

Application of the Gronwall–Bellman inequality leads to

$$\|\eta(t)\| \le \|u_{ext}(t)\| \exp\left[\int_{t-\tau}^{t} \|K\mathrm{e}^{(A-BK)(t-s)}B\|\,\mathrm{d}s\right].$$

If $\|u_{ext}\| \le \overline{U}$, the right hand side is bounded. Since $(A-BK)$ is Hurwitz, and the input of (21) is bounded, the state of the system remains bounded. Hence the delayed feedback system is BIBO stable. □

4 The Observation Problem

In [10], the dual problem of determining the initial condition for a system

$$\dot{x}(t) = Ax(t) + Bu(t), \quad y(t) = Cx(t) \tag{23}$$

but such that the observation available at time t is actually $z(t) = y(t - \tau)$, was considered. Guided by the first principle that the observer needs an internal model with a correction based on the discrepancy between the measured and simulated quantity, an observer that gives at time t an approximation for $x(t - \tau)$, was derived:

Theorem 5 *If (A, C) is an observable pair, the observer–predictor design can be "borrowed" from the delay-free case, with L associated with a given desired characteristic observer polynomial given by the Bass–Gura formula for a delay-free system. The estimator is given by*

$$\dot{\hat{x}}(t) = A\hat{x}(t) + \mathrm{e}^{A\tau}L[z(t) - C\mathrm{e}^{-A\tau}\hat{x}(t)] + \mathrm{e}^{A\tau}Bu(t-\tau) - \sigma\Sigma \tag{24}$$

where

$$\Sigma = \mathrm{e}^{A\tau}(A - LC)\mathrm{e}^{-A\tau}\int_{t-\tau}^{t} \mathrm{e}^{A(t-\theta)}Bu(\theta)\,\mathrm{d}\theta. \tag{25}$$

5 Time-Varying Delay

The proposed method of "borrowing" the state feedback" can also be adapted for systems with time-varying delays as shown in [4, 5]. A simple observation problem with a state dependent delay is discussed in [1]. However, there are restrictions to its feasibility. In [8, 9] we elaborated on possible inconsistencies when the derivative of the time delay exceeds one. Essentially $\dot{\tau} > 1$ imparts *noncausal* behavior to the time-delay system.

We provide a simple illustration of the problem: Denote by $t - \tau(t)$ the "backward" time, $t_b(t)$. If the delay-rate constraint is not satisfied, the function $t_b(t)$ no longer is a monotone function of time t. Consequently, more than one value of t may yield the same value of t_b. This implies that $x(t_b)$ and hence x for all t should be kept in memory indefinitely, as it may have to be reused at a future instant. See Fig. 1. This may be alleviated if the entire delay function $\tau(\cdot)$ (not only the past but also the future) is known at any instant. As the design of the controller essentially synthesizes the control signal at time t_b, a multi-valued $u(t_b)$ results, if for instance $t_b = t - \tau(t) = t' - \tau'(t')$ for $t \neq t'$. Indeed, in this case $u(t_b) = -K\mathrm{e}^{(A-BK)\tau}x(t_b)$ cannot be uniquely defined as τ needs to assume two different values at the same time.

Let us do the analysis in more detail. There are two viewpoints depending on the information structure [9].

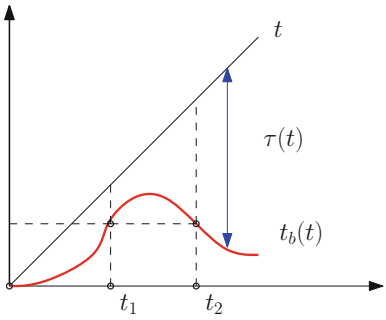

Fig. 1 Nonuniqueness problem

5.1 Backward Selection

At time t, the *delay* $\tau(t)$ is known and the state $x(t-\tau(t))$ is *selected* out of the past history to generate the feedback signal over a gain $K_{\tau(t)}$. In principle, this scheme allows $\dot{\tau} > 1$, however the problem then becomes unrealistic as an infinitely long delay line may be required in order to generate the feedback signal for each time t.

5.2 Forwarding

This is a physically more appropriate model. At time t, let it be known that whatever control signal is generated, it will not arrive at the system input until time $t + \hat{\tau}(t)$. Thus the forwarding[1] time or *advance* $\hat{\tau}(t)$ must be anticipated at time t. This means that the feedback system is modeled as

$$\dot{x}(t+\hat{\tau}(t)) = Ax(t+\hat{\tau}(t)) + B[u_{ex}(t+\hat{\tau}(t)) - K_{\hat{\tau}(t)}x(t)].$$

Let $t + \hat{\tau}(t) = T_f(t)$ be the "advanced" time. If $T_f(t) = t' > 0$ is monotone its inverse $t = \theta(t')$ exists and is also monotone. The corresponding delay at time t' is $\tau(t') = t' - \theta(t')$. The causality conditions $\tau > 0$ and $\dot{\tau} < 1$ imply then $\hat{\tau} > 0$ and $\dot{\hat{\tau}} > -1$. This guarantees that the synthesized feedback will only be used once, so that a unique applied gain can be assigned. This gain is

$$K_{\hat{\tau}(t)} = K\mathrm{e}^{(A-BK)\hat{\tau}(t)}. \tag{26}$$

[1]This notion of forwarding is different from the concept introduced by Praly for nonlinear control systems.

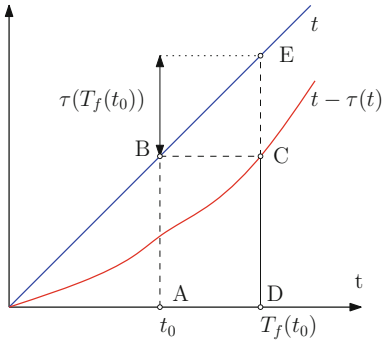

Fig. 2 Determining $T_f(t)$

The implications are clear. In order to be able to implement this gain, at time t, the knowledge of the delay $\tau(t + T(t))$ at a future time is necessary. If the delay is independent of the state, this means that the entire delay function needs to be known to the controller. In some cases, such as a periodic cases this may be realistic. It should also be clear again from the analysis that the method must fail if $\dot{\tau}(t) > 1$, as the time inversion of $t'(t)$ does not exist. In Fig. 2 we illustrate how $\tau(T_f(t))$ may be obtained graphically from the known future behavior of $\tau(t)$. At the present time t_0, indicated by point A, draw the vertical AB, with B on the t-graph. The horizontal line BC intersects $t_b(t) = t - \tau(t)$ at C, with coordinates $(T_f(t_0), T_f(t_0) = \tau(T_f(t_0))$. The segment CE has length $\tau(T_f(t_0))$.

5.3 State Dependent Delay

Here the problem is more complex. We sketch the simple case in the absence of an external input as illustration. First how is the deviating argument defined? Does it depend on the forward state or the backward state? Consider a closed loop model

$$\dot{x}(t) = Ax(t) + Bv(t - \tau(x(t))$$
$$v(t) = -K_\tau x(t).$$

If it is to behave as

$$\dot{x}_d = (A - BK)x_d(t),$$

then at time $t_b = t - \tau(x_d(t))$ the generated feedback signal should be

$$v(t_b) = -Kx_d(t_b + \tau(x_d(t))). \tag{27}$$

which is a noncausal structure ($t_b < t$). Assuming $x_d = x$ in the absence of an external input, this yields the anticipating form

$$v(t_b) = -Kx_d(t_b + \tau(\mathrm{e}^{(A-BK)\tau}x_d(t_b))).$$

Denoting $\hat{\tau}(x_d(t_b)) = \tau(\mathrm{e}^{(A-BK)\tau}x_d(t_b))$ this yields the implicit relation

$$\hat{\tau}(x_d(t)) = \tau(\mathrm{e}^{(A-BK)\hat{\tau}(x_d(t))}x_d(t)). \tag{28}$$

In some problems with state dependent delay, the delay and the state may be implicitly related, due to the physical structure of the problem. See for instance [1], where state and delay satisfy $c\tau = x(t) + x(t-\tau)$ as a result of signal propagation with speed c. This may be "solved" by Lagrange inversion, but convergence is an issue.

6 Conclusions

A unified framework for the design of a controller and observer for finite dimensional systems with delayed information was developed. The main principle is that one assumes that the goal can be reached, and then this information is "borrowed" to adjust the feedback signal. It was established that under certain conditions, this design leads to stable closed loop systems and/or observers. In particular, it was also pointed out that the causality condition $\dot{\tau} < 1$ played again a major role for the feasibility of the methodology if the gains are time varying or state dependent. Things can go very wrong if the causality is not satisfied.

Acknowledgements The author is indebted to the anonymous reviewers of the IFAC-TDS manuscript for their suggestions that substantially improved the original version of this paper and to Mr. A. Ahmed for correcting some erroneous formulas.

Appendix

Proof of Lemma 1.
Consider

$$u_{eq}(t) = K\int_{t-\tau}^{t} \mathrm{e}^{(A-BK)(t-\theta)}Bu(\theta)\,\mathrm{d}\theta,$$

and assume that $u(\cdot)$ has bounded energy, $\mathscr{E}_u$, in the interval $(t-\tau, t)$. Letting

$$z = \int_{t-\tau}^{t} \mathrm{e}^{(A-BK)(t-\theta)}Bu(\theta)\,\mathrm{d}\theta, \tag{29}$$

it is required to maximize $\mathscr{E}_{u_{eq}} = z^\top K^\top K z$ with constraint (29). Using Lagrangean methods, adjoin the constraints with Lagrange multipliers $\lambda \in \mathbb{R}^n$ and $\mu \in \mathbb{R}$

$$\mathscr{L} = \frac{1}{2} z^\top K^\top K z - \lambda^\top \left(z - \int_{t-\tau}^{t} \mathrm{e}^{(A-BK)(t-s)} B u(s)\, \mathrm{d}s \right) - \frac{\mu}{2} \left(\int_{t-\tau}^{t} u^\top(s) u(s)\, \mathrm{d}s - \mathscr{E}_u \right).$$

The first order variation is

$$\delta\mathscr{L} = \left(z^\top K^\top K - \lambda^\top \right) \delta z + \int_{t-\tau}^{t} \left(\lambda^\top \mathrm{e}^{(A-BK)(t-s)} B - \mu u^\top(s) \right) \delta u(s)\, \mathrm{d}s.$$

Stationarity requires, with the Du Bois-Reymond lemma,

$$\lambda = K^\top K z \tag{30}$$

$$\mu u(\theta) = B^\top \mathrm{e}^{(A-BK)^\top (t-\theta)} \lambda, \tag{31}$$

together with constraint (29) and

$$\int_{t-\tau}^{t} u^\top(s) u(s)\, \mathrm{d}s = \mathscr{E}_u. \tag{32}$$

Equations (30) and (31) yield

$$u(\theta) = \frac{1}{\mu} B^\top \mathrm{e}^{(A-BK)^\top (t-\theta)} K^\top K z, \tag{33}$$

since $\mu = 0$ surely is not maximizing. Substituting (33) in (29) yields

$$z = \frac{1}{\mu} \mathscr{R}_\tau K^\top K z,$$

from which in turn

$$\mu (Kz) = K \mathscr{R}_\tau K^\top (Kz), \tag{34}$$

expressing that Kz is an eigenvector of $K\mathscr{R}_\tau K^\top$ with eigenvalue μ.
If K has full rank, any vector in $\mathbb{R}^m$ can be written as Kz with $z \in \mathbb{R}^n$ for $m \leq n$. For instance take $z = K^\top (KK^\top)^{-1} v$ where v is an eigenvector of $K\mathscr{R}_\tau K^\top$ with eigenvalue μ. Equations (31) and (34) yield

$$v^\top K \mathscr{R}_\tau K^\top v = \mathscr{E}_u \mu^2. \tag{35}$$

and (34) with (35) $\mu \|v\|^2 = \mu^2 \mathscr{E}_u$. Finally, the norm of u_{eq} follows

$$\mathscr{E}_{u_{eq}} = \|Kz\|^2 = \|v\|^2 = \mu \mathscr{E}_u.$$

Hence $\mathscr{E}_{u_{eq}}$ is maximal if the largest eigenvalue of $K\mathscr{R}_\tau K^\top$ is chosen.

$$\max \mathscr{E}_{u_{eq}} = \lambda_{\max}(K\mathscr{R}_\tau K^\top)\,\mathscr{E}_u. \tag{36}$$

thus proving the lemma.

References

1. Ahmed, A., Verriest, E.I.: Estimator design for a subsonic rocket car (soft landing) based on state-dependent delay measurement. In: Proceedings of the 52-nd IEEE Conference on Decision and Control, Florence, Italy (2013)
2. Aminzare, Z., Sontag, E.: Contraction methods for nonlinear systems: a brief introduction and some open problems. In: Proceedings of the 53-d IEE Conference Decision and Control, pp. 3835–3847, Los Angeles, CA (2014)
3. Bekiaris-Liberis, N., Krstic, M.: Compensation of state-dependent input delay for nonsingular systems. IEEE Trans. Autom. Control **58**(2), 275–289 (2013)
4. Cacace, F., Germani, A., Manes, C.: An observer for a class of nonlinear systems with time varying observation delay. Syst. Control Lett. **59**(5), 305–312 (2010)
5. Cacace, F., Germani, A.: Manes C (2014) Exponential stabilization of linear systems with time-varying delayed state feedback via partial spectrum assignment. Syst. Control Lett. **69**(1), 47–52 (2014)
6. Ivanov, A., Liz, E., Trofimchuk, S.: Halanay inequality, Yorke 3/2 stability criterion and differential equations with maxima. Tohoku Math. J. **54**, 277–295 (2002)
7. Verriest, E.I: Riccati stability. In: Blondel, V., Megretski, A. (eds.) Unsolved Problems in Mathematical Systems and Control Theory, pp. 49–53. Princeton University Press (2004)
8. Verriest, E.I.: Well-posedness of problems involving time-varying delays. In: Proceedings of the MTNS-2010, pp. 1203–1210, Budapest, Hungary (2010)
9. Verriest, E.I.: Inconsistencies in systems with time-varying delays and their resolution. IMA J. Math. Control Inform. **28**, 147–162 (2011)
10. Verriest, E.I.: The principle of "borrowed feedback" and application to control and observation for systems with varying delay. In: Proceedings of the 12-th Workshop on Time-Delay Systems, Ann Arbor, MI (2015)
11. Walther, H.O.: On a model for soft landing with state-dependent delay. J. Dyn. Diff. Equ. **19**(3), 593–622 (2007)

A New Delay-Independent Stability Test for LTI Systems with Single Delay

Baran Alikoç and Ali Fuat Ergenç

Abstract A new method complying necessary and sufficient conditions to test delay-independent stability of the general linear time invariant (LTI) dynamics with single delay is presented. The method is based on investigating the location of zeros of an auxiliary characteristic polynomial obtained via Kronecker summation. The proposed approach enables to determine the exact regions of the unknown parameters, e.g., system and controller parameters, ensuring delay-independent stability.

1 Introduction

Stability and control design of time-delay systems are widely studied due to the effect of delay phenomena on system dynamics [1, 2]. The challenge in handling the characteristics of time-delayed systems arise from their nature of being infinite dimensional and yielding nonlinear eigenvalue problems. This paper deals with delay-independent stability (DIS), formally defined in [3] first, which indicates the stability of the system for all nonnegative values of delays whereas delay-dependent stability specifies the stability for a nonnegative subset of delays. Our main goal is to test DIS of a single delay LTI system and also to determine the region of system and/or controller parameters stabilizing the system independent of delay, in other words regardless of the delay value. This class of controllers is particularly important with the systems where the delayed feedback may cause critical and dangerous instabilities such as motion control, tank level control, high temperature furnace control. In these applications, controller has to drive the system to a stable operating point regardless of the delay where delay may occur due to a malfunction in the sensory system.

B. Alikoç (✉) · A.F. Ergenç
Department of Control and Automation Engineering, Istanbul Technical University, 34469 Istanbul, Maslak, Turkey
e-mail: baran.alikoc@itu.edu.tr

A.F. Ergenç
e-mail: ali.ergenc@itu.edu.tr

T. Insperger et al. (eds.), *Time Delay Systems*,
Advances in Delays and Dynamics 7, DOI 10.1007/978-3-319-53426-8_5

The research on stability and stabilization of time-delay systems can be classified according to the approach for the solution of the problem roughly speaking. One of the main approaches is the time domain approach based on Lyapunov–Razumikhin and Lyapunov–Krasovskii functionals [4, 5]. Another one is the frequency domain approach including frequency sweeping and matrix-pencil techniques, e.g., [1, 6–8] considering both delay-independent and dependent stability. Frequency domain techniques are mainly motivated by the characteristic root crossings on the imaginary axis where the delay-free system is stable. Practical algebraic tools in frequency domain to test DIS are being studied in recent years. [9] concerns DIS of single delay systems and investigates the roots of an improved rational function. [10] is presenting a new DIS test for multiple delay systems based on resultant theory and discriminant polynomials associated with infinite dimensional characteristic polynomial. Both papers are utilizing the features of Rekasius Transformation [11] and are useful in real arithmetics, however, are not convenient for literal parameters. Furthermore there are some algebraic methods to determine controller parameters guaranteeing DIS. A conservative method based on resultant theory and Descartes rule of signs for determining the boundaries of delay-independent stabilizing parameters is presented in [12] for multiple time-delay systems. A nonconservative method for single delay case is presented in [13] also based on resultant theory. Then the method is extended to multiple delay case using Sturm Sequences [14], however, it is required to test a set of real values in unknown parameter space in each region to determine if the region is delay-independent stable or not in both methods. This paper can be considered as a continuous work of the previous studies [15, 16] presenting a conservative methodology for multiple delay case. Although this paper is for single delay case, the approach is convenient to be extended to multiple delay case.

In this study, we consider general time-delay systems of retarded type with single uncertain constant delay. A nonconservative method to determine analytical boundaries of delay-independent stabilizing unknown parameters is improved. The method is based on the results of [17] utilizing Kronecker Summation and obtained auxiliary characteristic polynomial (*ACP*) which is self-inversive to explore the imaginary axis crossing roots of the characteristic equation of the system. The infinite dimensional delayed system is represented in terms of a finite dimensional polynomial with interspersed zeros among the unit circle. The problem of determining the region of unknown parameters for DIS is transformed into assigning a certain number of the zeros of the derivative of *ACP* inside the unit circle. For this purpose, an efficient zero location test with respect to the unit circle [18, 19] is utilized. Since the test is complying to necessary and sufficient conditions, the proposed method yields the exact boundaries of region of unknown parameter space for DIS. The key novelty of this method is that the method is not conservative, is practically implementable for literal parameters, and does not require parameter sweeping. Also there are no restrictions on the order of the system and the number of the parametric uncertainties.

The paper is organized as follows: In Sect. 2 preliminary definitions and statements of the study are given. Section 3 presents the main results for delay-

independent stability for LTI system with single delay. Section 4 contains example case studies. In the last section, conclusive remarks about the methodology are given.

2 Preliminaries

In the text, we use boldface notation for vector and matrix quantities. $\mathbb{R}$, $\mathbb{R}_+$ represent the set of real numbers and the set of nonnegative real numbers, respectively. Open left half, open right half, and the entire complex plane are represented as $\mathbb{C}_-$, $\mathbb{C}_+$, $\mathbb{C}$, respectively. Open unit disc, unit circle, and outside of unit circle are referred as $\mathbb{D}$, $\mathbb{T}$, and $\mathbb{S}$, respectively. Also, note that the "over-line" is used to represent being closed for the planes, e.g., $\overline{\mathbb{C}}_+$ for the closed right half complex plane.

2.1 Kronecker Sum and Delay-Independent Stability

We consider LTI single time-delay systems of retarded type. The general state space form is given as,

$$\dot{\mathbf{x}}(t) = \mathbf{A}(\mathbf{q})\mathbf{x}(t) + \mathbf{B}(\mathbf{q})\mathbf{x}(t-\tau) \tag{1}$$

where $\mathbf{x} \in \mathbb{R}^n$, $\mathbf{A}(\mathbf{q}) \in \mathbb{R}^{n\times n}$, $\mathbf{B}(\mathbf{q}) \in \mathbb{R}^{n\times n}$, $\mathbf{q} \in \mathbb{R}^r$ is a vector of unknown parameters and τ is the time delay.

The characteristic equation of the system (1) is derived as

$$CE(s,\tau,\mathbf{q}) = \det\left[s\mathbf{I} - \mathbf{A}(\mathbf{q}) - \mathbf{B}(\mathbf{q})e^{-\tau s}\right] = a_0(s,\mathbf{q}) + \sum_{k=1}^{n} a_k(s,\mathbf{q})e^{-k\tau s} = 0 \tag{2}$$

where $a_0(s,\mathbf{q})$ is a polynomial of n^{th} degree in s and $a_k(s,\mathbf{q})$ are polynomials of degree lower than n. In characteristic quasipolynomial $CE(s,\mathbf{q},\tau)$, there is no transcendental term $(e^{-k\tau s})$ multiplied by s^n because the delay system is retarded type. There are infinite number of characteristic roots since (2) is a transcendental equation. It is obvious that all the roots of characteristic equation (2) must lie on $\mathbb{C}_-$ for asymptotic stability for certain values of τ and $\mathbf{q}$. In other words, if no roots of (2) exist in $\overline{\mathbb{C}}_+$, the system is stable.

The frequency domain approach focuses on the characteristic roots that cross the imaginary axis rather than determining the location of infinitely many roots of (2) to determine stability. It has to be noted that this approach is valid when the delay-free system ($\tau = 0$) is stable. In [17], the problem of examining imaginary axis crossing of infinitely many characteristic roots is transformed into determination of the root locations of the auxiliary characteristic equation of which represents the system at the stability switching points for multiple delay systems. The Extended Kronecker Summation method is used to convert the infinite imaginary axis crossing problem

into finite unit circle crossing as in the following theorem. The theorem is given for single delay case in the interest of this study for simplicity.

Theorem 1 *Let the Auxiliary Characteristic Equation (ACE) of the system (1), with* $z = e^{-\tau s}$ *be as follows:*

$$ACE(z, \mathbf{q}) = \det \begin{bmatrix} \mathbf{A}(\mathbf{q}) \otimes \mathbf{I} + \mathbf{I} \otimes \mathbf{A}(\mathbf{q}) + \\ (\mathbf{B}(\mathbf{q}) \otimes \mathbf{I})\, z + (\mathbf{I} \otimes \mathbf{B}(\mathbf{q}))\, z^{-1} \end{bmatrix} = 0 \tag{3}$$

where $\otimes$ *denotes the Kronecker Product. Then, for the system (1) for a certain value set of* $\mathbf{q}$*, i.e.,* $\mathbf{q}^*$*, the following findings are equivalent:*

(i) A unitary complex number $z \in \mathbb{T}$ *satisfies ACE given in (3).*
(ii) There exists at least one pair of imaginary characteristic roots, $\pm\omega_c i$*, of (2).*
(iii) There exists a corresponding delay $\tau \in \mathbb{R}_+$ *which satisfies* $|z| = |e^{\pm\tau\omega_c i}| = 1$.

Proof Proof of the theorem is given in [17].

Theorem 1 states that one pair of imaginary characteristic roots, $\pm\omega_c i$, of (2) for a certain value of τ and $\mathbf{q}^*$ correspond to a unitary root of (3) necessarily and sufficiently.

DIS of a time-delay system represents that the delay system is stable regardless of the delay. For a system (1) ensuring DIS, none of the roots of the characteristic equation (2) must be on $\overline{\mathbb{C}}_+$ for all nonnegative values of the delay. Formal definition can be given as follows:

Definition 1 The system in (1) is said to be stable if

$$CE(s, \tau) \neq 0, \quad \forall s \in \overline{\mathbb{C}}_+ \tag{4}$$

where $CE(s, \tau)$ is given in (2). It is said that the system is delay-independent stable (DIS) if (4) holds for all $\tau \geq 0$.

Then the following theorem can be written with the perspective of Theorem 1 and Definition 1.

Theorem 2 *An LTI system (1) is delay-independent stable for a certain parameter set* $\mathbf{q}^*$ *if and only if the following conditions are satisfied simultaneously:*

(i) $\Re\left(\lambda_i\left[\mathbf{A}(\mathbf{q}^*) + \mathbf{B}(\mathbf{q}^*)\right]\right) < 0,\ i = 1, \ldots, n$
(ii) $Z = \{z \in \mathbb{T} \mid ACE(z) = 0\} = \emptyset$.

Proof In the first condition, the stability of the non-delayed system is guaranteed for the certain set of unknown parameters $\mathbf{q}^*$ by declaring the matrix $\mathbf{A}(\mathbf{q}^*) + \mathbf{B}(\mathbf{q}^*)$ is Hurwitz. In the second one, stating *ACE* has no roots on $\mathbb{T}$ assures that characteristic equation (2) has no $\pm i\omega_c$ roots on the imaginary axis for $\forall\tau \in \mathbb{R}_+$. Thus, the system is delay-independent stable and this condition is the result of root continuity property.

2.2 Bistritz Tabulation Method

In the literature, there are several methods to determine the location of zeros with respect to the unit circle for a given polynomial based on Schur–Chon matrices and Jury–Marden tables [20]. In this study, we present and utilize a different approach, Bistritz Tabulation, to determine the location of zeros with respect to the unit circle. The method is computationally efficient and easily implementable for unknown parameters. After giving the necessary definitions, the algorithm, and the theorems for the method are represented in this subsection. Then, the method is utilized on an auxiliary characteristic polynomial in the main results section.

Definition 2 Consider the polynomial with complex coefficients

$$P_n(z) = \sum_{i=0}^{n} d_i z^i \,. \tag{5}$$

Then the reciprocal of $P_n(z)$ is

$$P_n^{\#}(z) = \sum_{i=0}^{n} \overline{d}_{n-i} z^i = z^n \overline{P_n(1/\overline{z})} \tag{6}$$

where $\overline{(\cdot)}$ denotes the complex conjugate.

Definition 3 If $P_n(z) = P_n^{\#}(z)$ then the polynomial is called as *symmetric* or *self-inversive*.

Definition 4 $P_n(z)$ in (5) is called *normal* if $d_n \neq 0$. Otherwise it is called *abnormal*. In other words, being *normal* is the equivalence of formal degree (n) and the exact degree of the polynomial.

Definition 5 The *deficiency parameter*, λ_k, is the difference between the formal (i.e., expected) degree and the exact degree of a polynomial $P_k(z)$ where k denotes the degree of the polynomial. $P_k(z)$ is normal if $\lambda_k = 0$ and abnormal if $\lambda_k > 0$.

Bistritz Tabulation is a tabular method to determine the number of the zeros of a polynomial inside, on, and outside the unit circle ($\mathbb{D}, \mathbb{T}, \mathbb{S}$). It is presented in [18] for polynomials with real coefficients and then the study is extended for polynomials with complex coefficients in [21]. It is a Routh like tabulation method based on a three-term recursion of symmetric polynomials and the number of sign variations of these polynomials at $z = 1$. There are two kinds of singularities in the early mentioned papers. The method is improved to overcome one of the singularity types and a more compact form is given in [19].
For a polynomial $P_n(z)$ defined in (5), such that $P_n(1) \neq 0 \in \mathbb{R}$ and $d_n \neq 0$, the *regular* recursion algorithm [19] is as follows:

$$T_n(z) = \sum_{i=0}^{n} t_{ni} z^i = P_n(z) + P_n^{\#}(z) \tag{7}$$

$$T_{n-1}(z) = \sum_{i=0}^{n-1} t_{(n-1)i} z^i = \frac{P_n(z) - P_n^{\#}(z)}{z-1} \tag{8}$$

For $k = n-1, \ldots, 0$

$$\delta_{k+1} = \begin{cases} \frac{t_{(k+1)0}}{t_{k\lambda_k}}, & \text{if } T_k(z) \not\equiv 0 \\ 0, & \text{if } t_{(k+1)0} = 0 \\ \text{not required}, & \text{if } t_{(k+1)0} \neq 0 \ \ \& \ \ T_k(z) \equiv 0 \end{cases}$$

$$T_{k-1}(z) = z^{-1}\left[\left(\delta_{k+1} z^{\lambda_k} + \overline{\delta}_{k+1} z^{\lambda_k+1}\right) T_k(z) - T_{k+1}(z)\right]. \tag{9}$$

The following theorem is for counting the number of zeros inside and outside the unit circle in regular (i.e., nonsingular) case.

Theorem 3 (Zero Location for Nonsingular Case) *Consider $P_n(z)$ with the assumptions $P_n(1) \neq 0 \in \mathbb{R}$ and $d_n \neq 0$. Assume that the procedure is regular. Then,*

(i) number of zeros in $\mathbb{D}$: $\alpha_n = n - \nu_n$,
(ii) number of zeros in $\mathbb{S}$: $\gamma_n = \nu_n$

where $\nu_n = Var\left\{\sigma_n, \sigma_{n-1}, \ldots, \sigma_0\right\}$ such that $\sigma_k := T_k(1)$ and $Var\{\cdot\}$ denotes number of sign variations.

The only singularity situation which interrupts the regular recursion occurs if and only if a normal polynomial $T_\eta(z)$ ($\lambda_\eta = 0$) is followed by an identically zero polynomial, i.e., $T_{\eta-1}(z) \equiv 0$, in the given recursion algorithm. This occurs when a polynomial has unit circle and/or reciprocal zeros, i.e., conjugate pairs of zeros symmetrical to unit circle. Note that *ACE* in (3) has such roots. One can find the method to overcome singularities for proceeding the algorithm in [19]. We prefer not giving details since the singularity is handled for the polynomial of which the zeros are identical to the roots of *ACE* by means of a theorem. On the other hand, it is useful to present the following theorem to understand the effect of singularities on the zero distribution of the polynomial with respect to $\mathbb{T}$.

Theorem 4 (Zero Location for Singular Case) *Assume the algorithm in (7), (8), (9) is applied to a polynomial $P_n(z)$ in (5), such that $P_n(1) \neq 0 \in \mathbb{R}$ and $d_n \neq 0$, and a sequence of polynomials $\left\{T_k(z); k = n, \ldots, 0\right\}$ is produced after handling the singularities. Let "η" denote the degree after which a singularity occurred for the first time (with $\eta = 0$ denoting a nonsingular case). Then,*

(i) number of zeros in $\mathbb{D}$: $\alpha_n = n - \nu_n$,

(ii) number of zeros on $\mathbb{T}$*:* $\beta_n = 2\nu_\eta - \eta$,
(iii) number of zeros in $\mathbb{S}$*:* $\gamma_n = n - \alpha_n - \beta_n$

where $\nu_n = Var\left\{\sigma_n, \sigma_{n-1}, \ldots, \sigma_0\right\}$ *and* $\nu_\eta = Var\left\{\sigma_\eta, \sigma_{\eta-1}, \ldots, \sigma_0\right\}$ *such that* $\sigma_k := T_k(1)$. *Also, there are* $\eta - \nu_\eta$ *pairs of reciprocal zeros.*

Proof The detailed proofs of Theorems 3 and 4 can be found in [19].

One can utilize Theorem 4 to show none of the roots of the *ACE* is on the unit circle for DIS as stated in Theorem 2. However, firstly the singularity occurred in the *ACE* has to be treated. We prefer to present a corollary for DIS in the next section which removes the necessity of handling the singularity in the first step of recursion algorithm in Bistritz Tabulation.

3 Main Results

The two conditions given in Theorem 2 are the framework of DIS. Briefly, the delay-free system must be Hurwitz stable and *ACE* must have no unitary roots. Firstly, we would like to focus on the distinctive property of (3) which is also indicated in [15] for multiple delay case. Note that this function has a special form:

$$ACE(z, \mathbf{q}) = p(\frac{1}{z}, \mathbf{q}) + n(\mathbf{q}) + p(z, \mathbf{q}) \tag{10}$$

where $p(z, \mathbf{q})$ is a polynomial in terms of z. One can easily check the above observation by calculating the given determinant in (3) for system matrices $\mathbf{A}(\mathbf{q})$ and $\mathbf{B}(\mathbf{q})$ of any dimension "n" with literal parameters $\mathbf{q}$. Then, it is obvious that the roots of the *ACE* are identical to the zeros of the following Auxiliary Characteristic Polynomial (*ACP*)

$$ACP(z, q) = z^l ACE(z, \mathbf{q}) \tag{11}$$

where l is the degree of $p(z, \mathbf{q})$. Due to the structure indicated in (10), the *ACP* is a self-inversive polynomial of even degree $m = 2l$, as in Definition 3 and its reciprocal coefficients are equal. The zeros of self-inversive polynomials lie either on the unit circle $\mathbb{T}$ and/or occur in complex pairs which are symmetrical (reciprocal) to $\mathbb{T}$. This causes a singularity in recursion algorithm since the symmetrical polynomial produced by Eq. (8) is identically zero. Instead of trying to overcome the singularity in the first step, we employ the remarkable relationship of the critical points of the self-inversive polynomial (zeros of its derivative wrt z) and the zeros of the polynomial itself. It is stated as in the theorem below.

Theorem 5 *[24] Let P be a self-inversive polynomial of degree p. Suppose that P has exactly* β *zeros on the unit circle* $\mathbb{T}$ *(multiplicity included) and exactly* μ *critical points in the closed unit disc* $\overline{\mathbb{D}}$ *(counted according to multiplicity). Then,*

$$\beta = 2(\mu + 1) - p. \tag{12}$$

Proof The proof of the theorem can be found in [24] in detail.

Theorem 5 has a crucial role for establishing the criterion for DIS. In Theorem 2 it is stated that system (1) is delay-independent stable if its *ACE* has no roots on $\mathbb{T}$, i.e., *ACP* has no unitary zeros. It is cumbersome to check whether zeros are unitary, especially when unknown parameters are present. Notice that the number of the unitary roots of *ACP* is related to the number of its critical points in $\overline{\mathbb{D}}$. We then present the following theorem.

Theorem 6 *Consider an LTI system with single time-delay given in (1) with a certain parameter set* $\mathbf{q}^*$. *Defining the derivative of its auxiliary characteristic polynomial as*

$$D(z) := \frac{dACP(z)}{dz} \tag{13}$$

of degree $m-1$ *where the degree-m polynomial* $ACP(z)$ *is described in (3) and (11), the system (1) is delay-independent stable if and only if*

(i) $\Re\left(\lambda_i\left[\mathbf{A}(\mathbf{q}^*) + \mathbf{B}(\mathbf{q}^*)\right]\right) < 0,\ i = 1, \ldots, n$
(ii) $\nu = m/2$

where $\nu = Var\left\{\sigma_{m-1}, \sigma_{m-2}, \ldots, \sigma_0\right\}$ *such that* $\sigma_k = T_k(1)$ *are obtained by the recursion equations in (7), (8), (9) from* $D(z)$ *and* $Var\{\cdot\}$ *denotes the number of sign variations in a sequence.*

Proof For a Hurwitz stable delay-free system as declared in first condition above to be delay-independent stable, its *ACE* must have no roots on $\mathbb{T}$ (see Theorem 2). This also yields that self-inversive *ACP* must have no unitary zeros, i.e., $\beta = 0$ in Eq. (12). Considering Theorem 5, the number of zeros of $D(z)$ in $\overline{\mathbb{D}}$ must be $\mu = (m-2)/2$ to satisfy $\beta = 0$. From Theorems 3 and 4, the number of zeros of $D(z)$ in unit circle is $\mu = (m-1) - \nu$. Combining two equations for μ, we get $\nu = m/2$ indicating that the *ACP* and *ACE* have no roots on $\mathbb{T}$ yielding DIS.

Remark 1 The assumption $P_n(1) \neq 0 \in \mathbb{R}$, i.e., a zero of $P_n(z)$ at $z = 1$, to generate recursive polynomials given by (7), (8), (9), does not lead to a restriction in the theorem above for DIS. To have $D(1) = 0$, the *ACP* must have a zero at $z = 1$ with a multiplicity of at least two and since $z = e^{i\omega\tau}$, this can occur when there is an imaginary crossing $\pm i\omega$ for $\tau = 0$ or when there is an imaginary crossing at $\omega = 0$ for some τ. So, $D(1) = 0$ corrupts DIS and the assumption can be considered as a "weak" necessary condition.

In Theorem 6, necessary and sufficient conditions are given for DIS of LTI systems with single delay. Notice that it does not require any numerical calculation beyond simple algebraic operations, unlike other methods, e.g., [1, 22, 23] which include cumbersome numerical calculations such as frequency sweeping, finding spectral radius, or solving LMIs. As a result of Theorem 6, the following corollary can be written in case of the existence of unknown parameters.

Corollary 1 *Consider the system (1) and define the partial derivative of its auxiliary characteristic polynomial as*

$$D(z, \mathbf{q}) := \frac{\partial ACP(z, \mathbf{q})}{\partial z} \tag{14}$$

of degree $m-1$ where the degree-m polynomial $ACP(z, \mathbf{q})$ is described by (3) and (11). Then, the exact parameter set stabilizing the system independent of delay is

$$\mathbf{\Psi} = \left\{ \mathbf{q} \in \mathbb{R}^r | \ \ \mathfrak{R}\left(\lambda_i \left[\mathbf{A}(\mathbf{q}) + \mathbf{B}_1(\mathbf{q})\right]\right) < 0 \text{ and } \nu(\mathbf{q}) = m/2 \right\}, \ i = 1, \ldots, n \tag{15}$$

where $\nu(\mathbf{q}) = \mathrm{Var}\{\sigma_{m-1}(\mathbf{q}), \sigma_{m-2}(\mathbf{q}), \ldots, \sigma_0(\mathbf{q})\}$ such that $\sigma_l(\mathbf{q}) := T_l(1, \mathbf{q})$ are obtained by the recursion equations in (7, 8, 9) from $D(z, \mathbf{q})$ and $\mathrm{Var}\{\cdot\}$ denotes the number of sign variations.

The Corollary above can be used as a tool for delay-independent stabilizing controller design when $\mathbf{B}(\mathbf{q})$ is the matrix of state-feedback controller where $\mathbf{q}$ is the vector of gain parameters. The region of controller gain parameters which stabilize the system independent of delay is determined without conservativeness and parameter sweeping.

Remark 2 The *ACP* for the singe delay case is a polynomial with real coefficients so that $\delta_k = \overline{\delta}_k$ in (9) due to nonexistence of imaginary parts and the recursion equation (9) becomes

$$T_{k-1}(z) = z^{-1}\left[\delta_{k+1} z^{\lambda_k}(z+1)T_k(z) - T_{k+1}(z)\right] \tag{16}$$

allowing for effective computation in the recursion algorithm.

4 Case Studies

Example 1 Consider the time-delay system with single delay in [10] governed by

$$\dot{\mathbf{x}}(t) = \begin{bmatrix} 0 & 1 & 0 \\ 0 & 0 & 1 \\ -20 & -13 & -4.1 \end{bmatrix} \mathbf{x}(t) + \begin{bmatrix} 0 & 0 & 0.05 \\ 0.26 & 0 & 0 \\ 0 & 0.74 & 0 \end{bmatrix} \mathbf{x}(t-\tau). \tag{17}$$

The eigenvalues of the delay-free system ($\tau = 0$) are -2.167 and $-0.967 \pm i2.807$ which have negative real parts satisfying the first condition of Theorem 6. The auxiliary characteristic polynomial of the system (17) is

$$\begin{aligned} ACP(z) &= 8.903 \times 10^{-7} - 4.692 \times 10^{-5} z + 1.120 \times 10^{-3} z^2 \\ &-1.936 \times 10^{-2} z^3 + 0.270\ z^4 - 2.777\ z^5 + 8.867\ z^6 + 103.7\ z^7 \\ &-1031.\ z^8 - 1.769 \times 10^5 z^9 - 1031.\ z^{10} + 103.7\ z^{11} + 8.867\ z^{12} \\ &-2.777\ z^{13} + 0.270\ z^{14} - 1.936 \times 10^{-2} z^{15} + 1.120 \times 10^{-3} z^{16} \\ &-4.692 \times 10^{-5} z^{17} + 8.903 \times 10^{-7} z^{18}. \end{aligned} \tag{18}$$

The degree of the *ACP* in (18) is $m = 18$ and it is trivial to find its derivative (13), i.e., $D(z)$. After constructing the polynomials $T_k(z)$ by applying the recursion algorithm given in Eqs. (7), (8), (9) to $D(z)$, the sequence $\{\sigma_k\}$, such that $\sigma_k := T_k(1)$ for $k = 17, \ldots, 0$, is obtained as follows:

$$\begin{aligned} \{\sigma_k\} = \{&1.572 \times 10^6, -1.479 \times 10^6, -1.672 \times 10^7, 1.513 \times 10^6, \\ &2.533 \times 10^6, -2.168 \times 10^5, -2.511 \times 10^6, 1.405 \times 10^6, 1.969 \times 10^7, \\ &-1.393 \times 10^6, -2.065 \times 10^6, 1.212 \times 10^5, 2.082 \times 10^6, -1.659 \times 10^6, \\ &-1.698 \times 10^7, 1.640 \times 10^6, 1.606 \times 10^6, -3.217 \times 10^6\}. \end{aligned} \tag{19}$$

The sign variation in the list (19) is $\nu = 9$ and it is exactly $m/2 = 18/2$ as stated condition (*ii*) of Theorem 6 indicating the system is delay-independent stable. The result coincides with the result of the original study [10]. Note that, a polynomial $D(\omega)$ of degree 18 also obtained and the nonexistence of real ω roots is checked for DIS in [10].

Example 2 Consider the system below from [15]:

$$\dot{\mathbf{x}}(t) = \begin{bmatrix} 0 & 1 & 0 \\ 0 & 0 & 1 \\ -2.5 & -1.8 & -4 \end{bmatrix} \mathbf{x}(t) + \begin{bmatrix} 0 & 0 & 0 \\ 0 & 0 & 0 \\ -2\,\alpha & 0 & -1 \end{bmatrix} \mathbf{x}(t-\tau). \tag{20}$$

The characteristic equation of the system (20) is

$$CE(s, \alpha, \tau) = s^3 + 4s^2 + s^2 e^{-s\tau} + 1.8s + 2.5 + 2\alpha e^{-s\tau} = 0. \tag{21}$$

The delay-free system ($\tau = 0$) is stable when $-1.25 < \alpha < 1.45$, see Theorem 6. The partial derivative (14) of the corresponding *ACP* of degree $m = 6$ obtained by (3) and (11) is

$$\begin{aligned} D(z, \alpha) &= z^5(-37.5 + 201.1\alpha - 297.6\alpha^2 - 48\alpha^3) \\ &+z^4(-331 + 1441.\alpha - 2284\alpha^2) + z^3(-651.8 - 192.6\alpha + 428.8\alpha^2 - 96\alpha^3) \\ &+z^2(-1122. - 2110.\alpha + 3403.\alpha^2) + z(-325.9 - 96.32\alpha + 214.4\alpha^2 - 48\alpha^3) \\ &-66.2 + 288.3\alpha - 456.8\alpha^2. \end{aligned} \tag{22}$$

We get the sequence of variance coefficients $\{\sigma_k(\alpha)\}$, such that $\sigma_k(\alpha) := T_k(1, \alpha)$ for $k = 5, \ldots, 0$, applying the regular recursion algorithm in (7), (8), (9) to (22) as follows:

$$\sigma_5 = -6\,(13-4\alpha)^2\,(5+4\alpha)$$

$$\sigma_4 = 599 - \frac{4}{5}\alpha(-7619 + 4\alpha(3023 + 60\alpha))$$

$$\sigma_3 = \frac{-4(5-16\alpha)^2(5.319\times 10^4 + 8\alpha(-2.99\times 10^5 + 70\alpha(6227 + 600\alpha)))}{25(-287 + 8\alpha(109 + \alpha(-199 + 60\alpha)))}$$

$$\sigma_2 = \frac{\begin{array}{l}-6(7.107\times 10^7 + \ \alpha(6.789\times 10^8 + 8\alpha(-1.347\times 10^9 + 50\alpha(7.644\times 10^7 \\ \qquad +4\alpha(-1.514\times 10^7 + 40\alpha(1241 + 1950\alpha))))))\end{array}}{5(1.679\times 10^5 + 10\alpha(-1.572\times 10^5 + 40\alpha(6031 + 150\alpha)))}$$

$$\sigma_1 = \frac{\begin{array}{l}100(5-16\alpha)^4(4.251\times 10^7 + \ 32\alpha(8.056\times 10^6 + 5\alpha(-2.757\times 10^6 \\ \qquad +200\alpha(1106 + 135\alpha))))\end{array}}{\begin{array}{l}3(1.614\times 10^6 + \ 8\alpha(5.412\times 10^8 + 5\alpha(-9.469\times 10^8 + 20\alpha(1.232\times 10^8 \\ \qquad +100\alpha(-9.941\times 10^5 + 4\alpha(5013 + 1400\alpha))))))\end{array}}$$

$$\sigma_0 = -\frac{3}{25}(-5+4\alpha)(29+20\alpha)^2$$

Note that the delay-free stability condition is $-1.25 < \alpha < 1.45$ and it enforces $\sigma_5 < 0$ and $\sigma_0 > 0$. Thus, there may be ten possible sign variations in the sequence $\{\sigma_k\}$ which satisfy $\nu(\alpha) = m/2 = 3$ for DIS. The union of the regions for the unknown parameter satisfying $\nu = 3$ is found as $-0.134 < \alpha < 0.762$ by reducing the inequalities. The found range of α for DIS coincides with the numerical calculation where *ACE* has no unitary zeros as indicated in [15]. The DIS range for α found by the method complying sufficient condition in the mentioned paper is $0.135 < \alpha < 0.508$ and this result is highly conservative comparing to the proposed nonconservative result.

Example 3 A case for PD-controller design for a second order system is borrowed from [13] with the state space representation,

$$\dot{\mathbf{x}}(t) = \begin{bmatrix} 0 & 1 \\ -\omega_n^2 & -2\zeta\omega_n \end{bmatrix}\mathbf{x}(t) + \begin{bmatrix} 0 & 0 \\ -k_p & -k_d \end{bmatrix}\mathbf{x}(t-\tau) \tag{23}$$

where $\omega_n = 1$ and $\zeta = 0.95$. The characteristic equation of the system is

$$CE(s, k_p, k_d, \tau) = s^2 + 1.9s + k_d s e^{-s\tau} + k_p e^{-s\tau} + 1 = 0. \tag{24}$$

The delay-free system where $\tau = 0$ is Hurwitz stable for $k_p > -1$ and $k_d > -1.9$. The partial derivative (14) of the related *ACP* of degree $m = 4$ is

$$\begin{array}{l} D(z, k_p, k_d) = 7.6k_d + 7.22k_p + 2k_d^2k_p + (28.88 + 4k_d^2 + 22.8k_dk_p - 4k_p^2)z \\ + \left(22.8k_d + 21.66k_p + 6k_d^2k_p\right)z^2 + \left(4k_d^2 + 7.6k_dk_p + 4k_p^2\right)z^3. \end{array} \tag{25}$$

We obtain the elements of the sequence $\{\sigma_k(k_p, k_d)\}$, $k = 3, \ldots, 0$, such that $\sigma_k := T_k(1, k_p, k_d)$ as follows:

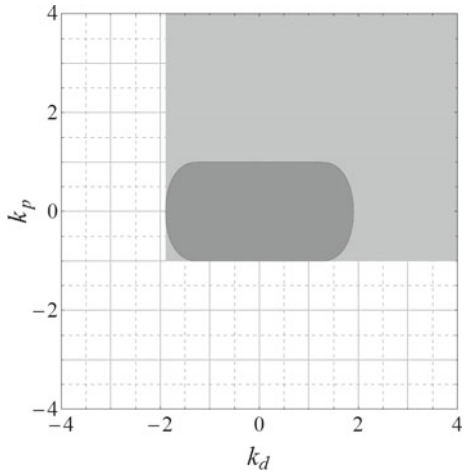

Fig. 1 Hurwitz stable region for the delay-free system (*light gray*) and delay-independent stabilizing region (*dark gray*) in PD-controller gain plane

$$\sigma_3 = -\frac{2}{25}(19 - 10k_d)^2(-1 + k_p)$$

$$\sigma_2 = \frac{4k_p^2\left(1.408 \times 10^4 + 200k_d^2\left(161 - 50k_d^2\right) - 4 \times 10^4 k_p^2\right)}{25\left(20(19 - 10k_d)k_d + (19 - 10k_d)^2 k_p - 200k_p^2\right)}$$

$$\sigma_1 = -\frac{722}{25} + 8k_d^2 + 16k_p^2$$

$$\sigma_0 = \frac{4}{25}(19 + 10k_d)^2(1 + k_p)$$

Note that $\nu(k_p, k_d) = 2$ must be satisfied for DIS as in Corollary 1. The stability condition for delay-free system enforces $\sigma_0 > 0$ and this also yields $\sigma_3 > 0$ since $\nu = 2$ is not possible for any combination of sign variations when $\sigma_3 < 0$. Consequently, there are three possible variations for $\{\sigma_2, \sigma_1\}$ as $\{+, -\}$, $\{-, +\}$, and $\{-, -\}$ which satisfies $\nu = 2$. The union of the regions of the PD-controller parameters satisfying $\nu = 2$, i.e., delay-independent stabilizing region of the parameters k_p and k_d, is shown in Fig. 1. The obtained region coincides with the results of the original paper [13].

5 Conclusion

A methodology preserving necessary and sufficient conditions, based on an auxiliary characteristic equation obtained via Kronecker summation is presented to test delay-independent stability of LTI systems with single delay. The method works for determining regions of DIS of systems with unknown parameters and for determining suitable state-feedback controllers ensuring DIS. The self-inversive property of

the auxiliary characteristic polynomial, and the Bistritz Tabulation method are utilized for efficient computation. The method does not require either parameter or frequency sweeping. Also, checking the roots of an obtained polynomial and point-wise testing in candidate DIS regions of parameter space is not needed like in alternative methods. On the other hand, finding the parameter regions for DIS may computationally be cumbersome when the system order "n" and correspondingly the degree of the auxiliary characteristic polynomial get higher. Because the possible combinations of sign variations in the sequence, $\{\sigma_k\}$, increases. To remedy this problem the condition for the number of zeros on the unit circle should be simplified in future work. Also, we plan to extend the obtained results for single delay case to multiple time-delay systems. In multiple delay case, the auxiliary characteristic polynomial should turn into a multivariable polynomial. The Bistritz method will be utilized for this multivariable polynomial problem.

References

1. Gu, K., Kharitonov, V.L., Chen, J.: Stability of Time-Delay Systems. Birkhauser, Boston, MA (2003)
2. Sipahi, R., Niculescu, S.I., Abdallah, C., Michiels, W., Gu, K.: Stability and stabilization of systems with time delay. IEEE Control Syst. Mag. **31**(1), 38–65 (2011)
3. Kamen, E.W.: Linear systems with commensurate time delays: Stability and stabilization independent of delay. IEEE Trans. Autom. Control **25**, 367–375 (1982)
4. Razumikhin, B.: Application of lyapunov's method to problems in the stability of systems with a delay. Automat. i Telemeh. **21**, 740–749 (1960)
5. Krasovskii, N.N.: Stability of Motion. Stanford University Press, Stanford (1963)
6. Chen, J.: On computing the maximal delay intervals for stability of linear delay systems. IEEE Trans. Autom. Control **40**(6), 1087–1093 (1995)
7. Chen, J., Latchman, H.A.: Frequency sweeping tests for stability independent of delay. IEEE Trans. Autom. Control **40**(9), 1640–1645 (1995)
8. Niculescu, S.I.: Stability and hyperbolicity of linear systems with delayed state: a matrix-pencil approach. IMA J. Math. Control Inf. **15**, 331–347 (1998)
9. Souza, F.O., De Oliveira, M.C., Palhares, R.M.: Stability independent of delay using rational functions. Automatica **45**(9), 2128–2133 (2009)
10. Delice, I.I., Sipahi, R.: Delay-independent stability test for systems with multiple time-delays. IEEE Trans. Autom. Control **57**(4), 963–972 (2012)
11. Rekasius, Z.V.: A stability test for systems with delays. In: Proceedings of Joint Automatic Control Conference (1980)
12. Delice, I.I., Sipahi, R.: Controller design for delay-independent stability of multiple time-delay systems via Descartes's rule of signs. In: IFAC Proceedings Volumes (IFAC-PapersOnline), pp. 144–149 (2010)
13. Nia, P.M., Sipahi, R.: Analytical boundaries of controller gains for delay-independent stability of LTI systems with single output delay. In: IFAC Proceedings Volumes (IFAC-PapersOnline), vol. 10, pp. 225–230 (2012)
14. Mahmoodi Nia, P., Sipahi, R.: Controller design for delay-independent stability of linear time-invariant vibration systems with multiple delays. J. Sound Vib. **332**(14), 3589–3604 (2013)
15. Ergenc, A.F.: A new method for delay-independent stability of time-delayed systems. Lecture Notes in Control and Information Sciences, vol. 423. Springer (2012)
16. Ergenc, A.F., Alikoc, B.: An experimental study for delay-independent state-feedback controller design. In: Proceedings of the 19th IFAC World Congress, vol. 19, pp. 6074–6079 (2014)

17. Ergenc, A.F., Olgac, N., Fazelinia, H.: Extended Kronecker summation for cluster treatment of LTI systems with multiple delays. SIAM J. Control Optim. **46**, 143–155 (2007)
18. Bistritz, Y.: Zero location with respect to the unit circle of discrete-time linear system polynomials. Proc. IEEE **72**(9), 1131–1142 (1984)
19. Bistritz, Y.: Zero location of polynomials with respect to the unit-circle unhampered by nonessential singularities. IEEE Trans. Circuits Syst. I: Fundam. Theory Appl. **49**(3), 305–314 (2002)
20. Marden, M.: The Geometry of the Zeros of a Polynomial in a Complex Variable. American Mathematical Society (1949)
21. Bistritz, Y.: A circular stability test for general polynomials. Syst. Control Lett. **7**(2), 89–97 (1986)
22. Chen, J., Xu, D., Shafai, B.: On sufficient conditions for stability independent of delay. IEEE Trans. Autom. Control **40**(9), 1675–1680 (1995)
23. Bliman, P.A.: Lyapunov equation for the stability of linear delay systems of retarded and neutral type. IEEE Trans. Autom. Control **47**(2), 327–335 (2002)
24. Sheil-Small, T.: Complex Polynomials. Cambridge University Press (2002)

Numerical Stability Test of Linear Time-Delay Systems of Neutral Type

Qi Xu, Gabor Stepan and Zaihua Wang

Abstract This paper begins with a brief discussion on the root location of linear time-delay systems of neutral type, to show its peculiar properties compared with time-delay systems of retarded type. Then it introduces a numerical stability test that can be carried out using a rough integral evaluation. The upper limit of the testing integral is estimated in two ways: parameter dependent or parameter independent. As an application of the testing method, the paper shows how to calculate the rightmost characteristic root(s) of a neutral delay differential equation with multiple delays.

1 Introduction

Time-delay systems of neutral type are described mathematically by neutral delay differential equations (NDDEs, for short) that involve at least one time delay in the derivative terms of the highest order, and they occur in many different engineering problems, such as in sway reduction on container cranes [1], traffic jam dynamics [2], self-balancing of a two-wheeled inverted pendulum [3], circuit dynamics [4], and so on. Compared with delay differential equations of retarded type (RDDEs, for short) that have no delayed derivative terms of the highest order, NDDEs exhibit some peculiar properties from the view point of stability. For example, a RDDE always has a finite number of characteristic roots in the right-half complex plane, but a NDDE may have infinite many characteristic roots in the right-half complex plane. The asymptotic stability of a RDDE is guaranteed if all the characteristic roots

Q. Xu
School of Mechanics and Engineering, Southwest Jiaotong University, Chengdu 610031, China

G. Stepan
Department of Applied Mechanics, Budapest University of Technology and Economics, Budapest 1521, Hungary

Z. Wang (✉)
State Key Laboratory of Mechanics and Control of Mechanical Structures, Nanjing University of Aeronautics and Astronautics, Nanjing 210016, China
e-mail: zhwang@nuaa.edu.cn

T. Insperger et al. (eds.), *Time Delay Systems*,
Advances in Delays and Dynamics 7, DOI 10.1007/978-3-319-53426-8_6

have negative real parts, but a NDDE may not be asymptotically stable when such a condition holds, because the infinitely many roots may have accumulation points on the imaginary axis. In addition, for NDDEs, these accumulation points' locations are not continuous with respect to time delays, hence an arbitrary small perturbation of time delays may destroy the stability of NDDEs [5–7].

Lots of methods, criteria, or algorithms are proposed for the stability analysis of DDEs [6, 8, 10, 11]. Lyapunov functionals and Lyapunov–Krasovskii functionals provide sufficient stability conditions for RDDEs and NDDEs, they work also for global stability analysis [12–14]. The semi-discretization method for RDDEs [15] has been generalized to NDDEs [16], which discretizes the delayed terms while the actual time dependencies are unchanged, and can be used also to study periodic continuous RDDEs and NDDEs.

Methods based on the analysis of characteristic functions of RDDEs can go back to 1942 [17]. The method of stability switch is effective in finding the exact stable intervals of a given parameter [11]. A different version of the stability switch method is based on introducing Rekasius's substitution, with which the critical conditions can be studied by means of polynomials without transcendentality [18–20]. The Argument Principle-based Nyquist criterion is developed to judge stability, by checking whether the number of unstable roots (characteristic roots in the right-half complex plane) is zero [21, 22]. The method proposed and developed in [10, 23] enables one to further calculate the exact number of unstable roots for RDDEs and most of NDDEs.

The definite integral method, see for example [24], is particularly effective in stability test of RDDEs. It has been extended to NDDEs [25]. This method calculates the number of unstable roots through an integral over a finite interval, whose upper limit can be roughly chosen as long as it is larger than certain value [26], hence the system stability can be easily determined. This chapter focuses on some issues about this method, such as why the stability analysis of a NDDE is more difficult than that of a RDDE, how the definite integral method can be applied effectively in judging the asymptotic stability, in plotting the stability domains and in calculating the rightmost characteristic root of NDDEs.

2 The Location of the Characteristic Roots of DDEs

The linear time-delay system under study is described by

$$\dot{x}(t) + \sum_{k=1}^{m} N_k \dot{x}(t-\tau_k) = Ax(t) + \sum_{k=1}^{m} B_k x(t-\tau_k) \tag{1}$$

where $x \in \mathbb{R}^n$, A, B_k, $N_k \in \mathbb{R}^{n\times n}$, and $\tau_k \geq 0$ are the time delays. The corresponding characteristic function is

$$f(\lambda) = \lambda^n + \sum_{k=0}^{n} \alpha_k(\mathrm{e}^{-\lambda\tau_1}, \ldots, \mathrm{e}^{-\lambda\tau_m})\lambda^{n-k} \tag{2}$$

where $\alpha_k(z_1, \ldots, z_m)$, $k = 0, 1, \ldots, n$, are real polynomials with respect to $z_1 = \mathrm{e}^{-\lambda\tau_1}$, $\ldots, z_m = \mathrm{e}^{-\lambda\tau_m}$. Equation (1) is a RDDE when $N_k = 0$ for all $k = 1, 2, \ldots, m$, that is, $\alpha_0(z_1, \ldots, z_m) \equiv 0$, while it is a NDDE when at least one $N_k \neq 0$ for some $k = 1, 2, \ldots, m$, that is, $\alpha_0(z_1, \ldots, z_m) \neq 0$. In case of NDDEs, the infinite number of characteristic roots may have accumulation points on the imaginary axis [11], so $x = 0$ is asymptotically stable if and only if the characteristic roots stay in the open left half complex plane and are uniformly bounded away from the imaginary axis. The second condition holds if

$$\sup_{\Re(\lambda)>0,\ |\lambda|\to\infty} \left|\alpha_0(\mathrm{e}^{-\lambda\tau_1}, \ldots, \mathrm{e}^{-\lambda\tau_m})\right| < 1\,, \tag{3}$$

where $\Re(z)$ stands for the real part of z. When $\alpha_0(z_1, \ldots, z_m) \equiv 0$, condition (3) is definitely true. Hence, the trivial solution $x = 0$ of a RDDE is asymptotically stable if and only if all the characteristic roots satisfy $\Re(\lambda) < 0$. [11].

For a better understanding of condition (3) and the root location, let us recall first that because the function $f(\lambda)$ is analytic in the whole complex plane, the roots of $f(\lambda)$ must be isolated. That is to say, any given point in the complex plane cannot be an accumulation point of the characteristic roots. For simplicity, consider the simplest NDDE in the form of

$$\dot{x}(t) + p\dot{x}(t-\tau) + ax(t) + bx(t-\tau) = 0\,. \tag{4}$$

The corresponding characteristic function is

$$f(\lambda) = (1 + p\mathrm{e}^{-\lambda\tau})\lambda + a + b\mathrm{e}^{-\lambda\tau}$$

where $\tau > 0$ is the time delay, and at least one of p and b is not zero. The DDE is of retarded type if $p = 0$, and it is of neutral type if $p \neq 0$. The root location of RDDEs is different from the one of NDDEs.

When $p = 0$, there must be a real number β such that all the roots of $f(\lambda))$ satisfy $\Re(\lambda) < \beta$. In fact, for $p = 0$, if $f(\lambda)$ has a series of roots $\lambda_k = \sigma_k + \omega_k\,\mathrm{i}$, $(k = 1, 2, \ldots)$, with $\sigma_k \to +\infty$ as $k \to +\infty$, then $f(\lambda_k) = 0$ gives

$$\sigma_k + a = -b\mathrm{e}^{-\sigma_k\tau}\cos\omega_k\tau \tag{5}$$

$$\text{and,}\quad \omega = b\mathrm{e}^{-\tau\,\sigma}\sin(\tau\,\omega) \tag{6}$$

which cannot be true because as $k \to +\infty$, the left-hand side of Eq. (5) goes to $+\infty$, while the right-hand side tends to 0. Thus, all roots of $f(\lambda)$ must be smaller than a finite number. Further calculation from Eq. (5) shows $\Re(\lambda) < |b| + |a|$.

Moreover, if $\Re(\lambda) < 0$ holds for all roots of $f(\lambda)$ and $f(\lambda)$ has a series of roots $\lambda_k = \sigma_k + \omega_k \mathrm{i}$, $(k = 1, 2, \ldots)$, with $\sigma_k \to 0$ as $k \to +\infty$, then $\omega_k \to \infty$ as $k \to +\infty$, because any given point in the complex plane cannot be an accumulation point of the characteristic roots. Thus, as $k \to +\infty$, the left-hand side of Eq. (6) goes to $+\infty$, while the right-hand side tends to $|b|$. Thus, if all roots of $f(\lambda)$ have negative real parts, then there must be a positive number ξ such that all the roots of $f(\lambda)$ satisfies

$$\Re(\lambda) < -\xi \,.$$

When $p \neq 0, f(\lambda) = 0$ leads to

$$\frac{\lambda + a}{p\lambda + b} = -\mathrm{e}^{-\lambda\tau} \,.$$

If $f(\lambda)$ has a series of roots $\lambda_k = \sigma_k + \omega_k \mathrm{i}$, $(k = 1, 2, \ldots)$, with $\sigma_k \to +\infty$ as $k \to +\infty$, one has

$$\left| \frac{\sigma_k + \omega_k \mathrm{i} + a}{p(\sigma_k + \omega_k \mathrm{i}) + b} \right| = \mathrm{e}^{-\sigma_k \tau} \,. \tag{7}$$

Then as $k \to +\infty$, the left-hand side and the right-hand side tend to $1/|p|$ and 0, respectively. This contradiction implies that there is a real number β such that $\Re(\lambda) < \beta$ holds for all roots of $f(\lambda)$. Similarly, if $f(\lambda)$ has a series of roots $\lambda_k = \sigma_k + \omega_k \mathrm{i}$, $(k = 1, 2, \ldots)$, with $\sigma_k \to -\infty$ as $k \to +\infty$, one has

$$\left| \frac{p(\sigma_k + \omega_k \mathrm{i}) + b}{\sigma_k + \omega_k \mathrm{i} + a} \right| = \mathrm{e}^{\sigma_k \tau} \,. \tag{8}$$

Then as $k \to +\infty$, the left-hand side and the right-hand side tend to $|p|$ and 0, respectively. The contradiction implies that there is a real number α such that $\Re(\lambda) > \alpha$ holds for all roots of $f(\lambda)$. Thus, there exist two real numbers α, β such that all the roots of $f(\lambda)$ satisfy $\alpha < \Re(\lambda) < \beta$.

If $\Re(\lambda) < 0$ holds for all roots of $f(\lambda)$ and $f(\lambda)$ has a series of roots $\lambda_k = \sigma_k + \omega_k \mathrm{i}$, $(k = 1, 2, \ldots)$, with $\sigma_k \to 0$ as $k \to +\infty$, then $\omega_k \to +\infty$ as $k \to +\infty$, thus Eq. (7) results in $|p| = 1$. This means that for $p = \pm 1$, the infinite many characteristic roots of $f(\lambda)$ may have accumulation point on the imaginary axis, even if all the roots have negative real parts only.

In fact, as shown in [29], with the help of multi-valued Lambert W function $W(z)$, the infinite many roots of $f(\lambda) = (1 + p\mathrm{e}^{-\lambda\tau})\lambda + a$ can be figured out with the help of auxiliary functions

$$F_k(\lambda) = \lambda + a - \frac{1}{\tau} W_k\left(-\tau\, \lambda\, \mathrm{e}^{a\tau}\right), \quad (k = 0, \pm 1, \pm 2, \ldots) \tag{9}$$

where $W_k(z)$ is the k-th branch of the Lambert W function. When $\tau = 0.3$, $a = 0.5$, $b = 0$, some characteristic roots are presented in Table 1, calculated by using Newton–Raphson iteration method for $F_k(\lambda)$ with proper initial values. As $k \to +\infty$,

Table 1 Some roots of $f(\lambda)$, calculated with the help of auxiliary functions $F_k(\lambda)$ [29]

Branch	Characteristic root	Branch	Characteristic root
−200	$-0.2572 \times 10^{-9} - 0.4178 \times 10^{4}\,\mathrm{i}$	1	$-0.3631 \times 10^{-2} + 0.1063 \times 10^{2}\,\mathrm{i}$
−100	$-0.9644 \times 10^{-9} - 0.2084 \times 10^{4}\,\mathrm{i}$	2	$-0.4200 \times 10^{-3} + 0.3147 \times 10^{2}\,\mathrm{i}$
−20	$-0.2498 \times 10^{-5} - 0.4084 \times 10^{3}\,\mathrm{i}$	3	$-0.1517 \times 10^{-3} + 0.5239 \times 10^{2}\,\mathrm{i}$
−10	$-0.1052 \times 10^{-4} - 0.1990 \times 10^{3}\,\mathrm{i}$	4	$-0.7747 \times 10^{-4} + 0.7333 \times 10^{2}\,\mathrm{i}$
−5	$-0.1052 \times 10^{-4} - 0.1990 \times 10^{3}\,\mathrm{i}$	5	$-0.4688 \times 10^{-4} + 0.9427 \times 10^{2}\,\mathrm{i}$
−4	$-0.7747 \times 10^{-4} - 0.7333 \times 10^{2}\,\mathrm{i}$	10	$-0.1052 \times 10^{-4} + 0.1990 \times 10^{3}\,\mathrm{i}$
−3	$-0.1517 \times 10^{-3} - 0.5239 \times 10^{2}\,\mathrm{i}$	20	$-0.2498 \times 10^{-5} + 0.4084 \times 10^{3}\,\mathrm{i}$
−2	$-0.4200 \times 10^{-3} - 0.3147 \times 10^{2}\,\mathrm{i}$	100	$-0.9644 \times 10^{-9} + 0.2084 \times 10^{4}\,\mathrm{i}$
−1	$-0.3631 \times 10^{-2} - 0.1063 \times 10^{2}\,\mathrm{i}$	200	$-0.2572 \times 10^{-9} + 0.4178 \times 10^{4}\,\mathrm{i}$
0	−0.2410	500	$-0.1386 \times 10^{-10} + 0.1046 \times 10^{5}\,\mathrm{i}$

the real and imaginary parts of the characteristic roots calculated from $F_k(\lambda)$ tend to 0 and ∞, respectively. That is to say, though all the roots of $f(\lambda)$ have negative real parts only, the infinite many characteristic roots have an accumulation point on the imaginary axis at the infinity.

Equation (8) implies also that when $|p| > 1$, there is at least one characteristic root with positive real part. In fact, for any roots $\lambda_k = \sigma_k + \omega_k\,\mathrm{i}$ of $f(\lambda)$, with all $\sigma_k < 0$ and $|\lambda_k| \to \infty$ as $k \to +\infty$, the right-hand side of Eq. (8) must be smaller than 1, while the left-hand side of Eq. (8) must be larger than 1 for sufficiently large k, because the limit of the left-hand side is $|p| > 1$ as $k \to +\infty$. As a result, in order that all the characteristic roots of $f(\lambda)$ of the Eq. (4) have negative real parts only and have no accumulation points on the imaginary axis, it is required that $|p| < 1$.

For NDDEs with multiple delays, the stability condition becomes more complicated: condition (3) is only a sufficient one which ensures that the characteristic roots' accumulation points locate in the open left complex plane (away from the imaginary axis). In some rare cases when condition (3) does not hold, the accumulation points can locate in the open left complex plane, and the corresponding NDDEs can be asymptotically stable. However, because the locations of the accumulation points are not continuous with respect to time delays, the accumulation points may show up discontinuously in the right-half complex plane if time delays are perturbed a little bit, the systems lose stability consequently [5]. In what follows, the stability analysis of the linear time-delay system (1) is studied under assumption (3), which guarantees that an asymptotically stable NDDE remains asymptotically stable when subjected to a very small perturbation.

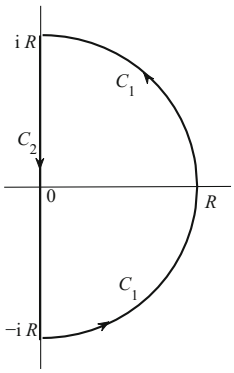

Fig. 1 The contour C of the line integral in Eq. (10)

3 Stability Test of NDDEs

3.1 Stability Criteria

The characteristic function $f(\lambda)$ is a meromorphic function in the right-half complex plane. If $f(\lambda)$ has no roots on the imaginary axis by assumption, then the Argument Principle can be used to represent the number $\mathcal{N}$ of all the unstable roots of $f(\lambda)$ that are located in the right-half complex plane, in terms of a limit of the total change in the argument $\Delta_C \arg(f(\lambda))$ over a contour $C = (C_1 + C_2)$ shown in Fig. 1, namely

$$\mathcal{N} = \lim_{R \to +\infty} \frac{\Delta_C \arg(f(\lambda))}{2\pi} . \tag{10}$$

The trivial solution $x = 0$ is asymptotically stable if and only if $\mathcal{N} = 0$. Equation (10) cannot be used directly for the calculation of $\mathcal{N}$, further effort is required to find a formula that is tractable for stability test. One way is to introduce an auxiliary function $W(\lambda)$ defined by

$$W(\lambda) = \frac{f(\lambda)}{1 + \alpha_0(z_1, \ldots, z_m)} = \lambda^n + \sum_{k=1}^{n} \xi_k(z_1, \ldots, z_m)\lambda^{n-k} \tag{11}$$

where $z_1 = \mathrm{e}^{-\lambda\tau_1}, \ldots, z_m = \mathrm{e}^{-\lambda\tau_m}$, and each $\xi_k(z_1, \ldots, z_m)$ is analytic with respect to $z_1, \ldots, z_m$. Straightforward calculation shows that

$$\mathcal{N} = \lim_{R \to +\infty} \frac{\Delta_C \arg(W(\lambda))}{2\pi} . \tag{12}$$

As proved in [25], one has

$$\mathscr{N} = \frac{n}{2} - \frac{1}{\pi}\arg(W(\omega\,\mathrm{i}))\Big|_{\omega=0}^{\omega\to+\infty} = \frac{n}{2} - \frac{1}{\pi}\int_0^{+\infty} \Re\left(\frac{W'(\omega\,\mathrm{i})}{W(\omega\,\mathrm{i})}\right)\mathrm{d}\omega\,, \tag{13}$$

where $\Re(z)$ stands for the real part of complex number z. Hence, the evaluation of $\mathscr{N}$ can be carried out exactly by using a rough estimation of the improper integral with a sufficiently large upper limit.

Theorem 1 *Assume that $f(\lambda)$ has no roots on the imaginary axis and condition (3) holds. The trivial solution $x = 0$ is asymptotically stable if and only if for sufficiently large $\Omega > 0$, one has*

$$\frac{1}{\pi}\int_0^{\Omega} \Re\left(\frac{W'(\omega\,\mathrm{i})}{W(\omega\,\mathrm{i})}\right)\mathrm{d}\omega > \frac{(n-1)\pi}{2}. \tag{14}$$

Moreover, as discussed in [25], for any $\Omega > 0$, the argument rule gives

$$\begin{aligned}\int_0^{\Omega} \Re\left(\frac{W'(\omega\,\mathrm{i})}{W(\omega\,\mathrm{i})}\right)\mathrm{d}\omega - \int_0^{\Omega} \Re\left(\frac{f'(\omega\,\mathrm{i})}{f(\omega\,\mathrm{i})}\right)\mathrm{d}\omega &= \arg(W(\omega\,\mathrm{i}))\Big|_{\omega=0}^{\omega=\Omega} - \arg(f(\omega\,\mathrm{i}))\Big|_{\omega=0}^{\omega=\Omega} \\ &= -\arg\left(1+\alpha_0(\mathrm{e}^{-\Omega\tau_1\mathrm{i}},\ldots,\mathrm{e}^{-\Omega\tau_m\mathrm{i}})\right)\,.\end{aligned}$$

Unlike for the case with $W(\lambda)$ where the improper integral

$$\int_0^{+\infty} \Re\left(\frac{W'(\omega\,\mathrm{i})}{W(\omega\,\mathrm{i})}\right)\mathrm{d}\omega$$

is convergent, the improper integral

$$\int_0^{+\infty} \Re\left(\frac{f'(\omega\,\mathrm{i})}{f(\omega\,\mathrm{i})}\right)\mathrm{d}\omega$$

is not convergent because $\lim_{\Omega\to+\infty}\arg\left(1+\alpha_0(\mathrm{e}^{-\Omega\tau_1\mathrm{i}},\ldots,\mathrm{e}^{-\Omega\tau_m\mathrm{i}})\right)$ does not exist. Actually, the complex number $1+\alpha_0(\mathrm{e}^{-\omega\tau_1\mathrm{i}},\ldots,\mathrm{e}^{-\omega\tau_m\mathrm{i}})$ is continuous and periodic with respect to ω when all the delays are commensurate, or continuous and quasi-periodic with respect to ω when the delays are incommensurate, thus, there must be a constant $0 < \gamma < \pi/2$ such that

$$\left|\arg\left(1+\alpha_0(\mathrm{e}^{-\omega\tau_1\,\mathrm{i}},\ldots,\mathrm{e}^{-\omega\tau_m\,\mathrm{i}})\right)\right| \le \frac{\pi}{2} - \gamma\,.$$

It follows that there is a number $\Omega_0 > 0$ such that for all $\Omega > \Omega_0$, one has [25]

$$\left|\mathscr{N} - \left(\frac{n}{2} - \frac{1}{\pi}\int_0^{\Omega} \Re\left(\frac{f'(\omega\,\mathrm{i})}{f(\omega\,\mathrm{i})}\right)\mathrm{d}\omega\right)\right| < \frac{1}{2}. \tag{15}$$

Considering that $\mathscr{N}$ is an integer, it can be derived from Eq. (15) that

$$\mathscr{N} = \text{round}\left(\frac{n}{2} - \frac{1}{\pi}\int_0^{\Omega} \Re\left(\frac{f'(\omega\,\mathrm{i})}{f(\omega\,\mathrm{i})}\right)\mathrm{d}\omega\right). \tag{16}$$

Therefore, the following theorem that uses the characteristic function $f(\lambda)$ is true, and the application of this theorem reduces the computational complexity in the stability test significantly.

Theorem 2 *Assume that $f(\lambda)$ has no roots on the imaginary axis and condition (3) holds. The trivial solution $x = 0$ is asymptotically stable if and only if for sufficiently large $\Omega > 0$, one has*

$$\mathscr{N} = \mathit{round}\left(\frac{n}{2} - \frac{1}{\pi}\int_0^{\Omega} \Re\left(\frac{f'(\omega\,\mathrm{i})}{f(\omega\,\mathrm{i})}\right)\mathrm{d}\omega\right) = 0. \tag{17}$$

3.2 Numerical Test

A successful application of Theorem 2 depends on the suitable selection of the upper limit in the testing integral. To this end, let

$$R(\omega) + S(\omega)\,\mathrm{i} = \mathrm{i}^{-n} f(\omega\,\mathrm{i})\,, \tag{18}$$

then $R(\omega)$ and $S(\omega)$ take the following form

$$\begin{aligned} R(\omega) &= (1 + b_0(\omega))\omega^n + b_1(\omega)\omega^{n-1} + \cdots, \\ S(\omega) &= c_0(\omega)\omega^n + c_1(\omega)\omega^{n-1} + \cdots, \end{aligned}$$

where $b_i(\omega)$, $c_i(\omega)$, $i = 0, 1, \ldots, n$ are functions with respect to $\cos(\omega\tau_j)$, $\sin(\omega\tau_j)$, $j = 1, \ldots, m$. Under condition (3), the leading coefficient of $R(\omega)$ is positive, thus $R(\omega) > 0$ for sufficiently large ω. Thus, the number of positive roots of $R(\omega)$ must be finite (if positive roots exist). Straightforward calculation shows that

$$\frac{\mathrm{d}}{\mathrm{d}\omega}\arctan\frac{S(\omega)}{R(\omega)} = \Re\left(\frac{f'(\omega\,\mathrm{i})}{f(\omega\,\mathrm{i})}\right). \tag{19}$$

Theorem 3 *Assume that assumption (3) holds, and $f(\lambda)$ has no roots on the imaginary axis. Let $\Omega_0(\tau_1, \ldots, \tau_m)$ be the maximal positive root of $R(\omega)$, then for all $\Omega > \Omega_0(\tau_1, \ldots, \tau_m)$ (if positive root does not exist, choose $\Omega = 0$), the integer $\mathscr{N}$ satisfies Eq. (16). In particular, the trivial solution $x = 0$ is asymptotically stable, namely $\mathscr{N} = 0$, if Eq. (17) is true for any $\Omega > \Omega_0(\tau_1, \ldots, \tau_m)$.*

The critical upper limit used in Theorem 3 depends on the delays and other system parameters. However, parameter-independent upper limit is preferable when some parameters, like the delays, are not fixed. Due to the harmonic periodicity of $\sin(\omega\tau_j)$

and $\sin(\omega\tau_j)$ in the coefficients of $R(\omega)$ in Eq. (18), each coefficient $b_i(\omega)$ has its infimum $\inf b_i(\omega)$ with respect to $\tau_1, \tau_2, \ldots, \tau_m$, which becomes independent of all delay parameters. Thus for $\omega > 0$,

$$R(\omega) \geqslant R_{\mathrm{L}}(\omega) \stackrel{\text{def}}{=} (1 + \inf b_0(\omega))\omega^n + \inf b_1(\omega)\omega^{n-1} + \cdots \tag{20}$$

where $R_{\mathrm{L}}(\omega)$ is a lower bound of $R(\omega)$. Let Ω_0 be the maximal positive root of $R_{\mathrm{L}}(\omega)$, then Ω_0 is independent of the delays and not less than the maximal positive root of $R(\omega)$. From Theorem 3, the following theorem holds.

Theorem 4 *Assume that assumption (3) holds and the characteristic function $f(\lambda)$ has no roots on the imaginary axis, then there exists a constant Ω_0 independent of the delays $\tau_1, \ldots, \tau_m$ such that $\mathscr{N}$ satisfies Eq. (16) for all $\Omega > \Omega_0$ and all delays. In particular, the trivial solution $x = 0$ is asymptotically stable, namely $\mathscr{N} = 0$, if Eq. (17) holds for any $\Omega > \Omega_0$.*

3.3 Illustrative Examples

Example 1 Consider the following neutral differential equation with single delay

$$\dot{x}(t) = \begin{bmatrix} -2 & 0 \\ 0 & -1 \end{bmatrix} x(t) + \begin{bmatrix} 0 & 0.5 \\ 0.5 & 0 \end{bmatrix} x(t-h) + \begin{bmatrix} 0.2 & 0 \\ 0 & 0.2 \end{bmatrix} \dot{x}(t-h)\,. \tag{21}$$

In [27], it is found using LMI method that the interval of h for the asymptotic stability is $h \in [0, 0.7516)$.

Following Theorem 4, the characteristic function of system (21) reads

$$f(\lambda) = \left(1 - 0.4\mathrm{e}^{-h\lambda} + 0.04\mathrm{e}^{-2h\lambda}\right)\lambda^2 + \left(3 - 0.6\mathrm{e}^{-h\lambda}\right)\lambda - 0.25\mathrm{e}^{-2h\lambda} + 2\,. \tag{22}$$

The two functions defined by Eqs. (18) and (20) read

$$\begin{aligned} R(\omega) = {} & \left(0.96 - 0.4\cos(h\omega) + 0.08\cos^2(h\omega)\right)\omega^2 + 0.6\sin(h\omega)\omega \\ & + 0.50\cos^2(h\omega) - 2.25\,, \\ R_{\mathrm{L}}(\omega) = {} & 0.56\omega^2 - 0.6\omega - 2.25\,. \end{aligned} \tag{23}$$

Thus the largest positive root of $R_{\mathrm{L}}(\omega)$ is $\Omega_0 \approx 2.611$, so we can take $\Omega = 2.7$ for calculating $\mathscr{N}$ using Eq. (16).

The result shown in Fig. 2 indicates that the system is always stable for a given range of $h \in [0, 100]$, which is much larger than $h \in [0, 0.7516)$ derived in [27] and indicates the high possibility that the system is delay-independent stable. Actually, further analytical analysis using the method of stability switch [11] shows that the system is asymptotically stable for all $h \in [0, +\infty)$.

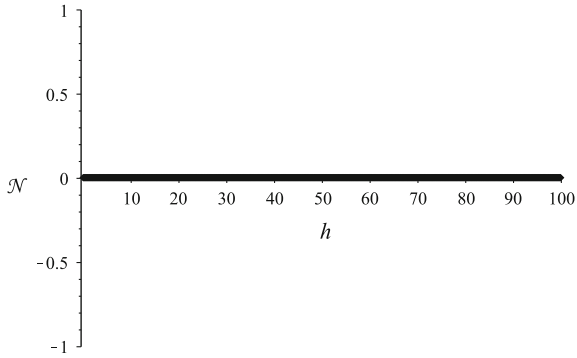

Fig. 2 The number of unstable roots $\mathcal{N}$ of system (21) with respect to $h \in [0, 100]$

Example 2 Consider a more complicated example described by the following neutral delay differential equation

$$\ddot{z}(t) + 2\zeta_1 \dot{z}(t) + z(t) + p\ddot{z}(t - \tau_1) + 2\zeta_2 \dot{z}(t - \tau_2) = 0\,. \tag{24}$$

A detailed stability analysis is made in [28] for the case of $\tau_1 = \tau_2 = \tau$. Below will be focused on the stability chart on (τ_1, τ_2)-plane, using the method of integral evaluation. First the characteristic function of system (21) takes the form of

$$f(\lambda) = \left(1 + p\mathrm{e}^{-\lambda\tau}\right)\lambda^2 + 2\left(\xi_1 + \xi_2\mathrm{e}^{-\lambda\tau}\right)\lambda + 1. \tag{25}$$

With fixed coefficients $p = 0.4, \xi_1 = 0.25, \xi_2 = 0.24$, one can find $R_{\mathrm{L}}(\omega)$ by following the same procedure used in Example 1:

$$R_{\mathrm{L}}(\omega) = 0.6\omega^2 - 0.48\omega - 1, \tag{26}$$

whose largest positive root is $\Omega_0 \approx 1.752$. Hence one can choose $\Omega = 1.8$ for calculating $\mathcal{N}$ using Eq. (16), for each meshed point in the parameter plane (τ_1, τ_2). Figure 3 shows the result of $\mathcal{N}$ with respect to $\{(\tau_1, \tau_2)|\tau_1 \in [0, 20], \tau_2 \in [0, 24]\}$, where the gray parts stand for the stable regions of $\mathcal{N} = 0$. It is worth mentioning that on the boundaries of the stable regions, the testing integral may become improper over the integral interval. However, in practice, with the well developed numerical integration methods such as the adaptive Gaussian quadrature one used for Fig. 3, the results shows both accuracy and efficiency.

4 Calculation of the Rightmost Characteristic Root

Consider a NDDE with $f(\lambda)$ defined in (2) as its characteristic function corresponding to the trivial solution. Let σ be the abscissa of $f(\lambda)$, defined by

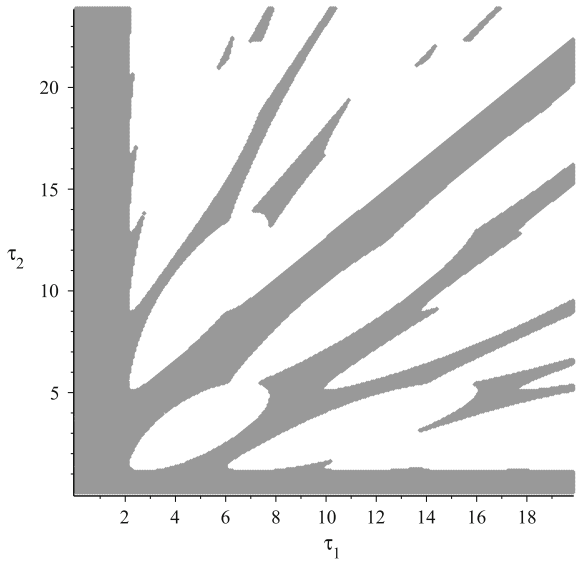

Fig. 3 The stable regions (*gray*) of system (24) with respect to the parameter plane $\{(\tau_1, \tau_2)|\tau_1 \in [0, 20], \tau_2 \in [0, 24]\}$, where $p = 0.4, \xi_1 = 0.25, \xi_2 = 0.24$

$$\sigma = \max\{\Re(\lambda) : f(\lambda) = 0\} .$$

If all the roots are simple, then the rightmost characteristic root is a real number σ, or a pair of conjugate complex numbers with σ as the real part. Under condition (3), the NDDE is asymptotically stable (unstable) if and only if $\sigma < 0$ ($\sigma > 0$). The larger the negative σ in absolute is, the more robustly stable the system is, and the faster the system response converges. Obviously, $f(\lambda) = 0$ has no roots on $\Re(\lambda) = \sigma$ if and only if $f(\sigma + \lambda) = 0$ has no roots on the imaginary axis. For the asymptotic stability, all the roots of $f(\sigma + \lambda) = 0$ have to be bounded away from the imaginary axis, so it is required that

$$\sup_{\substack{\Re(\lambda) > 0 \\ |\lambda| \to \infty}} \left|\alpha_0(\mathrm{e}^{-(\sigma+\lambda)\tau_1}, \ldots, \mathrm{e}^{-(\sigma+\lambda)\tau_m})\right| < 1 . \tag{27}$$

Due to the continuous dependence of the above supreme on σ, for all a that is close enough to σ, one has

$$\sup_{\substack{\Re(\lambda) > 0 \\ |\lambda| \to \infty}} \left|\alpha_0(\mathrm{e}^{-(a+\lambda)\tau_1}, \ldots, \mathrm{e}^{-(a+\lambda)\tau_m})\right| < 1 . \tag{28}$$

Assume that there is a real number a_1 such that for sufficiently large $\Omega > 0$ one has

$$\mathscr{N} = \mathrm{round}\left(\frac{n}{2} - \frac{1}{\pi}\int_0^{\Omega} \Re\left(\frac{f'(a_1 + \omega\,\mathrm{i})}{f(a_1 + \omega\,\mathrm{i})}\right) \mathrm{d}\omega\right) > 0 . \tag{29}$$

Hence the abscissa of $g(\lambda) \overset{def.}{=} f(a_1 + \lambda)$ must be positive. Thus, $a_1 < \sigma$. On the other hand, if there is a real number a_2 such that for sufficiently large $\Omega > 0$ one has

$$\mathscr{N} = \text{round}\left(\frac{n}{2} - \frac{1}{\pi}\int_0^{\Omega} \Re\left(\frac{f'(a_2 + \omega\,\mathrm{i})}{f(a_2 + \omega\,\mathrm{i})}\right) \mathrm{d}\omega\right) = 0\,. \tag{30}$$

Then the abscissa of $g(\lambda)$ must be negative. Thus, $a_2 > \sigma$. For such two numbers a_1, a_2, when $a_2 - a_1$ is small enough, the abscissa σ of $f(\lambda)$ can be estimated to be $\sigma_0 = (a_1 + a_2)/2$. Also, the real parts of the characteristic roots besides the rightmost root(s) can be estimated using the same procedure.

The real parts of the characteristic roots can be identified as follows: (i) Calculate the real part $R(\omega)$ of $\mathrm{i}^{-n} f(a + \omega\,\mathrm{i})$. (ii) Find an uniform upper limit Ω valid for a given interval of the value a using the lower bound $R_{\mathrm{L}}(\omega)$ of $R(\omega)$, where all the values of a should all satisfy Eq. (28). (iii) Figure out the number of unstable roots of $f(a + \lambda) = 0$ for each meshed point $a = a_i$ using

$$\mathscr{N} = \text{round}\left(\frac{n}{2} - \frac{1}{\pi}\int_0^{\Omega} \Re\left(\frac{f'(a_i + \omega\,\mathrm{i})}{f(a_i + \omega\,\mathrm{i})}\right) \mathrm{d}\omega\right)\,. \tag{31}$$

(iv) Estimate the real parts of the characteristic roots of $f(\lambda)$ by identifying the coordinates of a where $\mathscr{N}$ jumps from one integer to another. In particular, the rightmost root(s) corresponds to the coordinate(s) of a where $\mathscr{N}$ jumps from a positive integer directly to 0, while the other roots correspond to the coordinates of a where $\mathscr{N}$ jumps from one positive integer to another (smaller) positive one.

In order to calculate the rightmost root (or a pair of conjugate rightmost characteristic roots), an estimation ω_0 of the imaginary part ω of the rightmost characteristic root(s) can be found numerically from $f(\sigma_0 + \mathrm{i}\omega) \approx 0$. Each real root ω of $f(\sigma_0 + \mathrm{i}\omega) \approx 0$ corresponds to a possible characteristic root (finite and isolated) on the line $\Re(\lambda) = \sigma$. Then the exact rightmost characteristic root(s) can be obtained with the estimation $\sigma_0 + \mathrm{i}\omega_0$ using the Newton–Raphson iteration method with a few number of iterations:

$$\lambda_{i+1} = \lambda_i - \frac{f(\lambda_i)}{f'(\lambda_i)}, \quad i = 0, 1, 2, \ldots\,. \tag{32}$$

For a given tolerance $\varepsilon > 0$, the iteration is stopped if $|\lambda_{k+1} - \lambda_k| < \varepsilon$, see [25].

Example 3 Consider again the system (24) in Example 2 for demonstration. For fixed coefficients $p = 0.4, \xi_1 = 0.25, \xi_2 = 0.24$, as shown in Fig. 3, this system is stable when $\tau_1 = 8, \tau_2 = 10$. The real part $R(\omega)$ of $(\mathrm{i}^{-n})f(a + \lambda)$ takes the form of

$$\begin{aligned} R(\omega) = {} & \left(1 + 0.4\mathrm{e}^{-8a}\cos(8\omega)\right)\omega^2 - \left(0.8\mathrm{e}^{-8a}\sin(8\omega)\,a + 0.48\mathrm{e}^{-10a}\sin(10\omega)\right)\omega \\ & - \left(1 + 0.4\mathrm{e}^{-8a}\cos(8\omega)\right)a^2 - \left(0.48\mathrm{e}^{-10a}\cos(10\omega) + 0.5\right)a - 1\,. \end{aligned}$$

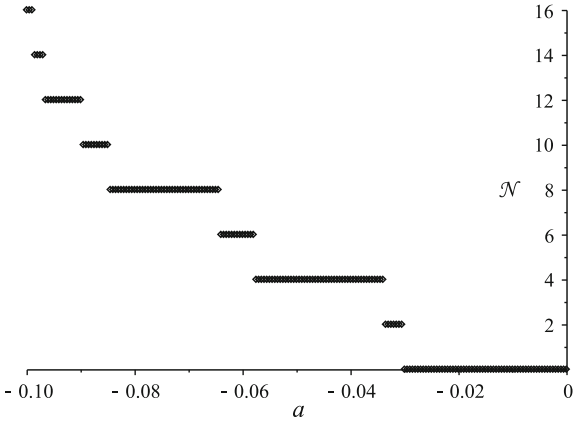

Fig. 4 The number of unstable roots of $f(a+\lambda)=0$ with respect to $a \in [-0.1, 0]$, for system (24) with $p = 0.4, \xi_1 = 0.25, \xi_2 = 0.24, \tau_1 = 8, \tau_2 = 10$

For a given range of $a \in [-0.1, 0]$, one has

$$R_{\mathrm{L}}(\omega) = (1 - 0.4\mathrm{e}^{0.8})\omega^2 - (0.8\mathrm{e}^{0.8} \cdot 0.1 + 0.48\mathrm{e})\omega - \left(1 + 0.4\mathrm{e}^{0.8}\right) \cdot 0.01 - (0.48\mathrm{e} + 0.5) \cdot 0.1 - 1,$$

whose largest positive root is about $\Omega_0 \approx 14.272$. Thus, one can choose $\Omega = 14.3$ as the upper limit of Eq. (31) for $a \in [-0.1, 0]$.

The results of $\mathcal{N}$ with respect to a in a given interval $[-0.01, 0]$ is shown in Fig. 4 using adaptive Gaussian quadrature method, from which we can see that $\mathcal{N}$ jumps 8 times, from 16 to 0, hence for system (24) with $p = 0.4, \xi_1 = 0.25, \xi_2 = 0.24, \tau_1 = 8$, and $\tau_2 = 10$, there are 8 pairs of conjugate characteristic roots whose real parts are larger than -0.01. The pair of rightmost roots corresponds to a value of a close to -0.033, where $\mathcal{N}$ jumps from 2 to 0, thus the abscissa σ, namely the real part of the rightmost roots, is close to -0.033. Further estimation of the imaginary part and refinement using iteration method find that the pair of rightmost roots is $\lambda = -0.0336 \pm 1.3725\mathrm{i}$.

5 Conclusions

Unlike that the real parts of the RDDEs' infinitely many characteristic roots go to negative infinity, the real parts of the NDDEs' infinitely many characteristic roots are bounded, which adds more complexity to the asymptotic stability of NDDEs. Under a special condition, the definite integral method is very effective in judging the stability of NDDEs by calculating the number of the unstable roots through a testing integral over a roughly chosen interval. It works not only in testing whether the NDDE is asymptotically stable or not, but also in finding the rightmost characteristic roots. In addition, with a properly chosen upper limit of the testing integral for calculating

the number of unstable roots, the stability domain can be easily determined in the parameter space. The proposed method is particularly useful for the stability test of NDDEs with multiple time delays.

Acknowledgements This work was supported by NSF of China under Grant 11372354, and by the Fund of the State Key Lab of Mechanics and Control of Mechanical Structures under Grant MCMS-0116K01.

References

1. Masoud, Z.N., Nayfeh, A.H.: Sway reduction on container cranes using delayed feedback controller. Nonlinear Dyn. **34**(3–4), 347–358 (2003)
2. Orosz, G., Wilson, R.E., Stepan, G.: Traffic jams: dynamics and control. Philos. Trans. Royal Soc. A: Math. Phys. Eng. Sci. **368**(1928), 4455–4479 (2010)
3. Xu, Q., Stepan, G., Wang, Z.H.: Balancing a wheeled inverted pendulum with a single accelerometer in the presence of time delay. J. Vib. Control (2015). doi:10.1177/1077546315583400
4. Bellen, A., Guglielmi, N., Ruehli, A.E.: Methods for linear systems of circuit delay differential equations of neutral type. IEEE Trans. Circuits Syst. I: Fundam. Theory Appl. **46**(1), 212–216 (1999)
5. Hale, J.K., Lunel, S.M.V.: Strong stabilization of neutral functional differential equations. IMA J. Math. Control Inf. **19**(1 and 2), 5–23 (2002)
6. Michiels, W., Niculescu, S.-I.: Stability and Stabilization of Time-Delay Systems (Advances in Design and Control). Society for Industrial and Applied Mathematics, PA (2007)
7. Zhang, L., Stepan, G.: Exact stability chart of an elastic beam subjected to delayed feedback. J. Sound Vib. (2016). doi:10.1016/j.jsv.2016.01.002
8. Erneux, T.: Applied Delay Differential Equations. Springer, London (2009)
9. Niculescu, S.-I.: Delay Effects on Stability: A Robust Control Approach. Springer, London (2001)
10. Stepan, G.: Retarded Dynamical Systems: Stability and Characteristic Functions. Longman Scientific & Technical Essex (1989)
11. Kuang, Y.: Delay Differential Equations: with Applications in Population Dynamics. Academic Press, London (1993)
12. Niculescu, S.-I.: A model transformation class for delay-dependent stability analysis. In: American Control Conference, pp. 314–318 (1999)
13. Gu, K., Niculescu, S.-I.: Additional dynamics in transformed time-delay systems. IEEE Trans. Autom. Control **45**(3), 572–575 (2000)
14. Ivanescu, D., Niculescu, S.-I., Dugard, L., Dion, J.-M., Verriest, E.I.: On delay-dependent stability for linear neutral systems. Automatica **39**(2), 255–261 (2003)
15. Insperger, T., Stepan, G.: Semi-discretization method for delayed systems. Int. J. Numer. Methods Eng. **55**, 503–518 (2002)
16. Insperger, T., Stepan, G., Janos, T.: Delayed feedback of sampled higher derivatives. Philos. Trans. Roy. Soc. A **368**, 469–482 (2010)
17. Pontryagin, L.S.: On the zeros of some elementary transcendental functions. Izvestiya Akademii Nauk. Seriya Matematicheskaya (Russian) **6**(3), 115–134 (1942). English translation (1955) in American Mathematical Society Translations, 2, 95–110
18. Olgac, N., Sipahi, R.: An exact method for the stability analysis of time-delayed linear time-invariant (LTI) systems. IEEE Trans. Autom. Control **47**(5), 793–797 (2002)
19. Olgac, N.: A practical method for analyzing the stability of neutral type LTI-time delayed systems. Automatica **40**(5), 847–853 (2004)

20. Sipahi, R., Olgac, N.: Complete stability analysis of neutral-type first order two-time-delay systems with cross-talking delays. SIAM J. Control Optim. **45**(3), 957–971 (2006)
21. Fu, M., Olbrot, A.W., Polis, M.: Robust stability for time-delay systems: the edge theorem and graphical tests. IEEE Trans. Autom. Control **34**(8), 813–820 (1989)
22. Fu, M., Olbrot, A.W., Polis, M.: The edge theorem and graphical tests for robust stability of neutral time-delay systems. Automatica **27**(4), 739–741 (1991)
23. Hassard, B.: Counting roots of the characteristic equation for linear delay-differential systems. J. Differ. Equ. **136**(2), 222–235 (1997)
24. Kolmanovskii, V., Myshkis, A.: Introduction to the Theory and Applications of Functional Differential Equations. Kluwer Academic Publishers, Dordrecht (1999)
25. Xu, Q., Wang, Z.H.: Exact stability test of neutral delay differential equations via a rough estimation of the testing integral. Int. J. Dyn. Control **2**(2), 154–163 (2014)
26. Xu, Q., Stepan, G., Wang, Z.H.: Delay-dependent stability analysis via delay-independent integral estimation. Automatica **70**(8), 153–157 (2016)
27. Park, J.H., Won, S.: Stability analysis for neutral delay-differential systems. J. Frankl. Inst. **337**, 1–9 (2000)
28. Kyrychko, Y.N., Blyuss, K.B., Hovel, P., Scholl, E.: Asymptotic properties of the spectrum of neutral delay differential equations. Dyn. Syst. Appl.: Int. J. **24**(3), 361–372 (2009)
29. Wang, Z.H.: Numerical stability test of neutral delay differential equations. Math. Probl. Eng. **2008**, 10. doi:10.1155/2008/698043. Article ID 698043

Utilizing Topological Data Analysis for Studying Signals of Time-Delay Systems

Firas A. Khasawneh and Elizabeth Munch

Abstract This chapter describes a new approach for studying the stability of stochastic delay equations by investigating their time series using topological data analysis (TDA). The approach is illustrated utilizing two stochastic delay equations. The first model equation is the stochastic version of Hayes equation—a scalar autonomous delay equation—where the noise is an additive term. The second model equation is the stochastic version of Mathieu's equation—a time-periodic delay equation. In the latter, noise is added via a multiplicative term in the time-periodic coefficient. The time series is generated using Euler–Maruyama method and a corresponding point cloud is obtained using the Takens' embedding. The point cloud is then analyzed using a tool from TDA known as persistent homology. The results of this study show that the described approach can be used for analyzing datasets of delay dynamical systems that are described using constant as well as time-periodic coefficients. The presented approach can be used for signals generated from both numerical simulation and experiments. It can be used as a tool to study the stability of stochastic delay equations for which there are currently a limited number of analysis tools.

1 Introduction

Delay differential equations are used widely in science and engineering to model systems whose evolution depends on their past history. Although the majority of delay equation models in the literature are assumed to be deterministic, their analysis is still not trivial due to their infinite-dimensional nature [1–3]. While the assumption of determinism is commonplace when investigating the evolution of natural and

F.A. Khasawneh (✉)
Mechanical Engineering, SUNY Polytechnic Institute, Utica, NY 13502, USA
e-mail: firas.khasawneh@sunyit.edu

E. Munch
Department of Mathematics and Statistics, University at Albany – SUNY, Albany, NY 12222, USA
e-mail: emunch@albany.edu

T. Insperger et al. (eds.), *Time Delay Systems*,
Advances in Delays and Dynamics 7, DOI 10.1007/978-3-319-53426-8_7

engineered systems, all processes are in fact inherently stochastic with many possible noise sources. For example, machining processes, which are often modeled using delay equations, can include stochasticity due to the variation of the material parameters [4, 5], external noise sources [6], and variations of the delay [7]. In addition to machining dynamics, stochastic delay differential equations (SDDEs) arise in many applications such as chemical kinetics [8] and genetic networks [9].

The analysis methods for the stability of stochastic delay systems are few or nonexistent in comparison to the available tools for deterministic DDEs. For some special SDDEs, stochastic calculus can be used to study the stability in moments [10]. When the delay is small, the SDDE can sometimes be approximated using a stochastic, non-delayed differential equation [11]. Alternatively, the moment stability of linear SDDEs with delays in the diffusion term only can be studied using semi-discretization [12]. The stability of the latter class of SDDEs can also be investigated using a Lyapunov approach [13].

Fourier transform and the power spectrum have also been used for data analysis especially when the signal is periodic. However, when the signal is non-periodic, the discrete Fourier transform (DFT) will result in errors unless when the signal meets a specific set of criteria [14]. Further, Fourier transform and other frequency-domain methods do not account for the signal evolution in time, e.g., trending, and are limited when analyzing time series with quasi-periodic motion [15]. Some of these limitations have been addressed successfully using time–frequency methods [16] and wavelets [17]. However, the topic of analyzing stochastic delay models remains an active and open research topic, and numerical simulation remains the most general approach for studying these models.

Simulation methods for stochastic differential equations such as Euler–Maruyama and Milstein were extended to SDDEs in [18–21] and [22], respectively. The simulated path-wise solutions can be easier to investigate than the original SDDE. Specifically, the paths generated by numerical simulation can be used for studying the mean square (or more generally, the pth mean) stability of the original SDDE [23–25]. Developing data analysis tools for the resulting data provides a benchmark for testing new analysis methods for SDDE, and allows the analysis of experimental data from real-world processes. One tool that has been successfully used recently for SDDEs is based on topological data analysis [26–28].

The idea behind this method is to use the Takens embedding [29] to turn a signal into a point cloud in high-dimensional space and analyze the resulting point cloud using persistence. In [30], it was shown that this method provides a framework to parameterize dynamics; the procedure is also amenable to combination with machine learning for automation [31]. Variations of this idea along with broader applications of topology have been used to study signals from human speech [32], wheezing in breathing signals [33], gene expression data [34–37], computer architecture [38, 39], and character animation [40]. See also Chap. 6 of [41] or [42] for the formulation of the procedure using cohomology.

In this study, we show that a TDA-based approach also applies to time-periodic stochastic delay equations with multiplicative noise. The model equation we use is the stochastic delayed damped Mathieu equation where the stochastic component is

introduced in the coefficient of the time-periodic term. In particular, we will use persistent homology [43–46] to automatically detect when changes in the system behavior indicative of instability occur near the stability boundary of the model equations.

2 Background

2.1 Takens Embedding

In order to study the time series, we use Takens embedding, a standard tool from time series analysis [15]. Given a time series $X(t)$, fix a lag parameter $\eta > 0$ and dimension $m \in \mathbb{Z}_{>0}$. Then the Takens embedding of the time series is a lift of the time series to the map

$$t \mapsto (X(t), X(t+\eta), X(t+2\eta), \ldots, X(t+(m-1)\eta)).$$

Via Takens theorem [29], we know that for most choices of m and η, the Takens embedding represents the underlying dynamics of the dynamical system. When we are provided with a discrete time series $X(t_n)$, the resulting embedding is a point cloud, which we investigate using persistent homology.

2.2 Persistent Homology

Persistent homology is a tool arising from the field of topological data analysis which gives a quantitative signature representing the shape of a data set. In the case of data coming from a Takens embedding, we are initially provided with a point cloud, a discrete set of points $\mathscr{P}$, in $\mathbb{R}^m$. Consider the example of Fig. 1. Initially, this data is simply a discrete set of points and thus, while we have an intuition for structure, none is directly seen in the data. To approximate this structure, we can place a disk of radius r centered at each point, and use the union of the disks as a proxy for the structure. Of course, choosing a radius which is too small yields no additional information as r may not be big enough for disks to intersect with neighboring disks. On the other hand, choosing a radius which is too large means that the union of disks sees no structure beyond one giant component, and thus still does not provide a useful representation of the shape. However, there is a collection of intermediate radii which do show that the structure of the point cloud is two circles. Thus, rather than requiring a single fixed radius to represent the structure, we look at the range of radii for which we have interesting structure.

To determine this range of radii, we adopt the following method. Starting from $r = 0$, let the radius grow and watch as features, in particular circles, appear and disappear. We say a circle is born at the radius at which it appears, and dies at the

radius at which it is filled in. Thus, for each circular structure, we get a point in $\mathbb{R}^2$, (birth radius, death radius). This data is stored in a *persistence diagram* as shown in the bottom right of Fig. 1.

The next question is how these features are determined. This is done using persistent homology, an emergent tool from the field of topological data analysis; see e.g., [47, 48] for a full introduction to homology and [43, 45] for an introduction to persistent homology. For any given topological space $\mathbb{X}$, which is the union of disks in our example above, homology[1] provides a vector space $H_k(\mathbb{X})$ for each dimension $k = 0, 1, 2, \ldots$. Lower dimensions are the most useful for our computational purposes here; in particular, the rank of the zero-dimensional homology group $H_0(\mathbb{X})$ gives the number of connected components, while the rank of the one-dimensional homology group $H_1(\mathbb{X})$ gives the number of loops in the space. To deal with the changing radius, let $\mathbb{X}_r$ be the union of disks of radius r for a given point cloud $\mathscr{P}$. Because we have inclusions $\mathbb{X}_r \subseteq \mathbb{X}_s$ for $r \leq s$, homology theory provides us with linear maps $H_k(\mathbb{X}_r) \to H_k(\mathbb{X}_s)$ between the homology groups. Let us restrict our attention to just one-dimensional homology, and to the radii for which there is a topological change in the union of disks $0 = r_0 < r_1 < r_2 < \cdots < r_n$; note that this is a subset of the collection of distances $\{\frac{1}{2}\|p - q\| \mid p, q \in \mathscr{P}\}$ since these are exactly the times when some pair of disks first touch. Then a generator $\gamma \in H_1(\mathbb{X}_{r_i})$ represents a circle which is born at radius r_i if it is not in the image of $H_1(\mathbb{X}_{r_{i-1}}) \to H_k(\mathbb{X}_{r_i})$. This circle dies at radius r_j if the image of γ in $H_1(\mathbb{X}_{r_j})$ is not contained in the image of $H_1(\mathbb{X}_{r_{i-1}})$ in $H_1(\mathbb{X}_{r_{j-1}})$, but is contained in the image of $H_1(\mathbb{X}_{r_{i-1}})$ in $H_1(\mathbb{X}_{r_j})$.

The persistence diagram is then drawn to show the birth/death pairs (r_i, r_j) for all generators representing circular structures. An example persistence diagram is given in the bottom left of Fig. 1. We often represent this persistence diagram as its collection of off-diagonal points in $\mathbb{R}^2$.

The persistence diagram is a particularly useful representation of the shape of the data since it is stable with respect to noise in the following sense. The space of persistence diagrams admits a metric, called the *bottleneck distance* d_B (see, e.g., [45] for a full definition). Say we have two point clouds $\mathscr{P}$ and $\mathscr{Q}$, giving rise to two filtrations $\{\mathbb{X}_{r_i}\}$ and $\{\mathbb{Y}_{s_i}\}$, and thus two persistence diagrams $\mathrm{Dgm}(\mathscr{P})$ and $\mathrm{Dgm}(\mathscr{Q})$. Then the diagrams satisfy the stability inequality

$$d_B(\mathrm{Dgm}(\mathscr{P}), \mathrm{Dgm}(\mathscr{Q})) \leq d_H(\mathscr{P}, \mathscr{Q}),$$

where d_H is the standard Hausdorff distance [49]. This, in particular, implies that if the point clouds are close, the diagrams will be close, thus making the persistence diagram a reasonable choice of representation for the shape even in the presence of noise. In addition, the persistence diagram can be computed in matrix multiplication time [50], thus making it a very useful computational tool. See also [51] for a comparison of available software packages.

[1] We are using homology with $\mathbb{Z}_2$ coefficients, hence $H_k(\mathbb{X})$ is always a vector space.

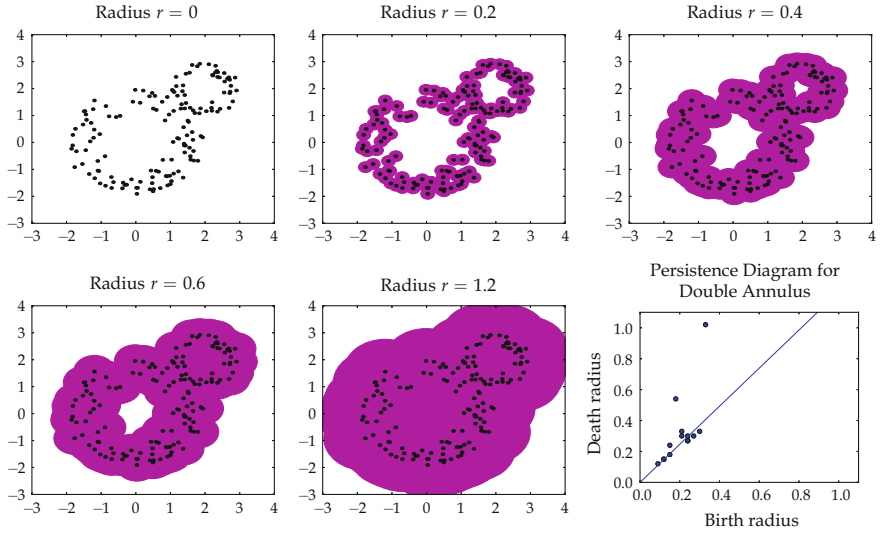

Fig. 1 Persistent homology is used to give a representation for the structure of the point cloud by growing disks around each point and using the union of the disks as an approximation of the structure. Each circular structure in the union of disks which is born at radius r and dies at radius s is represented by a point at (r, s) in the persistence diagram. Points far from the diagonal represent circular structures which lived the longest, and thus are considered to be representative of the true structure

2.3 Maximum Persistence

The points in the persistence diagram are all above the diagonal $\Delta = \{(x, x) \in \mathbb{R}^2\}$ since classes can only die after they are born. Note that points that are far from the diagonal represent circular structures which *persist* for a longer time; that is, they are present in the union of disks for a large collection of radii. Thus, these are often treated as representing inherent features of the point cloud $\mathscr{P}$. Points that are close to the diagonal appeared and disappeared almost immediately; thus, they are often treated as noise. For this project, we are particularly interested in differentiating between circular and non-circular point clouds. Thus, we will focus on the maximum persistence of a persistence diagram, defined as $\text{maxPers}(D) = \max_{(r,s)\in D} s - r$.

Consider the example of Fig. 2. The three signals on the top row come from the Hayes equation, discussed in Sect. 3.1 with $\delta = 0.03$ and parameters as listed in the top row. The second row gives the Takens embedding in two dimensions for each, and the last row gives the persistence diagrams for each. Note that as the Takens embedding becomes more circular, the persistence diagram has a more prominent off-diagonal point. The maximum persistence of each diagram is the distance from this point to the diagonal.

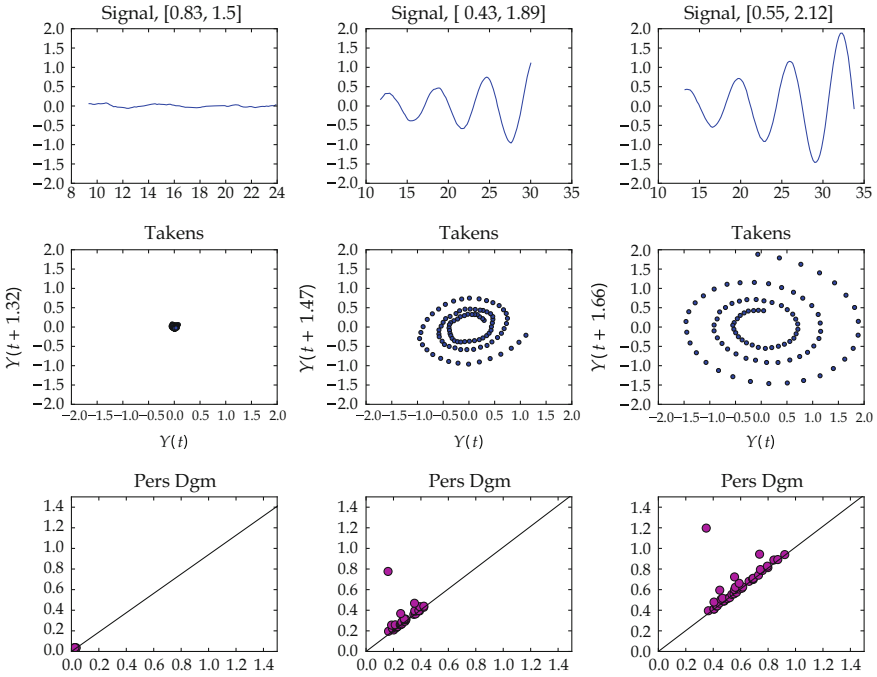

Fig. 2 Three signals, their associated Takens embeddings, and the resulting persistence diagrams for the stochastic Hayes equation (2). Note that as the signal becomes more periodic, the Takens embedding becomes more circular, and the persistence diagram has a more prominent off-diagonal point

3 Stochastic Model Equations

This section describes the equations that are used to generate the time series for the TDA approach. Two fundamental model equations are used [52]: Sect. 3.1 describes the stochastic Hayes equation, a scalar SDDE, while Sect. 3.2 shows the stochastic Mathieu equation as a model for an SDDE with time-periodic coefficients. In this study, all stochastic equations are interpreted in the Ito sense [53].

3.1 Scalar Autonomous SDDE: Stochastic Hayes Equation

The model equation for scalar autonomous DDEs is Hayes equation [52]. The deterministic version of Hayes equation is given by

$$\dot{x} = \alpha x(t) + \beta x(t - \tau), \tag{1}$$

where α and β are scalars while τ is the positive delay. The stability boundaries to this simple problem can be charted analytically [2], although in this study we use the spectral element method to find the stability boundaries the deterministic version of the model equations [54]. The stability diagram in the (a, τ) parameter space for the noise-free Hayes equation with $\beta = -\sqrt{2}$ is shown in Fig. 3a.

The scalar autonomous SDDE model is obtained by introducing noise to Hayes equation through additive terms according to

$$dx = (\alpha x(t) + \beta x(t - \tau))dt + \delta dB, \tag{2}$$

where τ is a constant delay, α and β are constants, δ is a parameter that represents the noise intensity, and B is a standard Brownian motion. This equation was used to illustrate stochastic resonance in [55]. Including noise in the model triggers stochastic resonance where the system behavior becomes oscillatory for values of τ near the boundary but still within the stable region for the deterministic system.

3.2 Time-Periodic SDDE: Stochastic Mathieu Equation

The model equation that will be used for time-periodic SDDE is Mathieu's equation [52, 56, 57] whose deterministic version is given by

$$\ddot{x}(t) + \kappa \dot{x}(t) + (a + \varepsilon \cos(2\pi/T)t)x(t) = bx(t - \tau), \tag{3}$$

where κ, a, ε and b are scalars, the time period is T, and the constant positive delay is τ. The stability diagram in the (a, b) parameter space is shown in Fig. 3b.

Now, if the coefficient of the time-periodic term becomes stochastic according to

$$\varepsilon = \hat{\varepsilon} + \delta \frac{dB}{dt}, \tag{4}$$

where $\hat{\varepsilon} = 1$ is the nominal value of ε while B is the standard Brownian motion, then the stochastic version of Eq. (3) can be written as

$$dX_1 = X_2 dt, \tag{5a}$$

$$dX_2 = \left(-\kappa X_2 - (a + \hat{\varepsilon} \cos t)X_1\right) dt - \delta \cos t X_1 dB, \tag{5b}$$

where the term multiplying dt is the drift term, while the term multiplying dB is the diffusion term. Notice that in this case we have multiplicative noise in the time-periodic term.

4 Results

This section starts by describing the simulation parameters in Sect. 4.1, and the persistence computation is discussed in Sect. 4.2. The results of the simulation for the stochastic Hayes SDDE described by Eq. (2) are shown in Sect. 4.3, and the results for Mathieu's SDDE, Eq. (5b), are shown in Sect. 4.4.

4.1 Numerical Simulation

Stochastic Hayes Equation (2) and stochastic Mathieu equation (5b) were simulated using the Euler–Maruyama method described in [18]. The resulting datasets were generated for each point on the grid used for generating the stability diagrams of Fig. 3. The simulation parameters used for each example are shown in Table 1. For irrational values of the delay τ, the delay term requires intermediate values of x that lie between any two Brownian increments. In this case, we picked the value of x at the left end of the increment, similar to the procedure used in [12].

The Brownian path was created using Python and the approach described in [58]. For each point in the parameter space grid, 5 realizations were generated. For each realization, Python's function *numpy.random.randn(seed = None)* was used to seed the random number generator using the system's clock in order to produce a different path in each run.

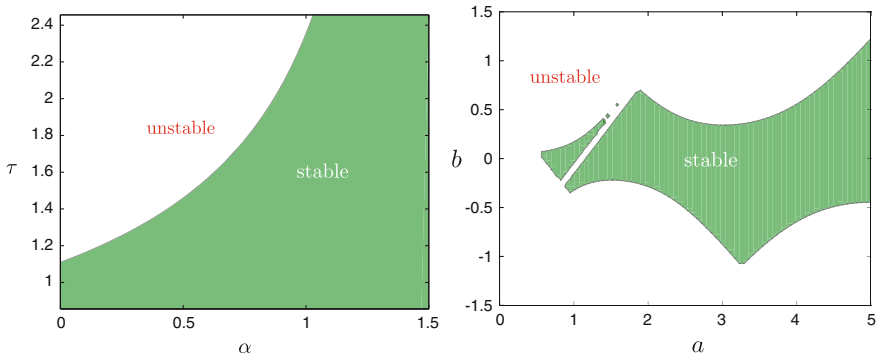

Fig. 3 On the *left*, the stability diagram corresponding to Eq. (2) with $\beta = -\sqrt{2}$. A grid of 50×50 in the (α, τ) was used. The spectral element method with one temporal element and an interpolating polynomial of order 20 was utilized to calculate the stability diagram [54]. On the *right*, the stability diagram corresponding to Eq. (3) with parameter values $\kappa = 0.2$, $\varepsilon = 1$, and $T = \tau = 2\pi$. An 80×80 grid was used in the (a, b) parameter space. One temporal element with an interpolating polynomial of order 20 was used

Table 1 The parameters used in the Euler–Maruyama simulation

	Stochastic Hayes	Stochastic Mathieu
Brownian path time step	$\delta t = \tau \times 2^{-11}$	$\delta t = \pi \times 2^{-9}$
Euler–Maruyama time step	$\Delta t = \tau \times 2^{-9}$	$\Delta t = \delta t = \pi \times 2^{-9}$
Simulation end time	$\tau \times 2^4$	$\pi \times 2^7$
History function for $t \in [-\tau, 0]$	$x = 0.1$	$x(t) = 0.001$ for $t = 0$, $x(t) = 0$ for $t < 0$

4.2 *Persistence Computation*

For each time series, the last K points were chosen, where K is 5,000 and 10,000 for the Hayes and Mathieu simulations, respectively. To further sparsify the data, every ℓ point was retained, where ℓ is 50 and 100, respectively. The resulting time series was embedded in $\mathbb{R}^3$ using the Takens embedding. The lag parameter η was chosen for each time series using the first zero of the autocorrelation function [15]. Persistence was computed using the M12 package [59] up to radius 100,000. For the purposes of drawing Figs. 4 and 5, only the maximum persistence for each diagram was retained. For each pair of parameter values, the five realizations yielded five persistence diagrams, and thus five values for maximum persistence. The heat maps in Figs. 4 and 5 show the average of these five values at each parameter pair.

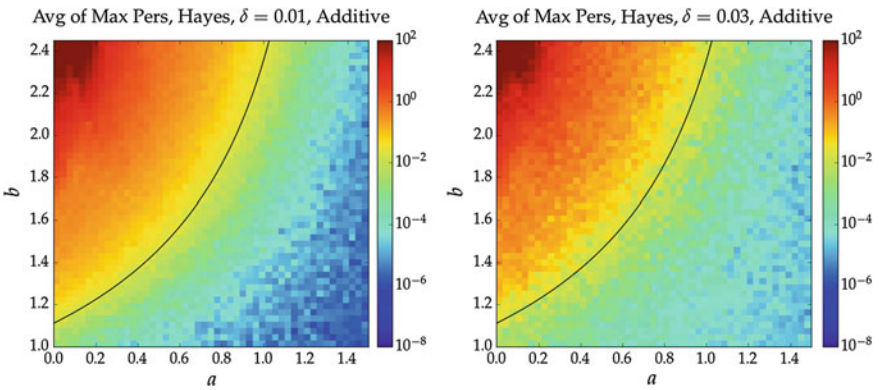

Fig. 4 Stability diagrams obtained using the described topological data analysis approach. The results represent the average maximum persistence of five realizations at every grid point for the stochastic Hayes equation with additive noise, Eq. (2). The *left* and *right* figures show the results for $\delta = 0.01$ and $\delta = 0.03$, respectively. For both cases, the stability diagram for the noise-free case shown in Fig. 3a is overlaid using a *black line*

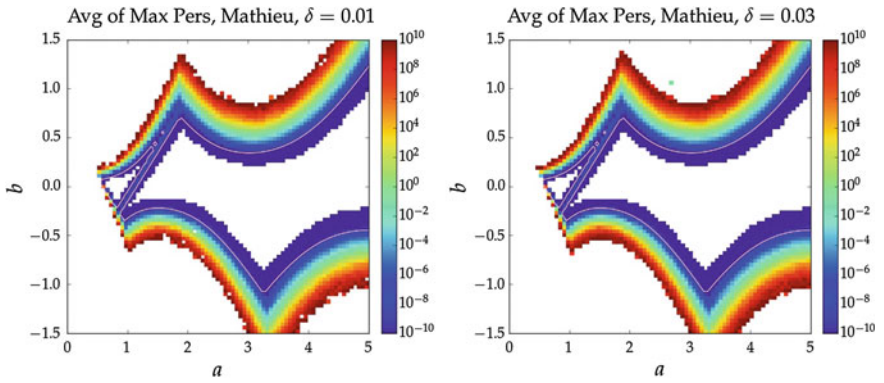

Fig. 5 Stability diagrams obtained using the described topological data analysis approach. The results represent the average maximum persistence of five realizations at every grid point. The *left* and the *right* figures show the results for the stochastic Mathieu equation, Eq. (5b), at noise levels $\delta = 0.01$ and $\delta = 0.03$, respectively. The stability diagram for the noise-free case shown in Fig. 3a is overlaid using a white line. Notice how the approach was capable of detecting the separate stability island to the *left* of the main stability lobe

4.3 Stocahstic Hayes Equation Results

The results of applying the described TDA approach to the stochastic Hayes equation are shown in Fig. 4. Two levels of noise were investigated: $\delta = 0.01$ (left figure) and $\delta = 0.03$ (right figure). The black line shows the stability boundary for the noise-free Hayes equation which was shown in Fig. 3. For this example, oscillatory behavior occurs as the parameter combination in the stable area below the shown boundary approaches the stability boundary [55]. The regions farthest from the boundary are characterized by a low average maximum persistence (10^{-8}), while maximum persistence increases closer to the boundary. Note how across the deterministic stability boundary the average persistence is two orders of magnitude higher. Farther above the stability boundary, the value of the average persistence keeps increasing up to 10^2 in the shown range.

4.4 Stochastic Mathieu Equation Results

Figure 5 shows the average maximum persistence for 5 iterations of the stochastic Mathieu equation (5b). Noise levels $\delta = 0.01$ and $\delta = 0.03$ are shown in the left and right panels of the figure, respectively. The overlaid white line represents the stability boundary for the noise-free Mathieu equation, which was shown in Fig. 3. Notice the jump in the magnitude of the average maximum persistence near the deterministic stability boundary. It is also interesting to see that the described TDA approach

was able to identify the separate stability island which is approximately centered at $(a, b) = (1, 0)$ to the left of the main stability lobe.

One observation to make here is that now there are white regions away from the colored stability boundaries. These white regions correspond to cases where the resulting persistence diagram was empty, thus leading to a maximum persistence value of NaN (not a number). The explanation for these regions and how stable and unstable regions can be delineated is included in Sect. 5.

5 Discussion

Stochastic Hayes equation: Figure 4 shows that persistence was able to provide a threshold for the stability of the stochastic Hayes equation for both noise levels: $\delta = 0.01$ and $\delta = 0.03$. Another observation is that the region around the boundary contains mixed values for maximum persistence. This reflects the phenomenon of stochastic resonance where noise can cause transitions between the stable and unstable attractors of the system [55].

Increasing the noise value from 0.01 in the left figure to 0.03 in the right figure caused the value of maximum persistence to increase far into the stable region. Nevertheless, the results still show the stability structure of the system and the stability threshold can still be distinguished. This figure shows that the average of the maximum persistence for the five iterations retained the stability information of the system. This contrasts the loss of information associated with pointwise averaging of the time series, as was shown in [28].

Stochastic Mathieu's equation: The stability results shown in Fig. 5 show that TDA can be used to ascertain the stability of SDDEs with time-periodic coefficients. However, the stability diagrams for the stochastic Mathieu's equation showed white regions away from the stability boundaries where the persistence diagram was empty. There are two main reasons why a persistence diagram might be empty as in the white regions of Fig. 5:

1. This occurred in the stable regions (the inside of the deterministic stability boundary) because the period at the end contained a stable solution, and therefore, the constructed point cloud was too clustered to pick up any classes in the persistence computation. To elaborate, if the point cloud is simply a mass, no one-dimensional features (loops) will be present, thus the diagram will be empty. This is likely what is occurring in the interior white regions bounded by blue (small) maximum persistence values.
2. On the other hand, unstable regions, which are the areas in the direction of the increasing gradient of the average maximum persistence, led to empty diagrams because the features were so far apart that they never died before the computation was finished, i.e., the code's upper limit of the maximum radius surrounding each point in the point cloud was reached.

It is easy to distinguish empty diagrams due to stable regions from their unstable counterparts. This can be achieved by observing the gradient of the maximum persistence. In Fig. 5, for example, it can be seen that the inner stable region is surrounded by low values of maximum persistence, while the unstable outer white region is consistent with the direction of the increasing gradient that corresponds to the value of the average maximum persistence. In practice, however, we expect this issue to be rarely encountered because with physical systems there often exist constraints or nonlinearities that prevent the system response from growing unboundedly. For example, in the literature of machining processes the oscillations of the tool during chatter will eventually cause the tool to jump out of the cut and experience free, damped oscillations. This means that the tool oscillations in reality will always remain bounded and will not grow indefinitely even when the system is in the chatter regime. This observation is true for other dynamical systems as well.

The presented results show that the described approach can be a viable tool for studying the stability of SDDEs using their time series. This is useful since the theory of stochastic differential equations in general and the theory of stochastic delay equations in particular are not nearly as developed as their deterministic counterparts. Therefore, the presented work can act as both an analysis and a benchmark tool as new methods and algorithms emerge.

Acknowledgements The authors would like to acknowledge financial support from the U.S. National Science Foundation through grants CMMI-1562012 and CMMI-1562459.

References

1. Hale, J.K., Lunel, S.V.: Introduction to Functional Differential Equations. Springer, New York (1993)
2. Stépán, G.: Retarded Dynamical Systems: Stability and Characteristic Functions. Wiley (1989)
3. Walther, H.-O.: Topics in delay differential equations. Jahresbericht der Deutschen Mathematiker-Vereinigung **116**(2), 87–114 (2014)
4. Buckwar, E., Kuske, R., L'Esperance, B., Soo, T.: Noise-sensitivity in machine tool vibrations. Int. J. Bifurc. Chaos **16**(08), 2407–2416 (2006)
5. Kuske, R.: Multiple-scales approximation of a coherence resonance route to chatter. Comput. Sci. Eng. **8**(3), 35–43 (2006)
6. Klamecki, B.E.: Enhancement of the low-level components of milling vibration signals by stochastic resonance. Proc. Inst. Mech. Eng. Part E J. Process Mech. Eng. **218**(1), 33–41 (2004)
7. Yilmaz, A., AL-Regib, E., Ni, J.: Machine tool chatter suppression by multi-level random spindle speed variation. J. Manuf. Sci. Eng. **124**(2), 208–216 (2002)
8. Barrio, M., Burrage, K., Leier, A., Tian, T.: Oscillatory regulation of Hes1: discrete stochastic delay modelling and simulation. PLoS Comput. Biol. **2**(9), e117 (2006)
9. Tian, T, Burrage, K., Burrage, P.M., Carletti, M.: Stochastic delay differential equations for genetic regulatory networks. J. Comput. Appl. Math. **205**(2), 696–707 (2007) (Special issue on evolutionary problems)
10. Mackey, M.C., Nechaeva, I.G.: Solution moment stability in stochastic differential delay equations. Phys. Rev. E **52**(4), 3366–3376 (1995)
11. Guillouzic, S., L'Heureux, I., Longtin, A.: Small delay approximation of stochastic delay differential equations. Phys. Rev. E **59**, 3970–3982 (1999)

12. Elbeyli, O., Sun, J.Q., Unal, G.: A semi-discretization method for delayed stochastic systems. Commun. Nonlinear Sci. Numer. Simul. **10**(1), 85–94 (2005)
13. Frank, T.D., Beek, P.J.: Stationary solutions of linear stochastic delay differential equations: applications to biological systems. Phys. Rev. E **64**, 021917 (2001)
14. McKelvey, T., Guerin, G.: Non-parametric frequency response estimation using a local rational model. In: 16th IFAC Symposium on System Identification the International Federation of Automatic Control Brussels, Belgium, July 11–13, 2012, vol. 16(1), pp. 49–54 (2012)
15. Kantz, H., Just, W., Baba, N., Gelfert, K., Riegert, A.: Fast chaos versus white noise: entropy analysis and a Fokker-Planck model for the slow dynamics. Phys. D Nonlinear Phenom. **187**(1–4), 200–213 (2004)
16. Fontanella, L., Granturco, M.: Spectral analysis in frequency and time domain for noisy time series. In: Bock, H.-H., Chiodi, M., Mineo, A. (eds.) Advances in Multivariate Data Analysis. Studies in classification, data analysis, and knowledge organization, pp. 67–79. Springer, Heidelberg (2004)
17. Yao, Z., Mei, D., Chen, Z.: On-line chatter detection and identification based on wavelet and support vector machine. J. Mater. Process. Technol. **210**(5), 713–719 (2010)
18. Buckwar, E.: Introduction to the numerical analysis of stochastic delay differential equations. J. Comput. Appl. Math. **125**(1–2), 297–307 (2000) (Numerical Analysis 2000. Vol. VI: Ordinary Differential Equations and Integral Equations)
19. Buckwar, E., Winkler, R.: Multi-step maruyama methods for stochastic delay differential equations. Stoch. Anal. Appl. **25**(5), 933–959 (2007)
20. Mao, X., Sabanis, S.: Numerical solutions of stochastic differential delay equations under local lipschitz condition. J. Comput. Appl. Math. **151**(1), 215–227 (2003)
21. Yuan, C., Glover, W.: Approximate solutions of stochastic differential delay equations with markovian switching. J. Comput. Appl. Math. **194**(2), 207–226 (2006)
22. Yaozhong, H., Mohammed, S.-E.A., Yan, F.: Discrete-time approximations of stochastic delay equations: the milstein scheme. Ann. Probab. **32**(1A), 265–314 (2004)
23. Baker, C.T.H., Buckwar, E.: Exponential stability in p-th mean of solutions, and of convergent euler-type solutions, of stochastic delay differential equations. J. Comput. Appl. Math. **184**(2), 404–427 (2005)
24. Luo, J.: A note on exponential stability in pth mean of solutions of stochastic delay differential equations. J. Comput. Appl. Math. **198**(1), 143–148 (2007)
25. Mao, X.: Exponential stability of equidistant euler-maruyama approximations of stochastic differential delay equations. J. Comput. Appl. Math. **200**(1), 297–316 (2007)
26. Khasawneh, F.A., Munch, E.: Exploring equilibria in stochastic delay differential equations using persistent homology. In: Proceedings of the ASME 2014 International Design Engineering Technical Conferences & Computers and Information in Engineering Conference, August 17–20, 2014, Buffalo, NY, USA (2014). Paper no. DETC2014/VIB-35655
27. Khasawneh, F.A., Munch, E.: Stability determination in turning using persistent homology and time series analysis. In: Proceedings of the ASME 2014 International Mechanical Engineering Congress & Exposition, November 14–20, 2014, Montreal, Canada (2014). Paper no. IMECE2014-40221
28. Khasawneh, F.A., Munch, E.: Chatter detection in turning using persistent homology. Mech. Syst. Signal Process. **70–71**, 527–541 (2016)
29. Takens, F.: Detecting strange attractors in turbulence. In: Rand, D., Young, L.-S. (eds.) Dynamical Systems and Turbulence. Warwick 1980. Lecture Notes in Mathematics, vol. 898, pp. 366–381. Springer, Heidelberg (1981)
30. de Silva, V., Skraba, P., Vejdemo-Johansson, M.: Topological analysis of recurrent systems. In: NIPS 2012 Workshop on Algebraic Topology and Machine Learning (2012)
31. Berwald, J., Gidea, M., Vejdemo-Johansson, M.: Automatic recognition and tagging of topologically different regimes in dynamical systems (2013). arXiv:1312.2482
32. Brown, K.A., Knudson, K.P.: Nonlinear statistics of human speech data. Int. J. Bifurc. Chaos **19**(07), 2307–2319 (2009)

33. Emrani, S., Gentimis, T., Krim, H.: Persistent homology of delay embeddings and its application to wheeze detection. IEEE Signal Process. Lett. **21**(4), 459–463 (2014)
34. Cohen-Steiner, D., Edelsbrunner, H., Harer, J., Mileyko, Y.: Lipschitz functions have l_p-stable persistence. Found. Comput. Math. **10**(2), 127–139 (2010)
35. Deckard, A., Anafi, R.C., Hogenesch, J.B., Haase, S.B., Harer, J.: Design and analysis of large-scale biological rhythm studies: a comparison of algorithms for detecting periodic signals in biological data. Bioinformatics **29**(24), 3174–3180 (2013)
36. Perea, J.A., Deckard, A., Harer, J., Haase, S.: Sw1pers: sliding windows and 1-persistence scoring; discovering periodicity in gene expression time series data (2013) (Preprint)
37. Perea, J.A., Harer, J.: Sliding windows and persistence: an application of topological methods to signal analysis. Found. Comput. Math. **15**(3), 799–838 (2015)
38. Alexander, Z.: A topology-based approach for nonlinear time series with applications in computer performance analysis. Ph.D. thesis, University of Colorado at Boulder (2012)
39. Alexander, Z., Meiss, J.D., Bradley, E., Garland, J.: Iterated function system models in data analysis: detection and separation. Chaos Interdiscip. J. Nonlinear Sci. **22**(2) (2012)
40. Vejdemo-Johansson, M., Pokorny, F.T., Skraba, P., Kragic, D.: Cohomological learning of periodic motion. Appl. Algebr. Eng. Commun. Comput. 1–22 (2015)
41. Robinson, M.: Topological Signal Processing. Springer (2014)
42. de Silva, V., Morozov, D., Vejdemo-Johansson, M.: Persistent cohomology and circular coordinates. Discret. Comput. Geom. **45**(4), 737–759 (2011)
43. Carlsson, G.: Topological pattern recognition for point cloud data. Acta Numer. **23**, 289–368 (2014). Survey
44. Edelsbrunner, H., Letscher, D., Zomorodian, A.: Topological persistence and simplification. In: Proceedings of the 41st Annual Symposium on Foundations of Computer Science, 2000, pp. 454 –463 (2000)
45. Edelsbrunner, H., Harer, J.: Computational Topology: An Introduction. American Mathematical Society (2010)
46. Zomorodian, A., Carlsson, G.: Computing persistent homology. Discret. Comput. Geom. **33**(2), 249–274 (2004)
47. Hatcher, A.: Algebraic Topology. Cambridge University Press (2002)
48. Munkres, J.R.: Elements of Algebraic Topology. Addison Wesley (1993)
49. Cohen-Steiner, D., Edelsbrunner, H., Harer, J.: Stability of persistence diagrams. Discrete Comput. Geom. **37**(1), 103–120 (2007)
50. Milosavljevic, N., Morozov, D., Skraba, P.: Zigzag persistent homology in matrix multiplication time. In: Proceedings of the 27th Annual Symposium on Computational Geometry (2011)
51. Otter, N., Porter, M.A., Tillmann, U., Grindrod, P., Harrington, H.A.: A roadmap for the computation of persistent homology (2015). arXiv: 1506.08903
52. Insperger, T., Stépán, G.: Semi-discretization for time-delay systems: stability and engineering applications. In: Stability Charts for Fundamental Delay-Differential Equations, pp. 13–37. Springer New York, New York (2011)
53. Oksendal, B.: Stochastic Differential Equations, 6th edn. Springer (2007)
54. Khasawneh, F.A., Mann, B.P.: A spectral element approach for the stability of delay systems. Int. J. Numer. Methods Eng. **87**(6), 566–592 (2011)
55. Klosek, M., Kuske, R.: Multiscale analysis of stochastic delay differential equations. Multiscale Model. Simul. **3**(3), 706–729 (2005)
56. Insperger, T., Stepan, G.: Stability chart for the delayed Mathieu equation. Proc. R. Soc. Lond. A **458**, 1989–1998 (2002)
57. Mathieu, E.: Memoire sur le mouvement vibratorie d'une membrane de forme elliptique. J. Math. **13**, 137–203 (1868)
58. Higham, D.J.: An algorithmic introduction to numerical simulation of stochastic differential equations. SIAM Rev. **43**(3), 525–546 (2001)
59. Harer, J., Slaczedek, J., Bendich, P.: Ripscollapse: Discrete Morse Theory and Fast Computation of One-Dimensional Persistence. Manuscript, Duke University (2014)

Stability and Control of Fractional Periodic Time-Delayed Systems

Eric A. Butcher, Arman Dabiri and Morad Nazari

Abstract In this chapter, two new methods are proposed to study the stability of linear fractional periodic time-delayed (FPTD) systems. First, the explicit harmonic balance (EHB) method is proposed to find necessary and sufficient conditions for fold, flip, and secondary Hopf transition curves in linear FPTD systems, from which the stability boundaries are obtained as a subset. Transition curves of the fractional damped delayed Mathieu equation are obtained by using the EHB method. Next, an approximated monodromy operator in a Banach space is defined for FPTD systems, which gives the linear map between two solutions. The fractional Chebyshev collocation (FCC) method is proposed to approximate this monodromy operator. The FCC method is outlined and illustrated with three practical problems including obtaining the parametric stability charts of the fractional Hayes equation and the fractional second-order system with delay, and designing an optimal linear periodic gain fractional delayed state feedback control for the damped delayed Mathieu equation.

1 Introduction

Delay differential equations occupy a place of central importance in all areas of science with a multitude of practical applications, see e.g. [1, 2]. The stability analysis of LTI delayed systems is more complicated than that of non-delayed systems because their characteristic equations (CEs) are in the form of exponential polynomials with infinite number of complex roots. Different stability criteria have been developed to approximate a subset of the infinite roots [3]. In LTI control systems with discrete delays, the stabilization problem in the frequency domain is that the

E.A. Butcher (✉) · A. Dabiri · M. Nazari
Aerospace and Mechanical Engineering Department, University of Arizona,
Tucson, AZ 85721, USA
e-mail: ebutcher@email.arizona.edu

A. Dabiri
e-mail: armandabiri@email.arizona.edu

M. Nazari
e-mail: moradnazari@email.arizona.edu

T. Insperger et al. (eds.), *Time Delay Systems*,
Advances in Delays and Dynamics 7, DOI 10.1007/978-3-319-53426-8_8

control law should be designed such that all of the closed-loop poles (eigenvalues) lie in the left-half plane, or at specific desired locations to ensure a specified response. One may consider a control law to only assign a value for the spectral abscissa [4]. Another strategy is to define a feedback control law with a large number of gains in order to obtain a desired closed-loop response with a large number of desired stable modes. This can be accomplished with either distributed delayed feedback and/or periodic control gains with an arbitrary number of Fourier coefficients [5]. The use of time-periodic control gains results in the closed-loop system having the form of a periodic system of DDEs.

The stability of time-periodic systems has been studied by using techniques such as perturbation and harmonic balance (HB) methods which employ Floquet theory to some degree [6–8]. The state transition matrix evaluated at the principal period is called the monodromy matrix, and its eigenvalues or Floquet multipliers indicate the stability of the system. Specifically, linear periodic ODEs are asymptotically stable when the eigenvalues of the monodromy matrix lie inside the unit circle [7]. On the other hand, the HB method is used to approximate periodic solutions and thus obtain transition curves for linear periodic systems or limit cycles for nonlinear systems [9]. The HB method works by expanding possible periodic solutions in a truncated Fourier series and balancing the coefficients of the individual harmonics, which requires extensive symbolic manipulations such as combining, extracting, and simplifying. The main drawback of using this method is computational inefficiency in large order periodic systems. Stability analysis of linear periodic DDEs is based on an infinite-dimensional extension of Floquet theory in which the eigenvalues of an infinite-dimensional monodromy operator determine the stability. Several methods have been proposed to approximate this monodromy operator. For instance, Chebyshev polynomial expansion and the Chebyshev collocation method are used to analyze the stability of periodic DDEs in [10, 11].

The idea of extending the order of the differential operator from an integer number to any fractional numbers was introduced by Leibniz [12]. Subsequently, a new field known as fractional calculus was founded. Fractional order models (FOMs) have been used in modeling a variety of different physical systems, and their advantages compared to those of integer order models have been demonstrated, e.g. [12–17]. Their ability to model physical processes with hereditary or memory properties (similar to time delay) has been demonstrated in [15]. For instance, the behavior of a viscoelastic material can be correctly described by a fractional model with a small number of model parameters compared to using a conventional integer order model with large number of model parameters [18]. Thus, a fractional operator is sufficient to describe the viscoelastic behavior of mechanical elements, e.g. viscoelastic dampers, which have been used in vibration control. On the other hand, in control of integer order plants, fractional order feedback controllers can be used. This strategy can provide extra design parameters and thus is capable of better meeting desired response specifications compared with conventional controllers such as PID control [16, 19]. The same general strategies for obtaining stability conditions for ODEs or DDEs are also extended for fractional differential equations (FDEs), but in exceptionally limited versions, e.g. [14, 20–23]. While numerical methods based on finite

differences or the spectral method have been proposed, e.g. [13, 24, 25], the nonlocal properties of the fractional operators usually result in slow convergence. Since the spectral method typically exhibits exponential convergence properties for integer order systems (in contrast to finite differences), the development of a spectral method based on Chebyshev collocation for stability analysis of fractional periodic time-delayed systems is one aim of this chapter.

Consequently, the purpose of this work is to study the stability of linear systems obtained from including these three phenomena (i.e., fractional order derivatives, periodic coefficients, and time delays). First, the explicit harmonic balance (EHB) method is introduced to obtain the Hill matrix in a computationally efficient manner, which yields the transition curves in the parametric stability chart. The efficiency of this method is demonstrated with the fractional damped delayed Mathieu equation. Next, a spectral method for periodic FDDEs is proposed, in which the approximate monodromy operator, whose eigenvalues yield the stability properties, is obtained using Chebyshev collocation and by invoking the short memory principle. The efficiency of the method is shown with the fractional Hayes equation, fractional second order system with delay, and the fractional delayed Mathieu equation. Finally, a technique is proposed to control periodic FDDEs with fractional delayed state feedback control. The control gains are optimized for minimum spectral radius of the closed-loop finite-time response. The proposed control strategy is applied to the unstable damped delayed Mathieu equation.

2 Caputo Fractional Derivative

Caputo's definition is the most popular definition of the fractional derivative among several proposed definitions for fractional operators because: (1) FDEs with Caputo fractional derivatives have integer order initial conditions, (2) a fractional derivative of a constant is zero, (3) FDEs give the same solution when the order is integer [12]. The left-sided fractional integral is defined based on the Cauchy nth fold integral as [12]

$$ {}_a\mathscr{J}_x^{\alpha} f(x) = \frac{1}{\Gamma(\alpha)} \int_a^x f(\xi)(x-\xi)^{\alpha-1} d\xi \tag{1} $$

where $a \in \mathbb{R}$, $\alpha \in [0, 1]$, and $\Gamma(\cdot)$ denotes the Gamma function. The left side Caputo derivative follows by using the left side fractional integral and integer derivative operator D as

$$ {}_a^C\mathscr{D}_x^{\alpha} f(x) = {}_a\mathscr{J}_x^{\lceil\alpha\rceil-\alpha} D^{\lceil\alpha\rceil} f(x) \tag{2} $$

in which $\lceil x \rceil$ is the ceiling function.

3 Transition Curves Using Explicit Harmonic Balance Method

3.1 Formulation

As shown in [26], a linear periodic FDDE of the form

$$A(t)\dot{x}(t) + B(t)\ \mathscr{D}_t^{\alpha} x(t) + C(t)\ \mathscr{D}_t^{\beta} x(t-\tau) = 0 \tag{3}$$

where x is an $n \times 1$ vector, and $A(t)$, $B(t)$ and $C(t)$ are $n \times n$ time-periodic matrices with period $T = 2\pi/\Omega$, can be expressed in algebraic form by using operational matrices. In [27], it is shown that, as in the case of Floquet theory for time-periodic ODEs and DDEs, the steady-state solution of (3) is the product of a periodic matrix and a function of an exponential matrix multiplied by time. Specifically, to obtain cyclic fold and flip instability the solution is assumed to be T- or $2T$-periodic, respectively. Thus, the solution can be expanded in a Fourier series and represented by a decomposed representation as

$$x(t) = \mathbf{p}_N^T\ I_{2N+1}\ \Theta^N_{\exp(\cdot)}(i\frac{\Omega}{2}t) \tag{4}$$

where $\mathbf{p}_N$ is the Fourier coefficient vector defined as $\mathbf{p}_N = [c_{-N}, c_{-(N-1)}, \ldots, c_{(N-1)}, c_N]^T$, where $c_i\ (i = -N, \ldots, N), N \in \mathbb{Z}$ is the ith coefficient of the Fourier series, and I_n is the $n \times n$ identity matrix. The operator $\Theta^N_{g(\cdot)}(z)$ is defined on the scalar function $g(\cdot)$ as

$$\Theta^N_{g(\cdot)}(z) := \left[g(-Nz), g(-(N-1)z), \ldots, g((N-1)z), g(Nz)\right]^T \tag{5}$$

This method decomposes the solution into harmonic terms $(\Theta^N_{\exp(\cdot)}(i\frac{\Omega}{2}t))$, unknown coefficients $(\mathbf{p}_N^T)$, and a core Hill matrix $(\mathfrak{H}_{\mathbf{p}_N})$ as

$$\mathbf{p}_N^T\ \mathfrak{H}_{\mathbf{p}_N}\ \Theta^N_{\exp(\cdot)}(i\frac{\Omega}{2}t) = 0 \tag{6}$$

in which the Hill matrix of the system is defined by linear operational matrices $(\mathscr{O}_{\mathbf{p}_N}(\cdot))$ with respect to $\mathbf{p}_n$ as

$$\mathfrak{H}_{\mathbf{p}_N} := \mathscr{O}_{\mathbf{p}_N}(A(t)\dot{x}(t)) + \mathscr{O}_{\mathbf{p}_N}\left(B(t)\ \mathscr{D}_t^{\alpha} x(t)\right) + \mathscr{O}_{\mathbf{p}_N}\left(C(t)\ \mathscr{D}_t^{\beta} x(t-\tau)\right) \tag{7}$$

Moreover, the operational matrices corresponding to when the state is multiplied by a scalar function $f(t)$, time-delayed by fixed delay τ, and operated on by a fractional derivative of order α are obtained as

$$f(t)p(t) \approx \mathbf{p}_N^T \, \mathscr{O}_{\mathbf{p}_N}\left(f(t)p(t)\right) \, \Theta^N_{\exp(\cdot)}(i\Omega t) \tag{8a}$$

$$\mathscr{O}_{\mathbf{p}_N}\left(p(t-\tau)\right) = \mathrm{diag}\left(\Theta^N_{\exp(\cdot)}(-i\Omega\tau)\right) \tag{8b}$$

$$\mathscr{O}_{\mathbf{p}_N}\left(\mathscr{D}_t^\alpha p(t)\right) = \mathrm{diag}\left(\Theta^N_{(\cdot)^\alpha}(\Omega)\right) e^{\alpha\frac{i\pi}{2}} \tag{8c}$$

in which $\mathscr{O}_{\mathbf{p}_N}\left(f(t)p(t)\right)$ is given by

$$\mathscr{O}_{\mathbf{p}_N}\left(f(t)p(t)\right) := \mathfrak{F}\left\{\mathbf{f}_N\right\} = \begin{bmatrix} f_0 & f_1 & f_2 & \cdots & f_{2N-2} & f_{2N-1} & f_{2N} \\ f_{-1} & f_0 & f_1 & \cdots & f_{N-3} & f_{N-2} & f_{2N-1} \\ f_{-2} & f_{-1} & f_0 & \cdots & f_{N-4} & f_{N-3} & f_{2N-2} \\ \vdots & \ddots & \ddots & \ddots & \ddots & \ddots & \vdots \\ f_{-(2N-2)} & f_{-(2N-3)} & f_{-(2N-4)} & \cdots & f_0 & f_1 & f_2 \\ f_{-(2N-1)} & f_{-(2N-2)} & f_{-(2N-3)} & \cdots & f_{-1} & f_0 & f_1 \\ f_{-2N} & f_{-(2N-1)} & f_{-(2N-2)} & \cdots & f_{-2} & f_{-1} & f_0 \end{bmatrix} \tag{9}$$

This is discussed in detail in [27] for the general case of multi-degree-of-freedom linear periodic FDDEs.

The necessary and sufficient condition to have a solution of the assumed form is that the Hill matrix should be singular, which gives the flip and fold transition curves. Moreover, for secondary Hopf instability, the Floquet multipliers are not ± 1 but lie on the unit circle as a complex conjugate pair. Floquet theory implies that to have a Floquet steady-state solution, $x(t)$ should be expanded as

$$x(t) = \mathbf{p}_N^T \left(I_{2N+1} e^{i\theta t} \right) \, \Theta^N_{\exp(\cdot)}(t) \tag{10}$$

All characteristic exponents should be in $[0, i\Omega) \in \mathbb{C}$. Note that the exponential term, $e^{i\theta t}(i\theta = \lambda)$, is multiplied by the periodic solution in Eq. (4). In general, adding this terms does not change the OMs, and only effects the operational matrices of time delayed and derivative terms (see Eqs. (8a)–(8c)) as

$$\mathscr{O}_{\mathbf{p}_N}\left(f(t)\, p(t-\tau)\right)_\theta = \mathrm{diag}\left(\Theta^{N\to N+\theta}_{\exp(\cdot)}(-i\frac{\Omega}{2}\tau)\right) \, \mathfrak{F}\left\{\mathbf{f}_N\right\} \tag{11}$$

$$\mathscr{O}_{\mathbf{p}_N}\left(f(t)\, \mathscr{D}_t^\alpha p(t)\right)_\theta = \mathrm{diag}\left(\Theta^{N\to N+\theta}_{(\cdot)^\alpha}(i\frac{\Omega}{2})\right) \mathfrak{F}\left\{\mathbf{f}_N\right\} \tag{12}$$

where for secondary Hopf instability the operational matrix by considering the exponential term of Hopf instability is indicated by $\mathscr{O}_{\mathbf{p}_N}(\cdot)_\theta$, and N is changed to $N+\theta$ in $\Theta^N_{(\cdot)}(\cdot)$.

3.2 Example: Fractional Damped Delayed Mathieu Equation

Consider the fractional damped delayed Mathieu equation of the form

$$\begin{aligned} &\ddot{x}(t) + (a + b\cos(\Omega t))\, x(t) = c\, {}_0^C\mathscr{D}_t^{\alpha} x(t-\tau) \\ &x(t) = \phi(t), \ -\tau \le t < 0, \end{aligned} \tag{13}$$

where $\Omega = 2\pi$ and $\tau = 1$. In this problem, the delayed term is combined with the fractional derivative. The Hill matrix is obtained by summation of all operational matrices as

$$\mathfrak{H}_{\mathbf{p}_N} := \mathscr{O}_{\mathbf{p}_N}\left(\mathscr{D}_t^2 x(t)\right) + \mathscr{O}_{\mathbf{p}_N}(a x(t)) + \mathscr{O}_{\mathbf{p}_N}(b\cos(2\pi t)\, x(t)) - \mathscr{O}_{\mathbf{p}_N}\left(c\mathscr{D}_t^{\alpha} x(t-\tau)\right) \tag{14}$$

in which

$$\mathscr{O}_{\mathbf{p}_N}\left(\mathscr{D}_t^2 x(t)\right) = \Theta^N_{(\cdot)^2}(i) = \operatorname{diag}\left(\left[-N^2 \ -(N-1)^2 \ \cdots \ -(N-1)^2 \ -N^2\right]\right) \tag{15a}$$

$$\mathscr{O}_{\mathbf{p}_N}(a x(t)) = a I_{2N+1} \tag{15b}$$

$$\mathscr{O}_{\mathbf{p}_N}(b\cos(2\pi t)\, x(t)) = \text{toeplitz}\left(\left[0\ 0\ {}^{b}/_{2}\ 0\ 0\ \cdots\ 0\right], \left[0\ 0\ {}^{b}/_{2}\ 0\ 0\ \cdots\ 0\right]\right) \tag{15c}$$

$$\mathscr{O}_{\mathbf{p}_N}\left(c\mathscr{D}_t^{\alpha} x(t-\tau)\right) = c\, \operatorname{diag}\left(\Theta^N_{(\cdot)^{\alpha}}(1)\right) e^{\alpha\frac{i\pi}{2}} \operatorname{diag}\left(\Theta^N_{\exp(\cdot)}(-i\tau)\right) \tag{15d}$$

where toeplitz (u, v) returns a nonsymmetric Toeplitz matrix, in which each descending diagonal from left to right is constant, with u as its first column and v as its first row.

Figure 1 shows the flip and fold transition curves of system (13) in different parametric stability charts. In the $a - b$ parametric stability chart, Fig. 1a, increasing the coefficient c of the delay term moves the transition curves on the a-axis. Figure 1b shows that the effect of increasing the fractional order is similar to adding damping to the system and separates the transition curves from the a-axis. Figure 1c shows the $b - c$ parametric stability chart when $\alpha = 0$. These transition curves are analogous to the Hsu–Bhatt–Vyshnegradskii stability chart when $b = 0$. By increasing b the first transition curve separates into two transition curves, which is indicated by the red box in this plot. Figure 1d demonstrates that the transition curves become in the form of closed contours when $\alpha = 0.5$.

4 Stability and Control Using the Fractional Chebyshev Collocation Method

4.1 Fractional Chebyshev Differentiation Matrix

The derivative of a function approximated by finite differences is obtained by interpolation of a local mth degree polynomial on m local points of an equispaced

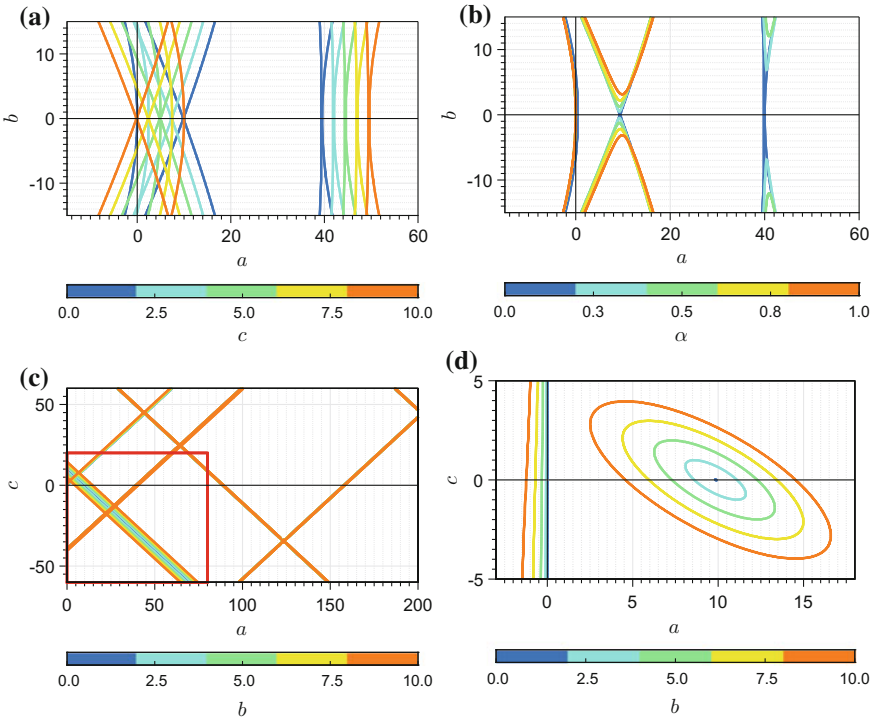

Fig. 1 Flip and fold transition curves for Eq. (13) in different parametric stability charts. **a** $\alpha = 0$ **b** $c = 0.5$ **c** $\alpha = 0$ **d** $\alpha = 0.5$

grid [28]. This results in a maximum accuracy $O(h^m)$. On the other hand, the main idea of spectral methods is the use of a global Nth degree polynomial that employs all N points inside the domain and achieves maximum accuracy [28, 29]. However, the accuracy of the result does not necessarily increase by increasing the degree of the polynomial. Moreover, if finite difference methods with equispaced collocation points are used, then the error of the interpolation increases when constructing a high degree polynomial interpolant. This error can be minimized by using nodes that are distributed more densely toward the edges of the interval. This is analogous to finding a basis with faster oscillation at the edges of the interval. It is shown in [28, 29] that interpolation at the Chebyshev–Gauss–Lobatto (CGL) points gives the minimum error out of all sets of polynomial bases, so the Chebyshev polynomials are ideal to be used in spectral methods.

The fractional Chebyshev differentiation matrix in the sense of Caputo, $\mathbb{D}^{\alpha}_{N+1}$, is a linear map that maps the discretized function at the CGL points onto the discretized fractional derivative of the function at those points, i.e.,

$$\mathbb{D}^{\alpha}_{N+1}\mathbf{x} = \left[{}^{C}_{t_0}\mathscr{D}^{\alpha}_{t} x\left(t_0\right) \; {}^{C}_{t_0}\mathscr{D}^{\alpha}_{t} x\left(t_1\right) \; \cdots \; {}^{C}_{t_0}\mathscr{D}^{\alpha}_{t} x\left(t_N\right) \right]^{T} \tag{16}$$

The fractional differentiation operational matrix in the sense of Caputo is obtained by using the discrete orthogonality relationship for the Chebyshev polynomials in [16–19].

4.2 Fractional Chebyshev Collocation Method

Consider a linear periodic fractional time-delayed system in the standard state-space form of

$$\begin{aligned} &{}_0^C\mathscr{D}_t^{(\alpha_1,\alpha_2,\ldots,\alpha_n)}\mathbf{x}(t) = A(t)\,\mathbf{x}(t) + F(t)\,\mathbf{x}(t-\tau) \quad \left(0 < \alpha_i \le 1, i = 1,2,\ldots,n\right) \\ &\mathbf{x}(t) = \phi(t), \quad -\tau \le t < 0 \end{aligned} \tag{17}$$

where $\mathbf{x}(t) \in \mathbb{R}^n$ is the state of the system, $A(t+T) = A(t)$ and $F(t+T) = F(t)$ are $n \times n$ matrices with period T, $\tau = T$ is the delay, $\phi(t)$ is the initial vector function in $[-\tau, 0]$, and

$${}_0^C\mathscr{D}_t^{(\alpha_1,\alpha_2,\ldots,\alpha_n)} \equiv \text{diag}\left({}_0^C\mathscr{D}_t^{\alpha_1}, {}_0^C\mathscr{D}_t^{\alpha_2}, \ldots, {}_0^C\mathscr{D}_t^{\alpha_n}\right) \tag{18}$$

Note that a different result is obtained if the lower terminal of the fractional operator is changed since the fixed lower terminal 0 in operator ${}_0^C\mathscr{D}_t^{(\alpha_1,\alpha_2,\ldots,\alpha_n)}$ indicates the nonlocal property, which requires a variable memory that enlarges over time, and hence it defines the degree of memory of the fractional operator. That is, the past states of the system are retained and used for the computations in the next step. This problem has been addressed in the literature and different solutions, such as the use of the short memory principle, have been proposed to overcome this limitation [13]. The short memory principle states that the solution of a fractional derivative can be approximated only by storing the most recent history of the function. In other words, the length of the memory is fixed. This principle is used to obtain an approximate monodromy operator for fractional periodic DDEs. For this purpose, the error bound from the short memory principle, $E(n,T,\alpha)$, is obtained by using Eqs. (1) and (2) with the fixed length memory T as

$$E(n,T,\alpha) = {}_0^C\mathscr{D}_t^{\alpha}\mathbf{x}(nT) - {}_{nT-T}^C\mathscr{D}_t^{\alpha}\mathbf{x}(nT) = \frac{1}{\Gamma(\alpha)}\int_0^T \dot{\mathbf{x}}(\xi)(nT-\xi)^{\alpha-1}d\xi, \tag{19}$$

in which for $M = \sup_{t\in[0,(n-1)T]}|\dot{\mathbf{x}}(t)|$, the error is bounded as $\|E(T,n,\alpha)\| \le MT^{1-\alpha}\left(n^{1-\alpha}-1\right)/\Gamma(2-\alpha)$. It should be noted that for values of α close to 1 this error is insignificant, and by decreasing the fractional order from unity the approximation error from using the short memory principle increases. It is shown in different examples that this method works efficiently, specifically for fractional orders close to one.

The initial function $\phi(t)$ of system (17) in Banach space $X = \mathscr{C}([-\tau, 0], \mathbb{R}^n)$ is denoted by $\mathscr{X}_0 \in X$, i.e., $\mathscr{X}_0 = \phi(\theta)$, $\theta \in [-\tau, 0]$. Similarly, $\mathbf{x}(t)$ in the time interval $t \in [(j-1)\tau, j\tau]$ is represented by $\mathscr{X}_j \in X$. In Sect. 3, it is shown that the steady-state solution of linear periodic FDDEs is a periodic function times an exponential function of time. Since the monodromy matrix B of a system of periodic ODEs can be defined in terms of the fundamental solution matrix $\Phi(t)$ as $B = \lim_{t\to\infty} \Phi^{-1}(t)\Phi(t+T)$, the steady-state monodromy operator of the linear periodic FDDE in Eq. (17) in Banach space X satisfies

$$\lim_{m\to\infty} \mathscr{X}_m = \lim_{m\to\infty} \mathscr{B}\left(\mathscr{X}_{m-1}\right) \tag{20}$$

By using the short memory principle, Eq. (20) can be rewritten in terms of an approximation for this monodromy operator $\tilde{\mathscr{B}} : X \to X$ as

$$\mathscr{X}_j \approx \tilde{\mathscr{B}}^j\left(\mathscr{X}_0\right) \tag{21}$$

where $\tilde{\mathscr{B}}^j(.) := \overbrace{\tilde{\mathscr{B}}(\tilde{\mathscr{B}}(\cdots \tilde{\mathscr{B}}(.)))}^{j}$.

In general, the monodromy operator does not have a closed form and it should be approximated using a suitable approximation technique. This can be accomplished by the discretization of the approximated monodromy operator at the CGL collocation points represented by the projections of the equispaced points on the lower halves of the semicircles in Fig. 2. If the number of CGL collocation points goes to infinity, then the approximations of the differentiation operator and any functions in Banach space X converge to their exact solution.

Let $\mathbf{X}_1$ and $\mathbf{X}_0$ be the discretized vectors of $\mathscr{X}_1$ and $\mathscr{X}_0$, respectively. Then, substituting these finite dimensional vectors into Eq. (17), the discretized version $\tilde{\mathbf{B}}$ of the operator $\tilde{\mathscr{B}}$ can be obtained as

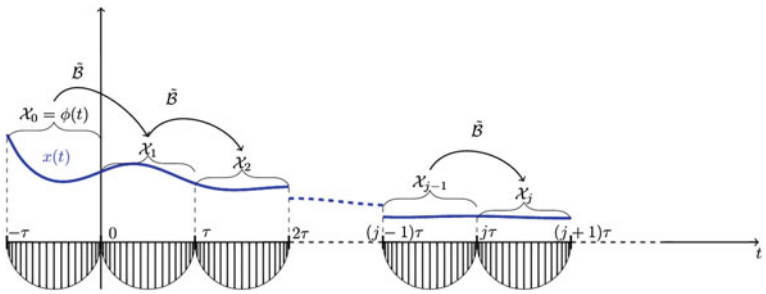

Fig. 2 Schematic representation of using the approximated monodromy operator to find the solution of linear periodic FDDEs (17) in Banach space X

$$\tilde{\mathbf{B}} \approx \left(\mathbf{D}'^{\tilde{\alpha}} - \bar{\mathbf{A}}\right)^{-1} \mathbf{F}'' \tag{22}$$

where $\mathbf{A}$ and $\mathbf{F}$ are the discretized finite dimensional matrices in the discretized Banach space corresponding to matrices $A(t)$ and $F(t)$ in Eq. (17), $(.)'$ is an operator that modifies the first row of a matrix as $[1\ 0\ 0\ \cdots\ 0]$, $(.)''$ is an operator that modifies the first row of a matrix as $[0\ 0\ \cdots\ 0\ 1]$, and $\bar{(.)}$ is an operator that sets the first row of a matrix to a zero row. Methods for calculating the discretized matrices $\mathbf{A}$ and $\mathbf{F}$ from the matrices $A(t)$ and $F(t)$ in Eq. (17) are found in [16]. The operator $\mathbf{D}^{\tilde{\alpha}}$ in Eq. (22) is defined as

$$\mathbf{D}^{\tilde{\alpha}} = \text{blkdiag}\left(\mathbb{D}_{N+1}^{\alpha_1}, \mathbb{D}_{N+1}^{\alpha_2}, ..., \mathbb{D}_{N+1}^{\alpha_n}\right) \tag{23}$$

where blkdiag $\left(A_1, A_2, ..., A_n\right)$ constructs a block diagonal matrix from input matrices A_i, $i = 1, 2, ..., n$ and $\mathbb{D}_{N+1}^{\alpha_i}$, $i = 1, 2, ..., n$ is the fractional order differentiation matrix at the CGL collocation points in $[0, T]$.

Since $\tilde{\mathbf{B}}$ is a discretized matrix approximation of operator $\tilde{\mathscr{B}}$, applying the induced norm $\|(\cdot)\|$ on the finite-dimensional discretization of Eq. (21), one can write

$$\left\|\mathbf{X}_j\right\| \leq \left\|\tilde{\mathbf{B}}\right\|^j \left\|\mathbf{X}_0\right\| \leq \rho^j \left\|\mathbf{X}_0\right\| \tag{24}$$

where ρ is the spectral radius of the discretized monodromy matrix $\tilde{\mathbf{B}}$. In reality the argument for the stability of the discretized operator being the same as that for the operator itself (assuming N is large enough) is due to the compactness of the monodromy operator; hence all (infinitely many) neglected eigenvalues are guaranteed to be clustered about the origin. Therefore, in the case of $\alpha_i \in \mathbb{N}$, $i = 1, 2, \ldots, n$, and for large enough values of N, the necessary and sufficient condition for the origin of system (17) to be asymptotically stable is that all the eigenvalues of $\tilde{\mathbf{B}}$ lie inside the unit circle. In the case of fractional orders, if the approximation error of using the short memory principle is insignificant, then asymptotically stability of the origin is guaranteed for large enough values of N.

4.3 Example: Stability of the Fractional Hayes Equation

Consider the fractional Hayes equation, defined here as the fractional order autonomous DDE with a single discrete delay given by

$$\begin{aligned} &{}_0^C\mathscr{D}_t^{\alpha} x(t) = a x(t) + b x(t-\tau) \quad (0 \leq \alpha \leq 2) \\ &x(t) = \phi(t), \quad -\tau \leq t \leq 0 \end{aligned} \tag{25}$$

where a and b are real constants. The characteristic equation of system (25) is

$$C(\lambda) = \lambda^{\alpha} - a - b e^{-\lambda\tau} = 0 \tag{26}$$

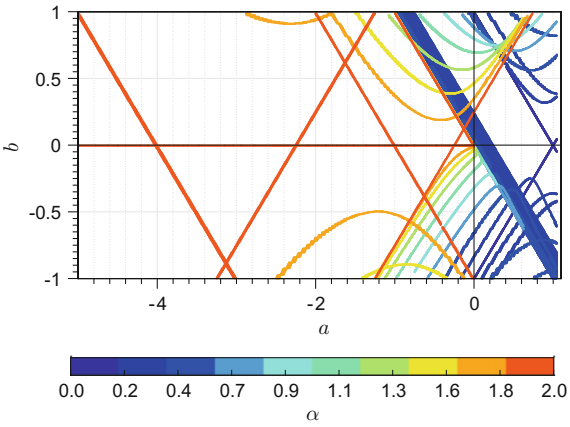

Fig. 3 Transition curves of the fractional Hayes equation on the first Riemann sheet for different values of α when $\tau = 2\pi$

when $\alpha = 0$, Eq. (25) is a linear map of the form $x_n = \frac{b}{1-a} x_{n-1}$, which is asymptotically stable if $\left|b/(1-a)\right| < 1$. If $\alpha = 1$, then Eq. (25) is a first-order DDE known as the Hayes equation, which is used in different biological models. The stability of the Hayes equation has been examined by different methods in the literature [3]. The stability boundary of the fractional Hayes equation is obtained if $\lambda = i\omega$, $\omega \in \mathbb{R}$, and ω is the solution of

$$(i\omega)^\alpha - a - be^{-i\omega\tau} = \omega^\alpha e^{i\alpha\frac{\pi}{2}} - a - be^{-i\omega\tau} = 0 \tag{27}$$

Figure 3 shows the numerical solution of Eq. (27) on the first Riemann sheet for different values of α when $\tau = 2\pi$. When $\alpha > 0$, the line $a = -b$ is an invariant transition curve for the system as it is independent of the fractional order. Figure 3 demonstrates that as the fractional order is varied from 1 to 2, the transition curves evolve from those of the Hayes equation to those of the second order system with delay with its recognizable triangular stability regions in the Hsu–Bhatt–Vyshnegradskii stability chart [3].

Studying the intersection point of the stability boundaries with b-axis is one way to evaluate the accuracy of the obtained boundaries. This intersection point is obtained by resolving Eq. (27) into real and imaginary parts when $a = 0$. That is,

$$\begin{cases} \text{Re} : \omega^\alpha \cos\left(\alpha\dfrac{\pi}{2}\right) = b\cos(\omega\tau) \\ \text{Im} : \omega^\alpha \sin\left(\alpha\dfrac{\pi}{2}\right) = -b\sin(\omega\tau) \end{cases} \tag{28}$$

which yields $-b|_{a=0} = \omega^\alpha = \left(\frac{\pi-\alpha\pi/2}{\tau}\right)^\alpha$. If $\alpha \to 0$, then $-b|_{a=0} \to 1$, and if $\alpha = 1$, then $-b|_{a=0} = \frac{\pi}{2\tau}$. Figure 4 shows the intersection point $-b|_{a=0}$ for different fractional orders and delays. In the case of the fractional Hayes equation, for $0 \le \alpha \le 1$,

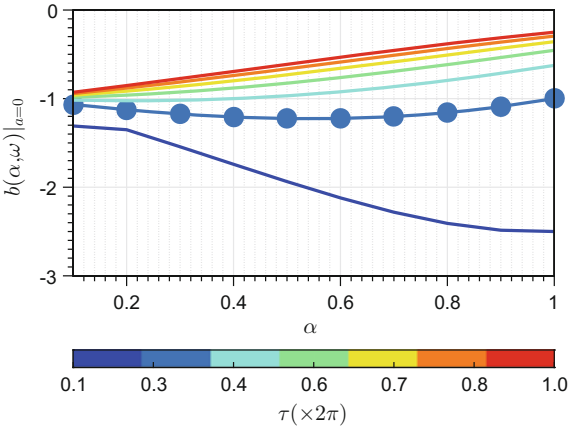

Fig. 4 The analytical solution of the stability boundary intersection $-b|_{a=0}$ with the b-axis for the fractional Hayes equation for different fractional orders and time-delays. The *line* with *solid circle* symbols is obtained when $\tau = \pi/2$, which is approximately 0.25 in the *color bar*, and shows the minimum variation in the intersection as $0 < \alpha < 1$

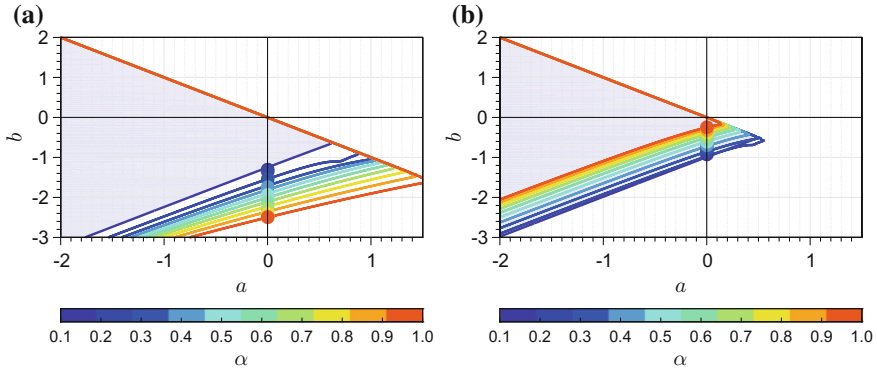

Fig. 5 The stability region of the fractional Hayes equation by using 20 CGL points for different values of the fractional order. The shaded regions indicate the stable boundaries for $\alpha = 0.1$, and the filled *circles* show the analytical solution of the b-axis stability boundary intersections. **a** $\tau = 1/10 \times 2\pi$ **b** $\tau = 2\pi$

the light blue line with solid circle symbols shows the minimum variation obtained when $\tau = \pi/2$. Moreover, this line is the margin of two different behaviors for the intersection point $-b|_{a=0}$. It monotonically decreases when $0 \leq \tau < \frac{\pi}{2}$, while it monotonically increases if $\frac{\pi}{2} < \tau \leq 2\pi$.

In the fractional Hayes equation when $b = 0$, Eq. (25) reduces to an FDE without time delay, whose stability can be analytically expressed by studying the location of its roots on the first Riemann sheet, i.e., $|\arg(a)| > \alpha\frac{\pi}{2}$. Figure 5 shows the approximated stability boundaries of the fractional Hayes equation by analyzing its

approximated monodromy matrix. The shaded regions are the stability boundaries for $\alpha = 0.1$, and the filled circles show the analytical solution of the b-axis stability boundary intersections. For small values of the fractional orders, the intersection points do not exactly overlap with the analytical results due to error associated with the short memory principle. However, by increasing the fractional order, the approximation improves and becomes closer to the analytical solution.

4.4 Example: Stability of the Fractional Second Order Equation with Delay

The fractional second order equation with delay can be expressed as

$$ {}_0^C\mathscr{D}_t^{2\gamma} x(t) = ax(t) + bx(t-\tau) \quad (0.5 < \gamma \leq 1) \tag{29} $$

If $\gamma = 1$, then the equation changes to a second order system with delay with its accompanying Hsu–Bhatt–Vyshnegradskii stability chart [3]. Since the CE of Eq. (29) is identical to Eq. (26) with $\alpha = 2\gamma$, the solution of its transition curves is easily obtained and is shown in Fig. 6. The FCC method with 25 CGL collocation points is used to find its stability regions as shown in Fig. 6. Figure 6a shows the effect on the stability boundaries by increasing γ from 0.5 to 1, in which at $\gamma = 1$ the stability boundaries are obtained from the Hsu–Bhatt–Vyshnegradskii stability chart. It should be noted that the stability boundaries given by the FCC method are analogous to the transition curves given in Fig. 3. If $\gamma = 1$ then Eq. (29) becomes the second order system with delay, to which a fractional damper can be added as

$$ {}_0^C\mathscr{D}_t^{2\gamma} x(t) = ax(t) + bx(t-\tau) + c\, {}_0^C\mathscr{D}_t^{\beta} x(t) \quad (0.5 < \gamma \leq 1) \tag{30} $$

where $c \in \mathbb{R}$. The stability plot of this system for the integer order damper and positive and negative damping coefficients is given in [3]. Figure 6b shows that adding a positive damping coefficient and increasing the order of the fractional damper enlarges the stable regions. Figure 6c demonstrates that increasing the fractional order of the damper shrinks the stable regions when the damping coefficient is negative. Figure 6d displays the influence of the damper coefficient for a first-order damper, where using a positive/negative damping coefficient enlarges/shrinks the stability domains.

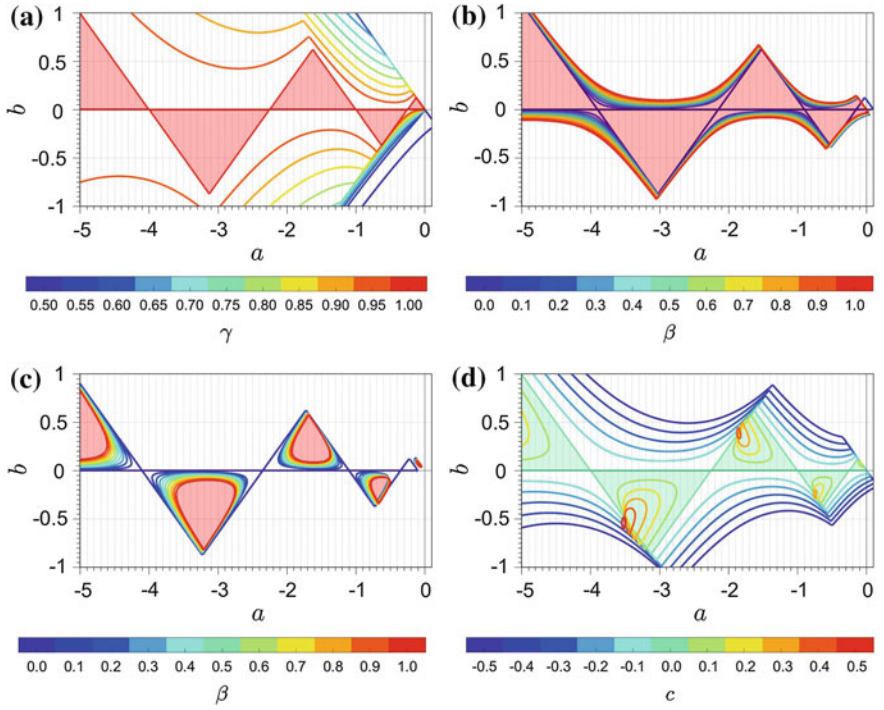

Fig. 6 The stability regions of system (30) with $\tau = 2\pi$ where the shaded regions indicate stable parameter sets for a specific value of the parameter in the *color bar*: **a** varying γ when $c = 0$, **b** β varying from 0 to 1 and $c = -0.1$, **c** β varying from 0 to 1 and $c = 0.1$, **d** c varying from -0.5 to 0.5 and $\beta = 0.5$

4.5 *Example: Control of the Fractional Damped Delayed Mathieu Equation*

In Sect. 3.2, the transition curves of the damped delayed Mathieu equation were obtained by the EHB method. Let $\tau = 1$, $\alpha = 0$, $\Omega = 2\pi$, and $c = 0.5$ in Eq. (13), and add a fractional delayed feedback control $u(t, \tau)$ (evaluated at $\tau = 1$ s) as

$$\begin{aligned} &\ddot{x}(t) + (a + b\cos(2\pi t))\, x(t) = 0.5x(t-1) + u(t) \\ &(x(t), \dot{x}(t)) = (1, 0), \ -1 \le t < 0 \end{aligned} \tag{31}$$

The stability regions of this system are shown in Fig. 7 in the $a - b$ parameter plane are obtained by using the FCC method when $u(t) = 0$. Comparing this figure with Fig. 1a reveals that the stability boundaries are a subset of the transition curves. Note that the $a = 0.2$ and $b = 0.1$ parameter set for the uncontrolled system corresponds to the unstable point denoted by a red solid circle in Fig. 7.

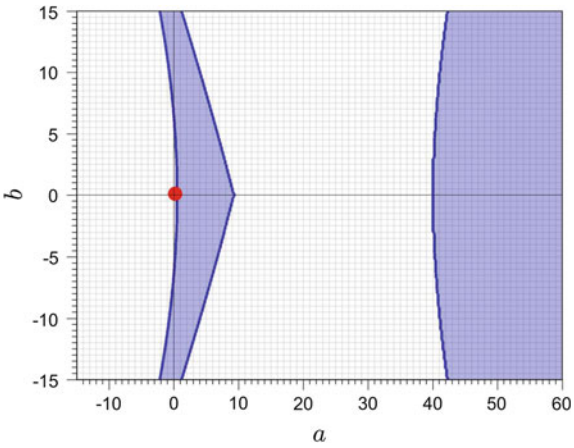

Fig. 7 Stability chart for uncontrolled system (31). The *red circle* point at $(a, b) = (0.2, 0.1)$ shows that the system is unstable at this set point. The *shaded* regions are stable

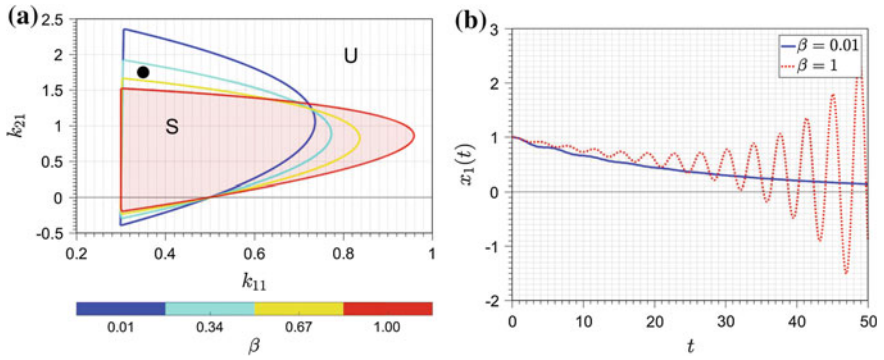

Fig. 8 **a** Stability chart for controlled system in Eq. (31) when the feedback control is chosen as Eq. (32) for a range of fractional order β. S and U denote the stable and unstable regions, respectively. The *shaded region* indicates the stable parameter sets for $\beta = 1$. **b** The responses of the system for the integer delayed feedback control (*red*) and the fractional delayed feedback control (*blue*, with $\beta = 0.01$), respectively, for $(k_{11}, k_{21}) = (0.35, 1.75)$ corresponding to the *black dot* in **a**

The fractional delayed feedback control is chosen to be of the form

$$u(t) = k_{11}\, x(t-1) + k_{21}\, {}_0^C\mathscr{D}_t^{\beta} x(t-1) \tag{32}$$

where $k_{11}, k_{21} \in \mathbb{R}$, and $0 \le \beta \le 1$. The stability chart of the closed-loop system is shown in Fig. 8a for different fractional orders. The system is stable inside the contours and unstable outside them. Figure 8a demonstrates how the stability boundaries enlarge horizontally and shrink vertically as the fractional order is decreased. According to this property, the use of fractional control is advantageous when

there are constraints in the selection of the control gains. For instance, for the case of $|k_{11} < 1|$ and $k_{21} > 1.5$, the feedback control can be chosen as $(k_{11}, k_{21}, \beta) = (0.35, 1.75, 0.01)$ which is shown by a black solid circle in Fig. 8a. The responses of the closed-loop system for $\beta = 1$ and $\beta = 0.01$ are shown in Fig. 8b. According to the figure, the closed-loop response is stable, for the choice of the control gains above, when the fractional order of the delayed feedback control is less than 0.5. Because of the closed stability region, it is feasible to find an optimal set $k_{11}^{opt}, k_{21}^{opt}$ for every fractional order for which the spectral radius ρ of the approximated monodromy matrix $\tilde{\mathscr{B}}$ is minimum. Consider changing the constant gains of the feedback control in Eq. (32) to periodic gains with two harmonics as

$$\begin{aligned} u(t) = &\left(k_{11} + k_{12}\cos(2\pi t) + k_{13}\sin(2\pi t)\right) x(t-1) + \\ &\left(k_{21} + k_{22}\sin(2\pi t) + k_{23}\cos(2\pi t)\right) {}_0^C\mathscr{D}_t^{\beta} x(t-1) \end{aligned} \tag{33}$$

where $k_{ij} \in \mathbb{R}$, $i = 1, 2$, $j = 1, 2, 3$. The six control gain coefficients k_{ij} are obtained by using an optimization algorithm where the optimization problem is defined by minimizing the spectral radius of the approximated monodromy matrix. To accomplish this, the `fmincon` function in the MATLAB Optimization Toolbox is used to minimize the spectral radius. The boundedness of the control gains are chosen as $k_{ij} < 2$ and the initial guess is chosen to be zero. Table 1 shows the optimal values of the periodic gains and the spectral radius for different values of the fractional order β. Note for the case of $\beta = 0.01$ that the fractional feedback term is approximately just the delayed position coordinate and hence adding control gain harmonics does not reduce the spectral radius significantly. As is illustrated in Fig. 9, however, for higher values of β it is seen that adding more gain harmonics results in a lower spectral radius and hence a faster convergence of the response. This benefit using periodic gains with optimization of the gain coefficients was also observed in the control of (integer order) periodic DDEs in [10].

Table 1 The optimal values of the periodic gains and the spectral radius of the discretized monodromy matrix for different values of the fractional order

β	$(k_{11}^{opt}, k_{21}^{opt}), \rho$	$(k_{11}^{opt}, k_{21}^{opt}, k_{12}^{opt}, k_{22}^{opt}), \rho$	$(k_{11}^{opt}, k_{21}^{opt}, k_{12}^{opt}, k_{22}^{opt}, k_{13}^{opt}, k_{23}^{opt}), \rho$
0.01	(0.37, 0.48), 0.59	(0.37, −0.23, 0.58, 0.23), 0.58	(0.37, −0.35, 0.26, 0.88, 0.99, 0.50), 0.58
0.34	(0.38, 0.39), 0.58	(0.37, −0.42, 0.53, 0.42), 0.57	(0.35, −0.89, 0.56, 0.71, 0.72, 0.71), 0.54
0.67	(0.39, 0.35), 0.56	(0.38, −0.60, 0.44, 0.40), 0.55	(0.34, −1.51, 0.82, 0.74, 0.56, 0.97), 0.46
1.00	(0.40, 0.35), 0.52	(0.38, −0.70, 0.52, 1.23), 0.39	(0.34, −1.67, 0.89, 0.64, 0.65, 0.14), 0.35

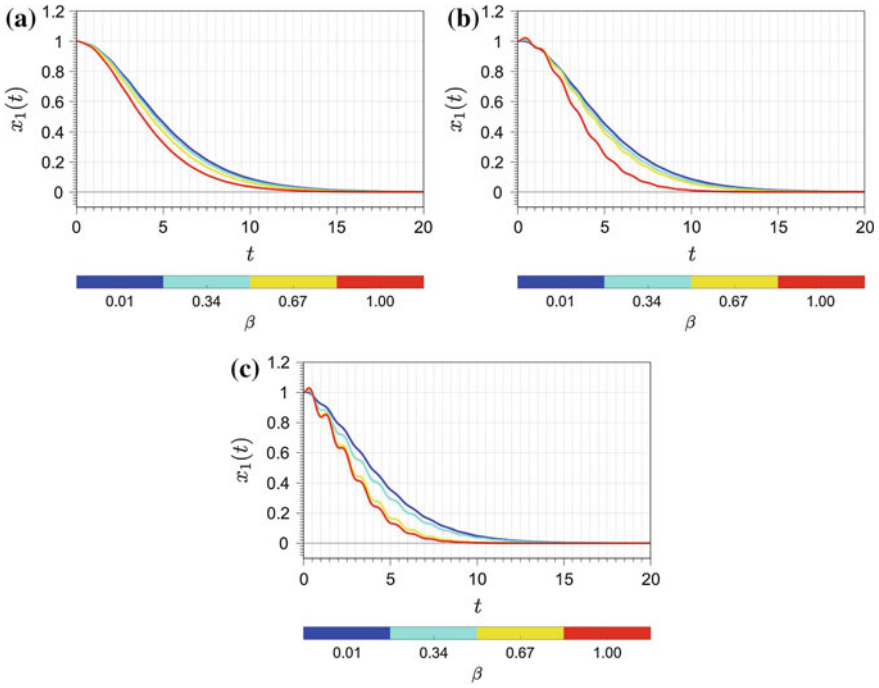

Fig. 9 The response of system (31) using the feedback control in (33). **a** Constant gains, see the second column of Table 1, **b** periodic gains with one harmonic included, see the third column of Table 1, **c** periodic gains with two harmonics included, see the fourth column of Table 1

5 Conclusions

In this chapter, two techniques were introduced to examine the transition curves and stability of linear periodic fractional delay differential equations (FDDEs). The explicit harmonic balance (EHB) method was first introduced to find the transition curves by employing operational matrices associated with a Fourier basis. It was shown that steady-state solutions of a linear periodic FDDE are of the form of a Floquet solution, i.e., a periodic function multiplied by an exponential function of time. Conditions for the existence of nontrivial solution in this form were obtained by setting the determinant of an infinite-dimensional matrix, i.e. the Hill's matrix, to zero. The approximation result was given by truncating the Hill's matrix. The efficiency of the EHB method was shown in finding transition curves of the fractional damped delayed Mathieu equation. Next, the fractional Chebyshev collocation (FCC) method was introduced to examine the stability of linear periodic FDDEs. By employing the abstract description of the solution's evolution in a Banach space and the short memory principle for fractional derivatives, the approximation of the monodromy operator was defined based on the state transition operator evaluated in the first period. The approximate solution was then obtained by discretizing the solu-

tion at Chebyshev–Gauss–Lobatto points. The advantages of the FCC method were illustrated in three different examples. In the first example, the fractional Hayes equation was introduced and its transition curves obtained analytically were compared to those obtained by the FCC method. In the second example, the stability of a second order differential equation with a fractional damper was discussed and the results were compared to the well-known Hsu–Bhatt–Vyshnegradskii stability chart. In the last example, the damped delayed Mathieu equation was considered and an optimal fractional delayed feedback control with periodic gains was proposed to stabilize the system. It was shown that using fractional feedback control is advantageous when there are constraints in the control gains and that using periodic control gains with optimization of the gain coefficients results in faster convergence of the response as compared to the constant gain feedback control.

References

1. Erneux, T.: Applied Delay Differential Equations, vol. 3. Springer Science & Business Media (2009)
2. Richard, J.-P.: Time-delay systems: an overview of some recent advances and open problems. Automatica **39**(10), 1667–1694 (2003)
3. Insperger, T., Stépán, G.: Semi-discretization method in delayed systems. Int. J. Numer. Methods Eng. **55**(5), 503–518 (2002)
4. Niculescu, S.-I.: Delay Effects in Stability: A Robust Control Approach, vol. 269. Springer Science & Business Media (2001)
5. Nazari, M., Butcher, E.A., Bobrenkov, O.A.: Optimal feedback control strategies in periodic delayed systems. Int. J. Dyn. Control **2**(1), 102–118 (2014)
6. Nayfeh, A.H.: Perturbation Methods. Wiley (2008)
7. Sinha, S., Butcher, E.A.: Symbolic computation of fundamental solution matrices in linear time-periodic dynamical systems. J. Sound Vib. **206**(1), 61–85 (1997)
8. Moiola, J.L., Chen, G.: Hopf Bifurcation Analysis. World Scientific (1996)
9. Nakhla, M.S., Vlach, J.: A piecewise harmonic balance technique in determination of periodic response of nonlinear systems. IEEE Trans. Circuits Syst. **23**(2), 85–91 (1976)
10. Butcher, E., Bobrenkov, O., Nazari, M., Torkamani, S.: Estimation and control in time-delayed dynamical systems using the chebyshev spectral continuous time approximation and reduced Liapunov-Floquet transformation. In: Sun, J.-Q., Ding, Q. (eds.) Recent Advances in Analysis and Control of Time-delayed Dynamical Systems, ch 8. World Scientific/Higher Education Press, Beijing (2013)
11. Butcher, E.A., Ma, H., Bueler, E., Averina, V., Szabo, Z.: Stability of linear time-periodic delay-differential equations via Chebyshev polynomials. Int. J. Numer. Methods Eng. **59**(7), 895–922 (2004)
12. Kilbas, A.A., Srivastava, H.M., Trujillo, J.J.: Theory and Applications of Fractional Differential Equations, vol. 204. Elsevier Science Inc. (2006)
13. Podlubny, I.: Fractional Differential Equations: An Introduction to Fractional Derivatives, Fractional Differential Equations, to Methods of their Solution and Some of Their Applications. Academic Press (1998)
14. Petras, I.: Fractional-Order Nonlinear Systems: Modeling, Analysis and Simulation. Springer Science & Business Media (2011)
15. Nigmatullin, R.R., Trujillo, J.J.: Mesoscopic fractional kinetic equations versus a Riemann-Liouville integral type. In: Sabatier, J., Agrawal, O.P., Machado, J.T. (eds.) Advances in Fractional Calculus, ch. 2, pp. 155–167. Springer (2007)

16. Dabiri, A., Nazari, M., Butcher, E.A.: Optimal fractional state feedback control for linear fractional periodic time-delayed systems. In: American Control Conference (ACC), Boston, MA, 6–8 July 2016
17. Dabiri, A., Butcher, E.A., Nazari, M.: One-dimensional impact problem in fractional viscoelastic models. In: International Design Engineering Technical Conferences & Computers and Information in Engineering Conference (IDETC/CIE), Charlotte, NC, 21–24 Aug 2016
18. Dabiri, A., Nazari, M., Butcher, E.A.: The spectral parameter estimation method for parameter identification of linear fractional order systems. In: American Control Conference (ACC), Boston, MA, 6–8 July 2016
19. Dabiri, A., Butcher, E.A., Poursina, M.: Fractional delayed control design for linear periodic systems. In: International Design Engineering Technical Conferences & Computers and Information in Engineering Conference (IDETC/CIE), Charlotte, NC, 21–24 Aug 2016
20. Fioravanti, A.R., Bonnet, C., Özbay, H., Niculescu, S.-I.: A numerical method in stability windows and unstable root-locus calculation in linear fractional time-delay systems. Automatica **48**(11), 2824–2830 (2012)
21. Mesbahi, A., Haeri, M.: Stability of linear time invariant fractional delay systems of retarded type in the space of delay parameters. Automatica **49**(5), 1287–1294 (2013)
22. Rand, R.H., Sah, S.M., Suchorsky, M.K.: Fractional Mathieu Equation. Commun. Nonlinear Sci. Numer. Simul. **15**(11), 3254–3262 (2010)
23. Debbouche, A., Torres, D.F.: Approximate controllability of fractional nonlocal delay semilinear systems in Hilbert spaces. Int. J. Control **86**(9), 1577–1585 (2013)
24. Lin, Y., Xu, C.: Finite difference/spectral approximations in the time-fractional diffusion equation. J. Comput. Phys. **225**(2), 1533–1552 (2007)
25. Weilbeer, M.: Efficient Numerical Methods in Fractional Differential Equations and their Analytical Background. Papierflieger (2005)
26. Dabiri, A., Nazari, M., Butcher, E.A.: Explicit harmonic balance method for transition curve analysis of linear fractional periodic time-delayed systems. In: 12th IFAC Workshop on Time Delay Systems TDS 2015, Ann Arbor, MI, 28–30 June 2015
27. Butcher, E.A., Dabiri, A., Nazari, M.: Transition curve analysis of linear fractional periodic time-delayed systems via explicit harmonic balance method. J. Comput. Nonlinear Dyn. **11**(4), 041005 (2016)
28. Trefethen, L.N.: Spectral Methods in MATLAB. Society for Industrial and Applied Mathematics, vol. 10 (2000)
29. Boyd, J.P.: Chebyshev and Fourier Spectral Methods. Courier (2001)

Design of Imaginary Spectrum of LTI Systems with Delays to Manipulate Stability Regions

Rifat Sipahi

Abstract This chapter is on the design problem of linear time-invariant (LTI) systems with delays. Our recent studies on the use of algebraic techniques, namely resultant and iterated discriminants operations, in connection with the well-known Rekasius transformation implemented on the system characteristic equation already revealed that it is indeed possible to compute the exact range of the imaginary spectrum of such systems. This know-how, which is the key toward understanding the stabilty/instability decomposition of the system, is utilized here to craft the imaginary spectrum of LTI systems with multiple delays, specifically with the aim to manipulate stability regions in a systematic manner in the delay parameter space.

1 Introduction

Many dynamical systems are affected by time delays, mainly because these systems may not obtain sensor measurements instantaneously and may require time to compute and/or prepare decisions to react to certain stimuli. Applications in this context are numerous from mechatronics, network control systems, and vibration control, to system dynamics and operations research, systems biology, and human-in-the-loop control [31].

The presence of delays can be detrimental to the behavior of dynamical systems, especially when such delays appear in a feedback loop setting. Delays may cause low performance and lead to instability if the controller in the loop is not properly designed. In the context of linear time-invariant (LTI) systems, this can be explained by delays unfavorably affecting system eigenvalues. Delay parameter can configure stable system eigenvalues in close proximity to the imaginary axis of the complex plane; a low performance indicator. It may also migrate these eigenvalues into the right-half complex plane, causing instability [32].

R. Sipahi (✉)
Department of Mechanical and Industrial Engineering, Northeastern University,
360 Huntington Avenue, Boston, MA 02115, USA
e-mail: rifat@coe.neu.edu

T. Insperger et al. (eds.), *Time Delay Systems*,
Advances in Delays and Dynamics 7, DOI 10.1007/978-3-319-53426-8_9

While delays have been largely considered to be detrimental to dynamic behavior, careful engineering of the feedback loop dynamics in the presence of delays can be beneficial for the system at hand. In this direction many studies have been published reporting how in some cases larger delays can stabilize an otherwise unstable system with smaller delays [1, 19, 21, 32]. Similarly, disturbance rejection capability of a feedback control system may be relatively satisfactory despite the presence of delays [21]. In some sense, all these phenomena can be considered analogous to the classical root locus problem whereby the delay parameter manipulates system eigenvalues on the complex plane, in certain ways that may lead to either detrimental or beneficial outcomes.

One of the most studied problems in the area of dynamical systems with time delays is the stability analysis of LTI systems with constant delays [4, 11, 12, 22]. These studies date back to early 1960s, and still today many problems remain open. A largely studied topic in the literature is regarding the stability decomposition of the system, either in the delay parameter space or in system parameter space [12, 30–32]. The objective is to reveal for what parameter ranges the system is stable/unstable, which in general requires the solution of a transcendental, hence infinite dimensional, eigenvalue problem. Along these lines many advancements have been reported, including those based on single and multiple delays, see [31] and the references therein. Irrespective of approach taken, all these results respect two fundamental and universal theorems, one regarding the continuity property of the real part of the system eigenvalues with respect to the parameter space [4], and the other regarding the stability/instability decomposition in the parameter space based on the well-known D-/tau-decomposition theorems [11, 15].

As per the above-mentioned theorems, it is known that stability/instability decomposition of a LTI system with L number of delays is made of countably many L-dimensional regions in the delay parameter space, where in each region the system is either stable or unstable. Moreover, these regions are separated by some "boundaries", i.e., L-dimensional hypersurfaces $\mathscr{H}$, where delays on these hypersurfaces yield at least one system eigenvalue that lies on the imaginary axis of the complex plane. In other words, these boundaries are strongly affected by the imaginary spectrum Ω of the LTI system [24].

Stability maps have been extremely valuable in visually presenting key information about the stability of an LTI system [12, 24, 31, 32]. These maps simply lay out which combinations of delays and/or system parameters would render the system stable. Moreover, parametric studies can be performed to investigate how stable regions change in favor of stability and/or certain design requirements. As expected, these regions will distort, shrink, and expand based on the aforementioned boundaries separating the stable regions from unstable ones. Therefore, understanding the mechanisms under which these boundaries are affected would be extremely valuable not only for the use of stability maps for analysis purposes, but more importantly manipulating these maps strategically in order to render a more desirable stability/instability decomposition.

While many studies published in the literature are for the "analysis" of time delay systems and revealing the corresponding stability maps, there is little information as to how to systematically influence stability maps. Currently, one option is to utilize the published tools, scan the parameter space of interest, produce a set of stability maps, and decide which parameter setting renders a more desirable stability/instability decomposition. Other than the trial–error nature of this approach, its one other main limitation is that it does not utilize the key information regarding how the stability boundaries are formed; specifically how these boundaries in the delay parameter space are dictated by the imaginary spectrum Ω of the dynamics.

Recent studies on frequency sweeping techniques [2] offer insight into the above formulated problem. For instance, in [10] authors utilized frequency sweeping techniques to demonstrate various shapes of stability maps being formed based on certain properties of Ω. In [8, 9, 14], these ideas were implemented in 3D stability maps whereby the authors systematically laid out those properties for the formation of different 3D stability volumes. In [25] authors computed 2/3D stability surfaces for problems with multiple fixed delays. In [6, 7, 26], our group tailored together algebraic techniques, namely resultant and iterated discriminants operations, in connection with the well-known Rekasius transformation [23] to compute the "exact range" of the imaginary spectrum Ω of LTI systems with multiple fixed and/or unknown delays. Moreover, this range may be a union of multiple distinct ranges, lower and upper bound of each of which can be computed precisely [5]. In this chapter, this know-how forms the basis to craft the imaginary spectrum of an LTI system with multiple delays, with the aim to influence the stability/instability decomposition of the system to ultimately expand or shrink stability regions systematically.

The chapter is organized as follows. In Sect. 2, preliminaries regarding the computation of the exact ranges of Ω are presented from our previous work. This is followed by Sect. 3 where an approach is presented to manipulate the spectrum in a strategic manner to be able to expand/shrink stability regions of stability maps. The chapter ends with discussions and future work in Sect. 4.

Notations are standard. The set of real and complex numbers are respectively denoted by $\mathbb{R}$ and $\mathbb{C}$, and n-dimensional real-valued vectors are in $\mathbb{R}^n$. The complex plane is a union of three disjoint sets, namely, the left-half complex plane $\mathbb{C}_-$, imaginary axis $j\mathbb{R}$, and right-half complex plane $\mathbb{C}_+$. The resultant of two polynomials $p(x)$ and $q(x)$ by eliminating x is denoted by $\mathscr{R}_x(p(x), q(x))$. Similarly, the discriminant of $p(x)$ eliminating x is expressed as $\mathscr{D}_x(p(x))$, which is equivalent to $\mathscr{R}_x(p(x), dp(x)/dx)$. For functions with more than one variable, the variable of interest for the parametric study is listed as the first argument separated from the remaining variables by a semi-column, e.g., $f(x; y, z)$. The real and imaginary parts of a complex number z are denoted respectively by $\mathfrak{R}(z)$ and $\mathfrak{I}(z)$.

2 Preliminaries

The class of LTI systems with multiple delays considered in this chapter is represented in the following state space form,

$$\frac{d}{dt}x(t) = \sum_{v=0}^{L} A_v x(t-\tau_v), \tag{1}$$

where delay τ_v is nonnegative, $x(t) \in \mathbb{R}^n$ is the state vector, delayed state vector x_{τ_v} is given by $x(t+\theta)$ with $\theta \in [-\tau_v, 0]$, A_v are $n \times n$ square matrices, L is a nonzero integer, and without loss of generality we have $0 = \tau_0 \leq \tau_1 \ldots \leq \tau_L$. The dynamics in (1) is known as *retarded* class systems since the highest derivative of the state is not influenced by any delay terms [32].

The characteristic function of the dynamics in (1) reads

$$f(s; e^{-s\tau_v}) := \det\left[sI - \sum_{v=0}^{L} A_v e^{-s\tau_v}\right], \tag{2}$$

where I is the $n \times n$ identity matrix and $s \in \mathbb{C}$ is the Laplace variable. The zeros s of (2), given $\tau_v = \tau_v^*$ and $A_v = A_v^*$, determine the stability of system (1). The system is stable if and only if all these zeros have negative real parts; otherwise it is unstable. Notice however that solving for s from (2) is challenging, if not impossible, mainly because (2) has infinitely many solutions due to the transcendental nature of exponential terms.

Although solving all the zeros of (2) is impossible, what is more critical is to compute the most relevant zeros, which are the dominant/rightmost roots of the dynamics. These roots are defined in the traditional sense as those with the largest real parts. Importantly, computing the dominant roots of (2) is nontrivial, and a number of elegant techniques addressing this technical problem was published, see a review in [31].

In terms of system's transition from stability to instability, or vice versa, one fundamental principle needed is the root continuity argument [4]. For retarded class systems, such as the one in (1), the spectral abscissa function defined as

$$\sigma = \sup\{\Re(s) | s \text{ is a zero of (2) given } \tau_v \geq 0, v = 1, \ldots, L\} \tag{3}$$

is continuous in the parameter space of delays, including in the vicinity of the origin of the delay parameter. This property is key to establishing a stability analysis framework. It implies that the stability of the system is preserved under sufficiently small perturbations on the delay parameter, and stability can be lost only if one of the eigenvalues of (1) touches the imaginary axis $j\mathbb{R}$ of the complex plane at $s = j\omega^*$ for some $\tau_v^* \geq 0$, i.e., when $\sigma = 0$.

Notice that, when an eigenvalue crosses over the imaginary axis at $s = j\omega^*$ as the delay parameter is perturbed from τ_v^* to $\tau_v^* + |\varepsilon|$, $|\varepsilon| \ll 1$, this does not necessarily mean that the system transitions from stable to unstable behavior, for two reasons. First of all, the system may already have unstable eigenvalues for τ_v^*. Second, the transition may not be necessarily toward the right-half complex plane $\mathbb{C}_+$. In other words, having an eigenvalue on the imaginary axis is only a necessary condition for a system to transition from stability to instability.

In light of the above rationale, stability analysis of (1) requires detecting all its imaginary eigenvalues, which is equivalent to solving the occurrence of $s = j\omega$ in the entire domain of the delay parameter space $\tau_v \geq 0$. This solution satisfies

$$F(j\omega; e^{-j\omega\tau_v}) := \det\left[j\omega I - \sum_{v=0}^{L} A_v e^{-j\omega\tau_v}\right] = 0, \tag{4}$$

where $\omega \geq 0$ without loss of generality.

2.1 Rekasius Transformation

Among many techniques published in the literature, one direction that can be taken to compute the roots of F in (4) is to utilize the well-known Rekasius transformation, which suggests replacing the exponential functions in (4) by a bilinear transformation. The single delay version of this transformation, $L = 1$, was proposed in [23], see also [20]; and especially its multiple delay versions lead to a large body of literature, starting with [28], see details in [24]. To simplify the presentation and notations, consider first the Rekasius transformation for the single delay case $\tau_1 = \tau$,

$$e^{-j\omega\tau} := \frac{1 - j\omega T}{1 + j\omega T}, \tag{5}$$

where $T \in \mathbb{R}$ is also known as the "pseudo-delay" [18]. It is extremely critical to note that the above transformation is not a Pade approximation, since the right-hand side term does not have τ but a new parameter T. Moreover, the transformation (5) is exact so long as both sides of the equation agree in modulus and phase. Since the modulus is unity on both sides, the only requirement for the transformation to be exact is the following condition derived from the phase condition,

$$\tau_k = \frac{2}{\omega}(\arctan(\omega T) \mp k\pi), \tag{6}$$

where $k \geq 0$ is an integer arising due to trigonometric identities.

Notice that from (6), it becomes apparent that an imaginary axis crossing at $s = j\omega$ will be created by infinitely many delay values $\tau = \tau_k$. Moreover, the system dynamics may have multiple crossings, $\Omega = \{\omega_1, \ldots, \omega_p, \ldots, \omega_P\}$. In this case, the delay

values causing these crossings are given by $\tau = \tau_k^{(p)}$, $p = 1, \ldots, P$, $k = 1, \ldots, \infty$. Detailed discussions on these principles can be found in [20, 24].

To give an example for the single delay case, let the characteristic equation in (4) on the imaginary axis $s = j\omega$ be

$$F(j\omega; e^{-j\omega\tau}) = j\omega + \alpha + \beta e^{-j\omega\tau} = 0, \tag{7}$$

which, after Rekasius transformation (5), becomes

$$\overline{F}(j\omega; T) = j\omega + \alpha + \beta \frac{1 - j\omega T}{1 + j\omega T} = 0, \tag{8}$$

where the term $1 + j\omega T \neq 0$ since T and ω are real quantities. In light of this, the above equation can be expanded by this term to obtain,

$$\tilde{F}(j\omega; T) = (j\omega + \alpha)(1 + j\omega T) + \beta(1 - j\omega T) = 0. \tag{9}$$

The interpretation of the system crossings in relationship to τ and T is as follows. The parametric equation in (9) has a root at $s = j\omega$ for some $T^* \in \mathbb{R}$ if and only if the original equation (7) has a root at $s = j\omega$ for some $\tau^* \geq 0$. The relationship between T^* and τ^* is established through (6). That is, for the root at $s = j\omega$ of (9) with $T = T^*$, the original equation (7) has a root also at $s = j\omega$, but for infinitely many delay values τ_k as formulated in (6) with one of those delays being τ^*.

With the above discussions, it is clear that one can study the algebraic polynomial (9) for its imaginary roots, as an alternative to studying the same roots from the transcendental equation (7), see the above cited studies. Once all (ω, T) pairs satisfying (9) are found, it is then straightforward to compute the delay values τ_k of the original system using (6).

In the case of multiple delays the approach requires one to deal with multiple T_v parameters [24, 29] where one applies the Rekasius transformation for each delay term independently,

$$e^{-j\omega\tau_v} := \frac{1 - j\omega T_v}{1 + j\omega T_v}, \tag{10}$$

with the inverse mapping condition

$$\tau_{v,k_v} = \frac{2}{\omega}(\arctan(\omega T_v) \mp k_v \pi), \tag{11}$$

considering a single crossing at $s = j\omega$. Notice however that in the case of multiple delays, the crossing set Ω does not have discrete crossing points, rather it is in general a continuous function of the delay parameters.[1] That is, the delays τ_{v,k_v} lie on L-dimensional hypersurfaces $\mathscr{H}$.

[1] Here we assume that the system indeed exhibits crossings. Otherwise Ω is an empty set, and the system is delay-independent stable, or unstable.

2.2 Stability Switchings and Their Relation to Ω

Let us now demonstrate how $\mathscr{H}$ in stability maps are obtained, and how the imaginary spectrum Ω of the LTI system plays a critical role in determining the stability/instability decomposition of the system.

Take the following scalar characteristic equation with two delays, $L = 2$,

$$F(j\omega; e^{-j\omega\tau_v}) = j\omega + \alpha + \beta_1 e^{-j\omega\tau_1} + \beta_2 e^{-j\omega\tau_2} = 0. \tag{12}$$

The equation corresponding to $\tilde{F}$ then becomes,

$$\begin{aligned}\tilde{F} = (j\omega + \alpha)(1 + j\omega T_1)(1 + j\omega T_2) + \beta_1(1 - j\omega T_1)(1 + j\omega T_2) \\ +\beta_2(1 - j\omega T_2)(1 + j\omega T_1) = 0,\end{aligned} \tag{13}$$

which holds if and only if its real and imaginary parts are zero, that is, the following equations must be satisfied,

$$\tilde{F}_r = \left((-\alpha + \beta_1 + \beta_2)\, T_1\, T_2 - T_1 - T_2\right)\omega^2 + \alpha + \beta_1 + \beta_2 = 0, \tag{14}$$

$$\tilde{F}_i = \left[-T_1\, T_2\, \omega^2 + \left((\alpha\ - \beta_1 + \beta_2)T_1 + (-\beta_2 + \alpha + \beta_1)\, T_2 + 1\right)\right]\omega = 0. \tag{15}$$

Given α, β_1, and β_2, the above polynomials can be solved in many different ways. One elegant implementation, which would work without a theoretical limitation on the order of polynomials, is to utilize the elimination theory. This process reduces these two polynomials into a single polynomial with one less variable of choice. The process starts with building a Sylvester matrix using the coefficients of the choice of variable for elimination. The necessary condition for (14) and (15) to hold is that this matrix is singular, i.e., its determinant is zero. The determinant of Sylvester matrix is also known as the "resultant" [33].

The resultant $\mathscr{R}_\omega(\tilde{F}_r(\omega), \tilde{F}_i(\omega))$ obtained by eliminating ω from (14) and (15) is calculated as a fourth order multinomial only in terms of T_1 and T_2. Zeros of $\mathscr{R}_\omega$ are "candidates" satisfying (14) and (15). At this point, one can scan $T_2 \in \mathbb{R}$ in a certain range and solve for $T_1 \in \mathbb{R}$ from $\mathscr{R}_\omega = 0$, and next use these T_1, T_2 pairs in (14) and (15) to check whether or not a common $\omega \geq 0$ solution exists. If it does, then the pairs (ω, T_1) and (ω, T_2) are used in (11) to compute the delay pairs $\tau_{1,k_1}, \tau_{2,k_2}$.

Another approach that can be utilized is to construct a Routh's array using (13) but with the Laplace variable s in place of $j\omega$ [24, 29]. In this case, one obtains a parametric array in terms of T_1, T_2, and can take advantage of some of the key features of the array to obtain the necessary and sufficient conditions for an imaginary crossing at $s = j\omega$ to occur. These conditions can indeed be extracted from the s^1 row element of the array being zero $R_1 = 0$, and the s^2 row elements R_{21} and R_{22} forming an auxiliary equation $R_{21}s^2 + R_{22} = 0$ with a root at $s = j\omega$ [24, 29]. For example, let $\alpha = 1$, and $\beta_1 = \beta_2 = 2$, then the conditions are given by

$$R_1 = \frac{(1-3T_2)T_1^2 + (-6T_2+1-3T_2^2)T_1 + T_2 + T_2^2}{R_{21}}, \tag{16}$$

$$R_{21} = T_2 + T_1 - 3T_1T_2, \quad \text{and} \quad R_{22} = 5. \tag{17}$$

A scanning of, e.g., T_2 can be performed to solve for the candidate T_1 from $R_1 = 0$, which can then be used in $R_{21}s^2 + R_{22} = 0$ to check if a root at $s = j\omega$ exists. If it does, a similar procedure is followed as explained above to compute the delay values $\tau_{1,k_1}, \tau_{2,k_2}$. Notice that ω is upper bounded for retarded class systems and it is known that R_{22} is in general a constant term. Hence $R_{21} \neq 0$, and zeros of R_1 can be checked only from its numerator.[2] Application of the above logic leads to the delay pairs $\tau_{1,k_1}, \tau_{2,k_2}$, where for each delay pair, the system has eigenvalues at $s = \mp j\omega$ on the imaginary axis. These delay values lie on $\mathscr{H}$ which in the case of two delays $L = 2$ are known as the "potential stability switching curves" (PSSC) of the system.

Furthermore, each delay pair on PSSC corresponds to at least one crossing frequency ω, that is, $\omega(\tau_1, \tau_2)$, with $(\tau_1, \tau_2) \in$ PSSC. Post processing of our computations for the above problem shows that $\omega \in \Omega = [0, 3.8728]$, with the extrema at $\omega = 0$ and $\omega = 3.8728$. Observe that for a fixed ω, $\omega \in \Omega$, the distance between delay points along any delay axis is given by $2\pi/\omega$, see (11) and also the concepts of kernel and offspring in [24, 29]. This corresponds, in the example at hand, respectively to delay points separated from each other by the maximal distance of infinite and the minimal distance of $2\pi/3.8728 = 1.6224$. Notice that the range of Ω arises as an "end result" of the above-described approaches, which unfortunately do not permit revealing the extrema of Ω in an analytical and systematic way.

3 Main Results: Manipulating the Stability Decomposition

3.1 *Rekasius Substitution with Frequency Sweeping*

Frequency sweeping has been utilized in solving many stability problems [2], and more recently was used to reveal 3D stability surfaces and/or characterize their geometries [8–10, 14, 25, 26]. In the context of the above example, the common roots of (14) and (15) can indeed be computed by scanning the ω variable instead of scanning the T_v variables. Interestingly, this is not a naive choice[3] as it offers new opportunities for multiple delay problems $L > 3$, revealed recently by our group [6, 26]. First, frequency sweeping helps extracting the "cross-sectional" views of

[2] These observations lead to a general proof that, except for possibly some special points in T_v, for a feasible $s = j\omega$ solution to exist the hypersurfaces formed by R_{21} and the numerator of R_1 do not intersect in the L-dimensional T_v parameter space [27].

[3] Notice that sweeping the frequency ω is not equivalent to sweeping T_v, $\omega\tau_v$, or ωT_v due to the intricate nonlinear relationships between (10) and (11), see also [5, 26].

PSSC in lower dimensions especially for problems with more than three delays and where some delays must be fixed "a priori". Since visualization of stability maps in dimensions larger than three is impossible, this approach is attractive. Second, it permits computing the exact upper/lower bounds of the set Ω, which as demonstrated in the next subsection will allow manipulating the concentration of PSSC, thereby the stability regions, in the delay parameter space.

With regard to obtaining cross-sectional views of PSSC, fix $\tau_v = \tau_v^*$ for all $v = 3, \ldots, L$ in (4). Then the exponential terms with $v = 3, \ldots, L$ must "not" undergo any transformations since transformations are valid only for uncertain delays [5, 26]. For this reason, it makes perfect sense to sweep ω and set these exponential terms to complex numbers. One is then left with only two variables (T_1, T_2) for each fixed ω sampled from a range $[0, \overline{\omega}]$, where $\overline{\omega}$ is known to be upper bounded. Using then the real and imaginary parts of the characteristic equation, one can compute the common $(T_1, T_2) \in \mathbb{R}^2$ roots, if they exist. Having (T_1, ω) and (T_2, ω) pairs at hand, the delay values $\tau_{1,k_1}, \tau_{2,k_2}$ can be easily calculated, corresponding to the a priori fixed τ_v^*, $v = 3, \ldots, L$, delay values [5, 6, 26, 27].

3.2 *Computing* $\sup(\Omega)$ *Using Iterated Discriminant Operations*

The maximal value $\overline{\omega} = \sup(\Omega)$ that the frequency ω will take is critical for two reasons. First of all, it determines the range of frequency sweeping and thus can help prevent unnecessary sweeping to much larger values than needed [5, 26]. Second, it determines the minimal distance between the delay points corresponding to this maximal frequency—the main focus of this chapter. This distance, which is $2\pi/\overline{\omega}$, determines how densely/sparsely the PSSC are packed in the delay parameter space. In some sense, larger $\overline{\omega}$ will cause the delay points to be produced more densely, and this will render many PSSC of the system per area. Conversely, smaller $\overline{\omega}$ will cause sparsely distributed PSSC on the delay plane, which will ultimately affect the size of stability regions.

On the other hand, the mechanisms of how $\overline{\omega}$ influences the concentration of stability/instability regions have so far not been investigated, mainly because it was not known until recently for the general problem how one would compute $\overline{\omega}$ analytically and systematically [6, 26, 27] without brute force computations and parameter scanning. The main idea in computing $\overline{\omega}$ lies in an optimization scheme developed by our group starting with [6]; later extended in [26] including delay-independent stability problems [5, 7, 16, 17], where one seeks for the extrema of ω from the common solutions of the surfaces $\tilde{F}_r(\omega; T_1, \ldots, T_L) = 0$ and $\tilde{F}_i(\omega; T_1, \ldots, T_L) = 0$. Since these surfaces are explicit functions of ω, a simple explicit solution of $\omega(T_1, \ldots, T_L)$ is impossible to obtain yet the elimination technique and resultants can be used to simplify the problem.

First of all, if $\tilde{F}_r = 0$ and $\tilde{F}_i = 0$ have common roots, then it is necessary that

$$\Theta_1(\omega; T_2, \ldots, T_L) := \mathscr{R}_{T_1}(\tilde{F}_r(\omega; T_1, \ldots, T_L), \tilde{F}_i(\omega; T_1, \ldots, T_L)), \tag{18}$$

is also zero. If an extremum of ω exists, then this extremum can be computed from Θ_1. Note that the necessary condition for this extremum to exist is that the following partial differential equations vanish, $\partial\omega/\partial T_v = 0, v = 2, \ldots, L$, so long as ω is a smooth function of T_v, see proofs and discussions on smoothness in [27]. Let us first study $v = 2$ using the constraint equation (18). Notice that in view of implicit function theorem, in a small neighborhood in T_v parameter space, we can express $\omega = \omega(T_1, \ldots, T_v)$. Considering smoothness properties hold, we can write,

$$\frac{\partial\Theta_1}{\partial\omega}d\omega + \frac{\partial\Theta_1}{\partial T_2}dT_2 = 0, \tag{19}$$

from which we have the following discussions. Since $\partial\omega/\partial T_v = 0$ must hold, whether the extremum of ω is a regular or a singular point, it is necessary but not sufficient that $\partial\Theta_1/\partial T_2 = 0$ obtained from (19) holds. In other words, for ω to exhibit an extremum, it is necessary that both $\Theta_1 = 0$ and its partial derivative with respect to T_2 must vanish. To find the common solutions between these two polynomials, we can once again utilize the resultant; this time by eliminating T_2,

$$\Theta_2(\omega; T_3, \ldots, T_L) := \mathscr{R}_{T_2}\left(\Theta_1(\omega; T_2, \ldots, T_L), \frac{\partial\Theta_1(\omega; T_2, \ldots, T_L)}{\partial T_2}\right), \tag{20}$$

which is nothing but the discriminant of Θ_1 with eliminating T_2,

$$\Theta_2(\omega; T_3, \ldots, T_L) := \mathscr{D}_{T_2}\left(\Theta_1(\omega; T_2, \ldots, T_L)\right). \tag{21}$$

With a similar logic as above, one can now focus on T_3 and solve the common roots between Θ_2 and $\partial\Theta_2/\partial T_3$, which leads to an "iterated discriminant" formulation,

$$\Theta_3(\omega; T_4, \ldots, T_L) := \mathscr{D}_{T_3}\left(\mathscr{D}_{T_2}\left(\Theta_1(\omega; T_2, \ldots, T_L)\right)\right). \tag{22}$$

Application of the above process successively on all T_v yields a single variable polynomial $\Theta_L(\omega) := D(\omega)$ only in terms of ω. For ω to exhibit an extremum, it is necessary that this polynomial is zero for some $T_v \in \mathbb{R}$ [5, 26].

In the above process, what we have done is to project the tangent lines of the $(L+1)-$dimensional surface to lower dimensions, where tangent lines touch the surface at points that are candidates for the extrema points. Now that $D(\omega)$ is obtained, its finite number of roots can be easily computed, ω_q, $q = 1, \ldots, \overline{q}$, and then one plugs in each candidate solution into Θ_{L-1} to solve for candidate $T_L \in \mathbb{R}$ solutions. These solutions are then plugged into Θ_{L-2} to solve for candidate $T_{L-1} \in \mathbb{R}$ solutions. If at the end of this process a candidate ω_q corresponds to $T = (T_1, \ldots, T_L) \in \mathbb{R}^n$ then this ω is in the set of extremum points.

For the example presented in (12), since we have only two T_v variables, one needs a resultant and a discriminant. The MAPLE code for this operation is,

```
> restart: a:=1: b1:=2: b2:=b1:
> f:=s+a+b1*exp(-tau1*s)+b2*exp(-tau2*s):
> Rk1:=(1-T1*s)/(1+T1*s): Rk2:=(1-T2*s)/(1+T2*s):
> h:=simplify(eval(f,{exp(-tau1*s)=Rk1, exp(-tau2*s)=Rk2})
*(1+T2*s)*(1+T1*s)): assume(T1,real,T2,real,omega,real):
> h:=eval(sort(collect(h,s),s),s=I*omega): fre:=Re(h):
> fim:=Im(h): with(LinearAlgebra): with(linalg):
> Theta[1]:=sort(simplify(det(SylvesterMatrix(fre,fim,T1)))
,omega): Theta[2]:=sort(simplify(det(SylvesterMatrix(
   Theta[1], diff(Theta[1],T2),T2))),omega);
```

which yields

$$\Theta_2(\omega) := \mathscr{D}_{T_2}\left(\mathscr{R}_{T_1}(\tilde{F}_r(\omega;T_1,T_2),\tilde{F}_i(\omega;T_1,T_2))\right), \tag{23}$$

$$= -4\omega^{13} + 68\omega^{11} - 108\omega^9 - 180\omega^7, \tag{24}$$

nonnegative real zeros of which $\{0, 1.732050808, 3.872983346\}$ are candidates for extrema points of Ω, ignoring repeated roots for a compact presentation.

It can be confirmed that only 0 and 3.872983346 correspond to $(T_1, T_2) \in \mathbb{R}^2$, hence $\overline{\omega} = 3.872983346$, which validates the computational results at the end of Sect. 2.2. Moreover, we can conclude that $\Omega = [0, 3.872983346]$. This is the only range in which ω must be scanned to compute *all* the PSSC. Needless to say, the above approach can be implemented on problems with any number of delays only limited by available computational power, and will become handy especially when $L > 2$ [26]. Furthermore, several trivial manipulations can be considered in this universal approach. For instance, the resultant can be expanded in different ways, e.g., using a homomorphism algorithm [3] as was done in [26]. Needless to say, resultant is unique, and regardless of how it is obtained, results in [26] stand.

3.3 Case Study

Now that an analytical technique to compute $\overline{\omega}$ is established, it becomes possible to consider parametric variations in the system characteristic equation, to investigate the changes in $\overline{\omega}$ which are inversely related to enlarged spacings between PSSC. Notice that it is impossible to estimate all possible intricate geometries of PSSC that may arise from the problem, and moreover Ω may be a union of multiple disjoint sets, each corresponding to different curve patterns. Nevertheless, "controlling" $\overline{\omega} = \sup(\Omega)$ will eventually allow for larger spacing between some segments of the PSSC, increasing the likelihood of larger stable regions.

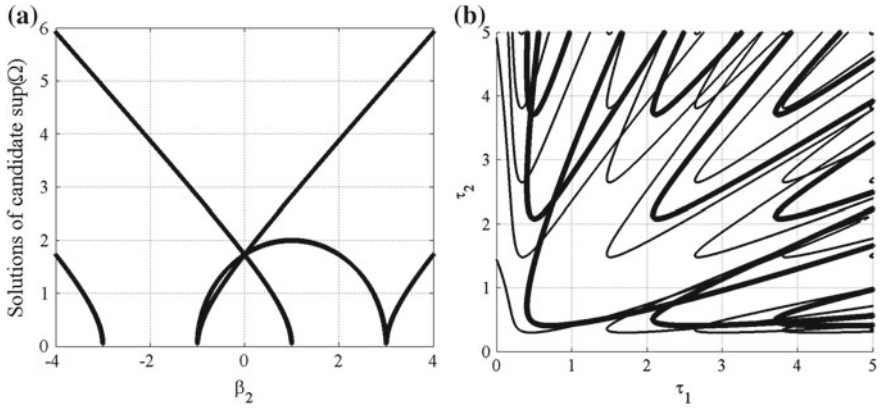

Fig. 1 **a** Positive real roots of $\Theta_2(\phi;\beta_2)=0$ with respect to β_2 are candidates for $\overline{\omega}=\sup(\Omega)$. For $\beta_2=2$ for instance, $\overline{\omega}\approx 3.8730$. **b** Potential stability switching curves (PSSC) computed with frequency sweeping with $\beta_2=2$ (*thick curves*) and $\beta_2=3.5$ (*thin curves*). With increase in $\overline{\omega}$ as β_2 is increased, PSSC per area is much denser

To study this idea, let us consider the first order system in (12) with β_2 as the tuning parameter. In this case, ignoring $\omega=0$ root as it cannot be the maxima, $\Theta_2(\omega)$ in (23) becomes a cubic polynomial in terms of $\phi:=\omega^2$, that is, $\Theta_2(\omega):=\Theta_2(\phi;\beta_2)$. On this polynomial, we can perform sensitivity analysis to study how $\overline{\omega}$ tends to change with respect to an increase in β_2. For example, take $\beta_2=2$ with $\omega=\overline{\omega}\approx 3.8730$ from the previous subsection. At this numerical setting, sensitivity function reads $\partial\omega/\partial\beta_2\approx 1.0327>0$, indicating that increasing β_2 with sufficiently small amount while respecting the conditions of the implicit function theorem will cause $\overline{\omega}$ to increase, which will ultimately lead to some delay points to be much closer to each other in the stability map.

Moreover, ϕ can be easily solved[4] from the cubic polynomial $\Theta_2(\phi;\beta_2)$ for a given β_2, and feasible candidate solutions must satisfy $\phi=\omega^2>0$. Solutions of candidate $\overline{\omega}$ are displayed in Fig. 2a for a range of β_2. As expected, for $\beta_2=2$, we have that $\overline{\omega}\approx 3.8730$, and $\omega=1.7320$ is not a feasible solution hence must be ignored. Using this figure, we can interpret how the spacings amongst PSSC are affected. For example, choice of $\beta_2=3.5$ corresponds to $\overline{\omega}=5.408$, which is larger than that for $\beta_2=2$ and hence PSSC should be more tightly packed in the stability maps. Furthermore, the lower bound of ω, which is zero for $\beta_2=2$ becomes 1.119 for $\beta_2=3.5$. In light of these, the minimal and maximal spacings between delay points for $\beta_2=2$ are $2\pi/3.872=1.622$ and $\lim_{\omega\to 0^+}2\pi/\omega\to+\infty$, while these spacings are respectively $2\pi/5.408=1.162$ and $2\pi/1.119=5.615$ for $\beta_2=3.5$. All these results can be easily checked by drawing PSSC; see Fig. 1b where we superimpose PSSC to compare the spacings. Upon request of an anonymous

[4]The number of positive real roots of polynomials can be assessed following algebraic tools. If this number is zero and $\omega\neq 0$, then Ω is an empty set hence the system maintains its stable/unstable characteristic irrespective of delays [13]. See also [5, 7, 17] for multiple delay treatments.

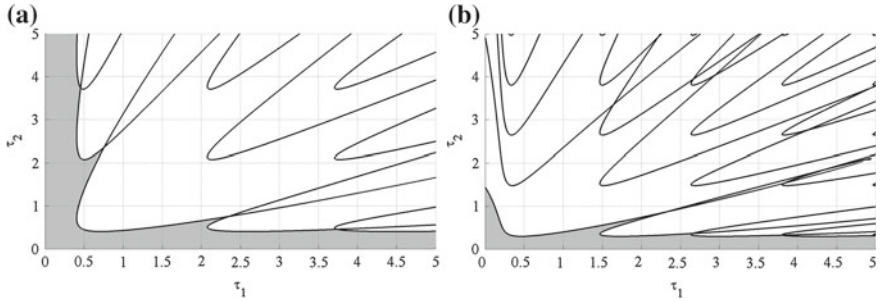

Fig. 2 **a** Stability map (stability regions shaded); $\beta_2 = 2$ case (PSSC: thick curves in Fig. 1b). **b** Stability map (stability regions *shaded*); $\beta_2 = 3.5$ case (PSSC: thin curves in Fig. 1b)

reviewer, next we separately present the stability regions (shaded) in Fig. 2; see [10, 24, 29, 31, 32] on the principles of systematically identifying stable regions.

4 Conclusions

Our recent results in computing the exact upper/lower bound of the imaginary crossing set of LTI multiple time delay systems are utilized here to "design" the imaginary spectrum of such systems to effectively manipulate the spacings in the delay parameter space where stability/instability is preserved. "Control" of the spectrum offers opportunities to design systems with certain stability properties, and certain vibration characteristics. Future work is to extend the presented work for more complicated problems of higher order and with multiple design parameters.

References

1. Abdallah, C.T., Dorato, P., Benites-Read, J., Byrne, R.: Delayed positive feedback can stabilize oscillatory systems. Proc. Am. Control Conf. (1993)
2. Chen, J., Latchman, H.A.: Frequency sweeping tests for asymptotic stability independent of delay. IEEE Trans. Autom. Control **40**(9), 1640–1645 (1995)
3. Collins, G.E.: The calculation of multivariate polynomial resultants. J. Assoc. Comput. Mach. **18**(4), 515–532 (1971)
4. Datko, R.: A Procedure for determination of the exponential stability of certain differential-difference equations. Q. Appl. Math. **36**, 279–292 (1978)
5. Delice, I.I.: Stability analysis of multiple time-delay systems with applications to supply chain management. Ph.D. Dissertation, Northeastern University, Boston, MA (2011)
6. Delice, I.I., Sipahi, R.: Exact upper and lower bounds of crossing frequency set and delay independent stability test for multiple time delayed systems. In: 8th IFAC Workshop on Time-Delay Systems, Sinaia, Romania (2009)
7. Delice, I.I., Sipahi, R.: Delay-independent stability test for systems with multiple time-delays. IEEE Trans. Autom. Control **57**(4), 963–972 (2012)

8. Gu, K., Naghnaeian, M.: On stability crossing set for general systems with three delays—part 1 and part 2. In: IFAC Workshop on Time Delay Systems, Sinaia, Romania (2009)
9. Gu, K., Naghnaeian, M.: Stability crossing set for systems with three delays. IEEE Trans. Autom. Control **56**(1), 11–26 (2011)
10. Gu, K., Niculescu, S.-I., Chen, J.: On Stability of crossing curves for general systems with two delays. J. Math. Anal. Appl. **311**, 231–253 (2005)
11. Lee, M.S., Hsu, C.S.: On the τ-decomposition method of stability analysis for retarded dynamical systems. SIAM J. Control **7**, 242–259 (1969)
12. Michiels, W., Niculescu, S.-I.: Stability and stabilization of time-delay systems: an eigenvalue-based approach. SIAM (2007)
13. Michiels, W., Niculescu, S.-I.: Characterization of delay-independent stability and delay-interference phenomena. SIAM J. Control Optim. **45**, 2138–2155 (2007)
14. Naghnaeian, M., Gu, K.: Stability crossing set for systems with two scalar-delay channels. Automatica **49**(7), 2098–2106 (2013)
15. Neimark, J.: *D*-subdivisions and spaces of quasi-polynomials. Prikl. Mat. Meh. **13**, 349–380 (1949)
16. Nia, P.M., Sipahi, R.: Controller design for delay-independent stability of linear time-invariant vibration systems with multiple delays. J. Sound Vib. **332**(14), 3589–3604 (2013)
17. Nia, P.M.: Control-parameter-space classification for delay-independent-stability of linear time-invariant time-delay systems; theory and experiments. Ph.D. Dissertation, Northeastern University, Boston, MA (2014)
18. Niculescu, S.-I.: Delay Effects on Stability: A Robust Control Approach. Springer, Heidelberg (2001)
19. Niculescu, S.-I., Michiels, W.: Stabilizing a chain of integrators using multiple delays. IEEE Trans. Autom. Control **49**(5), 802–807 (2004)
20. Olgac, N., Sipahi, R.: An exact method for the stability analysis of time-delayed LTI systems. IEEE Trans. Autom. Control **47**, 793–797 (2002)
21. Olgac, N., Sipahi, R., Ergenc, A.F.: Delay scheduling, an unconventional use of time delay for trajectory tracking. Mechatronics **17**, 199–206 (2007)
22. Popov, E.P.: The Dynamics of Automatic Control Systems. Pergamon Press, London (1962)
23. Rekasius, Z.V.: A stability test for systems with delays. In: Proceedings of 1980 Joint Automatic Control Conference, San Francisco, CA, article no. TP9-A (1980)
24. Sipahi, R.: Cluster Treatment of Characteristic Roots, CTCR, a unique methodology for the complete stability robustness analysis of linear time invariant multiple time delay systems against delay uncertainties. Ph.D. Dissertation, University of Connecticut, Storrs, CT (2005)
25. Sipahi, R., Delice, I.I.: Extraction of 3D stability switching hypersurfaces of a time delay system with multiple fixed delays. Automatica **45**, 1449–1454 (2009)
26. Sipahi, R., Delice, I.I.: Advanced clustering with frequency sweeping methodology for the stability analysis of multiple time-delay systems. IEEE Trans. Autom. Control **56**(2), 467–472 (2011)
27. Sipahi, R., Delice, I.I.: On some features of core hypersurfaces related to stability switching of LTI systems with multiple delays. IMA J. Math. Control Inf. **31**(2), 257–272 (2013)
28. Sipahi, R., Olgac, N.: Stability analysis of multiple time delayed systems using the direct method. In: ASME-IMECE Conference, Washington DC (2003)
29. Sipahi, R., Olgac, N.: Complete stability map of third order LTI multiple time delay systems. Automatica **41**, 1413–1422 (2005)
30. Sipahi, R., Olgac, N.: Stability robustness of retarded LTI systems with single delay and exhaustive determination of their imaginary spectra. SIAM J. Control Optim. **45**, 1680–1696 (2006)
31. Sipahi, R., Niculescu, S.-I., Abdallah, C.T., Michiels, W., Gu, K.: Stability and stabilization of systems with time delay, limitations and opportunities. IEEE Control Syst. Mag. **31**(1), 38–65 (2011)
32. Stépán, G.: Retarded Dynamical Systems: Stability and Characteristic Function. Longman Scientific, UK (1989)
33. Uspensky, J.V.: Theory of Equations. McGraw Hill, US (1948)

Algorithm for Robust Stability of Delayed Multi-Degree-of-Freedom Systems

Daniel Bachrathy, Marta Janka Reith and Gabor Stepan

Abstract Computation of the stability limits of systems with time delay is essential in many research and industrial applications. Most of the computational methods consider the exact model of the system, and do not take into account the uncertainties. However, the stability charts are highly sensitive to the change of some input parameters, especially to time delays. An algorithm has been developed to determine the robust stability limits of delayed dynamical systems, which is not sensitive to the fluctuations of selected parameters in the dynamic system. The algorithm is combined with the efficient Multi-Dimensional Bisection Method. The single-degree-of-freedom delayed oscillator is investigated first and the resultant robust stability limits are compared to the derived analytical results. For multi-degree-of-freedom systems, the system of equations of the robust stability limits are modified with the aim to reduce the computational complexity. The method is tested for the 2-cutter turning system with process damping.

1 Introduction

The determination of the stability of dynamical systems with time delay is of high importance for numerous industrial and research applications. Some of the most representative examples are cutting processes [12, 23, 25, 26], wheel shimmy [24], traffic jams [19] and human balancing [11].

One of the most important qualitative properties of dynamical systems is the stability of the equilibrium or the periodic motion. Stability is usually visualized in the form of so-called stability charts, which show the stability boundaries separating those parameter domains for which the system is stable or unstable.

D. Bachrathy (✉) · M.J. Reith · G. Stepan
Department of Applied Mechanics, BME, Műegyetem rkp. 5., Budapest 1111, Hungary
e-mail: bachrathy@mm.bme.hu

M.J. Reith
e-mail: reith@mm.bme.hu

G. Stepan
e-mail: stepan@mm.bme.hu

T. Insperger et al. (eds.), *Time Delay Systems*,
Advances in Delays and Dynamics 7, DOI 10.1007/978-3-319-53426-8_10

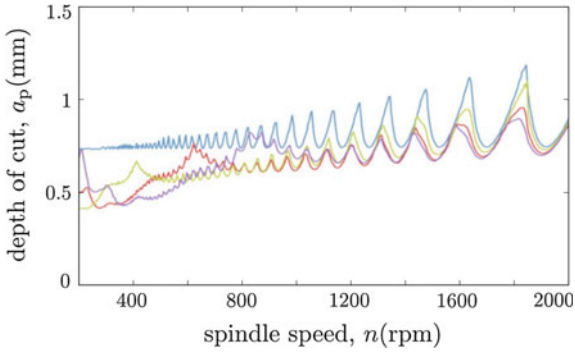

Fig. 1 Stability boundaries in the low spindle speed range for tool geometry optimization presented in [27]

There often exist problems, especially in the field of machining operations at low spindle speeds, where the computation of the stability boundaries requires very high computational effort and unnecessarily high resolution. This is caused by the dense and sharp line segments of the stability boundaries (so-called lobe structure), as it is visible for example in Fig. 1 [27]. In case of time-domain computations [12, 13, 27], a high degree of discretization is required for being able to obtain appropriate results. For instance, in frequency domain computations [1, 5, 6] for cutting processes, the lobe structure becomes dense for low spindle speed values (see Fig. 1), which requires high resolution of the stability chart and a continuously growing resolution in the chatter frequency parameter. However, these accurate boundaries are of no interest from practical point of view, thus the computation of the lower envelope of the lobe curves only might be sufficient.

Traditional computational methods consider exact models of the corresponding system and they do not take into account the uncertainties of the input parameters, in spite of the fact, that the results of these computations are highly sensitive to changes of some input parameters like the natural frequencies and time delays. In practice, these system parameters can only be determined with a limited accuracy.

The parameter uncertainty can be analysed based on the stability radius [17], which considers the perturbation of the elements of the system matrix. In [9] complex perturbation is applied, while [20] considers real valued perturbation. This stability radius method was also applied for time delayed systems in [16, 18].

In the present study, a different perturbation method is introduced in order to determine the robust stability limit. The presented algorithm is based on the direct perturbation of the time-delay parameter only. The main steps are presented based on the well-known mathematical model of the delayed oscillator. The resultant robust stability limit is obtained in the form of the lower envelope of the lobe structure. In order to decrease the computational time even further, the method is combined with an efficient numerical root-finding algorithm, the so-called Multi-Dimensional Bisection Method (MDBM) [2, 4]. These robust stability curves are given in analytical form too. Finally, the presented robust stability computation method is generalized

for multi-degree-of-freedom systems. The system of equations of the robust stability limits are reformulated to create a more efficient numerical scheme, which is applied to the 2-cutter turning model with process damping [22].

2 Robust Stability of Single-Degree-of-Freedom Systems

In this section, linear time-invariant systems are analysed, which can be described by the higher order delay differential equation with a single point delay in the following form:

$$\sum_{j=0}^{N} l_j \frac{\mathrm{d}^j x(t)}{\mathrm{d}t^j} + \sum_{k=0}^{N-1} r_k \frac{\mathrm{d}^k x(t-\tau)}{\mathrm{d}t^k} = 0\,, \tag{1}$$

where x is the scalar state variable, N is the order of the highest derivative, l_j and r_k are constant parameters and τ is the point delay. Note, that we do not deal with neutral equations, hence the highest order derivative term is not delayed.

The robust stability computation algorithm is presented along the model of the second order delayed oscillator (see [10]) given by the governing equation:

$$\ddot{x}(t) + \kappa \dot{x}(t) + \delta x(t) - b x(t-\tau) = 0\,, \tag{2}$$

where the time delay is $\tau = 2\pi$. Equation (2) is obtained from Eq. (1) with $N = 2$, $\mathbf{l} = [\delta, \kappa, 1]$ and $\mathbf{r} = [b, 0]$.

The corresponding stability charts are computed with the help of the D-subdivision method (for detailed description see [23])—main steps are summarized below. The characteristic function D of Eq. (1) can be found by substituting the trial function $x(t) = Ae^{\lambda t}$ into Eq. (1):

$$D = \sum_{j=0}^{N} l_j \lambda^j + \sum_{k=0}^{N-1} r_k \lambda^k \mathrm{e}^{-\lambda\tau}\,, \tag{3}$$

which yields the following characteristic function for the delayed oscillator:

$$D = \lambda^2 + \kappa\lambda + \delta - b e^{-\lambda\tau}\,. \tag{4}$$

The stability boundaries can be determined by substituting the critical value of the characteristic root $\lambda = \mathrm{i}\omega_\mathrm{c}$. The co-dimension 2 problem is defined by the real and imaginary parts of the characteristic equation in the parameter space of $(\mathbf{l}, \mathbf{r}, \omega_\mathrm{c})$:

$$\Re\left(D(\mathbf{l}, \mathbf{r}, \omega_\mathrm{c})\right) = 0 \tag{5}$$

$$\Im\left(D(\mathbf{l}, \mathbf{r}, \omega_\mathrm{c})\right) = 0. \tag{6}$$

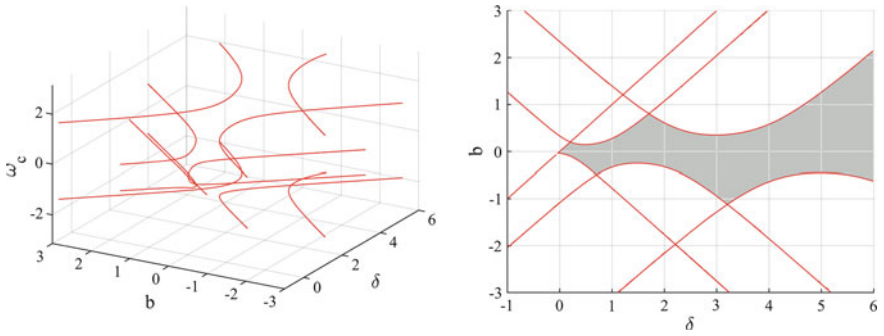

Fig. 2 Resulting curves for the delayed oscillator in the space of δ, b and ω_c (*left panel*) and its top view (*right panel*), where the stable area is *shaded* for $\kappa = 0.2$

The Multi-Dimensional Bisection Method (MDBM) [2, 4] is designed specifically for these types of root-finding problems, since it is able to find the submanifolds of the roots of a system of nonlinear equations in arbitrary parameter dimension and co-dimension. This robust technique can be used for the determination of multiple boundary curves and it can even find closed curves of stable and unstable islands in the stability chart automatically.

For Eq. (2) the free parameters are δ, b and ω_c, while κ is usually considered to be a constant representing damping. The roots of (5) and (6) are determined by MDBM for the test case and are presented in Fig. 2 for $\kappa = 0.2$. In the top view (right panel of Fig. 2) the resultant boundary curves form the border of the shaded stable area.

2.1 Parameter Uncertainty

Equation (2) can be considered as a dimensionless form of the governing equation of a mass-spring system with delayed control. The above computation method considers the exact model of this mechanical system and it does not take into account the uncertainty of the input parameters, like eigenfrequency and feedback delay. These parameters influence the dimensionless time delay, which is the main source of instability. To represent the effect of uncertainty in the delay parameter τ, numerous stability boundary curves were calculated for a set of time delays in the range $[0, 4\pi]$. These curves are plotted in Fig. 3. The intersection of the stable areas can be used as an approximation of the robust stability region (grey area in the right panel of Fig. 3).

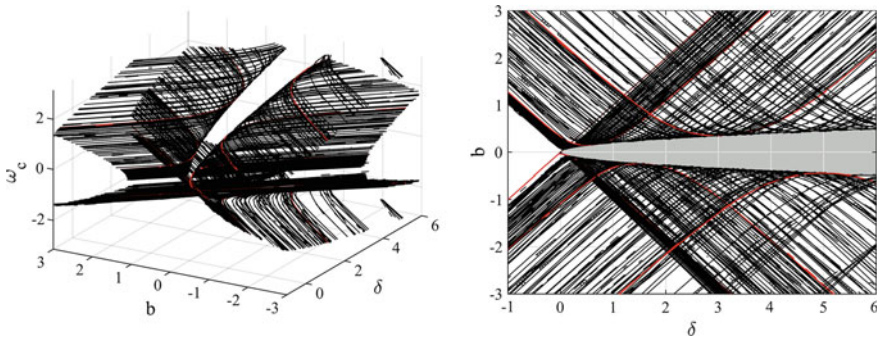

Fig. 3 Resulting curves for the delayed oscillator in the space of δ, b and ω_c (*left panel*) for different discrete τ values in the range $[0, 4\pi]$ (*black lines*) where the boundary curves from Fig. 2 are denoted by *red thick lines*. In the top view (*right panel*), the approximated robust stable area is *shaded* for $\kappa = 0.2$

2.2 Robust Stability Limit

The exact robust stability limit has to be computed for continuous time delay variation, however, the computation of the resultant boundaries presented in Fig. 3 was already time consuming, even for only 30 different τ values. To overcome this problem, a new idea was shown in [3], according to which the set of boundary curves can be connected to a surface by means of an additional parameter, which is defined as the regenerative phase shift parameter

$$\Phi := \mathrm{mod}(\tau\omega_c, 2\pi)\,. \tag{7}$$

This parameter has to be treated as an independent extra (time-delay perturbation) parameter in the exponential terms only. Consequently, the set of parameters for the characteristic function is extended by one and it yields:

$$D = \sum_{j=0}^{N} l_j \lambda^j + \sum_{k=0}^{N-1} r_k \lambda^k \mathrm{e}^{-\mathrm{i}\Phi}\,. \tag{8}$$

For the delayed oscillator, at the stability limit, the characteristic function is given in the form:

$$D = -\omega_c^2 + \mathrm{i}\kappa\omega_c + \delta - b e^{-\mathrm{i}\Phi}\,. \tag{9}$$

The application of MDBM is essential to solve the resultant co-dimension 2 problem in the extended parameter space. The resultant surface for Eq. (9) is plotted in Fig. 4.

The robust stability limit is defined by the envelope of this surface, where the surface is parallel to the ω_c axis in the 3D-representation in Fig. 4. It was found,

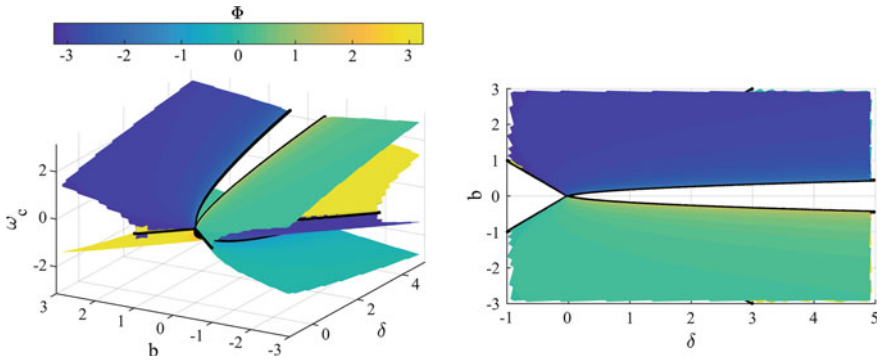

Fig. 4 Surface of the connected stability boundaries of the delayed oscillator in the space of δ, b, ω_c and Φ (*left panel*) and its top view (*right panel*). The envelope of the surface forms the robust stability limit given with *thick black lines* for $\kappa = 0.2$

that in the vicinity of the parameter points along the envelope, the real part of the critical roots λ of the characteristic equation (4) does not change as a function of the perturbation parameter. This condition can be described as follows:

$$\Re\left(\frac{\partial\lambda}{\partial\Phi}\right) = 0\,. \tag{10}$$

The left hand side of Eq. (10) can be determined by the implicit derivation of the characteristic equation [23], which results:

$$\frac{\mathrm{d}D(\lambda)}{\mathrm{d}\Phi} = 0 \tag{11}$$

$$\frac{\partial D}{\partial\lambda}\frac{\partial\lambda}{\partial\Phi} + \frac{\partial D}{\partial\Phi} = 0\,. \tag{12}$$

The extra condition (10) necessary for the computation of the robust stability limit can be written with the help of (12) as follows:

$$\Re\left(\frac{\partial\lambda}{\partial\Phi}\right) = \Re\left(-\frac{\frac{\partial D}{\partial\Phi}}{\frac{\partial D}{\partial\lambda}}\right) = 0\,. \tag{13}$$

In order to eliminate the division during the numerical implementation of Eq. (13), it is favourable to use the following rearranged form

$$\Im\left(\frac{\partial D}{\partial\omega_c}\,\overline{\frac{\partial D}{\partial\Phi}}\right) = 0\,, \tag{14}$$

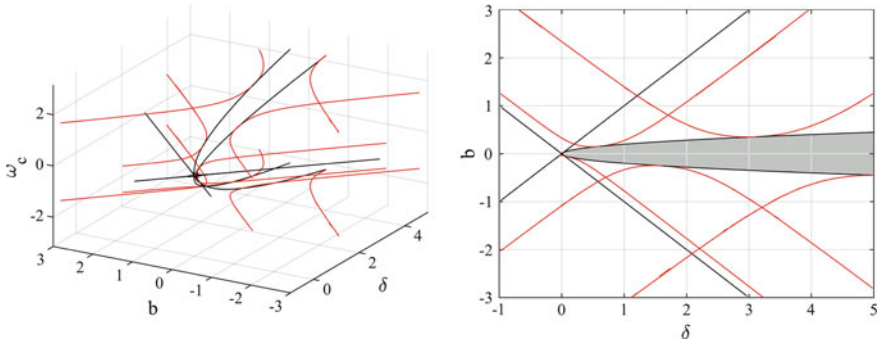

Fig. 5 Stability boundaries of the exact model of the delayed oscillator (*red lines*—see Fig. 2) and the corresponding robust stability limit given with black lines in the space of δ, b, ω_c and $\boldsymbol{\Phi}$ (*left panel*). In the top view (*right panel*) the robust stable area is *shaded* for $\kappa = 0.2$

in which the critical value $\lambda = \mathrm{i}\omega_c$ is considered and the bar denotes complex conjugate. This extra equation leads to:

$$\Re\left(\left(\sum_{j=1}^{N} l_j j\mathrm{i}(\mathrm{i}\omega_c)^{j-1} + \sum_{k=1}^{N-1} r_k k\mathrm{i}(\mathrm{i}\omega_c)^{k-1}\mathrm{e}^{-\mathrm{i}\boldsymbol{\Phi}}\right)\overline{\left(\sum_{k=0}^{N-1} r_k(\mathrm{i}\omega_c)^k\mathrm{e}^{-\mathrm{i}\boldsymbol{\Phi}}\right)}\right) = 0\,. \tag{15}$$

Note, that the last term in Eq. (15) was already computed during the evaluation of Eq. (8), which can be reused to decrease the computational time. For the delayed oscillator, the extra condition yields

$$\Re\left((-2\omega_c + \mathrm{i}\kappa)(be^{-\mathrm{i}\boldsymbol{\Phi}})\right) = 0\,. \tag{16}$$

Figure 5 shows the traditional stability chart and the robust stability limit of the delayed oscillator, which is determined by MDBM as a co-dimension 3 problem formed by (5), (6) and (16) in the 4-dimensional parameter space $(\delta, b, \omega_c, \boldsymbol{\Phi})$.

For 153 grid points along each parameter dimension, the computational time of the traditional stability limit curves was 3.5 s (Matlab 2014b; Intel Core i7-4710HQM CPU 2.50 GHz, 16 GB Memory). Thus, the set of stability curves in Fig. 3 was computed in approximately 105 s, while the robust stability limit in Fig. 5 was computed in 4.1 s, only. The computational effort for the robust stability limit is comparable with the time consumed for the computation of the traditional stability limit. Furthermore, the robust stability computation scheme is not only orders of magnitude faster than the approximating method applied for a discrete set of time delays, but it also delivers qualitatively better results in the form of continuous boundary lines, while the results in Fig. 3 present only segmented boundaries.

2.3 Analytical Results for Robust Stability of Delayed Oscillator

For the delayed oscillator, the system of equations (5), (6) and (13) defining the robust stability limit leads to:

$$-\omega_c^2 + \delta - b\cos(\Phi) = 0\,, \tag{17}$$

$$\kappa\omega_c + b\sin(\Phi) = 0\,, \tag{18}$$

$$-b\kappa\sin(\Phi) - 2b\omega_c\cos(\Phi) = 0\,. \tag{19}$$

This system can be solved analytically. The first set of results is

$$b = d \quad \omega_c = 0 \quad \Phi = 0\,, \tag{20}$$

$$b = -d \quad \omega_c = 0 \quad \Phi = \pm\pi\,, \tag{21}$$

which are straight robust stability lines corresponding to fold-type bifurcations, while the second set of solutions is:

$$b = \pm\kappa\sqrt{\delta - \kappa^2/4}\,, \tag{22}$$

$$\omega_c = \pm\sqrt{\delta - \kappa^2/2}\,, \tag{23}$$

$$\Phi = \pm\mathrm{acos}\left(\frac{\kappa}{4\delta - \kappa^2}\right)\,, \tag{24}$$

which represent the robust stability curves for Hopf-type bifurcations in case of $\delta > \kappa^2/2$.

3 Robust Stability of Multi-degree-of-Freedom Systems

Let us generalize Eq. (1) for multi-degree-of-freedom systems, which yields the following matrix equation:

$$\sum_{j=0}^{N} \mathbf{L}_j \frac{\mathrm{d}^j\mathbf{x}(t)}{\mathrm{d}t^j} + \sum_{k=0}^{N-1} \mathbf{R}_k \frac{\mathrm{d}^k\mathbf{x}(t-\tau)}{\mathrm{d}t^k} = 0\,, \tag{25}$$

where $\mathbf{x} \in \mathbb{R}^n$, N is the order of the highest derivative, $\mathbf{L}_j$ and $\mathbf{R}_k$ are coefficient matrices and τ is the point delay. The characteristic equation of Eq. (25) is determined based on the determinant

$$D := \det\left(\sum_{j=0}^{N} \mathbf{L}_j \lambda^j + \sum_{k=0}^{N-1} \mathbf{R}_k \lambda^k \mathrm{e}^{-\lambda\tau}\right) = 0 \tag{26}$$

using the trial solution $\mathbf{x}(t) = \mathbf{A}e^{\lambda t}$. Since Eq. (26) defines the characteristic equation, all steps described in Sect. 2 can be performed in order to obtain the robust stability limit. First, the regenerative phase shift parameter is introduced in the exponential terms based on Eq. (7), then the system of equations Eqs. (5) and (6) together with the extra condition Eq. (14) are solved by means of MDBM.

The derivative terms in Eq. (14) can be approximated by a finite difference method. This approximation is generally appropriate for numerical schemes. However, it can be determined in closed form, too. Based on this closed form equation, a rearranged form of Eq. (14) is created in order to make the computations more efficient.

3.1 Optimized Numerical Solution

In the extra condition for the robust stability computation given with Eq. (14), the derivative of a determinant must be computed. The closed form solution is provided by Jacobi's formula [14]:

$$\frac{\mathrm{d}}{\mathrm{d}x} \det(\mathbf{G}) = \mathrm{tr}\left(\mathrm{adj}(\mathbf{G}) \frac{\mathrm{d}\mathbf{G}}{\mathrm{d}x}\right), \tag{27}$$

where tr() denotes the trace and adj() is the adjugate matrix (the transpose of the cofactor matrix). Let us define the argument of the determinant of Eq. (26) as

$$\mathbf{G} = \sum_{j=0}^{N} \mathbf{L}_j \lambda^j + \sum_{k=0}^{N-1} \mathbf{R}_k \lambda^k \mathrm{e}^{-\lambda\tau}. \tag{28}$$

The computational effort for the adjugate matrix can be high, however, in our case, special conditions can be applied. Matrix $\mathbf{G}$ is singular due to Eq. (26), hence $\mathrm{rank}(\mathbf{G}) = n - 1$. If this holds, the $\mathrm{rank}(\mathrm{adj}(\mathbf{G})) = 1$, because the image of $\mathrm{adj}(\mathbf{G})$ is contained in the kernel of $\mathbf{G}$ that has dimension 1 by rank–nullity [15]. This means that the adjugate matrix can be expressed by

$$\mathrm{adj}(\mathbf{G}) = C\mathbf{e}_0 \circ \mathbf{e}_0^{\top}, \tag{29}$$

where $\circ$ denotes the vector direct product or dyadic product and $\mathbf{e}_0$ is the eigenvector belonging to the singular eigenvalue ($\mu = 0$) of matrix $\mathbf{G}$. Note, that the constant C depends on the non-singular eigenvalues of $\mathbf{G}$, however, it is not relevant in the further steps of the derivation since it will be cancelled. Equation (29) is valid if the multiplicity of the critical characteristic root is equal to one, otherwise $\mathrm{adj}(\mathbf{G}) = \mathbf{0}$

holds. The probability of this situation is very low, especially during the numerical analysis, thus these special cases are not treated here.

The computation of the only eigenvector $\mathbf{e}_0$ can be performed efficiently, e.g. with the inbuilt function `eigs` in Matlab. Alternatively, the simple textbook calculation can be used directly if we set the first element of $\mathbf{e}_0$ equal to 1, which leads to

$$\mathbf{e}_0 = [1\,,\, \mathbf{G}^{-1}_{(2:n)\times(2:n)}\mathbf{G}_{(1)\times(2:n)}]^\top\,. \tag{30}$$

For very special parameter sets ($e_{0,1} \approx 0$), this could result a poorly conditioned problem. If we consider the special form of the adjugate matrix as in Eq. (29) and the fact that the trace of a dyadic product is the same as the dot product, then Eq. (27) can be reformulated as:

$$\frac{\mathrm{d}}{\mathrm{d}x}\det(\mathbf{G}) = \mathbf{e}_0^\top \frac{\mathrm{d}\mathbf{G}}{\mathrm{d}x}\mathbf{e}_0\,. \tag{31}$$

The final form of Eq. (14) for multi-degree-of-freedom systems is

$$\mathfrak{I}\left(\left(\mathbf{e}_0^\top \frac{\partial \mathbf{G}}{\partial \omega_\mathrm{c}}\mathbf{e}_0\right)\overline{\left(\mathbf{e}_0^\top \frac{\partial \mathbf{G}}{\partial \boldsymbol{\Phi}}\mathbf{e}_0\right)}\right) = 0\,, \tag{32}$$

which leads to the following equation after the substitution of Eq. (28) and after performing the derivations:

$$\mathfrak{R}\left(\left(\mathbf{e}_0^\top\left(\sum_{j=1}^{N}\mathbf{L}_j j\mathrm{i}(\mathrm{i}\omega_\mathrm{c})^{j-1} + \sum_{k=1}^{N-1}\mathbf{R}_k k\mathrm{i}(\mathrm{i}\omega_\mathrm{c})^{k-1}\mathrm{e}^{-\mathrm{i}\boldsymbol{\Phi}}\right)\mathbf{e}_0\right)\overline{\left(\mathbf{e}_0^\top\left(\sum_{k=0}^{N-1}\mathbf{R}_k(\mathrm{i}\omega_\mathrm{c})^k\mathrm{e}^{-\mathrm{i}\boldsymbol{\Phi}}\right)\mathbf{e}_0\right)}\right) = 0. \tag{33}$$

Note, that this formula is only valid at the boundary of the robust stability area. If we are off the robust stability curve, then this equation is an approximation only, because $\mathbf{G}$ is not singular. For these off-boundary points $\mathbf{e}_0$ can be approximated by Eq. (30) or by the eigenvector belonging to the eigenvalue with the smallest magnitude.

If we decide to compute the eigenvector $\mathbf{e}_0$ by solving the eigenvalue–eigenvector problem, then the corresponding eigenvalue μ_0 with the smallest magnitude is also obtained as a side result, which can be used instead of the determinant in Eq. (26), because $\det(\mathbf{G}) = \prod_{m=1}^{n}\mu_m = 0$ if and only if $\mu_0 = 0$.

The above-presented robust stability computation method is applied for a two-cutter turning system with process damping.

3.2 *Robust Stability Limit of the Two-Cutter Turning with Process Damping*

In order to present the efficiency of the above presented robust stability computation method, it is applied for the test case of the two-cutter turning process with process damping. The model and the corresponding equation of motion of a two-cutter turning system is given in [21, 22] where the dynamics of the turret is also modelled. The simplified mechanical model is shown in Fig. 6. If the effect of process damping [7, 8, 26] is taken into account, too, then an extra damping coefficient appears, which is proportional to the time delay τ and thus the governing equation can be written in the form:

$$\mathbf{M}\ddot{\mathbf{x}}(t) + \left(\mathbf{C} + c_{\mathrm{p}}\tau\mathbf{E}\right)\dot{\mathbf{x}}(t) + \mathbf{K}\mathbf{x}(t) = k_{\mathrm{w}}\left(\mathbf{L}\mathbf{x}(t-\tau) - \mathbf{E}\mathbf{x}(t)\right) . \tag{34}$$

Here, $\mathbf{x}$ is the vector of the position coordinates of the tools and the turret (see Fig. 6), c_{p} denotes the process damping coefficient, k_{w} is the cutting coefficient. The coefficient matrices in Eq. (34) are given in Table 1.

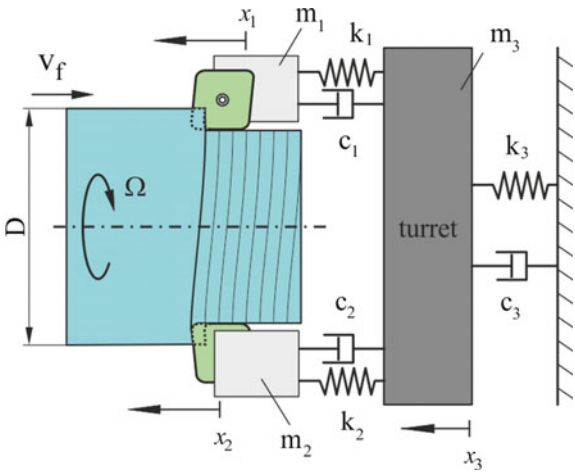

Fig. 6 Schematic representation of the two-cutter turning model. Tool 1 and tool 2 are coupled via the cutting force function, too, due to the surface regeneration effect

Table 1 The coefficient matrices in the governing equation of the two-cutter turning model

Mass matrix	Damping matrix	Stiffness matrix	Self coupling matrix	Cross coupling matrix
$\mathbf{M}$	$\mathbf{C}$	$\mathbf{K}$	$\mathbf{E}$	$\mathbf{L}$
$\begin{bmatrix} m_1 & 0 & 0 \\ 0 & m_2 & 0 \\ 0 & 0 & m_3 \end{bmatrix}$	$\begin{bmatrix} c_1 & 0 & -c_1 \\ 0 & c_2 & -c_2 \\ -c_1 & -c_2 & c_1+c_2+c_3 \end{bmatrix}$	$\begin{bmatrix} k_1 & 0 & -k_1 \\ 0 & k_2 & -k_2 \\ -k_1 & -k_2 & k_1+k_2+k_3 \end{bmatrix}$	$\begin{bmatrix} 1 & 0 & 0 \\ 0 & 1 & 0 \\ 0 & 0 & 0 \end{bmatrix}$	$\begin{bmatrix} 0 & 1 & 0 \\ 1 & 0 & 0 \\ 0 & 0 & 0 \end{bmatrix}$

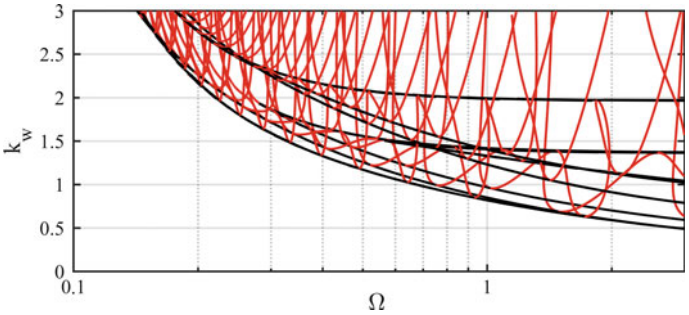

Fig. 7 Stability boundaries of the two-cutter turning system (*red lines*) and its robust stability limits (*black lines*) for the dimensionless parameters: $m_1 = m_2 = 1$, $m_3 = 10$, $c_1 = c_2 = 0.02$, $c_3 = 0.2$, $k_1 = 1$, $k_2 = 4$, $k_3 = 40$, $c_p = 0.03$. Note the logarithmic scale of Ω

The corresponding characteristic equation for $\lambda = \mathrm{i}\omega_c$ with the regenerative phase shift parameter Φ is given by:

$$\det\left(-\omega_c^2\mathbf{M} + \mathrm{i}\omega_c\mathbf{C} + \mathrm{i}c_p\tau\omega_c\mathbf{E} + \mathbf{K} - k_w\left(\mathbf{L}e^{-\mathrm{i}\Phi} - \mathbf{E}\right)\right) = 0\,, \tag{35}$$

Note, that the term $\tau\omega_c$ is replaced by Φ in the exponential term only, while in the damping term it is left as it is.

The resulting stability boundary curves (red) and the robust stability limit (black) are shown in Fig. 7 in the plane of the spindle speed $\Omega = 2\pi/\tau$ and the cutting coefficient k_w.

In spite of the high resolution of the computed stability chart, the dense stability lobe structure (red curves) becomes more and more inaccurate in the lower spindle speed range. It can be observed in Fig. 7 that the robust stability lines (black) are smooth in the whole spindle speed range for the same resolution, while the computational time is in the same range as for the stability computation.

4 Conclusion

In the present study, we have developed a method based on parameter perturbation for calculating the robust stability limits of systems of differential equations with point delay. One of the main benefits of the presented method is that it eliminates the sensitivity of the stability charts to the time delay parameter. Thus it can be efficiently used in cases where some of the input parameters are inaccurate.

In the proposed computation method, an additional perturbation parameter has to be introduced in order to find the resultant robust stability curves, which form the envelopes of the stability boundary lines. This increases the dimension of the parameter space by one, which requires the formulation of an additional condition for the

robust stability limit curve. Although the set of parameters and the system of equations are extended, the applied Multi-Dimensional Bisection Method can efficiently solve the equations without significant increase of computational time.

Future research is planned to extend this method to dynamical systems with multiple and/or distributed delays.

Acknowledgements The research leading to these results has received funding from the European Research Council under the European Unions Seventh Framework Programme (FP7/2007–2013) ERC Advanced grant agreement No. 340889. Furthermore, this paper was supported by the Hungarian Scientific Research Fund—OTKA PD-112983 and the Janos Bolyai Research Scholarship of the Hungarian Academy of Sciences.

References

1. Altintas, Y., Stepan, G., Merdol, D., Dombovari, Z.: Chatter stability of milling in frequency and discrete time domain. CIRP J. Manuf. Sci. Technol. **1**(1), 35–44 (2008). doi:10.1016/j.cirpj.2008.06.003
2. Bachrathy, D.: Multi-dimensional bisection method (mdbm)—fast computation of all the roots of a non-linear function for higher parameter dimension and co-dimension (2012)
3. Bachrathy, D.: Robust stability limit of delayed dynamical systems. Periodica Polytech., Eng. Mech. Eng. **59**(2), 74 (2015)
4. Bachrathy, D., Stepan, G.: Bisection method in higher dimensions and the efficiency number. Periodica Polytech., Mech. Eng. **56**(2), 81–86 (2012)
5. Bachrathy, D., Stepan, G.: Improved prediction of stability lobes with extended multi frequency solution. CIRP Ann. Manuf. Technol. (2013). doi:10.1016/j.cirp.2013.03.085
6. Budak, E., Altintas, Y.: Analytical prediction of chatter stability conditions for multi-degree of systems in milling. Trans. ASME J. Dyn. Syst. Measur. Control **120**, 22–30 (1998)
7. Budak, E., Tunc, L.T.: Identification and modeling of process damping in turning and milling using a new approach. CIRP Ann. Manuf. Technol. **59**(1), 403–408 (2010)
8. Eynian, M., Altintas, Y.: Chatter stability of general turning operations with process damping. J. Manuf. Sci. Eng. **131**(4), 10 (2009). doi:10.1115/1.3159047
9. Hinrichsen, D., Pritchard, A.J.: Stability radius for structured perturbations and the algebraic riccati eauation. Syst. Control Lett. **8**, 105–113 (1986)
10. Hsu, C.S., Bhatt, S.: Stability charts for second-order dynamical systems with time lag. J. Appl. Mech. **33**(1), 119–124 (1966)
11. Insperger, T., Milton, J., Stepan, G.: Acceleration feedback improves balancing against reflex delay. J. R. Soc. Interface **10**(79), 20120,763 (2012). doi:10.1098/rsif.2012.07631742-5662
12. Insperger, T., Stepan, G.: Semi-discretization for time-delay systems, 1st edn. Applied Mathematical Sciences, vol. 1. Springer (2011)
13. Khasawneh, F.A., Mann, B.P., Butcher, E.A.: Comparison between collocation methods and spectral element approach for the stability of periodic delay systems. In: 9th IFAC Workshop on Time Delay Systems, vol. 9, pp. 69–74 (2010)
14. Magnus, J.R., Neudecker, H., et al.: Matrix Differential Calculus with Applications in Statistics and Econometrics (1995)
15. Meyer, C.D.: Matrix Analysis and Applied Linear Algebra, vol. 2. SIAM (2000)
16. Michiels, W., Fridman, E., Niculescu, S.I.: Robustness assessment via stability radii in delay parameters. Int. J. Robust Nonlinear Control (2008). doi:10.1002/rnc.1385
17. Michiels, W., Niculescu, S.I.: Stability and Stabilization of Time-Delay Systems. Society for Industrial and Applied Mathematics, PA (2007)

18. Michiels, W., Roose, D.: An eigenvalue based approach for the robust stabilization of linear time-delay systems. Int. J. Control **76**(7), 678–686 (2003)
19. Orosz, G., Wilson, R.E., Stepan, G.: Traffic jams: dynamics and control. Philos. Trans. R. Soc. Lond. A Math. Phys. Eng. Sci. **368**(1928), 4455–4479 (2010). doi:10.1098/rsta.2010.0205
20. Qiu, L., Bernhardsson, B., Rantzer, A., Davison, E.J., Young, P.M., Doyle, J.C.: A formula for computation of the real stability radius. IMA Preprint Series # 1160 (1993)
21. Reith, M.J., Bachrathy, D., Stepan, G.: Comparing stability and dynamic behaviour of different multi-cutter turning models. In: ENOC 2014, Wien, 494, p. 2 (2014)
22. Reith, M.J., Stepan, G.: Exploitation of non-proportional damping in machine tools for chatter suppression. J. Mech. Mach. Theory submitted (2016)
23. Stepan, G.: Retarded Dynamical Systems. Longman, Harlow (1989)
24. Takacs, D.: Dynamics of towed wheels—nonlinear theory and experiments. Ph.D. Thesis, Budapest University of Technology and Economics, Department of Applied Mechanics (2011)
25. Tlusty, J., Spacek, L.: Self-excited vibrations on machine tools. Prague, Czech Republic: Nakl CSAV. [In Czech.] (1954)
26. Tobias, S.A.: Machine Tool Vibration. Blackie and Son Ltd, London (1965)
27. Zatarain, M., Dombovari, Z.: Stability analysis of milling with irregular pitch tools by the implicit subspace iteration method. Int. J. Dyn. Control **2**(1), 26–34 (2014)

Stability and Robustness Analysis of a Class of Cyclic Biological Systems

Mehmet Eren Ahsen, Hitay Özbay and Silviu-Iulian Niculescu

Abstract In the first part of this chapter, we do a local stability and robustness analysis of a model of cyclic biological network representing GRNs (Gene Regulatory Networks) under positive feedback. We present conditions leading to bistable behavior. In the second part, we analyze the GRN under negative feedback. Our analysis depends on an extension of the so-called secant condition, which gives a local stability condition. We deduce conditions leading to global stability of the network.

1 Introduction

One of the well-studied biochemical models is the Gene Regulatory Network (GRN) model, which is a cyclic nonlinear time-delayed feedback system described by n cascaded subsystems. A mathematical model for the GRN is given as

$$\begin{cases} \dot{x}_1(t) = -\lambda_1 x_1(t) + g_1(x_2(t)) \\ \dot{x}_2(t) = -\lambda_2 x_2(t) + g_2(x_3(t)) \\ \qquad \vdots \\ \dot{x}_n(t) = -\lambda_n x_n(t) + g_n(x_1(t-\tau)), \end{cases} \tag{1}$$

M.E. Ahsen (✉)
IBM Research, 1101 Route 134 Kitchawan Rd, Yorktown Heights, NY 10598, USA
e-mail: mahsen@us.ibm.com

H. Özbay
Department of Electrical and Electronics Engineering, Bilkent University,
06800 Ankara, Turkey
e-mail: hitay@bilkent.edu.tr

S.-I. Niculescu
Laboratory of Signals and Systems, UMR CNRS 8506, 3 rue Joliot Curie,
91192 Gif-sur-Yvette, France
e-mail: silviu.niculescu@lss.supelec.fr

T. Insperger et al. (eds.), *Time Delay Systems*,
Advances in Delays and Dynamics 7, DOI 10.1007/978-3-319-53426-8_11

where $\lambda_i > 0,\ i = 1, ..., n$ and each $g_i(x) : \mathbb{R}_+ \to \mathbb{R}_+$ is a Hill function of the form

$$g_i(x) = \begin{cases} \frac{a_i}{b_i + x^{m_i}} & \text{if} \quad i+1 \quad \text{represses} \quad i, \\ \frac{a_i x^{m_i}}{b_i + x^{m_i}} & \text{if} \quad i+1 \quad \text{activates} \quad i, \end{cases} \tag{2}$$

where $a_i > 0$, $b_i > 0$, and $m_i \in \mathbb{N}$ with $m_i \geq 1$, represent the parameters of the nonlinearities. If all the nonlinearities in (1) involve time delays with appropriate change of variables the system can be reduced to (1), see, e.g., [1].

The linearization of (1) around any of its equilibrium points leads to the following characteristic equation:

$$\chi(s) = \prod_{i=1}^{n} \left(\frac{s}{\lambda_i} + 1 \right) - ke^{-\tau s}, \tag{3}$$

where $\tau \geq 0$ represents the delay in the system, and $k \in \mathbb{R}$ is the DC gain of the linearized feedback system. The small-gain result, which can be found in [2] among others, provides a sufficient result for the stability of the characteristic function given in (3). A less conservative condition for the delay free system is the secant condition introduced in [3]. Accordingly, any characteristic equation of the form (3) with $k < 0$ is stable if the following condition (a.k.a. secant condition)

$$|k| \leq (\sec \frac{\pi}{n})^n$$

holds. In this paper, we use an extended version of the secant condition which includes time delays to analyze the characteristic function (3). We apply this new result to a time-delayed cyclic dynamical network under negative feedback analyzed in [4] and provide conditions for stability or existence of oscillations that depends only on the coefficients a_i, b_i, m_i of the Hill functions. We also do a robustness analysis of the network, and provide bounds on the perturbations in the parameters of the Hill functions of the GRN for it to stay locally asymptotically stable.

We also study the time-delayed cyclic dynamical network under positive feedback given in [5], where the authors prove that the system has always an equilibrium point x_{eq} such that the system is locally stable around x_{eq} independent of delay. This is consistent with the earlier result of [6], which states that a monotone dynamical system converges to one of its equilibrium. Here, we analyze the same GRN and show that the system can have at most two equilibrium points which are locally stable independent of delay. Moreover, when the GRN has exactly three equilibrium points, we show that two of the equilibrium points are stable independent of delay and the third equilibrium point is locally unstable independent delay. Hence, for any value of the delay the GRN exhibits bistable behavior.

2 Notation and Preliminary Results

This section contains some notation and preliminary results that are used throughout the chapter. For a given function f, f^m is used to denote the function obtained by m compositions of f. For a function $f : \mathbb{R}_+$ to $\mathbb{R}_+$, any point x is a fixed point if $f(x) = x$. Let a function f be defined from $\mathbb{R}_+$ to $\mathbb{R}_+$. Suppose it is at least three times continuously differentiable. Then, the Schwarzian derivative of the function f, denoted as $Sf(x)$, is given by the following expression (see [7]):

$$Sf(x) = \begin{cases} -\infty & \text{if } f'(x) = 0 \\ \dfrac{f'''(x)}{f'(x)} - \dfrac{3}{2}\left(\dfrac{f''(x)}{f'(x)}\right)^2 & \text{if } f'(x) \neq 0\,. \end{cases} \tag{4}$$

Hill functions, which are the main type of nonlinearity considered in the chapter, have negative Schwarzian derivatives. Next, we define a new function which is fundamental to the rest of the analysis.

$$g = (\frac{1}{\lambda_1} g_1) \circ (\frac{1}{\lambda_2} g_2) \circ \ldots \circ (\frac{1}{\lambda_n} g_n). \tag{5}$$

Definition 1 The gene regulatory network is said to be under *positive feedback* if

$$g'(x) > 0 \qquad \forall x \in (0, \infty).$$

Conversely, the gene regulatory network is said to be under *negative feedback* if the above inequality is reversed. We finish this section by citing a theorem which will be used for the analysis of the GRN under positive feedback.

Theorem 1 ([6]) *Consider the system* (1) *under positive feedback. Any solution of* (1) *with any nonnegative initial condition converges to one of its equilibrium points.*

3 The Secant Condition for Systems with Time Delays

Consider a linear plant with the following state space representation:

$$\dot{x}(t) = A_0 x(t) + Bu(t), \tag{6}$$

$$y(t) = Cx(t) \tag{7}$$

where

$$A_0 = \begin{bmatrix} -\lambda_1 & b_1 & 0 & \cdots & 0 \\ 0 & -\lambda_2 & b_2 & 0 \cdots & \vdots \\ 0 & 0 & \ddots & \ddots & 0 \\ \vdots & & \ddots & \ddots & b_{n-1} \\ 0 & \cdots & \cdots & 0 & -\lambda_n \end{bmatrix}$$

$$B = [0 \ \cdots \ 0 \ 1]^{\mathrm{T}}$$

$$C = [1 \ 0 \ \cdots \ 0].$$

It is assumed that $\lambda_i > 0$ for $i = 1, \ldots, n$, and $b_i \in \mathbb{R}$ for $i = 1, \ldots, n-1$. Suppose now we apply a delayed static output feedback control in the form

$$u(t) = b_n y(t - \tau),$$

where b_n is the constant controller gain. Then, the feedback system is described by state space equation

$$\dot{x}(t) = A_0 x(t) + A_1 x(t - \tau), \tag{8}$$

where $A_1 = b_n BC$. The characteristic function of the feedback system, $\det(sI - A_0 - A_1 e^{-\tau s})$, is of the following form

$$\chi(s) = \left(\prod_{i=1}^{n} (s/\lambda_i + 1) \right) - \beta e^{-\tau s} \tag{9}$$

$$\beta = \frac{\prod_{i=1}^{n} b_i}{\prod_{i=1}^{n} \lambda_i}. \tag{10}$$

If $\beta \geq 0$ then the small gain condition, $\beta < 1$, is both necessary and sufficient for the characteristic equation to be stable. Therefore, the system is unstable independent of delay if $\beta > 1$, see, e.g., [1]. The more interesting case is when $\beta < 0$. To analyze $\beta < 0$ case, define

$$k := -\beta,$$

which is positive. When $k > 0$ and $\tau = 0$, i.e., there is no time delay, the secant condition states that if

$$k < \left(\sec \frac{\pi}{n} \right)^n = \frac{1}{(\cos \frac{\pi}{n})^n}, \tag{11}$$

then, the characteristic function $\chi(s)$ is stable. A recent result of [8] extends the secant condition for systems with a time delay, i.e., $\tau > 0$. A similar result can be found in [9].

Proposition 1 ([8]) *Consider the system given by* (8)*, with* $\lambda_i > 0$ *for* $i = 1, \ldots, n$*, and assume that* $k > 0$*. Clearly, if* $k \leq 1$*, then the feedback system is stable for all* $\tau \geq 0$*. Suppose now* $k > 1$ *and* τ *is fixed. Let* $\lambda = \max_i \lambda_i$*. Then, if*

$$k < \left(\sec \frac{\pi}{n}\right)^n, \tag{12}$$

and

$$\tau < \frac{\pi - n \arccos\left(\sqrt[n]{1/k}\right)}{\omega_m} =: \tau_m, \tag{13}$$

where $\omega_m = \lambda\sqrt{\sqrt[n]{k^2} - 1}$*, then the system* (8) *is stable.*

Proof See [8] and its references for the proof. □

Let $x_{eq} = (x_1, ..., x_n)$ be an equilibrium point of the GRN system (1). It can be shown that the linearized system around the equilibrium is in the form (6)–(7), whose transfer function from input u to output y can be written as

$$R(s) := \left(1 - \frac{g'(x_1)e^{-\tau s}}{\prod_{i=1}^n \left(\frac{s}{\lambda_i} + 1\right)}\right)^{-1}. \tag{14}$$

When $g'(x_1) < 0$, the GRN is said to be under negative feedback. On the other hand, when $g'(x_1) > 0$ the GRN is said to be under positive feedback. In the next two sections, we analyze these two cases separately.

4 GRN Under Positive Feedback

In this section, we analyze the GRN (1) under positive feedback, i.e., $g'(x) > 0$. Moreover, we assume the network is homogeneous, i.e., $g_i(x) = f(x)$ and $\lambda_i = 1$. In the first part of this subsection, we will assume that

$$f'(x) < 0, \quad \forall x \in (0, \infty).$$

Then the system is under positive feedback if and only if n is even. Moreover, since f is strictly decreasing, it has a unique fixed point x_0. To continue, we borrow the following two results from [1].

Proposition 2 ([1]) *Consider the homogenous gene regulatory network* (1) *under positive feedback with* $f'(x) < 0$*. Moreover, suppose that* f *has negative Schwarzian derivative. Let* $x_0 > 0$ *denote the unique fixed point of* f*. Then,*

- *If* $|f'(x_0)| < 1$, *then the system has a unique equilibrium point which is stable independent of delay.*
- *If* $|f'(x_0)| > 1$, *then the system has three equilibrium points such that for any value of delay the system shows bistable behavior.*

Proposition 3 ([1]) *Consider the homogeneous network under positive feedback such that*

$$f(x) = \frac{a}{b + x^m}, \qquad a, b > 0, \quad m \in \{1,\ 2,\ 3, \dots\}.$$

If $m = 1$ *or a, b, m satisfy*

$$(\frac{a}{m})^m < (\frac{b}{m-1})^{m+1}, \tag{15}$$

then the system has a unique equilibrium point which is globally attractive. Otherwise, the system exhibits bistable behavior for any value of delay.

Biological systems are inherently noisy or uncertain; to model the uncertainty in the above system we assume that the nonlinearity function f is defined as follows:

$$f(x) = \varepsilon \frac{a}{b + x^m},$$

where $\varepsilon > 0$ can be different than 1. Then, we can show the following result.

Proposition 4 *Consider the homogeneous network under positive feedback such that*

$$f(x) = \varepsilon \frac{a}{b + x^m}, \qquad a, b > 0, \quad m \in \{1,\ 2,\ 3, \dots\}.$$

Moreover, assume that Eq. (15) *is satisfied and the network has a unique equilibrium. If*

$$\varepsilon \leq \frac{bm}{a(m-1)} \left(\frac{b}{m-1}\right)^{1/m}, \tag{16}$$

then the system has a unique equilibrium point which is globally attractive. Otherwise, the system exhibits bistable behavior for any value of delay.

Proof This result follows from Proposition 3, by letting $a = \varepsilon a$ in Eq. (15). □

Next, let us assume that each $f_i(x_i)$ satisfies

$$f_i(x) = \varepsilon_i \frac{a}{b + x^m}.$$

Next, result provides a sufficient condition for the system to converge to its unique equilibrium point. It is a generalization of Proposition (4).

Proposition 5 *Consider the homogeneous network under positive feedback such that*

$$f_i(x) = \varepsilon_i \frac{a}{b + x^m}, \qquad a, b > 0, \quad m \in \{1,\ 2,\ 3, \dots\}.$$

If for each i we have

$$a\ \varepsilon_i < b\ \sqrt[m]{\frac{b}{m-1}}, \tag{17}$$

then the system has a unique equilibrium point which is globally attractive.

Proof We will show that (17) implies $|g'(x_1)| < 1$, where x_1 is the first component of the equilibrium point which is also the unique fixed point of the function g. Then the result follows from Proposition 2. Note that the following equalities hold at the equilibrium point

$$x_i = \varepsilon_i \frac{a}{b + x_{i+1}^m} \quad i = 1, \dots, n \tag{18}$$

with $x_{n+1} := x_1$. We can calculate $|g'(x_1)|$ as

$$\begin{aligned} |g'(x_1)| &= \prod_{i=1}^{n} \frac{\varepsilon_i\ a\ m\ x_{i+1}^{m-1}}{(b + x_{i+1}^m)^2} \\ &= \frac{x_1 m x_2^{m-1}}{b + x_2^m} \cdots \frac{x_{n-1} m x_n^{m-1}}{b + x_n^m} \cdot \frac{x_n m x_1^{m-1}}{b + x_1^m} \\ &= \prod_{i=1}^{n} \frac{m x_i^m}{b + x_i^m} \end{aligned} \tag{19}$$

Now, if the following inequality holds for each i

$$\frac{m x_i^m}{b + x_i^m} < 1 \tag{20}$$

then $|g'(x_1)| < 1$. So, it is sufficient to check that (20) is satisfied for each i. Note that the function $f(x) = \frac{x^m}{b+x^m}$ is monotonically increasing for all $x > 0$. Also, from (18) we have

$$x_i < \varepsilon_i\ a/b.$$

Therefore, if $mf(\varepsilon_i a/b) < 1$ then (20) holds. In other words,

$$m \frac{(\varepsilon_i\ a/b)^m}{b + (\varepsilon_i\ a/b)^m} < 1 \quad \forall\ i = 1, \dots, n \tag{21}$$

implies $|g'(x_1)| < 1$. By re-arranging the terms in the above inequality, it is easy to see that (21) is equivalent to having

$$\varepsilon_i\, a < b \sqrt[m]{\frac{b}{m-1}}, \qquad \forall\, i = 1, \ldots, n,$$

which completes the proof. □

Next, we analyze the same homogeneous GRN when each nonlinearity has the following form:

$$g_i(x) = f(x) = \frac{ax^m}{b + x^m}.$$

Note that this time $g_i'(x) \geq 0$.

Proposition 6 *Consider the GRN* (1) *under positive feedback where for each i, the nonlinearity function* g_i *has the following form*

$$g_i(x) = f(x) = \frac{ax^m}{b + x^m}.$$

Then, $x_0 = (0, \ldots, 0) \in \mathbb{R}^n$ *is a locally stable equilibrium point of the system. Moreover, if*

$$\left(\frac{a}{m}\right)^m < \frac{b}{(m-1)^{m-1}}, \tag{22}$$

then there exists another locally stable equilibrium point $x_{eq} = (x_1, \ldots, x_1) \in \mathbb{R}^n_+$. *Otherwise,* x_0 *is the unique equilibrium point of* (1) *and all the solutions with positive initial conditions converge to* x_0.

Proof Note that $g_i(0) = 0$ for each i, so x_o is a equilibrium point of the GRN. Let $x_{eq} = (x_1, \ldots, x_1) \in \mathbb{R}^n_+$ be another equilibrium point of the GRN. Then,

$$x_1 = \frac{ax_1^m}{b + x_1^m} = f(x_1), \tag{23}$$

and the GRN is locally stable around x_{eq} if and only if

$$f'(x_1) < 1.$$

Let us define a new function

$$q(x) = x^m - ax^{m-1} + b,$$

and it is easy to verify that $q(x_1) = 0$. Moreover, for any x such that $q(x) = 0$ the point $x_e = (x, \ldots, x)$ is an equilibrium point of the GRN. Observe that $q(0) = q(a) = b$, $q(\infty) = \infty$, and

$$q'(x) = mx^{m-1} - a(m-1)x^{m-2},$$

which implies that $q(x)$ is decreasing for $x \leq a(m-1)/m$ and increasing for $x > a(m-1)/m$. This implies that $q(a(m-1)/m) \leq q(x)$ for all $x \in \mathbb{R}_+$. Then,

$$\begin{aligned}(\frac{a}{m})^m \leq \frac{b}{(m-1)^{m-1}} &\implies q(a(m-1)/m) \leq 0 \\ &\implies \exists x_1 > a(m-1)/m \text{s.t.} q(x_1) = 0. \end{aligned} \tag{24}$$

Then

$$f'(x_1) = \frac{bm}{b + a^m} \leq \frac{bm}{b + a^m(m-1/m)^m} \leq 1.$$

Therefore, $x_{eq} = (x_1, \ldots, x_1)$ is a locally stable equilibrium point of the GRN. Otherwise, if

$$(\frac{a}{m})^m > \frac{b}{(m-1)^{m-1}},$$

then the GRN has no other equilibrium point. □

Example 1 In this example, we consider the homogenous network under positive feedback. The dynamical model of the network is given as

$$\begin{aligned}\dot{x}_i(t) &= -x_i(t) + f(x_{i+1}(t)), \quad \text{for } i = 1, 2, 3 \\ \dot{x}_4(t) &= -x_4(t) + f(x_1(t-\tau)),\end{aligned} \tag{25}$$

where the function f is given as follows:

$$f(x) = \frac{3}{1 + x^3}. \tag{26}$$

Applying the inequality in (15), it is easily observed that

$$\left(\frac{a}{m}\right)^m = 1 > \left(\frac{b}{m-1}\right)^{m+1} = 0.0625.$$

Hence, the system shows bistable behavior for any value of delay. Now, the unique fixed point of the function f can be calculated as $x_0 = 1.164$. Moreover, the three equilibrium points of the system are found as

$$\begin{aligned}x_1 &= (1.164, 1.164, 1.164, 1.164), \\ x_2 &= (0.1075, 2.9963, 0.1075, 2.9963), \\ x_3 &= (2.9963, 0.1075, 2.9963, 0.1075).\end{aligned}$$

Hence, from Proposition 3 we expect bistable behavior. In Fig. 1 the solution converges to x_2, and in Fig. 2 the solution converges to x_3, which is in line with our theoretical expectations.

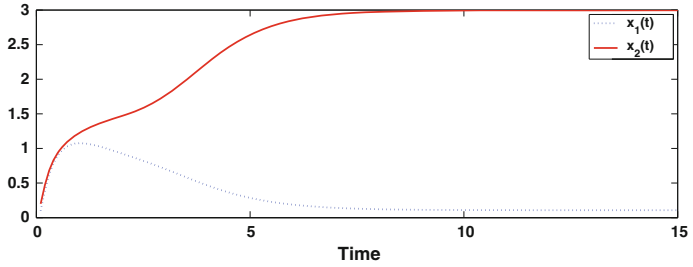

Fig. 1 Simulation of the system in Example 1 with initial conditions $x_{in} = (0.1, 0.2, 0.3, 0.4)$ and $\tau = 0$

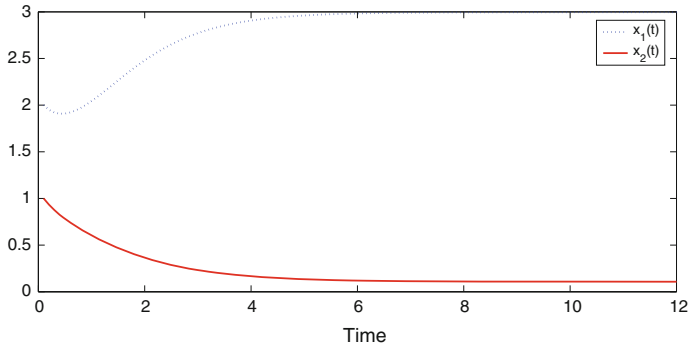

Fig. 2 Simulation of the system in Example 1 with initial conditions $x_{in} = (2, 1, 2, 1)$ and $\tau = 0$

5 GRN Under Negative Feedback

In this section, we will be analyzing the GRN model (1) network under negative feedback. Therefore, the following condition holds

$$g'(x) < 0, \quad \forall x \in (0, \infty).$$

Note that each $g_i(x) > 0$ for $x > 0$, so in order to have an equilibrium in the positive cone $\mathbb{R}^n_+$, we need $g(0) > 0$. Moreover, since $g'(x) < 0$ for all $x > 0$; the GRN has a unique equilibrium point. This comes from the fact that a decreasing function has a unique fixed point, see [1]. For the rest of this subsection, let $x_{eq} = [x_1, ..., x_n]^{\mathrm{T}}$ be the unique equilibrium point of the GRN. Then, the linearization of the GRN around x_{eq} results in a system in the form (8), with

$$b_1 = g_1'(x_2), \ \ldots, \ b_{n-1} = g_{n-1}'(x_n), \ b_n = g_n'(x_1).$$

Thus, the characteristic equation of the linearized system is of the form (9) where

$$\beta = \frac{g_1'(x_2)\cdots g_{n-1}'(x_n)\cdot g_n'(x_1)}{\prod_{i=1}^{n}\lambda_i}\,.$$

It is a simple exercise to check that

$$k = -\beta = -g'(x_1).$$

By the negative feedback assumption, $g'(x_1) < 0$, we have $k > 0$, and thus the result of Proposition 1 is applicable for this system. More precisely, (1) is locally stable around its equilibrium $x_{eq} = [x_1, ..., x_n]^{\mathrm{T}}$ independent of delay, if $|g'(x_1)| < 1$. Furthermore, (1) is locally stable around its equilibrium if

$$\kappa := \sqrt[n]{|g'(x_1)|} < \sec\frac{\pi}{n} \tag{27}$$

and

$$\tau < \frac{\pi - n\arccos(1/\kappa)}{\lambda\sqrt{\kappa^2-1}} =: \tau_m \tag{28}$$

where $\lambda = \max\{\lambda_1, \ldots, \lambda_n\}$. It is easy to verify that (27) is equivalent to

$$\cos\frac{\pi}{n} < 1/\kappa\,,$$

so $\arccos(1/\kappa) < \pi/n$.

Note that we only provide a local stability result around the unique equilibrium point of the GRN (1). Our results are inconclusive about the global behavior of the system. Nevertheless, in [4] it is shown that if $|g'(x_1)| < 1$ then the system is *globally stable* around its unique equilibrium point. The small gain condition $|g'(x_1)| < 1$ also implies delay independent stability of the linearized network. However, when $|g'(x_1)| > 1$, we cannot make any conclusions regarding the global stability of the system. Our extensive simulations suggest that the local stability of the system also implies the global stability of the network. The proof of such a result would most likely require a modified version of the Poincaré–Bendixson type of result obtained in [10]. A result to such direction with some additional assumptions is given in [9], where authors use integral quadratic constraints to show local stability implies global stability of the network.

Example 2 Consider the cyclic system:

$$\dot{x}_1(t) = -\lambda_1 x_1(t) + g_1(x_2(t)) \tag{29}$$

$$\dot{x}_2(t) = -\lambda_2 x_2(t) + g_2(x_1(t-\tau)), \tag{30}$$

where $\lambda_1 = 2$ and $\lambda_2 = 0.5$, $g_1(x) = \frac{6}{2+x^2}$, $g_2(x) = \frac{4x^2}{1+x^2}$ and $\tau > 0$. The unique equilibrium point of (29)–(30) is $x_e = [0.55, 1.86]^{\mathrm{T}}$, so we define $x_1 = 0.55$ and $x_2 =$

1.86. It is easy to verify that the fixed point of $g = (\frac{1}{\lambda_1} g_1) \circ (\frac{1}{\lambda_2} g_2)$ is $x_1 = 0.55$ and $g'(x) < 0$ for all $x > 0$, i.e., the cyclic system is under negative feedback. In particular,

$$k = -\frac{g_1'(x_2) \cdot g_2'(x_1)}{\lambda_1 \cdot \lambda_2} = 1.9447 = -g'(x_1)\,.$$

Hence $\kappa = \sqrt{1.9447} = 1.3945$. Since $\sec(\pi/2) = \infty$, the inequality (27) is automatically satisfied. By using (28) we compute $\tau_m = 0.8227$; whereas the exact delay bound τ_c for local stability around x_e is calculated numerically from the delay margin of the feedback system whose open loop transfer function is $G(s) = \frac{k}{(1+s/\lambda_1)(1+s/\lambda_2)}$ by using the Bode plots and `allmargin` command of Matlab: $\tau_c = 2.3585$. The conservatism introduced here is due to the fact that λ_1 and λ_2 differ by a factor of 4; in this case $\tau_c/\tau_m = 2.87$. We expect that as λ_1 and λ_2 get closer to each other, τ_m increases to τ_c.

Recall from the proof of Proposition 1 that the system is locally stable if

$$\tau < \frac{\pi - n \arccos(1/\kappa)}{\omega_c} \tag{31}$$

where $\kappa = \sqrt[n]{k}$ and ω_c is the solution of the equation

$$k^2 = \left(1 + \frac{\omega_c^2}{\lambda_1^2}\right) \cdots \left(1 + \frac{\omega_c^2}{\lambda_n^2}\right). \tag{32}$$

As mentioned before, analytical computation of ω_c is typically impossible especially when $n \geq 3$ and λ_i's are distinct. However, it is possible to determine another bound by re-writing (32) as

$$k^2 - 1 = \frac{\omega_c^{2n}}{\lambda_1^2 \cdots \lambda_n^2} + R(\omega_c)$$

where $R(\omega_c) \geq 0$ for all $\omega_c \in \mathbb{R}_+$, and $R(\omega_c)$ is an increasing function of ω_c. This motivates the definition of $\tilde{\omega}_m$ as the solution of

$$k^2 - 1 = \frac{\tilde{\omega}_m^{2n}}{\lambda_1^2 \cdots \lambda_n^2}$$

that is

$$\tilde{\omega}_m = \tilde{\lambda} \sqrt[2n]{k^2 - 1} \quad \text{where} \quad \tilde{\lambda} = \sqrt[n]{\lambda_1 \cdots \lambda_n}.$$

Clearly, $\omega_c \leq \tilde{\omega}_m$. Thus another estimate of τ_c is

$$\tau < \frac{\pi - n \arccos(1/\sqrt[n]{k})}{\tilde{\lambda} \sqrt[2n]{k^2 - 1}} =: \tilde{\tau}_m, \tag{33}$$

and we have $\tilde{\tau}_m \leq \tau_c$. In conclusion, for finding an estimate of ω_c, rather than taking the maximum of λ_i's, it may be preferable to use their geometric mean. See [11, 12] where similar analyses are conducted.

Returning to the numerical example, we see that $\tilde{\lambda} = 1$, and $\tilde{\omega}_m = 1.2915$; these give $\tilde{\tau}_m = 1.2383$. This represents an improvement in the estimate of τ_c: we now have $\tau_c/\tilde{\tau}_m = 1.9$.

However, we should point out that it is not always possible to compare τ_m and $\tilde{\tau}_m$ as illustrated by the following example. In (29)–(30) let us now take $\lambda_1 = 2$ and $\lambda_2 = 1$. Then, the equilibrium point shifts to $x_1 = 0.7441$, $x_2 = 1.4254$; linearization around this point gives the gain $k = 1.2975$. Then, we compute $\tau_c = 3.1035$, with $\omega_c = 0.7052$; the estimates are $\tau_m = 1.9646$ and $\tilde{\tau}_m = 1.666$. In conclusion, these two analytical bounds should be computed side by side and the larger one should be used as a lower bound of τ_c.

Next, we focus on the homogeneous network under negative feedback as such we assume each $g_i(x)$ is given as

$$g_i(x) = \varepsilon_i \frac{a}{b + x^m}, \tag{34}$$

where $a > 0$, $b > 0$, and $m \in \mathbb{N}$ with $m \geq 2$, are constants for each of the nonlinearities; the variables ε_i can be seen as perturbations from homogeneity of the network. Note that in order to have negative feedback n should be an odd number. The dependence of the global stability of the network on the parameters ε_i is determined by the following.

Proposition 7 *Consider the homogeneous GRN model given in* (1) *where each* g_i *is in the form* (34). *Let* $x_{eq} = [x_1, ..., x_n]^{\mathrm{T}}$ *denote the unique equilibrium point of the system. If for each i we have*

$$a\,\varepsilon_i < b\,\sqrt[m]{\frac{b}{m-1}}, \tag{35}$$

then the system is globally stable around its unique equilibrium point x_{eq}.

Proof The proof is similar to Proposition 5. □

6 Conclusions

We have studied homogenous GRN (1) under negative and positive feedback. For the positive feedback case, we derived sufficient conditions for the bistability of the GRN that depends only on the coefficients of the nonlinearity functions. Moreover, we did a robustness analysis and found necessary conditions that conserves the global asymptotic stability of the GRN. In the second part, we did a robustness

analysis the GRN under delayed negative feedback using an extended version of the secant condition. Similar to positive feedback case, we derived necessary conditions that conserves the local stability of the GRN.

References

1. Ahsen, M.E., Özbay, H., Niculescu, S.-I.: Analysis of Deterministic Cyclic Gene Regulatory Network Models with Delays. Birkhäuser (2015)
2. Özbay, H.: Introduction to Feedback Control Theory. CRC Press (1999)
3. Sontag, E.D.: Passivity gains and the 'secant condition' for stability. Syst. Control Lett. **55**, 177–183 (2006)
4. Ahsen, M., Özbay, H., Niculescu, S.-I.: On the analysis of a dynamical model representing gene regulatory networks under negative feedback. Int. J. Robust Nonlinear Control **24**, 1609–1627 (2014)
5. Ahsen, M.E., Özbay, H., Niculescu, S.-I.: Analysis of gene regulatory networks under positive feedback. In: Vyhlidal, T., Lafay, J.-F., Sipahi, R. (eds.) Delay Systems: From Theory to Numerics and Applications, pp. 127–140. Springer (2014a)
6. Hirsch, M.W., Smith, H.: Monotone dynamical systems. In: Cañada, D.P., Fonda, A. (eds.) Handbook of Differential Equations, Ordinary Differential Equations, vol. 2, pp. 239–357. Elsevier (2005)
7. Sedaghat, H.: Nonlinear Difference Equations: Theory with Applications to Social Science Models. Springer (2003)
8. Ahsen, M.E., Özbay, H., Niculescu, S.-I.: Analysis of a gene regulatory network model with time delay using the secant condition. IEEE Life Sci. Lett. **2**(2), 5–8 (June 2016)
9. Summers, E., Arcak, M., Packard, A.: Delay robustness of interconnected passive systems: an integral quadratic constraint approach. IEEE Trans. Autom. Control **58**, 712–724 (2013)
10. Mallet-Paret, J., Sell, G.R.: The Poincaré-Bendixson theorem for monotone cyclic feedback systems with delay. J. Differ. Equ. **125**(2), 441–489 (1996)
11. Wagner, J., Stolovitzky, G.: Stability and time-delay modeling of negative feedback loops. Proc. IEEE **96**, 1398–1410 (2008)
12. Arcak, M., Sontag, E.D.: Diagonal stability of a class of cyclic systems and its connection with the secant criterion. Automatica **42**(9), 1531–1537 (2006)
13. Arcak, M., Sontag, E.D.: A passivity-based stability criterion for a class of biochemical reaction networks. Math. Biosci. Eng. **5**, 1–19 (2008)
14. Enciso, G.A.: A dichotomy for a class of cyclic delay systems. Math. Biosci. **208**, 63–75 (2007)
15. Enciso, G.A.: On the asymptotic behavior of a cyclic biochemical system with delay. In: 45th IEEE Conference on Decision and Control, pp. 2388–2393 (2006)

Transformations from Variable Delays to Constant Delays with Applications in Engineering and Biology

Andreas Otto and Günter Radons

Abstract The transformation from systems with time-varying delays or state-dependent delays to systems with constant delays is studied. The transformation exists if the delay is defined by a transport with a variable velocity over a constant distance. In fact, time-varying or state-dependent delays, which are generated by such a mechanism, are common in engineering and biology. We study two paradigmatic time delay systems in more detail. For metal cutting processes, or more precisely turning with spindle speed variation, we show that the analysis of the machine tool vibrations via constant delays in terms of the spindle rotation angle is more advantageous than the conventional analysis of the vibrations with time-varying delays in the time domain. In a second example, motivated by the McKendrick equation modeling structured populations, we show that systems with variable delays and the equivalent systems with constant delays are, in addition, equivalent to partial differential equations with moving and constant boundaries.

1 Introduction

In many cases, the effects of time delays cannot be neglected for an accurate description of a dynamical system. For example, in control theory there can be time delays between the input, the output, and the internal state of the system [28]. In time-delayed feedback control schemes, a delayed feedback of the internal state is used for the stabilization of unstable periodic orbits in chaotic systems [31]. Delayed feedback and delay coupling is also intensively studied in biology [22, 24] and in the dynamics of semiconductor lasers [36], where especially synchronization phenom-

A. Otto (✉) · G. Radons
Institute of Physics, Chemnitz University of Technology, 09107 Chemnitz, Germany
e-mail: otto.a@mail.de

G. Radons
e-mail: radons@physik.tu-chemnitz.de

T. Insperger et al. (eds.), *Time Delay Systems*,
Advances in Delays and Dynamics 7, DOI 10.1007/978-3-319-53426-8_12

ena are studied [18]. In addition, there are systems with an intrinsic time delay, which does not appear due to an external feedback or coupling term. They can be found, for example, in climate dynamics [8], mechanical engineering [12, 17], or population dynamics [16, 35]. In general, a system with constant delay $r > 0$ can be described by a delay differential equation (DDE)

$$\mathbf{y}'(\varphi) = \mathbf{f}(\mathbf{y}(\varphi), \mathbf{y}(\varphi - r), \varphi), \tag{1}$$

where prime denotes differentiation with respect to φ and the vector field $\mathbf{f}$ depends not only on the instantaneous configuration $\mathbf{y}(\varphi)$ but also on the delayed configuration $\mathbf{y}(\varphi - r)$. In Eq. (1), the independent variable is specified by the unusual symbol φ. This is due to the fact that we use nonlinear time scale transformations in this paper for studying the relationship between DDEs with constant delays Eq. (1) and DDEs with variable delays

$$\dot{\mathbf{x}}(t) = \mathbf{g}(\mathbf{x}(t), \mathbf{x}(t - \tau(\mathbf{x}_t, t)), t), \tag{2}$$

where dot denotes the derivative with respect to t. In Eq. (2), the function $\mathbf{x}_t = \mathbf{x}(t + \theta)$, $\theta \in [-\tau_{\max}, 0]$ denotes the infinite dimensional state of the DDE, $\tau(\mathbf{x}_t, t)$ is the variable delay which may depend on the state and explicitly also on time and $\tau_{\max}$ is a threshold for the maximum delay. Examples for systems with time-varying delays $\tau(\mathbf{x}_t, t) = \tau(t)$ can be found in time-delayed feedback control [14, 37], synchronization [3], population dynamics [30], and machining [25, 38, 42]. Similarly, systems with state-dependent delays $\tau(\mathbf{x}_t, t) = \tau(\mathbf{x}_t)$ are studied motivated by adaptive time-delayed feedback control [27], laser dynamics [21], synchronization [29], population dynamics [16, 19, 34], and machine tool vibrations [13, 26, 40].

Whereas the mathematical theory for the analysis of DDEs with constant delay Eq. (1) is well-developed [9], there are open problems in the analysis of DDEs with state-dependent delay Eq. (2) [10, 33]. For example, in Eq. (2) the size of the state space, i.e., the interval size for the function $\mathbf{x}_t$, is not clear a priori. Typically, not even a threshold $\tau_{\max}$ for the maximum delay can be given in advance, which is associated with inconsistencies in the causal behavior of the DDE [39]. The problems with state-dependent delays can be avoided if the variable delay $\tau(\mathbf{x}_t, t)$ can be transformed to a constant delay r. The transformation from a system with variable delay Eq. (2) to a system with constant delay Eq. (1) goes back to the analysis of variable delay systems with analog and digital computers [4, 20, 32]. We show that variable delays, which can be transformed to constant delays, are equivalent to the delays, which are known as variable transport delays [44].[1] Even though, the transformation is known since more than 50 years, it has been used only rarely in applications. A few examples can be found in the control of flow processes [43], population dynamics [16, 34] and machine tool vibrations [26, 38, 40].

In this paper, the transformation from Eq. (2) with state-dependent delay to Eq. (1) with constant delay is studied systematically in Sect. 2. It turns out that the condition

[1] There is a specific *variable transport delay* block in the MATLAB/Simulink software environment for such type of delays.

for the existence of such a transformation is practically relevant in many real-world examples. As a paradigmatic example, the transformation from variable to constant delay is used in Sect. 3 for the analysis of machine tool vibrations, where the delay is time-varying due to an explicit variation of the spindle speed. In addition, in Sect. 4, we consider systems with a variable transport delay in structured population models, which are typically described by partial differential equations. We show the equivalence between the DDEs with variable and constant delays and partial differential equations (PDEs) with constant and moving boundaries.

2 Transformation from Variable Delay to Constant Delay

We apply a nonlinear time scale transformation $\varphi = \boldsymbol{\Phi}(\mathbf{x}(t), t)$ to the DDE with state-dependent delay Eq. (2) with the aim of changing the variable delay $\tau(\mathbf{x}_t, t)$ to a constant delay r. The function $\boldsymbol{\Phi}$ can depend explicitly on time t and on the configuration $\mathbf{x}(t)$, which itself depends on time t. For the sake of brevity, we define the function $\boldsymbol{\Phi}_{\mathbf{x}}(t) := \boldsymbol{\Phi}(\mathbf{x}(t), t)$, where the subscript $\mathbf{x}$ refers to the dependence on the configuration. The time scale transformation $\varphi = \boldsymbol{\Phi}_{\mathbf{x}}(t)$, $-\tau(\mathbf{x}_0, 0) \leq t < \infty$, is assumed to be bijective to guarantee a one-to-one mapping between the time t and the new variable φ. The inverse time scale transformation is denoted by $t = \boldsymbol{\Phi}_{\mathbf{x}}^{-1}(\varphi)$ with $-r \leq \varphi < \infty$. The instantaneous and delayed configuration of Eq. (2) can be given in terms of the new independent variable φ by

$$\mathbf{x}(t) = \mathbf{y}(\boldsymbol{\Phi}_{\mathbf{x}}(t)) = \mathbf{y}(\varphi), \quad \mathbf{x}(t - \tau(\mathbf{x}_t, t)) = \mathbf{y}\left(\boldsymbol{\Phi}_{\mathbf{x}}(t - \tau(\mathbf{x}_t, t))\right). \tag{3}$$

We are interested in a transformation to a constant delay r in the new representation, $\mathbf{y}\left(\boldsymbol{\Phi}_{\mathbf{x}}(t - \tau(\mathbf{x}_t, t))\right) = \mathbf{y}(\varphi - r)$. This yields the condition

$$\boldsymbol{\Phi}_{\mathbf{x}}(t - \tau(\mathbf{x}_t, t)) = \boldsymbol{\Phi}_{\mathbf{x}}(t) - r \quad \leftrightarrow \quad r = \int_{t-\tau(\mathbf{x}_t,t)}^{t} \dot{\boldsymbol{\Phi}}_{\mathbf{x}}(\theta) d\theta. \tag{4}$$

Note that $\boldsymbol{\Phi}_{\mathbf{x}}(t)$ depends on time t and on the instantaneous configuration $\mathbf{x}(t)$ at time t, whereas the associated delay $\tau(\mathbf{x}_t, t)$ in Eq. (4) depends also on the history of the configuration, and therefore, on the state $\mathbf{x}_t$ of the DDE. An equivalent representation of the system with variable delay Eq. (2) in terms of the new variables can be obtained by applying the time scale transformation to Eq. (2)

$$\mathbf{y}'(\varphi) = \left(\boldsymbol{\Phi}_{\mathbf{x}}^{-1}\right)'(\varphi)\mathbf{g}\left(\mathbf{y}(\varphi), \mathbf{y}(\varphi - r), \boldsymbol{\Phi}_{\mathbf{x}}^{-1}(\varphi)\right). \tag{5}$$

Equation (5) is similar to Eq. (1), which means that a system Eq. (2) with time-varying delay or state-dependent delay $\tau(\mathbf{x}_t, t)$ is equivalent to a DDE Eq. (1) with constant delay r if the condition Eq. (4) is fulfilled. The initial condition for the

transformed system Eq. (5) can be obtained from the initial condition of the original system Eq. (2) with the relationship Eq. (3). For state-dependent delays, the additional varying coefficient $\left(\boldsymbol{\Phi}_{\mathbf{x}}^{-1}\right)'(\varphi)$ in Eq. (5) is state-dependent as well, and uncovers the necessarily nonlinear behavior of systems with state-dependent delays.

The condition Eq. (4) for the existence of a transformation to constant delays is not only a purely mathematical condition. In fact, Eq. (4) describes a transport over the constant distance r with the variable velocity $\dot{\boldsymbol{\Phi}}_{\mathbf{x}}(t)$ and the corresponding delays are called variable transport delays [44] or threshold-type delays [16, 19, 34]. A time delay system with a state-dependent variable transport delay is illustrated in Fig. 1a. The configuration $\mathbf{x}(t)$ of the system is read at location zero on the left-hand side and imprinted on the square-shaped particles, which are transported by the conveyor belt. In a time delay system, the instantaneous configuration $\mathbf{x}(t)$ depends also on the imprinted configuration on the particles at the right-hand side of the conveyor belt at the location r, which is a delayed form $\mathbf{x}(t-\tau(\mathbf{x}_t,t))$ of the systems configuration. The time delay $\tau(\mathbf{x}_t,t)$ is equal to the traveling time for the transport of the particles over the distance r. The time- and state-dependence of the delay originates from the fact that the velocity $\dot{\boldsymbol{\Phi}}_{\mathbf{x}}(t)$ is time-varying and depends on the configuration $\mathbf{x}(t)$ of the system. In particular, the time delay is implicitly defined by Eq. (4), which is illustrated in Fig. 1b. The absolute distance covered by the particles is given by the function $\boldsymbol{\Phi}_{\mathbf{x}}(t)$, which defines a one-to-one mapping between time t (horizontal axis) and space φ (vertical axis). A vertical shift of the function $\boldsymbol{\Phi}_{\mathbf{x}}(t)$ by the constant distance r leads to a variable horizontal displacement between the two curves, which is equal to the variable transport delay $\tau(\mathbf{x}_t,t)$ (red lines). The system can be described either in the time domain by Eq. (2) with the variable transport delay $\tau(\mathbf{x}_t,t)$ or in the spatial domain by Eq. (1) with the constant delay r.

Typical examples for the existence of variable transport delays in engineering and biology are metal cutting processes and population dynamics, which are studied in

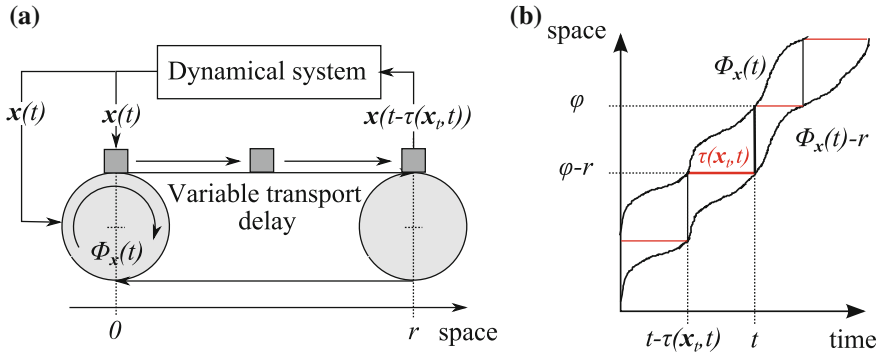

Fig. 1 **a** If the delay in a time delay system is defined by a transport with a variable velocity $\dot{\boldsymbol{\Phi}}_{\mathbf{x}}(t)$ over a constant distance r similar to the conveyor belt, the system can be described either by the DDE Eq. (2) with the variable delay $\tau(\mathbf{x}_t,t)$ or by the DDE Eq. (1) with the constant delay r. **b** Illustration of the relationship Eq. (4) between the variable delay $\tau(\mathbf{x}_t,t)$ and the constant delay r

detail in Sect. 3 and Sect. 4, respectively. In addition, variable transport delays can be found in automotive engineering [7]. In particular, such a delay appears in the modern electronic control of the air fuel ratio in spark ignition engines [6]. In this case, the constant delay r is a constant distance between the fuel injector and the oxygen sensor in the exhaust stream and the variable velocity $\dot{\Phi}_{\mathbf{x}}(t)$ is given by the exhaust gas flow rate, which varies with the injected fuel flow rate. Another example are FIFO buffers, where FIFO is an acronym for first-in first-out. In this example, the buffer size represents the constant transport distance r and a variable velocity $\dot{\Phi}_{\mathbf{x}}(t)$ of the transport can be realized by a modulation of the clock frequency [14].

Nevertheless, it should be made clear that not all variable delays are equivalent to constant delays. A counterexample, where a variable delay appears but the delay does not necessarily fulfill Eq. (4), is given by the state-dependent delay in the automatic soft landing problem [1, 41]. In this example, a finite propagation delay $\tau(x_t)$ is assumed for the signal propagation between the space vehicle and the ground. In particular, such a delay can be implicitly defined by

$$v\tau(x_t) = x(t - \tau(x_t)) + x(t), \tag{6}$$

where v denotes the constant speed of the signal and $x(t)$ specifies the moving distance of the vehicle to the ground. From the definition of the delay in Eq. (6), it is not clear whether Eq. (4) is satisfied and consequently a transformation to a constant delay r is possible. In fact, in this case it depends on the specific solution $x(t)$ whether a transformation to constant delay is possible or not.

2.1 Analysis of Systems with State-Dependent Variable Transport Delays

There are several difficulties in systems with state-dependent delays. Here we give some remarks that can be useful for the analysis of DDEs with state-dependent variable transport delays. One problem is that the delays are often only specified by an implicit relation similar to Eqs. (4) and (6). However, for the calculation of the solution of nonlinear DDEs with state-dependent delays with numerical solvers such as the MATLAB function *ddesd*, the state-dependent delay $\tau(\mathbf{x}_t, t)$ must be explicitly defined as a function of t and the configuration $\mathbf{x}(t)$. For DDEs with state-dependent delays as defined in Eq. (4) there are three ways to overcome this.

The first method is the interpretation of the state-dependent delay $\tau(\mathbf{x}_t, t)$ as an additional component $x_\tau(t)$ of the configuration $\mathbf{x}(t)$ of the delay system (cf. [7, 44]). In this case the state-dependent delay is equivalent to the corresponding component of the configuration, $x_\tau(t) := \tau(\mathbf{x}_t, t)$, and the dimension of the state space of the time delay system is increased by one. The differential equation for the additional component $x_\tau(t)$ can be obtained by differentiation of Eq. (4) with respect to time

$$\dot{x}_\tau(t) = 1 - \frac{\dot{\Phi}_{\mathbf{x}}(t)}{\dot{\Phi}_{\mathbf{x}}(t - x_\tau(t))}. \tag{7}$$

Note that the DDE Eq. (7) does only yield the correct state-dependent delay if the initial condition $x_\tau(0)$ for the delay component is chosen consistent with Eq. (4).[2] The second method uses the inverse time scale transformation $t = \Phi_{\mathbf{x}}^{-1}(\varphi)$ for the calculation of the state-dependent time delay

$$\tau(\mathbf{x}_t, t) = t - \Phi_{\mathbf{x}}^{-1}\left(\Phi_{\mathbf{x}}(t) - r\right). \tag{8}$$

Equation (8) can be obtained directly by rearranging Eq. (4). The function $\Phi_{\mathbf{x}}$ can be determined from the history of the configurations $\mathbf{x}(t)$ and its inverse $\Phi_{\mathbf{x}}^{-1}$ can be calculated numerically, for example, with Newton's method. In [44] the calculation of the delay via Eqs. (7) and (8) are compared, with the result that the performance of the second method with Eq. (8) was better. In this paper, a third method is proposed. It is based on the solution of the equivalent system with constant delay Eq. (1). The performance of this method is much better than the other two methods because a numerical solver for DDEs with constant delays can be used, which is faster than solvers for DDEs with varying delay. In this case the only extra effort is the numerical calculation of the inverse function $\Phi_{\mathbf{x}}^{-1}(\varphi)$ for the additional variable coefficient. Nevertheless, this is roughly the same effort compared to the calculation of the variable delay $\tau(\mathbf{x}_t, t)$ with Eq. (8). In fact, in many applications an explicit analytical expression can be derived for the additional state-dependent coefficient $\left(\Phi_{\mathbf{x}}^{-1}\right)'(\varphi)$, which means that the analysis of the equivalent system Eq. (5) with constant delay is much simpler than the analysis of the original system Eq. (2) with state-dependent delay [26].

Another difficulty appears in the linearization of DDEs with state-dependent delay, which is not straightforward because the delayed argument $\mathbf{x}(t - \tau(\mathbf{x}_t, t))$ depends itself on the state $\mathbf{x}_t$ of the DDE [10, 13, 33]. This difficulty vanishes if the system is analyzed in the spatial domain where no state-dependent delay appears. In this case, the linearization can be done in the conventional way. For the interested reader, the linearization of a system with state-dependent delay as a model for a turning process is provided in [13]. In comparison, the linearization and the stability analysis for the equivalent system with constant delay and variable coefficient can be found in [26]. Of course, the results of both methods are completely equivalent. However, not only the linearization but also the resulting linearized dynamics is more complex for the representation with variable delay. For example, if a periodic solution appears in the DDE Eq. (2) with state-dependent delay, the coefficients in the linearized dynamics and similarly the time delay becomes time-periodic. In contrast, if the system is at first transformed to a DDE with constant delay, the linearized dynamics can be characterized by a system with periodic coefficients but constant delay. Typically, the methods and software packages for the linear stability analysis

[2] No delayed values of $x_\tau(t)$ appear in the DDE system, and therefore, only an initial value $x_\tau(0)$ and no initial function must be specified for the additional component $x_\tau(t)$.

of DDEs with periodic coefficients are only applicable or at least optimized for systems with constant delays. A comparison of two numerical methods for the linear stability analysis of a DDE with variable delay and the analysis of the equivalent system with constant delays is given in the next Sect. 3.

3 Variable Transport Delays in Metal Cutting Dynamics

Machine tool dynamics is one of the above-mentioned fields, where time delay systems are studied intensively since more than 50 years. In Fig. 2a, a typical metal cutting process is illustrated schematically. Small variations of the chip thickness cause variations of the cutting force $\mathbf{F}$ that acts on the cutting tool and leads to structural displacements $\mathbf{x}(t)$ of the tool. The chip thickness, however, is not only determined by the instantaneous displacements $\mathbf{x}(t)$ of the tool but depends also on delayed displacements $\mathbf{x}(t-\tau)$, which characterize the outer surface of the chip. This is called regenerative effect and is the main reason for instabilities in metal cutting processes such as turning, boring, milling, drilling or grinding [2]. The time delay in machining is a variable transport delay as defined in Eq. (4), where $\dot{\Phi}_{\mathbf{x}}(t)$ is the angular velocity of the workpiece spindle. The constant delay r is either the full angle 2π or a constant fraction of the full angle of rotation of the spindle. For an ideal conventional process, the spindle speed is constant $\dot{\Phi}_{\mathbf{x}}(t) = \Omega_0$ and consequently a constant delay $\tau(\mathbf{x}_t, t) = \tau_0$ appears. However, in practice the process is not ideal and small variations of the relative spindle speed occur due torsional displacements of the workpiece or tangential displacements of the tool. These so-called passive spindle speed variations lead to a state-dependent delay [13, 26, 40]. On the other hand, an active variation of the spindle speed $\dot{\Phi}_{\mathbf{x}}(t) = \Omega(t)$ is used to stabilize the process by the effect of the resulting time-varying delay $\tau(t)$. Metal cutting processes including variable delays are treated in [25, 38, 42].

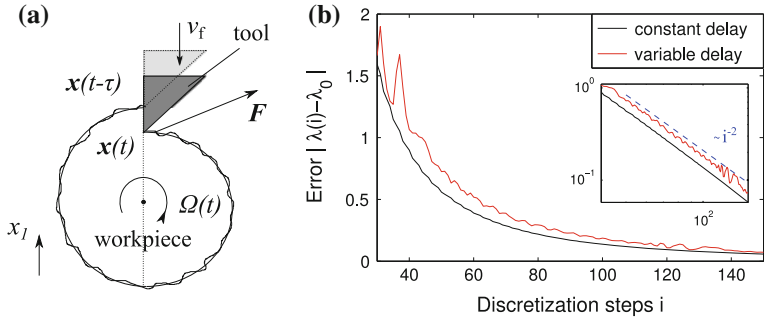

Fig. 2 **a** Regenerative effect in turning with spindle speed variation $\Omega(t)$. **b** Comparison of the error of the stability exponent $\lambda(i)$ between the semidiscretization method for constant delay and the semidiscretization method for time-varying delay

In this paper, we consider the turning process of Fig. 2a as a paradigmatic example for a more detailed investigation of the transformation. In this example, the spindle rotation angle φ in case of a spindle speed modulation can be characterized by

$$\varphi = \Phi(t) = \int_0^t \Omega(\theta) d\theta, \quad \Omega(t) = \Omega_0 \left(1 + A_m \cos(2\pi f_m t)\right). \tag{9}$$

where Ω_0 is the nominal spindle speed and A_m and f_m are the amplitude and the frequency of the spindle speed variation. The variable delay can be calculated from Eq. (8), where the constant delay r in the angular domain can be given by $r = 2\pi$. In this example, it is assumed that the spindle angle $\Phi_{\mathbf{x}}(t) = \Phi(t)$ does not depend on the configuration $\mathbf{x}(t)$ of the DDE but, in general, the spindle angle may also dependent on the displacements $\mathbf{x}(t)$ [26]. The main reason for dynamic variations of the cutting force in metal cutting are dynamic variations of the chip thickness $h(t)$. The modulus of the cutting force $F(t)$ on the tool can be determined from

$$F(t) = Kbh(t) = Kb \left(x_1(t - \tau(t)) - x_1(t)\right), \tag{10}$$

where K is the cutting force coefficient, b is the chip width, and $x_1(t)$ specifies relative displacements between the tool and the workpiece in normal direction (see Fig. 2a). The cutting force acts on the machine tool structure. For simplicity, here it is assumed that the structural dynamics can be described by a single harmonic oscillator. After converting the system to dimensionless variables, the dynamics can be described in state space representation with the tool velocity $x_2(t) = \dot{x}_1(t)$ by the first order linear DDE

$$\dot{\mathbf{x}}(t) = \mathbf{A}\mathbf{x}(t) + \mathbf{B}\mathbf{x}(t - \tau(t)), \tag{11}$$

where the coefficient matrices are specified by

$$\mathbf{A} = \begin{pmatrix} 0 & 1 \\ -(1+w) & -2\zeta \end{pmatrix}, \quad \mathbf{B} = \begin{pmatrix} 0 & 0 \\ w & 0 \end{pmatrix}. \tag{12}$$

In Eq. (12) ζ is the damping ratio of the harmonic oscillator and w is the dimensionless chip width, which is proportional to the real chip width b. The coefficient relating the dimensionless chip width w and the corresponding real chip width b at the lathe is determined by the cutting force coefficient K, the orientation, the modal mass and the eigenfrequency of the dominant eigenmode of the structure (see [11]).

3.1 Stability Analysis of Machine Tool Vibrations

Typically, the stability of machine tool vibrations is calculated from the time domain model Eq. (11). For example, the stability of Eq. (11) with periodic delay has been analyzed in [11] with the so-called semidiscretization method. On the other hand, it was shown in Sect. 2 that the system can be also described by a DDE with constant delay r and variable coefficient. According to Eq. (5), the equivalent system in the angular domain can be given by

$$\mathbf{y}'(\varphi) = \frac{1}{\Omega(\boldsymbol{\Phi}^{-1}(\varphi))} \left(\mathbf{A}\mathbf{y}(\varphi) + \mathbf{B}\mathbf{y}(\varphi - 2\pi)\right). \tag{13}$$

The condition of a one-to-one mapping between the time domain model Eq. (11) and the angular domain model Eq. (13) means a strictly positive spindle speed $\Omega(t) > 0$. In principle, there is no guarantee that this condition is fulfilled. However, if it is not fulfilled the cutting force model Eq. (10) does no longer hold, and therefore, Eq. (11) also does not adequately describe the process. Hence, we assume typical cutting conditions, where the turning process with spindle speed variation can be well described by Eq. (11) with variable delay τ and by the periodic system Eq. (13) with constant delay. In this case the semidiscretization for DDEs with periodic coefficients can be used for the stability analysis [12], where the inverse time scale transformation $\boldsymbol{\Phi}^{-1}(\varphi)$ for the determination of the variable coefficient was calculated numerically with Newton's method. Note that in many applications with state-dependent delay an explicit expression can be given for the inverse transformation $t = \boldsymbol{\Phi}^{-1}(\varphi)$.

In our previous work, we have shown that the results for the stability chart of both methods coincide very well [26]. In this paper, we compare the numerical accuracy and the convergence of the two numerical methods. In the semidiscretization method, the state of a time delay system $\mathbf{x}_t$ is approximated by the vector

$$\mathbf{z}(t) = \operatorname{cols}\left(\mathbf{x}(t), \mathbf{x}(t-h), \ldots, \mathbf{x}(t-ih)\right), \tag{14}$$

where h is the step size and i is the number of discretization steps. For the system with time-varying delay Eq. (11), the number of steps is chosen in such a way that $(i-1)h < \tau_{\max} \leq ih$. For the system with constant delay Eq. (13), the discretization is chosen such that the condition $(i-1)h < r \leq ih$ is fulfilled. This means, that for the system with variable delay a redundant state space is used. In other words, the state space is only completely used for $\tau(t) = \tau_{\max}$, whereas for other time steps with smaller delays $\tau(t)$ essential parts of the state are not used. In contrast, the state space for the system with constant delay is minimal (cf. [39]). With the variation of constant formula and a specific semidiscretization technique a finite dimensional monodromy matrix $\mathbf{M}$ can be constructed, which specifies the evolution of the discretized state $\mathbf{z}(t)$ of the DDE over one principle period T as

$$\mathbf{z}(T) = \mathbf{M}\mathbf{z}(0). \tag{15}$$

Details on the specific construction of the matrix $\mathbf{M}$ can be found in [12]. We remark that the step size of the discretization must be chosen in such a way that the principle period T is a multiple of the step size h with $kh = T$ and $k \in \mathbb{Z}$. The eigenvalues of the matrix $\mathbf{M}$ are the Floquet multipliers $e^{\mu T}$ of the system. For time delay systems, the matrix $\mathbf{M}$ approximates only a finite number of dominant Floquet multipliers, whereas the original continuous time delay system has, in general, infinitely many Floquet multipliers. The exponents μ are called characteristic or Floquet exponents and the maximum real part λ of the characteristic exponents can be used to determine the stability of the system. For a stability exponent $\lambda > 0$ the system is unstable, whereas the system is stable if the stability exponent $\lambda < 0$.

We have calculated the stability exponent λ with the semidiscretization method from Eq. (11) with time-varying delay and from Eq. (13) with periodic coefficients but constant delay. For both methods, the exponent λ is calculated as a function of the number of discretization steps i, thus $\lambda = \lambda(i)$. The computing time for the exponents $\lambda(i)$ is roughly the same for both methods because in both cases a $2(i+1)$-dimensional matrix is constructed nearly by the same technique. For the analysis of Eq. (11), the variable delay must be calculated with a numerical solver from Eq. (8), whereas for Eq. (13) the inverse function $\Phi^{-1}(\varphi)$ must be calculated numerically for the variable coefficient. In Fig. 2b, the error between the exponents $\lambda(i)$ and the accurate exponent $\lambda_0 = \lambda(500)$ is displayed. The parameters are $\zeta = 0.03$, $w = 0.24$ and a sinusoidal spindle speed variation with $A_m = 0.25, f_m = 1$ Hz and $\Omega_0 = 1200$ rpm is used. The error for the system with constant delay (black) is smaller than the error for the system with variable delay (red) and decreases uniformly, whereas fluctuations can be seen for the error of the exponent from the system with variable delay. The larger error for the method with variable delay can be explained by the fact that in this case the state space can not be completely used by the numerical method. Moreover, for the variable delay there are specific values for i, where the variable delay is approximated very accurately. In contrast, in some situations an increase of the number of steps deteriorate the approximation, which explains the fluctuations in the error for the system with variable delay. In general, for large i the error decreases quadratically with an increasing number of steps i for both methods, $|\lambda(i) - \lambda_0| \propto i^{-2}$. This is in agreement with theoretical estimations [12].

4 State-Dependent Delays in Structured Populations

In this section, we present partial differential equations with moving and constant boundaries as models for structured populations and show how they are related to DDEs with variable transport delays. We start with the PDE

$$\partial_t \tilde{\mathbf{u}}(t,a) + \partial_a \tilde{\mathbf{u}}(t,a) = -\mu \tilde{\mathbf{u}}(t,a) \tag{16}$$

with boundary and initial condition

$$\tilde{\mathbf{u}}(t,0) = \int_0^\infty \beta(a)\tilde{\mathbf{u}}(t,a)da, \quad \tilde{\mathbf{u}}(0,a) = \tilde{\mathbf{u}}_0(a). \tag{17}$$

This model is known as McKendrick equation, Sharpe–Lotka–McKendrick equation or von Foerster equation and is widely used for the description of populations $\tilde{\mathbf{u}}$ structured by the age a [5, 15, 23]. We consider a constant mortality rate μ, which leads to an exponential decrease of the population $\tilde{\mathbf{u}}$ for increasing age a. With the scaling $\tilde{\mathbf{u}}(t,a) = \mathrm{e}^{-\mu t}\,\mathbf{u}(t,a)$ the PDE Eq. (16) simplifies to $\partial_t \mathbf{u} + \partial_a \mathbf{u} = 0$. It is common to distinguish between the immature and the mature population separated by the boundary $a = \tau$. We assume that the birth rate of the immature and mature population is zero $\beta(a \le \tau) = 0$ and constant $\beta(a > \tau) = \beta_0$, respectively. By defining the scaled total number of adults

$$\mathbf{x}(t) = \int_\tau^\infty \mathbf{u}(t,a)da, \tag{18}$$

the population model Eq. (16) with boundary and initial condition Eq. (17) can be written as

$$\partial_t \mathbf{u}(t,a) + \partial_a \mathbf{u}(t,a) = 0, \quad \mathbf{u}(t,0) = \beta_0 \mathbf{x}(t), \quad \mathbf{u}(0,a) = \mathbf{u}_0(a). \tag{19}$$

The system Eq. (19) is an advection equation that describes, for example, the transport over the conveyor belt similar to Fig. 1a but with a constant velocity. The population $\mathbf{u}(t,a)$ can vary with time t and age a but remains constant along the characteristics of the PDE, that is $\mathbf{u}(t,a) = \mathbf{u}(t-a,0)$. In many applications there is a state-dependent boundary $\tau = \tau(\mathbf{x}_t)$ between the immature and the mature population defined by a threshold condition that is completely equivalent to the condition Eq. (4) [10, 16, 19, 34]. In the biological context, the threshold r, i.e., the associated constant delay, is a constant amount of food or a constant size that must be reached for maturity and $\dot{\boldsymbol{\Phi}}_{\mathbf{x}}(t)$ is the velocity of maturation that depends on the configuration $\mathbf{x}(t)$ of the system. This means that the model Eq. (19) is a PDE with moving boundary Eq. (18) with the state-dependent variable transport delay $\tau(\mathbf{x}_t)$.

In the following, we present a sequence of transformations, which relates the PDE Eq. (19) with moving boundary to a DDE with state-dependent delay, a DDE with constant delay and a PDE with constant boundaries. The transformations are summarized in Fig. 3. The time derivative of the boundary condition in Eq. (19) yields

$$\partial_t \mathbf{u}(t,0) = \beta_0 \dot{\mathbf{x}}(t) = \beta_0 \left(1 - \dot{\tau}(\mathbf{x}_t)\right) \mathbf{u}(t, \tau(\mathbf{x}_t)), \tag{20}$$

where the right-hand side is obtained from the differentiation of Eq. (18) with $\mathbf{u}(t,\infty) = \tilde{\mathbf{u}}(t,\infty) = 0$. Equation (20) is similar to the interconnected boundary con-

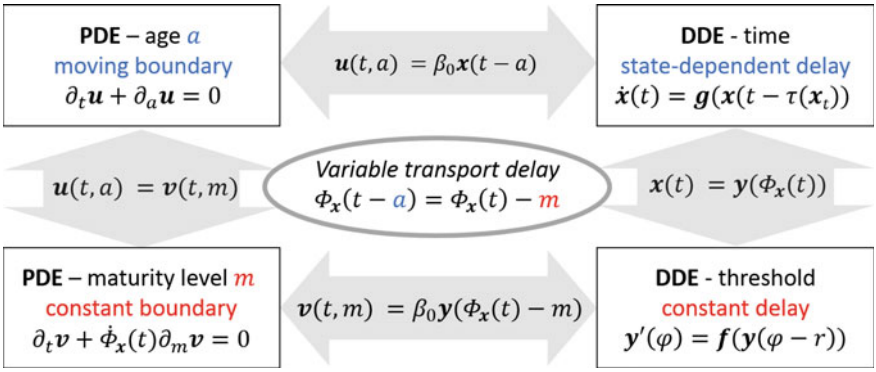

Fig. 3 Four equivalent representations of the same structured population model with a variable transport delay and the relationship between their configurations

ditions that can be found in typical PDE representations of DDEs [9]. If we use the property of constant solutions along the characteristics of Eq. (19), we get the DDE

$$\dot{\mathbf{x}}(t) = \beta_0 \frac{\dot{\boldsymbol{\Phi}}_{\mathbf{x}}(t)}{\dot{\boldsymbol{\Phi}}_{\mathbf{x}}(t-\tau(\mathbf{x}_t))} \mathbf{x}(t-\tau(\mathbf{x}_t)), \quad \mathbf{x}(-\theta) = \frac{1}{\beta_0}\mathbf{u}_0(\theta), \theta > 0, \tag{21}$$

where we have substituted Eq. (7) for the delay derivative. The velocity of maturation $\dot{\boldsymbol{\Phi}}_{\mathbf{x}}(t)$ is strictly positive because, for example, no adults will become juveniles again. Thus, the time scale transformation from Sect. 2 can be applied to Eq. (21), which leads to the DDE with constant delay

$$\mathbf{y}'(\varphi) = \beta_0 \left(\boldsymbol{\Phi}_{\mathbf{x}}^{-1}\right)'(\varphi - r)\mathbf{y}(\varphi - r), \quad \mathbf{y}(-\theta) = \frac{1}{\beta_0}\mathbf{u}_0\left(\boldsymbol{\Phi}_{\mathbf{x}}^{-1}(\theta)\right), \theta > 0. \tag{22}$$

Equation (22) describes the structured population in terms of the physiological time φ [34]. From Eq. (22) we can again construct a PDE by defining

$$\mathbf{v}(t,m) = \beta_0 \mathbf{y}(\boldsymbol{\Phi}_{\mathbf{x}}(t) - m) = \beta_0 \mathbf{x}\left(\boldsymbol{\Phi}_{\mathbf{x}}^{-1}(\boldsymbol{\Phi}_{\mathbf{x}}(t) - m)\right), \tag{23}$$

where m can be interpreted as the maturation level. The PDE that is associated to Eq. (23) can be written as

$$\partial_t \mathbf{v}(t,m) + \dot{\boldsymbol{\Phi}}_{\mathbf{x}}(t)\partial_m \mathbf{v}(t,m) = 0. \tag{24}$$

Equation (24) is an advection equation with variable velocity $\dot{\boldsymbol{\Phi}}_{\mathbf{x}}(t)$, which describes exactly the transport in Fig. 1a. The properties of the time delay system is given by the boundary condition and the initial condition

$$\partial_m \mathbf{v}(t,0) = \beta_0 \left(\boldsymbol{\Phi}_{\mathbf{x}}^{-1}\right)'(\boldsymbol{\Phi}_{\mathbf{x}}(t) - r)\mathbf{v}(t,r), \quad \mathbf{v}(0,m) = \mathbf{u}_0(-\boldsymbol{\Phi}_{\mathbf{x}}^{-1}(-m)), \tag{25}$$

where we have assumed that $\Phi_{\mathbf{x}}(0) = 0$. The description in terms of the maturation level m by Eq. (24) is, apart from an additional transformation $\tilde{\mathbf{v}}(t, m) = \mathbf{v}(t, m)\, \mathrm{e}^{-\mu t}$, equivalent to the representations in [19, 34]. The exact relationship between the configurations of the different representations of the population is presented in Fig. 3. The basis for the transformations is the relationship between age a and maturation level m of the population, which is presented in the center of Fig. 3 and is equivalent to the condition of a variable transport delay Eq. (4).

5 Conclusion

We have shown that the condition for the existence of a transformation from time-varying delays to constant delays is equivalent to the physical process of a transport with variable velocity over a constant distance. As a consequence, DDEs with these so-called variable transport delays are equivalent to DDEs with constant delays. In the same way, systems with state-dependent delays are equivalent to constant time delay systems if the delay originates from a transport with a state-dependent velocity over a constant distance. Indeed, we have found many examples in the literature, where the existence for a transformation to constant delay is fulfilled by the definition of the delay. One example, are the time delays in machining. For machine tool vibrations in a turning process with spindle speed variation, we have shown that the numerical analysis of the system with constant delay is advantageous in comparison to the analysis of the system with time-varying delay. Another example can be found in structured population models. In particular, for the McKendrick equation with a moving boundary originating from a threshold condition we have presented the equivalence between a PDE with a moving boundary, a DDE with a state-dependent delay, a DDE with a variable coefficient but constant delay and a PDE with a variable coefficient and constant boundaries.

References

1. Ahmed, A., Verriest, E.: Estimator design for a subsonic rocket car (soft landing) based on state-dependent delay measurement. IEEE Conf. Decis. Control 5698–5703 (2013)
2. Altintas, Y., Weck, M.: Chatter stability of metal cutting and grinding. CIRP Ann. **53**, 619–642 (2004)
3. Ambika, G., Amritkar, R.: Anticipatory synchronization with variable time delay and reset. Phys. Rev. E **79**, 056,206 (2009)
4. Bellman, R., Cooke, K.: On the computational solution of a class of functional differential equations. J. Math. Anal. Appl. **12**(3), 495–500 (1965)
5. Bocharov, G., Rihan, F.: Numerical modelling in biosciences using delay differential equations. J. Comput. Appl. Math. **125**, 183–199 (2000)
6. Bresch-Pietri, D., Chauvin, J., Petit, N.: Prediction-based stabilization of linear systems subject to input-dependent input delay of integral-type. IEEE Trans. Autom. Control **59**(9), 2385–2399 (2014)

7. Bresch-Pietri, D., Petit, N.: Implicit integral equations for modeling systems with a transport delay. In: Witrant, E., Fridman, E., Sename, O., Dugard,L. (eds.) Recent Results on Time-Delay Systems: Analysis and Control, pp. 3–21. Springer (2016)
8. Ghil, M., Zaliapin, I., Thompson, S.: A delay differential model of enso variability: parametric instability and the distribution of extremes. Nonlinear Proc. Geophys. **15**, 417–433 (2008)
9. Hale, J., Lunel, S.: Introduction to functional differential equations. Appl. Math. Sci. No. 99 (1993). Springer
10. Hartung, F., Krisztin, T., Walther, H.O., Wu, J.: Functional differential equations with state-dependent delays: theory and applications. In: Canada, A., Drabek, P., Fonda, A. (eds.) Handbook of Differential Equations: Ordinary Differential Equations, pp. 435–545. North-Holland (2006)
11. Insperger, T., Stépán, G.: Stability analysis of turning with periodic spindle speed modulation via semi-discretization. J. Vib. Control **10**(12), 1835–1855 (2004)
12. Insperger, T., Stépán, G.: Semi-Discretization for Time-Delay Systems: Stability and Engineering Applications. Springer (2011)
13. Insperger, T., Stépán, G., Turi, J.: State-dependent delay in regenerative turning processes. Nonlinear Dyn. **47**, 275–283 (2007)
14. Jüngling, T., Gjurchinovski, A., Urumov, V.: Experimental time-delayed feedback control with variable and distributed delays. Phys. Rev. E **86**, 046,213 (2012)
15. Keyfitz, B., Keyfitz, N.: The mckendrick partial differential equation and its uses in epidemiology and population study. Math. Comput. Model. **26**(6), 1–9 (1997)
16. Kuang, Y.: Delay Differential Equations: With Applications in Population Dynamics. Academic Press (1993)
17. Kyrychko, Y., Hogan, S.: On the use of delay equations in engineering applications. J. Vib. Control **16**, 943–960 (2010)
18. Lakshmanan, M., Senthilkumar, D.: Dynamics of Nonlinear Time-Delay Systems. Springer (2011)
19. Mahaffy, J.M., Bélair, J., Mackey, M.C.: Hematopoietic model with moving boundary condition and state dependent delay: applications in erythropoiesis. J. Theor. Biol. **190**(2), 135–146 (1998)
20. Margolis, S., O'Donnell, J.: Rigorous treatments of variable time delays. IEEE Trans. Electron. Comput. **12**(3), 307–309 (1963)
21. Martínez-Llinàs, J., Porte, X., Soriano, M.C., Colet, P., Fischer, I.: Dynamical properties induced by state-dependent delays in photonic systems. Nat. Commun. **6**, 7425 (2015)
22. Masoller, C., Torrent, M.C., García-Ojalvo, J.: Dynamics of globally delay-coupled neurons displaying subthreshold oscillations. Philos. Trans. R. Soc. A **367**(1901), 3255–3266 (2009)
23. McKendrick, A.G.: Applications of mathematics to medical problems. Proc. Edinb. Math. Soc. **44**, 98–130 (1925)
24. Orosz, G., Moehlis, J., Murray, R.M.: Controlling biological networks by time-delayed signals. Philos. Trans. R. Soc. A **368**(1911), 439–454 (2009)
25. Otto, A., Radons, G.: Application of spindle speed variation for chatter suppression in turning. CIRP J. Manuf. Sci. Technol. **6**(2), 102–109 (2013)
26. Otto, A., Radons, G.: The influence of tangential and torsional vibrations on the stability lobes in metal cutting. Nonlinear Dyn. **82**, 1989–2000 (2015)
27. Pyragas, V., Pyragas, K.: Adaptive modification of the delayed feedback control algorithm with a continuously varying time delay. Phys. Lett. A **375**(44), 3866–3871 (2011)
28. Richard, J.P.: Time-delay systems: an overview of some recent advances and open problems. Automatica **39**(10), 1667–1694 (2003)
29. Rosin, D.P., Rontani, D., Gauthier, D.J.: Synchronization of coupled boolean phase oscillators. Phys. Rev. E **89**, 042,907 (2014)
30. Schley, D., Gourley, S.: Linear stability criteria for population models with periodically perturbed delays. J. Math. Biol. **40**, 500–524 (2000)
31. Schuster, H.G., Schöll, E.: Handbook of Chaos Control. Wiley-VCH (2007)

32. Seddon, J., Johnson, R.: The simulation of variable delay. IEEE Trans. Comput. **C-17**, 89 –94 (1968)
33. Sieber, J.: Finding periodic orbits in state-dependent delay differential equations as roots of algebraic equations. Discrete Contin. Dyn. Syst. **32**(8), 2607–2651 (2012)
34. Smith, H.: Reduction of structured population models to threshold-type delay equations and functional differential equations: a case study. Math. Biosci. **113**(1), 1–23 (1993)
35. Smith, H.: An Introduction to Delay Differential Equations With Applications to the Life Sciences. Springer (2010)
36. Soriano, M.C., García-Ojalvo, J., Mirasso, C.R., Fischer, I.: Complex photonics: dynamics and applications of delay-coupled semiconductors lasers. Rev. Mod. Phys. **85**, 421–470 (2013)
37. Sugitani, Y., Konishi, K., Hara, N.: Experimental verification of amplitude death induced by a periodic time-varying delay-connection. Nonlinear Dyn. **70**(3), 2227–2235 (2012)
38. Tsao, T.C., McCarthy, M.W., Kapoor, S.G.: A new approach to stability analysis of variable speed machining systems. Int. J. Mach. Tools Manuf. **33**(6), 791–808 (1993)
39. Verriest, E.I.: Inconsistencies in systems with time-varying delays and their resolution. IMA J. Math. Control Inf. **28**(2), 147–162 (2011)
40. Voronov, S., Gouskov, A., Kvashnin, A., Butcher, E., Sinha, S.: Influence of torsional motion on the axial vibrations of a drilling tool. J. Comput. Nonlinear Dyn. **2**(1), 58–64 (2007)
41. Walther, H.O.: On a model for soft landing with state-dependent delay. J. Dyn. Differ. Equ. **19**(3), 593–622 (2006)
42. Zatarain, M., Bediaga, I., Muñoa, J., Lizarralde, R.: Stability of milling processes with continuous spindle speed variation: analysis in the frequency and time domains, and experimental correlation. CIRP Ann. **57**(1), 379–384 (2008)
43. Zenger, K., Niemi, A.: Modelling and control of a class of time-varying continuous flow processes. J Proc. Control **19**(9), 1511–1518 (2009)
44. Zhang, F., Yeddanapudi, M.: Modeling and simulation of time-varying delays. In: Proceedings of TMS/DEVS, p. 34. San Diego, CA, USA (2012)

Coupling Design for Consensus in Switching Topologies with Time-Varying Delays

Heitor J. Savino, Fernando O. Souza and Luciano C.A. Pimenta

Abstract This chapter presents a method to design the coupling strengths between the agents in a network of multi-agent systems in order to enable the group to achieve consensus on a given variable of interest while subject to time-varying delays and switching topologies. The multiple time-varying delays are considered to be nonuniform and nondifferentiable acting in the agents' control laws, and the topology switches are governed according to a continuous time Markov chain. The main result, formulated as conditions in the form of linear matrix inequalities, is obtained by analyzing the stability of an associated Markov jump linear system. The results are illustrated by a numerical example.

1 Introduction

In recent years, studies involving multi-agent systems have attracted the interest of researchers from several fields. Certainly, this comprehensiveness is due to advances in communication systems and its diversity of applications, such as multivehicle coordination [14], formation flight [5], swarm coordination [11], spacecraft formation [1], etc. An overview of multi-agent systems can be found in [2].

H.J. Savino (✉)
Graduate Program in Electrical Engineering, Universidade Federal de Minas Gerais, Belo Horizonte, MG, Brazil
e-mail: heitorjs@ufmg.br; savino@mit.edu

H.J. Savino
Department of Aeronautics and Astronautics, Massachusetts Institute of Technology, Cambridge, MA, USA

F.O. Souza · L.C.A. Pimenta
Department of Electronic Engineering, Universidade Federal de Minas Gerais, Belo Horizonte, MG, Brazil
e-mail: fosouza@cpdee.ufmg.br

L.C.A. Pimenta
e-mail: lucpim@cpdee.ufmg.br

T. Insperger et al. (eds.), *Time Delay Systems*,
Advances in Delays and Dynamics 7, DOI 10.1007/978-3-319-53426-8_13

One of the major concerns related to multi-agent systems is the one of determining a control law that allows a group of agents to achieve consensus on the value of a given magnitude, e.g., velocity and position. This is known as consensus problem.

The dynamics of interaction between neighbors for the coordination of a particle system moving in a plane was introduced in [21], showing that a distributed control law is able to govern all agents into a common direction. Concepts of algebraic graph theory were early introduced in [3, 7] to represent the relations between neighbors. In [10], the control law that dictates the interaction between agents and many particularities of the consensus problem were treated, such as directed and undirected networks, fixed or variable topologies, the time-delay effects, etc.

In practical applications, there always exist time-delays in the agents interactions. This is due to information processing, physical limitations in communication channels, time-response of actuators, etc. Based on this situation, many works have dealt with the consensus problem subject to time-delays. Some results in robust control-based approach considered constant delays for all the agents' interactions [8], others considered the analysis of the upper bound of multiple delays in high-order integrator dynamics [22], and yet there were other studies considering nonuniform nondifferentiable time-varying delays with upper and lower bounds for single-order integrator [16] and also high-order integrator [17]. An analytical result [18] shows the importance of studying consensus by time-intervals, showing how time-delays can improve or degrade the behavior of the system to achieve consensus.

Some works in the literature consider multi-agent systems subject to switching topology. In real environments, these switches are due to temporary communication losses or agents' failure, and/or changes in the arrangement of agents. A description of this problem can be seen in [10], whereas the switching topology is not stochastic. Currently, the switching topology has also been treated as a Markov process. In [23], analysis conditions for mean square consensus for second-order multi-agent system, with Markov switching topology, are formulated as linear matrix inequalities (LMIs). In [23], the authors also considered cases where the transition probability rates are not precisely known and the system is subject to constant time-delays. Switching topology as a Markov process was considered for the analysis of consensus with time-varying delays in [15]. In [19], these results were extended to the analysis of agents with high-order dynamics and uncertain probability rates.

The problem of designing the weights of the coupling strengths associated to the network communication links has also been considered. These weights are related to the information exchange topology and control gains. An analytical study and design of the coupling strengths considering time-delays is shown in [12] for fully connected networks, with a concept based on the placement of the rightmost eigenvalue of the Laplacian. An adaptive approach, aware of the instantaneous value of time-delay, is used in [13] to deal with time-varying delays. The design of the coupling strengths enable the multi-agent system to achieve consensus faster or in regions of time-delay where the system was previously unable to achieve consensus.

In this work, as an extension of [15], we present new LMI conditions to design the weights of the links between the agents in switching directed networks of multi-agent systems subject to time-varying delays in their control inputs, which are assumed to

belong to the intervals $0 \leq \tau_{ij}^{min} \leq \tau_{ij}(t) \leq \tau_{ij}^{max}$. The delays are considered to be non-differentiable and nonuniform, i.e., varying differently on each communication link. The proposed results are provided by using a transformation of the multi-agent system, so that the development here is based on the stability analysis of the transformed system. A numerical example is given to illustrate the effectiveness of the proposed method.

Throughout the paper, the following notation is used: I_n is the identity matrix of order n; $\mathbf{0}_n$ and $\mathbf{1}_n$ are column-vectors of zeros and ones, respectively, with dimension n; 0_n is a null matrix of order n; $M > 0$ (< 0) means that M is a positive (negative) definite matrix; M^T means the transpose matrix of M; $*$ denotes the symmetric block in a matrix; $M = [m_{ij}]$ for all $i,j \in [1, 2, \ldots, n]$ denotes a matrix

$$M = \begin{bmatrix} m_{1,1} & m_{1,2} & \ldots & m_{1,n} \\ m_{2,1} & m_{2,2} & \ldots & m_{2,n} \\ \vdots & \vdots & \ddots & \vdots \\ m_{n,1} & m_{n,2} & \ldots & m_{n,n} \end{bmatrix};$$

and $M = \text{diag}\{m_{11}, m_{22}, \ldots, m_{nn}\}$ denotes a diagonal matrix M composed of the elements m_{11}, m_{22}, …, m_{nn} in its main diagonal.

2 Background

2.1 Algebraic Graph Theory

A weighted directed graph is a representation of a set of nodes (or vertices), and a set of directed edges with assigned weights (or coupling strengths), indicating the information flow. Mathematically, a weighted directed graph is described by $\mathscr{G} = (\mathscr{V}, \mathscr{E}, \mathscr{W})$, with $\mathscr{V}$ representing the set of n nodes labeled as $v_1, v_2, \ldots, v_n$; $\mathscr{E}$ the set of edges, denoted by $e_{ij} = (v_i, v_j)$, where the first element v_i is said to be the parent node (tail) and the other v_j to be the child node (head); and $\mathscr{W}$ the set of weights associated to the edges, denoted by w_{ij}, that assign real nonnegative values to each e_{ij}.

Throughout the text, we consider switching topologies. Thus, let θ_t be the representation of the topology of the multi-agent system at the instant of time t, and $\ell = 1, 2, \ldots, s$ the image of θ_t, where s is the total number of topologies. Each topology is associated with a weighted directed graph $\mathscr{G}(\ell) = (\mathscr{V}, \mathscr{E}(\ell), \mathscr{W})$, with same set of vertices $\mathscr{V}$ and weights $\mathscr{W}$, but different sets of edges $\mathscr{E}(\ell)$.

Remark 1 Same edges e_{ij} in different graphs $\mathscr{G}(\ell)$ are associated to the same weights w_{ij}. An element w_{ij} may exist in $\mathscr{W}$ even if e_{ij} does not exist in $\mathscr{E}(\ell)$.

Consider the set $\bar{\mathscr{E}} = \bigcup_{\ell=1}^{s} \mathscr{E}(\ell)$, the union of all the edges in each graph $\mathscr{G}(\ell)$, for all $\ell = 1, 2, \ldots, s$. Thus, we define the Joint Graph $\bar{\mathscr{G}}$:

Definition 1 The Joint Graph $\bar{\mathcal{G}} = (\mathcal{V}, \bar{\mathcal{E}}, \mathcal{W})$ is the graph composed of the union of the edges in the subgraphs $\mathcal{G}(\ell)$, for all $\ell = 1, 2, \ldots, s$. The vertices $\mathcal{V}$ and weights $\mathcal{W}$ are the same for all $\mathcal{G}(\ell)$ and $\bar{\mathcal{G}}$.

In order to simplify the subscript notation, we assume a new ordered index k related to each edge, instead of the pair (i, j), such that $e_k(t) = e_{ji}(t)$, letting r represent total the number of directed edges in the Joint Graph $\bar{\mathcal{G}}$, such that $k = 1, \ldots, r$. The assignment of index k is outlined in Algorithm 1 with some other useful additional variables.

Algorithm 1: New indices k

```
Initialize: k ← 0;
forall i = 1, 2, ..., n do
    forall j = 1, 2, ..., n do
        if ∃e_ji ∈ ℰ̄, for ℰ̄ ∈ 𝒢̄ then
            k ← k + 1;
            w_k ← w_ji;  e_k ← e_ji;
            forall ℓ = 1, 2, ..., s do
                h_k(ℓ) ← zero column-vector of size n;
                h̄_k(ℓ) ← zero column-vector of size n;
                if ∃e_ji ∈ ℰ(ℓ) for ℰ ∈ 𝒢 then
                    h_k(ℓ) i-th entry ← 1;  h_k(ℓ) j-th entry ← −1;
                    h̄_k(ℓ) i-th entry ← 1;
```

From Algorithm 1, we will define the Laplacian matrices $L(\ell)$ for each $\mathcal{G}(\ell)$ in an alternative form, inspired by [6] and extended to directed networks, in which the weights of the edges can be conveniently displayed in the main diagonal of a matrix. This form plays an important role in the design method. Consider the index of each directed edge $e_{ij} \in \bar{\mathcal{E}}$ rewritten according to Algorithm 1, such that the edges are ordered as $e_k = e_{ji}$, with associated weights w_k, and vectors $h_k(\ell)$ and $\bar{h}_k(\ell)$ for each $\mathcal{G}(\ell)$. Also $k = 1, \ldots, r$ where r is the number of edges in the Joint Graph $\bar{\mathcal{G}}$. Thus, we define the Incidence matrix of each graph $\mathcal{G}(\ell)$ as $H(\ell) = [h_1(\ell) \ \ldots \ h_r(\ell)]$, and also the associated Heading matrix $\bar{H}(\ell) = [\bar{h}_1(\ell) \ \ldots \ \bar{h}_r(\ell)]$, both matrices of dimension $n \times r$. Additionally, write the coupling strengths, related to the weights $w_k = w_{ji}$ according to Algorithm 1, in a weight diagonal matrix $W \in \mathfrak{R}^{r \times r}$ in the ascending order of k. Then, the Laplacian matrix of each graph $\mathcal{G}(\ell)$ can be written according to the following Lemma.

Lemma 1 *Let $H(\ell) = [h_1(\ell) \ \ldots \ h_r(\ell)]$ be the $n \times r$ Incidence matrix, $\bar{H}(\ell) = [\bar{h}_1(\ell) \ \ldots \ \bar{h}_r(\ell)]$ be the $n \times r$ associated Heading matrix, and W be the $r \times r$ Weight diagonal matrix associated with a weighted directed graph $\mathcal{G}(\ell)$. Thus, the Laplacian matrix $L(\ell)$ can be written as*

$$L(\ell) = \bar{H}(\ell)\, WH^T(\ell). \tag{1}$$

Remark 2 The weights $w_k = w_{ji}$ are given in the main diagonal of W, i.e., $W = \text{diag}\{w_1, w_2, \ldots, w_r\}$.

3 Problem Formulation

3.1 Consensus Problem

A multi-agent system can be represented by a graph where the nodes represent agents, and the edges represent communication channels. Thus, consider a multi-agent system composed of n agents arranged in a directed network and the dynamics of each agent given by

$$\dot{x}_i(t) = u_i(\theta_t, t - \tau_{ij}(t)), \quad i = 1, 2, ..., n, \tag{2}$$

where $x_i \in \mathfrak{R}$ and $u_i \in \mathfrak{R}$ represent the state and the control input of the i-th agent, respectively, θ_t represents the topology of the multi-agent system at the instant of time t and is not subject to time-delays, and $\tau_{ij}(t)$ the time-varying delay of agent i related to j. The considered consensus protocol is given by

$$u_i(\theta_t, t) = -\sum_{j=1}^{n} a_{ij}(\theta_t)\big(x_i(t) - x_j(t)\big), \tag{3}$$

with

$$a_{ij}(\theta_t) = \begin{cases} w_{ji}, & \text{if } \exists e_{ji} \in \mathscr{E}(\theta_t) \\ 0, & \text{otherwise.} \end{cases} \tag{4}$$

We represent the delays by $\tau_{ij}(t) = \tau + \mu_{ij}(t)$, where τ is a constant value and $\mu_{ij}(t)$ are time-varying perturbations that satisfy $|\mu_{ij}(t)| \leq \bar{\mu} \leq \tau \ \forall \ (i,j)$, such that $\tau_{ij}(t) \in [\tau - \bar{\mu}, \tau + \bar{\mu}]$.

Moreover, we assume that θ_t is given by a continuous time Markov chain with discrete states given by $\mathscr{S} = \{1, 2, ..., s\}$ (s being the number of different topologies of the system), and a probability transition matrix $\Psi = [\psi_{pq}]$ defined by

$$\psi_{pq} = \mathbb{P}\{\theta_{t+\Delta} = q \mid \theta_t = p\} = \begin{cases} \pi_{pq}\Delta + o(\Delta) & p \neq q, \\ 1 + \pi_{pp}\Delta + o(\Delta) & p = q, \end{cases} \tag{5}$$

in which ψ_{pq} represents the probability of switching from topology p to q in an interval $\Delta > 0$ at given time t, for $p, q \in \mathscr{S}$, and where $\lim_{\Delta \to 0} \frac{o(\Delta)}{\Delta} = 0$. Also, π_{pq} represent the estimated rates in the transition rate matrix $\Pi = [\pi_{pq}]$ where $\pi_{pq} \geq 0$

for $q \neq p$, $\pi_{pp} = -\sum_{q=1,q\neq p}^{s} \pi_{pq}$, and consequently $\sum_{q=1}^{s} \pi_{pq} = 0$. Finally, denote $\nu = (\nu_1, \ldots, \nu_s)$ the initial distribution of the Markov chain.

We represent the multi-agent system using the Algebraic Graph Theory in Sect. 2.1. Thus, each state of the Markov chain is related to a network topology described by a graph $\mathcal{G}(\mathcal{E})$. Additionally, $\tau_{ij}(t)$, which is related to edge e_{ji}, has the index changed to $\tau_k(t)$ following Algorithm 1 to indicate the delay related to edge $e_k = e_{ji}$, with $k = 1, 2, \ldots, r$, where r is the number of edges in the Joint Graph $\bar{\mathcal{G}}$, i.e., the total number of different communication links in all the topologies.

Therefore, considering the agents' dynamics given by (2) with the consensus protocol in (3) and Algorithm 1, the multi-agent system is represented by

$$\dot{X}(t) = -\sum_{k=1}^{r} L_k(\theta_t) X(t - \tau_k(t)), \tag{6}$$

where $X(\cdot) = [x_1(\cdot)\ x_2(\cdot)\ \ldots\ x_n(\cdot)]^T$ and $L_k(\theta_t)$ is the Laplacian matrix of the subgraph connections associated only with the delay $\tau_k(t)$ on the topology θ_t. Note that $\sum_{k=1}^{r} L_k(\theta_t) = L(\theta_t)$, with $L(\theta_t)$ the Laplacian matrix of all edge connections on the topology θ_t. Also, $L_k(\theta_t)$ is simply a zero matrix whenever $e_k \notin \mathcal{E}(\theta_t)$.

Before progressing further, in order to formalize the problem of consensus analysis with stochastic switching topology, we assume the following definition.

Definition 2 [9] Under stochastic switching topology, the multi-agent system (6) reaches mean-square consensus if, for all $i \neq j$, $\lim_{t\to\infty} \mathbb{E}||x_i(t) - x_j(t)|| \to 0$ hold in the mean square sense for any initial distribution $\nu = (\nu_1, \ldots, \nu_s)$ of θ_t and initial state conditions.

3.2 Auxiliary Results

In this section, we recall some results from the literature, especially from [15, 19], presenting how to construct a transformed multi-agent system, such that its stability dictates if the multi-agent system in (6) achieves consensus. Thus consider the following lemma.

Lemma 2 *Under stochastic switching topology, the multi-agent system* (6) *reaches mean-square consensus if its associated transformed system given by*

$$\dot{z}(t) = -\sum_{k=1}^{r} \bar{L}_k(\theta_t) z(t - \tau_k(t)), \tag{7}$$

where $\bar{L}_k(\theta_t) \in \mathbb{R}^{(n-1)\times(n-1)}$ *and*

$$\bar{L}_k(\theta_t) = U L_k(\theta_t) \bar{U},\ \textit{with}\ U = [\boldsymbol{I}_{n-1}\ \ -I_{n-1}]\ \textit{and}\ \bar{U}^T = [\boldsymbol{0}_{n-1}\ \ -I_{n-1}]^T, \tag{8}$$

is stochastically stable in the mean-square sense, i.e., $\lim_{t\to\infty} \mathbb{E}\left[z^T(t)z(t)\right] \to 0$ *holds in the mean-square sense for any initial distribution* $\nu = (\nu_1, \ldots, \nu_s)$ *of* θ_t *and initial state conditions.*

The previous lemma follows directly from [15, 19], combining [15] [Proposition 2] and [19] [Definition 1]. The transformed system presented in the previous lemma is obtained based on the disagreement of the state variables of the multi-agent system, see also [20], by defining the new variable:

$$z_i(t) = x_1(t) - x_{i+1}(t),$$

such that for the consensus to be achieved, it is necessary that $\lim_{t\to\infty} z_i(t) = 0$ with $i = 1, 2, \ldots, n-1$. Therefore, based on the stability of the transformed system (7) we can assess consensus of (6).

Finally, before presenting the main result of this chapter, consider the definition.

Definition 3 [4] Consider a stochastic process defined by $\{\theta_t,\ t \in [0, +\infty)\}$. Then, the infinitesimal generator $\mathscr{L}$ applied in a function $f(\theta_t)$ is given by

$$\mathscr{L}f(\theta_t) = \lim_{\Delta\to 0} \mathbb{E}\left[\frac{f(\theta_{t+\Delta}) - f(\theta_t)}{\Delta}\right]. \tag{9}$$

Hereinafter, for a more compact notation of the stochastic variables, θ_t is replaced by the subscript index ℓ, if no confusion occurs; e.g., $Y(\theta_t)$ is replaced by Y_ℓ. Note that the infinitesimal generator $\mathscr{L}$ of a stochastic function is the natural stochastic analog of the deterministic derivative.

4 Consensus Design of Coupling Strengths

In the following, we state and prove the main result in this chapter in the form of a theorem. The theorem presents conditions based on linear matrix inequalities that are computationally solved. The feasibility of the LMI conditions is able to design the proper coupling strengths of the communication links to enable consensus.

Theorem 1 *Consider the multi-agent system in* (6) *with* $\tau > 0$, $\tau \geq \bar{\mu} \geq 0$, *and* $\Pi = [\pi_{pq}]$, *whose* π_{pq} *are the transition rates from topologies* p *to* q, $\forall p, q \in \mathscr{S}$, $\mathscr{S} = \{1, 2, ..., s\}$ *where* s *is the number of different topologies, and multiple time-delays* $\tau_k \in [\tau - \bar{\mu}, \tau + \bar{\mu}]$, *for* $k = 1, 2, \ldots, r$ *according to Algorithm 1. Then, the multi-agent system* (6) *achieves consensus in the mean-square sense with the designed coupling strengths* w_k *given as in Remark 2, if there exist:* $(n-1) \times (n-1)$ *matrices* $P_\ell = P_\ell^T$, Q_ℓ, $R_1 = R_1^T$, R_2, $R_3 = R_3^T$, $S_\ell = S_\ell^T$, *and* $Z = Z^T$; *a* $r \times r$ *diagonal matrix* W_d; *and a scalar* f; *such that the following LMIs hold* $\forall \ell = 1, 2, ..., s$:

$$\begin{bmatrix} P_\ell & Q_\ell \\ * & \frac{1}{\tau}S_\ell \end{bmatrix} > 0, \qquad \bar{R} = \begin{bmatrix} R_1 & R_2^T \\ R_2 & R_3 \end{bmatrix} > 0, \tag{10}$$

and

$$\begin{bmatrix} \boldsymbol{\Phi}_\ell & \Gamma_\ell \\ * & -\bar{\mu}Z \end{bmatrix} < 0, \tag{11}$$

with

$$\boldsymbol{\Phi}_\ell = \begin{bmatrix} \phi_\ell^{1,1} & \phi_\ell^{1,2} & -Q_\ell + \frac{1}{\tau}R_3 - U\bar{H}_\ell W_d H_\ell^T \bar{U} & -\frac{1}{\tau}R_2 + \sum_{m=1}^{s} \pi_{\ell m} Q_m \\ * & \phi^{2,2} & -U\bar{H}_\ell W_d H_\ell^T \bar{U} & Q_\ell \\ * & * & -\frac{1}{\tau}R_3 - S_\ell & \frac{1}{\tau}R_2 \\ * & * & * & -\frac{1}{\tau}R_1 + \frac{1}{\tau}\sum_{m=1}^{s} \pi_{\ell m} S_m \end{bmatrix}, \tag{12}$$

where $\phi_\ell^{1,1} = Q_\ell + Q_\ell^T + \tau R_1 - \frac{1}{\tau}R_3 + S_\ell + \sum_{m=1}^{s} \pi_{\ell m} P_m$, $\phi_\ell^{1,2} = P_\ell + \tau R_2^T - fI_{n-1}$, $\phi^{2,2} = \tau R_3 + 2\bar{\mu}Z - 2fI_{n-1}$, *and* $\Gamma_\ell^T = (\bar{\mu}U\bar{H}_\ell W_d H_\ell^T \bar{U})^T \begin{bmatrix} I_{n-1} & I_{n-1} & 0_{n-1} & 0_{n-1} \end{bmatrix}$.

Thus, the designed weights $w_k \in \mathscr{W}$ *of the coupling strengths, related to the edges* $e_k \in \bar{\mathscr{E}}$, *are given in the diagonal of* $W = \frac{1}{f}W_d$.

Proof Due to Lemma 2, stochastic stability in the mean-square sense of system (7) implies mean-square consensus for the system (6). Thus, the proof of this theorem relies on the fact that if the conditions presented here are satisfied, the system (7) will be stochastically stable in the mean-square sense.

First, we show that if the proposed LMIs are satisfied, then $V(z(t), \ell) > 0$ and $\mathscr{L}V(z(t), \ell) < 0$ hold, where $\mathscr{L}$ is the infinitesimal generator operator given in Definition 3, and $V(z(t), \ell)$ is the Lyapunov–Krasovskii stochastic functional [15]:

$$V(z_t, \ell) = V_1(z(t), \ell) + V_2(z_t, \ell) + V_3(z_t) + V_4(z_t, \ell) + V_5(z_t), \tag{13}$$

where z_t corresponds to $z(\sigma)$ for $\sigma \in [t - \tau - \bar{\mu},\ t]$,

$$V_1(z(t), \ell) = z^T(t) P_\ell z(t), \tag{14}$$

$$V_2(z_t, \ell) = 2z^T(t) Q_\ell \int_{t-\tau}^{t} z(\xi) d\xi, \tag{15}$$

$$V_3(z_t) = \int_{-\tau}^{0} \int_{t+\zeta}^{t} \bar{z}^T(\xi) \bar{R} \bar{z}(\xi) d\xi d\zeta, \tag{16}$$

$$V_4(z_t, \ell) = \int_{-\tau}^{0} z^T(t+\xi) S_\ell z(t+\xi) d\xi, \tag{17}$$

$$V_5(z_t) = \int_{-\bar{\mu}}^{\bar{\mu}} \int_{t-\tau+\zeta}^{t} \dot{z}^T(\xi) Z \dot{z}(\xi) d\xi d\zeta, \tag{18}$$

given $\bar{z}(\xi) = \begin{bmatrix} z(\xi) \\ \dot{z}(\xi) \end{bmatrix}$, $P_\ell = P_\ell^T$, Q_ℓ, $\bar{R} = \bar{R}^T = \begin{bmatrix} R_1 & R_2^T \\ R_2 & R_3 \end{bmatrix}$, $S_\ell = S_\ell^T$, and $Z = Z^T$.

Next, we present the condition for $V(z_t, \ell) > 0$ to be satisfied. Applying the Jensen Inequality in (13), we have

$$V(z_t,\ell) \geq \eta^T \begin{bmatrix} P_\ell & Q_\ell \\ * & \frac{1}{\tau} S_\ell \end{bmatrix} \eta + \int_{-\tau}^{0} \int_{t+\zeta}^{t} \bar{z}^T(\xi) \bar{R} \bar{z}(\xi) d\xi d\zeta + \int_{-\bar{\mu}}^{\bar{\mu}} \int_{t-\tau+\zeta}^{t} \dot{z}^T(\xi) Z \dot{z}(\xi) d\xi d\zeta,$$

with $\eta^T = \begin{bmatrix} z^T(t) & \int_{-\tau}^{0} z^T(t+\xi) d\xi \end{bmatrix}$.

Note that, if LMIs in (10) hold, then the first and the second terms of the right side of the inequality (19) are positive. Also, if the LMI (11) holds, then the term $-Z$ in the main diagonal is definite negative, which implies that the third term on the right side of inequality (19) is positive. Thus, a sufficient condition to check if $V(z_t, \ell) > 0$, is to verify if LMIs (10) and (11) are satisfied.

Now, we prove the LMI condition to guarantee that $\mathscr{L}V(z_t, \ell) < 0$. Initially, consider the following null term:

$$0 = 2f[z^T(t) + \dot{z}^T(t)] \left[-\dot{z} - \sum_{k=1}^{r} \bar{L}_{k\ell} z(t - \tau_k(t)) \right], \tag{19}$$

$$= 2f[z^T(t) + \dot{z}^T(t)] \left[-\dot{z} - \sum_{k=1}^{r} \bar{L}_{k\ell} \left(z(t-\tau) - \int_{-\tau_k(t)}^{-\tau} \dot{z}(t+\xi) d\xi \right) \right], \tag{20}$$

$$= 2f[z^T(t) + \dot{z}^T(t)] \left[-\dot{z}(t) - \bar{L}_\ell z(t-\tau) \right] + v(t), \tag{21}$$

where f is a scalar variable, $\bar{L}_\ell = \sum_{k=1}^{r} \bar{L}_{k\ell}$, and

$$v(t) = \sum_{k=1}^{r} \int_{-\tau_k(t)}^{-\tau} 2\Lambda \bar{L}_{k\ell} \dot{z}(t+\xi) d\xi, \quad \text{with} \quad \Lambda = [z^T(t) f + \dot{z}^T(t) f]. \tag{22}$$

Then, applying the inequality $2a^T b \leq a^T X a + b^T X^{-1} b$ in (22), where a^T and b are vectors chosen as $\Lambda \bar{L}_{k\ell}$ and $\dot{z}(t+\xi)$, respectively, and X is a positive definite matrix chosen $X^{-1} = \dfrac{Z}{r}$, we have

$$v(t) \leq \sum_{k=1}^{r} \int_{-\tau_k(t)}^{-\tau} (\Lambda \bar{L}_{k\ell}) r Z^{-1} (\Lambda \bar{L}_{k\ell})^T d\xi + \sum_{k=1}^{r} \int_{-\tau_k(t)}^{-\tau} \dot{z}^T(t+\xi) \frac{Z}{r} \dot{z}(t+\xi) d\xi \quad . \tag{23}$$

We take upper limits for the integrals in (23) to obtain

$$v(t) \leq \sum_{k=1}^{r} (\Lambda \bar{L}_{k\ell}) \bar{\mu} r Z^{-1} (\Lambda \bar{L}_{k\ell})^T + \int_{t-\tau-\bar{\mu}}^{t-\tau+\bar{\mu}} \dot{z}^T(\xi) Z \dot{z}(\xi) d\xi. \tag{24}$$

From Eq. (8) and Lemma 1 we have that

$$f\bar{L}_\ell = UfL_\ell\bar{U} = U\bar{H}_\ell W_d H_\ell^T \bar{U} \tag{25}$$

making $fW = W_d$, where W_d is a diagonal matrix defined similarly to W in Remark 2. Thus, the null term (21) with the upper bound (24) of $v(t)$, can be rewritten as

$$\begin{aligned} 0 \leq 2[z^T(t) + \dot{z}^T(t)] \left[-f\dot{z}(t) - U\bar{H}_\ell W_d H_\ell^T \bar{U} z(t-\tau)\right] \\ + \sum_{k=1}^{r} (\Lambda\bar{L}_{k\ell})\bar{\mu} r Z^{-1} (\Lambda\bar{L}_{k\ell})^T + \int_{t-\tau-\bar{\mu}}^{t-\tau+\bar{\mu}} \dot{z}^T(\xi) Z \dot{z}(\xi) d\xi, \end{aligned} \tag{26}$$

Moreover, invoking the operator of the infinitesimal generator in (13), we have

$$\mathscr{L}V(z_t, \ell) = \mathscr{L}V_1(z(t), \ell) + \mathscr{L}V_2(z_t, \ell) + \mathscr{L}V_3(z(t)) + \mathscr{L}V_4(z_t, \ell) + \mathscr{L}V_5(z(t)), \tag{27}$$

where

$$\mathscr{L}V_1 = \dot{z}^T(t) P_\ell z(t) + z^T(t) P_\ell \dot{z}(t) + z^T(t) \left(\sum_{m=1}^{s} \pi_{\ell m} P_m \right) z(t),$$

$$\mathscr{L}V_2 = 2\dot{z}^T(t) Q_\ell \int_{t-\tau}^{t} z(\xi) d\xi + 2z^T(t) \left[Q_\ell \int_{t-\tau}^{t} \dot{z}(\xi) d\xi + \sum_{m=1}^{s} \pi_{\ell m} Q_m \int_{t-\tau}^{t} z(\xi) d\xi \right],$$

$$\mathscr{L}V_3 = \bar{z}^T(t) \tau \bar{R} \bar{z}(t) - \int_{t-\tau}^{t} \bar{z}^T(\xi) \bar{R} \bar{z}(\xi) d\xi,$$

$$\mathscr{L}V_4 = z^T(t) S_\ell z(t) - z^T(t-\tau) S_\ell z(t-\tau) + \int_{-\tau}^{0} z^T(t+\xi) \left(\sum_{m=1}^{s} \pi_{\ell m} S_m \right) z(t+\xi) d\xi,$$

$$\mathscr{L}V_5 = \dot{z}^T(t) 2\bar{\mu} Z \dot{z}(t) - \int_{t-\tau-\bar{\mu}}^{t-\tau+\bar{\mu}} \dot{z}^T(\xi) Z \dot{z}(\xi) d\xi.$$

Expanding $\bar{R}$ and $\bar{z}$, adding the upper bound of the null term (26), and applying Jensen Inequality in (28), Eq. (27) becomes

$$\mathscr{L}V(z_t, \ell) \leq \Upsilon^T \boldsymbol{\Phi}_\ell \Upsilon + \sum_{k=1}^{r} (\Lambda\bar{L}_{k\ell})\bar{\mu} r Z^{-1} (\Lambda\bar{L}_{k\ell})^T, \tag{28}$$

where $\Upsilon^T = [z^T(t)\ \dot{z}^T(t)\ z^T(t-\tau)\ \int_{-\tau}^{0} z^T(t+\xi) d\xi]$ and $\boldsymbol{\Phi}_\ell$ is given in (12). Writing $\Lambda\bar{L}_{k\ell} = \Upsilon^T \gamma f \bar{L}_{k\ell}$ with $\gamma^T = [I_{n-1}\ I_{n-1}\ 0_{n-1}\ 0_{n-1}]$, we can write (28) as

$$\mathscr{L}V(z_t, \ell) \leq \Upsilon^T \left[\sum_{k=1}^{r} \left(\boldsymbol{\Phi}_\ell + (\gamma f \bar{L}_{k\ell})\bar{\mu} r Z^{-1} (\gamma f \bar{L}_{k\ell})^T \right) \right] \Upsilon, \tag{29}$$

Then, the negativeness of the right side of the inequality in (29) is a sufficient condition to guarantee that $\mathscr{L}V(z_t, \ell) < 0$. Thus, the term in the brackets is imposed negative definite. Using Schur's complement we obtain

$$\sum_{k=1}^{r} \begin{bmatrix} \frac{1}{r}\boldsymbol{\Phi}_\ell & \bar{\mu}\gamma f \bar{L}_{k\ell} \\ * & -\frac{\bar{\mu}}{r}Z \end{bmatrix} = \begin{bmatrix} \boldsymbol{\Phi}_\ell & \bar{\mu}\gamma f \bar{L}_\ell \\ * & -\bar{\mu}Z \end{bmatrix} < 0, \tag{30}$$

which, replacing $f\bar{L}_\ell$ by (25) leads to the LMI condition in (11). Thus, if LMI (11) holds, then $\mathscr{L}V(z_t, \ell) < 0$.

Finally, it is shown that if LMIs in (10) and (11) hold, then the system in (7) is stochastically stable in the mean-square sense. Assume that the LMIs in the theorem are satisfied then $V(z_t, \ell) > 0$ and $\mathscr{L}V(z_t, \ell) \leq -\alpha z^T(t)z(t)$ is true for some sufficiently small $\alpha > 0$. Then, as in [19], applying the expectancy we obtain $\mathbb{E}\left[V(z_t, \ell)\right] > 0$ and $\mathbb{E}\left[\mathscr{L}V(z_t, \ell)\right] \leq -\alpha\mathbb{E}\left[z^T(t)z(t)\right]$, which applying the generalized Itô's formula yields

$$\mathbb{E}\left[V(z_t, \ell)\right] - V(z(0), \ell_0) = \int_0^t \mathbb{E}\left[\mathscr{L}V(z(\xi), \ell)\right] d\xi \leq -\alpha \int_0^t \mathbb{E}\left[z^T(t)z(t)\right] d\xi,$$

where ℓ_0 is the arbitrary initial topology at $t = 0$. Thus, $\int_0^t \mathbb{E}\left[z^T(\xi)z(\xi)\right] d\xi < \frac{V(z(0), \ell_0)}{\alpha}$, which implies $\lim_{t\to\infty} \mathbb{E}\left[z^T(t)z(t)\right] \to 0$. Therefore, if the LMIs proposed hold, the system (7) is stochastically stable in the mean-square sense. Consequently, the system (6) achieves consensus according to Lemma 2. □

5 Numerical Example

In order to illustrate the applicability of the method, we consider a team of four agents that must achieve consensus on a given variable x_i, for $i = 1, \ldots, 4$, assuming time-varying delayed control inputs and intermittent communication.

We model the intermittent communication with a network topology switching between the graphs $\mathscr{G}(1)$ and $\mathscr{G}(2)$. These two topologies are illustrated in Fig. 1, also showing the representation of the time-delays $\tau_{ij} = \tau_k$, for $k = 1, \ldots, 6$ the edge index according to Algorithm 1.

In this example, it is worth noting that when the system is on the topology $\mathscr{G}(2)$, the agents 3 and 4 do not receive information from the other agents, therefore if the system never leaves this topology it will not reach consensus, unless the agents 3 and 4 are in consensus occasionally.

Initially, to represent the multi-agent system as in (6) we have that $r = 6$, which is the total number of links in the Joint graph $\bar{\mathscr{G}}$, i.e., subject to six delays. Also,

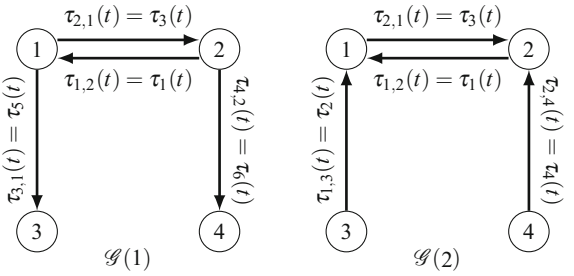

Fig. 1 Graphs $\mathcal{G}(1)$ and $\mathcal{G}(2)$ representing the two possible topologies of the multi-agent system

the subgraphs $\mathcal{G}(\ell)$ are associated with the following Incidence matrix $H(\ell)$ and Heading matrix $\bar{H}(\ell)$:

$$H(1) = \begin{bmatrix} 1 & 0 & -1 & 0 & -1 & 0 \\ -1 & 0 & 1 & 0 & 0 & -1 \\ 0 & 0 & 0 & 0 & 1 & 0 \\ 0 & 0 & 0 & 0 & 0 & 1 \end{bmatrix}, \quad \bar{H}(1) = \begin{bmatrix} 1 & 0 & 0 & 0 & 0 & 0 \\ 0 & 0 & 1 & 0 & 0 & 0 \\ 0 & 0 & 0 & 0 & 1 & 0 \\ 0 & 0 & 0 & 0 & 0 & 1 \end{bmatrix}, \tag{31}$$

and

$$H(2) = \begin{bmatrix} 1 & 1 & -1 & 0 & 0 & 0 \\ -1 & 0 & 1 & 1 & 0 & 0 \\ 0 & -1 & 0 & 0 & 0 & 0 \\ 0 & 0 & 0 & -1 & 0 & 0 \end{bmatrix}, \quad \bar{H}(2) = \begin{bmatrix} 1 & 1 & 0 & 0 & 0 & 0 \\ 0 & 0 & 1 & 1 & 0 & 0 \\ 0 & 0 & 0 & 0 & 0 & 0 \\ 0 & 0 & 0 & 0 & 0 & 0 \end{bmatrix}, \tag{32}$$

where the indices $\ell = 1$ and $\ell = 2$ are associated to the topologies $\mathcal{G}(1)$ and $\mathcal{G}(2)$. Thus, we have $s = 2$ the number of topologies and $n = 4$ the number of agents.

Moreover, assume that the switching topology dynamics is described by a continuous time Markov chain with the transition rate matrix $\Pi = \begin{bmatrix} -1 & 1 \\ 1 & -1 \end{bmatrix}$. Besides, consider that the system is subject to nondifferentiable and nonuniform time-varying delays $\tau_k(t) \in [\tau - \bar{\mu}, \tau + \bar{\mu}]$, for $k = 1, \ldots, 6$.

In order to illustrate the applicability of the main result proposed in this work, we run a numerical simulation considering the multi-agent system (6) with data presented in this section and choosing $\tau = 0.7$ and $\bar{\mu} = 0.3$, such that the time-delays can vary in the interval $\tau_k(t) \in [0.40, 1.00]$, for all k. Figure 2 shows an example for the variation of $\tau_1(t)$ in this interval.

Initially, we consider the systems without any design for the coupling strengths, i.e., all the weights of the coupling strengths $w_k = 1$ and simulate the system for 50 s. During this simulation, consensus could not be achieved. Figure 3 shows the state trajectories of the multi-agent system and the disagreement of the agents. In Fig. 4, the switches of the topology are shown.

Next, we use Theorem 1 to design proper weights. So, for $\tau = 0.7$, $\bar{\mu} = 0.3$, $\Pi = \begin{bmatrix} -1 & 1 \\ 1 & -1 \end{bmatrix}$, and the topologies described by $H(1)$, $\bar{H}(1)$ in (31), and $H(2)$, $\bar{H}(2)$ in

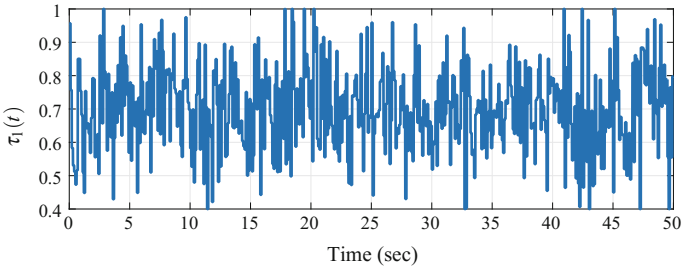

Fig. 2 Illustration of behavior of delay $\tau_1(t)$. The illustration of the others delays are omitted since they present similar behavior

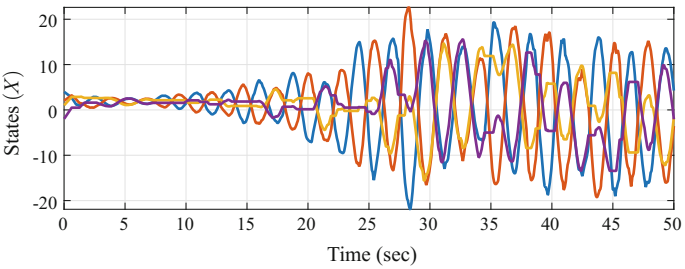

Fig. 3 State trajectories of the multi-agent system in the numerical example without any design of the coupling strengths. The initial states of the agents are $X(0) = [4 \;\; 2 \;\; 1 \;\; -2]^T$

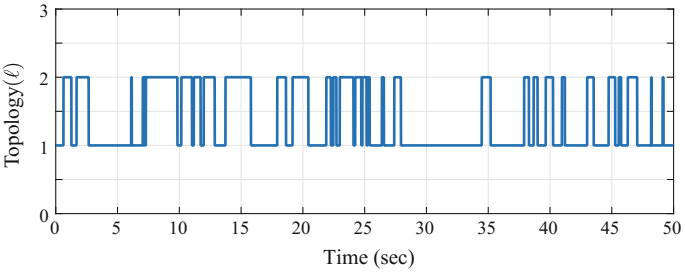

Fig. 4 Switches of the topology for one simulation, where $l = 1, 2$ are the Markov chain states

(32), we run the LMI conditions obtaining feasible solution for $W = \frac{1}{f} W_d$, where f and W_d are LMI variables with values returned by the LMI solver, which results $W = \text{diag}\{0.1392,\ 0.1244,\ 0.2880,\ 0.0900,\ 0.4825,\ 0.3751\}$ such that w_k are given in its main diagonal, from w_1 to w_6, respectively.

With the designed coupling strengths, we simulate the system for 20 s to show that consensus is achieved, as illustrated in Fig. 5.

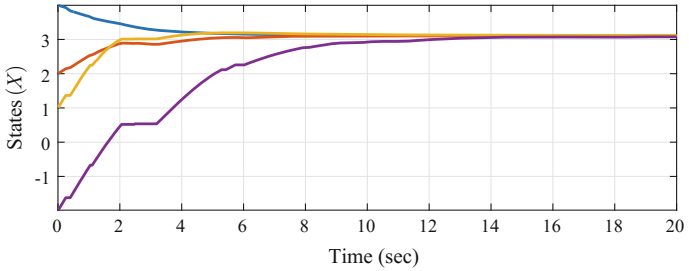

Fig. 5 State trajectories of the multi-agent system in the numerical example with the designed coupling strengths

6 Conclusion

In this chapter, it is studied the consensus problem of multi-agent systems, considering nondifferentiable and nonuniform time-varying delays and switching topology according to a continuous time Markov chain. The main result provides LMI conditions to design proper weights for the coupling strengths between the agents, such that the system can achieve consensus in regions of time-delay that were previously not enabling consensus.

References

1. Beard, R.W., Lawton, J., Hadaegh, F.: A coordination architecture for spacecraft formation control. IEEE Trans. Control Syst. Technol. **9**, 777–790 (2001)
2. Cao, Y., Yu, W., Ren, W., Chen, G.: An overview of recent progress in the study of distributed multi-agent coordination. IEEE Trans. Ind. Inform. **9**, 427–438 (2013)
3. Fax, J.A., Murray, R.M.: Graph Laplacians and stabilization of vehicle formations. In: Proceedings of the 15th IFAC World Congress, pp. 283–288 (2002)
4. Fei, Z., Gao, H., Shi, P.: New results on stabilization of Markovian jump systems with time delay. Automatica **45**, 2300–2306 (2009)
5. Giulietti, F., Pollini, L., Innocenti, M.: Autonomous formation flight. IEEE Control Syst. Mag. **20**, 34–44 (2000)
6. Godsil, C., Royle, G.F.: Algebraic graph theory. In: Graduate Texts in Mathematics, vol. 207. Springer, New York (2001)
7. Jadbabaie, A., Lin, J., Morse, A.S.: Coordination of groups of mobile autonomous agents using nearest neighbor rules. IEEE Trans. Autom. Control **48**, 988–1001 (2003)
8. Lin, P., Jia, Y., Li, L.: Distributed robust H_∞ consensus control in directed networks of agents with time-delay. Syst. Control Lett. **57**, 643–653 (2008)
9. Miao, G., Xu, S., Zhang, B., et al.: Mean square consensus of second-order multi-agent systems under Markov switching topologies. IMA J. Math. Control Inf. **31**, 151–164 (2014)
10. Olfati-Saber, R., Murray, R.M.: Consensus problems in networks of agents with switching topology and time-delays. IEEE Trans. Autom. Control **49**, 1520–1533 (2004)
11. Pimenta, L.C.A., Pereira, G.A.S., Michael, N., et al.: Swarm coordination based on smoothed particle hydrodynamics technique. IEEE Trans. Robot. **29**, 383–399 (2013)

12. Qiao, W., Sipahi, R.: A linear time-invariant consensus dynamics with homogeneous delays: analytical study and synthesis of rightmost eigenvalues. SIAM J. Control Optim. **51**, 3971–3992 (2013)
13. Qiao, W., Sipahi, R.: Delay-dependent coupling for a multi-agent LTI consensus system with inter-agent delays. Phys. D: Nonlinear Phenom. **267**, 112–122 (2014)
14. Ren, W., Beard, R.W., Atkins, E.M.: Information consensus in multivehicle cooperative control: collective group behavior through local interaction. IEEE Control Syst. Mag. **27**, 71–82 (2007)
15. dos Santos Jr., C.R.P., Souza, F.O., Savino, H.J.: Consensus analysis in multi-agent systems subject to delays and switching topology. In: Proceedings of the 12th IFAC Workshop Time Delay Systems, pp. 147–152 (2015)
16. Savino, H.J., Souza, F.O., Pimenta, L.C.A.: Consensus with convergence rate in directed networks with multiple non-differentiable input delays. In: Proceedings of the IEEE International Symposium on Intelligence Control, pp. 252–257 (2014)
17. Savino, H.J., Souza, F.O., Pimenta, L.C.A.: Consensus with guaranteed convergence rate of high-order integrator agents in the presence of time-varying delays. Int. J. Syst. Sci. **47**, 2475–2486 (2016)
18. Savino, H.J., Souza, F.O., Pimenta, L.C.A.: Consensus on time-delay intervals in networks of high-order integrator agents. In: Proceedings of the 12th IFAC Workshop Time Delay Systems, pp. 153–158 (2015)
19. Savino, H.J., dos Santos Jr, C.R.P., Souza, F.O., et al.: Conditions for consensus of multi-agent systems with time-delays and uncertain switching topology. IEEE Trans. Ind. Electron. **63**, 1258–1267 (2016)
20. Sun, Y.G., Wang, L.: Consensus of multi-agent systems in directed networks with nonuniform time-varying delays. IEEE Trans. Autom. Control **54**, 1607–1613 (2009)
21. Vicsek, T., Czirók, A., Ben-Jacob, E., et al.: Novel type of phase transition in a system of self-driven particles. Phys. Rev. Lett. **75**, 1226–1229 (1995)
22. Zhang, Q., Niu, Y., Wang, L., et al.: Average consensus seeking of high-order continuous-time multi-agent systems with multiple time-varying communication delays. Int. J. Control Autom. Syst. **9**, 1209–1218 (2011)
23. Zhao, H., Xu, S., Yuan, D.: An LMI approach to consensus in second-order multi-agent systems. Int. J. Control Autom. Syst. **9**, 1111–1115 (2011)

Analysis of a Model-Free Predictor for Delay Compensation in Networked Systems

Xinyi Ge, Yingshi Zheng, Mark J. Brudnak, Paramsothy Jayakumar, Jeffrey L. Stein and Tulga Ersal

Abstract One important challenge with networked systems is that communication delays can significantly deteriorate system performance. This chapter proposes a model-free predictor framework to compensate for communication delays and improve networked system performance, where the term "model-free" indicates that the predictor does not need to know the dynamic equations governing the system. The motivation to pursue a model-free approach lies in its robustness, ease of design, and implementation. The proposed predictor has a first-order time delay system structure with only one design parameter. Stability of the predictor is analyzed for constant delays and the range of the design parameter to guarantee a stable predictor is established as a function of the network time delay. Since ensuring stability does not necessarily guarantee a good performance, understanding when the predictor can perform well and what its limitations are also critical. To this end, a frequency-domain analysis is given, through which the relationship between the predictor design parameter, time delay, and steady-state performance is revealed. Fundamental limitations of the predictor at higher frequencies are laid out. Finally, this analysis is confirmed on a case study. The case study further allows for testing the

X. Ge · Y. Zheng · J.L. Stein · T. Ersal (✉)
Department of Mechanical Engineering, University of Michigan,
Ann Arbor, MI 48109, USA
e-mail: tersal@umich.edu

X. Ge
e-mail: gexinyi@umich.edu

Y. Zheng
e-mail: zhengys@umich.edu

J.L. Stein
e-mail: stein@umich.edu

M.J. Brudnak · P. Jayakumar
U.S. Army TARDEC, Warren, MI 48092, USA
e-mail: mark.j.brudnak.civ@mail.mil

P. Jayakumar
e-mail: paramsothy.jayakumar.civ@mail.mil

T. Insperger et al. (eds.), *Time Delay Systems*,
Advances in Delays and Dynamics 7, DOI 10.1007/978-3-319-53426-8_14

transient performance of the predictor in closed loop with the networked system, and shows that the predictor holds significant potential to alleviate the negative impact of communication delays, even if its high frequency performance may be limited.

1 Introduction

Networked systems are systems that are coupled through information exchange over a communication channel. Example applications include tele-operation, network control, and networked hardware-in-the-loop simulation systems.

Typically, the communication channel introduces delays, which could deteriorate the system performance significantly and could even destabilize the system. The literature presents many techniques to address this challenge. Some of these techniques leverage the system models. For example, in the tele-operation literature, model predictive control has been applied to time delay systems to predict future commands with maximized tracking performance [1]. Methods to predict operator inputs have been developed [2]. The network control system literature describes many techniques to handle both deterministic [3, 4] and stochastic network delays [5–8]. When system models are not available, other methods can be used. For example, researchers from the tele-operation field designed a PD-type predictor in the form of prediction of observation [9] and extended it to a state predictor based on solution trajectories of the dynamics [10]. The passivity approach guarantees stability without requiring knowledge about system dynamics [11]; however, this guarantee comes at the expense of performance [12]. Networked hardware-in-the-loop simulation literature presents learning-based methods to ensure a high-fidelity integration with no or minimal knowledge about the system [13–15]. However, these methods are more suitable in an experimental setting, where experiments can be repeated under controlled environments.

In this work, the predictor-based idea is pursued further, but with the specific unique goal of achieving a robust, easy-to-design, and easy-to-implement solution by eliminating the need for a dynamic model of the system. In particular, this work first leverages the principles of sliding mode control to derive the dynamics of a model-free predictor. This approach avoids the need to know the dynamic equations of the system and requires only the knowledge of the output equations that pertain to the coupling variables. The result is a predictor that is a first-order time delay system with a single design parameter. The relationship between the design parameter of this predictor and time delay is established to ensure a stable predictor for constant delays. Then, the performance characteristics of the predictor is analyzed through a frequency-domain study. Specifically, this analysis reveals the relationship between the design parameter of the predictor, time delay, and predictor's steady-state performance. This helps establish the fundamental performance limitations of the predictor beyond a certain frequency determined by the time delay. Finally, a case study is performed to validate this analysis and further study the transient performance of the

predictor. The case study demonstrates that the predictor can perform well in transient even when its high-frequency steady-state performance can be very limited.

The rest of the chapter is organized as follows. Section 2 presents the problem formulation using a generic networked system framework, introduces the proposed model-free predictor, including the stability analysis result, and performs the frequency-domain analysis on the steady-state performance of the predictor. In Sect. 3, the predictor is applied to a networked motor-gear-shaft system to evaluate the transient performance of the predictor. Conclusions are given in Sect. 4.

2 Predictor-Based Framework

2.1 General Framework

Consider the generic networked system with communication delay as shown in Fig. 1a. System 1 and System 2 are the two remote systems that are coupled over the network, where the network is considered as a pure, constant delay. If the delays from System 1 to System 2 and from System 2 to System 1 are denoted as τ_1 and τ_2, respectively, then there is a total delay of $\tau_1 + \tau_2$ between System 1 sending out a signal to and receiving the response from System 2. This delay distorts the networked system dynamics and reduces performance. It may even cause instability.

To alleviate the negative impact of communication delay, a predictor-based framework as illustrated in Fig. 1b is considered. The site of System 1 contains a predictor for System 2 that aims to predict the non-delayed response of System 2. Instead of interacting with System 2 directly over the network, System 1 interacts with System 2 indirectly through its predictor and without delay. The vectors $x_{1r}(t)$ and $x_{2r}(t)$ contain only the states related to the calculation of the coupling signals; i.e., the signals $y_1(t)$ and $y_2(t)$ that are communicated over the network to establish the coupling between the remote systems. Note that when the predictors are introduced as shown

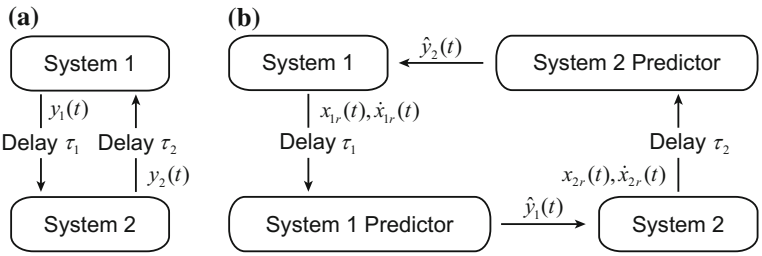

Fig. 1 A generic networked system with (**a**) direct coupling over the delayed communication channel and (**b**) coupling through the predictor-based framework

in Fig. 1b, $x_r(t)$ and its derivative $\dot{x}_r(t)$ are communicated over the network instead of the original coupling signal $y(t)$ in Fig. 1a.

The System 2 Predictor receives the information about System 2 with the delay τ_2. Ensuring that the System 2 Predictor can track the outputs of System 2 satisfactorily despite the delay is the problem of interest. A similar predictor structure applies to the site of System 2, as well.

The literature has previously addressed this control problem by explicitly expressing the dynamics of System 1 and System 2 within the predictors for System 1 and System 2, respectively [16]. In this chapter, an alternative method is considered, which is inspired by the notion of sliding surface in sliding mode control and is described next.

2.2 Predictor Design

Sliding mode control is a nonlinear control technique that reduces the problem of controlling a higher order system to controlling a first-order system [17]. This is achieved by defining a sliding surface in the phase plane and applying a switching control input that forces the system to slide along that surface. The advantages of this method include robustness to disturbances, parameter variations, and un-modeled dynamics.

Consider a nonlinear system of the form

$$\dot{x}_f(t) = f\left(x_f(t)\right) + g\left(x_f(t)\right) u_f(t) \tag{1}$$

where $x_f(t)$ and $u_f(t)$ are the states and inputs of the system, and $f(\cdot)$ and $g(\cdot)$ are nonlinear functions. The subscript f is introduced to distinguish the full state vector $x_f(t)$ from the state vector $x_r(t)$, $x_r \subseteq x_f$, which contains only the states related to the calculation of the coupling signals.

A sliding surface is defined in the phase plane as

$$\mathscr{S} = \left(\frac{d}{dt} + \lambda\right) x_f(t) = 0 \tag{2}$$

where λ determines the slope of the surface. A controller can then be designed to transform the original dynamics (1) to the first-order dynamics of the sliding surface (2) [17].

The sliding mode control approach has been utilized in the literature to create a model-based observer by employing in the local site a model of the remote system and using a sliding mode controller to ensure that the states of the model track the states of the remote system closely [16]. In contrast, the key idea of this chapter is to use the sliding surface concept to derive a dynamic equation for a model-free predictor.

To this end, define the error between the state of the predictor $\hat{x}(t)$ and the actual state of the remote system $x_r(t)$ as:

$$e(t) := x_r(t) - \hat{x}(t) \tag{3}$$

Define a sliding surface for the error system as

$$\mathscr{S} = \left(\frac{d}{dt} + \lambda\right) e(t) = 0 \tag{4}$$

Without any communication delays, keeping the error system on this surface could be achieved with the following dynamic equation for the predictor state

$$\dot{\hat{x}}(t) = \dot{x}_r(t) + \lambda \left(x_r(t) - \hat{x}(t)\right) \tag{5}$$

In reality, however, the remote signals x_r and $\dot{x}_r$ are available only with a delay. Thus, (5) becomes:

$$\dot{\hat{x}}(t) = \dot{x}_r(t-\tau) + \lambda \left(x_r(t-\tau) - \hat{x}(t)\right) \tag{6}$$

where the second term on the right-hand side now involves a difference between the delayed remote state $x_r(t-\tau)$ and the current predictor state $\hat{x}(t)$. That would cause the predictor to track the delayed remote state $x_r(t-\tau)$ instead of the current remote state $x_r(t)$ and render the predictor obsolete. Furthermore, $x_r(t-\tau) - \hat{x}(t)$ cannot be meaningfully referred to as state error when states from different time instances are compared. Hence, for a more useful and meaningful definition of error, (6) is modified to also delay the predictor state, resulting in the following predictor design:

$$\begin{aligned} \dot{\hat{x}}(t) &= \dot{x}_r(t-\tau) + \lambda(x_r(t-\tau) - \hat{x}(t-\tau)) \\ \hat{y}(t) &= h(\hat{x}(t)) \end{aligned} \tag{7}$$

where $h(\cdot)$ is the output function of the predictor, which gives an estimate of the non-delayed response of the remote system, i.e., $\hat{y}(t)$. The resulting predictor is a first-order time delay system with λ being the only design parameter. Assuming $h(\cdot)$ is perfectly known, the goal of the predictor is to drive its states, $\hat{x}(t)$, as close as possible to the coupling-related states of the remote system, $x_r(t)$. Note that no knowledge about the system dynamics is used in the predictor; i.e., neither $f(\cdot)$, nor $g(\cdot)$ appears in (7). The delay τ can be measured by synchronizing the clocks on both sides of the communication channel and time-stamping the packets.

2.3 Stability Analysis

When (7) is used as the predictor, the error system will stay on the sliding surface defined by (4) only when the time delay τ is zero. Hence, it is critical to establish the

stability of the error system for nonzero time delay. Towards this end, substituting (7) into the time derivative of (3), the following results can be derived:

$$\begin{aligned}\dot{e}(t) &= \dot{x}_r(t) - \dot{\hat{x}}(t) \\ &= \dot{x}_r(t) - \dot{x}_r(t-\tau) - \lambda(x_r(t-\tau) - \hat{x}(t-\tau)) \\ &= \dot{x}_r(t) - \dot{x}_r(t-\tau) - \lambda e(t-\tau) \\ &= -\lambda e(t-\tau) + \dot{u}(t)\end{aligned} \tag{8}$$

where $u(t)$ is the coupling error over the communication channel and is an external input to the error system. It is defined as:

$$u(t) := x_r(t) - x_r(t-\tau) \tag{9}$$

The stability of (8) is given by the roots of the following characteristic equation:

$$s + \lambda e^{-s\tau} = 0 \tag{10}$$

where s is the complex frequency variable. Hence, the asymptotically stability of predictor is guaranteed for constant delays if and only if the following relationship holds [18]:

$$0 < \lambda < \frac{\pi}{2\tau} \tag{11}$$

2.4 Frequency-Domain Analysis

The stability criterion (11) is useful to choose a λ for a given time delay τ, such that the predictor is stable. However, it does not provide any insight into the performance of the predictor. Therefore, this section provides a frequency-domain analysis for a steady-state performance evaluation of the predictor.

Consider the communication channel and predictor as shown in Fig. 2, where the state tracking error $e(t)$ and the coupling error over the communication channel $u(t)$ are shown explicitly. The following transfer function from the input $u(t)$ to the output $e(t)$ is then obtained from (8):

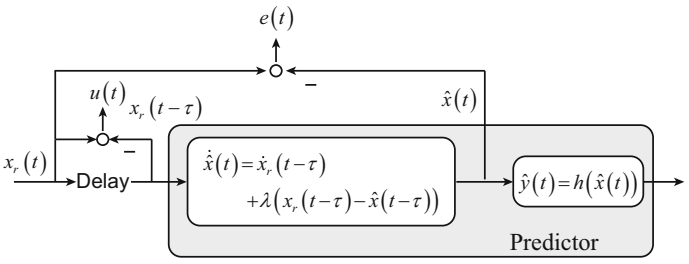

Fig. 2 Visual representation of the variables used in the performance analysis of the predictor

$$\frac{E(s)}{U(s)} = \frac{s}{s + \lambda e^{-\tau s}} \tag{12}$$

Ideally, the state tracking error should be zero to completely eliminate the delay effect. Hence, a good choice of the design parameter λ should not only guarantee the predictor's stability, but also minimize $e(t)$. From a frequency-domain perspective, the gain of the transfer function (12) should be less than one at all frequencies such that the coupling error u is attenuated at each frequency. If the magnitude of $E(j\omega)/U(j\omega)$ is larger than one at a given frequency ω, then the coupling error at that frequency is amplified, which could lead to a bad predictor performance even if the predictor is stable.

The Bode plots of (12) for various values of τ and λ are shown in Figs. 3 and 4. All $\{\lambda, \tau\}$ pairs shown satisfy the stability criterion (11). A number of observations can be made in these figures regarding the performance characteristics of the predictor. First, Fig. 3 illustrates that the steady state tracking performance is better at low frequencies for larger λ values. However, it is not always the case that larger λ gives better steady state tracking. Namely, within the range of about 90–200 rad/s, small λ values may be a better choice for this example delay value, since larger λ values lead to an overshoot above 0 dB in the magnitude plot. Furthermore, at higher frequencies, the predictor is less effective in terms of attenuating the state tracking error, since the magnitude remains close to 0 dB regardless of the λ value chosen, i.e., the magnitude of $E(j\omega)/U(j\omega)$ is approximately one for large ω values. Finally, Fig. 4 shows that it is more difficult for the proposed predictor to be effective as the delay τ becomes larger, since the frequency range corresponding to a magnitude smaller than 0 dB becomes smaller as delay increases.

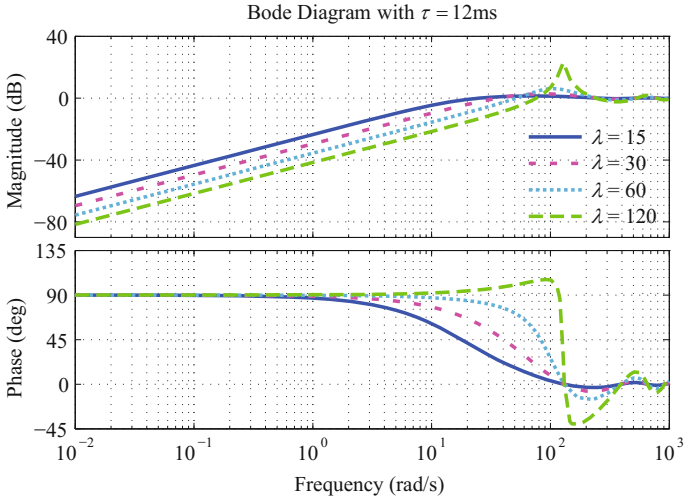

Fig. 3 Bode plot of (12) with $\tau = 12$ ms for various λ values

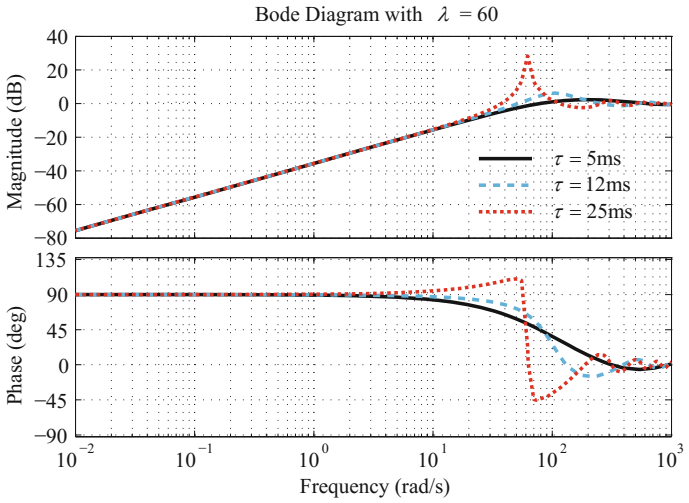

Fig. 4 Bode plot of (12) with $\lambda = 60$ for various τ values

Thus, (12) establishes the relationship between the steady-state performance of the predictor, its design parameter λ, and the time delay τ. Hence, this analysis is important to understand some fundamental, frequency-domain performance characteristics of the predictor. It is still unknown, however, how the predictor will perform in transient when introduced into a system as shown in Fig. 1b. This motivates the case study in the next section.

3 Case Study

A case study is performed in this section to validate the analysis above and also gain some insight into the transient performance of the predictor.

Consider the example system shown in Fig. 5. This example simulates a networked motor-shaft-gear system, where System 1 includes a DC motor, a pair of gears, two shafts, and two bearings. A motor voltage V is given to drive the DC motor, which rotates the motor shaft connected to a gear pair. The output shaft gives a shaft torque. Bearings are mounted on both shafts; therefore, viscous dampings R_{v1} and R_{v2} are introduced for the motor shaft and the output shaft, respectively. The compliance of the motor shaft is neglected, whereas the compliance of the output shaft is taken into account. System 2 consists of a gear pair, a shaft, a fly wheel and two bearings. The input is the shaft torque from System 1, which drives the gear pair. The gear pair drives the shaft, which is connected to a fly wheel. There are two bearings, with viscous frictions R_v and R_{v4}, at both ends of this shaft. There is viscous damping R_{v3} along with the gear pair. For a closed-loop coupling, System 1 needs the shaft speed ω_s from the remote site and System 2 needs the shaft torque

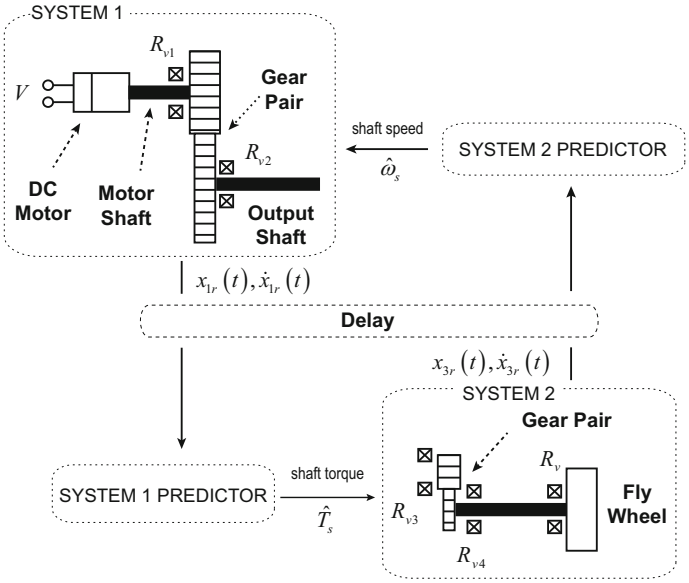

Fig. 5 Networked motor-shaft-gear system with constant communication delay

T_s from the remote site. The one-way communication delay between the systems is $\tau = 12$ ms. The output of interest of the entire system is the difference of the angular displacement of the two ends of the output shaft in System 1, $\Delta\theta$. The dynamics of the individual systems are given as:

System 1:

$$\begin{bmatrix} \dot{x}_{1r} \\ \dot{x}_{2f} \end{bmatrix} = \begin{bmatrix} 0 & 500 \\ -0.56 & -1.5 \end{bmatrix} \begin{bmatrix} x_{1r} \\ x_{2f} \end{bmatrix} + \begin{bmatrix} 0 & -1 \\ 0.00074 & 0 \end{bmatrix} \begin{bmatrix} V \\ \omega_s \end{bmatrix}$$
$$y_1 = T_s = 10x_{1r} \tag{13}$$

System 2:

$$\begin{aligned} \dot{x}_{3r} &= -0.13x_{3r} + 0.28T_s \\ y_2 &= \omega_s = 20x_{3r} \end{aligned} \tag{14}$$

The Bode plots of the two systems are shown in Fig. 6. The coupling-related states for System 1 and System 2 are x_{1r} and x_{3r}, respectively. With the coupling signal output equations for System 1 and System 2 known, the equations for the two predictors are given by:

System 1 Predictor:

$$\begin{aligned} \dot{\hat{x}}_1(t) &= \dot{x}_{1r}(t-\tau) + \lambda(x_{1r}(t-\tau) - \hat{x}_1(t-\tau)) \\ \hat{y}_1(t) &= \hat{\omega}_s = 10\hat{x}_1(t) \end{aligned} \tag{15}$$

System 2 Predictor:

$$\begin{aligned}\dot{\hat{x}}_3(t) &= \dot{x}_{3r}(t-\tau) + \lambda(x_{3r}(t-\tau) - \hat{x}_3(t-\tau)) \\ \hat{y}_2(t) &= \hat{T}_s = 20\hat{x}_3(t)\end{aligned} \tag{16}$$

Note that the same λ is used in this case study in both predictors only for simplicity. In general, different values can be used. To characterize the time-domain performance of the predictors, the 2-norm of the differences between the simulation results with predictors and the simulation results for the ideal case (i.e., when there is no communication delay) is used. To characterize the performance improvement relative to the case when predictors are not used, a normalized version of the performance metric is also considered, where normalization is done with respect to the 2-norm of the simulation results for the delayed case without predictors. Mathematically, the performance metric p and its normalized version p_n are given as:

$$p = ||r - r_i||_2, \quad p_n = \frac{||r - r_i||_2}{||r_d - r_i||_2} \tag{17}$$

where r is the simulation output trajectory vector (in this case, r is $\Delta\theta$) with subscripts i and d standing for the ideal and delayed cases without predictors, respectively. Best performance is achieved when $p = p_n = 0$; i.e., when the impact of delay is completely attenuated. $p_n > 1$ would mean that the predictors worsen the performance, and $p_n < 1$ would mean that the predictors improve the performance compared to the case when predictors are not used.

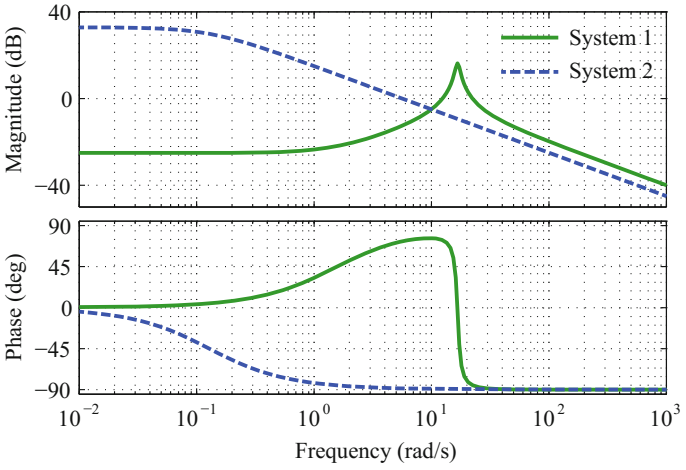

Fig. 6 Bode plot of System 1 (from ω_s to y_1) and System 2 (from T_s to y_2)

The simulation is run for 80 s using a sinusoidal voltage input $V = 50sin(\omega t) + 50$ volts and zero initial conditions. Performance metrics p_n and p for various ω and λ values are summarized in Table 1. Note that all λ values yield stable predictors according to (11). $\lambda = 0$ corresponds to the case when predictors are not used. The predictors are effective at all excitation frequencies tested and, in general, a larger λ value corresponds to better predictor performance in terms of attenuating the effect of delay as can be seen by the smaller p_n values. Two specific ω values will be discussed further to aid with the comparison between the frequency-domain analysis of Sect. 2.4 and the time-domain simulation results.

When ω is 1 rad/s, the output of interest $\Delta\theta$ for the ideal case (no delay), delayed case, and delayed case with predictors ($\lambda = 15$ and $\lambda = 120$) is shown in Fig. 7 for the first 9 s. With delay introduced into the system, the output of interest deviates significantly from the ideal case. When predictors are added into the system, the delay effect is reduced, with a larger λ value leading to a better performance.

The state tracking error for the System 2 Predictor is shown in Fig. 8 for two λ values. Note that for different λ values, the coupling errors may be different. Figure 8 shows that with the larger λ value, the predictor gives a faster state tracking response, and the ratio of the magnitude of state tracking error to the magnitude of coupling

Table 1 Performance metrics for different λ values and excitation frequencies over a simulation time window of 80 s; a smaller metric value indicates better performance

	ω (rad/s)	1	10	30	100	400
p	$\lambda = 0$	8.2	10.5	11.3	8.3	8.2
p_n	$\lambda = 15$	26.6 %	26.6 %	27.7 %	26.7 %	26.6 %
	$\lambda = 30$	7.8 %	8.1 %	9.0 %	7.8 %	7.8 %
	$\lambda = 60$	3.3 %	3.6 %	4.2 %	3.3 %	3.3 %
	$\lambda = 120$	1.6 %	1.7 %	2.0 %	1.6 %	1.6 %

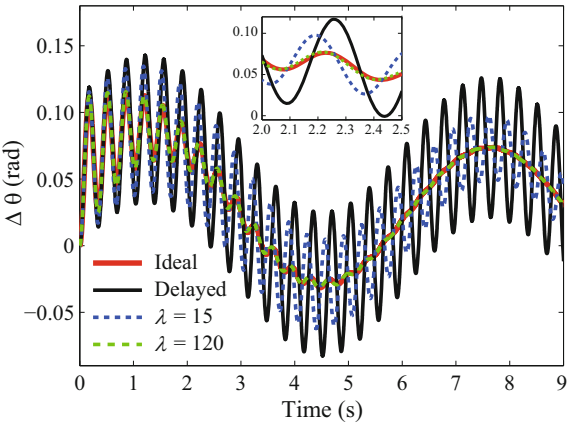

Fig. 7 Output of interest for $\omega = 1$ rad/s

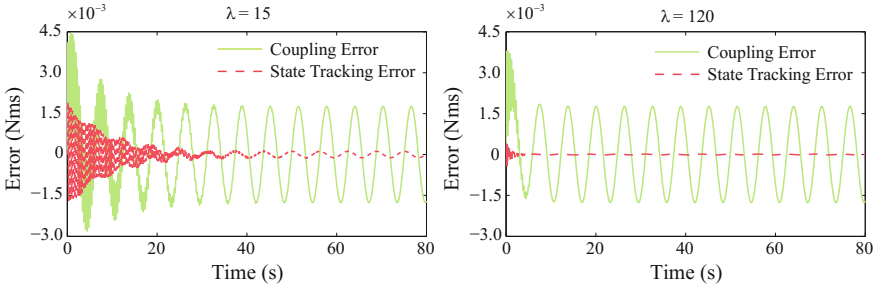

Fig. 8 System 2 predictor performance for $\omega = 1$ rad/s

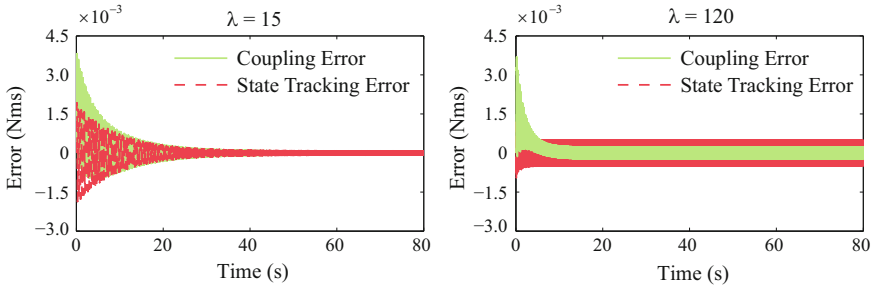

Fig. 9 System 2 predictor performance for $\omega = 100$ rad/s

error becomes smaller in steady state, which is consistent with the frequency-domain analysis in Sect. 2.4.

The same analysis also showed, however, that at higher frequencies the predictors would be less effective in terms of reducing the coupling error. Nevertheless, in this case study, p_n is reduced as effectively even when ω is larger. Here, the results obtained with $\omega = 100$ rad/s will be used as an example to explain the reason behind this observation.

For this particular frequency, according to Fig. 3, using $\lambda = 15$ does not make much difference in the coupling error, whereas $\lambda = 120$ yields a steady-state performance that is even worse than the case without any predictors. Indeed, the coupling and state tracking errors shown in Fig. 9 confirm this analysis. In steady state, the amplitude of the coupling and state tracking errors are almost the same for $\lambda = 15$, and state tracking error is worse than the coupling error for $\lambda = 120$. The reason why the predictors are still effective in terms of p_n is because of the combination of two facts. The first fact is that p_n captures the transient response, as well. The transient response does not only include the excitation frequency itself, but also the lower frequencies, where the predictors are effective. The second fact is the low-pass-filter nature of the systems, which places more emphasis on the lower frequency performance and attenuates the higher frequency signals. Thus, even though the performance of the predictors is very limited at higher frequencies, even amplifying

the coupling errors for certain λ values, this reduced performance does not have a significant impact on the system response. Figure 10 shows the output of interest for $\omega = 100$ rad/s for the first 9 s of the simulation to highlight the transient performance of the predictors.

Figure 11 shows the coupling error trajectory for $\omega = 100$ rad/s when the predictors are not used. Note that without the predictors the convergence speed to steady state is much slower compared to Fig. 9. Figure 9 also shows that a higher λ value gives a faster response, even though it leads to a higher steady-state error. Hence, depending on the frequency, there may be a trade-off between faster transient response and lower steady-state error.

This case study illustrates that even though the frequency-domain analysis in Sect. 2.4 points out a limited steady-state performance of the predictors at higher frequencies, the predictors may still be helpful, especially if those higher frequencies are beyond the system's bandwidth and the transient response is of interest.

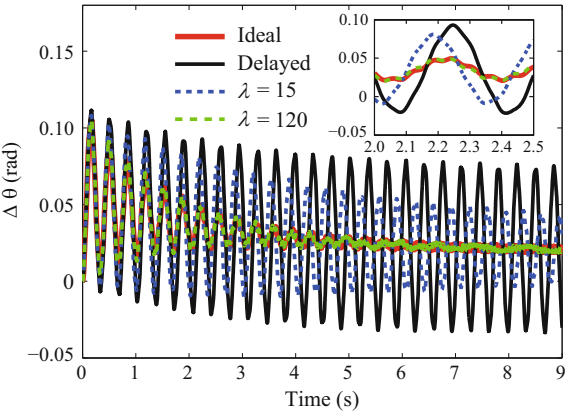

Fig. 10 Output of interest for $\omega = 100$ rad/s

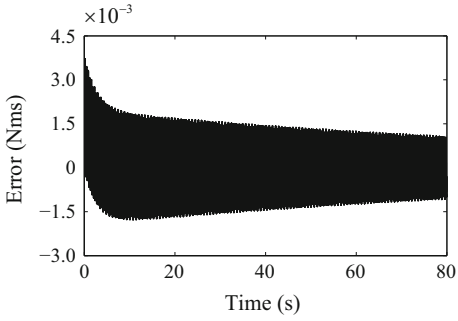

Fig. 11 Coupling error for $\omega = 100$ rad/s when predictors are not used

4 Conclusion

A model-free predictor framework is proposed to compensate for communication delays in networked systems. The predictor is a first-order time delay system with a single design parameter λ. After the relationship between λ and the predictor's stability is established, a frequency-domain analysis is provided to gain insight into the relationship between the steady-state performance of the predictor, its design parameter, and time delays. The frequency-domain analysis thus lays out the fundamental steady-state performance characteristics of the predictor. The case study confirms this analysis, but also illustrates the time-domain, transient performance of the predictor. The main conclusion is that the predictor has significant potential to attenuate the negative impact of delays, especially if the systems exhibit a low-pass-filter type behavior that puts more emphasis on the performance at lower frequencies and thus makes the performance limitations of the predictor at higher frequencies less consequential.

These results encourage further research to fully develop and understand this predictor framework. Performance under stochastic delays is of particular interest. Future work also needs to focus on closed-loop stability, as the stability of the predictor does not automatically guarantee closed-loop stability.

References

1. Bemporad, A.: Predictive control of teleoperated constrained systems with unbounded communication delays. In: IEEE Conference on Decision and Control, pp. 2133–2138 (1998)
2. Smith, C., Jensfelt, P.: A predictor for operator input for time-delayed teleoperation. Mechatronics **20**(7), 778–786 (2010)
3. Lian, F.-L., Moyne, J., Tilbury, D.: Network design consideration for distributed control systems. IEEE Trans. Control Syst. Technol. **10**(2), 297–307 (2002)
4. Montestruque, L.A., Antsaklis, P.J.: On the model-based control of networked systems. Automatica **39**(10), 1837–1843 (2003)
5. Nilsson, J.: Real-time control systems with delay. Ph.D. Dissertation, Lund Institute of Technology (1998)
6. Goktas, F.: Distributed control of systems over communication networks. Ph.D. Dissertation, University of Pennsylvania (2000)
7. Liu, G.-P., Xia, Y., Rees, D., Hu, W.: Design and stability criteria of networked predictive control systems with random network delay in the feedback channel. IEEE Trans. Syst. Man Cybern. Part C: Appl. Rev. **37**(2), 173–184 (2007)
8. Wang, R., Liu, G.-P., Wang, W., Rees, D., Zhao, Yun-Bo: H-inf control for networked predictive control systems based on the switched Lyapunov function method. IEEE Trans. Ind. Electron. **57**(10), 3565 (2010)
9. Kawada, H., Namerikawa, T.: Bilateral control of nonlinear teleoperation with time varying communication delays. In: American Control Conference, pp. 189–194 (2008)
10. Yoshida, K., Namerikawa, T., Sawodny, O.: A state predictor for bilateral teleoperation with communication time delay. In: IEEE Conference on Decision and Control, pp. 4590–4595 (2008)
11. Anderson, R.J., Spong, M.W.: Bilateral control of teleoperators with time delay. IEEE Trans. Autom. Control **34**(5), 494–501 (1989)

12. Lawrence, D.A.: Stability and transparency in bilateral teleoperation. IEEE Trans. Robot. Autom. **9**(5), 624–637 (1993)
13. Ersal, T., Brudnak, M., Salvi, A., Kim, Y., Siegel, Jason B., Stein, Jeffrey L.: An iterative learning control approach to improving fidelity in internet-distributed hardwarein-the-loop simulation. J. Dyn. Syst. Meas. Control **136**(6), 061012 (2014)
14. Ersal, T., Gillespie, R.B., Brudnak, M.J., Stein, J.L., Fathy, Hosam K.: Effect of coupling point selection on distortion in internet-distributed hardware-in-the-loop simulation. Int. J. Veh. Des. **61**(1–4), 67–85 (2013)
15. Ge, X., Brudnak, M.J., Stein, J.L., Ersal, T.: A norm optimal iterative learning control framework towards internet-distributed hardware-in-the-loop simulation. In: American Control Conference, pp. 3802–3807 (2014)
16. Goodell, J., Compere, M., Simon, M., Smith, W., Wright, R., Brudnak, M.: Robust control techniques for state tracking in the presence of variable time delays. SAE Technical Paper 2006-01-1163 (2006)
17. Slotine, J.J.E., Li, W.: Applied Nonlinear Control, vol. 199, no. 1. Englewood Cliffs, NJ, Prentice-hall (1991)
18. Hale, J.: Theory of Functional Differential Equations. Springer, New York (1977)

Predictor Feedback for Extremum Seeking with Delays

Tiago Roux Oliveira and Miroslav Krstic

Abstract In this paper, we derive the design and analysis for scalar gradient extremum seeking (ES) subject to arbitrarily long input–output delays, by employing a predictor with a perturbation-based estimate of the Hessian. Exponential stability and convergence to a small neighborhood of the unknown extremum point can be guaranteed. This result is carried out using backstepping transformation and averaging in infinite dimensions. Generalization of the results for Newton-based ES is also indicated. Some simulation examples are presented to illustrate the performance of the delay-compensated ES control scheme.

1 Introduction

Despite of the large number of publications on extremum seeking (ES) [1–7], there is no work which rigorously deals with ES in the presence of delays. Indeed, this is a very challenging problem, because ES is all about convergence, with a good convergence rate, whereas a delay, when it is simply ignored, directly restricts the convergence rate or destabilizes the closed-loop system.

In the present paper, we give an answer to this question by considering scalar gradient ES and Newton-based ES [5, 7] under input–output delays. Predictor feedback [8–11] is the most effective methodology to deal with arbitrary delays. However, it requires a known model. In our problem, the nonlinear map to be optimized is unknown. Thus, we present a new approach for prediction feedback based on perturbation-based estimates of the model. The stability analysis is rigorously obtained via backstepping transformation [11] and averaging in infinite dimensions

T.R. Oliveira (✉)
Department of Electronics and Telecommunication Engineering,
State University of Rio de Janeiro (UERJ), Rio de Janeiro, RJ 20550-900, Brazil
e-mail: tiagoroux@uerj.br

M. Krstic
Department of Mechanical and Aerospace Engineering,
University of California—San Diego (UCSD), La Jolla, CA 92093-0411, USA
e-mail: krstic@ucsd.edu

T. Insperger et al. (eds.), *Time Delay Systems*,
Advances in Delays and Dynamics 7, DOI 10.1007/978-3-319-53426-8_15

[12, 13]. The perturbation-based (averaging-based) scheme rises due to the necessity of estimating the unknown second derivative (Hessian) of the nonlinear convex-concave map, or its inverse [3, 5].

We start in Sect. 2 formulating the real-time ES control problem under time delays. In Sect. 3, it is introduced the predictor design for delay compensation in scalar gradient ES as well as the exponential stability analysis with explicit Lyapunov–Krasovskii functionals. Section 4 briefly discusses the generalization of the perturbation-based predictor design for Newton-based ES [5, 7]. Section 5 presents a numerical example to illustrate the convergence of the proposed extremum seeking with delay compensation to a small neighborhood of the desired extremum. Finally, Sect. 6 concludes the paper identifying some open problems for future research directions.

Notation and Norms: The 2−norm of a finite-dimensional (ODE) state vector $X(t)$ is denoted by single bars, $|X(t)|$. In contrast, norms of functions (of x) are denoted by double bars. By default, $\|\cdot\|$ denotes the spatial $L_2[0,D]$ norm, i.e., $\|\cdot\| = \|\cdot\|_{L_2[0,D]}$. Since the PDE state variable $u(x,t)$ is a function of two arguments, taking a norm in one of the variables makes the norm a function of the other variable. For example, the $L_2[0,D]$ norm of $u(x,t)$ in $x \in [0,D]$ is $\|u(t)\| = \left(\int_0^D u^2(x,t)dx\right)^{1/2}$, see [11]. The partial derivatives of $u(x,t)$ are denoted by $u_t(x,t)$ and $u_x(x,t)$ or, occasionally, by $\partial_t u_{\text{av}}(x,t)$ and $\partial_x u_{\text{av}}(x,t)$ to refer the operator for its average signal $u_{\text{av}}(x,t)$. As defined in [14], big $\mathcal{O}(\epsilon)$ notation is used to quantify approximations or order of magnitude relation of vector functions, valid for "ϵ sufficiently small".

2 Problem Statement

Scalar ES considers applications in which the goal is to maximize (or minimize) the output $y \in \mathfrak{R}$ of an unknown nonlinear static map $Q(\theta)$ by varying the input $\theta \in \mathfrak{R}$. Here, we additionally assume that there is a *constant and known* delay $D \geq 0$ in the actuation path or measurement system such that the measured output is given by

$$y(t) = Q(\theta(t-D)). \tag{1}$$

For notation clarity, we assume that our system is output-delayed in the following presentation and block diagrams. However, the results in this paper can be straightforwardly extended to the input–delay case since any input delay can be moved to the output of the static map. The case when input delays D_{in} and output delays D_{out} occur simultaneously could also be handled, by assuming that the total delay to be counteract would be $D = D_{\text{in}} + D_{\text{out}}$, with $D_{\text{in}}, D_{\text{out}} \geq 0$. Without loss of generality, let us consider the maximum seeking problem such that the maximizing value of θ is denoted by θ^*. For the sake of simplicity, we also assume that the nonlinear map is at least locally quadratic, i.e.,

$$Q(\theta) = y^* + \frac{H}{2}(\theta - \theta^*)^2 , \tag{2}$$

in some neighborhood of the extremum point (θ^*, y^*), where besides the constants $\theta^* \in \mathfrak{R}$ and $y^* \in \mathfrak{R}$ being unknown, the scalar $H < 0$ is the unknown Hessian of the static map. By plugging (2) into (1), we obtain the *quadratic static map with delay* of interest

$$y(t) = y^* + \frac{H}{2}(\theta(t - D) - \theta^*)^2 . \tag{3}$$

3 Gradient Extremum Seeking with Delays

Let $\hat{\theta}$ be the estimate of θ^* and

$$\tilde{\theta}(t) = \hat{\theta}(t) - \theta^* \tag{4}$$

be the *estimation error*. From Fig. 1, the *error dynamics* can be written as

$$\dot{\tilde{\theta}}(t - D) = U(t - D) . \tag{5}$$

Moreover, one has

$$G(t) = M(t)y(t) , \quad \theta(t) = \hat{\theta}(t) + S(t) , \tag{6}$$

where the dither signals are given by

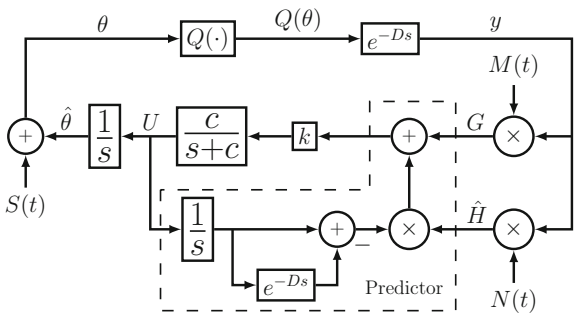

Fig. 1 Block diagram of the basic prediction scheme for output-delay compensation in gradient ES. The predictor feedback with a perturbation-based estimate of the Hessian obeys Eq. (18), the dither signals are given by $S(t) = a\sin(\omega(t + D))$ and $M(t) = \frac{2}{a}\sin(\omega t)$ and the demodulating signal is $N(t) = -\frac{8}{a^2}\cos(2\omega t)$

$$S(t) = a\sin(\omega(t+D))\,, \quad M(t) = \frac{2}{a}\sin(\omega t)\,, \tag{7}$$

with nonzero perturbation amplitude a and frequency ω. The sinusoid feature of the signals in (7) is only one possible choice—many other perturbations, from square waves to stochastic noise, can be used in lieu of it, provided they are of zero mean [6, 15]. The same is valid for $N(t)$ in the signal

$$\hat{H}(t) = N(t)y(t)\,, \tag{8}$$

applied to obtain an estimate of the unknown Hessian H, where the demodulating signal $N(t)$ is given by

$$N(t) = -\frac{8}{a^2}\cos(2\omega t)\,. \tag{9}$$

In [5], it was proved that

$$\frac{1}{\Pi}\int_0^{\Pi} N(\sigma)yd\sigma = H\,, \quad \Pi = 2\pi/\omega\,, \tag{10}$$

if a quadratic map as in (2) is considered. In other words, the average version $\hat{H}_{\text{av}} = (Ny)_{\text{av}} = H$.

3.1 Predictor Feedback with an Estimate of the Hessian

By using the averaging analysis, we can verify that the average version of the signal $G(t)$ in (6) is given by

$$G_{\text{av}}(t) = H\tilde{\theta}_{\text{av}}(t-D)\,. \tag{11}$$

From (5), the following average models can be obtained:

$$\dot{\tilde{\theta}}_{\text{av}}(t-D) = U_{\text{av}}(t-D)\,, \quad \dot{G}_{\text{av}}(t) = HU_{\text{av}}(t-D)\,, \tag{12}$$

where $U_{\text{av}} \in \mathfrak{R}$ is the resulting average control for $U \in \mathfrak{R}$.

In order to motivate the predictor feedback design, the idea here is to compensate for the delay by feeding back the future state $G(t+D)$, or $G_{\text{av}}(t+D)$ in the equivalent average system. Given any stabilizing gain $k > 0$ for the undelayed system, our wish is to have a control that achieves

$$U_{\text{av}}(t) = kG_{\text{av}}(t+D)\,, \quad \forall t \geq 0\,, \tag{13}$$

and it appears to be non-implementable since it requires future values of the state. However, by applying the variation of constants formula to (12) we can express the future state as

$$G_{\text{av}}(t+D) = G_{\text{av}}(t) + H\int_{t-D}^{t} U_{\text{av}}(\sigma)d\sigma\,, \tag{14}$$

which gives the future state $G_{\text{av}}(t+D)$ in terms of the average control signal $U_{\text{av}}(\sigma)$ from the past window $[t-D, t]$. It yields the following feedback law:

$$U_{\text{av}}(t) = k\left[G_{\text{av}}(t) + H\int_{t-D}^{t} U_{\text{av}}(\sigma)d\sigma\right]. \tag{15}$$

Hence, from (14) and (15), the average feedback law (13) can be obtained indeed as desired. Consequently,

$$\dot{\tilde{\theta}}_{\text{av}}(t) = kG_{\text{av}}(t+D)\,, \quad \forall t \geq 0\,. \tag{16}$$

Therefore, from (11), one has

$$\frac{d\tilde{\theta}_{\text{av}}(t)}{dt} = kH\tilde{\theta}_{\text{av}}(t)\,, \quad \forall t \geq D\,, \tag{17}$$

with an exponentially attractive equilibrium $\tilde{\theta}^e_{\text{av}} = 0$, since $k > 0$ in the control design and $H < 0$ by assumption.

In the next section, we show that the control objectives can still be achieved if a simple modification of the above basic predictor-based controller, which employs a low-pass filter, is applied. In this case, we propose the following infinite-dimensional and averaging-based predictor feedback in order to compensate the delay [16]

$$U(t) = \frac{c}{s+c}\left\{k\left[G(t) + \hat{H}(t)\int_{t-D}^{t} U(\tau)d\tau\right]\right\}, \tag{18}$$

where $c > 0$ is sufficiently large, i.e., the predictor feedback is of the form of a low-pass filtered non-average version of (15). This low-pass filtering is particularly required in the stability analysis when the averaging theorem in infinite dimensions [12, 13] is invoked. The predictor feedback (18) is averaging-base (perturbation-based) because $\hat{H}$ is updated according to the estimate (8) of the unknown Hessian H, satisfying the averaging property (10).

3.2 Stability Analysis

The main stability results are stated in the next theorem.

Theorem 1 *Consider the closed-loop system in Fig. 1 with delayed output (3). There exists $c^* > 0$ such that, $\forall c \geq c^*$, $\exists\ \omega^*(c) > 0$ such that, $\forall \omega > \omega^*$, the closed-loop delayed system (5) and (18), with $G(t)$ in (6), $\hat{H}(t)$ in (8) and state $\tilde{\theta}(t-D)$, $U(\sigma)$,*

$\forall \sigma \in [t-D, t]$, has a unique exponentially stable periodic solution in t of period $\Pi = 2\pi/\omega$, denoted by $\tilde{\theta}^{\Pi}(t-D)$, $U^{\Pi}(\sigma)$, $\forall \sigma \in [t-D, t]$, satisfying, $\forall t \geq 0$:

$$\left(\left| \tilde{\theta}^{\Pi}(t-D) \right|^2 + \left[U^{\Pi}(t) \right]^2 + \int_{t-D}^{t} \left[U^{\Pi}(\tau) \right]^2 d\tau \right)^{1/2} \leq \mathscr{O}(1/\omega) \tag{19}$$

Furthermore,

$$\limsup_{t \to +\infty} |\theta(t) - \theta^*| = \mathscr{O}(a + 1/\omega)\,, \tag{20}$$

$$\limsup_{t \to +\infty} |y(t) - y^*| = \mathscr{O}(a^2 + 1/\omega^2)\,. \tag{21}$$

Proof The demonstration follows the **Steps 1** to **8** below.

Step 1: Transport PDE for Delay Representation

According to [11], the delay in (5) can be represented using a transport PDE as

$$\dot{\tilde{\theta}}(t-D) = u(0,t)\,, \tag{22}$$

$$u_t(x,t) = u_x(x,t)\,, \quad x \in [0, D]\,, \tag{23}$$

$$u(D,t) = U(t)\,, \tag{24}$$

where the solution of (23) and (24) is

$$u(x,t) = U(t + x - D)\,. \tag{25}$$

Step 2: Equations of the Closed-Loop System

First, substituting $S(t)$ given in (7) into $\theta(t)$ in (6), we obtain

$$\theta(t) = \hat{\theta}(t) + a \sin(\omega(t + D))\,. \tag{26}$$

Now, plug (4) and (26) into (3) so that the output is given in terms of $\tilde{\theta}$:

$$y(t) = y^* + \frac{H}{2}(\tilde{\theta}(t-D) + a \sin(\omega t))^2\,. \tag{27}$$

By plugging $M(t)$ given in (7) into $G(t)$ in (6), (9) into (8) and representing the integrand in (18) using the transport PDE state, one has

$$U(t) = \frac{c}{s+c}\left\{k\left[G(t) + \hat{H}(t)\int_0^D u(\sigma,t)d\sigma\right]\right\}, \tag{28}$$

$$G(t) = \frac{2}{a}\sin(\omega t)y(t), \tag{29}$$

$$\hat{H}(t) = -\frac{8}{a^2}\cos(2\omega t)y(t). \tag{30}$$

Plug (27) into (29) and (30), and then the resulting (29) and (30) into (28). By extracting the common factor y in the resulting version of (28), one has

$$\begin{aligned} U(t) = \frac{c}{s+c}\Bigg\{k\Bigg[y^* + \frac{H}{2}(\tilde{\theta}(t-D) + a\sin(\omega t))^2\Bigg] \\ \times\left[\frac{2}{a}\sin(\omega t) - \frac{8}{a^2}\cos(2\omega t)\int_0^D u(\sigma,t)d\sigma\right]\Bigg\}. \end{aligned} \tag{31}$$

By expanding the binome in (31), we obtain

$$\begin{aligned} U(t) = \frac{c}{s+c}\Bigg\{k\Bigg[y^* + \frac{H}{2}\tilde{\theta}^2(t-D) + \\ + Ha\sin(\omega t)\tilde{\theta}(t-D) + \frac{a^2H}{2}\sin^2(\omega t)\Bigg] \\ \times\left[\frac{2}{a}\sin(\omega t) - \frac{8}{a^2}\cos(2\omega t)\int_0^D u(\sigma,t)d\sigma\right]\Bigg\}. \end{aligned} \tag{32}$$

Finally, substituting (32) into (24), we can rewrite (22)–(24) as

$$\dot{\tilde{\theta}}(t-D) = u(0,t), \tag{33}$$

$$u_t(x,t) = u_x(x,t), \quad x \in [0,D], \tag{34}$$

$$\begin{aligned} u(D,t) &= \frac{c}{s+c}\left\{k\left[y^* + \frac{H}{2}\tilde{\theta}^2(t-D) + Ha\sin(\omega t)\tilde{\theta}(t-D) + \frac{a^2H}{2}\sin^2(\omega t)\right]\right. \\ &\quad \left.\times\left[\frac{2}{a}\sin(\omega t) - \frac{8}{a^2}\cos(2\omega t)\int_0^D u(\sigma,t)d\sigma\right]\right\} \\ &= \frac{c}{s+c}\left\{k\left[y^*\frac{2}{a}\sin(\omega t) - y^*\frac{8}{a^2}\cos(2\omega t)\int_0^D u(\sigma,t)d\sigma + \frac{H}{a}\tilde{\theta}^2(t-D)\sin(\omega t)\right.\right. \\ &\quad -\frac{4H}{a^2}\tilde{\theta}^2(t-D)\cos(2\omega t)\int_0^D u(\sigma,t)d\sigma + 2H\sin^2(\omega t)\tilde{\theta}(t-D) \\ &\quad -\frac{8H}{a}\sin(\omega t)\tilde{\theta}(t-D)\cos(2\omega t)\int_0^D u(\sigma,t)d\sigma + aH\sin^3(\omega t) \\ &\quad \left.\left.-4H\sin^2(\omega t)\cos(2\omega t)\int_0^D u(\sigma,t)d\sigma\right]\right\} \\ &= \frac{c}{s+c}\left\{k\left[y^*\frac{2}{a}\sin(\omega t) - y^*\frac{8}{a^2}\cos(2\omega t)\int_0^D u(\sigma,t)d\sigma + \frac{H}{a}\tilde{\theta}^2(t-D)\sin(\omega t)\right.\right. \end{aligned} \tag{35}$$

$$-\frac{4H}{a^2}\tilde{\theta}^2(t-D)\cos(2\omega t)\int_0^D u(\sigma,t)d\sigma + H\tilde{\theta}(t-D) - H\cos(2\omega t)\tilde{\theta}(t-D)$$
$$-\frac{4H}{a}[\sin(3\omega t)-\sin(\omega t)]\tilde{\theta}(t-D)\int_0^D u(\sigma,t)d\sigma + \frac{3aH}{4}\sin(\omega t)$$
$$-\frac{aH}{4}\sin(3\omega t) - 2H\cos(2\omega t)\int_0^D u(\sigma,t)d\sigma + [H+H\cos(4\omega t)]\int_0^D u(\sigma,t)d\sigma\Bigg]\Bigg\}\,.$$

Step 3: Average Model of the Closed-Loop System

Now denoting

$$\tilde{\vartheta}(t) = \tilde{\theta}(t-D)\,, \tag{36}$$

the average version of system (33)–(35) is

$$\dot{\tilde{\vartheta}}_{\rm av}(t) = u_{\rm av}(0,t), \tag{37}$$
$$\partial_t u_{\rm av}(x,t) = \partial_x u_{\rm av}(x,t), \quad x\in[0,D]\,, \tag{38}$$
$$\frac{d}{dt}u_{\rm av}(D,t) = -cu_{\rm av}(D,t) + ckH\left[\tilde{\vartheta}_{\rm av}(t) + \int_0^D u_{\rm av}(\sigma,t)d\sigma\right] \tag{39}$$

where in the last line we have simply set all the averages of the sine and cosine functions of ω, 2ω, 3ω and 4ω to zero. Moreover, the filter $c/s+c$ is also represented in the state-space form. The solution of the transport PDE (38) and (39) is given by

$$u_{\rm av}(x,t) = U_{\rm av}(t+x-D)\,. \tag{40}$$

Step 4: Backstepping transformation, its inverse and the target system

Consider the infinite-dimensional backstepping transformation of the delay state

$$w(x,t) = u_{\rm av}(x,t) - kH\left[\tilde{\vartheta}_{\rm av}(t) + \int_0^x u_{\rm av}(\sigma,t)d\sigma\right]\,, \tag{41}$$

which maps the system (37)–(39) into the target system

$$\dot{\tilde{\vartheta}}_{\rm av}(t) = kH\tilde{\vartheta}_{\rm av}(t) + w(0,t)\,, \tag{42}$$
$$w_t(x,t) = w_x(x,t)\,, \quad x\in[0,D]\,, \tag{43}$$
$$w(D,t) = -\frac{1}{c}\partial_t u_{\rm av}(D,t)\,. \tag{44}$$

Using (41) for $x = D$ and the fact that $u_{\text{av}}(D,t) = U_{\text{av}}(t)$, from (44) we get (39), i.e.,

$$U_{\text{av}}(t) = \frac{c}{s+c}\left\{kH\left[\tilde{\vartheta}_{\text{av}}(t) + \int_0^D u_{\text{av}}(\sigma,t)d\sigma\right]\right\}. \tag{45}$$

Let us now consider $w(D,t)$. It is easily seen that

$$w_t(D,t) = \partial_t u_{\text{av}}(D,t) - kHu_{\text{av}}(D,t), \tag{46}$$

where $\partial_t u_{\text{av}}(D,t) = \dot{U}_{\text{av}}(t)$. The inverse of (41) is given by

$$u_{\text{av}}(x,t) = w(x,t) + kH\left[e^{kHx}\tilde{\vartheta}_{\text{av}}(t) + \int_0^x e^{kH(x-\sigma)}w(\sigma,t)d\sigma\right]. \tag{47}$$

Plugging (44) and (47) into (46), we get

$$w_t(D,t) = -cw(D,t) - kHw(D,t) - (kH)^2\left[e^{kHD}\tilde{\vartheta}_{\text{av}}(t) + \int_0^D e^{kH(D-\sigma)}w(\sigma,t)d\sigma\right] \tag{48}$$

Step 5: Lyapunov–Krasovskii Functional

Now consider the following Lyapunov functional

$$V(t) = \frac{\tilde{\vartheta}_{\text{av}}^2(t)}{2} + \frac{a}{2}\int_0^D (1+x)w^2(x,t)dx + \frac{1}{2}w^2(D,t), \tag{49}$$

where the parameter $a > 0$ is to be chosen later. We have

$$\begin{aligned}
\dot{V}(t) &= kH\tilde{\vartheta}_{\text{av}}^2(t) + \tilde{\vartheta}_{\text{av}}(t)w(0,t) + a\int_0^D (1+x)w(x,t)w_x(x,t)dx + w(D,t)w_t(D,t)\\
&= kH\tilde{\vartheta}_{\text{av}}^2(t) + \tilde{\vartheta}_{\text{av}}(t)w(0,t) + \frac{a(1+D)}{2}w^2(D,t)\\
&\quad -\frac{a}{2}w^2(0,t) - \frac{a}{2}\int_0^D w^2(x,t)dx + w(D,t)w_t(D,t)\\
&\le kH\tilde{\vartheta}_{\text{av}}^2(t) + \frac{\tilde{\vartheta}_{\text{av}}^2(t)}{2a} - \frac{a}{2}\int_0^D w^2(x,t)dx + w(D,t)\left[w_t(D,t) + \frac{a(1+D)}{2}w(D,t)\right].
\end{aligned}$$

Reminding that $k > 0$ and $H < 0$, let us choose $a = -1/(kH)$. Then,

$$\dot{V}(t) \le -\frac{1}{2a}\tilde{\vartheta}_{\text{av}}^2(t) - \frac{a}{2}\int_0^D w^2(x,t)dx + w(D,t)\left[w_t(D,t) + \frac{a(1+D)}{2}w(D,t)\right]. \tag{50}$$

Now we consider (50) along with (48). With a completion of squares, we obtain

$$\dot{V}(t) \leq -\frac{1}{4a}\tilde{\vartheta}_{\text{av}}^2(t) - \frac{a}{4}\int_0^D w^2(x,t)dx + a\left|(kH)^2 e^{kHD}\right|^2 w^2(D,t) \tag{51}$$
$$+\frac{1}{a}\left\|(kH)^2 e^{kH(D-\sigma)}\right\|^2 w^2(D,t) + \left[\frac{a(1+D)}{2} - kH\right] w^2(D,t) - cw^2(D,t)\,.$$

To obtain (51), we have used

$$-w(D,t)\left\langle (kH)^2 e^{kH(D-\sigma)}, w(\sigma,t)\right\rangle \leq |w(D,t)|\left\|(kH)^2 e^{kH(D-\sigma)}\right\| \|w(t)\|$$
$$\leq \frac{a}{4}\|w(t)\|^2 + \frac{1}{a}\left\|(kH)^2 e^{kH(D-\sigma)}\right\|^2 w^2(D,t)\,, \tag{52}$$

where the first inequality is the Cauchy–Schwarz and the second is Young's, the notation $\langle\cdot,\cdot\rangle$ denotes the inner product in the spatial variable $\sigma \in [0\,, D]$, on which both $e^{kH(D-\sigma)}$ and $w(\sigma,t)$ depend, and $\|\cdot\|$ denotes the L_2 norm in σ. Then, from (51), we arrive at

$$\dot{V}(t) \leq -\frac{1}{4a}\tilde{\vartheta}_{\text{av}}^2(t) - \frac{a}{4(1+D)}\int_0^D (1+x)w^2(x,t)dx - (c-c^*)w^2(D,t)\,, \tag{53}$$

where

$$c^* = \frac{a(1+D)}{2} - kH + a\left|(kH)^2 e^{kHD}\right|^2 + \frac{1}{a}\left\|(kH)^2 e^{kH(D-\sigma)}\right\|^2\,. \tag{54}$$

From (54), it is clear that an upper bound for c^* can be obtained from known lower and upper bounds of the unknown Hessian H. Hence, from (53), if c is chosen such that $c > c^*$, we obtain

$$\dot{V}(t) \leq -\mu V(t)\,, \tag{55}$$

for some $\mu > 0$. Thus, the closed-loop system is exponentially stable in the sense of the full state norm

$$\left(|\tilde{\vartheta}_{\text{av}}(t)|^2 + \int_0^D w^2(x,t)dx + w^2(D,t)\right)^{1/2}\,, \tag{56}$$

i.e., in the transformed variable $(\tilde{\vartheta}_{\text{av}}\,, w)$.

Step 6: Exponential Stability Estimate (in L_2 norm) for the Average System (37)–(39)

To obtain exponential stability in the sense of the norm

$$\left(|\tilde{\vartheta}_{\text{av}}(t)|^2 + \int_0^D u_{\text{av}}^2(x,t)dx + u_{\text{av}}^2(D,t)\right)^{1/2}, \tag{57}$$

we need to show there exist positive numbers α_1 and α_2 such that $\alpha_1\Psi(t) \le V(t) \le \alpha_2\Psi(t)$ where $\Psi(t) := |\tilde{\vartheta}_{\text{av}}(t)|^2 + \int_0^D u_{\text{av}}^2(x,t)dx + u_{\text{av}}^2(D,t)$, or equivalently,

$$\Psi(t) := |\tilde{\theta}_{\text{av}}(t-D)|^2 + \int_{t-D}^t U_{\text{av}}^2(\tau)d\tau + U_{\text{av}}^2(t), \tag{58}$$

using (36) and (40). This is straightforward to establish using (41), (47), (49) and employing the Cauchy–Schwarz inequality and other calculations, as in the proof of Theorem 2.1 in [11]. Hence, with (55), we get

$$\Psi(t) \le \frac{\alpha_2}{\alpha_1} e^{-\mu t}\Psi(0), \tag{59}$$

which completes the proof of exponential stability.

Step 7: Invoking Averaging Theorem

First, note that the closed-loop system (5) and (18) can be rewritten as

$$\dot{\tilde{\theta}}(t-D) = U(t-D), \tag{60}$$

$$\dot{U}(t) = -cU(t) + c\left\{k\left[G(t) + \hat{H}(t)\int_{t-D}^t U(\tau)d\tau\right]\right\}, \tag{61}$$

where $z(t) = [\tilde{\theta}(t-D), U(t)]^T$ is the state vector. Equation (61) is simply the differential equation of (18). Moreover, from $G(t)$ in (6) and $\hat{H}(t)$ in (8), one has

$$\dot{z}(t) = f(\omega t, z_t), \tag{62}$$

where $z_t(\Theta) = z(t+\Theta)$ for $-D \le \Theta \le 0$ and f is an appropriate continuous functional, such that the averaging theorem by [12] and [13] can be directly applied considering $\omega = 1/\varepsilon$.

From (59), the origin of the average closed-loop system (37)–(39) with transport PDE for delay representation is exponentially stable. Then, according to the averaging theorem [12, 13], for ω sufficiently large, (33)–(35) has a unique exponentially stable periodic solution around its equilibrium (origin) satisfying (19).

Step 8: Asymptotic Convergence to a Neighborhood of the Extremum (θ^*, y^*)

By using the change of variables (36) and then integrating both sides of (22) within the interval $[t, \sigma + D]$, we have

$$\tilde{\vartheta}(\sigma + D) = \tilde{\vartheta}(t) + \int_t^{\sigma+D} u(0, s)ds\,. \tag{63}$$

From (25), we can rewrite (63) in terms of U, namely

$$\tilde{\vartheta}(\sigma + D) = \tilde{\vartheta}(t) + \int_{t-D}^{\sigma} U(\tau)d\tau\,. \tag{64}$$

Now, note that $\tilde{\theta}(\sigma) = \tilde{\vartheta}(\sigma + D)\,,\ \forall \sigma \in [t - D, t]$. Hence,

$$\tilde{\theta}(\sigma) = \tilde{\theta}(t - D) + \int_{t-D}^{\sigma} U(\tau)d\tau\,, \quad \forall \sigma \in [t - D, t]\,. \tag{65}$$

By applying the supremum norm in both sides of (65), we have

$$\begin{aligned}
\sup_{t-D\le\sigma\le t} \left|\tilde{\theta}(\sigma)\right| &= \sup_{t-D\le\sigma\le t} \left|\tilde{\theta}(t - D)\right| + \sup_{t-D\le\sigma\le t} \left|\int_{t-D}^{\sigma} U(\tau)d\tau\right| \\
&\le \sup_{t-D\le\sigma\le t} \left|\tilde{\theta}(t - D)\right| + \sup_{t-D\le\sigma\le t} \int_{t-D}^{t} |U(\tau)|\, d\tau \\
&\le \left|\tilde{\theta}(t - D)\right| + \int_{t-D}^{t} |U(\tau)|\, d\tau \quad \text{(Cauchy-Schwarz)} \\
&\le \left|\tilde{\theta}(t - D)\right| + \left(\int_{t-D}^{t} d\tau\right)^{1/2} \times \left(\int_{t-D}^{t} |U(\tau)|^2\, d\tau\right)^{1/2} \\
&\le \left|\tilde{\theta}(t - D)\right| + \sqrt{D}\left(\int_{t-D}^{t} U^2(\tau)d\tau\right)^{1/2}.
\end{aligned} \tag{66}$$

Now, it is easy to check

$$\left|\tilde{\theta}(t - D)\right| \le \left(\left|\tilde{\theta}(t - D)\right|^2 + \int_{t-D}^{t} U^2(\tau)d\tau\right)^{1/2}, \tag{67}$$

$$\left(\int_{t-D}^{t} U^2(\tau)d\tau\right)^{1/2} \le \left(\left|\tilde{\theta}(t - D)\right|^2 + \int_{t-D}^{t} U^2(\tau)d\tau\right)^{1/2}. \tag{68}$$

Using (67) and (68), one has

$$\left|\tilde{\theta}(t-D)\right|+\sqrt{D}\left(\int_{t-D}^{t}U^2(\tau)d\tau\right)^{1/2}\leq\ (1+\sqrt{D})\left(\left|\tilde{\theta}(t-D)\right|^2+\int_{t-D}^{t}U^2(\tau)d\tau\right)^{1/2} \quad (69)$$

From (66), it is straightforward to conclude that

$$\sup_{t-D\leq\sigma\leq t}\left|\tilde{\theta}(\sigma)\right|\leq(1+\sqrt{D})\left(\left|\tilde{\theta}(t-D)\right|^2+\int_{t-D}^{t}U^2(\tau)d\tau\right)^{1/2} \quad (70)$$

and, consequently,

$$\left|\tilde{\theta}(t)\right|\leq(1+\sqrt{D})\left(\left|\tilde{\theta}(t-D)\right|^2+\int_{t-D}^{t}U^2(\tau)d\tau\right)^{1/2}. \quad (71)$$

Inequality (71) can be given in terms of the periodic solution $\tilde{\theta}^{\Pi}(t-D)$, $U^{\Pi}(\sigma)$, $\forall\sigma\in[t-D,t]$ as follows

$$\left|\tilde{\theta}(t)\right|\leq(1+\sqrt{D})\left(\left|\tilde{\theta}(t-D)-\tilde{\theta}^{\Pi}(t-D)+\tilde{\theta}^{\Pi}(t-D)\right|^2\right.$$
$$\left.+\int_{t-D}^{t}\left[U(\tau)-U^{\Pi}(\tau)+U^{\Pi}(\tau)\right]^2d\tau\right)^{1/2}. \quad (72)$$

By applying Young's inequality and some algebra, the right-hand side of (72) and $\left|\tilde{\theta}(t)\right|$ can be majorized by

$$\left|\tilde{\theta}(t)\right|\leq\sqrt{2}\,(1+\sqrt{D})\left(\left|\tilde{\theta}(t-D)-\tilde{\theta}^{\Pi}(t-D)\right|^2+\left|\tilde{\theta}^{\Pi}(t-D)\right|^2\right.$$
$$\left.+\int_{t-D}^{t}\left[U(\tau)-U^{\Pi}(\tau)\right]^2d\tau+\int_{t-D}^{t}\left[U^{\Pi}(\tau)\right]^2d\tau\right)^{1/2}. \quad (73)$$

From the averaging theorem [12, 13], we have $\tilde{\theta}(t-D)-\tilde{\theta}^{\Pi}(t-D)\to0$ and $\int_{t-D}^{t}\left[U(\tau)-U^{\Pi}(\tau)\right]^2d\tau\to0$, exponentially. Hence,

$$\limsup_{t\to+\infty}|\tilde{\theta}(t)|=\sqrt{2}\,(1+\sqrt{D})\times\left(\left|\tilde{\theta}^{\Pi}(t-D)\right|^2+\int_{t-D}^{t}[U^{\Pi}(\tau)]^2d\tau\right)^{1/2}. \quad (74)$$

From (19) and (74), we can write $\limsup_{t\to+\infty}|\tilde{\theta}(t)|=\mathcal{O}(1/\omega)$. From (4) and reminding that $\theta(t)=\hat{\theta}(t)+S(t)$ with $S(t)=a\sin(\omega(t+D))$, one has that $\theta(t)-\theta^*=\tilde{\theta}(t)+S(t)$. Since the first term in the right-hand side is ultimately of order $\mathcal{O}(1/\omega)$ and the second term is of order $\mathcal{O}(a)$, then (20) is achieved. Finally, from (3) and (20), we get (21). □

4 Newton-Based Extremum Seeking with Delays

The advantages of Newton-based over gradient ES in the absence of delays were deeply studied in [5, 7] and the discussion can be summarized in the fact that the former removes the dependence of the convergence rate on the unknown second derivative (Hessian) of the nonlinear map to be optimized. The guarantee of this property even in the presence of delays was proved in a companion paper [17], where we estimate the Hessian's inverse rather than only the Hessian. In this new predictor design, the delay compensation can be achieved with an arbitrarily assigned convergence rate, thus, improving the controller performance.

In the next theorem, we present the control law for the delay-compensated Newton-based ES illustrated in Fig. 2.

Theorem 2 *The same stability results of Theorem 1 are guaranteed for the maximum seeking Newton algorithm under delays, where the nonlinear map is at least locally quadratic* $y(t) = y^* + \frac{H}{2}(\theta(t-D) - \theta^*)^2$, *with* $y(t)\,,\ \theta(t) \in \mathfrak{R}$ *and* $\theta^*\,, y^*$ *and* $H < 0$ *being unknown scalars. The additive dither is* $S(t) = a\sin(\omega(t+D))$ *and the predictor feedback with perturbation-based estimate of the Hessian's inverse is*

$$U(t) = \frac{c}{s+c}\left\{-k\left[z(t) + \int_{t-D}^{t} U(\tau)d\tau\right]\right\}, \tag{75}$$

$$z(t) = \Gamma(t)G(t)\,, \quad G(t) = \frac{2}{a}\sin(\omega t)y(t)\,, \tag{76}$$

$$\dot{\Gamma} = \omega_r\Gamma - \omega_r\hat{H}\Gamma^2\,, \quad \hat{H}(t) = -\frac{8}{a^2}\cos(2\omega t)y(t)\,, \tag{77}$$

for scalars: $k\,,\ \omega_r > 0$ *arbitrary,* $a > 0$ *arbitrarily small and* $c\,,\ \omega > 0$ *sufficiently large. For more details, see [17, Theorem 1].*

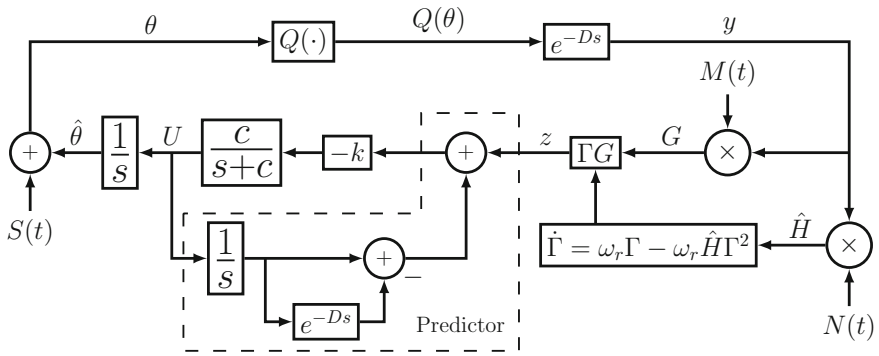

Fig. 2 Block diagram of the basic prediction scheme for output-delay compensation in Newton-based ES. The dither signals are given by $S(t) = a\sin(\omega(t+D))$ and $M(t) = \frac{2}{a}\sin(\omega t)$ and the demodulating signal is $N(t) = -\frac{8}{a^2}\cos(2\omega t)$

5 Simulation Example

In order to evaluate the proposed extremum seeking with delay compensation, the following static quadratic map is considered

$$Q(\theta) = 5 - (\theta - 2)^2\,, \tag{78}$$

subject to an output delay of $D = 5\,\mathrm{s}$. According to (78), the extremum point is $(\theta^*,\ y^*) = (2,\ 5)$ and the Hessian of the map is $H = -2$. We present numerical simulations of the predictor (18), where $\hat{H}$ is given by (8) and $c = 20$. We perform our tests with the following parameters: $a = 0.2$, $\omega = 10$, $k = 0.2$, and $\theta(0) = 0$.

Figure 3 shows the system output $y(t)$ in 3 situations: (a) free of output delays, (b) in the presence of output delay but without any delay compensation and (c) with output-delay and predictor-based compensation.

Figure 4 presents relevant variables for ES. The red curves are shown when the proposed predictor is applied in comparison to the free of delays case (with blue curves). It is clear that the remarkable evolution of our prediction scheme in

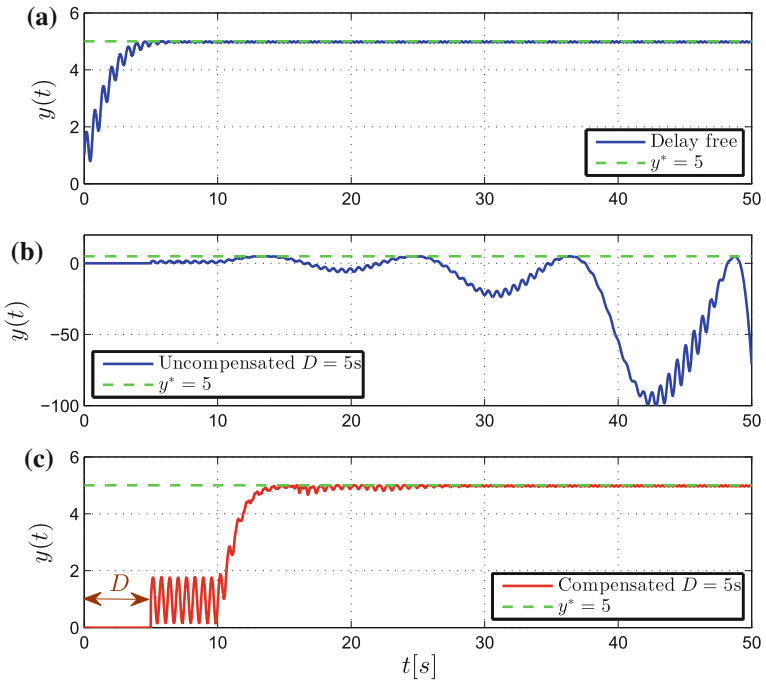

Fig. 3 Gradient-based ES plus output delay (time response of $y(t)$): **a** basic ES works well without delays; **b** ES goes unstable in the presence of delays; **c** predictor fixes this

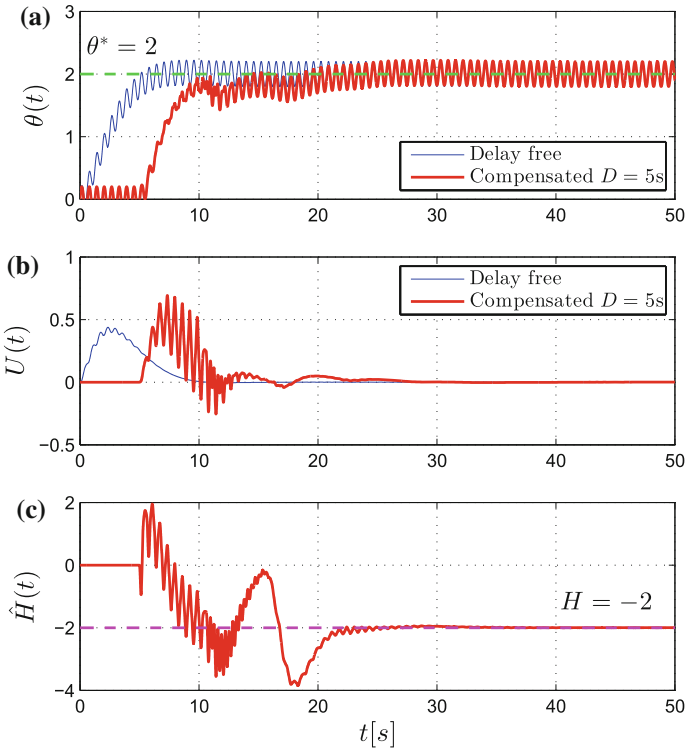

Fig. 4 **Gradient-based ES plus output delay**: **a** time response of the parameter $\theta(t)$; **b** control signal $U(t)$; **c** Hessian's estimate $\hat{H}(t)$

searching the maximizer $\theta^* = 2$ and the perturbation-based Hessian's estimation of $H = -2$.

The issue of robustness to the approximation of the integral terms for prediction was raised by Mondié and Michiels in [10]. It was subsequently showed by Mirkin [18] that it is simply the result of a poor choice of the approximation scheme for the integral. Furthermore, numerical approximation schemes that are robust have been provided recently in [19]. In our simulation results, the safe implementation of Eq. (18) could be verified and the proposed perturbation-based predictor has shown robustness to numerical approximations.

6 Conclusions

Two new predictor feedback strategies with perturbation-based estimate of the Hessian and its inverse are introduced to cope with input–output delays in gradient and Newton-based extremum seeking controllers. The resulting approaches preserve

exponential stability and convergence of the system output to a small neighborhood of the extremum point, despite the presence of actuator and sensor delays. A rigorous demonstration is given by exploring backstepping transformation and averaging theory in infinite dimensions. While the convergence rate of the gradient method is dictated by the unknown Hessian, the Newton-based scheme is independent of it and thus the delay compensation can be achieved with an arbitrarily assigned convergence rate, improving the controller performance. The results presented here are given for scalar plants, but the extension to the multivariable maps with output delays or multiple and distinct input delays can be found in [20] and [21], respectively. Robustness of the predictor feedback to small perturbations in the delay is proved in [22]. Thus, generalization to include uncertain and time-varying delays are possible directions for future research.

Acknowledgements The first author thanks the Brazilian funding agencies CAPES, CNPq, and FAPERJ for the financial support.

References

1. Adetola, V., Guay, M.: Guaranteed parameter convergence for extremum-seeking control of nonlinear systems. Automatica **43**, 105–110 (2007)
2. Tan, Y., Nesić, D., Mareels, I.M.Y., Astolfi, A.: On global extremum seeking in the presence of local extrema. Automatica **45**, 245–251 (2009)
3. Nesić, D., Tan, Y., Moase, W.H., Manzie, C.: A unifying approach to extremum seeking: adaptive schemes based on the estimation of derivatives. In: IEEE Conference on Decision and Control, Atlanta, pp. 4625–4630 (2010)
4. Oliveira, T.R., Hsu, L., Peixoto, A.J.: Output-feedback global tracking for unknown control direction plants with application to extremum-seeking control. Automatica **47**, 2029–2038 (2011)
5. Ghaffari, A., Krstić, M., Nesić, D.: Multivariable Newton-based extremum seeking. Automatica **48**, 1759–1767 (2012)
6. Liu, S.-J., Krstić, M.: Stochastic Averaging and Stochastic Extremum Seeking. Springer (2012)
7. Krstić, M.: Extremum seeking control. In: Samad, T., Baillieul, J. (eds.)Encyclopedia of Systems and Control. Springer (2014)
8. Artstein, Z.: Linear systems with delayed controls: a reduction. IEEE Trans. Autom. Control **27**, 869–879 (1982)
9. Richard, J.-P.: Time-delay systems: an overview of some recent advances and open problems. Automatica **39**, 1667–1694 (2003)
10. Mondié, S., Michiels, W.: Finite spectrum assignment of unstable time-delay systems with a safe implementation. IEEE Trans. Autom. Control **48**, 2207–2212 (2003)
11. Krstić, M.: Delay Compensation for Nonlinear, Adaptive, and PDE Systems. Birkhaüser (2009)
12. Hale, J.K., Lunel, S.M.V.: Averaging in infinite dimensions. J. Integral Equ. Appl. **2**, 463–494 (1990)
13. Lehman, B.: The influence of delays when averaging slow and fast oscillating systems: overview. IMA J. Math. Control Inf. **19**, 201–215 (2002)
14. Khalil, H.K.: Nonlinear Systems. Prentice Hall, 3rd edn. (2002)
15. Tan, Y., Nesić, D., Mareels, I.: On the choice of dither in extremum seeking systems: a case study. Automatica **44**, 1446–1450 (2008)
16. Krstić, M.: Lyapunov tools for predictor feedbacks for delay systems: inverse optimality and robustness to delay mismatch. Automatica **44**, 2930–2935 (2008)

17. Oliveira, T.R., Krstić, M.: Newton-based extremum seeking under actuator and sensor delays. In: 12th IFAC Workshop on Time Delay Systems, Ann Arbor, pp. 304–309 (2015)
18. Mirkin, L.: On the approximation of distributed-delay control laws. Syst. Control Lett. **51**, 331–342 (2004)
19. Karafyllis, I., Krstić, M.: Numerical schemes for nonlinear predictor feedback. Math. Control Signals Syst. **26**, 519–546 (2014)
20. Oliveira, T.R., Krstić, M., Tsubakino, D.: Multiparameter extremum seeking with output delays. In: American Control Conference, Chicago, pp. 152–158 (2015)
21. Oliveira, T.R., Krstić, M., Tsubakino, D.: Extremum seeking subject to multiple and distinct input delays. In: 54th IEEE Conference on Decision and Control, Osaka, pp. 5635–5641 (2015)
22. Bekiaris-Liberis, N., Krstic, M.: Robustness of nonlinear predictor feedback laws to time- and state-dependent delay perturbations. Automatica **49**, 1576–1590 (2013)

Improving Stability Margins via Time-Delayed Vibration Control

A. Galip Ulsoy

Abstract Time-delayed vibration control of a two degree-of-freedom mechanical system approximates state-derivative feedback and reduces sensitivity and improves the stability margins. Additional sensors are not required since state derivatives are approximated using available measurements and time delays. A Lambert W method based design approach is used to solve the resulting delay differential equations. Simulation results demonstrate excellent performance with improved stability margins over state feedback control only.

1 Introduction

Control systems are designed based on nominal plant models, but variations in parameters often occur. Thus, research in robust control design explicitly considers such uncertainties in the design process. For example, use of state-derivative feedback, in addition to state feedback (SF), can reduce closed-loop system sensitivity to plant parameter variations and disturbance inputs Haraldsdottir et al. [7, 8]. However, state plus state-derivative feedback (SSD) is difficult to implement because sensors are needed to measure the state derivatives in addition to the states. Even measuring all the states is too restrictive in many engineering applications. Thus, measuring state derivatives as well as states is often impractical.

Recent research has proposed the use of time delays in the controller to approximate the state derivatives to improve stability margins [11–13]. In this paper that proposed time-delay control (TDC) approach is applied to the vibration control of a two degree-of-freedom (DOF) mechanical system. The simulation results demonstrate significant improvements in stability margins for TDC over SF control only, without requiring any additional sensors.

A.G. Ulsoy (✉)
Mechanical Engineering, University of Michigan, Ann Arbor, MI 48109-2125, USA
e-mail: ulsoy@umich.edu

T. Insperger et al. (eds.), *Time Delay Systems*,
Advances in Delays and Dynamics 7, DOI 10.1007/978-3-319-53426-8_16

2 Theory

A single-input single-output (SISO) linear time invariant (LTI) plant in state equation form can be represented as

$$\dot{\mathbf{x}} = \mathbf{A}\mathbf{x} + \mathbf{B}u; \quad y = \mathbf{C}\mathbf{x} \tag{1}$$

Assuming all states, **x**(t), are measurable a SF controller,

$$u(t) = -\mathbf{K}\mathbf{x}(t) \tag{2}$$

yields the closed-loop system equations

$$\dot{\mathbf{x}} = \mathbf{A}_c\mathbf{x} + \mathbf{B}u = (\mathbf{A} - \mathbf{B}\mathbf{K})\mathbf{x}; \quad y = \mathbf{C}\mathbf{x} \tag{3}$$

If (**A, B**) is controllable, then **K** can be selected (e.g., via optimal control or eigenvalue assignment) to achieve desired closed-loop performance. If all states are not measured, but (**A, C**) is observable, then one can also design a state estimator, or observer, to estimate the states from the output Anderson and Moore [1]. Furthermore, SF controllers achieve not only the desired closed-loop performance, but also excellent robustness as measured by stability margins. However, the use of a state estimator will reduce the stability margins Safonov [10].

2.1 Sensitivity Reduction via State Derivative Feedback

Consider SSD feedback control Haraldsdottir et al. [7] of the system in (1):

$$u(t) = -\mathbf{F}\mathbf{x}(t) - \mathbf{G}\dot{\mathbf{x}}(t) \tag{4}$$

The closed-loop system then becomes

$$\dot{\mathbf{x}}(t) = \mathbf{A}_c\mathbf{x}(t) = (\mathbf{I} + \mathbf{B}\mathbf{G}^{-1})(\mathbf{A} - \mathbf{B}\mathbf{F})\mathbf{x}(t) \tag{5}$$

One can first select **K** in (2) to obtain the desired $\mathbf{A_c}$ in (3), then select **G** based on sensitivity considerations and to ensure invertibility of (**I** + **BG**), and finally determine **F** from (5) given $\mathbf{A_c}$, **G**, **A,** and **B**. The SSD feedback gives exactly the same closed-loop eigenstructure as SF control, but, for appropriate values of **G**, SSD can reduce eigenvalue sensitivity to variations in the parameters of **A** and **B**, improve the stability margins, and also reduce the effects of any external disturbances acting on the system. The benefits of SSD feedback over SF control can be significant Haraldsdottir et al. [7] and Ulsoy [12, 13], however, state derivatives must now be measured in addition to the states.

2.2 Approximation via Time Delay

In practice, it is difficult to measure the state derivatives to implement SSD feedback. Thus, one can implement the following TDC:

$$u(t) = -\mathbf{K_p}\mathbf{x}(t) - \mathbf{K_d}\mathbf{x}(t-h), \tag{6}$$

where h is a constant time delay. The closed-loop system becomes

$$\dot{\mathbf{x}}(t) = (\mathbf{A} - \mathbf{B}\mathbf{K}_p)\mathbf{x}(t) - \mathbf{B}\mathbf{K}_d\mathbf{x}(t-h) = \mathbf{A}_c\mathbf{x}(t) + \mathbf{A}_d\mathbf{x}(t-h) \tag{7}$$

The system in (7) is a retarded delay differential equation (DDE) and has an infinite eigenspectrum. However, as $h \to 0$ (7) can be viewed as an approximation to the closed-loop system in (5) with SSD feedback. Consider the backward difference approximation, for small h

$$\dot{\mathbf{x}}(t) = \frac{\mathbf{x}(t) - \mathbf{x}(t-h)}{h} \tag{8}$$

Then the SSD feedback control can be approximated as

$$\begin{aligned} u(t) &= -\mathbf{F}\mathbf{x}(t) - \mathbf{G}\dot{\mathbf{x}}(t) \\ &\approx -\mathbf{F}\mathbf{x}(t) - (1/h)\mathbf{G}(\mathbf{x}(t) - \mathbf{x}(t-h)) \\ &= -(\mathbf{F} + (1/h)\mathbf{G})\mathbf{x}(t) + (1/h)\mathbf{G}\mathbf{x}(t-h) \end{aligned} \tag{9}$$

Comparing (6) and (9) one obtains

$$\mathbf{K}_p = (\mathbf{F} + (1/h)\mathbf{G}); \quad \mathbf{K}_d = -(1/h)\mathbf{G} \tag{10}$$

If one selects h to be sufficiently small, and $\mathbf{G}$ to reduce sensitivity, the closed-loop system in (7) will have the specified closed-loop eigenstructure and desired performance, as with SF control only, plus reduced sensitivity, as with SSD feedback control. However, (7) is a DDE and its analysis, to select the appropriate value of h and to confirm closed-loop performance and robustness, is challenging.

2.3 Solution of Delay Differential Equations

One would like to see the performance of the closed-loop system in (7) be close to that specified by $\mathbf{A_c}$ in (3) or (5). The system of DDEs in (7) possesses an infinite number of eigenvalues due to the presence of the delay h. However, the overall system response, as in higher order linear systems without delay, will be dominated by the system eigenvalues closest to the imaginary axis; that is the rightmost

eigenvalues in the s-plane. These rightmost eigenvalues will determine stability as well as transient response characteristics, such as settling time and overshoot Yi et al. [19]. A method, based on the Lambert W function, has been developed that enables the analysis of LTI time-delay systems as in (7) to obtain rightmost eigenvalues and the time response Yi et al. [18]. Other DDE analysis tools, e.g., Breda et al. [3], could also be utilized. However, only the Lambert W approach is considered here and is found to be convenient and efficient for the problem at hand. This method, which will be utilized here to establish the performance of the closed-loop system in (7) by computing the rightmost eigenvalues and time response, is briefly summarized below.

The solution to an autonomous system of DDEs, as in (7), can be represented by an infinite series Yi et al. [18]

$$\mathbf{x}(t) = \sum_{k=-\infty}^{\infty} e^{\mathbf{S}_k t}\mathbf{C}_k^I, \tag{11}$$

where the coefficients $\mathbf{C}_k^I$ depend on a pre-shape function $\boldsymbol{\phi}(t)$, $-h \leq t < 0$, and

$$\mathbf{S}_k = \frac{1}{h}\mathbf{W}_k(\mathbf{A_d}h\mathbf{Q}_k) + \mathbf{A_c} \tag{12}$$

are the solution matrices, where the matrix $\mathbf{Q}_k$ satisfies

$$\mathbf{W}_k(\mathbf{A_d}h\mathbf{Q}_k)e^{\mathbf{W}_k(\mathbf{A_d}h\mathbf{Q}_k)+\mathbf{A_c}h} = \mathbf{A_d}h \tag{13}$$

An iterative numerical solution of (13) yields the matrix $\mathbf{Q}_k$, which is then substituted into (12) to obtain $\mathbf{S}_k$. The rightmost eigenvalues of (7) can then be obtained from the eigenvalues of $\mathbf{S}_k$, for $k = 0, \pm 1, \ldots, \pm m$, where $m =$ nullity $(\mathbf{A_d})$. The series solution in (11) converges as k is increased.

Software routines available in the *LambertW_DDE Toolbox* can be utilized to compute both the rightmost eigenvalues and the time response Yi et al. [16]. The methods and software have been successfully applied to a variety of engineering problems Yi et al. [17–19] and Ulsoy [12]. However, in some cases convergence problems can occur in numerically solving (13) for $\mathbf{Q_k}$ Wei et al. [14]. This convergence issue has also been discussed, for a second-order DDE example, in Cepeda-Gomez and Michiels [4, 5] where it is shown that the initialization of $\mathbf{Q_k}$ has an important influence on which eigenvalues the method converges to. In this paper an initial value of $\mathbf{Q}_k = e^{-h\mathbf{A}_c}$ has been used throughout without any significant convergence problems. All the cases considered for the two DOF mechanical system in Sect. 3 converged to the rightmost eigenvalues, but some cases were found to converge more rapidly than others.

2.4 Stability Margins

A standard measure of robustness for control of SISO systems are the gain margin (*GM*) and phase margin (*PM*). For a closed-loop unity feedback system, as in Fig. 1, these stability margins are determined from a frequency response (i.e., Bode or Nyquist) plot of the loop transfer function *C(s)G(s)*. A typical control design rule-of-thumb is to specify $GM > 6$ dB and $PM > 30 - 40°$. The time-delay margin is characterized by the minimum time delay $h > 0$ such that the closed-loop system becomes unstable. For example, a pure time delay of h seconds has the transfer function $G_D(s) = e^{-sh}$, which in the frequency domain has a constant gain of one (i.e., 0 dB) and a phase of $-\omega h$. When $\omega h = \pi$ radians the delay introduces a phase lag of 180°. Thus, if the desired closed-loop bandwidth is ω_{bw}, then delays of $h \ll \pi/\omega_{bw}$ are desired Franklin et al. [6]. Published research on stability margins for systems with time delays is limited Bergmans [2] and Lee et al. [9].

3 Two DOF Mechanical Vibration Control

Consider a two DOF mechanical vibration control problem, similar to the robust control benchmark problem in Wie and Bernstein [15]. The system is shown in Fig. 2, and the sensor (on mass m_2) and actuator (on mass m_1) are noncolocated. Such noncolocated systems are known to be sensitive to model uncertainty, and have been the subject of numerous robust control studies. The system can be described by the state equations

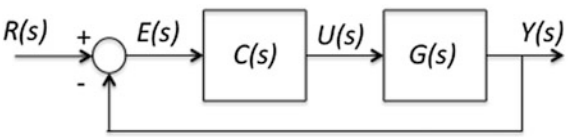

Fig. 1 Block diagram of SISO unity feedback control system with controller *C(s)* and plant *G(s)*

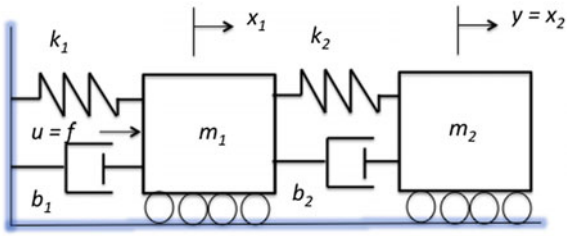

Fig. 2 Schematic of a two degree-of-freedom mass–spring–damper system

$$\begin{Bmatrix} \dot{x}_1 \\ \dot{x}_2 \\ \dot{x}_3 \\ \dot{x}_4 \end{Bmatrix} = \begin{bmatrix} 0 & 0 & 1 & 0 \\ 0 & 0 & 0 & 1 \\ a_{31} & a_{32} & a_{33} & a_{34} \\ a_{41} & a_{42} & a_{43} & a_{44} \end{bmatrix} \begin{Bmatrix} x_1 \\ x_2 \\ x_3 \\ x_4 \end{Bmatrix} + \begin{Bmatrix} 0 \\ 0 \\ (\frac{1}{m_1}) \\ 0 \end{Bmatrix} u$$

$$a_{31} = -(\frac{k_1 + k_2}{m_1}); \quad a_{32} = (\frac{k_2}{m_1}); \quad a_{33} = -(\frac{b_1 + b_2}{m_1});$$

$$a_{34} = (\frac{b_2}{m_1}); \quad a_{41} = (\frac{k_2}{m_2}); \quad a_{42} = -(\frac{k_2}{m_2}); \tag{14}$$

$$a_{43} = (\frac{b_2}{m_2}); \quad a_{44} = -(\frac{b_2}{m_2})$$

$$y = \begin{bmatrix} 0 & 1 & 0 & 0 \end{bmatrix} \begin{Bmatrix} x_1 \\ x_2 \\ x_3 \\ x_4 \end{Bmatrix}$$

and the transfer function of the system is given by

$$G(s) = \frac{Y(s)}{U(s)}$$

$$= \frac{(1/m_1)((b_2/m_2)s + (k_2/m_2))}{s^4 + a_3 s^3 + a_2 s^2 + a_1 s + a_0} \tag{15}$$

$$a_3 = ((\frac{b_1 + b_2}{m_1}) + (\frac{b_2}{m_2})); \quad a_2 = ((\frac{k_1 + k_2}{m_1}) + (\frac{k_2}{m_2}) + (\frac{b_1 b_2}{m_1 m_2}))$$

$$a_1 = (\frac{b_2 k_1 + k_2 b_1}{m_1 m_2}); \quad a_0 = (\frac{k_1 k_2}{m_1 m_2})$$

where $y = x_2$ and $u = f$. With parameter values $m_1 = m_2 = k_1 = k_2 = 1$ and $b_1 = b_2 = 0.1$, the open-loop system response is lightly damped (i.e., open-loop poles at $-0.1309 \pm 1.6127i$ and $-0.0191 \pm 0.6177i$), with a 2% settling time of $t_s \approx 210$ s. The goal is to design a controller to achieve a closed-loop settling time of $t_s \approx 4$ s with no overshoot (i.e., dominant closed-loop damping ratio $\zeta \approx 1$).

The SF controller, $u = -\mathbf{Kx} = -K_1 x_1 - K_2 x_2 - K_3 x_3 - K_4 x_4$, which requires measurement of the position and velocity of both masses, gives the closed-loop system equations as in (14) but with $u = 0$ and

$$a_{31} = -(\frac{k_1 + k_2 + K_1}{m_1}); \quad a_{32} = (\frac{k_2 - K_2}{m_1})$$

$$a_{33} = -(\frac{b_1 + b_2 + K_3}{m_1}); \quad a_{44} = (\frac{b_2 - K_4}{m_1}) \tag{16}$$

The SF controller can also be represented in transfer function form (Fig. 1) as

$$C(s) = (K_1(\frac{s^2 + (b_2/m_2)s + (k_2/m_2)}{(b_2/m_2)s + (k_2/m_2)}) + K_2 + K_3 s(\frac{s^2 + (b_2/m_2)s + (k_2/m_2)}{(b_2/m_2)s + (k_2/m_2)}) + K_4 s) \tag{17}$$

Selecting the desired closed-loop eigenvalues at $s_1 = s_2 = -2$, and $s_3 = s_4 = -2.5$, gives the gains $\mathbf{K} = [23 \quad 1 \quad 8.7 \quad 33.7]$. The closed-loop response, with $t_s \approx 4$ s and no overshoot as desired, is shown in Fig. 3. The stability margins can be determined from the Bode plot of *C(s)G(s)* in Fig. 4 to be $GM = \infty$ and $PM = 71.8°$, so this system has the desired performance as well as excellent stability margins. The SF controller requires measurement of all of the four states (i.e., position and velocity of both masses) to implement.

3.1 SSD Control of Two DOF Mechanical System

For the same two DOF system next consider the SSD feedback controller

$$\begin{aligned} u &= -\mathbf{F}\mathbf{x} - \mathbf{G}\dot{\mathbf{x}} \\ &= -F_1 x_1 - F_2 x_2 - F_3 x_3 - F_4 x_4 \\ &\quad - G_1 \dot{x}_1 - G_2 \dot{x}_2 - G_3 \dot{x}_3 - G_4 \dot{x}_4 \end{aligned} \tag{18}$$

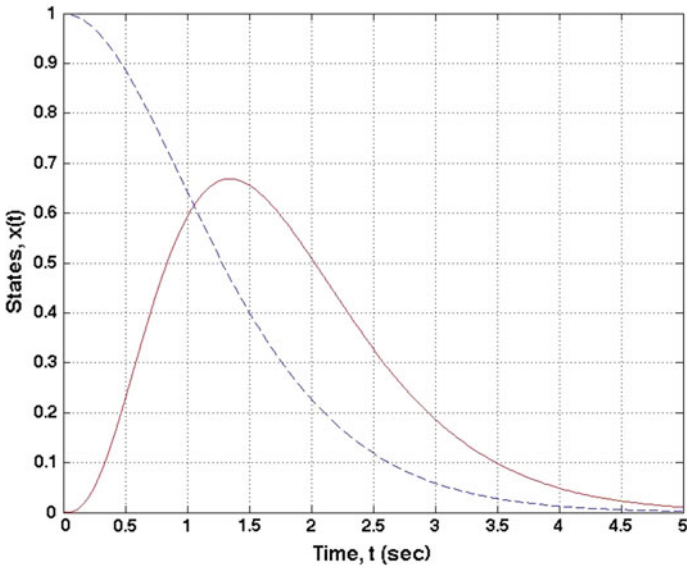

Fig. 3 Response x(t) of two DOF system with SF control ($K_1 = 23$, $K_2 = 1$, $K_3 = 8.7$, $K_4 = 33.7$) to initial condition $x(0) = (0\ 1\ 0\ 0)^T$. *Solid red line*: x_1, *dashed blue line*: x_2

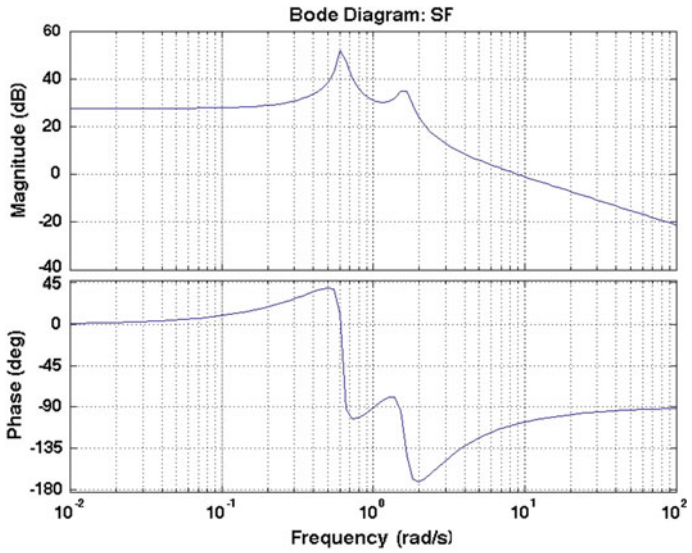

Fig. 4 Loop transfer function Bode plot for SF control ($K_1 = 23$, $K_2 = 1$, $K_3 = 8.7$, $K_4 = 33.7$) of a two DOF system. $GM = \infty$ and $PM = 71.8°$

The SSD controller requires measurement of positions, velocities, and accelerations of both masses and its transfer function is

$$\begin{aligned} C(s) = &(F_1(\frac{s^2 + (b_2/m_2)s + (k_2/m_2)}{(b_2/m_2)s + (k_2/m_2)}) + F_2 \\ &+ (F_3 + G_1)s(\frac{s^2 + (b_2/m_2)s + (k_2/m_2)}{(b_2/m_2)s + (k_2/m_2)}) \\ &+ (F_4 + G_2)s + G_3 s^2(\frac{s^2 + (b_2/m_2)s + (k_2/m_2)}{(b_2/m_2)s + (k_2/m_2)}) + G_4 s^2 \end{aligned} \tag{19}$$

The closed-loop system becomes as in (14), with $u = 0$, and

$$\begin{aligned} a_{31} &= -[k_1 + k_2 + F_1 + k_2(G_4/m_2)]/(m_1 + G_3); \\ a_{32} &= [k_2 - F_2 + k_2(G_4/m_2)]/(m_1 + G_3); \\ a_{33} &= -[G_1 + b_1 + b_2 + F_3 + b_2(G_4/m_2)]/(m_1 + G_3); \\ a_{34} &= -[G_2 - b_2 + F_4 - b_2(G_4/m_2)]/(m_1 + G_3); \end{aligned} \tag{20}$$

To achieve the same closed-loop eigenvalues (i.e., −2, −2, −2.5, and −2.5) as with SF, select **G**, then determine **F** from

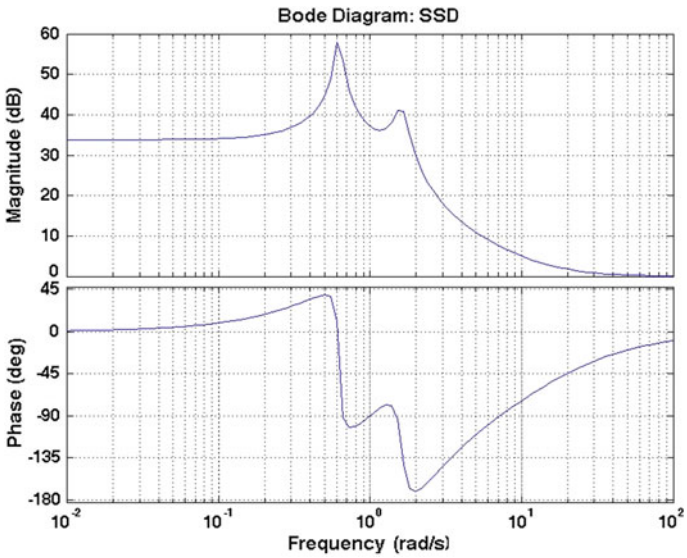

Fig. 5 Loop transfer function Bode plot for SSD control of a two DOF system. $GM = \infty$ and $PM = 180°$. (improvement in PM of 108.2°. over SF control)

$$\begin{aligned} F_1 &= -a(m_1 + G_3) - k_2(G_4/m_2) - k_1 - k_2 \\ F_2 &= -b(m_1 + G_3) + k_2(G_4/m_2) + k_2 \\ F_3 &= -c(m_1 + G_3) - G_1 - b_2(G_4/m_2) - b_1 - b_2 \\ F_4 &= -d(m_1 + G_3) - G_2 + b_2(G_4/m_2) + b_2 \end{aligned} \tag{21}$$

Selecting $G_1 = G_2 = G_4 = 0$ and $G_3 = 1.0$, one obtains $F_1 = 48$, $F_2 = 1$, $F_3 = 17.6$, and $F_4 = 67.3$ to achieve the same closed-loop $\mathbf{A_c}$ as for SF control, and exactly the same response as in Fig. 3, but with stability margins of $GM = \infty$ and $PM = 180°$ (Fig. 5). So the system with SSD control has a 108.2° increase in the PM compared to state feedback only. The disadvantage is that now one needs to measure not only positions and velocities of the two masses, but also their accelerations to implement SSD control. In the next section, the use of the approximation in (8) is considered to achieve improved stability margins compared to state feedback only, but using only measurement of positions and velocities.

3.2 Approximate SSD Control of Two DOF System

Consider the SSD controller in the previous section, but approximate the state derivative term using (8). The resulting TDC (i.e., approximate SSD control) is

$$
\begin{aligned}
u(t) = & -\mathbf{K_p}\mathbf{x}(t) - \mathbf{K_d}\mathbf{x}(t-h) = \\
& -K_{p1}x_1(t) - K_{p2}x_2(t) - K_{p3}x_3(t) - K_{p4}x_4(t) \\
& -K_{d1}x_1(t-h) - K_{d2}x_2(t-h) - K_{d3}x_3(t-h) - K_{d4}x_4(t-h)
\end{aligned} \tag{22}
$$

This controller only requires measurement of positions and velocities of the two masses (i.e., same as SF control) and has the transfer function

$$
\begin{aligned}
C(s) = & [(K_{p1} + K_{d1}e^{-sh})(\frac{s^2 + (b_2/m_2)s + (k_2/m_2)}{(b_2/m_2)s + (k_2/m_2)}) \\
& + (K_{p2} + K_{d2}e^{-sh}) \\
& + (K_{p3} + K_{d3}e^{-sh})s(\frac{s^2 + (b_2/m_2)s + (k_2/m_2)}{(b_2/m_2)s + (k_2/m_2)}) \\
& + (K_{p4} + K_{d4}e^{-sh})s]
\end{aligned} \tag{23}
$$

The closed-loop system is given by

$$
\dot{\mathbf{x}}(t) = \mathbf{A_c}\mathbf{x}(t) + \mathbf{A_d}\mathbf{x}(t-h) \tag{24}
$$

where all elements of $\mathbf{A_c}$ and $\mathbf{A_d}$ are zero, except for

$$
\begin{aligned}
& a_{c13} = a_{c24} = 1; \quad a_{c31} = -(\frac{k_1 + k_2 + K_{p1}}{m_1}) \\
& a_{c32} = (\frac{k_2 - K_{p2}}{m_1}); \quad a_{c33} = -(\frac{b_1 + b_2 + K_{p3}}{m_1}) \\
& a_{c34} = (\frac{b_2 + K_{p4}}{m_1}); \quad a_{c41} = (\frac{k_2}{m_2}); \quad a_{c42} = -(\frac{k_2}{m_2}) \\
& a_{c43} = (\frac{b_2}{m_2}); \quad a_{c44} = -(\frac{b_2}{m_2}); \quad a_{d31} = -(\frac{K_{d1}}{m_1}) \\
& a_{d32} = -(\frac{K_{d2}}{m_1}); \quad a_{d33} = -(\frac{K_{d3}}{m_1}); \quad a_{d34} = -(\frac{K_{d4}}{m_1})
\end{aligned} \tag{25}
$$

The controller gains $\mathbf{K_p}$ and $\mathbf{K_d}$ are determined from (10). For example, using the same SSD gains $\mathbf{F}$ and $\mathbf{G}$ as in the previous subsection, one obtains the gains $K_{d1} = K_{d2} = K_{d4} = 0$, $K_{d3} = -G_3/h = -1/h$, $K_{p1} = F_1$, $K_{p2} = F_2$, $K_{p4} = F_4$, and $K_{p3} = F_3 + G_3/h = F_3 + 1/h$.

Table 1 presents results for selected values of delay h. The closed-loop response of the system with approximate SSD control for $h = 0.1$ is almost identical to the response with SF control in Fig. 3. The loop transfer function Bode plot for $h = 0.1$ is shown in Fig. 6. Note that for $h = 0.1$ s the $PM = 80°$, which is 8.2° larger than the SF control. This improvement in PM increases as h becomes smaller (Table 1), and the gain margin is infinite.

Table 1 Gains, rightmost eigenvalues, and phase margins for system in (24) with TDC (i.e., approximate SSD control) with $G_1 = G_2 = G_4 = 0$ and $G_3 = 1.0$ for selected values of h. As $h \to 0$ the PM increases and the rightmost eigenvalues approach the desired values of -2.0 and -2.5

Time delay h	Gains K_p & K_d	Rightmost eigenvalues	PM (deg)
0.001	$K_{d1} = K_{d2} = K_{d4} = 0$; $K_{d3} = -1000$; $K_{p1} = 48$; $K_{p2} = 1$; $K_{p3} = 1017.6$; $K_{p4} = 67.3$	$-1.92 \pm 0.16i$ $-2.57 \pm 0.30i$	164
0.005	$K_{d1} = K_{d2} = K_{d4} = 0$; $K_{d3} = -200$; $K_{p1} = 48$; $K_{p2} = 1$; $K_{p3} = 217.6$; $K_{p4} = 67.3$	$-1.85 \pm 0.22i$ $-2.62 \pm 0.52i$	146
0.01	$K_{d1} = K_{d2} = K_{d4} = 0$; $K_{d3} = -100$; $K_{p1} = 48$; $K_{p2} = 1$; $K_{p3} = 117.6$; $K_{p4} = 67.3$	$-1.79 \pm 0.26i$ $-2.64 \pm 0.68i$	134
0.05	$K_{d1} = K_{d2} = K_{d4} = 0$; $K_{d3} = -20$; $K_{p1} = 48$; $K_{p2} = 1$; $K_{p3} = 37.6$; $K_{p4} = 67.3$	$-1.63 \pm 0.34i$ $-2.58 \pm 1.20i$	95.1
0.1	$K_{d1} = K_{d2} = K_{d4} = 0$; $K_{d3} = -10$; $K_{p1} = 48$; $K_{p2} = 1$; $K_{p3} = 27.6$; $K_{p4} = 67.3$	$-1.54 \pm 0.38i$ $-2.43 \pm 1.49i$	80

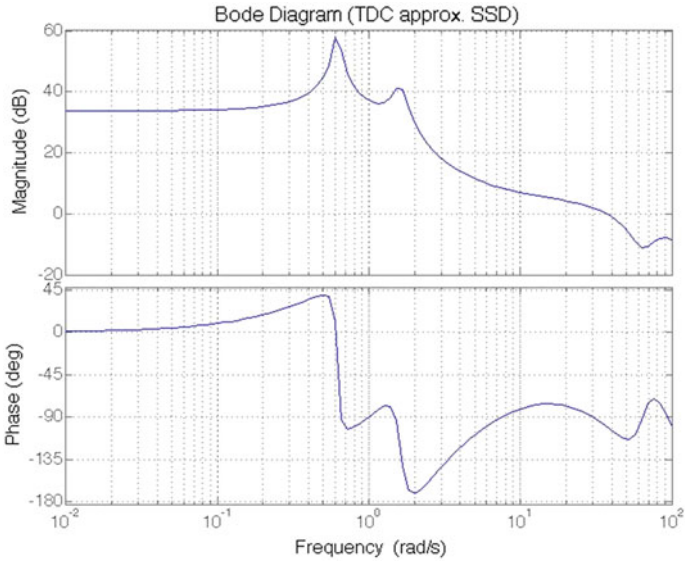

Fig. 6 Loop transfer function Bode plot for TDC (i.e., approximate SSD control, $h = 0.1$) of two DOF system. $GM = \infty$, $PM = 80°$. (improvement in PM of 8.2°. over SF control)

4 Summary and Conclusions

This simulation study has demonstrated that time delays can be used to reduce sensitivity and improve robustness by approximating the state derivatives in a SSD feedback controller. First an ideal SSD controller, assuming measurement of state derivatives, is designed Haraldsdottir et al. [7]. Then the state derivatives are approximated with a time delay using backward differencing. Recently developed methods and software, based on the Lambert W function approach for analysis of time-delay systems, are used to help select a suitable delay time, h, for a specific SSD gain, $\mathbf{G}$ Yi et al. [16]. The proposed method is demonstrated by application to the SISO vibration control of a two DOF mechanical system, with only measurement of positions and velocities of both masses. Simulations show that the specified performance can be achieved with improved stability margins for TDC when compared to SF control only.

The key topic for future research is to consider the effects of output measurement noise. The extension of the results presented here to multi-input multi-output LTI systems, and to observer-based controllers, appears to be relatively straightforward but is also a topic for future research. As is the "design problem" where given a desired PM and/or GM one can determine the gains for the TDC and the appropriate delay time h. One could also consider other (e.g., higher order) approximations in place of Eq. (8).

References

1. Anderson, B.D.O., Moore, J.B.: Optimal Control: Linear Quadratic Methods. Prentice-Hall (1990)
2. Bergmans, J.W.M.: Effect of loop delay on phase margin of First-Order and Second-Order control loops. IEEE Trans. Circ. Syst. **52**(10), 621–625 (2005)
3. Breda, D., Maset, S., Vermiglio, R.: TRACE-DDE: a tool for robust analysis and characteristic equations for delay differential equations. In: Loiseau, J.J., Michiels, W., Niculescu, S., Sipahi, R. (eds.), Topics in Time Delay Systems, pp. 145–155. Springer (2009)
4. Cepeda-Gomez, R., Michiels, W.: Special cases in using the Matrix Lambert W Function for the stability analysis of Higher-Order linear systems with time delay. In: Proceedings of the 12th IFAC Workshop on Time Delay Systems, Ann Arbor, MI. IFAC-PapersOnLine, vol. 48, No. 12, pp. 7–12 (2015)
5. Cepeda-Gomez, R., Michiels, W.: Some special cases in the stability analysis of Multi-Dimensional Time-Delay systems using the Matrix Lambert W Function. Automatica **53**, 339–345 (2015)
6. Franklin, G.F., Powell, J.D., Emami-Naeini, A.: Feedback Control of Dynamic Systems. Pearson Prentice-Hall (2010)
7. Haraldsdottir, A., Kabamba, P.T., Ulsoy, A.G.: Sensitivity reduction by state derivative feedback. ASME J. Dyn. Syst. Meas. Control **110**(1), 84–93 (1988)
8. Haraldsdottir, A., Kabamba, P.T., Ulsoy, A.G.: Control of linear systems by output proportional plus derivative feedback. ASME J. Dyn. Syst. Meas. Control **112**(1), 27–34 (1990)
9. Lee, T., Watkins, J.M., Emami, T.: A Unified approach for stabilization of arbitrary order Continuous-Time and Discrete-Time transfer functions with delay. In: Proceedings of the IEEE Conference on Decision and Control, pp. 2100–2105 (2007)
10. Safonov, M.G.: Stability and Robustness of Multivariable Feedback Systems. MIT Press (1980)
11. Ulsoy, A.G.: Improving stability margins via time delay control. In: Proceedings of ASME IDETC, Portland, OR, Paper DETC2013-12076 (2013)
12. Ulsoy, A.G.: Time-Delayed control of SISO systems for improved stability margins. ASME J. Dyn. Syst. Measur. Control **137**(4), 12 (2015)
13. Ulsoy, A.G.: Time-Delayed vibration control of Two Degree-Of-Freedom mechanical system for improved stability margins. In: Proceedings of the 12th IFAC Workshop on Time Delay Systems, Ann Arbor, MI. IFAC-PapersOnLine, vol. 48, No. 12, pp. 1–6 (2015)
14. Wei, F., Bachrathy, D., Orosz, G., Ulsoy, A.G.: Spectrum design using distributed delay. Int. J. Dyn. Control **2**(2), 26–234 (2014)
15. Wie, B., Bernstein, D.S.: Benchmark problem for robust control design (1992 ACC Version). In: Proceedings of American Control Conference, pp. 2047–2048 (1992)
16. Yi, S., Duan, S., Nelson, P.W., Ulsoy, A.G.: Analysis and control of time delay systems using the lambert WDDE toolbox. In: Vyhlidal, T., Lafay, J.F., Sipahi, R. (eds.) Delay Systems: From Theory to Numerics and Applications, vol. 1 of the Series Advances in Delays and Dynamics, pp. 271–284. Springer (2014)
17. Yi, S., Nelson, P.W., Ulsoy, A.G.: Design of Observer-Based feedback control for Time-Delay systems with application to automotive powertrain control. J. Franklin Inst. **347** (1), 358–376 (2010)
18. Yi, S., Nelson, P.W., Ulsoy, A.G.: Time Delay Systems: Analysis and Control using the Lambert W Function. World Scientific (2010)
19. Yi, S., Nelson, P.W., Ulsoy, A.G.: Robust control and Time-Domain specifications for systems of delay differential equations via eigenvalue assignment. ASME J. Dyn. Syst. Meas. Control **132**(3), 7 (2010)

A Delay-Based Spacing Policy for Vehicle Platooning: Analysis and Control

B. Besselink and K.H. Johansson

Abstract Reducing inter-vehicular distances and the formation of groups of closely spaced vehicles have the potential to increase traffic flow, reduce congestion, and reduce fuel consumption. In this chapter, such vehicle platoons subject to a delay-based spacing policy are considered and the design of distributed controllers is pursued. Specifically, it is shown that the use of the delay-based spacing policy ensures that all vehicles in the platoon track the same velocity profile in the spatial domain, which offers advantages as road properties such as hills, bends, or road speed limits are specified in this domain. The proposed controller exploits delayed information about the preceding vehicle to achieve string-stable platoon behavior. In addition, a relaxation of the delay-based spacing policy is presented that exploits more information about the preceding vehicle. This extended delay-based spacing policy is shown to lead to improved platoon behavior. The results are illustrated by means of simulations.

1 Introduction

Platooning amounts to the formation of automatically controlled groups of closely spaced vehicles, which has the potential to increase traffic flow and reduce congestion [1]. Moreover, platooning offers a reduced aerodynamic drag and therefore reduces fuel consumption and emissions, particularly for heavy-duty vehicles [2]. These clear economical and ecological advantages have led to a large interest in the efficient control of vehicle platoons, with an early work given by [3]. Many results have followed since, e.g., [4, 5].

B. Besselink (✉)
Johann Bernoulli Institute for Mathematics and Computer Science,
University of Groningen, Groningen, The Netherlands
e-mail: b.besselink@rug.nl

K.H. Johansson
Department of Automatic Control and ACCESS Linnaeus Centre,
KTH Royal Institute of Technology, Stockholm, Sweden
e-mail: kallej@kth.se

T. Insperger et al. (eds.), *Time Delay Systems*,
Advances in Delays and Dynamics 7, DOI 10.1007/978-3-319-53426-8_17

The so-called spacing policy, which specifies the desired inter-vehicular distance as a function of the velocity of two neighboring vehicles, largely determines the dynamics of a platoon and is therefore of crucial importance. The most common examples are the constant spacing [6] and constant headway [7, 8] policies. However, experiments with heavy-duty vehicles driving over hilly terrain in [2] have shown that these spacing policies might lead to undesirable platoon behaviors as they might require follower vehicles to accelerate while climbing a hill in an attempt to maintain the desired gap to their predecessor. Due to limited engine power, this might be infeasible. Fundamentally, these undesired dynamics are due to the fact that the constant spacing and constant headway policies do not guarantee that all vehicles in a platoon track the same velocity profile in the spatial domain. As the required velocity profile of a platoon is constrained by the spatial domain (due to, e.g., hills, bends, or road speed limits), this provides a fundamental limitation for the use of these spacing policies in practice.

These aspects have led to the analysis of the so-called delay-based spacing policy in [9] (see also [10] for an early discussion on spacing policies). In this policy, a vehicle tracks a time-delayed version of the trajectory of its predecessor, which can be shown to lead to velocity profiles that are equal in the spatial domain. In fact, the analysis and control design in [9] is performed using space (rather than time) as the independent variable.

This chapter builds on the work of [9], but takes a time-domain perspective. This leads to the following contributions.

First, distributed controller design for vehicle platooning in the time domain is presented, which leads to a controller that is easier to interpret and implement. To this end, an alternative characterization of the delay-based spacing policy is exploited. In addition, it is shown that a relaxation of the delay-based spacing policy on the basis of the velocity tracking error leads to string-stable platoon behavior, implying that perturbations do not amplify as they propagate through the platoon. Here, it is also observed that tracking of the delay-based spacing policy only requires time-delayed information about the preceding vehicle, making this approach inherently robust to (small) delays in wireless communication between vehicles.

Second, a further relaxation of the delay-based spacing policy is introduced that exploits more information about the preceding vehicle in the control design. In particular, rather than only using delayed information, a distributed-delay approach is taken in which also the current state of the predecessor is included. It is shown that the use of this additional information can lead to improved platoon performance in the sense that the propagation of perturbations through the platoon can be further suppressed.

Before developing the points introduced above, it is stressed that the role of delays is different than in other works on delays in vehicle systems. Namely, in these works, the delay is generally regarded as a detrimental effect as a result of wireless inter-vehicle communication (see, e.g., [11, 12]), whereas, in the current work, the delay specifies the desired inter-vehicle spacing.

The remainder of this chapter is organized as follows. Section 2 introduces the delay-based spacing policy that is used throughout this chapter, whereas control

design and analysis for this spacing policy is presented in Sect. 3. A distributed-delay approach to improve platoon performance is presented in Sect. 4. Sections 5 and 6 present a numerical evaluation of the proposed control strategies and the conclusions, respectively.

2 A Delay-Based Spacing Policy for Platooning

The dynamics of a platoon of vehicles is largely determined by the spacing policy, which specifies the desired inter-vehicular distance within a platoon, as illustrated in Fig. 1. With s_i and $s_{\text{ref},i}$ the actual and desired position, respectively, of the i-th vehicle in the platoon, the delay-based spacing policy

$$s_{\text{ref},i}(t) = s_{i-1}(t - \Delta t), \tag{1}$$

is considered, with delay $\Delta t > 0$. In this spacing policy, which is discussed in [9] (see also [10]), a vehicle tracks a time-delayed version of the trajectory of its predecessor. When this spacing policy is perfectly tracked, each vehicle in the platoon achieves the same velocity on the same point on the road. This is formalized as follows [9].

Lemma 1 *Consider the kinematics* $\dot{s}_i(t) = v_i(t)$ *and assume* $s_i(t) = s_{\text{ref},i}(t)$ *and* $v_i(t) > 0$ *for all* $t \in \mathbb{R}$. *Then, (1) holds if and only if,*[1] *for all s,*

$$v_i(s) = v_{i-1}(s). \tag{2}$$

Lemma 1 provides the main motivation for the use of the delay-based spacing policy (1). Namely, the desired velocity of a vehicle is generally determined by spatial properties such as the road speed limit, but also bends and hills. It is therefore important to reflect this in the spacing policy, especially for large platoons. Existing spacing policies as the constant spacing [6] and constant headway [7, 8] policies do not share the property (2) and, as a result, might result in undesirable or even infeasible platoon behavior. An example is given by heavy-duty vehicles driving over a hilly road, where the last vehicle in a platoon does not always experience the same road grade as the first vehicle in the platoon. As a result, the last vehicle might not have sufficient engine power to maintain the platoon formation when, for example, a constant inter-vehicle spacing is required. This effect is observed in experiments in [2], whereas a more thorough motivation for the use of the delay-based spacing policy (1) can be found in [9].

In this work, the synthesis of distributed controllers for a platoon formation is pursued according to the delay-based spacing policy. Specifically, motivated by the above discussion, the control objectives are twofold. Namely, a control strategy is sought that, first, ensures that each vehicle in the platoon tracks a desired reference

[1] The slight abuse of notation $v_i(t)$ and $v_i(s)$ is used to indicate the velocity of vehicle i as a function of time and space, respectively.

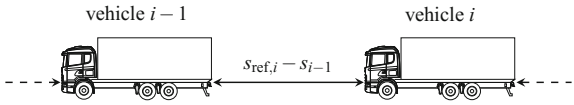

Fig. 1 Desired spacing policy $s_{\mathrm{ref},i}(t) - s_{i-1}(t)$ between vehicles in a platoon

velocity profile $v_{\mathrm{ref}}(\cdot)$ specified in the spatial domain, and, second, maintains a platoon formation by tracking the desired delay-based spacing policy (1).

Here, it is noted that these two objectives are aligned due to Lemma 1. Finally, the following assumption is made on the reference velocity profile.

Assumption 1 The reference velocity profile $v_{\mathrm{ref}}(\cdot)$ satisfies (for some $v_{\min}$) $v_{\mathrm{ref}}(s) \geq v_{\min} > 0$ for all $s \geq 0$ and is twice continuously differentiable.

3 Platoon Control Design and Stability Analysis

A platoon of $N+1$ vehicles is considered, where the index set $\mathscr{I}_0 := \{0, 1, \ldots, N\}$ represents the lead vehicle with index 0 and the follower vehicles with indices in the set $\mathscr{I} := \{1, 2, \ldots, N\}$. Following, e.g., [5, 13], each vehicle is modeled as

$$\begin{aligned} \dot{s}_i(t) &= v_i(t), \\ \dot{v}_i(t) &= a_i(t), \\ \tau \dot{a}_i(t) &= -a_i(t) + u_i(t). \end{aligned} \tag{3}$$

Here, $s_i(t) \in \mathbb{R}$, $v_i(t) \in \mathbb{R}$, and $a_i(t) \in \mathbb{R}$ denote the position, velocity, and acceleration of vehicle $i \in \mathscr{I}_0$, respectively. The control input $u_i(t) \in \mathbb{R}$ represents the desired acceleration, whereas the final equation in (3) can be regarded as the actuator dynamics of the vehicle with time constant $\tau > 0$. The dynamics (3) can be the result of applying feedback linearization to a more complex nonlinear vehicle model, see [5].

As stated in Sect. 2, the design of a controller is pursued that tracks, first, the desired velocity profile $v_{\mathrm{ref}}(\cdot)$ specified in the spatial domain, and, second, the delay-based spacing policy (1). In order to achieve the first objective, the relative velocity error e_i is introduced as

$$e_i(t) := \frac{v_i(t)}{v_{\mathrm{ref}}(s_i(t))} - 1, \tag{4}$$

for each $i \in \mathscr{I}_0$. It will be shown later that this choice for the velocity tracking error allows for obtaining relevant (string stability) properties of the controlled platoon. Next, it can be shown that choosing the input u_i in (3) as

$$u_i(t) = a_i(t) + \tau v_{\mathrm{ref}}(s_i(t))\tilde{u}_i - \tau v_{\mathrm{ref}}(s_i(t))\left(3\,\frac{\mathrm{d}}{\mathrm{d}s}\frac{1}{v_{\mathrm{ref}}(s)}\bigg|_{s=s_i(t)} v_i(t)a_i(t) + \frac{\mathrm{d}^2}{\mathrm{d}^2 s}\frac{1}{v_{\mathrm{ref}}(s)}\bigg|_{s=s_i(t)} v_i^3(t)\right) \tag{5}$$

achieves feedback linearization of the final two equations in (3) with respect to the output (4). Namely, after applying the feedback linearizing control (5), the dynamics (3) can be written as

$$\begin{aligned} \dot{s}_i(t) &= v_{\mathrm{ref}}(s_i(t))\big(1 + e_i(t)\big), \\ \ddot{e}_i(t) &= \tilde{u}_i(t), \end{aligned} \tag{6}$$

for $i \in \mathscr{I}_0$. Here, the definition (4) is exploited and $\tilde{u}_i(t) \in \mathbb{R}$.

Whereas e_i in (4) provides a characterization of the velocity tracking error corresponding to the first control objective, a measure for the tracking error related to the desired spacing policy (1) is introduced next to target the second control objective. Specifically, the spacing tracking error Δ_i, $i \in \mathscr{I}$, is defined as

$$\Delta_i(t) := \int_{s_{i-1}(t-\Delta t)}^{s_i(t)} \frac{1}{v_{\mathrm{ref}}(s)}\,\mathrm{d}s, \tag{7}$$

where it is noted that the property $v_{\mathrm{ref}}(s) \geq v_{\min}$ (see Assumption 1) guarantees that $\Delta_i(t) = 0$ if and only if $s_i(t) = s_{i-1}(t - \Delta t)$, which corresponds to the desired spacing policy. The time-differentiation of Δ_i in (7) yields

$$\dot{\Delta}_i(t) = \frac{v_i(t)}{v_{\mathrm{ref}}(s_i(t))} - \frac{v_{i-1}(t-\Delta t)}{v_{\mathrm{ref}}(s_{i-1}(t-\Delta t))} = e_i(t) - e_{i-1}(t - \Delta t), \tag{8}$$

such that the definition of the spacing tracking error Δ_i is in agreement with the definition of the velocity tracking error e_i in (4).

However, rather than directly using Δ_i as in (7) in the control design, controllers will be synthesized that aim at asymptotically achieving $\delta_i(t) = 0$, where δ_i is defined as

$$\delta_i(t) := \Delta_i(t) + h e_i(t), \tag{9}$$

for $i \in \mathscr{I}$ and with $h > 0$. It is recalled that the two terms in (9) correspond to the spacing tracking error (7) and velocity tracking error (4), such that (9) can be regarded as a relaxation of the desired spacing policy. In particular, it allows the spacing between vehicles to increase if the follower vehicle drives at higher speed than the reference velocity. This will be shown to lead to a suppression of perturbations as they propagate through the string of vehicles, as is generally referred to as string stability. Even though the desired spacing is given by (1), the definition in (9) will be referred to as the delay-based spacing policy.

In order to obtain a controller that asymptotically achieves $\delta_i(t) = 0$, (9) is differentiated (three times) with respect to time to yield

$$\dddot{\delta}_i(t) = \tilde{u}_i(t) - \tilde{u}_{i-1}(t - \Delta t) + h\dot{\tilde{u}}(t). \tag{10}$$

Here, (8) as well as the dynamics in velocity tracking error coordinates (6) are exploited. Next, by regarding $\tilde{u}_i$ as a controller state, a virtual input $\xi_i \in \mathbb{R}$ can be introduced as

$$\xi_i(t) := h\dot{\tilde{u}}_i(t) + \tilde{u}_i(t), \tag{11}$$

for $i \in \mathscr{I}$. After choosing the virtual input ξ_i as

$$\xi_i(t) = -\left(k_0\delta_i(t) + k_1\dot{\delta}_i(t) + k_2\ddot{\delta}_i(t)\right) + \tilde{u}_{i-1}(t - \Delta t), \tag{12}$$

it is readily seen that the following closed-loop dynamics is obtained

$$\dddot{\delta}_i(t) + k_2\ddot{\delta}_i(t) + k_1\dot{\delta}_i(t) + k_0\delta_i(t) = 0 \tag{13}$$

for $i \in \mathscr{I}$. Consequently, the controller parameters k_j, $j \in \{0, 1, 2\}$ can be chosen (e.g., by the Routh–Hurwitz criterion or pole placement techniques) to achieve asymptotic stability of the dynamics (13), which asymptotically achieves $\delta_i(t) = 0$ for δ_i as in (9). The subspace for which $\delta_i = 0$ plays a similar role as the sliding surface in sliding mode control. In the final part of this section, it will be shown that asymptotically achieving $\delta_i = 0$ indeed reaches the objectives of tracking the desired reference velocity and delay-based spacing policy, characterized through e_i in (4) and Δ_i in (7), respectively.

At this point, it is worth noting that the total controller for the follower vehicles $i \in \mathscr{I}$ is given by the feedback linearizing part (5), the controller dynamics (11), and the feedback (12). This latter part relies on measurements of δ_i (obtained through (9)) and its time derivatives as well as the controller state of the preceding vehicle $\tilde{u}_{i-1}$, see (12).

Remark 1 The controller state $\tilde{u}_{i-1}$ in (12) can be obtained through (wireless) communication between vehicles. As only a delayed version of $\tilde{u}_{i-1}$ is required for the control of vehicle i, this control approach is inherently robust to (small) time delays in this communication. In Sect. 4, an approach will be discussed that also exploits information about the preceding vehicle in the interval $(t - \Delta t, t]$ in an attempt to improve platoon performance.

Remark 2 The controller presented above targets tracking of the desired delay-based spacing policy and only applies to the follower vehicles with indices in $\mathscr{I}$. The lead vehicle (with index $i = 0$) can be controlled to track the desired reference velocity profile v_{ref} by exploiting the same feedback linearizing controller (5) and choosing $\tilde{u}_0$ as

$$\tilde{u}_0(t) = -l_0 e_0(t) - l_1 \dot{e}_0(t). \tag{14}$$

It follows immediately from (6) with $\tilde{u}_0$ in (14) that the velocity error dynamics is asymptotically stable whenever $l_j > 0$ for $j \in \{0, 1\}$.

In the remainder of this section, stability properties of the controlled platoon are analyzed. Here, it is noted that asymptotic stability of the dynamics for δ_i in (13) does not directly imply that the desired delay-based spacing policy is achieved. This can be observed by considering the definition of δ_i in (9). Namely, after applying (8), it follows that (9) can be written as

$$h\dot{\Delta}_i(t) = -\Delta_i(t) + \delta_i(t) - he_{i-1}(t - \Delta t), \tag{15}$$

for $i \in \mathscr{I}$, such that the specific choice of δ_i in (9) induces the dynamics (15). Consequently, the total dynamics of the follower vehicles are given by the dynamics (13) and (15). Note that this dynamics follows from the vehicle dynamics (6) with the dynamic controller (11) and feedback (12) using the coordinates (7) and (9).

When the lead vehicle employs the controller discussed in Remark 2, the total platoon asymptotically achieves tracking of the desired velocity profile and the delay-based spacing policy. This is formalized as follows.

Theorem 1 *Consider the closed-loop platoon dynamics (13), (15) for $i \in \mathscr{I}$ and the lead vehicle controller (14). Then, the origin $\Delta_i = \delta_i = \dot{\delta}_i = \ddot{\delta}_i = 0$, $i \in \mathscr{I}$ and $e_0 = \dot{e}_0 = 0$ is asymptotically stable if and only if the controller parameters satisfy $k_0 > 0$, $k_1 > 0$, $k_2 > 0$ such that $k_1 k_2 > k_0$ and $l_0 > 0$, $l_1 > 0$.*

Proof The proof will be based on induction on the index of the follower vehicles, where the first vehicle is considered in the first step.

It is clear from the controller (14) and the dynamics $\ddot{e}_0 = \tilde{u}_0$ (see (6)) that the equilibrium $e_0 = \dot{e}_0 = 0$ is asymptotically stable under the conditions in the statement of the theorem. Consequently, the lead vehicle achieves tracking of the desired reference velocity $v_{\mathrm{ref}}(\cdot)$, as follows from the definition of e_i in (4).

A follower vehicle with index i satisfying the dynamics (9), (7) is considered in order to establish the inductive step. First, it is noted that the dynamics for δ_i in (9) is independent of the state Δ_i and is asymptotically stable under the conditions of the theorem. This follows from the Routh–Hurwitz criterion, e.g., [14]. Next, consider the dynamics for Δ_i in (7). Introduction of the function $V(\Delta_i) = \frac{1}{2} h \Delta_i^2$ and time-differentiation of V along the trajectories of (15) yields

$$\tfrac{\mathrm{d}}{\mathrm{d}t} V(\Delta_i(t)) \leq -(1 - \alpha)|\Delta_i(t)|^2, \qquad \forall \alpha |\Delta_i(t)| > |\delta_i(t) - he_{i-1}(t - \Delta t)|, \tag{16}$$

for any α such that $0 < \alpha < 1$. This implies that the dynamics (15) is input-to-state stable (see [15]) with respect to the input $\delta_i(t) - he_{i-1}(t - \Delta t)$.

Taking $i = 1$, it is recalled that the relative velocity error dynamics of the lead vehicle is asymptotically stable, such that e_{i-1} vanishes (as it is generated by an asymptotically stable system). Similarly, δ_i vanishes due to asymptotic stability of

(13). Consequently, the dynamics of the first follower vehicle and the lead vehicle form a cascade interconnection of the input-to-state stable dynamics for Δ_i, whose total inputs result from the asymptotically stable dynamics for δ_i and the asymptotically stable dynamics for e_0. Due to the input-to-state stability property, this cascade it itself asymptotically stable (see [16]). Moreover, e_i can be regarded as an output of this asymptotically stable cascaded system (through (9)), which therefore vanishes as well. Induction on the vehicle index i then leads to the desired result. □

The result of Theorem 1 ensures the closed-loop stability of the desired delay-based spacing policy, regardless of the value of the delay Δt ($\Delta t \geq 0$). However, this does not guarantee that any disturbances caused by velocity tracking errors of the lead vehicle do not amplify through the platoon. The following result provides a bound on the amplification of velocity tracking errors.

Theorem 2 *Consider the spacing policy (9), let $\delta_i(t) = 0$ for all t, and assume that $\Delta_i(0) = 0$, $i \in \mathscr{I}$. Let the velocity tracking error of the lead vehicle be such that $e_0(t) = 0$ for all $t \leq 0$. Then, the velocity tracking errors e_i of the follower vehicles satisfy*

$$\|e_i\|_2 \leq \|e_{i-1}\|_2 \tag{17}$$

for all $i \in \mathscr{I}$. Here $\|e_i\|_2$ denotes the $\mathscr{L}_2$ signal norm, i.e., $\|e_i\|_2^2 = \int_0^\infty |e_i(t)|^2 \, \mathrm{d}t$.

Proof In order to prove the theorem, consider the dynamics (15) induced by the spacing policy (9). Setting $\delta_i = 0$, the transfer function from e_{i-1} to e_i can be obtained as

$$H_\delta(s) = \frac{1}{hs+1} e^{-s\Delta t}, \tag{18}$$

where the relation $he_i = \Delta_i$ (see (9) for $\delta_i = 0$) is used. It then follows that the $\mathscr{H}_\infty$-norm of H_δ, defined as $\|H_\delta\|_\infty = \sup_{\omega \in \mathbb{R}} |H_\delta(j\omega)|$, satisfies $\|H_\delta\|_\infty = 1$. This proves the result (17) through the Parseval identity. □

The result in Theorem 2 provides a so-called string-stability property, which ensures that velocity tracking errors do not amplify as they propagate through the platoon. An early reference on string stability is [17], whereas a recent overview is given in [13]. It is noted that the dynamics for δ_i in (13) is independent of the velocity tracking error, such that the assumption $\delta_i = 0$ is not restrictive. In fact, (17) holds for any controller that renders $\delta_i = 0$ in (9) invariant. As such, it is clear that the string-stability property in Theorem 2 is a direct result of the choice of the spacing policy (9) rather than the details of the controller design. Note that the controller parameters determine the speed of convergence towards the subspace on which $\delta_i = 0$, see (13).

Remark 3 The design of controllers achieving the delay-based spacing policy (1) was first pursued in [9]. However, rather than directly addressing the time delay Δt

in the time domain as pursued in the current work, the results in [9] rely on a formulation in which space (rather than time) is taken as the independent variable. By taking a time-domain approach, the results in this chapter allow for a more insightful interpretation. Moreover, this approach allows for considering more advanced spacing policies, as will be discussed in the next section.

4 Platoon Control Performance

In the previous section, control design on the basis of the delay-based spacing policy (9) was shown to achieve desirable string-stability properties (see Theorem 2). Here, it is recalled that the controller of a given vehicle relies on delayed information on its preceding vehicle, where the size of the delay corresponds to the desired time gap Δt in the spacing policy (1). This is particularly apparent from the definition of the spacing tracking error (7) and the feedback control part (12).

Consequently, information about the preceding vehicle in the time interval $(t - \Delta t, t]$, although available, is not exploited in the controller. In the current section, it will be shown that this additional information can be employed to improve the performance of the controlled platoon.

In particular, the delay-based spacing policy (9) is extended as

$$\eta_i(t) = \Delta_i(t) + he_i(t) - kp_{i-1}(t), \tag{19}$$

with $i \in \mathscr{I}$, $h > 0$, $k \geq 0$, and where p_{i-1} is defined as

$$p_{i-1}(t) = \int_{-\Delta t}^{0} e^{-\alpha(\Delta t+\theta)} e_{i-1}(t+\theta)\, \mathrm{d}\theta. \tag{20}$$

The influence of this additional term (20), with $\alpha \geq 0$, can be understood by considering the case $\eta_i = 0$ in (19) (this will be, similar to before, the control objective). Namely, the term p_{i-1} provides an additional relaxation of the desired delay-based spacing policy (7) by allowing a momentarily shorter inter-vehicular distance ($\Delta_i(t) > 0$) when the preceding vehicle drives faster than desired in the time interval $(t - \Delta t, t]$ ($p_{i-1}(t) > 0$). Note that the delay-based spacing policy (1) requires tracking of the trajectory of the preceding vehicle subject to the delay Δt. As such, information on e_{i-1} in the interval $(t - \Delta t, t]$, as characterized through p_{i-1} in (20), can be regarded as preview information of "future" behavior of the velocity of the preceding vehicle. This information is weighted using the kernel $e^{-\alpha(\Delta t+\theta)}$, which ensures (for $\alpha > 0$) that data in the near "future" (for θ close to $-\Delta t$) has the highest importance.

A controller on the basis of the extended delay-based spacing policy η_i in (19) can be synthesized using a similar approach as discussed in Sect. 3 for the spacing policy δ_i in (9). Therefore, in the remainder of this section, it will be assumed that $\eta_i(t) = 0$ in (19) and the performance of this extended spacing policy will be analyzed by

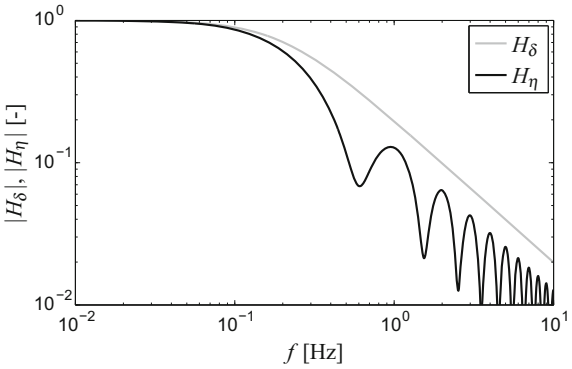

Fig. 2 Comparison of the frequency response functions $H_\delta(j\omega)$ in (18) and $H_\eta(j\omega)$ in (21), corresponding to the spacing policies (9) (for $\delta_i = 0$) and (19) (for $\eta_i = 0$), respectively. The parameter values are $\Delta t = 1$, $h = 0.8$, $k = 0.6$, and $\alpha = 0.9$

considering its transfer function, in analogy to (18) in Theorem 2. Specifically, the transfer function from e_{i-1} to e_i is obtained as

$$H_\eta(s) = \frac{1}{hs+1} e^{-s\Delta t} + \frac{ks}{hs+1} \frac{e^{-\alpha\Delta t} - e^{-s\Delta t}}{s-\alpha}. \tag{21}$$

Here, the expression (8) is used, whereas the right-most term in (21) is the result of the distributed delay in (20).

In order to compare the behavior of the extended spacing policy (19) with transfer function (21) to that of the spacing policy (9) with transfer function (18), the magnitude of their frequency response functions is depicted in Fig. 2. From this figure it is clear that the extended delay-based spacing policy characterized by H_η also ensures that perturbations in the velocity tracking error do not amplify to the string of vehicles, as was proven for the delay-based spacing policy δ_i in (9) in Theorem 2. In fact, the extended spacing policy η_i in (19) achieves a better suppression of disturbances, in particular for higher frequencies. Consequently, the use of the extended spacing policy (19) is expected to lead to increased performance of the controlled platoon. This will be verified through simulations in Sect. 5.

Remark 4 The implementation of the extended delay-based spacing policy (19) requires the evaluation of the integral in (20). However, the computation of this term cannot be obtained as the solution of a differential equation, as this involves an unstable pole-zero cancelation (at $s = \alpha$, see (21)). Instead, an online numerical computation of the integral term in $p_{i-1}(t)$ is required. It is remarked that these issues are also encountered in the finite spectrum assignment problem, which features a similar integral term. For an overview and computational approaches in this framework, see [18] and the references therein.

Table 1 Parameter values for the vehicle dynamics (3), spacing policy (9) and controller (5), (11) and (12). The lead vehicle is controlled through (14)

τ	1 (s)	l_0	2.00 (s^{-2})	k_0	7.92 (s^{-3})
Δt	1 (s)	l_1	2.82 (s^{-1})	k_1	11.96 (s^{-2})
h	0.8 (s)			k_2	6.00 (s^{-1})

5 Evaluation

The performance of the controller designed in Sect. 3 as well as the spacing policies δ_i in (9) and η_i in (19) is evaluated by means of simulations.

First, a platoon of eleven vehicles (i.e., $N = 10$ follower vehicles) is considered using the controller given by (5), (11), and (12). For the parameter values in Table 1, the tracking of the reference velocity profile $v_{\text{ref}}(\cdot)$ and delay-based spacing policy (9) is considered in Fig. 3. Herein, the initial conditions for the velocity profiles are randomly chosen and deviate from the equilibrium point. From this figure, it is clear that the equilibrium $e_i(t) = 0$, which corresponds to $v_i(t) = v_{\text{ref}}(s_i(t))$, is asymptotically stable. The same holds for the spacing tracking error Δ_i, indicating that the desired inter-vehicular spacing is obtained. To further illustrate the first point, the velocities v_i are depicted as a function of s_i in Fig. 4, from which it can be seen

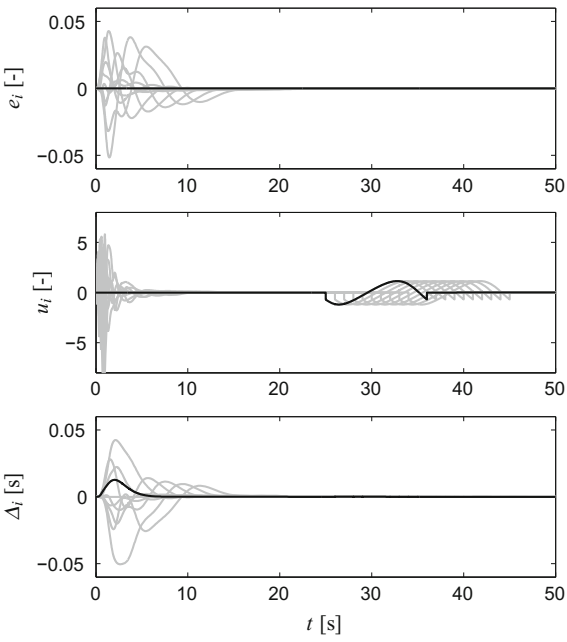

Fig. 3 Velocity tracking error e_i (*top*) and control input u_i (*middle*) for the lead vehicle (in *black*) and $N = 10$ follower vehicles (in *gray*) for non-equilibrium initial conditions and velocity reference $v_{\text{ref}}(s) = 20 - 1.75(1 - \cos(0.02\pi(s - 500)))$ for $500 \leq s \leq 700$ and $v_{\text{ref}}(s) = 20$ otherwise. Spacing errors Δ_i (*bottom*) are shown for the first follower vehicle (in *black*) and remaining follower vehicles (in *gray*)

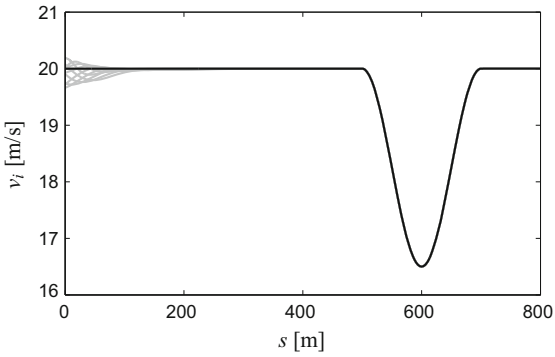

Fig. 4 Velocity v_i in the spatial domain for the lead vehicle (in *black*) and follower vehicles (in *gray*) corresponding to the simulation in Fig. 3

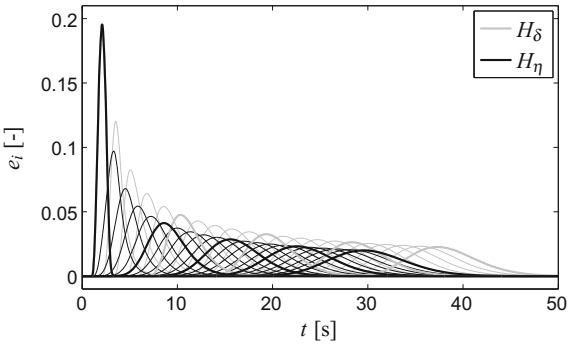

Fig. 5 Velocity tracking error e_i for the spacing policies (9) (in *gray*) and (19) (in *black*) for a platoon of $N = 20$ follower vehicles. The initial perturbation e_0 as well as the trajectories of vehicles 5, 10, 15, and 20 are shown in *thicker lines* for easy comparison. The parameter values correspond to those in Fig. 2

that all vehicles achieve the same velocity profile in the spatial domain as stated in Lemma 1.

Second, the spacing policy δ_i in (9) and extended spacing policy η_i in (19) are considered. Here, it is assumed that the spacing policies are tracked perfectly, i.e., $\delta_i(t) = 0$ and $\eta_i(t) = 0$ for all t and $i \in \mathscr{I}$, such that the design of controllers is not explicitly addressed. This case corresponds to the frequency response functions in Fig. 2. Figure 5 shows the velocity tracking errors of a platoon of $N = 20$ follower vehicles in case the lead vehicle experiences a perturbation e_0, which is considered as an input to the total platoon. It is clear that, for both spacing policies, the influence of this perturbation is decreased as it propagates through the platoon. In addition, as can also be seen in the frequency response function in Fig. 2, the extended delay-based spacing policy η_i in (19) achieves a larger suppression of disturbances and therefore a better performance. In fact, the disturbances are also handled earlier in time due to the distributed-delay term in (20). Here, it is recalled that the repeated application of (18) always leads to a delay of Δt seconds before a disturbance is propagated from a vehicle to its immediate follower. Finally, Fig. 6 shows the corresponding spacing tracking error, which confirms these observations and indicates an even more apparent benefit of the extended spacing policy (19).

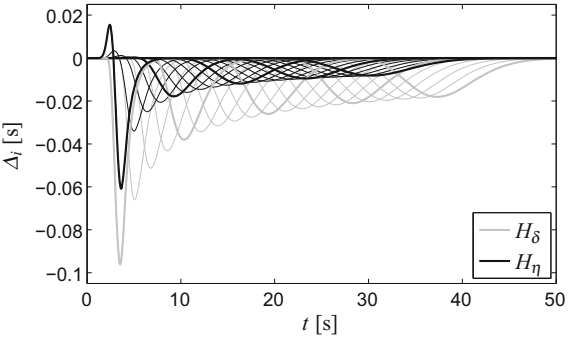

Fig. 6 Spacing tracking error Δ_i for the spacing policies (9) (in *gray*) and (19) (in *black*) for a platoon of $N = 20$ follower vehicles, corresponding to the velocity tracking errors in Fig. 5

6 Conclusions

The design of distributed platoon controllers for a delay-based spacing policy is discussed in this work, leading to platoon behavior in which all vehicles track the same velocity profile in the spatial domain. It is shown that a relaxation of this spacing policy leads to string-stable platoon behavior. Contrary to earlier results in [9], control design and analysis were done in the time domain (rather than the spatial domain), leading to a controller that is easier to interpret and implement. In addition, the time-domain approach allows for an extension of the delay-based policy. Herein, more information about the preceding vehicle is used by taking a distributed-delay approach, which is shown to lead to improved platoon behavior.

Future work will focus on further developing this distributed-delay approach, with particular emphasis on the implementation of this extended delay-based spacing policy and the resulting controller.

Acknowledgements This research is financially supported by the European Union Seventh Framework Programme under the project COMPANION, the Swedish Research Council, and the Knut and Alice Wallenberg Foundation.

References

1. Varaiya, P.: Smart cars on smart roads: problems of control. IEEE Trans. Autom. Control **38**(2), 195–207 (1993)
2. Alam, A., Besselink, B., Turri, V., Mårtensson, J., Johansson, K.H.: Heavy-duty vehicle platooning towards sustainable freight transportation: a cooperative method to enhance safety and efficiency. IEEE Control Syst. Mag. **35**(6), 34–56 (2015)
3. Levine, W., Athans, M.: On the optimal error regulation of a string of moving vehicles. IEEE Trans. Autom. Control, AC **11**(3), 355–361 (1966)
4. Peppard, L.E.: String stability of relative-motion PID vehicle control systems. IEEE Trans. Autom. Control **19**(5), 579–581 (1974)
5. Stanković, S.S., Stanojević, M.J., Šiljak, D.D.: Decentralized overlapping control of a platoon of vehicles. IEEE Trans. Control Syst. Technol. **8**(5), 816–832 (2000)

6. Swaroop, D., Hedrick, J.K.: Constant spacing strategies for platooning in automated highway systems. J. Dyn. Syst. Measur. Control **121**(3), 462–470 (1999)
7. Ioannou, P.A., Chien, C.C.: Autonomous intelligent cruise control. IEEE Trans. Veh. Technol. **42**(4), 657–672 (1993)
8. Swaroop, D., Hedrick, J.K., Chien, C.C., Ioannou, P.: A comparison of spacing and headway control laws for automatically controlled vehicles. Veh. Syst. Dyn. **23**(1), 597–625 (1994)
9. Besselink, B., Johansson, K.H.: Control of platoons of heavy-duty vehicles using a delaybased spacing policy. In: Proceedings of the 12th IFAC Workshop on Time Delay Systems, Ann Arbor, USA, pp. 364–369 (2015)
10. Newell, G.F.: A simplified car-following theory: a lower order model. Transp. Res. Part B: Methodol. **36**(3), 195–205 (2002)
11. Ge, J.I., Orosz, G.: Dynamics of connected vehicle systems with delayed acceleration feedback. Transp. Res. Part C: Emerg. Technol. **46**, 46–64 (2014)
12. Öncü, S., Ploeg, J., van de Wouw, N., Nijmeijer, H.: Cooperative adaptive cruise control: network-aware analysis of string stability. IEEE Trans. Intell. Transp. Syst. **15**(4), 1527–1537 (2014)
13. Ploeg, J., van de Wouw, N., Nijmeijer, H.: Lp string stability of cascaded systems: application to vehicle platooning. IEEE Trans. Control Syst. Technol. **22**(2), 786–793 (2014)
14. Antsaklis, P.J., Michel, A.N.: Linear Systems. Birkhäuser, Boston, USA (2006)
15. Sontag, E.D.: Smooth stabilization implies coprime factorization. IEEE Trans. Autom. Control **34**(4), 435–443 (1989)
16. Khalil, H.K.: Nonlinear Systems, 3rd edn. USA, Prentice Hall, Upper Saddle River (2002)
17. Fenton, R.E., Cosgriff, R.L., Olson, K., Blackwell, L.M.: One approach to highway automation. Proc. IEEE **56**(4), 556–566 (1968)
18. Michiels, W., Niculescu, S.-I.: Stability and Stabilization of Time-Delay Systems: An Eigenvalue-Based Approach. SIAM, Philadelphia, USA (2007)

To Delay or Not to Delay—Stability of Connected Cruise Control

Jin I. Ge, Gábor Orosz, Dávid Hajdu, Tamás Insperger and Jeff Moehlis

Abstract The dynamics of connected vehicle systems are investigated where vehicles exchange information via wireless vehicle-to-vehicle (V2V) communication. In particular, connected cruise control (CCC) strategies are considered when using different delay configurations. Disturbance attenuation (string stability) along open chains is compared to the linear stability results using ring configuration. The results are summarized using stability diagrams that allow one to design the control gains for different delay values. Critical delay values are calculated and trade-offs between the different strategies are pointed out.

J.I. Ge (✉) · G. Orosz
Department of Mechanical Engineering, University of Michigan,
Ann Arbor, MI 48109, USA
e-mail: gejin@umich.edu

G. Orosz
e-mail: orosz@umich.edu

D. Hajdu
Department of Applied Mechanics, Budapest University of Technology and Economics,
Budapest 1111, Hungary
e-mail: hajdu@mm.bme.hu

T. Insperger
Department of Applied Mechanics, Budapest University of Technology and Economics
and MTA-BME Lendület Human Balancing Research Group, Budapest 1111, Hungary
e-mail: insperger@mm.bme.hu

J. Moehlis
Department of Mechanical Engineering, University of California, Santa Barbara,
CA 93106, USA
e-mail: moehlis@engineering.ucsb.edu

T. Insperger et al. (eds.), *Time Delay Systems*,
Advances in Delays and Dynamics 7, DOI 10.1007/978-3-319-53426-8_18

1 Introduction

Vehicular traffic has been fascinating researchers for decades and most of the early work has been focused on understanding how humans drive, in particular, how they control the longitudinal motion of vehicles [4, 7, 8]. In the last few decades, the so-called optimal velocity model [2, 10] gained popularity since this can reproduce a plethora of different large-scale traffic patterns observed empirically [20]. It also became evident that human drivers often trigger traffic jams due to their large reaction times and limited perception range [15].

In order to bypass this problem, the concept of adaptive cruise control (ACC) was created where the distance to the vehicle ahead is monitored by range sensors (e.g., radar, lidar) and the vehicle is actuated accordingly [11, 19]. By appropriate control design, one may guarantee attenuation of velocity perturbations between consecutive vehicles that is called string stability in the literature [18]. However, a relatively large penetration of ACC vehicles is required to change the behavior of the overall traffic flow [3], which may be difficult to reach due to the relatively high cost. Also, while the sensing delay of an ACC vehicle is significantly smaller than the human reaction time, it is still only able to monitor the motion of the vehicle immediately ahead.

Wireless vehicle-to-vehicle (V2V) communication can be used to obtain information from beyond the line of sight. Initial attempts focused on constructing platoons of ACC vehicles where the information broadcast by a designated platoon leader is utilized by the following vehicles. This strategy, called cooperative adaptive cruise control (CACC) [12, 21], can significantly improve the performance of the system but it requires all vehicles to be equipped with sensors and communication devices, and the number of vehicles involved is limited by the communication range. To eliminate such limitations the concept of connected cruise control (CCC) has been put forward that allows the inclusion of human-driven vehicles that may or may not broadcast information [1, 5, 13, 16, 22]. CCC utilizes all available information from multiple vehicles ahead and may be used to assist the human drivers, to complement sensor-based algorithms, or to automatically control the longitudinal motion of the vehicle. This increased flexibility makes CCC scalable for large connected vehicle systems.

However, intermittencies and packet drops lead to time delays in CCC. Such communication delays are typically larger than the sensing delays in ACC, though they are still smaller than human reaction time. Typically, one may expect that larger delays lead to degraded performance but time-delay systems may present counterintuitive behavior in terms of stability [9, 17]. In this paper, we investigate the simplest CCC scenario when each CCC vehicle utilizes information from the vehicle immediately ahead. While the received V2V information is delayed by the communication delay, information measured by on-board sensors may be available (almost) instantaneously. In this paper, we are asking the question whether one shall use these instantaneous values or shall delay them with the communication delay. We compare the different control strategies using stability charts where we identify gain combinations ensuring plant stability (stability in the lack of disturbances) and string

stability (attenuation of velocity disturbances arising ahead). We also identify trade-offs between the different strategies.

2 Modeling and Control Design with Delays

We consider connected cruise control strategies where each vehicle receives motion information from the vehicle immediately ahead via wireless V2V communication and uses this information to control its longitudinal motion. In particular, we consider control strategies of the form

$$\begin{aligned} \dot{s}(t) &= v(t)\,, \\ \dot{v}(t) &= F\big(s(t), v(t), s(t-\tau), v(t-\xi), s_{\mathrm{L}}(t-\sigma), v_{\mathrm{L}}(t-\sigma)\big)\,, \end{aligned} \tag{1}$$

where the dot stands for differentiation with respect to time t. Also, s, and s_{L} denote the position of the front bumpers of the vehicle and its immediate predecessor (called the leader), while v and v_{L} denote the corresponding velocities; see Fig. 1. The communication delay σ is caused by intermittencies and packet drops while the delays τ and ξ can be set when designing the controller. More precisely, we assume that the quantities s and v are available instantaneously through on-board sensors of high sampling rate but one may still use the delayed values in the control design as explained below. Indeed, τ and ξ may be set to zero or to be equal to σ.

In this paper, we base our control design on the optimal velocity model and consider three different delay scenarios, but all results can be generalized to car-following models of the general form (1); see [6, 15]. The first scenario is given by

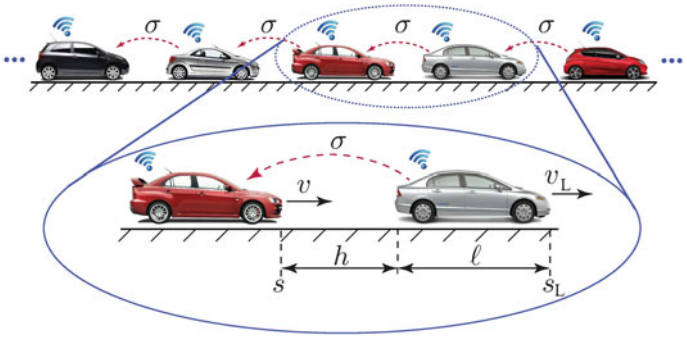

Fig. 1 Connected vehicles system where each vehicle receives information from the vehicle immediately ahead with the communication delay σ as indicated by the *red-dashed arrows*. The system can be constructed as the concatenation of leader–follower pairs shown below where the positions, the velocities, the headway, and the vehicle length are highlighted

$$\begin{aligned}\dot{s}(t) &= v(t)\,,\\ \dot{v}(t) &= \alpha\big(V(s_{\mathrm{L}}(t-\sigma)-s(t-\sigma)-\ell)-v(t-\sigma)\big)+\beta\big(W(v_{\mathrm{L}}(t-\sigma))-v(t-\sigma)\big)\,,\end{aligned} \tag{2}$$

which corresponds to matching all delays in the controller to the communication delay. Here, ℓ represents the length of the vehicle ahead (see Fig. 1) while the delayed value of the headway $h = s_{\mathrm{L}} - s - \ell$ appears in the monotonously increasing range policy function

$$V(h) = \begin{cases} 0 & \text{if} \quad h \le h_{\mathrm{st}}\,,\\ F(h) & \text{if} \quad h_{\mathrm{st}} < h < h_{\mathrm{go}}\,,\\ v_{\max} & \text{if} \quad h \ge h_{\mathrm{go}}\,. \end{cases} \tag{3}$$

That is, for small headways the vehicle intends to stop for safety reasons while for large headways it intends to travel with a chosen maximum speed. Between these we assume $F(h)$ to be strictly monotonously increasing such that $F(h_{\mathrm{st}}) = 0$ and $F(h_{\mathrm{go}}) = v_{\max}$. The simplest choice may be

$$F(h) = v_{\max}\frac{h-h_{\mathrm{st}}}{h_{\mathrm{go}}-h_{\mathrm{st}}}\,, \tag{4}$$

that is depicted in Fig. 2a where the time gap $T_{\mathrm{gap}} = (h_{\mathrm{go}} - h_{\mathrm{st}})/v_{\max}$ is highlighted. Notice that T_{gap} is constant for headway range $h_{\mathrm{st}} < h < h_{\mathrm{go}}$. However, the corresponding range policy is non-smooth at h_{st} and h_{go} which may lead to a "jerky ride". Thus, in this paper we use

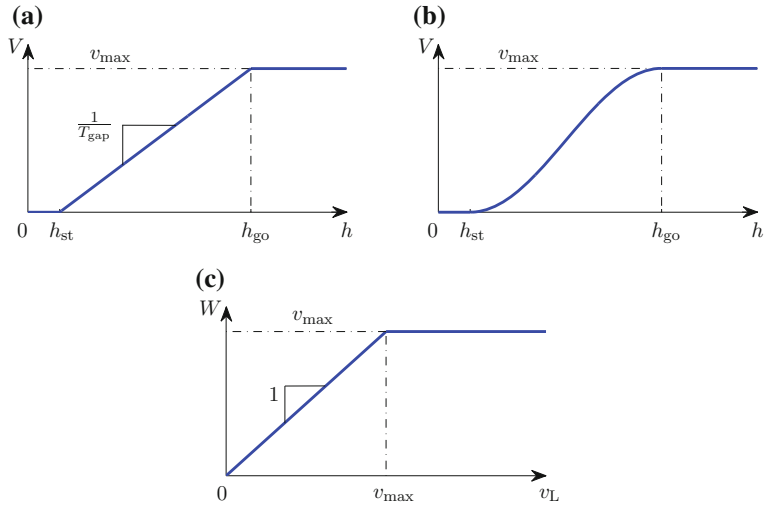

Fig. 2 **a**, **b** Range policies (3) with the middle sections given by (4) and (5). **c** Saturation function (6)

$$F(h) = \frac{v_{\max}}{2}\left(1 - \cos\left(\pi \frac{h - h_{\mathrm{st}}}{h_{\mathrm{go}} - h_{\mathrm{st}}}\right)\right), \tag{5}$$

that makes the range policy smooth as shown in Fig. 2b. Indeed, one may design range policies with higher level of smoothness as shown in [13].

The second term on the right-hand side of (2) contains the saturation function

$$W(v_{\mathrm{L}}) = \begin{cases} v_{\mathrm{L}} & \text{if} \quad v_{\mathrm{L}} \le v_{\max}\,, \\ v_{\max} & \text{if} \quad v_{\mathrm{L}} > v_{\max}\,, \end{cases} \tag{6}$$

shown in Fig. 2c, that is introduced to avoid the situation that the vehicle follows a leader whose velocity is larger than $v_{\max}$. Notice that when the leader's velocity is smaller than $v_{\max}$, the delayed value of the derivative of the headway $\dot{h} = v_{\mathrm{L}} - v$ appears on the right-hand side. Thus, in model (2) all quantities on the right hand side have clear physical meaning and we only compare quantities at the same time moment. When presenting the results below we use the numbers $h_{\mathrm{st}} = 5$ m, $h_{\mathrm{go}} = 35$ m, and $v_{\max} = 30$ m/s that corresponds to traffic data for human drivers [15].

Let us assume that the leader is traveling with a constant speed, that is, $s_{\mathrm{L}}(t) = v^* t + \bar{s}_{\mathrm{L}}$ and $v_{\mathrm{L}}(t) \equiv v^*$, where $0 < v^* < v_{\max}$ and $\bar{s}_{\mathrm{L}}$ is given by the initial condition. Then the follower admits the equilibrium

$$s(t) = v^* t + \bar{s}\,, \quad v(t) \equiv v^*\,, \quad \bar{s}_{\mathrm{L}} - \bar{s} - \ell = V^{-1}(v^*) = F^{-1}(v^*) := h^*\,. \tag{7}$$

In the vicinity of the equilibrium we define the time gap as $T_{\mathrm{gap}} = 1/V'(h^*) = 1/F'(h^*)$ which indeed changes with the equilibrium headway h^* (or equivalently with the equilibrium velocity v^*). Note that for $v^* = 0$ any constant headway smaller than h_{st} is possible while for $v^* = v_{\max}$ any constant headway larger than h_{go} may occur; see (3). For $v^* > v_{\max}$ no equilibrium exists and the headway between the leader and follower increases in time.

Since time delays often lead to instabilities and undesired oscillations in dynamic systems, one may try to eliminate some delays on the right hand side of (2). For example, the model

$$\begin{aligned} \dot{s}(t) &= v(t)\,, \\ \dot{v}(t) &= \alpha\big(V(s_{\mathrm{L}}(t-\sigma) - s(t-\sigma) - \ell) - v(t)\big) + \beta\big(W(v_{\mathrm{L}}(t-\sigma)) - v(t-\sigma)\big)\,, \end{aligned} \tag{8}$$

still contains the delayed values of the headway $h = s_{\mathrm{L}} - s - \ell$ and its derivative $\dot{h} = v_{\mathrm{L}} - v$ (when $v_{\mathrm{L}} \le v_{\max}$), but we consider the instantaneous value of the velocity v (as it may be measured by on-board sensors). The model (8) still satisfies the equilibrium (7) but in the first term on the right-hand side we compare a delayed value with an instantaneous value.

To further eliminate delays one may consider

$$\begin{aligned} \dot{s}(t) &= v(t)\,, \\ \dot{v}(t) &= \alpha\big(V(s_{\mathrm{L}}(t-\sigma) - s(t-\sigma) - \ell) - v(t)\big) + \beta\big(W(v_{\mathrm{L}}(t-\sigma)) - v(t)\big)\,, \end{aligned} \tag{9}$$

where both terms on the right-hand side compare delayed values to instantaneous values. In fact, the velocity difference in the second term can be created since the leader's velocity is received via wireless communication while the vehicle's own velocity is measured on board. This is not accessible when using range sensors to measure the headway and its derivative. The model (9) also satisfies the equilibrium (7).

One may argue that the delay in the position s may be neglected as well. However, in this case the desired equilibrium (7) cannot be achieved by the system. In particular, the equilibrium headway becomes $\bar{s}_{\mathrm{L}} - \bar{s} - \ell = V^{-1}(v^*) + v^*\sigma$ that may lead to safety hazards.

In the next section, we will compare the three models (2), (8) and (9) in terms of the stability and disturbance attenuation in the vicinity of the equilibrium (7) by plotting stability charts for different values of the communication delay σ.

3 Linear Stability Analysis

In order to analyze the behavior of the models proposed above, we consider two different configurations. In the *open chain configuration*, $N+1$ vehicles are placed on a straight road such that the motion of the head vehicle is prescribed. Then the system is viewed as an input–output system, such that the speed of the head vehicle v_{N+1} serves as the input and the speed of the tail vehicle v_1 serves as an output. In the *ring-road configuration*, N vehicles are placed on a circular road of length $L + N\ell$ (yielding $h^* = L/N$ and the periodic boundary conditions $s_{N+1} = s_1$, $v_{N+1} = v_1$).

When considering vehicles with identical range policies, there exists a uniform flow equilibrium where all vehicles travel with the same velocity while keeping the same headway; see (7). Our goal is to choose the gain parameters α and β such that the velocity perturbations are attenuated as they propagate backward along the vehicle chain, and the system is able to maintain the uniform flow equilibrium [13].

In order to analyze the dynamics in the vicinity of the equilibrium (7) one may define the perturbations $\tilde{s}_{\mathrm{L}}(t) = s_{\mathrm{L}}(t) - v^*t - \bar{s}_{\mathrm{L}}$, $\tilde{v}_{\mathrm{L}}(t) = v_{\mathrm{L}}(t) - v^*$, $\tilde{s}(t) = s(t) - v^*t - \bar{s}$, $\tilde{v}(t) = v(t) - v^*$ and linearize the above models about the equilibrium. In particular, model (2) results in

$$\begin{aligned} \dot{\tilde{s}}(t) &= \tilde{v}(t)\,, \\ \dot{\tilde{v}}(t) &= \alpha f^*\,(\tilde{s}_{\mathrm{L}}(t-\sigma) - \tilde{s}(t-\sigma)) + \beta\tilde{v}_{\mathrm{L}}(t-\sigma) - (\alpha+\beta)\tilde{v}(t-\sigma)\,, \end{aligned} \tag{10}$$

where we introduced the notation $f^* = V'(h^*) = F'(h^*)$. In this paper, we consider the equilibrium $v^* = 15$ m/s, that is, $h^* = 20$ m yielding the maximum $f^* = \pi/2$ 1/s; see (3, 5). This corresponds to the minimum value of the time gap $T_{\text{gap}} = 1/f^*$, which gives the worst case scenario in terms of stability.

Taking the Laplace transform with zero initial conditions one may derive the transfer function

$$\Gamma(s) = \frac{\tilde{V}(s)}{\tilde{V}_{\text{L}}(s)} = \frac{\beta s + \alpha f^*}{\mathrm{e}^{s\sigma} s^2 + (\alpha + \beta) s + \alpha f^*}, \tag{11}$$

where $\tilde{V}(s)$ and $\tilde{V}_{\text{L}}(s)$ denote the Laplace transform of $\tilde{v}(t)$ and $\tilde{v}_{\text{L}}(t)$, respectively. The transfer function allows us to evaluate stability and the amplitude ratio between the input and the output in steady state when applying sinusoidal input.

In order to ensure *plant stability* (that is, $\tilde{s}(t) \to 0$, $\tilde{v}(t) \to 0$ as $t \to 0$ when $\tilde{s}_{\text{L}}(t) \equiv 0$ and $\tilde{v}_{\text{L}}(t) \equiv 0$) one needs to make sure that the infinitely many poles of the transfer function (11) are located in the left half complex plane. In order to determine the stability boundary in the parameter plane of α and β, we consider two different types of stability loss. When a real pole crosses the imaginary axis, substituting $s = 0$ into the characteristic equation $\mathrm{e}^{s\sigma} s^2 + (\alpha + \beta) s + \alpha f^* = 0$ yields the stability boundary

$$\alpha = 0\,. \tag{12}$$

On the other hand, when a complex conjugate pair of poles crosses the imaginary axis, substituting $s = \mathrm{i}\Omega$ with $\Omega > 0$ into the characteristic equation and separating the real and imaginary parts result in the stability boundary

$$\begin{aligned} \alpha &= \frac{\Omega^2 \cos(\Omega\sigma)}{f^*}\,, \\ \beta &= \Omega \sin(\Omega\sigma) - \alpha\,, \end{aligned} \tag{13}$$

that is parameterized by the angular frequency Ω.

In the special case of $\sigma = 0$, (12) remains the same while (13) simplifies to $\beta = -\alpha$ as shown by the thick black lines in Fig. 3a. One may use the Routh–Hurwitz criteria to show that plant stability is achieved above the lines in the top right corner. For different values of $\sigma > 0$ the curves (12) and (13) are shown as thick black curves in the (β, α)-plane in Fig. 4a, c, e. One may apply Stépán's formulae [17] and show that stability is maintained inside the lobe-shaped domain. As the delay is increased, the plant stable domain shrinks and the size of the domain tends to zero as the delay is increased to infinity.

To ensure *string stability*, that is, attenuation of velocity perturbations between the leader and the follower, we consider sinusoidal excitation $\tilde{v}_{\text{L}}(t) = v_{\text{L}}^{\text{amp}} \sin(\omega t)$, which (assuming plant stability) leads to the steady state response $\tilde{v}^{\text{ss}}(t) = v^{\text{amp}} \sin(\omega t + \psi)$, where $v^{\text{amp}}/v_{\text{L}}^{\text{amp}} = |\Gamma(\mathrm{i}\omega)|$ and $\psi = \angle\Gamma(\mathrm{i}\omega)$. Requiring $|\Gamma(\mathrm{i}\omega)| < 1$ for all $\omega > 0$ ensures attenuation of sinusoidal signals and, as superposition holds for

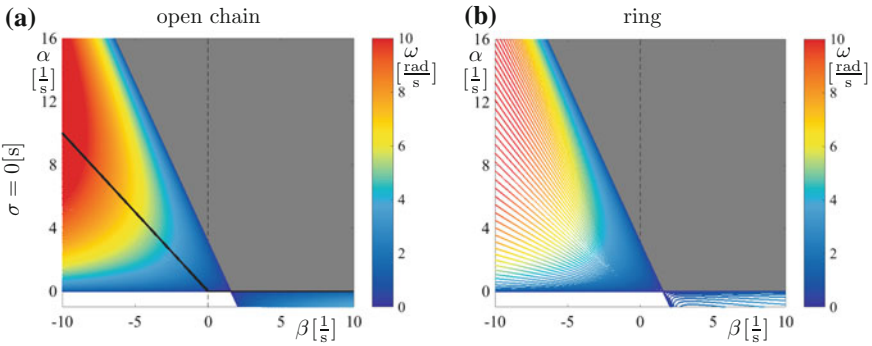

Fig. 3 Stability diagrams for the system (10) for $\sigma = 0$ using the open chain configuration (*left*) and the ring configuration (*right*). The system is plant stable above the thick *black lines*. The *gray-shaded* region indicates string stability while coloring refers to the oscillation frequencies as indicated by the *color bar*

linear systems, for the linear combination of those signals. This condition may be rewritten as $\omega^2 P(\omega) > 0$ where

$$P(\omega) = \omega^2 + 2\alpha\beta + \alpha^2 - 2(\alpha + \beta)\omega \sin(\omega\sigma) - 2\alpha f^* \cos(\omega\sigma)\,. \tag{14}$$

The stability boundaries can be identified corresponding to the minima of P becoming negative at $\omega_{\mathrm{cr}} > 0$ that is defined by

$$\begin{aligned} P(\omega_{\mathrm{cr}}) &= 0\,, \\ \frac{\partial P}{\partial \omega}(\omega_{\mathrm{cr}}) &= 0\,, \end{aligned} \tag{15}$$

while satisfying $\frac{\partial^2 P}{\partial \omega^2}(\omega_{\mathrm{cr}}) > 0$. Solving this for α and β one may obtain the string stability boundaries parameterized by ω_{cr} as

$$\begin{aligned} \alpha &= a \pm \sqrt{a^2 + b}\,, \\ \beta &= \frac{\omega_{\mathrm{cr}} + \alpha f^* \sigma \sin(\omega_{\mathrm{cr}}\sigma)}{\sin(\omega_{\mathrm{cr}}\sigma) + \omega_{\mathrm{cr}}\sigma \cos(\omega_{\mathrm{cr}}\sigma)} - \alpha\,, \end{aligned} \tag{16}$$

where

$$\begin{aligned} a &= \frac{\omega_{\mathrm{cr}}(f^*\sigma - 1) + f^* \sin(\omega_{\mathrm{cr}}\sigma)\cos(\omega_{\mathrm{cr}}\sigma)}{(2f^*\sigma - 1)\sin(\omega_{\mathrm{cr}}\sigma) - \omega_{\mathrm{cr}}\sigma\cos(\omega_{\mathrm{cr}}\sigma)}\,, \\ b &= \frac{\omega_{\mathrm{cr}}^2\big(\sin(\omega_{\mathrm{cr}}\sigma) - \omega_{\mathrm{cr}}\sigma\cos(\omega_{\mathrm{cr}}\sigma)\big)}{(2f^*\sigma - 1)\sin(\omega_{\mathrm{cr}}\sigma) - \omega_{\mathrm{cr}}\sigma\cos(\omega_{\mathrm{cr}}\sigma)}\,. \end{aligned} \tag{17}$$

For $\omega_{\rm cr} = 0$, the equalities $|\Gamma(0)| = 1$ and $\frac{\partial|\Gamma|}{\partial\omega}(0) = 0$ always hold. Thus for string stability we need $\frac{\partial^2|\Gamma|}{\partial\omega^2}(0) < 0$ which is equivalent to $P(0) = \alpha(\alpha + 2\beta - 2f^*) > 0$. That is, one of the boundaries is equivalent to the plant stability boundary (12) while the other is given by

$$\alpha = 2(f^* - \beta)\,. \tag{18}$$

Notice that this zero-frequency boundary does not depend on the delay σ.

In the special case of $\sigma = 0$, only the string stability boundaries (12) and (18) appear as shown by the straight lines bounding the gray string stable domain in Fig. 3a. The coloring outside the string stable area corresponds to the solution of $P(\omega) = \omega^2 + \alpha(\alpha + 2\beta - 2f^*) = 0$ for the frequency ω. The coloring indicates that string stability is lost for low frequencies. For different values of $\sigma > 0$ the stability boundaries (12, 16–18) enclose the gray-shaded string stability domain in the (β, α)-plane as depicted in Fig. 4a, c, e. The coloring outside the string stable area corresponds to the solution of $P(\omega) = 0$ for the frequency ω (cf. (14)). When there exist multiple solutions we use the largest ω value. The coloring indicates that when leaving the string stable area toward the left, string stability is still lost at low frequencies. On the other hand, leaving the area to the right, high-frequency string instability occurs. To demonstrate this behavior we marked the points A, B, C on Fig. 4a and plot the corresponding amplification ratios as a function of the frequencies in Fig. 5a. Indeed, for case B the amplification ratio stays below 1 for all frequencies. For cases A and C it exceeds 1 for low and high frequencies, respectively.

One may observe that as the delay σ increases the string stable domain shrinks and for $\sigma = 0.3$ s it almost disappears. In fact, there exists a critical value of the delay such that for $\sigma > \sigma_{\rm cr}$ there exist no gain combinations that can ensure string stability. To calculate the critical delay one may use the L'Hospital rule to show that for $\omega_{\rm cr} \to 0$ formulae (16, 17) yield the points

$$\begin{aligned}(\alpha^+,\, \beta^+) &= \left(\frac{2f^*\sigma - 1}{\sigma(f^*\sigma - 1)},\, \frac{2(f^*\sigma)^2 - 4f^*\sigma + 1}{2\sigma(f^*\sigma - 1)}\right),\\ (\alpha^-,\, \beta^-) &= \left(0,\, \frac{1}{2\sigma}\right),\end{aligned} \tag{19}$$

which are located along the stability boundary around the yellow shading in Fig. 4a. These points move closer to each other when the delay increases and coincide when the delay takes the value

$$\sigma_{\rm cr} = \frac{1}{2f^*} = \frac{T_{\rm gap}}{2}\,. \tag{20}$$

Finally notice that for an open chain of $N + 1$ vehicles, one may derive the head-to-tail transfer function $(\Gamma(s))^N = \tilde{V}_1(s)/\tilde{V}_{N+1}(s)$ between the head vehicle $N + 1$ and

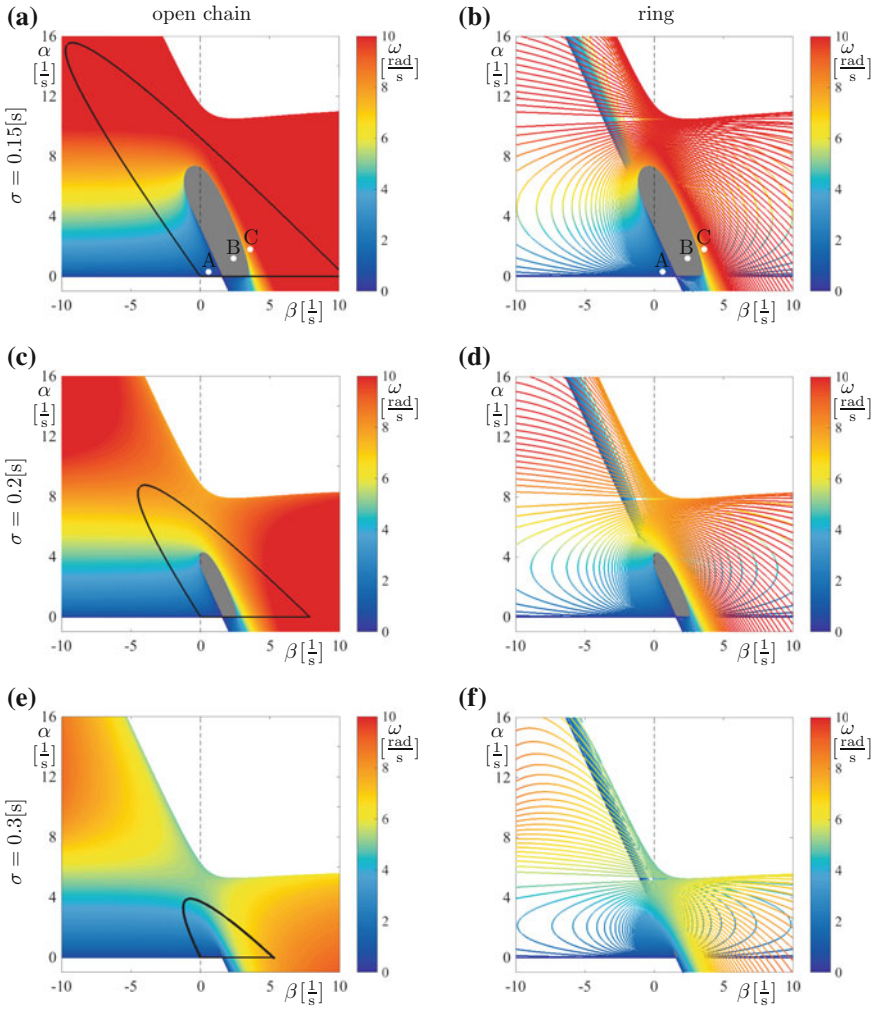

Fig. 4 Stability diagrams for the system (10) for different delay values as indicated using the open chain configuration (*left*) and the ring configuration (*right*). The system is plant stable within the lobe-shaped domain enclosed by the thick *black curve*. The *gray-shaded* region indicates string stability while coloring refers to the oscillation frequencies as indicated by the *color bar*

the tail vehicle 1. Thus, the string stability condition still remains the same independent of N.

When having N vehicles on a ring-road, one may define the state $X = [\tilde{s}_1, \tilde{v}_1, \ldots, \tilde{s}_N, \tilde{v}_N]^T$ where T denotes the transpose. Then (10) can be written into the compact form

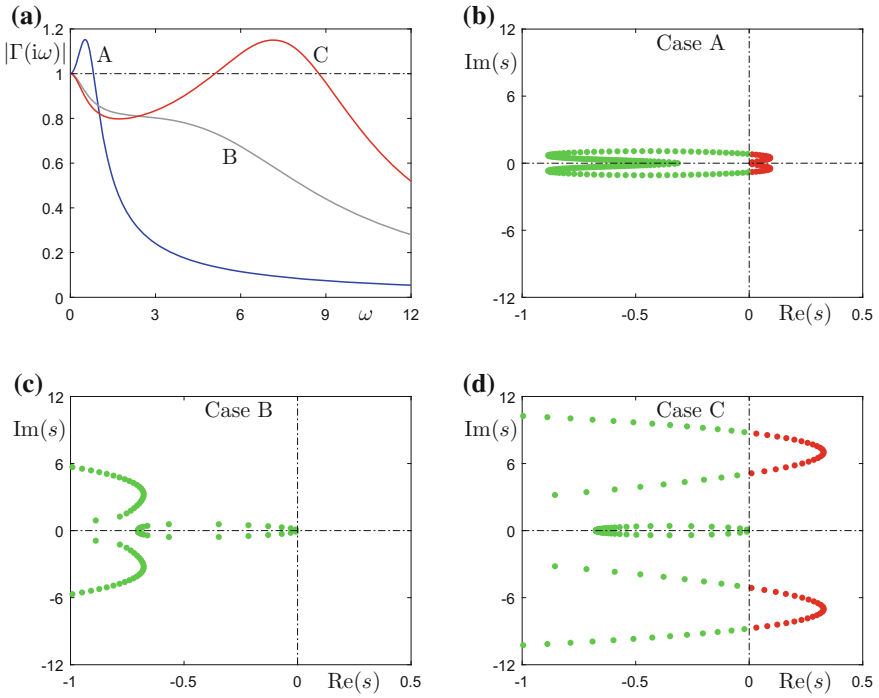

Fig. 5 **a** Amplification ratios for the points marked A, B, C in Fig. 4a, b when considering two consecutive cars in an open chain. **b**, **c**, **d** Corresponding characteristic roots in case of the ring configuration

$$\begin{aligned}\dot{X}(t) &= (\mathbf{I}\otimes\mathbf{a})X(t) + (\mathbf{I}\otimes\mathbf{b}+\mathbf{R}\otimes\mathbf{c})X(t-\sigma)\\ &= \begin{bmatrix}\mathbf{a} & & \\ & \ddots & \\ & & \mathbf{a}\end{bmatrix}X(t) + \begin{bmatrix}\mathbf{b} & \mathbf{c} & \\ & \ddots & \ddots \\ & & \mathbf{b} \\ \mathbf{c} & & \mathbf{b}\end{bmatrix}X(t-\sigma)\,,\end{aligned} \tag{21}$$

where $\otimes$ denotes the Kronecker product and $\mathbf{I}$ is the N-dimensional identity matrix. Also, the N-dimensional matrix $\mathbf{R}$ is given by

$$\mathbf{R} = \begin{bmatrix}0 & 1 & 0 & \cdots & 0\\ 0 & 0 & 1 & \ddots & \vdots\\ \vdots & & \ddots & \ddots & 0\\ 0 & 0 & \cdots & 0 & 1\\ 1 & 0 & \cdots & 0 & 0\end{bmatrix}, \tag{22}$$

while the two-dimensional nonzero blocks are

$$\mathbf{a} = \begin{bmatrix} 0 & 1 \\ 0 & 0 \end{bmatrix}, \quad \mathbf{b} = \begin{bmatrix} 0 & 0 \\ -\alpha f^* & -(\alpha+\beta) \end{bmatrix}, \quad \mathbf{c} = \begin{bmatrix} 0 & 0 \\ \alpha f^* & \beta \end{bmatrix}. \tag{23}$$

Then one can block-diagonalize the matrices in (21) using the coordinate transformation

$$X = (\mathbf{T} \otimes \mathbf{I})Z, \tag{24}$$

where the N-dimensional matrix $\mathbf{T}$ is constructed from the eigenvectors of $\mathbf{R}$ while $\mathbf{I}$ is the two-dimensional identity matrix. This yields

$$\dot{Z}(t) = \begin{bmatrix} \mathbf{a} & & & \\ & \ddots & & \\ & & \ddots & \\ & & & \mathbf{a} \end{bmatrix} Z(t) + \begin{bmatrix} \mathbf{b}+\mathbf{c} & & & \\ & \mathbf{b}+\mathrm{e}^{\mathrm{i}\frac{2\pi}{N}}\mathbf{c} & & \\ & & \ddots & \\ & & & \mathbf{b}+\mathrm{e}^{\mathrm{i}\frac{2(N-1)\pi}{N}}\mathbf{c} \end{bmatrix} Z(t-\sigma), \tag{25}$$

where $\mathrm{e}^{\mathrm{i}\frac{2k\pi}{N}}$, for $k = 0, 1, \ldots, N-1$ are the eigenvalues of the matrix $\mathbf{R}$ in (22). The corresponding eigenvectors, that constitute the columns of $\mathbf{T}$ in (24), are given by $[1, \mathrm{e}^{\mathrm{i}\frac{2k\pi}{N}}, \mathrm{e}^{\mathrm{i}\frac{2k\pi}{N}2}, \ldots, \mathrm{e}^{\mathrm{i}\frac{2k\pi}{N}(N-1)}]^{\mathrm{T}}$, for $k = 0, 1, \ldots, N-1$. Thus, the physical meaning of k is a discrete wave number of the appearing traveling waves and the corresponding spatial wavelengths are $\Lambda = (L + N\ell)/k$ for $k \leq N/2$ and $\Lambda = (L + N\ell)/(N-k)$ for $k > N/2$. In other words, the same spatial pattern arises for wave numbers k and $N-k$.

The block-diagonal matrices in (25) allow us to analyze the stability of the traveling waves separately for each wave number k. In particular, using the trial solution $Z(t) \sim \mathrm{e}^{st}$ one may obtain the characteristic equation

$$\prod_{k=0}^{N-1} \det\left[s\mathbf{I} - \mathbf{a} - \left(\mathbf{b} + \mathrm{e}^{\mathrm{i}\frac{2k\pi}{N}}\mathbf{c}\right)\mathrm{e}^{-s\sigma}\right] = 0. \tag{26}$$

Using the definitions (23), this yields

$$\mathrm{e}^{s\sigma}s^2 + (\alpha+\beta)s + \alpha f^* - \left(\beta s + \alpha f^*\right)\mathrm{e}^{\mathrm{i}\frac{2k\pi}{N}} = 0 \tag{27}$$

for $k = 0, 1, \ldots, N-1$. Notice that using the transfer function (11) and the periodic boundary conditions imply $(\Gamma(s))^N = 1$ and taking the N-th root results in the characteristic equation (27).

The system is stable if the characteristic roots are located in the left half complex plane for all k. To determine the corresponding stability boundaries we consider the critical scenarios when characteristic roots cross the imaginary axis. For wavenumber $k = 0$, one may notice $s = 0$ satisfies (27) for all values of α and β. This corresponds to the translational symmetry of the ring configuration: the system is invariant when shifting all vehicles with the same distance along the road [14]. For wavenumbers $k > 0$, substituting $s = 0$ into (27) yields the stability boundary (12).

On the other hand, when considering that a pair of complex conjugate roots crosses the imaginary axis, substituting $s = \pm \mathrm{i}\omega$ into (27) results in the stability boundaries

$$\begin{aligned} \alpha &= \frac{\omega^2 \left(\cos(\omega\sigma) - \cos(\omega\sigma - \frac{2k\pi}{N}) \right)}{-\omega \sin(\frac{2k\pi}{N}) + 2f^* \left(1 - \cos(\frac{2k\pi}{N})\right)}, \\ \beta &= \frac{-\omega^2 \cos(\omega\sigma) + f^*\omega \left(\sin(\omega\sigma) - \sin(\omega\sigma - \frac{2k\pi}{N}) \right)}{-\omega \sin(\frac{2k\pi}{N}) + 2f^* \left(1 - \cos(\frac{2k\pi}{N})\right)} \end{aligned} \tag{28}$$

for $k = 0, 1, \ldots, N-1$ as depicted in Fig. 3b and in Fig. 4b, d, f for different values of the delay σ while considering $N = 100$ vehicles. Each curve is parameterized by the frequency ω as highlighted by the color code. Notice the remarkable similarity between the stability charts shown in the left and the right of Fig. 4 despite the fact that panels (a, c, e) correspond to the steady state response of the open chain while panels (b, d, f) correspond to the transient response of the ring configuration. To further emphasize this similarity we plot the characteristic roots (the solutions of (27)) in the complex plane in Fig. 5b, c, d for the points marked A, B, C in Fig. 4b. For cases A and C the crossing frequencies in Fig. 5a and in Fig. 5b, d show a good correspondence.

Linearizing the model (8) about the equilibrium (7) yields

$$\begin{aligned} \dot{\tilde{s}}(t) &= \tilde{v}(t)\,, \\ \dot{\tilde{v}}(t) &= \alpha f^* \left(\tilde{s}_{\mathrm{L}}(t-\sigma) - \tilde{s}(t-\sigma)\right) + \beta \tilde{v}_{\mathrm{L}}(t-\sigma) - \alpha \tilde{v}(t) - \beta \tilde{v}(t-\sigma)\,. \end{aligned} \tag{29}$$

Taking the Laplace transform with zero initial conditions we obtain the transfer function

$$\Gamma(s) = \frac{\tilde{V}(s)}{\tilde{V}_{\mathrm{L}}(s)} = \frac{\beta s + \alpha f^*}{\mathrm{e}^{s\sigma}(s^2 + \alpha s) + \beta s + \alpha f^*}\,. \tag{30}$$

The corresponding plant stability boundaries are given by (12) and

$$\begin{aligned} \alpha &= \frac{\Omega^2 \cos(\Omega\sigma)}{f^* - \Omega \sin(\Omega\sigma)}\,, \\ \beta &= \Omega \sin(\Omega\sigma) - \alpha \cos(\Omega\sigma)\,, \end{aligned} \tag{31}$$

that are shown as thick black curves in the (β, α)-plane in Fig. 6a, c, e. Applying Stépán's formulae [17] shows that the system is plant stable when parameters are chosen from the region above the black curves. Again, increasing the delay leads to smaller plant stable domains.

In this case, the string stability condition can be rewritten as $\omega Q(\omega) > 0$ where

$$Q(\omega) = \omega^3 + \alpha^2\omega - 2(\alpha^2 f^* + \beta\omega^2)\sin(\omega\sigma) + 2(\alpha\beta - \alpha f^*)\omega\cos(\omega\sigma)\,. \tag{32}$$

For $\omega_{cr} > 0$ the string stability boundaries can be obtained by substituting P with Q in (15) which yields

$$\begin{aligned} &\sum_{p=0}^{3} a_p \alpha^p = 0\,, \\ &\beta = \frac{\omega_{cr}^3 + \alpha^2 \omega_{cr} - 2\alpha f^* \big(\alpha \sin(\omega_{cr}\sigma) + \omega_{cr} \cos(\omega_{cr}\sigma)\big)}{2\omega_{cr}\big(\omega_{cr} \sin(\omega_{cr}\sigma) - \alpha \cos(\omega_{cr}\sigma)\big)}\,, \end{aligned} \tag{33}$$

where

$$\begin{aligned} a_0 &= \omega_{cr}^4 \cos(\omega_{cr}\sigma)\big(-\sin(\omega_{cr}\sigma) + \omega_{cr}\sigma\cos(\omega_{cr}\sigma)\big)\,, \\ a_1 &= \omega_{cr}^2 \cos(\omega_{cr}\sigma)\big(\omega_{cr}^2\sigma\sin(\omega_{cr}\sigma) - 2f^*\sin(\omega_{cr}\sigma)\cos(\omega_{cr}\sigma) + 2\omega_{cr}\cos(\omega_{cr}\sigma) - 2f^*\omega_{cr}\sigma\big)\,, \\ a_2 &= \omega_{cr}\cos(\omega_{cr}\sigma)\big(\omega_{cr}\sin(\omega_{cr}\sigma) - 4f^*\sin^2(\omega_{cr}\sigma) + \omega_{cr}^2\sigma\cos(\omega_{cr}\sigma)\big)\,, \\ a_3 &= \cos(\omega_{cr}\sigma)\big(\omega_{cr}^2\sigma\sin(\omega_{cr}\sigma) + 2f^*\sin(\omega_{cr}\sigma)\cos(\omega_{cr}\sigma) - 2f^*\omega_{cr}\sigma\big)\,. \end{aligned} \tag{34}$$

For $\omega_{cr} = 0$, the inequality $\frac{\partial^2|\Gamma|}{\partial\omega^2}(0) < 0$ is equivalent to $\frac{\partial Q}{\partial\omega}(0) = \alpha\big((1 - 2f^*\sigma)\alpha + 2\beta - 2f^*\big) > 0$, that yields the boundaries (12) and

$$\alpha = \frac{2(f^* - \beta)}{1 - 2f^*\sigma}\,. \tag{35}$$

That is, in this case, the gradient of the zero-frequency boundary is influenced by the delay as shown by the boundary on the left of the gray string stable region in Figs. 3a and 6a, c, e. Here the coloring corresponds to the solution of $Q(\omega) = 0$ for the frequency ω (cf.(32)). Again, on the left string stability is lost at low frequencies while on the right high-frequency string instability occurs. The string stable domain is not closed from above but it still shrinks as the delay increases and it disappears when the delay exceeds

$$\sigma_{cr} \approx \frac{0.785}{f^*} = 0.785\, T_{gap}\,, \tag{36}$$

but this value cannot be calculated analytically.

When comparing Figs. 4a, c, e and 6a, c, e one may notice a trade-off. While the critical delay is significantly larger in the latter case, it also requires larger gains to make the systems string stable as the delay is increased. This may be difficult to achieve in practice due to the saturation of the actuators.

In case of the ring configuration we may still write the system into the form (21) where $\mathbf{R}$ is still given by (22), but the blocks are given by

$$\mathbf{a} = \begin{bmatrix} 0 & 1 \\ 0 & -\alpha \end{bmatrix}\,, \quad \mathbf{b} = \begin{bmatrix} 0 & 0 \\ -\alpha f^* & -\beta \end{bmatrix}\,, \quad \mathbf{c} = \begin{bmatrix} 0 & 0 \\ \alpha f^* & \beta \end{bmatrix}\,. \tag{37}$$

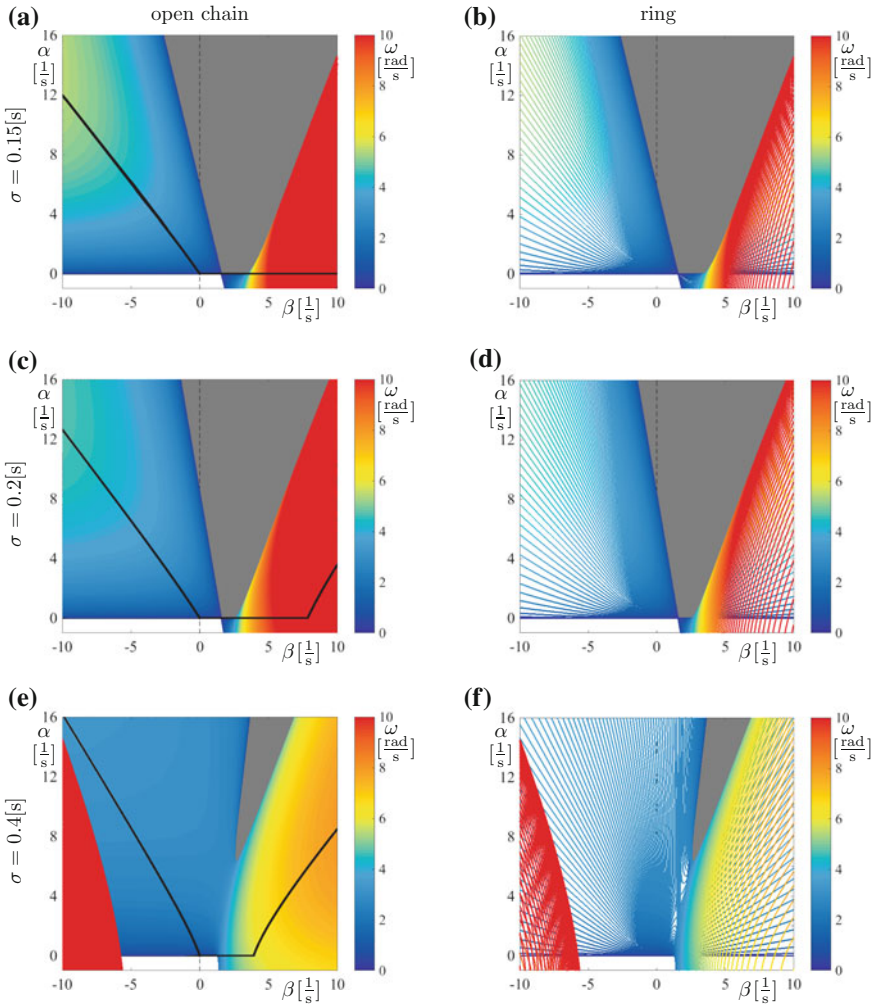

Fig. 6 Stability diagrams for the system (29) using the open chain configuration (*left*) and the ring configuration (*right*). The same notation is used as in Fig. 4

After obtaining the block-diagonal form (25) we can obtain the characteristic equation in the form (26) that yields

$$e^{s\sigma}\left(s^2 + \alpha s\right) + \beta s + \alpha f^* - \left(\beta s + \alpha f^*\right)e^{i\frac{2k\pi}{N}} = 0 \tag{38}$$

for $k = 0, 1, \dots, N-1$. The corresponding stability boundaries are given by

$$\begin{aligned} \alpha &= \frac{\omega^2\big(\cos(\omega\sigma) - \cos(\omega\sigma - \frac{2k\pi}{N})\big)}{-\omega\big(\sin(\omega\sigma) - \sin(\omega\sigma - \frac{2k\pi}{N})\big) + 2f^*\big(1 - \cos(\frac{2k\pi}{N})\big)}\,, \\ \beta &= \frac{-\omega^2 + f^*\omega\big(\sin(\omega\sigma) - \sin(\omega\sigma - \frac{2k\pi}{N})\big)}{-\omega\big(\sin(\omega\sigma) - \sin(\omega\sigma - \frac{2k\pi}{N})\big) + 2f^*\big(1 - \cos(\frac{2k\pi}{N})\big)} \end{aligned} \tag{39}$$

for $k = 0, 1, \dots, N-1$ as depicted in Fig. 6b, d, f for different values of the delay σ while considering $N = 100$ vehicles. Again, comparing panels (a, c, e) to panels (b, d, f) shows very good correspondence with each other.

Finally, the linearization of (9) about the equilibrium (7) takes the form

$$\begin{aligned} \dot{\tilde{s}}(t) &= \tilde{v}(t)\,, \\ \dot{\tilde{v}}(t) &= \alpha f^*\left(\tilde{s}_{\mathrm{L}}(t-\sigma) - \tilde{s}(t-\sigma)\right) + \beta\tilde{v}_{\mathrm{L}}(t-\sigma) - (\alpha+\beta)\tilde{v}(t)\,, \end{aligned} \tag{40}$$

and the corresponding transfer function is given by

$$\Gamma(s) = \frac{\tilde{V}(s)}{\tilde{V}_{\mathrm{L}}(s)} = \frac{\beta s + \alpha f^*}{\mathrm{e}^{s\sigma}\left(s^2 + (\alpha+\beta)s\right) + \alpha f^*}\,. \tag{41}$$

Then the plant stability boundaries are given by (12) and

$$\begin{aligned} \alpha &= \frac{\Omega^2}{f^*\cos(\Omega\sigma)}\,, \\ \beta &= \Omega\tan(\Omega\sigma) - \alpha\,, \end{aligned} \tag{42}$$

that are displayed as thick black curves in Fig. 7a, c, e. According to Stépán's formulae [17] the system is plant stable above the curves and increasing the delay still deteriorates plant stability (though this effect is not so pronounced when comparing to the other two cases discussed above).

Again the string stability condition can be written as $\omega R(\omega) > 0$ where

$$R(\omega) = \omega^3 + \alpha^2\omega + 2\alpha\beta\omega - 2\alpha f^*(\alpha+\beta)\sin(\omega\sigma) - 2\alpha f^*\omega\cos(\omega\sigma)\,, \tag{43}$$

and substituting P with R in (15) results in the string stability boundaries

$$\begin{aligned} \alpha &= \hat{a} \pm \sqrt{\hat{a}^2 + \hat{b}}\,, \\ \beta &= \frac{\omega_{\mathrm{cr}}^3 + \alpha^2\omega_{\mathrm{cr}} - 2\alpha f^*\left(\alpha\sin(\omega_{\mathrm{cr}}\sigma) + \omega_{\mathrm{cr}}\cos(\omega_{\mathrm{cr}}\sigma)\right)}{2\alpha\left(f^*\sin(\omega_{\mathrm{cr}}\sigma) - \omega_{\mathrm{cr}}\right)}\,, \end{aligned} \tag{44}$$

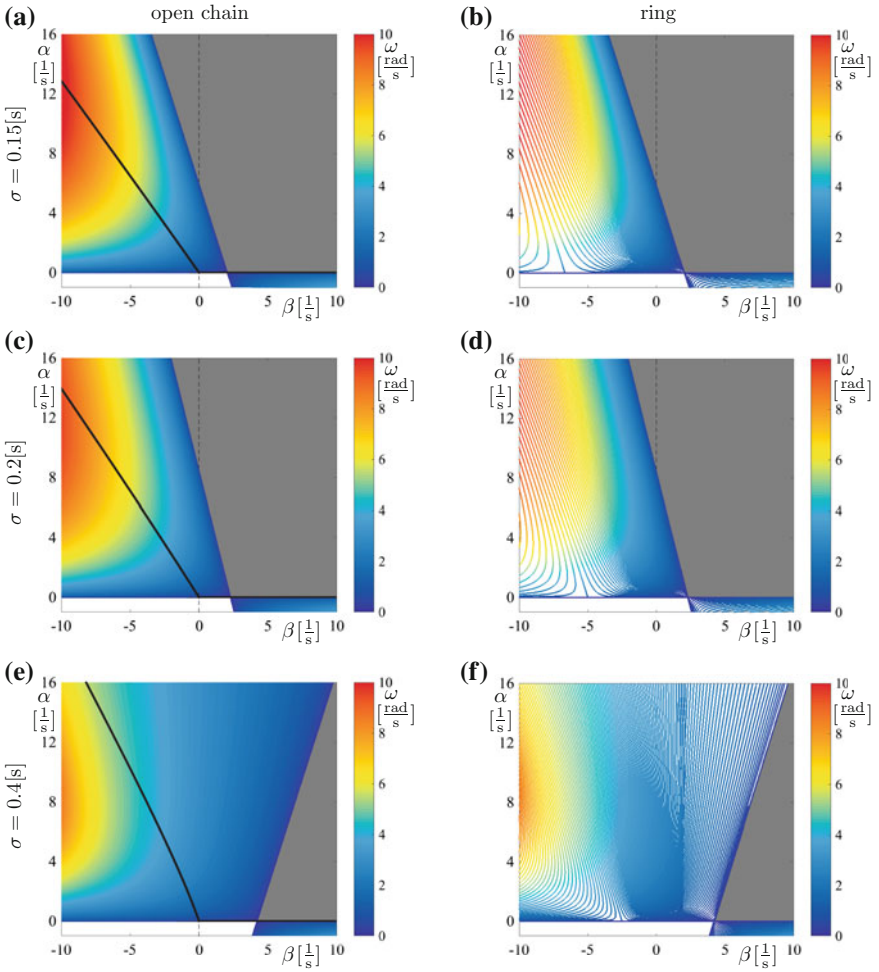

Fig. 7 Stability diagrams for the system (40) using the open chain configuration (*left*) and the ring configuration (*right*). The same notation is used as in Fig. 4

where

$$\begin{aligned}\hat{a} &= \frac{-\omega_{\text{cr}}^2\sigma\sin(\omega_{\text{cr}}\sigma) - f^*\sin(\omega_{\text{cr}}\sigma)\cos(\omega_{\text{cr}}\sigma) + f^*\omega_{\text{cr}}\sigma}{\sin(\omega_{\text{cr}}\sigma) - \omega_{\text{cr}}\sigma\cos(\omega_{\text{cr}}\sigma)}\,,\\ \hat{b} &= \frac{\omega_{\text{cr}}^2\left(3f^*\sin(\omega_{\text{cr}}\sigma) - f^*\omega_{\text{cr}}\sigma\cos(\omega_{\text{cr}}\sigma) - 2\omega_{\text{cr}}\right)}{f^*\left(\sin(\omega_{\text{cr}}\sigma) - \omega_{\text{cr}}\sigma\cos(\omega_{\text{cr}}\sigma)\right)}\,.\end{aligned} \tag{45}$$

However, we remark that these do not give stability boundaries in the physically realistic parameter ranges.

For $\omega_{\rm cr} = 0$, we obtain $\frac{\partial R}{\partial \omega}(0) = \alpha\big((1-2f^*\sigma)\alpha + 2(1-f^*\sigma)\beta - 2f^*\big) > 0$, that yields the boundaries (12) and

$$\alpha = \frac{2\big(f^* - (1-f^*\sigma)\beta\big)}{1-2f^*\sigma}\,. \tag{46}$$

That is, both the gradient and the position of the zero-frequency boundary is influenced by the delay which can be observed when looking at the left boundary in Figs. 3a and 6a, c, e. As shown by the coloring, only low-frequency string instability occurs and the gray string stable domain is open from above and from the right. By investigating when the gradient of (46) becomes zero one can calculate the critical delay

$$\sigma_{\rm cr} = \frac{1}{f^*} = T_{\rm gap}\,, \tag{47}$$

above which the string stable domain disappears.

Again comparing Figs. 4a, c, e, 6a, c, e, and 7a, c, e one may notice that the critical delay increases but larger gains are required to make the system string stable which may not be possible due to the limitation of the actuators.

In case of the ring configuration (25) contains

$$\mathbf{a} = \begin{bmatrix} 0 & 1 \\ 0 & -(\alpha+\beta) \end{bmatrix}, \quad \mathbf{b} = \begin{bmatrix} 0 & 0 \\ -\alpha f^* & 0 \end{bmatrix}, \quad \mathbf{c} = \begin{bmatrix} 0 & 0 \\ \alpha f^* & \beta \end{bmatrix}, \tag{48}$$

while (26) yields

$$\mathrm{e}^{s\sigma}\big(s^2 + (\alpha+\beta)s\big) + \beta s + \alpha f^* - \alpha f^* \mathrm{e}^{\mathrm{i}\frac{2k\pi}{N}} = 0\,, \tag{49}$$

resulting in the stability boundaries

$$\begin{aligned} \alpha &= \frac{\omega^2\big(1-\cos(\omega\sigma - \frac{2k\pi}{N})\big)}{\omega\sin(\omega\sigma - \frac{2k\pi}{N}) + f^*\big(1-\cos(\frac{2k\pi}{N}) + \cos(\omega\sigma) - \cos(\omega\sigma - \frac{2k\pi}{N})\big)}\,, \\ \beta &= \frac{-\omega^2 + f^*\omega\big(\sin(\omega\sigma) - \sin(\omega\sigma - \frac{2k\pi}{N})\big)}{\omega\sin(\omega\sigma - \frac{2k\pi}{N}) + f^*\big(1-\cos(\frac{2k\pi}{N}) + \cos(\omega\sigma) - \cos(\omega\sigma - \frac{2k\pi}{N})\big)} \end{aligned} \tag{50}$$

for $k = 0, 1, \ldots, N-1$ as shown in Fig. 7b, d, f for different σ values and $N = 100$ vehicles. Indeed, panels (a, c, e) show very good correspondence with panels (b, d, f).

4 Conclusion

The effect of time delays has been investigated in connected cruise control scenarios where each vehicle controls its longitudinal motion based on the V2V information received from the vehicles immediately ahead. In order to evaluate the stability of uniform traffic flow we considered open chain and ring configurations and our results show that these configurations give the same results when the number of vehicles is large enough. We also demonstrated that as the delay increases the stable areas shrink, and that when the delay exceeds a critical value no gain combinations can stabilize the uniform flow. Moreover, using the instantaneous values of quantities measured on board may not necessarily improve the performance. On one hand, one may increase the critical value of the delay, but on the other hand it requires larger gains to stabilize the system (that may not be available due to actuator limitations). Thus, it may in fact be beneficial to delay the values of the on-board quantities to achieve high-performance CCC design.

References

1. Avedisov, S.S., Orosz, G.: Nonlinear network modes in cyclic systems with applications to connected vehicles. J. Nonlinear Sci. **25**, 1015–1049 (2015)
2. Bando, M., Hasebe, K., Nakanishi, K., Nakayama, A.: Analysis of optimal velocity model with explicit delay. Phys. Rev. E **58**(5), 5429–5435 (1998)
3. Davis, L.C.: Effect of adaptive cruise control systems on traffic flow. Phys. Rev. E **69**(6), 066–110 (2004)
4. Gazis, D.C., Herman, R., Rothery, R.W.: Nonlinear follow-the-leader models of traffic flow. Oper. Res. **9**(4), 545–567 (1961)
5. Ge, J.I., Orosz, G.: Dynamics of connected vehicle systems with delayed acceleration feedback. Trans. Res. Part C **46**, 46–64 (2014)
6. Ge, J.I., Orosz, G.: Optimal control of connected vehicle systems with communication delay and driver reaction time. IEEE Trans. Intell. Trans. Syst. (2016) (published online). doi:10.1109/TITS.2016.2633164
7. Greenshields, B.D.: Studying traffic capacity by new methods. J. Appl. Psychol. **20**(3), 353–358 (1936)
8. Herman, R., Montroll, E.W., Potts, R.B., Rothery, R.W.: Traffic dynamics: analysis of stability in car following. Oper. Res. **7**(1), 86–106 (1959)
9. Insperger, T., Stépán, G.: Semi-Discretization for Time-Delay Systems: Stability and Engineering Applications. Applied Mathematical Sciences, vol. 178. Springer (2011)
10. Kesting, A., Treiber, M.: How reaction time, update time, and adaptation time influence the stability of traffic flow. Comput. Aided Civ. Infrastruct. Eng. **23**(2), 125–137 (2008)
11. Liang, C.Y., Peng, H.: Optimal adaptive cruise control with guaranteed string stability. Veh. Syst. Dyn. **32**(4–5), 313–330 (1999)
12. Öncü, S., Ploeg, J., van de Wouw, N., Nijmeijer, H.: Cooperative adaptive cruise control: network-aware analysis of string stability. IEEE Trans. Intell. Trans. Syst. **15**(4), 1527–1537 (2014)
13. Orosz, G.: Connected cruise control: modelling, delay effects, and nonlinear behaviour. Veh. Syst. Dyn. **54**(8), 1147–1176 (2016)
14. Orosz, G., Stépán, G.: Subcritical Hopf bifurcations in a car-following model with reaction-time delay. Proc. R. Soc. A **462**(2073), 2643–2670 (2006)

15. Orosz, G., Wilson, R.E., Stépán, G.: Traffic jams: dynamics and control. Philos. Trans. R. Soc. A **368**(1928), 4455–4479 (2010)
16. Qin, W.B., Gomez, M.M., Orosz, G.: Stability and frequency response under stochastic communication delays with applications to connected cruise control design. IEEE Trans. Intell. Trans. Syst. **18**(2), 388–403 (2017)
17. Stépán, G.: Retarded Dynamical Systems: Stability and Characteristic Functions, Pitman Research Notes in Mathematics, vol. 210. Longman (1989)
18. Swaroop, D., Hedrick, J.K.: String stability of interconnected systems. IEEE Trans. Autom. Control **41**(3), 349–357 (1996)
19. Swaroop, D., Hedrick, J.K., Chien, C.C., Ioannou, P.A.: A comparision of spacing and headway control laws for automatically controlled vehicles. Veh. Syst. Dyn. **23**(8), 597–625 (1994)
20. Wagner, P.: Fluid-dynamical and microscopic description of traffic flow - a data-driven comparison. Philos. Trans. R. Soc. A **368**(1928), 4481–4495 (2010)
21. Wang, M., Daamen, W., Hoogendoorn, S.P., van Arem, B.: Rolling horizon control framework for driver assistance systems. Part II: cooperative sensing and cooperative control. Trans. Res. Part C **40**, 290–311 (2014)
22. Zhang, L., Orosz, G.: Motif-based analysis of connected vehicle systems: delay effects and stability. IEEE Trans. Intell. Trans. Syst. **17**(6), 1638–1651 (2016)

H-infinity Filtering for Cloud-Aided Semi-active Suspension with Delayed Information

Zhaojian Li, Ilya Kolmanovsky, Ella Atkins, Jianbo Lu and Dimitar Filev

Abstract This chapter presents an H_∞ filtering framework for cloud-aided semi-active suspension system with time-varying delays. In this system, road profile information is downloaded from a cloud database to facilitate onboard estimation of suspension states. Time-varying data transmission delays are considered and assumed to be bounded. A quarter-car linear suspension model is used and an H_∞ filter is designed with both onboard sensor measurements and delayed road profile information from the cloud. The filter design procedure is designed based on linear matrix inequalities (LMIs). Numerical simulation results are reported that illustrate the fusion of cloud-based and onboard information that can be achieved in Vehicle-to-Cloud-to-Vehicle (V2C2V) implementation.

1 Introduction

The interest in employing cloud computing for automotive applications is growing to support computation and data intensive tasks [1–3]. The cloud can provide access to "big data" as well as real-time crowd-sourced information. Smart utilization of on-demand cloud resources can increase situation awareness and provide additional

Z. Li (✉) · I. Kolmanovsky · E. Atkins
Department of Aerospace Engineering, University of Michigan,
1221 Beal Avenue, Ann Arbor, MI 48109, USA
e-mail: zhaojli@umich.edu

I. Kolmanovsky
e-mail: ilya@umich.edu

E. Atkins
e-mail: ematkins@umich.edu

J. Lu · D. Filev
Research & Advanced Engineering, Ford Motor Company, 2101 Village Rd,
Dearborn, MI 48124, USA
e-mail: jlu10@ford.com

D. Filev
e-mail: dfilev@ford.com

T. Insperger et al. (eds.), *Time Delay Systems*,
Advances in Delays and Dynamics 7, DOI 10.1007/978-3-319-53426-8_19

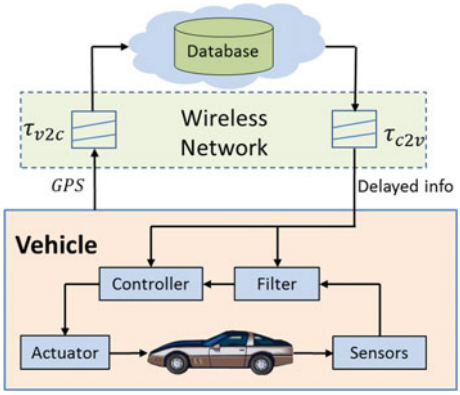

Fig. 1 Info-based V2C2V system with time delays

functionality. In addition, computation and data intensive tasks can be outsourced to the cloud, enabling advanced and computation intensive algorithms to be implemented in real time. While embedded vehicle processors remain essential for time-critical applications, cloud computing can extend current control functionalities with additional functions to enhance performance [1].

Numerous automotive functions have been identified as candidates for Vehicle-to-Cloud-to-Vehicle (V2C2V) implementations [2]. In particular, a cloud-aided safety-based route planning system has been proposed that exploits road risk index database and real-time factors like traffic and weather, and generates a "safe" route [4, 5]. A cloud-based road anomaly detection and crowd-sourcing framework has been proposed in [6–8]. The cloud-aided vehicle semi-active suspension control system is another potential application [9], in which road profile data from the cloud is exploited. In this chapter, we consider the state estimation problem for the cloud-aided semi-active suspension system.

While cloud database can provide large quantity of information, its use for vehicle control is hindered by inevitable time delays in information transmission. While there are proposed mechanisms (e.g., exploiting multiple communication channels [10]) to alleviate the effects of time delays, it is well acknowledged that delays can cause system instability and performance degradation and thus have to be considered in control and filter design. The architecture of V2C2V system with time delays is illustrated in Fig. 1. When needed, the vehicle can send a data request together with its GPS coordinates to the cloud. Then the cloud will send the requested data to the vehicle. The messages are exchanged with a wireless communication channel where vehicle-to-cloud delay (τ_{v2c}) and cloud-to-vehicle delay (τ_{c2v}) occur.

In this chapter, we consider the design of an observer for a V2C2V semi-active suspension system. Unlike traditional white noise road disturbance treatment [11–13], in our system road profile information is downloaded from the cloud to facilitate the suspension state estimation. There are two main approaches in filter design for linear systems. One is H_2 filtering which minimizes estimation error variance. The other is H_∞ filtering which is based on H_∞ performance criterion. H_∞ techniques

are popular in stability analysis and filter design, even in cases with time delays [14, 15]. In this chapter, we develop a H_∞ filtering approach for V2C2V semi-active suspension with time-varying information delays. The filter design is reduced to linear matrix inequalities (LMIs), which can be solved by standard LMI solvers.

This chapter is an extension of our previous conference paper [16]. The main contribution of this chapter is the illustration of the potential to fuse cloud-based and onboard measurements in V2C2V systems to facilitate state estimation and the developments of H-infinity filtering framework for handling communication delays.

The rest of this chapter is organized as follows. In Sect. 2, we present the preliminaries and problem formulation of the H_∞ filtering for info-based V2C2V semi-active suspension system. In Sect. 3, stability and H_∞ filter performance analysis results are presented and derived in terms of LMIs. Section 4 presents the design procedure for the H_∞ filter. Numerical simulations are developed in Sect. 5. Section 6 concludes the chapter.

2 Problem Formulation

In this chapter, we consider the filtering problem for cloud-aided semi-active suspension. Quarter-car models are often used for suspension control design [11–13], because they are simple yet capture many important characteristics of the full-car model. A quarter-car model, with 2 degrees of freedom (DOF) as shown in Fig. 2, is used. M_s and M_{us} represent the car body (sprung) mass and the tire and axles (unsprung mass), respectively. The spring and shock absorber with adjustable damping ratio constitute the suspension system, connecting sprung (body) and unsprung (wheel assembly) masses. The tire is modeled as a spring with stiffness k_{us} and its damping ratio is assumed to be negligible in the suspension formulation. From Fig. 2, we have the following equations of motion:

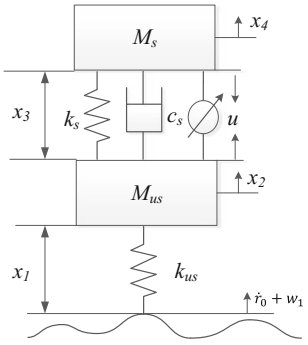

Fig. 2 Semi-active suspension dynamics

$$\begin{aligned}
\dot{x}_1 &= x_2 - \alpha w - \dot{r}_o, \\
M_{us}\dot{x}_2 &= -k_{us}x_1 + k_s x_3 + c_s(x_4 - x_2) + u, \\
\dot{x}_3 &= x_4 - x_2, \\
M_s\dot{x}_4 &= -k_s x_3 - c_s(x_4 - x_2) - u,
\end{aligned} \tag{1}$$

where x_1 is the tire deflection from equilibrium; x_2 is the unsprung mass velocity; x_3 is the suspension deflection from equilibrium; x_4 is the sprung mass velocity; $\dot{r}_o$ represents the deterministic *velocity* disturbance due to the known road profile; w represents the unknown road disturbance and α is a scaling factor; c_s is the constant damping and u is adjustable damper force; k_s and k_{us} are suspension and tire stiffness, respectively.

Defining $x = [x_1 \quad x_2 \quad x_3 \quad x_4]^T$, the suspension system model can be written as

$$\dot{x} = Ax + Bu + B_r\dot{r}_o + B_w w, \tag{2}$$

where

$$A = \begin{bmatrix} 0 & 1 & 0 & 0 \\ -\frac{k_{us}}{M_{us}} & -\frac{c_s}{M_{us}} & \frac{k_s}{M_{us}} & \frac{c_s}{M_{us}} \\ 0 & -1 & 0 & 1 \\ 0 & \frac{c_s}{M_s} & -\frac{k_s}{M_s} & -\frac{c_s}{M_s}p \end{bmatrix}, B = \begin{bmatrix} 0 \\ \frac{1}{M_{us}} \\ 0 \\ -\frac{1}{M_s} \end{bmatrix}, \tag{3}$$

$$B_r = [-1 \quad 0 \quad 0 \quad 0]^{\mathrm{T}}, \quad B_w = [-\alpha \quad 0 \quad 0 \quad 0]^{\mathrm{T}}.$$

For vehicles equipped with semi-active suspension, measurements of vertical wheel velocity (x_2), suspension deflection (x_3) and body velocity (x_4) are typically available, while tire deflection is hard to measure. Let y_0 denote the measurements and z denote the objective signal to be estimated, we augment (2) as follows,

$$\begin{aligned}
\dot{x} &= Ax + Bu + B_r\dot{r}_o + B_w w, \\
y_0 &= [x_2 \quad x_3 \quad x_4]^{\mathrm{T}} = C_0 x + D_0 w, \\
z &= x,
\end{aligned} \tag{4}$$

where $C_0 = [0_{3\times 1} \quad I_3]$.

Figure 3 illustrates the developed cloud-based vehicle software agent that has access to stored vehicle parameters (M_{us}, M_s, k_{us}, k_s, R, $c_{s,i}$), receives vehicle state estimate, $\hat{x}$, vehicle longitudinal velocity, v_{car}, wheel speed, ω, and GPS coordinates, and sends road profile information, $\dot{r}_o$ for use by onboard vehicle state estimator. The received road profile will be delayed in the wireless communication channel. Thus, we will have a delayed measurement of the road profile onboard, that is,

$$y_1(t) = \dot{r}_0(t - \tau(t)) + D_1 w(t), \tag{5}$$

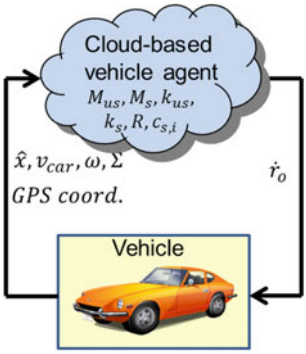

Fig. 3 V2C2V suspension control system

where $\tau(t)$ is the time-varying delay.

Assumption 1 The time delay $\tau(t)$ is time varying and $\tau_m \leq \tau(t) \leq \tau_M$, where τ_m and τ_M are the lower and upper bound of the delay. In the sequel, we use τ to represent $\tau(t)$ when there is no confusion.

For the filter design, we assume that the road profile is modeled as $\ddot{r}_0 = D_r w$, and we let $u(t) \equiv 0$. Then combining (4) and defining the augmented state as $x_a = [x^{\mathrm{T}} \quad \dot{r}_0^{\mathrm{T}}]^{\mathrm{T}}$ and augmented measurement output $y_a = \begin{bmatrix} y_0^{\mathrm{T}} & y_1^{\mathrm{T}} \end{bmatrix}^{\mathrm{T}}$, we have

$$\begin{aligned} \dot{x}_a(t) &= A_a x_a(t) + B_a w(t), \\ y_a(t) &= C_{a0} x_a(t) + C_{a1} x_a(t - \tau(t)) + D_a w(t), \\ z(t) &= E_a x_a(t), \end{aligned} \tag{6}$$

where $A_a = \begin{bmatrix} A & B_r \\ 0 & 0 \end{bmatrix}$, $B_a = \begin{bmatrix} B_w \\ D_r \end{bmatrix}$, $C_{a0} = \begin{bmatrix} C_0 & 0 \\ 0 & 0 \end{bmatrix}$, $C_{a1} = \begin{bmatrix} 0 & 0 \\ 0 & I \end{bmatrix}$, $D_a = \begin{bmatrix} D_0 \\ D_1 \end{bmatrix}$, $E_a = [I \quad 0]$.

A linear time invariant filter for system (6) has the following form:

$$\begin{aligned} \dot{\hat{x}}(t) &= K_A \hat{x}(t) + K_B y_a(t), \\ \hat{z}(t) &= K_C \hat{x}(t), \\ \hat{x}(0) &= x_a(0), \, \hat{x}(s) = 0, \forall s \in [-\tau, 0]. \end{aligned} \tag{7}$$

Let $\eta(t) = \begin{bmatrix} x_a(t) \\ \hat{x}(t) \end{bmatrix}$ denote the extended state. Then we have the following dynamics

$$\begin{aligned} \dot{\eta}(t) &= \bar{A}\eta(t) + \bar{A}_d x_a(t - \tau) + \bar{B} w(t), \\ e(t) &\triangleq z(t) - \hat{z}(t) = \bar{C}\eta(t), \end{aligned} \tag{8}$$

where

$$\bar{A} = \begin{bmatrix} A_a & 0 \\ K_B C_{a0} & K_A \end{bmatrix}, \quad \bar{A}_d = \begin{bmatrix} 0 \\ K_B C_{a1} \end{bmatrix}, \quad \bar{B} = \begin{bmatrix} B_a \\ K_B D_a \end{bmatrix}, \quad \bar{C} = [E_a \quad -K_C].$$

The desired H_∞ filter problem addressed in this chapter can be formulated as follows: given system (6) and a prescribed level of noise attenuation $\gamma > 0$, determine a linear filter in the form (7) such that the filtering error system is asymptotically stable and

$$\sup_{w \in L_2[0,\infty)} \frac{\|e(t)\|_2^2}{\|w\|_2^2} < \gamma^2. \tag{9}$$

Before ending this section, we present the following lemmas which will be used in the proofs of subsequent sections.

Lemma 1 ([17]) *The linear matrix inequalities*

$$S = \begin{bmatrix} S_{11} & S_{12} \\ S_{12}^T & S_{22} \end{bmatrix} < 0,$$

where $S_{11} = S_{11}^T$ *and* $S_{22} = S_{22}^T$ *are equivalent to*

$$S_{11} < 0, \quad S_{22} - S_{12}^T S_{11}^{-1} S_{12} < 0$$

or

$$S_{22} < 0, \quad S_{11} - S_{12} S_{22}^{-1} S_{12}^T < 0.$$

Lemma 1 is the well-known Schur complement lemma.

Lemma 2 ([18]) *Let X, Y be real constant matrices of compatible dimensions. Then*

$$X^T Y + Y^T X \le \varepsilon X^T X + \frac{1}{\varepsilon} Y^T Y$$

holds for any $\varepsilon > 0$.

Lemma 3 ([19]) *If f, g:* $[a \quad b] \to \mathbb{R}^n$ *are similarly ordered, that is,*

$$(f(x) - f(y))^T (g(x) - g(y)) \ge 0, \quad \forall x, y \in [a, b], \tag{10}$$

then,

$$\frac{1}{b-a} \int_a^b f(x) g(x) dx \ge \left[\frac{1}{b-a} \int_a^b f(x) dx\right] \left[\frac{1}{b-a} \int_a^b g(x) dx\right]. \tag{11}$$

Lemma 3 is a Chebyshev's inequality under similarly ordered conditions.

3 H_∞ Performance Analysis

In this section, sufficient conditions of existence of the H_∞ filter are derived as LMIs.

Theorem 1 *Let K_A, K_B, K_C be given matrices and γ be a given positive scalar. If there exist symmetric matrices $P > 0$, $Q_1 > 0$, $Q_2 > 0$, satisfying*

$$\begin{bmatrix} \Psi & P\bar{B} & \bar{C}^T & \Gamma \\ * & -\gamma^2 I + \tau_M Q_2 & 0 & 0 \\ * & * & -I & 0 \\ * & * & * & -\frac{1}{\tau_M} diag\{Q_1, Q_2\} \end{bmatrix} < 0 \tag{12}$$

where

$$\Psi = P[\bar{A} + \bar{A}_d I_0] + [\bar{A} + \bar{A}_d I_0]^T P + \tau_M I_0^T Q_1 I_0, \quad \Gamma = [P\bar{A}_d A_a \quad P\bar{A}_d B_a], \quad I_0 = [I \quad 0],$$

then the error system (8) is asymptotically stable and satisfies (9).

Proof Note:

$$\begin{aligned} x_a(t-\tau) &= x_a(t) - \int_{t-\tau}^{t} \dot{x}_a(s) ds \\ &= x_a(t) - \int_{t-\tau}^{t} [A_a x_a(s) + B_a w(s)] ds. \end{aligned} \tag{13}$$

Substituting (13) into (8) leads to

$$\dot{\eta}(t) = [\bar{A} + \bar{A}_d I_0]\eta(t) - \bar{A}_d \int_{t-\tau}^{t} [A_a x_a(s) + B_a w(s)] ds + \bar{B} w(t). \tag{14}$$

We next show the stability of the error system (8). Let us consider the following Lyapunov functional candidate

$$V(\eta(t)) = V_0(\eta(t)) + V_1(\eta(t)) + V_2(\eta(t)), \tag{15}$$

where

$$V_0(\eta(t)) = \eta^{\mathrm{T}}(t) P \eta(t),$$

$$V_1(\eta(t)) = \int_{-\tau_M}^{0} \int_{t+\theta}^{t} x_a^{\mathrm{T}}(s) Q_1 x_a(s) ds d\theta,$$

$$V_2(\eta(t)) = \int_{-\tau_M}^{0} \int_{t+\theta}^{t} w^{\mathrm{T}}(s) Q_2 w(s) ds d\theta.$$

In view of (14), we have

$$\begin{aligned}\dot{V}_0(\eta(t)) =&\eta^{\mathrm{T}}(t)\big[P[\bar{A}+\bar{A}_dI_0]+[\bar{A}+\bar{A}_dI_0]^{\mathrm{T}}P\big]\eta(t)\\ &-2\eta^{\mathrm{T}}(t)P\bar{A}_d\Big[A_a\int_{t-\tau}^{t}x_a(s)ds+B_a\int_{t-\tau}^{t}w(s)ds\Big]+2\eta^{\mathrm{T}}(t)P\bar{B}w(t).\end{aligned}\tag{16}$$

Let $X^{\mathrm{T}}=-\eta^{\mathrm{T}}(t)P\bar{A}_dA_aQ_1^{-\frac{1}{2}}$, $\varepsilon=\tau$, $Y=Q_1^{\frac{1}{2}}\int_{t-\tau}^{t}x_a(s)ds$. Using Lemma 2, we obtain

$$\begin{aligned}-2\eta^{\mathrm{T}}(t)P\bar{A}_dA_a\int_{t-\tau}^{t}x_a(s)ds\le&\ \tau\eta^{\mathrm{T}}(t)[P\bar{A}_dA_aQ_1^{-1}A_a^{\mathrm{T}}\bar{A}_d^{\mathrm{T}}P]\eta(t)\\ &+\frac{1}{\tau}\int_{t-\tau}^{t}x_a^Tds Q_1\int_{t-\tau}^{t}x_a(s)ds.\end{aligned}\tag{17}$$

Using Lemma 3, we have

$$\int_{t-\tau}^{t}x_a^T(s)dsQ_1\int_{t-\tau}^{t}x_a(s)ds\le\tau\int_{t-\tau}^{t}x_a^{\mathrm{T}}(s)Q_1x_a(s)ds.\tag{18}$$

From (17) and (18), it follows that

$$\begin{aligned}-2\eta^{\mathrm{T}}(t)P\bar{A}_dA_a\int_{t-\tau}^{t}x_a(s)ds\le&\ \tau\eta^{\mathrm{T}}(t)[P\bar{A}_dA_aQ_1^{-1}A_a^{\mathrm{T}}\bar{A}_d^{\mathrm{T}}P]\eta(t)\\ &+\int_{t-\tau}^{t}x_a^TQ_1x_a(s)ds.\end{aligned}\tag{19}$$

Similarly,

$$\begin{aligned}-2\eta^{\mathrm{T}}(t)P\bar{A}_dB_a\int_{t-\tau}^{t}w(s)ds\le&\ \tau\eta^{\mathrm{T}}(t)P\bar{A}_dB_aQ_2^{-1}B_a^{\mathrm{T}}\bar{A}_d^{\mathrm{T}}P\eta(t)\\ &+\int_{t-\tau}^{t}w^{\mathrm{T}}(s)Q_2w(s)ds.\end{aligned}\tag{20}$$

Combining (16)–(20) yields

$$\begin{aligned}\dot{V}_0(\eta(t))\le&\ \eta^{\mathrm{T}}(t)\big[P[\bar{A}+\bar{A}_dI_0]+[\bar{A}+\bar{A}_dI_0]^{\mathrm{T}}P\big]\eta(t)\\ &+\tau\eta^{\mathrm{T}}(t)[P\bar{A}_dA_aQ_1^{-1}A_a^{\mathrm{T}}\bar{A}_d^{\mathrm{T}}P]\eta(t)\\ &+\int_{t-\tau}^{t}x_a^T(s)Q_1x_a(s)ds\\ &+\tau\eta^{\mathrm{T}}(t)P\bar{A}_dB_aQ_2^{-1}B_a^{\mathrm{T}}\bar{A}_d^{\mathrm{T}}P\eta(t)\\ &+\int_{t-\tau}^{t}w^{\mathrm{T}}(s)Q_2w(s)ds+2\eta^{\mathrm{T}}(t)P\bar{B}w(t).\end{aligned}\tag{21}$$

Simple computations yield

$$\dot{V}_1(\eta(t)) = -\int_{t-\tau_M}^{t} x_a^{\mathrm{T}}(s)Q_1x_a(s)ds + \tau_M x_a^{\mathrm{T}}(t)Q_1x_a(t) \tag{22}$$

Also,

$$\dot{V}_2(\eta(t)) = \tau_M w^{\mathrm{T}}(t)Q_2w(t) - \int_{t-\tau_M}^{t} w^{\mathrm{T}}(s)Q_2w(s)ds. \tag{23}$$

Combining (21), (22) and (23), we obtain

$$\begin{aligned}\dot{V}(\eta(t)) &\le \eta^{\mathrm{T}}(t)\big[P[\bar{A}+\bar{A}_dI_0] + [\bar{A}+\bar{A}_dI_0]^{\mathrm{T}}P\big]\eta(t)\\ &\quad + \tau_M\eta^{\mathrm{T}}(t)[P\bar{A}_dA_aQ_1^{-1}A_a^{\mathrm{T}}\bar{A}_d^{\mathrm{T}}P]\eta(t)\\ &\quad + \tau_M\eta^{\mathrm{T}}(t)P\bar{A}_dB_aQ_2^{-1}B_a^{\mathrm{T}}\bar{A}_d^{\mathrm{T}}P\eta(t)\\ &\quad + \tau_M x_a^{\mathrm{T}}(t)Q_1x_a(t) + \tau_M w^{\mathrm{T}}(t)Q_2w(t) + 2\eta^{\mathrm{T}}(t)P\bar{B}w(t)\\ &= [\eta^{\mathrm{T}}(t)\, w^{\mathrm{T}}(t)]\boldsymbol{\Phi}\begin{bmatrix}\eta(t)\\ w(t)\end{bmatrix},\end{aligned} \tag{24}$$

where

$$\boldsymbol{\Phi} = \begin{bmatrix}\Psi & P\bar{B}\\ \bar{B}^{\mathrm{T}}P & \tau_MQ_2\end{bmatrix} + \begin{bmatrix}\tau_M\Gamma diag\{Q_1^{-1},\, Q_2^{-1}\}\Gamma^{\mathrm{T}} & 0\\ 0 & 0\end{bmatrix}.$$

Using Lemma 1, it is straightforward to check that (12) implies $\boldsymbol{\Phi} < 0$, which concludes the proof of stability.
Now let us define an H_∞ performance J_T as follows:

$$J_T = \int_0^T [e^{\mathrm{T}}(t)e(t) - \gamma^2 w^{\mathrm{T}}(t)w(t)]dt.$$

Then we have

$$\begin{aligned}J_T &= \int_0^T [e^{\mathrm{T}}(t)e(t) - \gamma^2 w^{\mathrm{T}}(t)w(t)]dt\\ &= \int_0^T [e^{\mathrm{T}}(t)e(t) - \gamma^2 w^{\mathrm{T}}(t)w(t) + \dot{V}(\eta(t)) - \dot{V}(\eta(t))]dt\\ &= \int_0^T [e^{\mathrm{T}}(t)e(t) - \gamma^2 w^{\mathrm{T}}(t)w(t) + \dot{V}(\eta(t))]dt - V(\eta(T))\\ &\le \int_0^T [\eta^{\mathrm{T}}(t)\, w^{\mathrm{T}}(t)]\Theta\begin{bmatrix}\eta(t)\\ w(t)\end{bmatrix}dt,\end{aligned} \tag{25}$$

where

$$\Theta = \begin{bmatrix} \Psi + \bar{C}^{\mathrm{T}}\bar{C} & P\bar{B} \\ \bar{B}^{\mathrm{T}}P & -\gamma^2 I + \tau_M Q_2 \end{bmatrix} + \begin{bmatrix} \tau_M \Gamma diag\{Q_1^{-1}, Q_2^{-1}\}\Gamma^{\mathrm{T}} & 0 \\ 0 & 0 \end{bmatrix}. \tag{26}$$

Using Schur complement as in Lemma 1, it is straight to check that (12) implies $\Theta < 0$ and consequently

$$J_T < 0 \quad \forall T > 0,$$

and it follows that

$$J_\infty = \int_0^\infty [e^{\mathrm{T}}(t)e(t) - \gamma^2 w^{\mathrm{T}}(t)w(t)]dt < 0,$$

that is $\|e\|_2 \leq \gamma \|w\|_2$. This concludes the proof of Theorem 1.

4 Filter Design

In this section, we present the design of filter gains K_A, K_B and K_C in (7).
We note that using Schur complement, it can be shown that (12) is equivalent to

$$\begin{bmatrix} \Psi_1 & P\bar{B} & \bar{C}^{\mathrm{T}} & \Gamma_1 \\ * & -\gamma^2 I + \tau_M Q_2 & 0 & 0 \\ * & * & -I & 0 \\ * & * & * & -1/\tau_M \mathscr{Q} \end{bmatrix} < 0, \tag{27}$$

where

$$\Psi_1 = P[\bar{A} + \bar{A}_d I_0] + [\bar{A} + \bar{A}_d I_0]^{\mathrm{T}} P, \quad \Gamma_1 = [P\bar{A}_d A_a \; P\bar{A}_d B_a \; I_0^{\mathrm{T}}],$$

$$\mathscr{Q} = diag\{Q_1, Q_2, Q_1^{-1}\}.$$

Assume that P and P^{-1} can be decomposed as follows,

$$P = \begin{bmatrix} Y & N \\ N^{\mathrm{T}} & W_1 \end{bmatrix}, \quad P^{-1} = \begin{bmatrix} X & M \\ M^{\mathrm{T}} & W_2 \end{bmatrix}. \tag{28}$$

Then $PP^{-1} = I$ implies

$$\begin{cases} YX + NM^{\mathrm{T}} = I, \\ YM + NW_2 = 0, \\ N^{\mathrm{T}}X + W_1 M^{\mathrm{T}} = 0. \end{cases} \tag{29}$$

Define

$$\boldsymbol{\Phi}_1 = \begin{bmatrix} X & I \\ M^{\mathrm{T}} & 0 \end{bmatrix}, \quad \boldsymbol{\Phi}_2 = \begin{bmatrix} I & Y \\ 0 & N^{\mathrm{T}} \end{bmatrix}. \tag{30}$$

It can be shown that

$$P\boldsymbol{\Phi}_1 = \boldsymbol{\Phi}_2 \tag{31}$$

and

$$\boldsymbol{\Phi}_1^{\mathrm{T}} P \boldsymbol{\Phi}_1 = \begin{bmatrix} X & I \\ I & Y \end{bmatrix} > 0. \tag{32}$$

Define the following matrices $\mathscr{A}$, $\mathscr{B}$, $\mathscr{C}$:

$$\begin{cases} \mathscr{A} = YA_aX + NK_B(C_{a0} + C_{a1})X + NK_AM^{\mathrm{T}}, \\ \mathscr{B} = NK_B, \\ \mathscr{C} = K_CM^{\mathrm{T}}. \end{cases} \tag{33}$$

With direct matrix calculation, pre- and post-multiplying (27) by $diag\{\boldsymbol{\Phi}_1^{\mathrm{T}}, I, I, I\}$ and $diag\{\boldsymbol{\Phi}_1, I, I, I\}$, respectively, yields

$$\begin{bmatrix} T_1 & T_2 & T_3 & T_4 \\ * & -\gamma^2 + \tau_M Q_2 & 0 & 0 \\ * & * & -I & 0 \\ * & * & * & -1/\tau_M \mathscr{Q} \end{bmatrix} < 0, \tag{34}$$

where

$$T_1 = \begin{bmatrix} A_aX + XA_a^{\mathrm{T}} & A_a + \mathscr{A}^{\mathrm{T}} \\ A_a^{\mathrm{T}} + \mathscr{A} & \begin{pmatrix} YA_a + A_a^{\mathrm{T}}Y + \mathscr{B}(C_{a0} + C_{a1}) \\ +(C_{a0} + C_{a1})^{\mathrm{T}}\mathscr{B}^{\mathrm{T}} \end{pmatrix} \end{bmatrix},$$

$$T_2 = \begin{bmatrix} B_a \\ YB_a + \mathscr{B}D_a \end{bmatrix}, \quad T_3 = \begin{bmatrix} XE_a^{\mathrm{T}} - \mathscr{C}^{\mathrm{T}} \\ E_a^{\mathrm{T}} \end{bmatrix},$$

$$T_4 = \begin{bmatrix} 0 & 0 & X \\ \mathscr{B}C_{a1}A_a & \mathscr{B}C_{a1}B_a & I \end{bmatrix}.$$

Thus, if there exist symmetric matrices $X > 0$, $Y > 0$ and matrices $\mathscr{A}$, $\mathscr{B}$, $\mathscr{C}$ that satisfy (34), then the H_∞ criterion is satisfied and filter gains can be obtained by solving (33). We next give the following Lemma which can be used to design the filter.

Theorem 2 *If there exist symmetric matrices $X > 0$, $Y > 0$ and matrices $\mathscr{A}$, $\mathscr{B}$, $\mathscr{C}$ that satisfy (34) and (32) with a given positive constant γ, then there exist matrices K_A, K_B, K_C such that the error system (8) is stable and (9) is satisfied. The filter gains are*

$$K_A = N^{-1}[\mathscr{A} - YA_aX - \mathscr{B}(C_{a0} + C_{a1})X](M^T)^{-1},$$

$$K_B = N^{-1}\mathscr{B}, \quad K_C = \mathscr{C}(M^T)^{-1}.$$

Proof (32) guarantees that there is a positive definite matrix P that can be decomposed as in (28). Then it is easy to check that defined K_A, K_B, K_C and P satisfies (12).

Remark: To implement the algorithm, first solve LMIs (32) and (34) to get X, Y, $\mathscr{A}$, $\mathscr{B}$ and $\mathscr{C}$. Then using $MN^{\mathrm{T}} = I - XY$ as in (29), M and N can be obtained by singular value decomposition. Then define $\boldsymbol{\Phi}_1$ and $\boldsymbol{\Phi}_2$ as in (30), P can be solved using (31). Then the filter gains can be computed as in Theorem 2.

5 Simulations

In this section, we present numerical simulations to illustrate the effectiveness of our designed filter. The simulation parameters are illustrated in Table 1. For simulations, a road segment over a 10 s horizon is modeled as follows,

$$\dot{r}_o(t) = \begin{cases} 0.15 \cdot \sin \pi(t-1) & 1s \le t \le 3s, \\ 0.2 \cdot \sin \pi/2t & 4s \le t \le 8s, \\ 0 & \text{otherwise.} \end{cases}$$

See Fig. 4. Let $\gamma = 0.5$ and $\tau_M = 0.5$ s, we aim at a filter in form of (7) such that (9) is satisfied. Applying Theorem 1 with MATLAB LMI toolbox, filter gains K_A, K_B and K_C in (7) are obtained.

With the obtained filter, estimates of x_3 and x_4 are shown in Figs. 5 and 6, respectively. Plots of estimates of x_1 and x_2 are not shown due to space limit. The H_∞ filter performance is compared with a Kalman filter assuming no knowledge of the road profile information. It can be seen that by using road profile from the cloud with small delays (e.g., 0.2 s), our designed H_∞ filtering has better performances than the traditional Kalman filter. However, with larger time delays, the estimation performance can be worse than the Kalman filter. Note that from practical standpoint, the delays in V2C2V system can be reduced if sufficient communication bandwidth and onboard memory storage is available so that the road profile information can be transmitted in advance.

Table 1 Simulation parameters

m_s	m_{us}	k_s	k_{us}	c_s	α
290 kg	60 kg	16800 N/m	19000 N/m	200 N · s/m	0.1

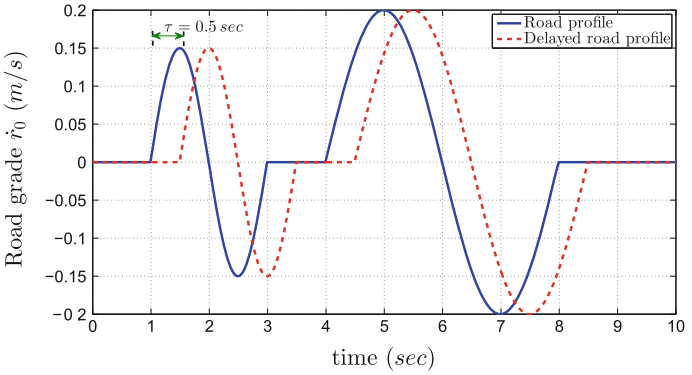

Fig. 4 Road grade profile ($\dot{r}_0$)

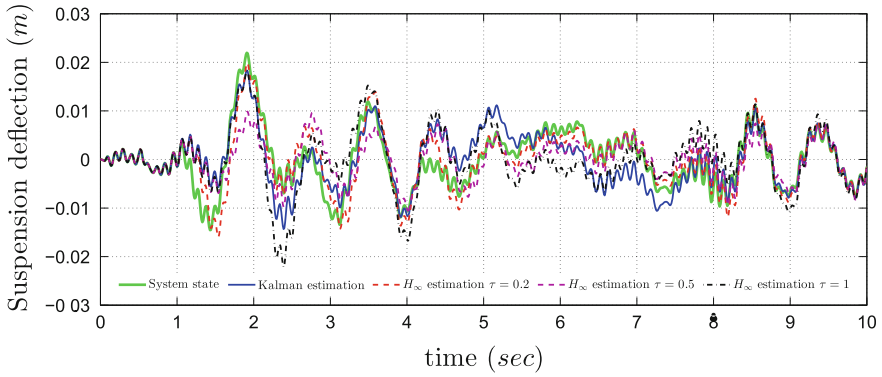

Fig. 5 Suspension deflection x_3

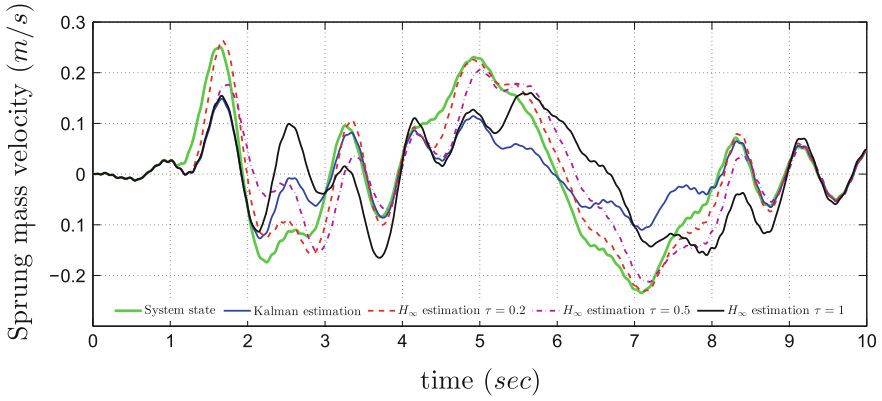

Fig. 6 Sprung mass velocity x_4

6 Conclusions

In this chapter we studied an H_∞ filtering problem for cloud-aided semi-active suspension where road profile information was sent from the cloud to the vehicle to compliment onboard measurements. We have studied this problem under the assumption that there are delays in transmitting the information from the cloud to the vehicle. Sufficient conditions of existence of the H_∞ filter were given in terms of linear matrix inequalities. The explicit expressions of the filter parameters were derived. A numerical example illustrated that the proposed filter framework has a potential for performance than traditional Kalman filter when the communication delay is not very large.

References

1. Filev, D., Lu, J., Hrovat, D.: Future mobility: integrating vehicle control with cloud computing. ASME Dyn. Syst. Control Mag. **1**, 18–24 (2013)
2. Fernando, N., Loke, S.W., Rahayu, W.: Mobile cloud computing: a survey. Fut. Gen. Comput. Syst. **29**(1), 84–106 (2013) (Including Special section: AIRCC-NetCoM 2009 and Special section: Clouds and Service-Oriented Architectures)
3. Mangharam, R.: The car and the cloud: automotive architectures for 2020. The Bridge **42**(4) (2012)
4. Li, Z., Kolmanovsky, I., Atkins, E., Lu, J., Filev, D., Michelini, J.: Cloud aided safety-based route planning. In: 2014 IEEE International Conference on Systems, Man, and Cybernetics (SMC), pp. 2495–2500 (2014)
5. Li, Z., Kolmanovsky, I., Atkins, E., Lu, J., Filev, D.P., Michelini, J.: Road risk modeling and cloud-aided safety-based route planning. IEEE Trans. Cybern. (99), 1–11 (2015)
6. Li, Z., Kolmanovsky, I., Atkins, E., Lu, J., Filev, D.: Road anomaly estimation: Model based pothole detection. In: American Control Conference (ACC), pp. 1315–1320 (2015)
7. Li, Z., Filev, D.P., Kolmanovsky, I., Atkins, E., Lu, J.: A new clustering algorithm for processing GPS-based road anomaly reports with a mahalanobis distance. IEEE T. Intel. Trans. Syst. (99), 1–9 (2016)
8. Li, Z., Kolmanovsky, I.V., Kalabić, U.V., Atkins, E.M., Lu, J., Filev, D.P.: Optimal state estimation for systems driven by jump-diffusion process with application to road anomaly detection. IEEE T. Control Syst. Tech. (99), 1–10 (2016)
9. Li, Z., Kolmanovsky, I., Atkins, E., Lu, J., Filev, D., Michelini, J.: Cloud aided semi-active suspension control. In: 2014 IEEE Symposium on Computational Intelligence in Vehicles and Transportation Systems (CIVTS), pp. 76–83 (2014)
10. Li, Z., Yin, X., Kolmanovsky, I., Lu, J., Filev, D., Atkins, E.: Robust h$^\infty$ control for a class of networked uncertain systems with multiple channels subject to Markovian switching. In: 2015 54th IEEE Conference on Decision and Control (CDC), pp. 6856–6861 (2015)
11. Vassal, C., Savaresi, S., Spelta, C., Sename, O., Dugard, L.: A methodology for optimal semi-active suspension systems performance evaluation. In: 49th IEEE Conference on Decision and Control, Atlanta, GA, pp. 2892–2897 (2010)
12. Giorgetti, N., Bempoard, A., Tseng, H., Hrovat, D.: Hybrid model predictive control application towards optimal semi-active suspension. In: Proceedings of the IEEE International Symposium on Industrial Electronics, Dubronvnik, Croatia, pp. 391–398 (2005)
13. Miller, L.R.: Tuning passive, semi-active, and fully active suspension systems. In: Proceedings of the 27th IEEE Conference on Decision and Control, 1988, pp. 2047–2053. IEEE (1988)

14. Zhang, L., Shi, P., Boukas, E.-K., Wang, C.: Robust $l_2 - l_\infty$ filtering for switched linear discrete time-delay systems with polytopic uncertainties. IET Control Theory Appl. **1**, 722–730 (2007)
15. Yin, X., Zhang, L., Zhu, Y., Wang, C., Li, Z.: Robust control of networked systems with variable communication capabilities and application to a semi-active suspension system. In: IEEE/ASME Trans. Mechatron. (99), 1–1 (2016)
16. Li, Z., Kolmanovsky, I., Atkins, E., Lu, J., Filev, D.: H_∞ filtering for cloud-aided semi-active suspension with delayed road information. In: IFAC-PapersOnLine **48**(12), 275–280 (2015). 12th IFAC Workshop on Time Delay Systems (TDS) 2015, Ann Arbor, Michigan, USA, 28–30 June 2015
17. Boyd, S., El Ghaoui, L., Feron, E., Balakrishnan, V.: Linear Matrix Inequalities in System and Control Theory, vol. 15. Studies in Applied Mathematics. SIAM, Philadelphia (1994)
18. Boukas, E.-K., Liu, Z.-K.: Deterministic and Stochastic Time-Delay Systems. Springer-Verlag, New York Inc, Secaucus, NJ, USA (2002)
19. El Farissi, A., Latreuch, Z.: New type of chebychev-grss inequalities for convex functions. Acta Universitatis Apulensis **30**, 235–245 (2012)

Analysis of Time Delays in Quadrotor Systems and Design of Control

Stephen K. Armah and Sun Yi

Abstract In analyzing and designing control for unmanned aerial vehicles (UAVs), existence of transmission delays caused by wireless communication is one of the critical challenges. Estimation of the delays and analysis of their effects are not straightforward. A delay estimation method is introduced using transient responses of a quadrotor type of UAVs and analytical solutions of delay differential equations (DDEs). Experimental data sets in the time domain are compared to the predicted ones based on the analytical solutions of DDEs. The Lambert W function-based approach for first-order DDEs is used for the analysis. The dominant characteristic roots among an infinite number of roots are obtained in terms of coefficients and the delay. The effects of the time delay on the responses are analyzed via root locations. Based on the estimation result, proportional- plus-velocity controllers are proposed to improve transient altitude responses.

1 Introduction

Time delays exist in autonomous dynamic systems when signals are transmitted wirelessly. Estimation of the delays and understanding of their effects on the performance of dynamic systems is an important topic in many applications [1]. Estimating delays is a challenging problem and has attracted great research interests [2] [3]. Although considerable efforts have been made on parameter estimation, as for time-delay identification there are still many open problems and there is no common approach due to the lack of analytical solutions to delay equations and difficulty in formulation [4–6].

Autonomous control of quadrotor types of unmanned aerial vehicles (UAVs) has been the focus of active research during the past decades. One of the challenges in

S.K. Armah (✉) · S. Yi
Department of Mechanical Engineering, North Carolina A&T State University, Greensboro, NC 27411, USA
e-mail: skarmah@aggies.ncat.edu

S. Yi
e-mail: syi@ncat.edu

T. Insperger et al. (eds.), *Time Delay Systems*,
Advances in Delays and Dynamics 7, DOI 10.1007/978-3-319-53426-8_20

designing effective control systems for UAVs is the existence of signal transmission delay, which has nonlinear effects on the flight performance. A controller designed using a non-delayed system model may result in disappointingly slow and oscillating responses due to the delays. For autonomous aerial robots, typical values of the time delay have been known to be around 0.4 ± 0.2 s [7] or 0.2 s [8]. For large delays (e.g., larger than 0.2 s), the system response might not be stabilized or converged due to the dramatic increase in torque. This poses a significant challenge [9]. Since its effect is not trivial the delay need be estimated and considered in designing controllers.

In this chapter, an estimation method introduced in [6] is studied further and applied to a quadrotor type of UAV, Parrot AR.Drone 2.0. The UAV is controlled with MATLAB/Simulink through WiFi, which introduces a time delay to its dynamics as shown in Sect. 3. The overall time delay is attributed to: (1) the processing capability of the host computer, (2) the electronic devices processing the motion signals, e.g., actuation, (3) the measurement reading devices, e.g., the distance between the ultrasonic sensor, for reading the altitude, and the surface can affect the delay, and (4) the software, on the host computer, being used to implement the controllers. For UAVs wireless communication delays may not be critical when all the controllers are on board. However, delays have significant effects when the control software is run on an external computer and signals are transmitted wirelessly. For example, the experiments on the drone in this chapter were conducted using MATLAB/Simulink on an external computer, and decoding process of navigation data (yaw, pitch, roll, altitude, etc.) contributes to the delay. Also, the numerical solvers in the software introduce additional delay.

Most methods for transfer function identification assume that the delay is already known or just ignore the delays and their effects [10]. Several approaches to estimation of delay have been introduced in the literature. Those include finite dimensional Chebyshev spectral continuous time approximation (CTA) [11]. The finite dimensional CTA was used to approximately solve delay differential equations (DDEs) for the estimation of constant and time-varying delays. In addition, cross-correlation method [12], graphical methods [13, 14], a cost function for a set of time delays in a certain range [15], and frequency-domain maximum likelihood [16] have been used for delay estimation. This chapter presents a method to estimate the time delay in the altitude control system of quadrotor types of UAVs using the approach based on the analytical solutions to DDEs [6]. The altitude dynamics is assumed to be linear time-invariant (LTI) first order and the time delay is incorporated into the model as an explicit parameter. In real applications, drones fly around and the time delay may vary. Here, the delay is not restricted to be a multiple of the sampling interval. Experimental data and analytical solutions of infinite dimensional continuous DDEs are used for estimation. The approach in this chapter is inspired by the well-known time-domain description of step responses of LTI ordinary differential equations (ODEs). Measured transient responses are compared to time-domain descriptions obtained by using the dominant characteristic roots based on the Lambert W function written in terms of system parameters including the delay. Proportional (P) controllers are used to generate the responses for estimation. The effects of the time delay on the transient responses and stability are analyzed. Then, proportional-plus-velocity (PV) control

is designed to obtain better transient responses. This chapter continues with introduction of the approach used for estimating the system's time delay in Sect. 2 with an example. A description of quadrotor's altitude model and the AR.Drone 2.0 control system are provided in Sect. 3. In Sect. 4 the estimation results are summarized. Concluding remarks and future work are presented in Sect. 5.

2 Time-Delay Estimation Using Characteristic Roots

The estimation problem can be formulated using an analytical solution form to DDEs in terms of the scalar Lambert W function [6]. Consider the first-order scalar homogenous DDE:

$$\dot{z}(t) - a_o z(t) - a_1 z(t - T_d) = 0, \tag{1}$$

The characteristic equation of (1) is given by

$$s - a_o - a_1 e^{(-sT_d)} = 0. \tag{2}$$

Then, the characteristic equation in (2) is solved as [17]

$$s = \frac{1}{T_d} W(T_d a_1 e^{(-a_o T_d)}) + a_o. \tag{3}$$

The Lambert W function is defined as $W(x)e^{W(x)} = x$ [18]. As seen in (3), the characteristic root, s, is expressed analytically in terms of parameters, a_o, a_1, and the time delay, T_d. The solution form in (3) enables one to determine how the time delay is involved in the solution and, thus, response. Furthermore, how each parameter affects each characteristic root. Thus, it is possible to formulate estimation of time delays in an analytic way. The Lambert W function is already embedded as *lambertw* in MATLAB [17]. The equation in (2) has an infinite number of roots. Each root is distinguished using branches, $k = -\infty, \ldots, -1, 0, 1, \ldots, \infty$, of the Lambert W function. For first-order scalar DDEs, it has been proved that the rightmost characteristic roots are always obtained by using the principal branch, $k = 0$, and/or $k = -1$ [19]. For the DDE in (1), one has to consider two possible cases for rightmost characteristic roots: characteristic equations of DDEs as in (2) can have one real dominant root or two complex conjugate dominant roots. Thus, when estimating time delays using characteristic roots, it is required to decide whether it is the former or the latter [6].

For ODEs, an estimation technique using the logarithmic decrement provides an effective way to estimate the damping ratio. The technique makes use of the characteristic roots in terms of ζ and ω_n:

$$s = -\zeta\omega_n \pm j\omega_n\sqrt{(1 - \zeta^2)} \tag{4}$$

of second-order ODEs. The variables ζ and ω_n are obtained from the transient response of the system, and different approaches can be applied depending on the nature of the response: oscillatory and non-oscillatory. Here, the transient properties for oscillatory responses ($0 < \zeta < 1$) are used. Property such as the maximum overshoot in percentile, $M_o(\%)$, is related to ζ, as

$$M_o(\%) = 100e^{\left(\frac{-\zeta\pi}{\sqrt{(1-\zeta^2)}}\right)} \tag{5}$$

For a stable system, the dominant roots, s, lie in the left-hand complex plane. Then, ζ is computed as

$$\zeta = \frac{|Re(s)|}{\sqrt{(Re(s))^2 + (Im(s))^2}} \tag{6}$$

Then, the drone control system with the unknown T_d is estimated by the following steps:

Step 1: Measure the maximum overshoot from the experimental transient data,
Step 2: Calculate ζ based on the system altitude response using (5),
Step 3: Solve the nonlinear equation (6) with $s = \frac{1}{T_d} W(T_d a_1 e^{(-a_o T_d)}) + a_o$ for T_d. Equation (6) has only one unknown, which is the time delay, T_d.

The equation in Step 3 can be solved using a nonlinear solver (e.g., *fsolve* in MATLAB). The above method using the dominant characteristic roots assumes that the dominant ones are substantially closer to the imaginary axis than subdominant ones [6]. If not, estimation results may be inaccurate.

2.1 Example: Internet-Based Control

An example for a simple Internet-based feedback control is presented to illustrate how to use the above estimation technique. When tele-operating systems are run through private media variation of the transmission delay value is very small. Thus, the delay can be assumed to be constant and can be well modeled. The Internet, on the other hand, is a public and shared resource in which many end users transmit data through the network simultaneously. The route for transmission between two end points is not fixed and varies dynamically. Also, traffic jams may be caused when too many users use the same route simultaneously. The transmission latency of such public network is difficult to estimate and predict. Time delay is one of the critical obstacles in realizing reliable Internet-based process control systems [20].

The system in Fig. 1 has a plant of an integrator with proportional feedback control. The error, $e(t)$, is calculated in the first PC (PC 1) and sent to the second PC (PC 2). Then, the control input, $u(t) = Ke(t)$, is sent back to the PC1, where K is the

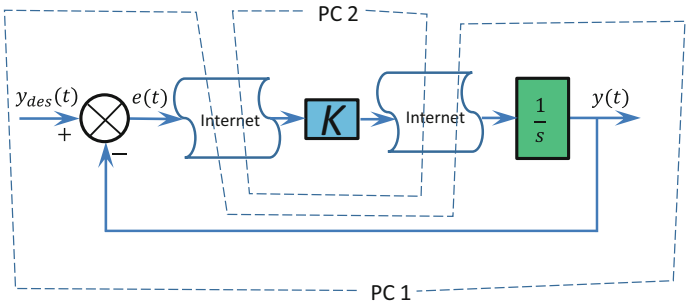

Fig. 1 A plant of an integrator is stabilized with proportional feedback control. The signals are transmitted through Internet using the 'UDP' block of Simulink

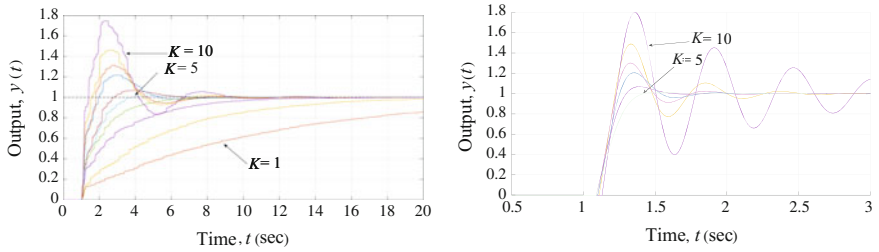

Fig. 2 Outputs for various control gain, K, with Internet delay (*left*) and artificial delay using estimated values in Table 1 (*right*)

control gain. The signals are transmitted through Internet using the 'UDP' blocks of Simulink.

Figure 2 (left) shows response, $y(t)$, of the system. If there is no time delay, the system has one real characteristic root, $-K$. Increases in the values of the control gain, K, do not yield overshoots (the closed-loop system is first order). But when K is greater than 5, overshoots are observed. The observed overshoots are summarized in Table 1.

Table 1 The results in Fig. 2 (left) are summarized

K	1–4	5	6	7	8	9	10
$M_p(\%)$	none	1.7%	7%	22%	31.5%	46%	75%
Estimated T_d (s)	n/a	0.09	0.09	0.104	0.104	0.11	0.13
Rightmost roots	n/a	−9.2	−8.1	−5.2	−4.4	−3.0	−1.0
		$\pm 7.2i$	$\pm 9.6i$	$\pm 10.8i$	$\pm 11.8i$	$\pm 12.1i$	$\pm 11.4i$
Damping ratio (ζ)	n/a	0.7898	0.6454	0.4315	0.3431	0.2373	0.0902

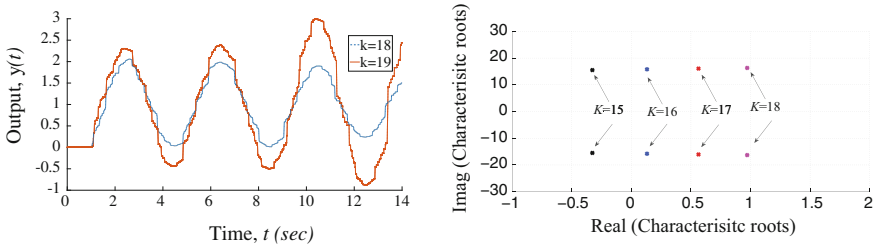

Fig. 3 Internet-based feedback control: when the gain is greater than 19, the output diverge and the controlled system become unstable (*left*). On the other hand, from the position of the rightmost characteristic roots, when the gain is greater than 15 the system is unstable ($T_d = 0.1$ s)

Using the three steps explained above using Eqs (4)–(6), the time delay caused by communication was estimated as summarized in Table 1. All the estimated values, T_d, are not exactly same and they vary from 0.09 to 0.13 s. This variation may happen partly due to Internet delays varying with time and sampling of signals. Also, it may be caused by ignoring other subdominant characteristic roots.

The estimation result can be used for stability analysis. When the value $T_d = 0.1$ s is used for simulation the gain, K, greater than 19 makes the system unstable. Refer to Fig. 3 (left). If the delay is assumed to be zero, no gain value larger than zero makes the system unstable in theory. When the gain is greater than 19 the output diverges over time and the controlled system become unstable. When the rightmost roots are obtained using the Lambert W function the gain greater than 16 makes the system unstable (Fig. 3 (right)). Although the two values (19 and 16) are not exactly same the stability analysis with the estimated time delay provides an approximate stability boundary. Note that using the estimation technique using 'Maximum overhoot' gives relatively good predictions of overshoots (Fig. 2) and stability (Fig. 3). But when the time scales of the simulation and experiment results are compared, there is a difference. Refer to the responses in Fig. 2. This difference is observed in the Internet-based control example above and drone control results to be shown later as well. This needs be studied further.

3 Altitude Model and Control System

This method is applied to control of quadrotors. Quadrotors are typically modeled based on three coordinate systems attached to it; the body-fixed frame, vehicle frame, and global inertial frame. They have six degrees of freedom in terms of position and attitude defined using the Euler angles. The quadrotor has four rotors, labeled 1 to 4, mounted at the end of each cross arm. The rotors are driven by electric motors having electronic speed controllers. The vehicle's total mass is m and total upward thrust, $T(t)$, on the vehicle given by [21]

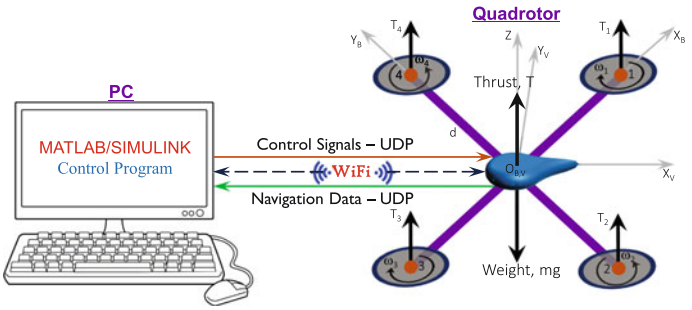

Fig. 4 The drone's navigation data is sent to the PC though WiFi. Then, the altitude error and control signal are calculated and sent back to the drone

$$T(t) = \sum_{i=1}^{i=4} T_i(t) \tag{7}$$

and $T_i(t) = a\omega_i^2(t)$, $i = 1, 2, 3$, and 4, where $\omega_i(t)$ is the rotor angular speed and $a > 0$ is the thrust constant. The equation of motion in the z-direction can be obtained as follows (refer to Fig. 4)

$$\ddot{z}(t) = \frac{4a\omega^2(t)}{m} - g \tag{8}$$

where $\omega(t)$ is the rotor's average angular speed necessary to generate $T(t)$. Thus, only the speed $\omega(t)$ needs be controlled to regulate the altitude, $z(t)$, of the quadrotor, since m, a, and g are constants.

According to the AR.Drone 2.0 SDK documentation, $z(t)$ is controlled by applying a reference vertical speed, $\dot{z}_{ref}(t)$, as control input. The speed, $\dot{z}_{ref}(t)$, has to be constrained to be between -1 and 1 m/s, to prevent damage. The drone's flight management system sampling time, T_s is 0.065 s, which is also the sampling time at which the control law is executed and the navigation data received.

The control block diagram for the drone's altitude motion regulation is shown in Fig. 5. The altitude motion dynamics in (8) is used to determine $\omega(t)$ from $\dot{z}(t)$. The rotors rotate at the equal speed, $\omega(t)$, which will generate $T(t)$ to make $z(t)$ reach the reference ($z_{des} = 1m$). These computations take place in the onboard control system programmed in C. In this chapter, the motor dynamics is assumed to be very fast such that the altitude control system can be represented by a first-order system using an integrator. Under such assumption, the control input, $\dot{z}_{app}(t)$, to the first-order system is approximated to be equal to the actual vertical speed, $\dot{z}(t)$, of the drone. Thus, a first-order model is used for the analytical determination of the time delay and for obtaining the simulation altitude responses. This simplification for control of quadrotor types of UAVs has been used and experimentally verified in the literature [22, 23]. The drone navigation data (from the sensors, cameras, and battery) is received and the control signals are sent using AT commands by UDP protocols.

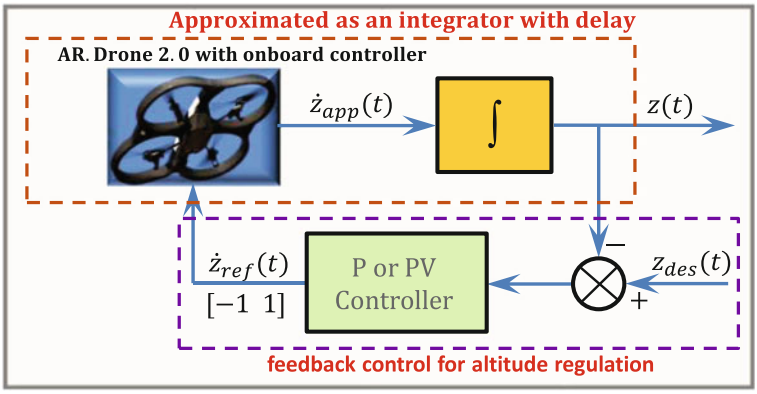

Fig. 5 Diagram for altitude control of the AR. Drone 2.0

AT commands are the combination of short text strings sent to the drone to control its actuation. The drone has ultrasound sensors for ground altitude measurement (at the bottom of the quadrotor). It has 1 GHz 32 bit ARM Cortex A8 processor, 1GB DDR2 RAM at 200 MHz, and USB 2.0 high speed for extensions.

3.1 P and PV Control

The system has an integrator, 1/s, in the closed-loop transfer function as shown in Fig. 5. Thus, only P and PV feedback controllers are used to regulate vertical speed signal. PV control, unlike proportional-plus-derivative (PD) control, does not induce numerator dynamics. The P-feedback controller is used to create transient responses to be used for estimation of the time delay. Based on the estimation, the PV feedback controller is designed to improve the transient response. The transfer function of the time-delay closed-loop system with the P controller is given by

$$\frac{Z(s)}{Z_{des}(s)} = \frac{K_P e^{-sT_d}}{s + K_P e^{-sT_d}} \tag{9}$$

This time-delay system is a retarded type. The characteristic equation is transcendental and the number of the characteristic roots is infinite. The characteristic roots have imaginary parts, which introduce oscillations in outputs, $z(t)$. Comparing the characteristic equation of the closed-loop system in (9) to the first-order system in (2), the coefficients are found as $a_o = 0$ and $a_1 = -K_P$.

The effect of T_d on the drone's altitude response is studied using analytical, simulation, and experimental approaches with the P controller. Then, suitable PV controller gains, K_p and K_v, are obtained to improve on the transient response performance. A high pass filter (HPF) with damping ratio, $\zeta_f = 1.0$ was used for the

derivative controller. A natural frequency value, ω_f, for the filter was selected by tuning and the use of the Bode plot. The transfer function of the time-delay closed-loop system for the PV controller, neutral type, is given by

$$\frac{Z(s)}{Z_{des}(s)} = \frac{K_P e^{-sT_d}}{s + (K_P + K_v s)e^{-sT_d}} \tag{10}$$

The characteristic equations of the neutral types of delay systems cannot be solved by using the Lambert W function [17]. Instead, a numerical method is used to obtain the roots [24].

4 Results and Discussion

4.1 Estimation of Time Delay

First, the drone's altitude responses were collected for several values of K_p, as shown in Fig. 6. Note that if there is no delay in the system ($T_d = 0$), the characteristic root is $-K_p$ (refer to Eq. (9)), which is a real number. Thus, there should be no overshoot in the response. Also, increase in K_p moves the root more to the left in the complex plane and does not destabilize the system. However, as seen in Fig. 6, when the gain, K_p, is higher than 1.0, the output has a nonzero overshoot due to delay in the control loop. Therefore, the delay does have nontrivial effects on response and need to be precisely estimated and considered in designing effective control. Note that for ease of analyzing the responses are shifted to start at (0 s, 0 m).

It was also observed that the saturation applied to the control input has a nonlinear effect on the system's response, especially as K_p increases. After comparing

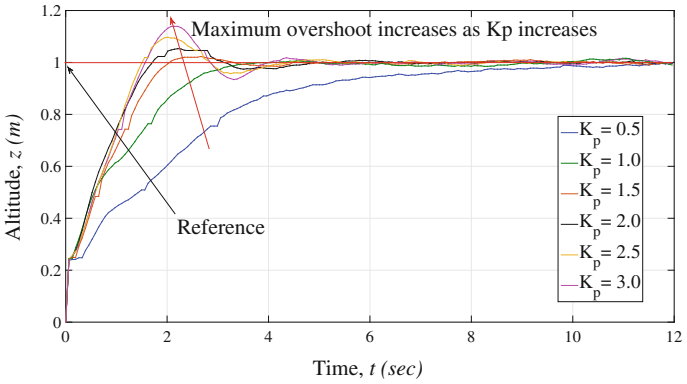

Fig. 6 Measured altitude responses with the gain, K_p, varying from 0.5 to 3

simulation results to experimental data, it was found that the value $K_p = 1.31$ gives a response with a sufficient overshoot for delay estimation with a minimum effect of saturation.

4.2 Numerical Method

Table 2 shows a summary of the simulation altitude responses transient properties by varying T_d at $K_p = 1.31$, where N is a real constant tuning parameter. The drone altitude responses from navigation data of 5 tests (Flights 1–5) with $K_p = 1.31$ are shown in Fig. 7. The measured M_o values are 2.30, 2.29, 2.30, 2.27, and 0.60%. When the values $M_o = 2.30\%$ from the first four flights excluding the last are used to estimate the time delay, as shown in the simulation results in Table 2 the delay T_d is estimated as $5.6646T_s$, which is 0.3682 s.

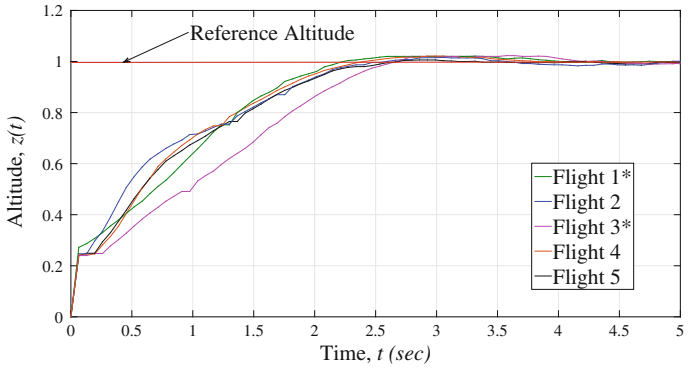

Fig. 7 Experimented altitude responses: $K_p = 1.31$. The measured M_o values are 2.30, 2.29, 2.30, 2.27, and 0.60 %

Table 2 The maximum overshoots of the simulated altitude responses with $K_p = 1.31$

N	$T_d = NT_s$	$M_o(\%)$
4.0000	0.2600	0.000
5.0000	0.3250	0.419
5.6000	0.3640	2.067
5.6640	0.3682	2.298
5.6646	0.3682	2.300
5.6660	0.3683	2.305
5.7000	0.3705	2.429

4.3 Use of Characteristic Roots

The drone altitude responses oscillate and have overshoots as shown in Figs. 6 and 7. Thus, it is assumed that the system has two complex conjugate dominant roots. The maximum overshoot values are used to determine the damping ratio, ζ. When $M_o = 2.30\%$ is used ζ is computed as 0.7684 using Eq. (5). Applying the steps described in Sect. 2, the delay T_d is determined as 0.3598 s. This value is close to the numerical method result (0.3682 s) but the two values are not exactly same. This discrepancy can come from simulation errors and noise in measuring altitudes. Then, the estimated result is used for stability analysis. Again, when stability is predicted assuming no delay any K_p value larger than zero does not destabilize the system. However, as shown in Fig. 8, if K_p is greater than 5, the amplitude of the altitude response grows over time and the system is unstable. The estimated delay value can explain this result. When the value ($T_d = 0.36$ s) is used, the simulated responses obtained by using Simulink agree with the experimental stability result (Fig. 9 (left)). Also, the roots calculated using the Lambert W function-based method shows that when K_p is greater than 5, the rightmost roots are placed in the right half plane (RHP) and, thus, unstable (Fig. 9 (right)).

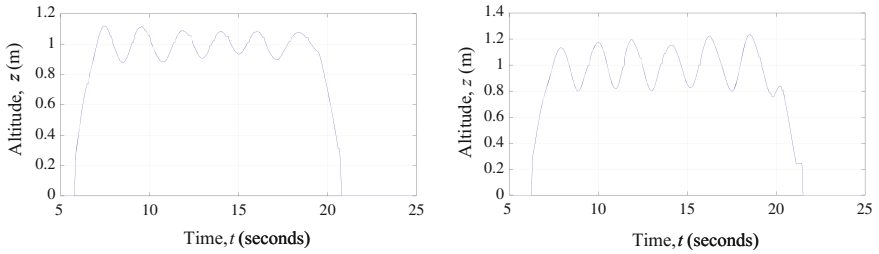

Fig. 8 The altitude responses with K_p is 4 (*left*) and 5 (*right*). If the control gain is greater than 5, the system becomes unstable

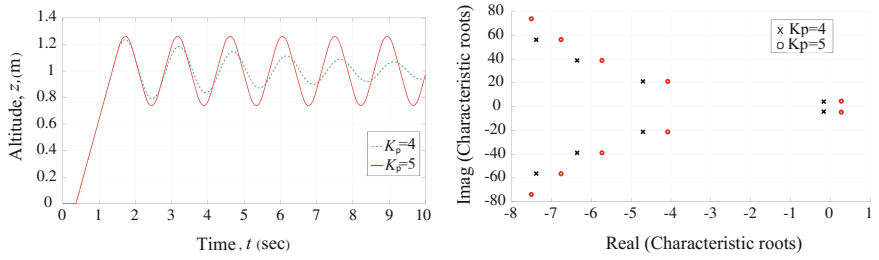

Fig. 9 Simulation also confirms that when K_p is larger than 5, the system becomes unstable (*left*). The rightmost roots crosses the imaginary axis when $K_p > 5$

4.4 PV Control

The PV control used to control altitude of the drone system is designed based on the time delay, 0.36 s, estimated using the analytical method. A MATLAB-based software package [24] was used to study the stability of the neutral type time-delay system, by solving the characteristic equation from the transfer function in Eq. (10). The closed-loop system characteristic roots within a specified region are then plotted for various K_v values. Figure 10 shows the spectrum distribution of the characteristic roots. When the rightmost (i.e., dominant) roots for each case are considered the value $K_v = 0.3$ yields the most stable rightmost roots ($s = -3.32$). For PV control, addition of K_v reduces the maximum overshoot for the same gain value, $K_p = 2$, while maintaining fast response time. But when K_v is greater than 0.97 the roots cross the imaginary axis, and the system becomes unstable. Thus, the estimated time delay value enables stability analysis before implementing.

The corresponding simulation altitude responses for the system were also obtained for the various K_v values, which are not shown in this chapter. It can be seen that as K_v increases at $K_p = 2.0$ and $T_d = 0.36$ s, M_o decreases but the rise time becomes longer. At higher values of K_v, the response oscillates and the system becomes unstable. This is also observed in Fig. 10, that as K_v increases (higher than 0.5) the roots moves back to the right increasing the instability in the system.

Based on these analyses, a controller gain set of $K_p = 2.0$ and $K_v = 0.3$ was selected for the most stable closed-loop system response with transient properties

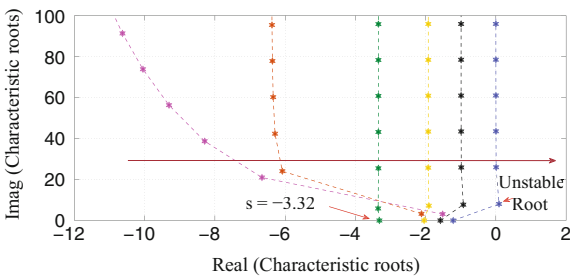

Fig. 10 The characteristic roots of the system with PV control with $K_p = 2.0$ and $T_d = 0.36$ s

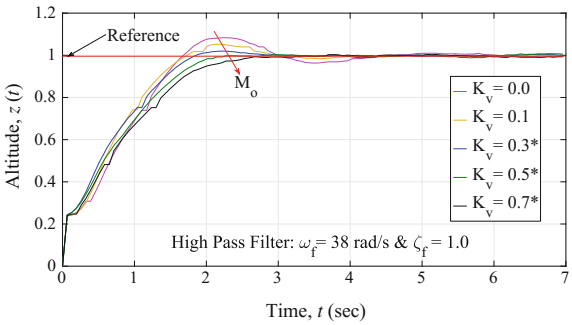

Fig. 11 Experimented PV controller altitude responses with $K_p = 2.0$

of $M_o < 1\,\%$ and $t_s < 2$ s after simulations using Simulink. Using these controller gains, the HPF was included in the simulation control system, and its effects on the altitude transient response, at different ω_f, were studied. It is observed that at lower ω_f values the response oscillates, and at higher values the response distorts [25]. The oscillations and the distortions effects were reduced by using the high-order solver, *ode8* (Dormand-Prince). After trial-and-errors HPF with $\omega_f = 38$ rad/s and $\zeta_f = 1.0$ were selected, with poles of -38 repeated. Now, looking at the poles distribution of the system in Fig. 10, it is observed that the poles of this filter are located much farther to the left than the poles of the PV feedback closed-loop system. Thus, this filter will respond faster, therefore, it has only a minor effect on the drone's altitude transient response. The filter's cutoff frequency was determined as 5.68 rad/s (0.90 Hz).

Figure 11 shows the experimented altitude responses and their corresponding transient properties, with the HPF and $K_p = 2.0$, for different K_v values. It was observed that as the K_v value increases M_o decreases but the responses become slower. The PV controller with $K_v = 0.3$ and $K_p = 2.0$, which has the most stable root ($s = -3.32$) in Fig. 10, gives the best performance in terms of the 2% settling time (1.86 s). As K_v increases, the maximum overshoot decreases but the settling time becomes longer. For example, the PV controller with $K_v = 0.7$ and $K_p = 2.0$, which has the rightmost roots as ($s = -0.93 \pm 7.71i$) and yields 2.47 s for the 2% settling time.

5 Conclusion

This study demonstrated how to use analytical solutions for ODEs and DDEs to estimate the time delay in Internet-based feedback control and quadrotor types of UAVs. Through numerical and analytical approaches, the time delay was estimated as 0.37 s and 0.36 s for the quadrotor, respectively. In the estimation of the time delay, an appropriate P controller was used and the gain that minimizes the effect of the applied control signal saturation on the system's response was selected. The effect of the time delay on the drone's altitude response was analyzed including system stability conditions. The PV controller was designed for improved transient responses based on the rightmost roots calculated using the estimated delay value.

The simulations and experiments were conducted using a high-order solver of MATLAB/Simulink, *ode8* (Dormand-Prince). Investigation through trials revealed that selection of the solver had significant effects on the drone's altitude response. The HPF performance was constrained by the type of solver used and the filter performed better with the high-order solvers. Also, discretization of continuous systems can cause additional errors [26]. These are being investigated further by the authors.

In future, multiaxis dynamics of the drone system considering attitude (pitch, roll, and yaw) and lateral motions (x and y) can be considered for estimating and incorporating the time delay in designing control systems. This problem is significantly more challenging, since the equation of motions are coupled and more complex than that

of the altitude motion. Furthermore, the presented time-delay estimating methods can be extended to general systems of DDEs (higher than first order). Also adaptive control that is updated based on the real-time estimation of delays can be studied.

Acknowledgements This material is based on research sponsored by Air Force Research Laboratory and OSD under agreement number FA8750-15-2-0116. The U.S. Government is authorized to reproduce and distribute reprints for Governmental purposes notwithstanding any copyright notation thereon.

References

1. Armah, S., Yi, S.: Altitude regulation of quadrotor types of UAVs considering communication delays. In: 12th IFAC Workshop on Time Delay Systems, pp. 263–268 (2015)
2. Azadegan, M., Beheshti, M.T., Tavassoli, B.: Using AQM for performance improvement of networked control systems. Int. J. Control Autom. Syst. **13**(3), 764–772 (2015)
3. Kchaou, M., Tadeo, F., Chaabane, M., Toumi, A.: Delay-dependent robust observer-based control for discrete-time uncertain singular systems with interval time-varying state delay. Int. J. Control Autom. Syst. **12**(1), 12–22 (2014)
4. Belkoura, L., Richard, J.P., Fliess, M.: Parameters estimation of systems with delayed and structured entries. Automatica **45**(5), 1117–1125 (2009)
5. Richard, J.P.: Time-delay systems: an overview of some recent advances and open problems. Automatica **39**(10), 1667–1694 (2003)
6. Yi, S., Choi, W., Abu-Lebdeh, T.: Time-delay estimation using the characteristic roots of delay differential equations. Am. J. Appl. Sci. **9**(6), 955–960 (2012)
7. Vásárhelyi, G., Virágh, C., Somorjai, G., Tarcai, N., Szorenyi, T., Nepusz, T., Vicsek, T.: Outdoor flocking and formation flight with autonomous aerial robots. In: 2014 IEEE/RSJ International Conference on Intelligent Robots and Systems (IROS 2014), pp. 3866–3873 (2014)
8. Sa, I., Corke, P.: System identification, estimation and control for a cost effective open-source quadcopter. In: 2012 IEEE International Conference on Robotics and Automation (ICRA), pp. 2202–2209 (2012)
9. Ailon, A., Arogeti, S.: Study on the effects of time-delays on quadrotor-type helicopter dynamics. In: 2014 22nd Mediterranean Conference of Control and Automation (MED), pp. 305–310 (2014)
10. Wang, Q.G., Zhang, Y.: Robust identification of continuous systems with dead-time from step responses. Automatica **37**(3), 377–390 (2001)
11. Torkamani, S., Butcher, E.A.: Delay, state, and parameter estimation in chaotic and hyperchaotic delayed systems with uncertainty and time-varying delay. Int. J. Dyn. Control **1**(2), 135–163 (2013)
12. He, H., Yang, T., Chen, J.: On time delay estimation from a sparse linear prediction perspective. J. Acoust. Soc. Am. **137**(2), 1044–1047 (2015)
13. Ahmed, S., Huang, B., Shah, S.: Parameter and delay estimation of continuous-time models using a linear filter. J. Process Control **16**(4), 323–331 (2006)
14. Mamat, R., Fleming, P.: Method for on-line identification of a first order plus dead-time process model. Electron. Lett. **31**(15), 1297–1298 (1995)
15. Saha, D.C., Rao, G.P.: Identification of continuous dynamical systems: the poisson moment functional (PMF) approach, vol. 56. Springer (1983)
16. Pintelon, R., Van Biesen, L.: Identification of transfer functions with time delay and its application to cable fault location. IEEE Trans. Instrum. Measur. **39**(3), 479–484 (1990)
17. Yi, S., Nelson, P.W., Ulsoy, A.G.: Time-Delay Systems: Analysis and Control Using the Lambert W Function. World Scientific (2010)

18. Corless, R.M., Gonnet, G.H., Hare, D.E.G., Jeffrey, D.J., Knuth, D.E.: On the Lambert W function. Adv. Comput. Math. **5**(4), 329–359 (1996)
19. Shinozaki, H., Mori, T.: Robust stability analysis of linear time-delay systems by Lambert W function: some extreme point results. Automatica **42**(10), 1791–1799 (2006)
20. Yang, S.H.: Internet-Based Control Systems Design and Applications. Springer, London (2010)
21. Corke, P.: Robotics, vision and control: fundamental algorithms in MATLAB, vol. 73. Springer Science & Business Media (2011)
22. Hoffmann, G.M., Huang, H., Waslander, S.L., Tomlin, C.J.: Quadrotor helicopter flight dynamics and control: theory and experiment. In: Proceedings of the AIAA Guidance, Navigation, and Control Conference, vol. 2 (2007)
23. Hoffmann, G.M., Waslander, S.L., Tomlin, C.J.: Quadrotor helicopter trajectory tracking control. In: AIAA Guidance, Navigation and Control Conference and Exhibit, pp. 1–14 (2008)
24. Vyhlidal, T., Ziítek, P.: Mapping based algorithm for large-scale computation of quasi-polynomial zeros. IEEE Trans. Autom. Control **54**(1), 171–177 (2009)
25. Armah, S., Yi, S., Choi, W.: Design of feedback control for quadrotors considering signal transmission delays. Int. J. Control Autom. Syst. (accepted)
26. Yepes, A.G., Freijedo, F.D., Doval-Gandoy, J., Lopez, O., Malvar, J., Fernandez-Comesa, P.: Effects of discretization methods on the performance of resonant controllers. IEEE Trans. Power Electron. **25**(7), 1692–1712 (2010)

Experimental Validation of Robust Chatter Control for High-Speed Milling Processes

N. van de Wouw, N.J.M. van Dijk, A. Schiffler, H. Nijmeijer and E. Abele

Abstract This chapter presents results on the design and experimental implementation and testing of robust controllers for the high-speed milling process for the purpose of avoiding chatter vibrations. Chatter vibrations are intimately related to the delay nature of the cutting process inherent to milling and should be avoided to ensure a high product quality. A design approach based on μ-synthesis is used to synthesize a controller that avoids chatter vibrations in the presence of model uncertainties and while respecting key performance specifications. The experimental validation of this controller on a benchmark setup, involving a spindle system including an active magnetic bearing, shows that chatter can be robustly avoided while significantly increasing the material removal rate, i.e., the productivity.

N. van de Wouw (✉)
Department of Mechanical Engineering, Eindhoven University of Technology,
Eindhoven, The Netherlands
e-mail: N.v.d.Wouw@tue.nl

N. van de Wouw
Department of Civil, Environmental & Geo-Engineering, University of Minnesota,
Minneapolis, USA

N. van de Wouw
Delft Center for Systems and Extra Control, Delft University of Technology,
Delft, The Netherlands

N.J.M. van Dijk
Philips Innovation Services, Eindhoven, The Netherlands
e-mail: niels.van.dijk@philips.com

A. Schiffler
Schaeffler Technologies AG & Co. KG, Schweinfurt, Germany
e-mail: andreas.schiffler@schaeffler.com

H. Nijmeijer
Department of Mechanical Engineering, Eindhoven University of Technology,
Eindhoven, The Netherlands
e-mail: H.Nijmeijer@tue.nl

E. Abele
Institut Für Produktionsmanagement, Technologie und Werkzeugmaschinen,
Technische Universität Darmstadt, Darmstadt, Germany
e-mail: abele@ptw.tu-darmstadt.de

T. Insperger et al. (eds.), *Time Delay Systems*,
Advances in Delays and Dynamics 7, DOI 10.1007/978-3-319-53426-8_21

1 Introduction

Chatter is an instability phenomenon in machining processes. The occurrence of (regenerative) chatter results in an inferior workpiece quality due to heavy vibrations of the cutter. Moreover, a high noise level is produced, the tool wears out rapidly and damage to the spindle unit may be caused, inducing high manufacturing costs. The occurrence of chatter can be visualized in so-called stability lobes diagrams (SLD). In a SLD, the chatter stability boundary between a stable cut (i.e. without chatter) and an unstable cut (i.e. with chatter) is visualized in terms of spindle speed and depth of cut (two key parameters characterizing the productivity).

The present day manufacturing industry demands high-precision products manufactured at a high productivity rate. This feeds the desire for the design of dedicated control strategies, which are able to actively alter the chatter stability boundary such that a higher productivity becomes feasible while avoiding chatter.

Three distinct approaches exist in literature to control chatter. The first method involves adjusting process parameters (i.e. spindle speed, feed per tooth or chip load) such that a stable working point is chosen [7, 25]. Although chatter can be eliminated by adaptation of process parameters, this methodology does not enlarge the domain of stable operation points toward those of higher productivity. A second method is to disturb the regenerative (delay) effect by continuous spindle speed modulation, see [26, 30]. Although the stability boundary is altered by spindle speed modulation, see [15], the method cannot be used in the case of high-speed milling since the modulation speed is limited by the inertia and actuation power of the spindle. The third method is to passively or actively alter the machine dynamics to favorably shape the chatter boundary. There are passive chatter suppression techniques that use dampers ([20]) or vibration absorbers ([28]). Active chatter control in milling has mainly been focused on the active damping of machine dynamics, see [11, 19], or workpiece, see [31]. Damping the machine or workpiece dynamics, either passively or actively, results in a uniform increase of the stability boundary for all spindle speeds. To enable more dedicated shaping of the stability boundary (e.g. lifting the SLD locally around a specific spindle speed), the regenerative (delay) effect should be taken into account during chatter controller design. In [23], an optimal state feedback observer-controller combination with integral control in the case of turning was designed. Recently, Chen and Knospe [5] developed three different chatter control strategies in the case of turning: speed-independent control, speed-specified control, and speed interval control.

Recently, in [8, 9] an active chatter control strategy based μ-synthesis has been proposed with the following benefits. First, using this approach, controllers can be designed that guarantee chatter-free cutting operations in an a priori defined range of process parameters, such as the spindle speed and depth of cut. Second, the approach explicitly takes the regenerative (delay) effect, responsible for chatter, into account in the milling models serving as basis for controller design. Third, robust stabilization of high-speed milling operations is achieved in the presence of model uncertainties (regarding the spindle-tool dynamics), while minimizing the control effort needed.

In this chapter, we experimentally validate controllers designed using the approach in [8, 9] on an experimental benchmark setup equipped with Active Magnetic Bearings (AMB) in the spindle, also used in [18] for chatter control using active damping techniques. Section 2 presents the dynamic model of the milling process in the form of a nonlinear time-varying delay differential equation (DDE) and a simplified DDE model used in the scope of controller design is introduced. In Sect. 3, the experimental setup is described and the experimental identification of the model for the setup is discussed. Section 4 presents the controller design approach used and the resulting controller design for the experimental setup. Finally, experimental results are presented that illustrate the effectiveness of this chatter control approach to improve the material removal rate of the milling process while guaranteeing the avoidance of chatter. Section 5 concludes this chapter.

2 High-Speed Milling Process

2.1 Comprehensive Milling Model

A model of the milling process will be described below, see e.g., [3, 13, 17, 27] for more details. In Fig. 1, a schematic representation of the milling process is depicted. The predefined motion of the tool with respect to the workpiece is characterized in terms of the static chip thickness $h_{j,\mathsf{stat}}(t) = f_z \sin \phi_j(t)$, where f_z is the feed per tooth and $\phi_j(t)$ the rotation angle of the j-th tooth of the tool with respect to the y (normal) axis. However, the total chip thickness $h_j(t)$ also depends on the interaction between the cutter and the workpiece. This interaction causes cutter vibrations resulting in a dynamic displacement $\underline{v}_t(t) = \left[v_{t,x}(t)\, v_{t,y}(t)\right]^T$ of the tool, see Fig. 1, which is superimposed on the predefined tool motion and results in a wavy workpiece surface. The next tooth encounters this wavy surface, generated by the previous tooth, and, in turn, generates its own waviness. This is called the regenerative effect. The difference between the current and previous wavy surface generates the dynamic chip thickness, denoted by $h_{j,\mathsf{dyn}}(t) = \left[\sin \phi_j(t) \cos \phi_j(t)\right] \left(\underline{v}_t(t) - \underline{v}_t(t-\tau)\right)$ with $\tau = 60/(zn)$ the delay, z the number of teeth and n the spindle speed in revolutions per minute (rpm). Hence, the total chip thickness removed by tooth j at time t equals $h_j(t) = h_{j,\mathsf{stat}}(t) + h_{j,\mathsf{dyn}}(t)$. Here, a circular tooth path is assumed, while in reality the tooth path is trochoidal, see [14]. For high radial immersion cuts (such as the full immersion cuts considered here), the circular tool path model forms a good approximation, also in terms of the prediction of the chatter stability boundary, see [14].

The cutting force model relates the total chip thickness to the forces acting at the tool tip. The tangential and radial forces, F_t and F_r in Fig. 1, for a single tooth j, are described by the following exponential cutting force model:

$$F_{t_j}(t) = g_j\big(\phi_j(t)\big) K_t\, a_p\, h_j(t)^{x_F},\ F_{r_j}(t) = g_j\big(\phi_j(t)\big) K_r\, a_p\, h_j(t)^{x_F}, \tag{1}$$

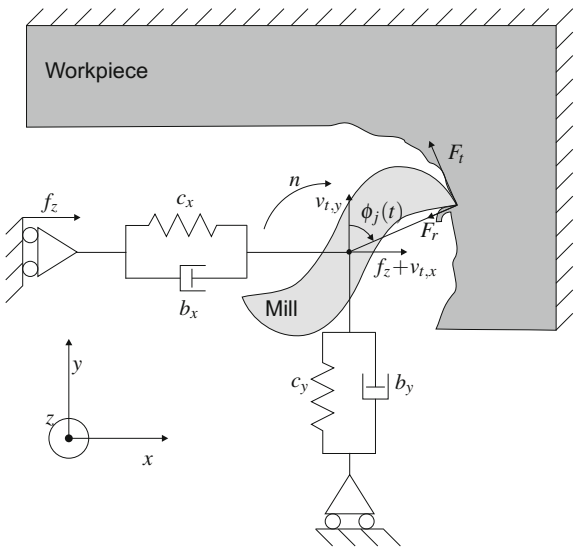

Fig. 1 Schematic representation of the milling process

where $0 < x_F \leq 1$ and $K_t, K_r > 0$ are cutting parameters which depend on the workpiece material. Moreover, a_p is the axial depth of cut. The function $g_j\big(\phi_j(t)\big)$ in (1) describes whether a tooth is in or out of cut:

$$g_j\big(\phi_j(t)\big) = \begin{cases} 1, & \phi_s \leq \phi_j(t) \leq \phi_e \wedge h_j(t) > 0, \\ 0, & \text{else}, \end{cases} \tag{2}$$

where ϕ_s and ϕ_e are the entry and exit angles of the cut, respectively. The total cutting forces in the x- and y-directions, $\underline{F}_t(t) = \left[F_{t,x}(t)\ F_{t,y}(t)\right]^T$, can be obtained by summing over all z teeth:

$$\begin{aligned} \underline{F}_t(t) = a_p \sum_{j=0}^{z-1} g_j\big(\phi_j(t)\big) \Big(\Big(& h_{j,\text{stat}}(t) \\ & + \left[\sin\phi_j(t)\ \cos\phi_j(t)\right]\big(\underline{v}_t(t) - \underline{v}_t(t-\tau)\big) \Big)^{x_F} \mathbf{S}_j(t) \begin{bmatrix} K_t \\ K_r \end{bmatrix} \Big) \end{aligned} \tag{3}$$

with $\mathbf{S}_j(t) = \begin{bmatrix} -\cos\phi_j(t) & -\sin\phi_j(t) \\ \sin\phi_j(t) & -\cos\phi_j(t) \end{bmatrix}$.

The cutting force interacts with the machine (spindle and tool) dynamics, which are modeled with a linear multi-input-multi-output (MIMO) state-space model,

$$\begin{aligned} \dot{\underline{x}}(t) &= \mathbf{A}\underline{x}(t) + \mathbf{B}_t\underline{F}_t(t) + \mathbf{B}_a\underline{F}_a(t), \\ \underline{v}_t(t) &= \mathbf{C}_t\underline{x}(t), \quad \underline{v}_a(t) = \mathbf{C}_a\underline{x}(t), \end{aligned} \tag{4}$$

where $\underline{x}(t)$ is the state. $\underline{F}_a(t) = \left[F_{a,x}(t)\ F_{a,y}(t)\right]^T$ denote the control forces, where $F_{a,x}(t)$ and $F_{a,y}(t)$ are the control forces acting in the x- and y-direction, respectively. Moreover, $\underline{v}_a(t)$ represents the measured displacements available for feedback (see Sect. 4).

Substitution of (3) into (4) results in the nonlinear, nonautonomous delay differential equations (DDE) describing the dynamics of the milling process:

$$\begin{aligned}\dot{\underline{x}}(t) &= \mathbf{A}\underline{x}(t) + \mathbf{B}_a\underline{F}_a(t) + \mathbf{B}_t a_p \sum_{j=0}^{z-1} g_j\left(\phi_j(t)\right)\Big(\Big(h_{j,\mathrm{stat}}(t) \\ &\quad + \left[\sin\phi_j(t)\ \cos\phi_j(t)\right]\mathbf{C}_t\left(\underline{x}(t) - \underline{x}(t-\tau)\right)\Big)^{x_F}\mathbf{S}(t)\begin{bmatrix}K_t\\K_r\end{bmatrix}\Big), \\ \underline{v}_a(t) &= \mathbf{C}_a\underline{x}(t).\end{aligned} \tag{5}$$

2.2 Stability of the Milling Process and Its Relation to Chatter

The static chip thickness $h_{j,\mathrm{stat}}(t)$ is periodic with period time $\tau = \frac{60}{zn}$. In general, the uncontrolled (i.e. $\underline{F}_a(t) \equiv 0$) milling model (5) has a periodic solution $\underline{x}^*(t)$ with period time τ, see [14]. In the absence of chatter, this periodic solution is (locally) asymptotically stable and when chatter occurs it is unstable. Hence, the chatter stability boundary can be analyzed by studying the (local) stability properties of the periodic solution $\underline{x}^*(t)$. Hereto, the milling model is linearized about the periodic solution $\underline{x}^*(t)$ for zero control input (i.e. $\underline{F}_a(t) \equiv 0$) yielding the following linearized dynamics in terms of perturbations $\tilde{\underline{x}}(t)$ ($\underline{x}(t) = \underline{x}^*(t) + \tilde{\underline{x}}(t)$):

$$\begin{aligned}\dot{\tilde{\underline{x}}}(t) &= \mathbf{A}\tilde{\underline{x}}(t) + a_p\mathbf{B}_t\sum_{j=0}^{z-1}\mathbf{H}_j(\phi_j(t))\mathbf{C}_t(\tilde{\underline{x}}(t) - \tilde{\underline{x}}(t-\tau)) + \mathbf{B}_a\underline{F}_a(t), \\ \tilde{\underline{v}}_a(t) &= \mathbf{C}_a\tilde{\underline{x}}(t),\end{aligned} \tag{6}$$

where

$$\mathbf{H}_j(\phi_j(t)) = g_j\left(\phi_j(t)\right)x_F(f_z\sin\phi_j(t))^{x_F-1}\mathbf{S}(t)\begin{bmatrix}K_t\\K_r\end{bmatrix}\begin{bmatrix}\sin\phi_j(t)\\\cos\phi_j(t)\end{bmatrix}^T. \tag{7}$$

The linearized model (6), (7) is a delayed, periodically time-varying system. As described in [3], for full immersion cuts it is sufficient to average the dynamic cutting forces $\sum_{j=0}^{z-1}\mathbf{H}_j(\phi_j(t))$ over the tool path such that the milling model becomes time-invariant. Since the cutter is only cutting when $\phi_s \le \phi_j \le \phi_e$ the averaged cutting forces are given by

$$\bar{\mathbf{H}} = \frac{z}{2\pi} \int_{\phi_s}^{\phi_e} \sum_{j=0}^{z-1} \mathbf{H}_j(\phi) \mathrm{d}\phi. \tag{8}$$

Then, a linear time-invariant model of the milling process is obtained by combining (6) with $\sum_{j=0}^{z-1} \mathbf{H}_j(\phi_j(t))$ replaced by $\overline{\mathbf{H}}$ and $\overline{\mathbf{H}}$ given in (8). The characteristic equation of the linear DDE (6), with $\sum_{j=0}^{z-1} \mathbf{H}_j(\phi_j(t))$ replaced by $\overline{\mathbf{H}}$ and $\overline{\mathbf{H}}$ given in (8), is then given as

$$\det(\mathbf{I} - a_p \mathbf{G}_{tt}(i\omega)\overline{\mathbf{H}}(1 - e^{-i\omega\tau})) = 0, \tag{9}$$

where $\mathbf{G}_{tt}(i\omega) = \mathbf{C}_t(i\omega\mathbf{I} - \mathbf{A})^{-1}\mathbf{B}_t$ represents the frequency response function (FRF) from cutting forces at the tooltip to tooltip displacements. The chatter stability boundary can be obtained by solving (9) for depth of cut a_p and delay τ as e.g. discussed in [3], see also [16].

2.3 Model Simplification for Control

In support of the usage of robust control synthesis techniques as in [8, 9], we construct a finite-dimensional model approximation using a Padé approximation (see also [5]). Hereto, the delayed (perturbation) tool vibrations $\underline{\tilde{v}}_t(t-\tau) = \mathbf{C}_t\tilde{q}(t-\tau)$ are approximated by Padé approximation denoted by $\tilde{v}_p(t)$, such that $\underline{\tilde{v}}_t(t-\tau) = \mathbf{C}_t\tilde{q}(t-\tau) \approx \underline{\tilde{v}}_p(t)$. The milling model in (6) with cutting force averaging, defined in (8), and Padé approximation is given as,

$$\begin{aligned}
\begin{bmatrix} \dot{\tilde{q}}(t) \\ \dot{\tilde{q}}_p(t) \end{bmatrix} &= \begin{bmatrix} \mathbf{A} + a_p\mathbf{B}_t\overline{\mathbf{H}}(\mathbf{C}_t - \mathbf{D}_p\mathbf{C}_t) & -a_p\mathbf{B}_t\overline{\mathbf{H}}\mathbf{C}_t \\ \mathbf{B}_p\mathbf{C}_t & \mathbf{A}_p \end{bmatrix} \begin{bmatrix} \tilde{q}(t) \\ \tilde{q}_p(t) \end{bmatrix} + \begin{bmatrix} \mathbf{B}_a \\ \mathbf{0} \end{bmatrix} \underline{F}_a(t), \\
\underline{\tilde{v}}_a(t) &= \mathbf{C}_a\underline{\tilde{q}}(t),
\end{aligned} \tag{10}$$

where $\mathbf{A}_p, \mathbf{B}_p, \mathbf{C}_p$ and $\mathbf{D}_p$ denote matrices of the state-space description of the Padé approximation (with state $\tilde{q}_p(t)$). The order of the Padé approximation will be based on a desired level of accuracy regarding the predicted chatter stability boundary using the model with Padé approximation, see [9].

In the next section, the experimental identification of the milling model introduced above will be discussed. Subsequently, the following steps in model identification will be pursued: (1) the identification of the cutting model the spindle-tool dynamics, i.e., the parameters K_t, K_r and X_F in (7), (2) the identification of the spindle-tool dynamics, i.e., the matrices A, B_t, B_a, C_t and C_a in (4) and (3) the identification of uncertainties in these spindle-tool dynamics (needed in support of the design of chatter controllers that are robust in the presence of such uncertainties that are unavoidable in practice).

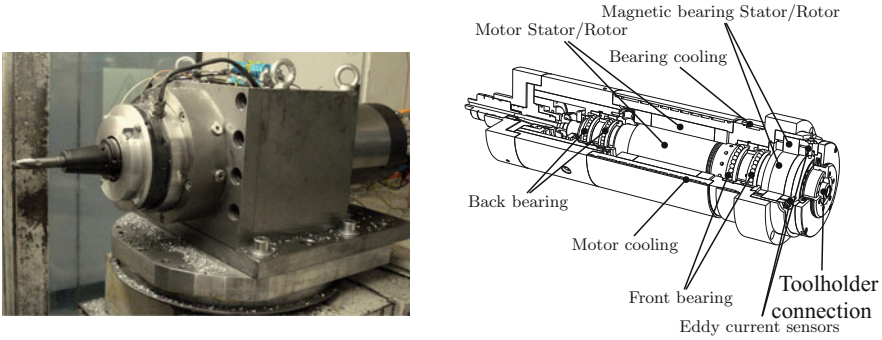

(a) Photo. (b) Schematic representation.

Fig. 2 The experimental setup. An active magnetic bearing (AMB) is integrated into a machine spindle between the front bearings and toolholder connection. *Source* Institut für Produktionsmanagement, Technologie und Werkzeugmaschinen (PTW), Technische Universität Darmstadt, Germany

3 Experimental Setup and Model Identification

3.1 Experimental Setup

The experimental setup, used in this chapter, is designed and realized at the Institut für Produktionsmanagement, Technologie und Werkzeugmaschinen (PTW) of the Technische Universität Darmstadt, Germany. In Fig. 2, a photo and schematic overview of the spindle with integrated Active Magnetic Bearing (AMB) can be found. It can be seen that the active magnetic bearing, to be used as actuator, is integrated in the spindle and is placed between the front bearings and the toolholder. Moreover, two eddy current sensors are employed to measure the spindle shaft motion relative to the spindle housing. In this way, the setup can serve as a testbed for a proof of principle in order to test the active chatter control strategy in practice. The specifications of the spindle and AMB, taken from [18], are listed in Table 1. The same spindle with integrated AMB has been used in [18] for chatter control using active damping techniques.

3.2 Identification of the Experimental Setup

In this section, we first concisely describe the result of experiments aiming at the identification of (1) the parameters of the cutting force model, (2) a parametric model of the spindle and actuator dynamics and (3) uncertainties in the spindle dynamics, see [6] for details. Next, the SLD of the experimental setup will be determined

Table 1 Specifications of the experimental setup

Spindle		AMB	
max. Power	80 kW	Number of poles	8
max. spindle speed	24,000 rpm	Nominal airgap	0.4 mm
		Pre-magnetizing current	5 A
		max. input current	10 A
		max. static force	600 N
		Bandwidth current controller	1000 Hz

through dedicated milling experiments as well as using the obtained model for the purpose of model validation.

Identification of the cutting force model parameters. Cutting tests have been performed to experimentally identify the parameters, K_t, K_r and x_F of the cutting force model (3). Hereto, full immersion cuts in aluminum 7075 have been performed while measuring the cutting forces using a dynamometer. The parameters are obtained by fitting the model on the experimentally obtained cutting forces in feed and normal direction using least squares optimization as outlined in [12]. The corresponding parameters are given by $K_t = 585.00$ N/mm$^{1+x_f}$, $K_r = 210.04$ N/mm$^{1+x_f}$ and $x_F = 0.7654$.

Identification of the spindle-actuator dynamics. Next, the nominal model of the spindle and actuator dynamics is determined experimentally. The model consists of four inputs (the input voltage to the current controller which drives the AMB and the force acting at the tooltip in feed (x)- and normal (y)-direction) and four outputs (displacements in feed (x)- and normal (y)-direction measured at the AMB location and the tooltip). In order to determine the frequency response functions (FRF), corresponding to this input/output set, the tooltip is excited using an impulse hammer while the accelerations at the tooltip are measured using an accelerometer and AMB displacements are measured using the eddy current sensors. The FRF matrix $\mathbf{G}$ of the spindle dynamics is defined as follows:

$$\mathbf{G}(i\omega) = \begin{bmatrix} \mathbf{G}_x(i\omega) & \mathbf{0} \\ \mathbf{0} & \mathbf{G}_y(i\omega) \end{bmatrix}, \text{ with } \mathbf{G}_\alpha(i\omega) = \begin{bmatrix} \mathbf{G}_{tt,\alpha}(i\omega) & \mathbf{G}_{ta,\alpha}(i\omega) \\ \mathbf{G}_{at,\alpha}(i\omega) & \mathbf{G}_{aa,\alpha}(i\omega) \end{bmatrix} \tag{11}$$

and $\alpha \in \{x, y\}$. Herein, $\mathbf{G}_{kl,x}(i\omega)$ (and $\mathbf{G}_{kl,y}(i\omega)$) denote the FRF with output $k \in \{a, t\}$ and input $l \in \{a, t\}$, where t and a indicate tooltip and bearing excitation/response, respectively. All the experiments are conducted at standstill. It is well-known that the spindle dynamics is generally dependent on the spindle speed [1, 21]. Such spindle speed dependency of the dynamics of experimental setup will be modeled by including uncertainty in the spindle-actuator dynamics model, see below. Based on the measured data, a parametric model is fitted to the obtained

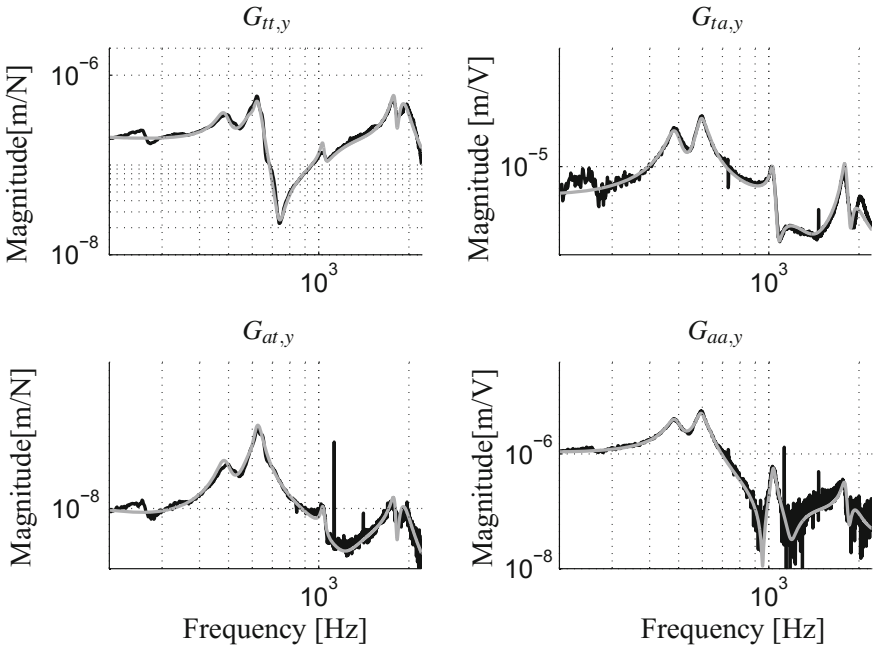

Fig. 3 Frequency response measurements (*black*) and fitted parametric model (*gray*) in normal (y) direction

frequency response functions. The multivariable model is described using polynomial matrix fraction descriptions ([4]). The parameters of the model are determined using Sanathanan–Koerner (SK) iteration, see [22].

In Fig. 3, the amplitude of the measured frequency response functions (FRFs) and corresponding parametric models in normal (y)-direction is given (information on the FRFs in the feed (x)-direction can be found in [6]). Especially near resonances, the fitted frequency response data and experimental data are quite comparable. The presented parametric model has a total of 30 states (14 in feed direction and 16 states in normal direction).

Identification of spindle-actuator dynamics uncertainties. To support the design of controllers that are robust for uncertainties in the milling machine dynamics, such uncertainties are identified here for the experimental setup under study. [12] concludes that the sensitivity of the SLD with respect to the spindle dynamics is considerably larger than the sensitivity to the parameters of the cutting force model. Consequently, during the controller design, uncertainties in the spindle-actuator model will be included. The following key sources of uncertainties in the model of the spindle-actuator dynamics are recognized: (1) uncertainty due to spindle speed dependent dynamics, (2) uncertainty due to unmodeled dynamics.

First, the uncertainty due to spindle speed dependent dynamics arises due to gyroscopic effects in the rotor and the spindle speed dependent bearing stiffness, see [21],

which results in a change of the low-frequent stiffness and a change in the eigenfrequencies of the spindle-actuator dynamics. The change in the low-frequency stiffness is compensated for by scaling the nominal model of the spindle-actuator dynamics. The associated scaling factor is determined by dividing the average value of the magnitude of the measured FRF $\mathbf{G}_{aa,k,n}$ (which is the only FRF from (11) that can be measured for a rotating spindle) from input voltage of the current controller to measured displacements $\underline{v}_a(t)$ at spindle speed n by the average value of magnitude of the FRF $\mathbf{G}_{aa,k,0}$ measured at standstill over a certain frequency range.

Second, in order to deal with changing eigenfrequencies due to spindle speed induced uncertainty (mainly due to changing bearing stiffness [1, 2, 21]), parametric uncertainties will be used to consider uncertain spindle modes. Here, uncertainty in the resonances is modeled as a parametric uncertainty in the eigenfrequencies of the associated resonances, see [6, 18]. Moreover, the uncertainty due to unmodeled dynamics is mainly due to the limited order of the parametric model which results in a deviation between the measured and modeled FRFs at higher frequencies. Moreover, at high frequencies the signal-to-noise ratio of the eddy current sensors becomes small, as can be seen from the measured FRFs in Fig. 3. Therewith, the structure of the model at high frequencies is unknown and the uncertainty is modeled using a (frequency-dependent) dynamic additive uncertainty.

In order to determine the uncertainties in the spindle-actuator dynamics of the experimental setup, FRFs from AMB input voltage to eddy current displacements $\underline{v}_a(t)$ have been measured for several spindle speeds. In this case, only the response at the bearing location can be measured. In Fig. 4, the amplitudes of the measured FRFs in feed and normal direction are given for several spindle speeds. This figure shows that there indeed is a significant change in the stiffness due to the spindle speed dependent dynamics. From now on, when a reference to the nominal model is made, it implies the model in which the scaling is absorbed. Figure 4 also shows that the first bending mode (which lies around 550 Hz) shifts as a function of the spindle speed. The gray area in this figure shows the uncertainty model for uncertainties on the resonances. Moreover, it can be seen that especially at frequencies above approximately 800 Hz the structure of the model (which is determined using measured data

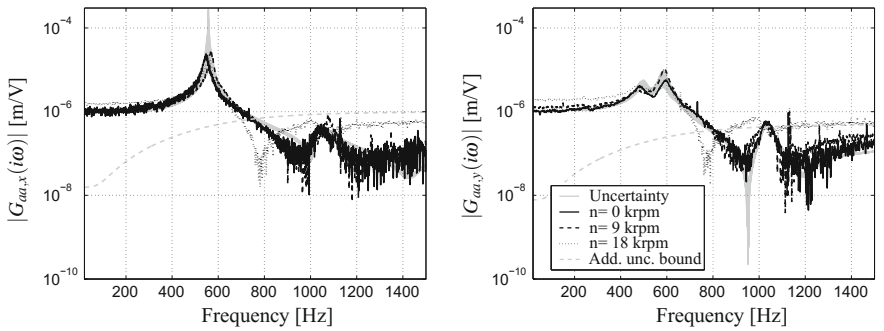

(a) feed direction. (b) normal direction.

Fig. 4 Frequency response data for bearing excitation experiments for several spindle speeds and uncertainty modeling

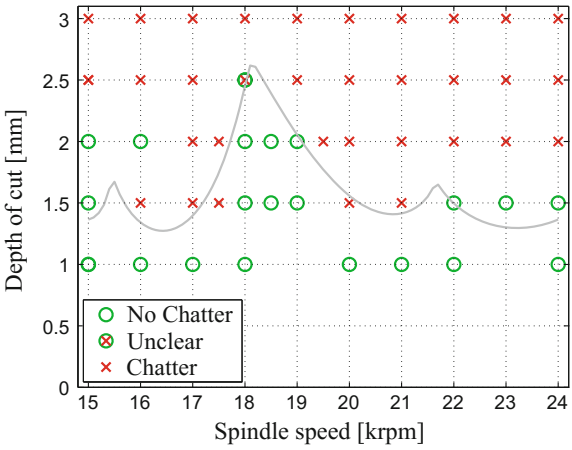

Fig. 5 Experimental (*o,x*) and (nominal) model-based (*gray line*) stability lobes diagram of the experimental setup

at standstill) does not match the measured FRFs. Based on these results, we model the uncertainties on the eigenfrequencies around 550 Hz by parametric uncertainties and add an additive uncertainty, see Fig. 4, to cope with the differences observed at higher frequencies. The measured spindle speed dependent spindle-actuator dynamics clearly lie inside the uncertainty set of the uncertain model of the spindle-actuator model.

3.2.1 Stability Lobes Diagram

First, stability lobes diagrams (SLD) are calculated using the open-loop linearized non autonomous model of the milling process (6) for the obtained parameters for the cutting force model and the *nominal* scaled parametric models of the spindle-actuator dynamics as presented above. The SLD is also determined experimentally. Hereto, cuts in aluminum 7075 have been made with the experimental setup as described in Sect. 3.1 for several spindle speeds and depth of cuts. Based on a visible inspection of the workpiece and the observed sound during the cut, a cut is marked with or without chatter. The resulting experimentally obtained SLD and the model-based SLD, calculated using the semi-discretization method ([16]), are presented in Fig. 5. It can be seen that the calculated SLD fits sufficiently well to the experimentally obtained SLD.

4 Control Approach and Validation

In this section, first a high-level description of the adopted chatter control approach will be given and next experimental results obtained with this approach will be presented.

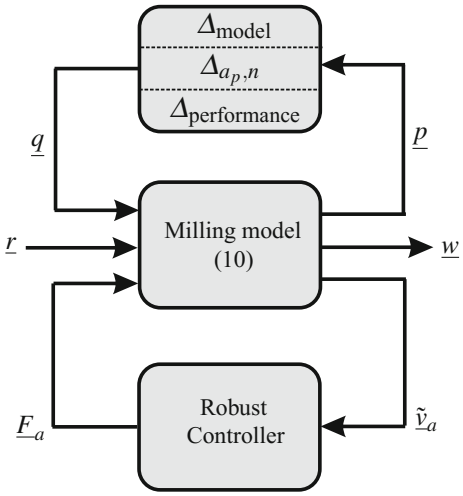

Fig. 6 Generalized plant framework, including uncertainties, used for controller synthesis

4.1 Chatter Control Approach

We employ the approach described in [8, 9] to design robust chatter controllers; for the sake of brevity only a high-level description of the approach is provided here.

In support of controller synthesis, a generalized plant framework as depicted in Fig. 6 is used. The main goal of the controller to be designed is to stabilize the dynamics (10), which implies that absence of chatter vibrations (at least locally). Figure 6 expresses that the controller used measured outputs $\underline{\tilde{v}}_a$, being the perturbation displacements in the active magnetic bearing. As the perturbation variants of these displacements cannot be directly measured, an online estimation algorithm for $\underline{\tilde{v}}_a$ as presented in [7] is used. The controller produces the forces $\underline{F}_a$ applied in the AMB. The uncertainty block consists of three parts: (1) Δ_{model} reflects the model uncertainty as identified in Sect. 3.2, (2) $\Delta_{a_p,n}$ reflects an uncertainty in the depth of cut a_p and the spindle speed n, which ensures that the controller stabilizes the milling process for an entire range of these parameters, and (3) $\Delta_{\text{performance}}$ embeds performance specifications for the controller, see [24], mainly related to limiting the control sensitivity, which in turn guarantees the limitation of the required control action. $\underline{p}$ and q represent an input–output pair needed in the interconnection between the plant dynamics and the uncertainty models. Finally, $\underline{r}$ reflects disturbances and measurement noise, while the performance output $\underline{z}$ represents the (weighted) control action. Now, a μ-synthesis approach, as proposed in [8, 9], is used to design linear, dynamic controllers that guarantee robustness with respect to these uncertainties.

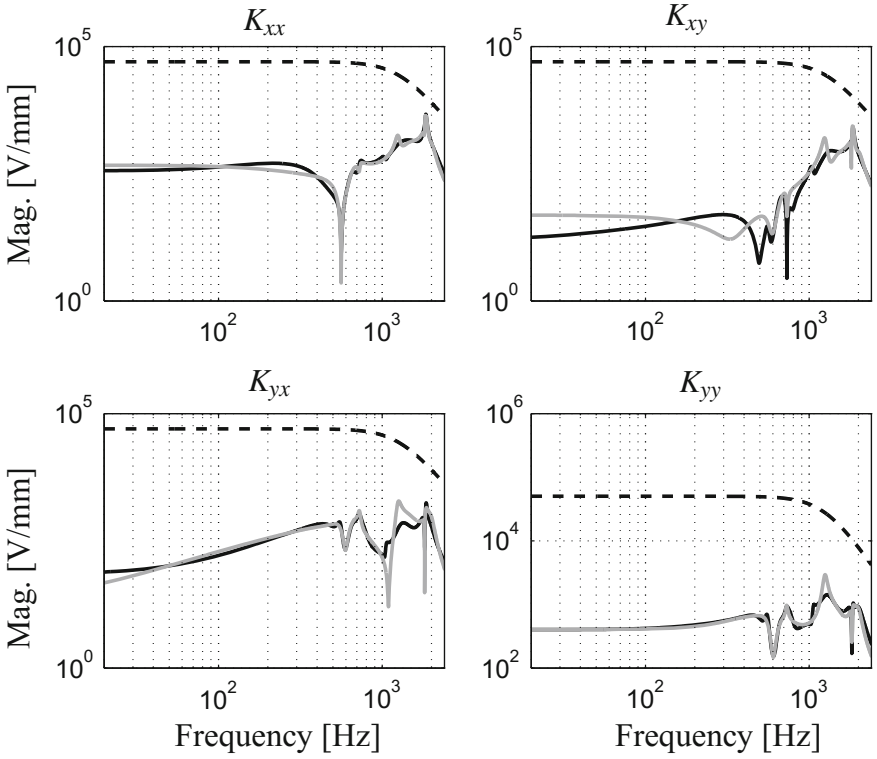

Fig. 7 Magnitude of the FRF for the full-order (*black*) and reduced-order (*gray*) controllers along with the inverse of the performance weighting function (*dashed*)

4.2 Chatter Controller Design

The SLD of the uncontrolled system in Fig. 5 shows that the productivity of the system measured in terms of the material removal rate (MMR) can be significantly increased when the critical depth of cut a_p is increased in the spindle speed range above 20,000 rpm. To this end, a controller for a single spindle speed of $n = 23{,}000$ rpm has been designed. The controller is designed by employing D-K-iteration with a bisection scheme to find the largest depth of cut $\overline{a}_p$ such that robust stability and performance is guaranteed. This yields a 98-th order controller that guarantees robust stability up to a depth of cut $\overline{a}_p = 2$ mm. Closed-loop model reduction yields a 19-th order controller for which robust stability and performance is still guaranteed up to $\overline{a}_p = 2$ mm. Magnitude plots of the high-order and reduced-order controllers are given in Fig. 7. It can be seen that the resulting controllers exhibit highly dynamical characteristics.

Next, closed-loop SLD diagrams are determined using the nominal linearized nonautonomous model of the milling model in (5) and the controller obtained above. The resulting closed-loop model-based SLDs along with the open-loop and

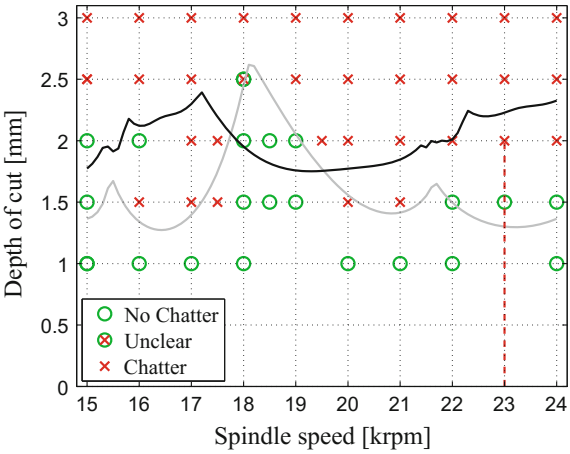

Fig. 8 Experimental (o, x) SLD and model-based (*solid lines*) SLD of the open-loop system (*gray*) and the closed-loop system for the reduced-order controller (*black*) using the nominal spindle dynamics

experimentally obtained SLD, as already presented in Sect. 3.2.1, are given in Fig. 8. The domain of stable operating points (in terms of the depth of cut) as guaranteed by the μ-synthesis is (for the model) given by the vertical dashed line: $\overline{a}_p = 2$ mm. The maximum achievable depth of cut (as obtained through computation of the SLD is given by $a_{p,max} = 2.23$ mm, as opposed to $a_{p,max} = 1.3$ mm for the open-loop case, which implies an increase of more than 70% in depth of cut.

4.3 Experimental Results

The robust controller, presented above, has been implemented and tested on the experimental setup. Before the results from a milling test are presented, first measurements are performed to determine the process sensitivity FRF of the closed-loop system in both feed and normal direction. The obtained FRFs are compared to measurements of the open-loop plant. Hereto, the AMB is excited using a 'pseudo-random binary sequence' signal, for a rotating spindle at $n = 23{,}000$ rpm while measuring the response using the eddy current sensors. The resulting magnitudes of the FRFs in feed and normal direction are given in Fig. 9.[1] From these figures, it can be concluded that the controller alters the spindle dynamics, where the first bending mode of the spindle is damped (especially in the normal direction) and a resonance is created at approximately 1510 Hz which is close to the second harmonic of the tooth passing excitation frequency ($2f_{tpe} = 2 \cdot \frac{2 \cdot 23{,}000}{60} \approx 1533$ Hz). As shown in [9], this characteristic of the closed-loop dynamics induces the raising of the SLD at the desired spindle speed (in this case 23,000 rpm), see Fig. 8.

Next, a full immersion cutting test has been performed at 23,000 rpm for a depth of cut of 2.5 mm using the controller with spindle-actuator uncertainty included in the controller design. Notice that chatter occurs for the open-loop at this depth of

[1]Note that in this case the tooltip dynamics, which are of interest for calculating the SLD, cannot be measured since the spindle is rotating.

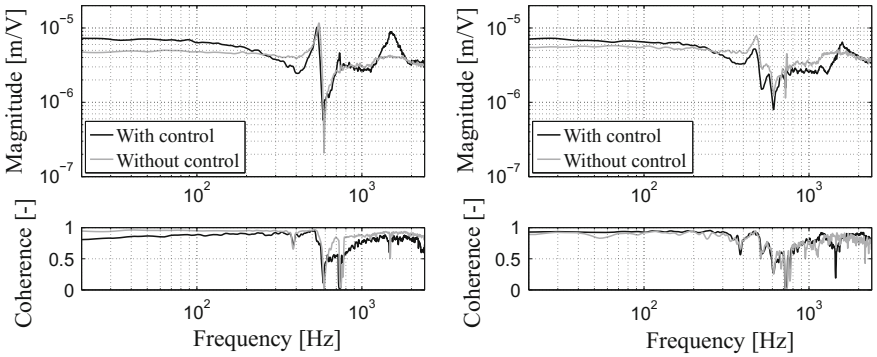

Fig. 9 Magnitude and coherence of the measured closed-loop process sensitivity and open-loop FRF from current controller input voltage to measured bearing displacements for $n = 23{,}000$ rpm

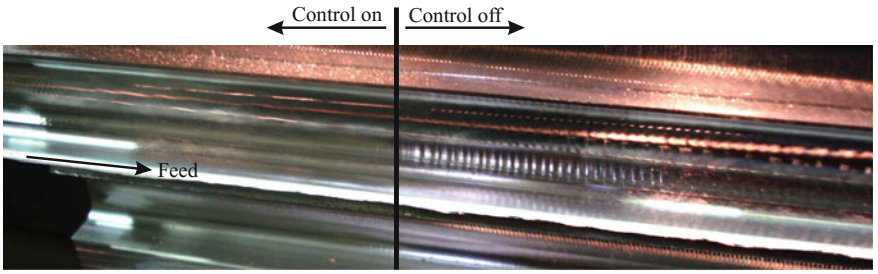

Fig. 10 Photo of the workpiece for an experiment at $n = 23{,}000$ rpm for a depth of cut of $a_p = 2.5$ mm, where in the first part of the cut the controller is on and is switched off after approximately 100 mm

cut, see Fig. 5. At the start of the cut, the controller is switched on. When the cutter is approximately 100 mm inside the material (in feed direction), the controller is switched off. After switching the controller off, chatter marks become visible on the workpiece. A picture of a part of the resulting workpiece is given in Fig. 10. It can be seen that, at the start of the cut, no chatter marks are visible on the workpiece, whereas chatter marks appear on the workpiece when the controller has been switched off.

Summarizing, it can be said that the working principle of the active chatter control design methodology has been illustrated in practice. With active chatter control for a single spindle speed, the depth of cut could be increased to 2.5 mm which is an increase of approximately 66% as compared to the experimentally uncontrolled obtained SLD in Fig. 5 at the same spindle speed.

5 Conclusions

This chapter has presented results on the experimental validation of an active control strategy for the avoidance of chatter vibrations in the high-speed milling process. In particular, a recently proposed robust control strategy [8, 9] has been tested on an experimental setup of a spindle with integrated Active Magnetic Bearing (AMB). The experimental results illustrate the effectiveness of the controller to robustly stabilize the milling process (i.e., avoid chatter) in the presence of significant model uncertainty and to achieve a significantly higher material removal rate while avoiding chatter.

Further research is needed on the following topics to promote the adoption of these techniques in industrial practice: (1) the development of robust online estimation techniques for chatter or alternatively the development of output feedback control techniques that do not need the estimation of the chatter (perturbation) vibrations, but can function with full vibrational measurements in the spindle, see e.g., [10, 29], and (2) further industrial development of active spindle systems including sensing and actuation techniques supporting the control techniques validated here.

Acknowledgements This work was supported by the Dutch Ministry of Economic affairs within the framework of Innovation Oriented Research Programmes (IOP) Precision Technology. We also thank E. J. J. Doppenberg and J. A. J. Oosterling (TNO Science and Industry, The Netherlands) for fruitful discussion on the topic of this research.

References

1. Abele, E., Kreis, M., Roth, M.: Electromagnetic actuator for in process non-contact identification of spindle-tool frequency respons functions. In: CIRP 2nd International Conference on High Performance Cutting, Vancouver, Canada, paper no. 103 (2006)
2. Abele, E., Schiffler, A., Rothenbücher, S.: System identification during milling via active magnetic bearing. Prod. Eng. Res. Dev. **1**(3), 309–314 (2007)
3. Altintas, Y.: Manufacturing Automation. Cambridge University Press, Cambridge, UK (2000)
4. de Callafon, R., de Roover, D., Van den Hof, P.: Multivariable least squares frequency domain identification using polynomial matrix fraction descriptions. In: Proceedings of the 35th IEEE Conference on Decision and Control, Kobe, Japan, vol. 2, pp. 2030–2035 (1996)
5. Chen, M., Knospe, C.R.: Control approaches to the suppression of machining chatter using active magnetic bearings. IEEE Trans. Control Syst. Technol. **15**(2), 220–232 (2007)
6. van Dijk, N.: Active chatter control in high-speed milling processes. PhD thesis, Eindhoven University of Technology. http://www.dct.tue.nl/New/Wouw/phdthesisvandijk2011.pdf (2011)
7. van Dijk, N.J.M., Doppenberg, E.J.J., Faassen, R.P.H., van de Wouw, N., Oosterling, J.A.J., Nijmeijer, H.: Automatic in-process chatter avoidance in the high-speed milling process. J. Dyn. Syst. Meas. Control **132**(3), 031,006 (14 pp) (2010a)
8. van Dijk, N.J.M., van de Wouw, N., Doppenberg, E.J.J., Oosterling, J.A.J., Nijmeijer, H.: Chatter control in the high-speed milling process using μ-synthesis. In: Proceedings of the American Control Conference, pp. 6121–6126, Baltimore, MD, USA (2010b)

9. van Dijk, N.J.M., van de Wouw, N., Doppenberg, E.J.J., Oosterling, J.A.J., Nijmeijer, H.: Robust active chatter control in the high-speed milling process. IEEE Trans. Control Syst. Technol. **20**(4), 901–917 (2012)
10. van Dijk, N.J.M., van de Wouw, N., Nijmeijer, H.: Fixed-structure robust controller design for chatter mitigation in high-speed milling. Int. J. Robust Nonlinear Control **25**(17), 34953514 (2015)
11. Dohner, J.L., Lauffer, J.P., Hinnerichs, T.D., Shankar, N., Regelbrugge, M.E., Kwan, C.M., Xu, R., Winterbauer, B., Bridger, K.: Mitigation of chatter instabilities in milling by active structural control. J. Sound Vib. **269**(1–2), 197–211 (2004)
12. Faassen, R.: Chatter prediction and control for high-speed milling: Modelling and experiments. PhD thesis, Eindhoven University of Technology (2007)
13. Faassen, R.P.H., van de Wouw, N., Oosterling, J.A.J., Nijmeijer, H.: Prediction of regenerative chatter by modelling and analysis of high-speed milling. Int. J. Mach. Tools Manuf. **43**(14), 1437–1446 (2003)
14. Faassen, R.P.H., van de Wouw, N., Nijmeijer, H., Oosterling, J.A.J.: An improved tool path model including periodic delay for chatter prediction in milling. J. Comput. Nonlinear Dyn. **2**(2), 167–179 (2007)
15. Insperger, T., Stépán, G.: Stability analysis of turning with periodic spindle speed modulation via semi-discretisation. J. Vib. Control **10**, 1835–1855 (2004)
16. Insperger, T., Stépán, G.: Updated semi-discretization method for periodic delay-differential equations with discrete delay. Int. J. Num. Methods Eng. **61**(1), 117–141 (2004)
17. Insperger, T., Stépán, G., Bayly, P.V., Mann, B.P.: Multiple chatter frequencies in milling processes. J. Sound Vib. **262**(2), 333–345 (2003)
18. Kern, S.: Erhöhung der prozessstabilität durch aktive dämpfung von frässpindeln mittels elektromagnetischer aktoren. PhD thesis, Technische Universität Darmstadt, Darmstadt, Germany (2009)
19. Kern, S., Ehmann, C., Nordmann, R., Roth, M., Schiffler, A., Abele, E.: (2006) Active damping of chatter vibrations with an active magnetic bearing in a motor spindle using μ-synthesis and an adaptive filter. In: The 8th International Conference on Motion and Vibration Control
20. Liu, K.J., Rouch, K.E.: Optimal passive vibration control of cutting process stability in milling. J. Mater. Process. Technol. **28**(1–2), 285–294 (1991)
21. Rantatalo, M., Aidanpä, J., Göransson, B., Norman, P.: Milling machine spindle analysis using fem and non-contact spindle excitation and response measurement. Int. J. Mach. Tools Manuf. **47**(7–8), 1034–1045 (2007)
22. Sanathanan, C., Koerner, J.: Transfer function synthesis as a ratio of two complex polynomials. IEEE Trans. Autom. Control **8**(1), 56–58 (1963)
23. Shiraishi, M., Yamanaka, K., Fujita, H.: Optimal control of chatter in turning. Int. J. Mach. Tools Manuf. **31**(1), 31–43 (1991)
24. Skogestad, S., Postlethwaite, I.: Multivariable Feedback Control: Analysis and Design, 2nd edn. Wiley, Chichester (2005)
25. Smith, S., Delio, T.: Sensor-based chatter detection and avoidance by spindle speed. J. Dyn. Syst. Meas. Control **114**(3), 486–492 (1992)
26. Soliman, E., Ismail, F.: Chatter suppression by adaptive speed modulation. Int. J. Mach. Tools Manuf. **37**(3), 355–369 (1997)
27. Stépán, G.: Modelling nonlinear regenerative effects in metal cutting. Philos. Trans. R. Soc. A: Math. Phys. Eng. Sci. **359**(1781), 739–757 (2001). doi:10.1098/rsta.2000.0753
28. Tarng, Y.S., Kao, J.Y., Lee, E.C.: Chatter suppression in turning operations with a tuned vibration absorber. J. Mater. Process. Technol. **105**(1), 55–60 (2000)
29. van de Wouw, N., van Dijk, N.J.M., Nijmeijer, H.: Pyragas-type feedback control for chatter mitigation in high-speed milling. In: Proceedings of the A12th IFAC Workshop on Time Delay Systems, Ann-Arbor, MI, USA (2015)
30. Yilmaz, A., AL-Regib, E., Ni, J.: Machine tool chatter suppression by multi-level random spindle speed variation. J. Manuf. Sci. Eng. **124**(2), 208–216 (2002)
31. Zhang, Y., Sims, N.D.: Milling workpiece chatter avoidance using piezoelectric active damping: a feasibility study. Smart Mater. Struct. **14**(6), N65–N70 (2005)

Time-Delay Identification for Linear Systems: A Practical Method Using the Frequency Response Function

Xiaoxu Zhang and Jian Xu

Abstract The present paper gives a comprehensive study on delay parameter identification in linear system with time-delayed control. For the cases when the state matrix is prior known and is prior unknown, identification algorithms are provided. For the former case, delay identifiability depends on the measurability of the outputs that serve as the delayed feedback; while for the latter case, the external input information, including the positions where the delayed control acts, is also a necessity. The algorithms are stated in a unified programming scheme because the main steps for the two cases are basically the same. To verify the algorithm, an experiment on an active vibration absorber and a simulation on an active truss are performed. The results show a good convergence and preciseness of the proposed algorithm.

1 Introduction

Extensive studies [1, 2] show that time delay not only determines the controller's precision, but also affects the stability of the closed-loop system. From the demand of accurate parameter tuning, time-delay calibration has become an indispensable work in control strategy design.

The delay identification study starts from the case with single time delay. Such system is identifiable [3] if the solution of the model system is identical to the object system over a time period that is larger than the maximum delay. For systems with multiple time delays, the identifiability [4, 5] is ensured if the system is weakly controllable, and the input is sufficiently rich. Several adaptive algorithms [6–8] for time-delay parameter identification have been proposed, in which time-domain samples are utilized. Such algorithms require prior information about the initial conditions over a time period that is larger than the maximum time delay, which is

X. Zhang · J. Xu (✉)
School of Aerospace Engineering and Applied Mechanics, Tongji University, Shanghai 200092, China
e-mail: xujian@tongji.edu.cn

T. Insperger et al. (eds.), *Time Delay Systems*,
Advances in Delays and Dynamics 7, DOI 10.1007/978-3-319-53426-8_22

challenging because the time delay is undetermined. To overcome the drawbacks in time-domain algorithms, frequency-domain algorithms [9, 10], based on frequency response function (FRF), have been developed. In a proportional input–output signal with single time delay, the FRF is a complex exponential function whose phase lag slope directly indicates the signal's time delay. In this sense, the FRF becomes a valuable data source for delay identification and therefore calls for further investigations.

For instance, the parameter identifiability in condition of incomplete measurements, a common case in unlimited degree-of-freedom (DOF) systems, has not yet been discussed. Meanwhile, corresponding identification algorithm, using FRF samples, also needs further development.

Focusing on these issues, the study of this paper is organized as follows. In Sect. 2, the FRF of the time-delayed linear system is given first. The delay parameter's identifiability is discussed on cases when the state matrix is prior known and prior unknown, and corresponding parameter identification algorithms are constructed. In Sect. 3, an experiment of an active vibration absorber is applied for algorithm verification to the former case, and a numerical simulation of an active planar truss is designed for algorithm verification to the latter case. As for the last section, some comments on the proposed parameter identification algorithm are given.

2 Problem Statement and Algorithm Construction

The differential equation of linear time-delayed systems is given by

$$\dot{\mathbf{x}}(t) = \mathbf{A}\mathbf{x}(t) + \sum_{l=1}^{L} \mathbf{D}_l \mathbf{x}(t-\tau_l) + \mathbf{g}(t), \tag{1}$$

where $\mathbf{x} \in \mathbb{R}^M$ is the output state, $\mathbf{g} \in \mathbb{R}^M$ is the input state, $\mathbf{A} \in \mathbb{R}^{M\times M}$ is the state matrix, L is the number of distinct time delays, M is the dimension of $\mathbf{x}$, $\mathbf{D}_l \in \mathbb{R}^{M\times M}$, and τ_l are unknown time-delay parameters that need to be identified. Applying Fourier transform to Eq. (1) yields its FRF representation, which is given by

$$(j\omega\mathbf{E} - \mathbf{A})\mathbf{X}(j\omega) - \mathbf{G}(j\omega) = \left(\sum_{l=1}^{L} \mathbf{D}_l e^{-j\omega\tau_l}\right)\mathbf{X}(j\omega), \tag{2}$$

where j is the pure imaginary unit, ω is the frequency, $\mathbf{X}(j\omega)$ is the Fourier transform of $\mathbf{x}(t)$, $\mathbf{G}(j\omega)$ is the Fourier transform of $\mathbf{g}(t)$, and $\mathbf{E}$ is a unit matrix. When $\mathbf{X}(j\omega)$ and $\mathbf{G}(j\omega)$ are partly measurable, they can be rewritten as

$$\mathbf{X}(j\omega) = \mathbf{U}_o \mathbf{X}_o(j\omega) + \mathbf{U}_{uo} \mathbf{X}_{uo}(j\omega), \tag{3}$$

and

$$\mathbf{G}(j\omega) = \mathbf{V}_e \mathbf{G}_e(j\omega) + \mathbf{V}_{ue} \mathbf{G}_{ue}(j\omega), \tag{4}$$

respectively, where $\mathbf{X}_o(j\omega) \in \mathbb{C}^{M_o}$ is the sub-state of the measurable output, and $\mathbf{X}_{uo}(j\omega) \in \mathbb{C}^{M-M_o}$ is the complementary state of the unmeasurable output, $\mathbf{U}_o \in \mathbb{R}^{M \times M_o}$ and $\mathbf{U}_{uo} \in \mathbb{R}^{M \times (M-M_o)}$ are elementary matrices that map $\mathbf{X}_o(j\omega)$ and $\mathbf{X}_{uo}(j\omega)$ into the full state space; besides, $\mathbf{G}_e \in \mathbb{C}^{M_e}$ is the measurable external state input, $\mathbf{G}_{ue}(j\omega) \in \mathbb{C}^{M-M_e}$ is the unmeasurable external state input, $\mathbf{V}_e \in \mathbb{R}^{M \times M_e}$ and $\mathbf{V}_{ue} \in \mathbb{R}^{M \times (M-M_e)}$ are elementary matrices that map $\mathbf{G}_e(j\omega)$ and $\mathbf{G}_{ue}(j\omega)$ into full state. For example, suppose $\mathbf{X}(j\omega) \in \mathbb{C}^3$ and the measurable points are $X_2(j\omega)$ and $X_3(j\omega)$, then

$$\mathbf{X}_o(j\omega) = \begin{pmatrix} X_2(j\omega) \\ X_3(j\omega) \end{pmatrix}, \ \mathbf{X}_{uo}(j\omega) = X_1(j\omega), \ \mathbf{U}_o = \begin{pmatrix} 0 & 0 \\ 1 & 0 \\ 0 & 1 \end{pmatrix}, \text{ and } \mathbf{U}_{uo} = \begin{pmatrix} 1 \\ 0 \\ 0 \end{pmatrix}.$$

Furthermore, we may put exciters only at the excitation measurable points so that $\mathbf{G}_{ue}(j\omega)$ can be conveniently set as $\mathbf{0}$. Hence, Eq. (4) can be conveniently written as

$$\mathbf{G}(j\omega) = \mathbf{V}_e \mathbf{G}_e(j\omega). \tag{5}$$

Substituting Eqs. (3) and (5) into Eq. (2) yields

$$\begin{aligned}(j\omega \mathbf{E}_M - \mathbf{A})(\mathbf{U}_o \mathbf{X}_o(j\omega) + \mathbf{U}_{uo} \mathbf{X}_{uo}(j\omega)) = &\left(\sum_{l=1}^{L} e^{-j\omega\tau_l} \mathbf{D}_l \right) \mathbf{U}_o \mathbf{X}_o(j\omega) + \mathbf{V}_e \mathbf{G}_e(j\omega) \\ &+ \left(\sum_{l=1}^{L} e^{-j\omega\tau_l} \mathbf{D}_l \right) \mathbf{U}_{uo} \mathbf{X}_{uo}(j\omega),\end{aligned} \tag{6}$$

where we can find that if we want to identify $\mathbf{D}_l$ and τ_l from this equation, the unmeasurable state $\mathbf{X}_{uo}(j\omega)$ should be eliminated first. To do so, different identifiability conditions should be discussed according to the deterministic of $\mathbf{A}$.

2.1 Parameter Identification with Prior Known State Matrix

Theorem 1 *If the system's state matrix* $\mathbf{A}$ *is prior known, and the outputs that serve as delayed control are measurable, then the time delay* τ_l *and the delay governing matrix* $\mathbf{D}_l$ *are identifiable.*

Proof Since $\mathbf{A}$ is prior known, the impedance matrix $j\omega\mathbf{E}_M - \mathbf{A}$ is invertible. Accordingly Eq. (6) can be written as

$$\begin{aligned}\mathbf{U}_o\mathbf{X}_o(j\omega) + \mathbf{U}_{uo}\mathbf{X}_{uo}(j\omega) = \mathbf{H}(j\omega)\left(\sum_{l=1}^{L} e^{-j\omega\tau_l}\mathbf{D}_l\right)\mathbf{U}_o\mathbf{X}_o(j\omega) + \mathbf{H}(j\omega)\mathbf{V}_e\mathbf{G}_e(j\omega) \\ + \mathbf{H}(j\omega)\left(\sum_{l=1}^{L} e^{-j\omega\tau_l}\mathbf{D}_l\right)\mathbf{U}_{uo}\mathbf{X}_{uo}(j\omega),\end{aligned} \tag{7}$$

where $\mathbf{H}(j\omega) = (j\omega\mathbf{E}_M - \mathbf{A})^{-1}$ is the complete transfer matrix. Left multiplying $\mathbf{U}_o^T$ to both sides of Eq. (7), and taking into account that $\mathbf{U}_o^T\mathbf{U}_o = \mathbf{E}_{M_o}$ and $\mathbf{U}_o^T\mathbf{U}_{uo} = \mathbf{0}$ yield

$$\begin{aligned}\mathbf{X}_o(j\omega) = \mathbf{U}_o^T\mathbf{H}(j\omega)\left(\sum_{l=1}^{L} e^{-j\omega\tau_l}\mathbf{D}_l\right)\mathbf{U}_o\mathbf{X}_o(j\omega) + \mathbf{U}_o^T\mathbf{H}(j\omega)\mathbf{V}_e\mathbf{G}_e(j\omega) \\ + \mathbf{U}_o^T\mathbf{H}(j\omega)\left(\sum_{l=1}^{L} e^{-j\omega\tau_l}\mathbf{D}_l\right)\mathbf{U}_{uo}\mathbf{X}_{uo}(j\omega).\end{aligned} \tag{8}$$

Furthermore, since the delayed control only uses signal that belongs to the measurable output, we alternatively rewrite $\mathbf{D}_l$ as

$$\mathbf{D}_l = \mathbf{K}_l\mathbf{U}_o^T, \tag{9}$$

where $\mathbf{K}_l \in \mathbb{R}^{M\times M_o}$ is the compact delay governing matrix. Substituting Eq. (9) into Eq. (8) yields

$$\mathbf{X}_o(j\omega) - \mathbf{U}_o^T\mathbf{H}(j\omega)\mathbf{V}_e\mathbf{G}_e(j\omega) = \mathbf{U}_o^T\mathbf{H}(j\omega)\left(\sum_{l=1}^{L} e^{-j\omega\tau_l}\mathbf{K}_l\right)\mathbf{X}_o(j\omega), \tag{10}$$

where the unmeasured state $\mathbf{X}_{uo}(j\omega)$ is eliminated. Hence, to prove the delay parameters' identifiability, we just need to further verify that Eq. (10) promises the unique solution of $\mathbf{K}_l$ and τ_l.

Suppose that the parameters satisfying Eq. (10) are not unique, which means there are other parameters like $\tilde{\mathbf{K}}_r$ and $\tilde{\tau}_r$ satisfying the same FRF, namely,

$$\mathbf{X}_o(j\omega) - \mathbf{U}_o^T\mathbf{H}(j\omega)\mathbf{V}_e\mathbf{G}_e(j\omega) = \mathbf{U}_o^T\mathbf{H}(j\omega)\left(\sum_{r=1}^{L} e^{-j\omega\tilde{\tau}_r}\tilde{\mathbf{K}}_r\right)\mathbf{X}_o(j\omega). \tag{11}$$

Subtracting Eq. (11) from Eq. (10) yields

$$\mathbf{U}_o^T\mathbf{H}(j\omega)\left(\sum_{l=1}^{L} e^{-j\omega\tau_l}\mathbf{K}_l - \sum_{r=1}^{L} e^{-j\omega\tilde{\tau}_r}\tilde{\mathbf{K}}_r\right)\mathbf{X}_o(j\omega) = \mathbf{0}. \tag{12}$$

Because $\mathbf{H}(j\omega)$ and $\mathbf{X}_o(j\omega)$ are not always zero when the frequency ω varies, we further get

$$\sum_{l=1}^{L} e^{-j\omega\tau_l}\mathbf{K}_l - \sum_{r=1}^{L} e^{-j\omega\tilde{\tau}_r}\tilde{\mathbf{K}}_r = \mathbf{0} \tag{13}$$

from Eq. (12). Applying the inverse Fourier transform on Eq. (13) yields

$$\begin{aligned}\lim_{n\to\infty}\left(\frac{\tau_l}{2\pi n}\int_0^{\frac{2\pi n}{\tau_l}}\left(\sum_{l=1}^{L} e^{-j\omega\tau_l}\mathbf{K}_l - \sum_{r=1}^{L} e^{-j\omega\tilde{\tau}_r}\tilde{\mathbf{K}}_r\right)e^{j\omega\tau_l}d\omega\right)\\ = \mathbf{K}_l - \sum_{r=1}^{L}\delta(\tau_l-\tilde{\tau}_r)\tilde{\mathbf{K}}_r = \mathbf{0},\end{aligned} \tag{14}$$

where $\delta(\tau_l-\tilde{\tau}_r)$ is the Kronecker delta function, which gives $\delta(\tau_l-\tilde{\tau}_r)=1$ for $\tau_l=\tilde{\tau}_r$ and $\delta(\tau_l-\tilde{\tau}_r)=0$ for the other values. Therefore, Eq. (14) indicates that $\tau_l=\tilde{\tau}_r$ and $\mathbf{K}_l=\tilde{\mathbf{K}}_r$, and consequently the uniqueness of delay parameters are certified. #

The next step, after the analysis of the parameter identifiability, is the identification of $\mathbf{K}_l$ and τ_l from Eq. (10). Note that the right-hand side of Eq. (10) is strongly nonlinear with respect to τ_l, the closed-form solution cannot be derived in general. We can, however, use the Newton-Raphson method to solve Eq. (10) in an iterative way, for instance.

Suppose that the real parameters are the sum of the initial parameters and their increments, i.e.

$$\begin{cases}\mathbf{K}_l = \mathbf{K}_l^0 + \Delta\mathbf{K}_l^0\\ \tau_l = \tau_l^0 + \Delta\tau_l^0\end{cases}. \tag{15}$$

Substituting Eq. (15) into Eq. (10) and eliminating higher order terms yield

$$\mathbf{R}^0(j\omega) = \mathbf{U}_o^T\mathbf{H}(j\omega)\left(\sum_{l=1}^{L}\left(e^{-j\omega\tau_l^0}\Delta\mathbf{K}_l^0 - j\omega e^{-j\omega\tau_l^0}\mathbf{K}_l^0\Delta\tau_l^0\right)\right)\mathbf{X}_o(j\omega), \tag{16}$$

where

$$\mathbf{R}^0(j\omega) := \mathbf{X}_o(j\omega) - \mathbf{U}_o^T\mathbf{H}(j\omega)\mathbf{V}_e\mathbf{G}_e(j\omega) - \mathbf{U}_o^T\mathbf{H}(j\omega)\left(\sum_{l=1}^{L} e^{-j\omega\tau_l^0}\mathbf{K}_l^0\right)\mathbf{X}_o(j\omega)$$

is called the residue term. If τ_l^0 and $\mathbf{K}_l^0$ are exact parameters of the system, then it can be verified that $\mathbf{R}^0(j\omega)=\mathbf{0}$. Equation (16) is a matrix equation about $\Delta\mathbf{K}_l^0$, and it can be vectorized to

$$\mathbf{R}^0(j\omega)=\mathbf{X}_o^T(j\omega)\otimes\left(\mathbf{U}_o^T\mathbf{H}(j\omega)\right)\left(\mathbf{Q}_K^0(j\omega)\quad\mathbf{Q}_\tau^0(j\omega)\right)\begin{pmatrix}\Delta\mathbf{K}_{vec}^0\\ \Delta\boldsymbol{\tau}^0\end{pmatrix}\in\mathbb{C}^{M_o},\tag{17}$$

where

$$\mathbf{Q}_K^0(j\omega)=\left(e^{-j\omega\tau_1^0}\mathbf{E}_{MM_o}\quad e^{-j\omega\tau_2^0}\mathbf{E}_{MM_o}\quad\ldots\quad e^{-j\omega\tau_L^0}\mathbf{E}_{MM_o}\right)\in\mathbb{C}^{MM_o\times MM_oL},$$
$$\mathbf{Q}_\tau^0(j\omega)=-j\omega\left(e^{-j\omega\tau_1^0}\mathbf{V}\left(\mathbf{K}_1^0\right)\quad e^{-j\omega\tau_2^0}\mathbf{V}\left(\mathbf{K}_2^0\right)\quad\ldots\quad e^{-j\omega\tau_L^0}\mathbf{V}\left(\mathbf{K}_L^0\right)\ \ldots\right)\in\mathbb{C}^{MM_o\times L},$$

$$\Delta\mathbf{K}_{vec}^0=\begin{pmatrix}\mathbf{V}\left(\Delta\mathbf{K}_1^0\right)\\ \mathbf{V}\left(\Delta\mathbf{K}_2^0\right)\\ \vdots\\ \mathbf{V}\left(\Delta\mathbf{K}_L^0\right)\end{pmatrix}\in\mathbb{R}^{MM_oL},\quad\text{and}\quad\Delta\boldsymbol{\tau}^0=\begin{pmatrix}\Delta\tau_1^0\\ \Delta\tau_2^0\\ \vdots\\ \Delta\tau_L^0\end{pmatrix}\in\mathbb{R}^L$$

Here $\otimes$ is the Kronecker product [11] of two matrices, $\mathrm{V}(\bullet)$ is the vectorization [12] of a matrix, and $\mathbf{E}_{MM_o}$ is an $MM_o\times MM_o$ unit matrix. To make Eq. (17) invertible, we consider different FRF samples. Suppose that the frequency series is ω_n, where $n=1,2,\ldots,N$, Eq. (17) can be augmented to

$$\boldsymbol{\Psi}^0=\boldsymbol{\Phi}^0\begin{pmatrix}\Delta\mathbf{K}_{vec}^0\\ \Delta\boldsymbol{\tau}^0\end{pmatrix},\tag{18}$$

where

$$\boldsymbol{\Psi}^0=\begin{pmatrix}\mathbf{R}^0(j\omega_1)\\ \mathbf{R}^0(j\omega_2)\\ \vdots\\ \mathbf{R}^0(j\omega_N)\end{pmatrix}\in\mathbb{C}^{NM_o}$$

and

$$\boldsymbol{\Phi}^0=\begin{pmatrix}\mathbf{X}_o^T(j\omega_1)\otimes\mathbf{H}(j\omega_1)\left(\mathbf{Q}_K^0(j\omega_1)\quad\mathbf{Q}_\tau^0(j\omega_1)\right)\\ \mathbf{X}_o^T(j\omega_2)\otimes\mathbf{H}(j\omega_2)\left(\mathbf{Q}_K^0(j\omega_2)\quad\mathbf{Q}_\tau^0(j\omega_2)\right)\\ \vdots\\ \mathbf{X}_o^T(j\omega_N)\otimes\mathbf{H}(j\omega_N)\left(\mathbf{Q}_K^0(j\omega_N)\quad\mathbf{Q}_\tau^0(j\omega_N)\right)\end{pmatrix}\in\mathbb{C}^{NM_o\times(MM_oL+L)}.$$

When $N>(MM_oL+L)/M_o$, $\boldsymbol{\Phi}^0$ is full column rank. Thus the solution of increments can be given from Eq. (18) as

$$\begin{pmatrix}\Delta\mathbf{K}_{vec}^0\\ \Delta\boldsymbol{\tau}^0\end{pmatrix}=\left(\left(\boldsymbol{\Phi}^0\right)^T\boldsymbol{\Phi}^0\right)^{-1}\left(\boldsymbol{\Phi}^0\right)^T\boldsymbol{\Psi}^0,\tag{19}$$

and the iteration equation can be consequently given as

$$\begin{pmatrix} \mathbf{K}_{vec}^{i+1} \\ \boldsymbol{\tau}^{i+1} \end{pmatrix} = \begin{pmatrix} \mathbf{K}_{vec}^{i} \\ \boldsymbol{\tau}^{i} \end{pmatrix} + \begin{pmatrix} \Delta\mathbf{K}_{vec}^{i} \\ \Delta\boldsymbol{\tau}^{i} \end{pmatrix} = \begin{pmatrix} \mathbf{K}_{vec}^{i} \\ \boldsymbol{\tau}^{i} \end{pmatrix} + \left(\left(\boldsymbol{\Phi}^{i}\right)^{T} \boldsymbol{\Phi}^{i} \right)^{-1} \left(\boldsymbol{\Phi}^{i}\right)^{T} \boldsymbol{\Psi}^{i}. \quad (20)$$

2.2 Parameter Identification with Prior Unknown State Matrix

Theorem 2 *If the system's transfer matrix, which is derived from the measurable external inputs and the measurable outputs, can be acquired before delayed control activating; and the delayed control only acts measurable outputs onto positions where external input can be measured, then the time delay* τ_l *and the delay governing matrix* $\mathbf{D}_l$ *are identifiable.*

Proof As for the first condition, the transfer matrix derived from measurable inputs and measurable outputs can be mathematically written as

$$\mathbf{H}(j\omega) = \mathbf{U}_o^T (j\omega \mathbf{E}_M - \mathbf{A})^{-1} \mathbf{V}_e, \quad (21)$$

where $\mathbf{U}_o$ and $\mathbf{V}_e$ are the same as that shown in Eqs. (3) and (4). As for the second condition, the specified delay governing matrix can be mathematically written as

$$\mathbf{D}_l = \mathbf{V}_e \mathbf{K}_l \mathbf{U}_o^T, \quad (22)$$

where $\mathbf{K}_l \in \mathbb{R}^{M_e \times M_o}$ denotes the compacted delay governing matrix. Substituting Eqs. (21) and (22) into Eq. (6), and taking into account that $\mathbf{U}_o^T \mathbf{U}_o = \mathbf{E}_{M_o}$ and $\mathbf{U}_o^T \mathbf{U}_{uo} = \mathbf{0}$ yield

$$\mathbf{X}_o(j\omega) - \mathbf{H}(j\omega)\mathbf{G}_e(j\omega) = \mathbf{H}(j\omega)\left(\sum_{l=1}^{L} e^{-j\omega\tau_l} \mathbf{K}_l \right) \mathbf{X}_o(j\omega), \quad (23)$$

where the undetermined elements like $\mathbf{A}$ and $\mathbf{X}_{uo}(j\omega)$ are all eliminated.

Similarly, we can also verify the delay parameters' uniqueness by the reduction-to-absurdity procedure. Note that the difference of parameter identifiability between prior known $\mathbf{A}$ and prior unknown $\mathbf{A}$ is that the former only follows output observing rule, whereas the latter needs to follow both input observing and output observing rules.

Using the same Newton-Raphson procedure, the increment equation of Eq. (23) is given by

$$\mathbf{R}^0(j\omega) = \mathbf{X}_o^T(j\omega) \otimes \mathbf{H}(j\omega) \begin{pmatrix} \mathbf{Q}_K^0(j\omega) & \mathbf{Q}_\tau^0(j\omega) \end{pmatrix} \begin{pmatrix} \Delta\mathbf{K}_{vec}^0 \\ \Delta\boldsymbol{\tau}^0 \end{pmatrix}, \quad (24)$$

where

$$\mathbf{R}^0(j\omega) := \mathbf{X}_o(j\omega) - \mathbf{H}(j\omega)\mathbf{G}_e(j\omega) - \mathbf{H}(j\omega)\left(\sum_{l=1}^{L} e^{-j\omega\tau_l^0}\mathbf{K}_l^0\right)\mathbf{X}_o(j\omega),$$
$$\mathbf{Q}_K^0(j\omega) = \left(e^{-j\omega\tau_1^0}\mathbf{E}_{M_eM_o} \quad e^{-j\omega\tau_2^0}\mathbf{E}_{M_eM_o} \quad \dots \quad e^{-j\omega\tau_L^0}\mathbf{E}_{M_eM_o}\right),$$

and the other terms are in the same form as in Eq. (17). Considering different FRF samples, we can construct the same increment solution as the one shown by Eq. (20).

2.3 Algorithm Programing

It is obvious that except for some matrix constructions, the procedures of delay identification with prior known **A** and prior unknown **A** are basically identical, and thus they can be combined into a unified algorithm scheme.

Furthermore, when initial parameters are set improperly, the iteration given by Eq. (20) may act as an intensive numerical oscillation, which affects the convergence of the iteration significantly. In order to fix this issue, we add a relaxation factor into this equation to get

$$\begin{pmatrix} \mathbf{K}_{vec}^{i+1} \\ \boldsymbol{\tau}^{i+1} \end{pmatrix} = \begin{pmatrix} \mathbf{K}_{vec}^{i} \\ \boldsymbol{\tau}^{i} \end{pmatrix} + \left(1 - e^{-\zeta i}\right)\left(\left(\boldsymbol{\Phi}^i\right)^T\boldsymbol{\Phi}^i\right)^{-1}\left(\boldsymbol{\Phi}^i\right)^T\boldsymbol{\Psi}^i, \tag{25}$$

where ζ is called the artificial damping ratio. In practice, let ζ be small if the initial condition is at low confidence level, otherwise it can be set larger to accelerate the iteration. The recommended damping ratio is from 3% to 10%.

In applications, the active control may connect only a few nodes, which means that the delay governing vector $\mathbf{K}_{vec}$ is sparse. In this case, the calculation related to the zero elements can be saved by a linear compacting transformation, i.e.,

$$\mathbf{K}_{vec} = \mathbf{T}\tilde{\mathbf{K}}_{vec}, \tag{26}$$

where $\mathbf{T}$ is a linear mapping and $\tilde{\mathbf{K}}_{vec}$ is the compacted vector that only contains distinct elements. For example, suppose that there are two different delays in the control system and their delay governing matrices are

$$\mathbf{K}_1 = \begin{pmatrix} 0 & d_1 \\ 0 & 0 \end{pmatrix} \quad \text{and} \quad \mathbf{K}_2 = \begin{pmatrix} d_2 & 0 \\ d_2 & 0 \end{pmatrix},$$

respectively, then

$$\mathbf{K}_{vec} = \begin{pmatrix} 0 & 0 & d_1 & 0 & d_2 & d_2 & 0 & 0 \end{pmatrix}^T.$$

It has only two distinct elements, i.e., d_1 and d_2, thus the compacted vector and the linear mapping can be written as

$$\tilde{\mathbf{K}}_{vec} = \begin{pmatrix} d_1 \\ d_2 \end{pmatrix}, \quad \text{and} \quad \mathbf{T} = \begin{pmatrix} 0 & 0 & 1 & 0 & 0 & 0 & 0 & 0 \\ 0 & 0 & 0 & 0 & 1 & 1 & 0 & 0 \end{pmatrix}^T.$$

Hence, the iteration Eq. (25) is adapted to

$$\begin{pmatrix} \tilde{\mathbf{K}}_{vec}^{i+1} \\ \boldsymbol{\tau}^{i+1} \end{pmatrix} = \begin{pmatrix} \tilde{\mathbf{K}}_{vec}^{i} \\ \boldsymbol{\tau}^{i} \end{pmatrix} + \begin{pmatrix} \Delta\tilde{\mathbf{K}}_{vec}^{i} \\ \Delta\boldsymbol{\tau}^{i} \end{pmatrix} = \begin{pmatrix} \tilde{\mathbf{K}}_{vec}^{i} \\ \boldsymbol{\tau}^{i} \end{pmatrix} + \left(\left(\boldsymbol{\Phi}^i\right)^T \boldsymbol{\Phi}^i \right)^{-1} \left(\boldsymbol{\Phi}^i\right)^T \boldsymbol{\Psi}^i, \quad (27)$$

where

$$\boldsymbol{\Phi}^i = \begin{pmatrix} \mathbf{X}_o^T(j\omega_1) \otimes \mathbf{H}(j\omega_1) \left(\mathbf{Q}_K^i(j\omega_1)\mathbf{T} \quad \mathbf{Q}_\tau^i(j\omega_1) \right) \\ \mathbf{X}_o^T(j\omega_2) \otimes \mathbf{H}(j\omega_2) \left(\mathbf{Q}_K^i(j\omega_2)\mathbf{T} \quad \mathbf{Q}_\tau^i(j\omega_2) \right) \\ \vdots \\ \mathbf{X}_o^T(j\omega_N) \otimes \mathbf{H}(j\omega_N) \left(\mathbf{Q}_K^i(j\omega_N)\mathbf{T} \quad \mathbf{Q}_\tau^i(j\omega_N) \right) \end{pmatrix}.$$

Finally, the programing flow chart of the combined delay identification procedure can be drawn as shown in Fig. 1.

3 Experimental and Numerical Verification

In the above section, parameter identifiability and corresponding algorithms are discussed for different cases. To verify their practicability, the experiment on a simple active vibration absorber and the simulation on an active truss with multiple degree-of-freedoms are applied.

3.1 Experiment Verification for Prior Known State Matrix

The vibration absorber, shown in Fig. 2, generally consists of six parts. The first part is a steel block (mark 1) acting as the payload on the absorber. The blue bar under the payload (mark 2) is the aluminum holder hanged on the ceiling of the yellow frame (mark 6) by two pairs of sheet springs (mark 5a). The lower blue bar (mark 3) is the absorber holder that connects the payload holder by sheet springs (mark 5b) and links the linear actuator (mark 4) by carbon fiber coupler, where the actuator's stator is fixed on the yellow frame. The yellow frame is made of hard aluminum alloy so that it can be treated as a rigid body.

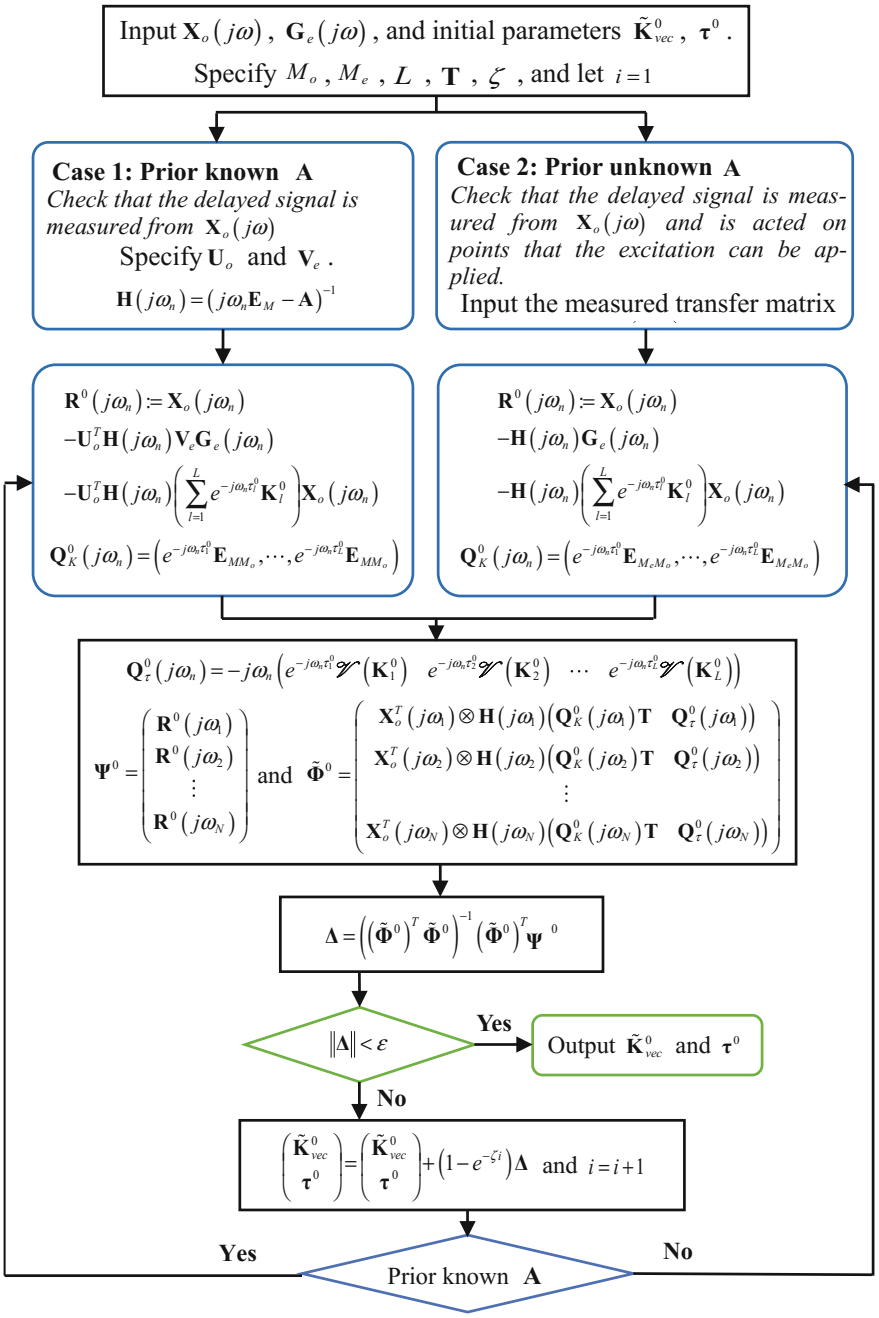

Fig. 1 The flow chart of delay parameter identification

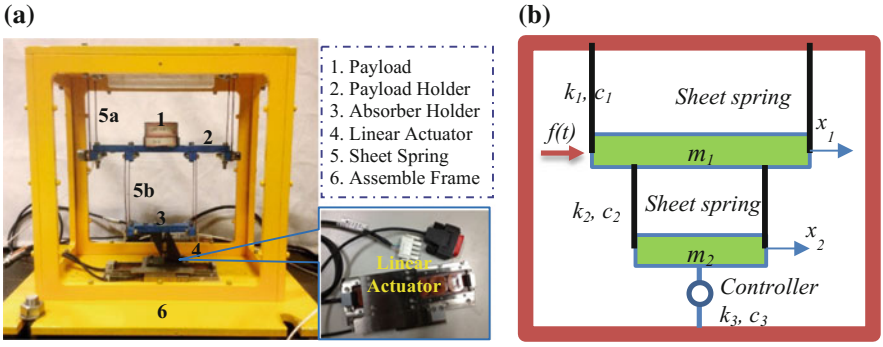

Fig. 2 Vibration absorber. **a** Real device; **b** Schematic view

The controller measures the lower holder's displacement, i.e., x_2, delays it in RAM for a period τ, and then proportionally outputs it to the linear actuator. Note that the controller costs time in signal transmitting and calculating, the reference signal that is actually exported is $x_2(t-\tau-\tau_{in})$, where τ is the delay given in the programmer and τ_{in} is the controller's inherent delay. Besides, the power amplifier in linear actuator has its gain factor, although it should be tuned to 1, so that the actual output of the actuator is $gkx_2(t-\tau-\tau_{in})$, where g is the gain factor of the power amplifier and k is the proportion set in the programmer. The task of this experiment is identifying the gain factor g and the inherent time delay τ_{in} in the actuator. τ is set as 0 ms in the programmer and k is set as −400 N/m, −350 N/m, …, −100 N/m, 100 N/m, 150 N/m, …, 400 N/m, respectively, so that the identification's accuracy can be evaluated comprehensively.

The equation of motion of the device can be written as

$$\begin{cases} m_1\ddot{x}_1 + c_1\dot{x}_1 + c_2(\dot{x}_1 - \dot{x}_2) + k_1x_1 + k_2(x_1 - x_2) = f(t) \\ m_2\ddot{x}_2 + c_2(\dot{x}_2 - \dot{x}_1) + c_3\dot{x}_2 + k_2(x_2 - x_1) + k_3x_2 = gkx_2(t-\tau_{in}) \end{cases}. \tag{28}$$

Let $(x_1 \quad x_2 \quad x_3 \quad x_4)^T = (x_1 \quad x_2 \quad \dot{x}_1 \quad \dot{x}_2)^T$, Eq. (28) can be rewritten into the standard form as Eq. (1) shows, where

$$\mathbf{A} = \begin{pmatrix} 0 & 0 & 1 & 0 \\ 0 & 0 & 0 & 1 \\ -\frac{k_1+k_2}{m_1} & \frac{k_2}{m_1} & -\frac{c_1+c_2}{m_1} & \frac{c_2}{m_1} \\ \frac{k_2}{m_2} & -\frac{k_2+k_3}{m_2} & \frac{c_2}{m_2} & -\frac{c_2+c_3}{m_2} \end{pmatrix}, \quad \mathbf{D}_1 = \begin{pmatrix} 0 & 0 & 0 & 0 \\ 0 & 0 & 0 & 0 \\ 0 & 0 & 0 & 0 \\ 0 & \frac{gk}{m_2} & 0 & 0 \end{pmatrix},$$

$$\mathbf{g}(t) = \begin{pmatrix} 0 \\ 0 \\ f(t) \\ 0 \end{pmatrix},$$

and $\tau_1 = \tau_{in}$. Using modal analysis method, the system's structural parameters are calibrated as $m_1 = 0.8027\,\text{kg}$, $m_2 = 0.3827\,\text{kg}$, $c_1 = 2.5238\,\text{Ns/m}$, $c_2 = -0.4728\,\text{Ns/m}$, $c_3 = 8.7934\,\text{Ns/m}$, $k_1 = 2271.2284\,\text{N/m}$, $k_2 = 1469.8869\,\text{N/m}$, and $k_3 = 185.6448\,\text{N/m}$.

Since the state matrix $\mathbf{A}$ is prior known, Theorem 1 can be applied to determine the identifiability of the delay parameters. Note that the delayed control only uses x_2 as its reference signal, we just need to measure $X_2(j\omega)$ to identify g and τ_{in}. According to the algorithm shown in Fig. 1, the specifications should be given as

$$M_o = 1,\ M_e = 1,\ L = 1,\ \tilde{\mathbf{K}}^0_{vec} = g^0,\ \boldsymbol{\tau}^0 = \tau^0_{in},\ \mathbf{X}_o(j\omega) = X_2(j\omega),\ \mathbf{G}_e = F(j\omega),$$
$$\mathbf{T} = (0 \quad 0 \quad 0 \quad k/m_2)^T,\ \mathbf{U}_o = (0 \quad 1 \quad 0 \quad 0)^T,\ \mathbf{V}_e = (0 \quad 0 \quad 1 \quad 0)^T.$$

Substituting these parameters into the algorithm, the gain factor g and inherent delay τ_{in} are identified and shown in Fig. 3, where their mean values are calibrated to be 1.1626 and 7.7986 ms, respectively.

In order to verify the identification's accuracy, these mean values are substituted into Eq. (28) to predict the system's FRF, where k is set as 200 N/m and τ is set as 70 ms. The comparison of the predicted FRF and the experimental FRF is shown in Fig. 4. As can be seen, the predicted FRF considering the inherent delay fits the experimental FRF precisely, whereas the FRF neglecting the internal delay biases a lot.

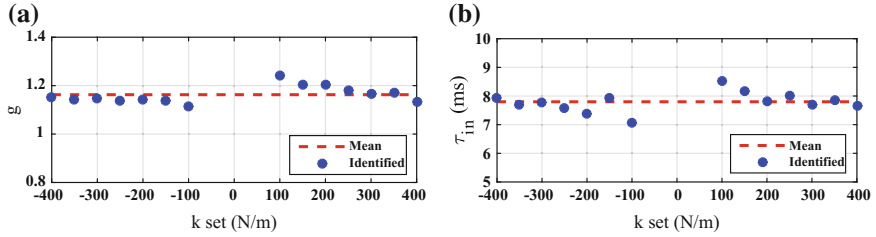

Fig. 3 The identified parameters and errors. **a** Gain factor; **b** Inherent time delay

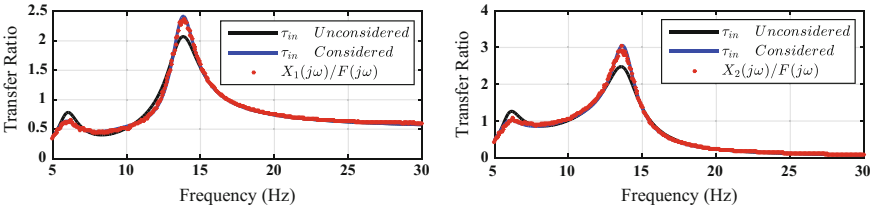

Fig. 4 The frequency response with 70 ms programmer delay

3.2 Numerical Verification for Prior Unknown State Matrix

Truss structure is usually used in the environment that requires large span but light weight, e.g., the solar panel skeleton or the antenna holder on the spacecraft. The payload is often mounted at the tip of the structure. To stabilize the payload, active control is introduced into the structure. Figure 5 shows a simple truss structure with tip mass. For this kind of mechanism, the monitoring of all nodes is impossible, otherwise it would cost too much space or resource from the carrier. Thus, laying out as few sensors and monitors as possible is a practical problem for dynamic monitoring and parameter identification.

The structure shown in Fig. 5 has 11 nodes, which means 22 degrees of freedoms in the horizontal and vertical directions. Suppose that the feedback point is node 11 and the delayed control is embedded in active elements 0^1–2 and 0^2–1 with different time delays. Besides, suppose that the truss structure is made of aluminum, i.e., the mass density is 2700 kg/m^3 and the Young's modulus is 69 GPa; the distance between nodes is 0.8 m; the cross-sectional area is 5 cm^2 and the tip mass is 10 kg. In system model, let

$$\begin{pmatrix} x_{2i-1} \\ x_{2i} \end{pmatrix} = \begin{pmatrix} u_i \\ v_i \end{pmatrix},$$

where $i = 1, 2, \ldots, 11$ is the node number. As can be seen, there are so many degree-of-freedoms that the calibration of $\mathbf{A}$ is a difficult task. For this case, Theorem 2 can be applied for delay parameter identification.

Theorem 2 implies that if we want to identify delay parameters connecting the reference node 11 and the active nodes 1 and 2, the output measurement should contain node 11 and the input measurement should contain nodes 1 and 2. To simplify the identification, we just set the output measurement as u_{11} and v_{11}, i.e., $\mathbf{X}_o(j\omega) = (\, X_{21}(j\omega) \quad X_{22}(j\omega)\,)^T$, and set the input measurement as $\mathbf{G}_e(j\omega) = (\, G_1(j\omega) \quad G_3(j\omega)\,)^T$. Thus the transfer matrix estimated before control activating can be specified as

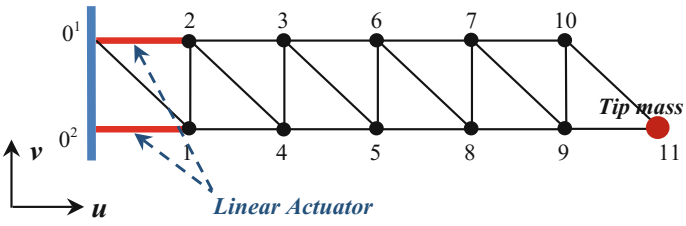

Fig. 5 The planar truss structure with a tip mass

$$\mathbf{H}(j\omega) = \begin{pmatrix} H_{21,1}(j\omega) & H_{21,3}(j\omega) \\ H_{22,1}(j\omega) & H_{22,3}(j\omega) \end{pmatrix},$$

which is much easier to be acquired compared with the entire transfer function in 22 freedoms.

As for the concrete control plan, suppose that the horizontal displacement of node 11 is proportionally acted on the active elements with one time delay, and the vertical displacement of node 11 is proportionally acted on the active elements with another time delay, thus the delay coupling matrix could be written as

$$\mathbf{K}_1 = \begin{pmatrix} d_1 & 0 \\ d_2 & 0 \end{pmatrix} \quad \text{and} \quad \mathbf{K}_2 = \begin{pmatrix} 0 & d_3 \\ 0 & d_4 \end{pmatrix},$$

where $d_1 = -7.70\,\text{N/μm}$, $d_2 = -4.20\,\text{N/μm}$, $d_3 = -3.30\,\text{N/μm}$, $d_4 = 3.90\,\text{N/μm}$, $\tau_1 = 17.00\,\text{ms}$, $\tau_2 = 34.00\,\text{ms}$. Accordingly, the vectorized form can be written as $\mathbf{K}_{vec} = (\,d_1 \quad d_2 \quad 0 \quad 0 \quad 0 \quad 0 \quad d_3 \quad d_4\,)^T$, which can be compacted to $\tilde{\mathbf{K}}_{vec} = (\,d_1 \quad d_2 \quad d_3 \quad d_4\,)^T$ with the linear transformation

$$\mathbf{T} = \begin{pmatrix} 1 & 0 & 0 & 0 & 0 & 0 & 0 & 0 \\ 0 & 1 & 0 & 0 & 0 & 0 & 0 & 0 \\ 0 & 0 & 0 & 0 & 0 & 0 & 1 & 0 \\ 0 & 0 & 0 & 0 & 0 & 0 & 0 & 1 \end{pmatrix}^T.$$

In parameter identification, the specifications are set as $M_o = 2$, $M_e = 2$, and $L = 2$. The initial parameters are set as $d_1^0 = -9.63\,\text{N/μm}$, $d_2^0 = -5.25\,\text{N/μm}$, $d_3^0 = -4.13\,\text{N/μm}$, $d_4^0 = 4.88\,\text{N/μm}$, $\tau_1^0 = 14.45\,\text{ms}$, and $\tau_2^0 = 39.10\,\text{ms}$. The iteration processes of different parameters are shown in Fig. 6.

It can be seen that the iteration converges to the set parameters very fast. Furthermore, the residue error of every iteration step, i.e., $\left\|\mathbf{\Psi}^i\right\|$, is calculated to verify the algorithm's accuracy. The result is shown in Fig. 7. It can be seen that the error converges to zero within 30 steps.

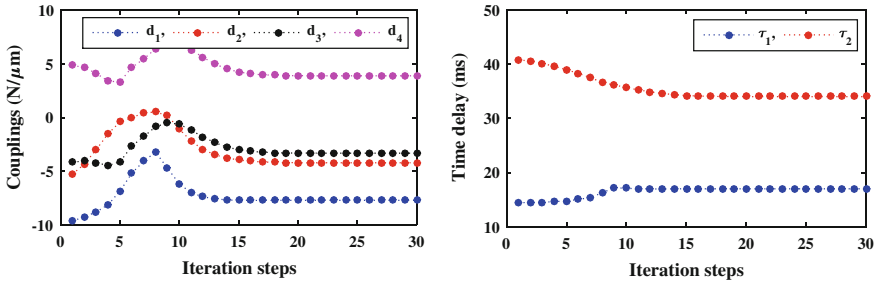

Fig. 6 Iteration process of delay parameter identification

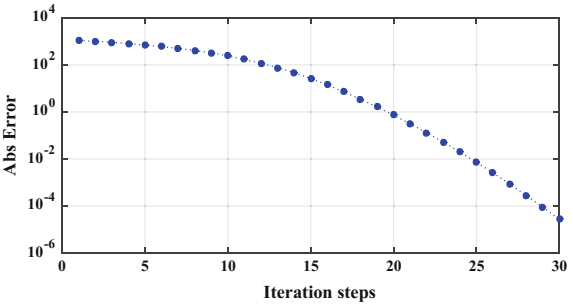

Fig. 7 Iteration process of the norm of redundant term

4 Conclusions

The delay parameter identifiabilities and corresponding estimation algorithms for different cases are systematically studied in this paper. From comprehensive analysis, some highlights of this paper can be drawn as follows.

a. This algorithm is very friendly in experimental application. The source data used for parameter identification is the frequency response function, which is a common function embedded in most general data analyzers.
b. This algorithm is versatile on delay identification problems in linear system. It considers cases that the state matrix is prior known and prior unknown. It has no limitations in the number of degree-of-freedoms or the number of time delays.
c. This algorithm ensures rapid convergence. The Newton-Raphson method is proved to be convergent in the neighborhood of the fixed point, while the relaxation factor prevents numerical oscillation so that the convergence speed is accelerated.

Acknowledgements This research is supported by the National Natural Science Foundation of China under Grant No. 11572224.

References

1. Richard, J.P.: Time-delay systems: an overview of some recent advances and open problems. Automatica **39**(10), 1667–1694 (2003)
2. Xu, J., Chung, K.W.: Effects of time delayed position feedback on a van der Pol-Duffing oscillator. Physica D **180**(1), 17–39 (2003)
3. Verduyn Lunel, S.M.: Parameter identifiability of differential delay equations. Int. J. Adapt. Control Signal Process. **15**(6), 655–678 (2001)
4. Belkoura, L., Orlov, Y.: Identifiability analysis of linear delay differential systems. IMA J. Math. Control Inf. **19**(1 and 2), 73–81 (2002)
5. Orlov, Y., Belkoura, L., Richard, J.P., Dambrine, M.: On identifiability of linear time-delay systems. IEEE Trans. Autom. Control **47**(8), 1319–1324 (2002)

6. Orlov, Y., Belkoura, L., Richard, J.P., Dambrine, M.: Adaptive identification of linear time-delay systems. Int. J. Robust Nonlinear Control **13**(9), 857–872 (2003)
7. Gomez, O., Orlov, Y., Kolmanovsky, I.V.: On-line identification of SISO linear time-invariant delay systems from output measurements. Automatica **43**(12), 2060–2069 (2007)
8. Orlov, Y., Kolmanovsky, I.V., Gomez, O.: Adaptive identification of linear time-delay systems: from theory toward application to engine transient fuel identification. Int. J. Adapt. Control Signal Process. **23**(2), 150–165 (2009)
9. Björklund, S., Ljung, L.: An improved phase method for time-delay estimation. Automatica **45**(10), 2467–2470 (2009)
10. Liu, T., Gao, F.: A frequency domain step response identification method for continuous-time processes with time delay. J. Process Control **20**(7), 800–809 (2010)
11. Van Loan, C.F.: The ubiquitous Kronecker product. J. Comput. Appl. Math. **123**(1), 85–100 (2000)
12. Hardy, Y., Steeb, W.H.: Vec-operator, Kronecker product and entanglement. Int. J. Algebra Comput. **20**(01), 71–76 (2010)

Analysis of Thermoacoustic Instability: A Time-Delay System Approach

Umut Zalluhoglu and Nejat Olgac

Abstract This study is on the analysis of thermoacoustic instability on a Rijke tube. This phenomenon results from a coupling between the heat release rate fluctuations and acoustic pressure. The simplified dynamics is modeled as a linear time-invariant multiple time-delayed system of neutral type. The conditions leading to unstable operation are identified using the Cluster Treatment of Characteristic Roots (CTCR) paradigm. This method assesses the stability of time-delay systems exhaustively and non-conservatively in the space of system parameters. Several experimental tests are conducted on a laboratory scale Rijke tube setup, and their results are used to verify the analytical findings.

1 Introduction

A major problem in the modern-day gas turbines is the thermoacoustic instability (TAI). Although it is a one-and-half century old problem, especially last two decades have seen numerous scientific advances in its prediction and control [2, 3, 17, 25–27]. Its complexity emanates from the dynamic coupling between acoustic and thermal events in an enclosure. A regionally confined unsteady heat release drives a series of acoustic waves within the combustor. These waves return and influence their own source (the heat release) after some acoustic reflections and time delays. Such a regenerative mechanism may ultimately cause instability, which is reflected in the form of pressure fluctuations with growing amplitudes within the combustion chamber.

In order to better understand the TAI phenomenon, many researchers focus on simple thermoacoustic devices, such as the Rijke tube [21]. First discovered in 1859, it consists of a cylindrical tube with a heat source placed inside, as shown in Fig. 1.

U. Zalluhoglu · N. Olgac (✉)
University of Connecticut, 191 Auditorium Rd., Storrs, CT 06269-3139, USA
e-mail: olgac@engr.uconn.edu

T. Insperger et al. (eds.), *Time Delay Systems*,
Advances in Delays and Dynamics 7, DOI 10.1007/978-3-319-53426-8_23

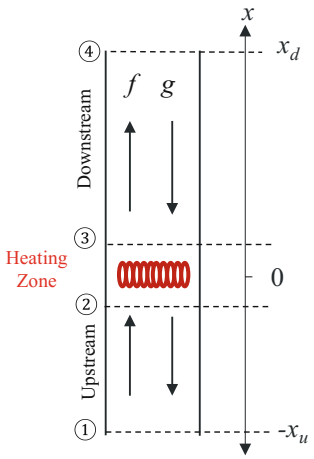

Fig. 1 Schematic representation of Rijke tube

It is commonly accepted in the literature [3] that the thermoacoustic dynamics remains within linear realm until instabilities set in. When it becomes unstable, however, the pressure fluctuations grow exponentially, which is a typical linear system property. After they reach to certain levels which invite nonlinearities, they eventually settle into a limit cycle behavior.

To detect the "onset" of instability, we focus on the linearized dynamics, following the procedure in Dowling [2]. This leads to a linear time-invariant, multiple time-delay system of neutral type. Earlier investigations utilize the Nyquist method to tackle its stability analysis [2, 3]. It is, however, not practical if one aims to analyze stability over a broad range of the system parameters [18].

The systems and mathematics literature has a strong evidence of advances in the time-delay systems (TDS) in the last two decades [20]. Numerical stability analysis algorithms are also developed such as semi-discretization method by Insperger and Stépán [10], DDE-BIFTOOL by Engelborghs et al. [4], TRACE-DDE by Breda et al. [1], and quasi-polynomial mapping-based rootfinder (QPmR) by Vyhlidal and Zitek [23]. They approximate the characteristic root distribution of TDS for given delay compositions. Nevertheless, a high computational demand arises when stability is of concern in a broader parametric space, since they are determine stability in a pointwise fashion. Lyapunov–Krasovskii approaches are also developed for the stability determination of TDS [8]. However, they provide only conservative results and are strongly dependent on the selection of the Lyapunov–Krasovskii functionals. Alternatively, cluster treatment of characteristic roots (CTCR) paradigm is deployed here to remedy such shortfalls [14, 15]. CTCR creates exhaustive and non-conservative "stability maps" in the domain of the system parameters.

The text consists of the following segments: Sect. 2 contains the mathematical model of the Rijke tube dynamics. Section 3 reviews the highlights of the CTCR paradigm. Section 4 is devoted to theoretical findings and their experimental validation.

An abbreviated version of this book chapter can be found in [24], which is presented by the authors at the 12th IFAC Workshop on Time Delay systems. Sections 2 and 4 are expanded in this study with the inclusion of new figures and additional discussions.

2 The Mathematical Model

The mathematical model of the thermoacoustic dynamics in the Rijke tube is derived under some commonly applied assumptions [2, 3, 16]: (i) the airflow is induced by natural buoyancy, therefore has low velocity and negligibly small Mach number; (ii) the heating zone is narrow compared to the tube length; (iii) the average (mean) flow quantities such as density $\bar{\rho}$ and the speed of sound $\bar{c}$ are assumed as constant along the tube; and (iv) the acoustic waves are considered as one dimensional.

Here, we reformulate the model from a control systems perspective. The thermoacoustic dynamics is governed by the first principles of conservation of mass, momentum, and energy [2]. When linearized under the aforementioned assumptions, the pressure and velocity fluctuations in the tube obey the following linear wave equation:

$$\frac{\partial^2 \tilde{p}}{\partial t^2} - \bar{c}^2 \frac{\partial^2 \tilde{p}}{\partial x^2} = 0, \tag{1}$$

where overscript $\tilde{\bullet}$ denotes the nonsteady (i.e., fluctuating) component, whereas $\bar{\bullet}$ represents the steady (mean) component of the quantity $\bullet$. Following the d'Alembert's solution of the linear wave equation [3] and the linearized momentum equation

$$\bar{\rho} \frac{\partial \tilde{u}}{\partial t} + \frac{\partial \tilde{p}}{\partial x} = 0, \tag{2}$$

the pressure and velocity fluctuations can be expressed as superposition of forward and backward traveling acoustic waves, $f(x,t)$ and $g(x,t)$, respectively:

$$\tilde{p}(x,t) = f(t - x/\bar{c}) + g(t + x/\bar{c}) \tag{3}$$

$$\tilde{u}(x,t) = [f(t - x/\bar{c}) - g(t + x/\bar{c})]/\bar{\rho}\,\bar{c}. \tag{4}$$

As shown in Fig. 1, x is the position along the tube, where $x = 0$ corresponds to location of the heater. At the tube ends $x = -x_u$ and $x = x_d$, where x_u and x_d denote the distances between ①–② and ③–④ (the upstream and downstream sides from the heating zone), respectively.

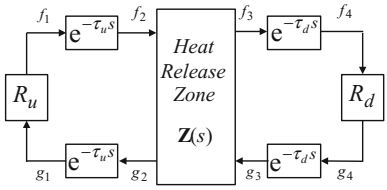

Fig. 2 Block diagram representation of Rijke tube dynamics

The block diagram of the overall dynamics is given in Fig. 2. In this representation, the system variables are the forward and backward progressing acoustic waves $f_i(t)$ and $g_i(t)$. They form the main flow variables, pressure, and velocity fluctuations at any cross section as per (3) and (4). The subscript $i = 1, 2, 3, 4$ denotes the cross sections in Fig. 1, where these functions are evaluated. The time delays $\tau_u = x_u/\bar{c}$ and $\tau_d = x_d/\bar{c}$ correspond to the travel times of acoustic waves moving at the speed of sound. In order to derive causal relationships between each variable, we start with expressing $(f_2(t)\, g_3(t))^{\mathrm{T}}$ as the delayed version of $(f_1(t)\, g_4(t))^{\mathrm{T}}$ as

$$\begin{pmatrix} f_2(t) \\ g_3(t) \end{pmatrix} = \begin{pmatrix} f_1(t-\tau_u) \\ g_4(t-\tau_d) \end{pmatrix}. \tag{5}$$

In Laplace domain, (5) transforms into

$$\begin{pmatrix} F_2(s) \\ G_3(s) \end{pmatrix} = \mathbf{T}(s) \begin{pmatrix} F_1(s) \\ G_4(s) \end{pmatrix}, \quad \mathbf{T}(s) = \begin{pmatrix} \mathrm{e}^{-\tau_u s} & 0 \\ 0 & \mathrm{e}^{-\tau_d s} \end{pmatrix}. \tag{6}$$

Next, we identify the dynamics representing the thermoacoustic coupling. The conservation of mass, momentum, and energy equations, when used with (3) and (4) across the heating zone results in

$$\begin{pmatrix} -1 & 1 \\ \frac{1}{\gamma-1} & \frac{1}{\gamma-1} \end{pmatrix} \begin{pmatrix} g_2(t) \\ f_3(t) \end{pmatrix} = \begin{pmatrix} 1 & -1 \\ \frac{1}{\gamma-1} & \frac{1}{\gamma-1} \end{pmatrix} \begin{pmatrix} f_2(t) \\ g_3(t) \end{pmatrix} + \begin{pmatrix} 0 \\ \frac{\tilde{Q}(t)}{A\bar{c}} \end{pmatrix}, \tag{7}$$

where γ is the heat capacity ratio, A is the cross-sectional area of the tube, and $\tilde{Q}(t)$ is the unsteady heat release rate [2]. $\tilde{Q}(t)$ is influenced by the velocity fluctuations at the heating zone, $\tilde{u}_2(t)$ [7]. In Laplace domain this relation is represented by

$$\tilde{Q}(s)/\tilde{u}_2(s) = a/(bs+1), \tag{8}$$

where a and b act as gain and time constant, affected by mean heat release $(\bar{Q})$, mean flow velocity $(\bar{u}_2)$, and the heater geometry. Evaluating (4) at cross section ② and taking its Laplace transform gives

$$\tilde{u}_2(s) = [F_2(s) - G_2(s)]/\bar{\rho}\bar{c}. \tag{9}$$

Substituting (8) and (9) in Laplace transform of (7), one obtains

$$\begin{pmatrix} G_2(s) \\ F_3(s) \end{pmatrix} = \mathbf{Z}(s) \begin{pmatrix} F_2(s) \\ G_3(s) \end{pmatrix}, \mathbf{Z}(s) = \frac{1}{s+Z+W} \begin{bmatrix} Z & s+W \\ s+2Z+W & -Z \end{bmatrix}, \tag{10}$$

where $Z = a(\gamma - 1)/(2Ab\bar{c}^2\bar{\rho})$ and $W = 1/b$. Next, we express the relationship between $(\, g_2(t) \quad f_3(t) \,)^{\mathrm{T}}$ and $(\, g_1(t) \quad f_4(t) \,)^{\mathrm{T}}$ similar to (5) and (6) as

$$\begin{pmatrix} g_1(t) \\ f_4(t) \end{pmatrix} = \begin{pmatrix} g_2(t-\tau_u) \\ f_3(t-\tau_d) \end{pmatrix} \rightarrow \begin{pmatrix} G_1(s) \\ F_4(s) \end{pmatrix} = \mathbf{T}(s) \begin{pmatrix} G_2(s) \\ F_3(s) \end{pmatrix}. \tag{11}$$

The boundary conditions at cross sections ① and ④ can be characterized by the reflection coefficients R_u and R_d, which account for the acoustic losses at the tube ends. This leads to the following expression:

$$\begin{pmatrix} F_1(s) \\ G_4(s) \end{pmatrix} = \mathbf{R} \begin{pmatrix} G_1(s) \\ F_4(s) \end{pmatrix}, \quad \mathbf{R} = \begin{pmatrix} R_u & 0 \\ 0 & R_d \end{pmatrix}. \tag{12}$$

Now that all the transfer matrices are obtained, (6), (10), (11), and (12) can be combined to close the loop in Fig. 2 as

$$\begin{pmatrix} F_1(s) \\ G_4(s) \end{pmatrix} = \mathbf{RT}(s)\mathbf{Z}(s)\mathbf{T}(s) \begin{pmatrix} F_1(s) \\ G_4(s) \end{pmatrix}. \tag{13}$$

Which can be rewritten as

$$\mathbf{M}(s) \begin{pmatrix} F_1(s) \\ G_4(s) \end{pmatrix} = 0, \quad \mathbf{M}(s) = \mathbf{I} - \mathbf{RT}(s)\mathbf{Z}(s)\mathbf{T}(s). \tag{14}$$

In (14), $\mathbf{M}(s)$ represents the overall system matrix, determinant of which gives the characteristic equation of the system as

$$CE(s, .\tau_u, \tau_d) = \det[\mathbf{M}(s)] = 0. \tag{15}$$

To simplify the notation, we introduce a delay vector $(\tau_1, \tau_2) = (2\tau_u, 2\tau_d)$ and express the characteristic equation as

$$\begin{aligned} CE(s, \tau_1, \tau_2) = {} & 2Ab\bar{c}^2\bar{\rho}\left(R_u R_d \mathrm{e}^{-(\tau_1+\tau_2)s} - 1\right)s + R_d a(1-\gamma)\mathrm{e}^{-\tau_2 s} \\ & + R_u a(\gamma-1)\mathrm{e}^{-\tau_1 s} - 2A\bar{c}^2\bar{\rho} + R_u R_d\left(2A\bar{c}^2\bar{\rho} + a\gamma - a\right)\mathrm{e}^{-(\tau_1+\tau_2)s} + a(1-\gamma) = 0. \end{aligned} \tag{16}$$

It is a quasi-polynomial involving two independent delays (τ_1, τ_2), which are related to (x_u, x_d) by $\tau = 2x/\bar{c}$ and vary with the tube length and heater location. The rest of the parameters in (16) are taken as constants.

3 Stability Analysis Methodology

The Rijke tube dynamics falls into the class of linear time-invariant multiple time-delay systems with two delays, as discussed in the previous section. Its exponential stability is completely determined by the roots of its characteristic polynomial in (16). In general form, it can be written as

$$CE(s,\tau_1,\tau_2)=\sum_{i=0}^{n}\sum_{j=0}^{m}\sum_{k=0}^{l}P_{ijk}\mathrm{e}^{-(j\tau_1+k\tau_2)s}s^i=0, \tag{17}$$

where n is the order of the characteristic polynomial, m and l are the highest order of commensurate of delays τ_1 and τ_2, respectively. The highest order term in (17) involves delays, and thus it is representative of a *neutral* time-delay system. Next, we give two theorems that determine the stability of this class of systems.

Theorem 1 *The exponential stability of a neutral time-delay system with some given delays requires the dynamics governed by its associated difference equation to be stable. Therefore, as a necessary condition, all the zeros of*

$$D(s,\tau_1,\tau_2)=\sum_{j=0}^{m}\sum_{k=0}^{l}P_{njk}\mathrm{e}^{-(j\tau_1+k\tau_2)s}=0 \tag{18}$$

have to lie in the left half of the complex plane [13].

Theorem 2 *The necessary and sufficient condition for the exponential stability of* (17) *is that all its infinitely many zeros should (i) lie in the open left half plane and (ii) be bounded away from the imaginary axis* [9]. *The proof is suppressed here.*

Theorem 1 guarantees the condition (ii) in Theorem 2. Once it is satisfied, delay-dependent stability posture of the system can be determined by CTCR. Leaving the details on the paradigm to Olgac et al. [14, 15], a brief review is presented next.

For a linear time-invariant TDS characterized by (17) to switch the stability posture, the characteristic roots should cross the imaginary axis, say at $\pm\omega\mathrm{i}$ for some delays $\boldsymbol{\tau}\in\Re^{2+}$. We use $\langle\boldsymbol{\tau},\omega\rangle$ notation to indicate their causal correspondence. In order to assess the stability of the system exhaustively, all delay compositions for which (17) has an imaginary root should be determined. We denote the complete set of such imaginary root frequencies with $\boldsymbol{\Omega}$, and the corresponding root set with $\mathbf{S}_\Omega$ as

$$\begin{aligned}\boldsymbol{\Omega}&=\left\{\omega|CE(s=\pm\omega\mathrm{i},\boldsymbol{\tau})=0,\boldsymbol{\tau}\in\Re^{2+},\omega\in\Re\right\}\\ \mathbf{S}_\Omega&=\left\{s=\pm\omega\mathrm{i}|\omega\in\boldsymbol{\Omega}\right\}.\end{aligned} \tag{19}$$

It is trivial to observe from (17) that an imaginary root $s=\pm\omega\,\mathrm{i}$ corresponding to $\boldsymbol{\tau}\in\Re^{2+}$ will be repeated infinitely many times as

$$(\tau_{1j}, \tau_{2k}) = \left(\tau_1 + \frac{2\pi}{\omega} j, \tau_2 + \frac{2\pi}{\omega} k\right), \quad j = 0, 1, \ldots, \quad k = 0, 1, \ldots \tag{20}$$

These trajectories divide the delay domain into encapsulated regions in which the *number of unstable roots*, *NU*, is fixed (see D-Subdivision method by Kolmanovskii and Nosov [11]). Consequently, any stability reversal can only occur at the boundaries of these regions. The system is declared stable when $NU = 0$. One needs to determine the boundaries of these infinitely many regions exhaustively for a complete stability declaration. The following two propositions bring a discipline to this chaotic looking picture.

Proposition 1 *There are only a manageably small number of trajectories in* (τ_1, τ_2) *space called the* kernel hypercurves [22]

$$\wp_0 = \left\{ \boldsymbol{\tau} | \langle \boldsymbol{\tau}, \omega \rangle, \boldsymbol{\tau} \in \Re^{2+}, \omega \in \boldsymbol{\Omega}, 0 \le \tau_1 \le \frac{2\pi}{\omega}, 0 \le \tau_2 \le \frac{2\pi}{\omega} \right\}. \tag{21}$$

Here, $\wp_0$ represents the loci of the smallest τ_1 and τ_2 combinations for which the characteristic equation has an imaginary root at $s \in \mathbf{S}_\Omega$. The remaining hypercurves are created from this set, $\wp_0$, using the pointwise translation property in (20) for $j, k > 0$. They are called the *offspring hypercurves*, and denoted by $\wp_{jk}$ where j and k identify the jth and kth generation offspring in τ_1 and τ_2, respectively. Consequently, the complete set of hypercurves, $\wp$, becomes

$$\wp = \wp_0 \cup \left(\cup_{j=1}^{\infty} \cup_{k=1}^{\infty} \wp_{jk} \right). \tag{22}$$

Any point on the trajectories of kernel, $\wp_0$, imposes its $\omega \in \boldsymbol{\Omega}$ signature identically onto its offspring, $\wp_{jk}$. Thus, the imaginary root set $\mathbf{S}_\Omega$ remains invariant from kernel to offspring. The set $\wp$ constitutes the complete distribution of (τ_1, τ_2) where the characteristic Eq. (17) has root sets containing at least one pair of imaginary roots, $\mathbf{S}_\Omega$.

The root tendency (*RT*) for an imaginary characteristic root $s \in \mathbf{S}_\Omega$, along a delay axis (say τ_1), is defined by

$$RT|_{s=\omega i}^{\tau_1} = \operatorname{sgn}\left[\operatorname{Re}\left(\frac{\partial s}{\partial \tau_1} \right) \Big|_{s=\omega i} \right]. \tag{23}$$

This property indicates the evolution direction of the imaginary root $\pm\omega$i (to the left or the right half of the complex plane) as we pass through a hypercurve in (τ_1, τ_2) space by increasing one delay (τ_1) infinitesimally.

Proposition 2 *At* $s \in \mathbf{S}_\Omega$ *as* τ_1 *(or* τ_2*) increases at a point on a kernel and its corresponding offspring, the root tendency* $RT|_s^{\tau_1}$ *(or* $RT|_s^{\tau_2}$*) remains invariant so long as the other delay* τ_2 *(or* τ_1*) is kept fixed. This feature, in essence, declares the stabilizing (or destabilizing) transitions across the regional boundaries defined by* $\wp$.

In light of these propositions, one can establish the stability outlook of the system by generating its stability map in (τ_1, τ_2) domain. Among various methods to determine the complete set of kernel and offspring hypercurves, we use the spectral delay space (SDS) method [5, 6]. In this approach, a new coordinate set, $(\nu_1, \nu_2) = (\tau_1\omega, \tau_2\omega)$, is defined that confines the kernel and offspring hypercurves in two-dimensional blocks of 2π length. The building block (BB) contains the *building hypercurves*, which later transform to kernel hypercurves in (τ_1, τ_2) domain. By stacking the BB in (ν_1, ν_2) domain, *reflection hypercurves* are obtained. They transform to the offspring hypercurves in (τ_1, τ_2) domain. Once the complete set of kernel and offspring hypersurfaces, $\wp$, is obtained, *RT* is evaluated and the complete stability map of the system is revealed.

4 Main Results

In this section, stability of the Rijke tube is assessed using the CTCR paradigm and these analytical findings are then compared with the results from several experimental tests. Three cylindrical glass tubes of different lengths are heated with an electrical coil, which is powered through a variac. The temperatures below and above the heater are measured via two thermocouples. A piezoelectric microphone is utilized to record the sound pressure close to the downstream end. The data acquisition of the measured pressure is performed at 8000 Hz sampling rate.

The operational parameters that represent our experiment are measured and taken as $R_u = R_d = -0.93$, $\gamma = 1.4$, $A = 7.5\,\text{cm}^2$, $\bar{\rho} = 1.2\,\text{kg/m}^3$, $\bar{c} = 340\,\text{m/s}$, $a = 200$, and $b = 0.002$. Substituting these parameters in the characteristic equation given in (16), we obtain the following normalized form:

$$\begin{aligned} CE(s, \tau_1, \tau_2) = (1 - 0.865\mathrm{e}^{-(\tau_1+\tau_2)s})s + 178.78\mathrm{e}^{-\tau_1 s} \\ - 178.78\mathrm{e}^{-\tau_2 s} - 598.71\mathrm{e}^{-(\tau_1+\tau_2)s} + 692.23 = 0. \end{aligned} \tag{24}$$

The coefficient of the highest order s term in (24) that corresponds to the associated difference equation is

$$D(s, \tau_1, \tau_2) = 1 - 0.865\mathrm{e}^{-(\tau_1+\tau_2)s} = 0, \tag{25}$$

which implies $|\mathrm{e}^{-(\tau_1+\tau_2)s}| = 1.156 > 1$, meaning that all the infinitely many roots of (25) have $\mathrm{Re}(s) < 0$. Thus the associated difference equation for this dynamics is stable for all delay values (i.e., it is "strongly" stable [9]). Next, the CTCR procedure is implemented to generate the stability map of the Rijke tube in (τ_1, τ_2) domain. The SDS representation of (24) with the respective building (red) and reflection (blue) hypercurves is obtained in Fig. 3a. Again, they carry the kernel and offspring signature respectively. The frequency variation is color coded on the building block in Fig. 3b.

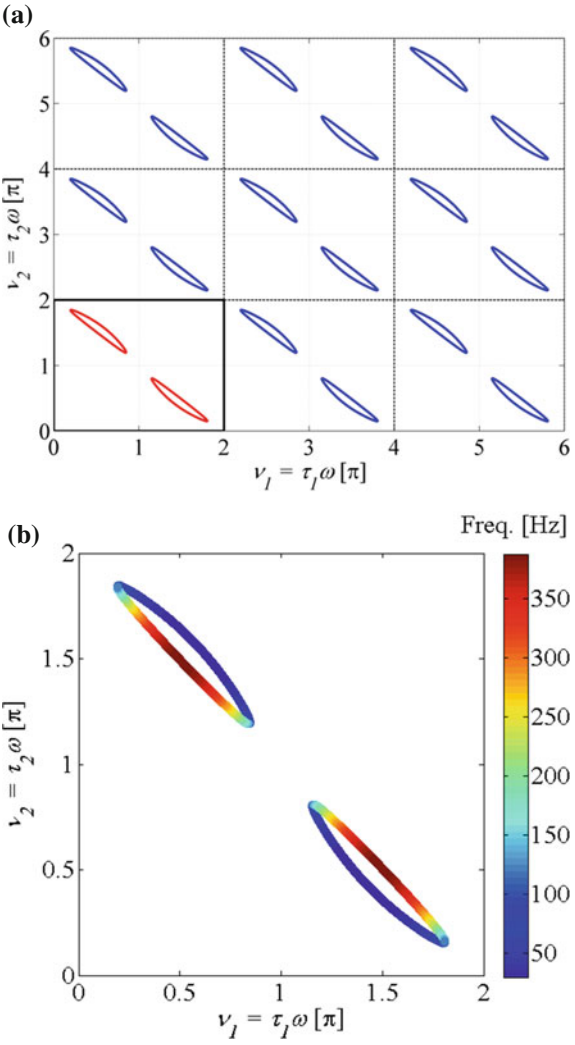

Fig. 3 **a** SDS representation of the system. Building block (BB) is in *black solid* frame. **b** Frequency variation on the building block

The CTCR-generated stability map is given in Fig. 4a. To facilitate visualization it is displayed in (x_u, x_d) space rather than delay space (τ_1, τ_2). The kernel and offspring hypercurves are colored in red and blue, respectively. The stable regions are shaded in gray. A series of experimental tests are conducted on three different tube lengths ($L = x_u + x_d = 0.51$ m, 1.02 m, and 1.22 m), which are represented by black parallel lines. Any point on these lines depicts a certain heater location determined by x_u and x_d. To test the structure at any heater location, we energize the heating element, and wait until the temperature difference below and above the heater reaches steady state. If the recorded pressure perturbations attain a noticeable

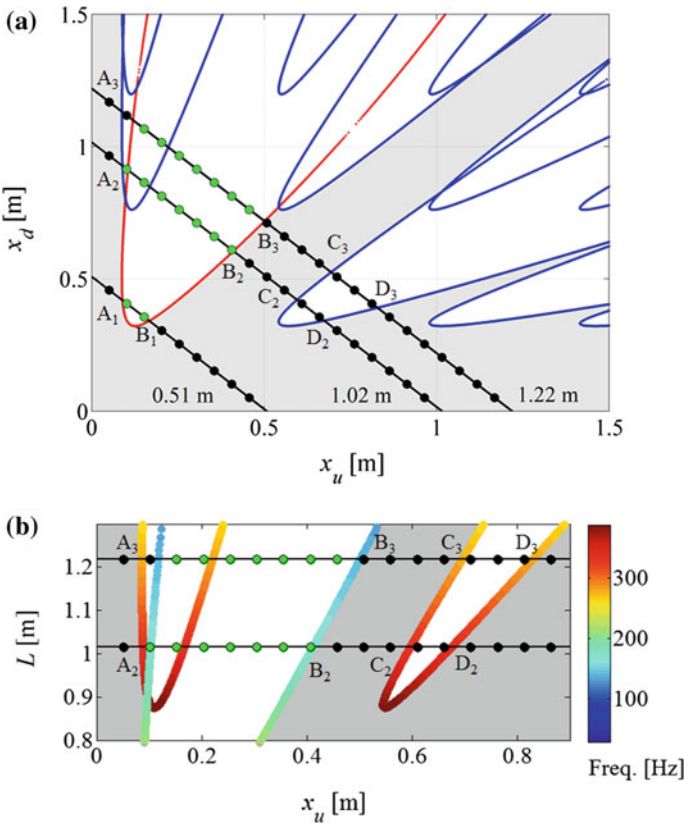

Fig. 4 **a** CTCR stability map of the Rijke tube in (x_u, x_d) space, and experimental validation. **b** Frequency distribution on the kernel and offspring hypercurves in (x_u, L) space

level, the system is declared unstable. The unstable declared operating points are marked with green, while the stable ones are marked with black circles.

The agreement between experimental TAI detection overlaid on the stability chart of CTCR is remarkable, especially for the intervals A_1B_1, A_2B_2, and A_3B_3. These intervals correspond to the case when the heater is located at the lower half of the tubes $(x_u < x_d)$. In accordance with Matveev [12] and Raun et al. [19], it is not possible to destabilize the Rijke tube when the heater is located at the midpoint $(x_u = x_d)$ or when it is close to tube ends.

Some minor disagreements are observed when the heater is located at the upper half of the tube $(x_u > x_d)$, such as C_2D_2 (for 1.02 m tube) and C_3D_3 (for 1.22 m) intervals. At such locations, instability is driven by higher modes of the dynamics, instead of the fundamental (first) mode [19]. In Fig. 4b, the stability map is redrawn in (x_u, L) domain, where L is the tube length. The frequencies at the stability boundaries near A_2B_2 and A_3B_3 contain higher frequencies as in C_2D_2 and C_3D_3 as well as lower frequencies (of blue tone). It is well known that higher power input is

required to excite the higher frequency modes of the dynamics than those of lower frequencies. As we do not have high enough power at the present test setting, these investigations are left for future studies. The stability disagreements at higher frequencies might also be attributed to the lack of nonlinear damping features that were unaccounted for in the mathematical model. For instance, Matveev [12] reports that the reflections of the acoustic waves at the tube ends are in fact weaker for the secondary (higher) modes. In addition, the pressure oscillations at higher frequencies tend to have lower signal-to-noise ratio, which are more difficult to record. Our experimental equipment might have also failed to capture such sound levels.

The modal characteristics of the Rijke tube are studied during an unstable operation, next. In Fig. 4a it is declared that TAI occurs for the 1.22-m-length tube when the heater is located at $(x_u, x_d) = (0.20\,\text{m}, 1.02\,\text{m})$. At this operating point, the recorded sound pressure is shown in Fig. 5a, where the instability and nonlinear limit cycle can be observed. As the zoomed-in figure in Fig. 5b shows, the pressure oscillations grow exponentially at the onset of instability. This is linear system

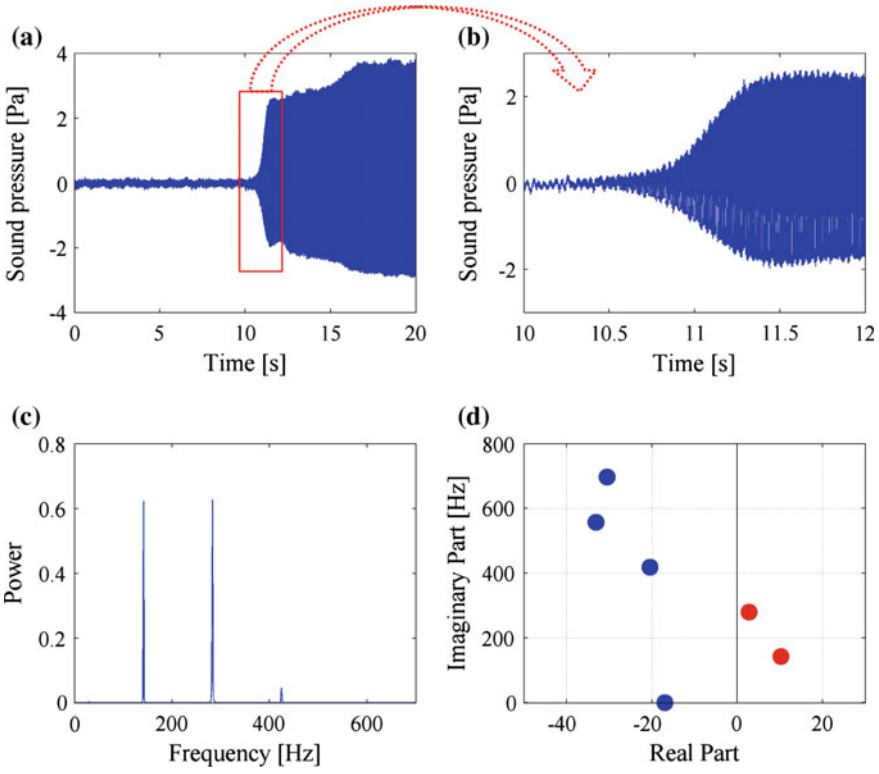

Fig. 5 **a** Time trace of the recorded sound pressure; **b** zoomed-in view of the onset of instability; **c** power spectral density of the interval in (**b**); **d** QPmR-generated dominant poles; all for 1.22-m-length tube with the heater located at $(x_u, x_d) = (0.20\,\text{m}, 1.02\,\text{m})$

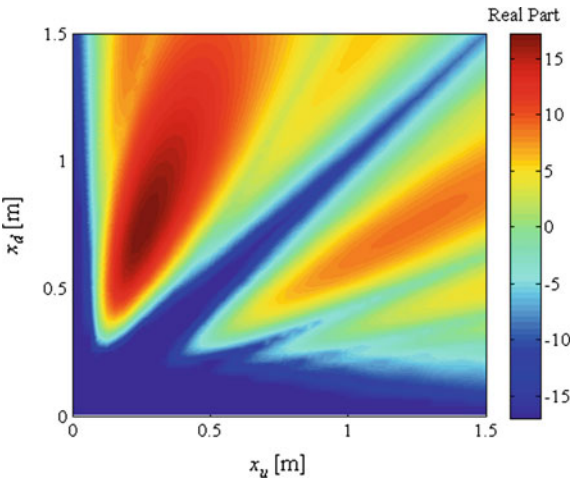

Fig. 6 **a** The distribution of the real part of the system's dominant characteristic root at various operating points over the (x_u, x_d) space

behavior, and thus it can be claimed that the linearized mathematical model described in Sect. 2 is sufficient to predict TAI. A fast Fourier transformation is performed at the onset of instability and corresponding spectral power density is obtained as shown in Fig. 5c. In Fig. 5d, the approximate characteristic root locations of (24) are shown, generated with the QPmR algorithm. The imaginary parts of the unstable roots match well with the detected frequencies in Fig. 5c, supporting the accuracy of the mathematical model and stability analysis.

The real parts of the dominant roots are next examined from the system stability and dominant impulse response perspectives. We deploy QPmR algorithm to approximate the characteristic roots of Eq. (24) on a dense enough grid within the time-delay space (τ_1, τ_2). In Fig. 6, the real part of the dominant characteristic root of (24) is color coded in (x_u, x_d) space. To keep the color distribution uniform across the map, the operating points at which $\mathrm{Re}(s_{\mathrm{dom}}) < -17$ are plotted with dark blue, the same color with $\mathrm{Re}(s_{\mathrm{dom}}) = -17$ (especially at the grid points close to the origin). In general, it can be observed that the growth rates for $(x_u < x_d)$ are larger than the growth rates for $(x_u > x_d)$. Therefore, instability is expected to be more violent when the heater is placed at the lower half of the tube. This might be a reason why we could experimentally observe TAI within the intervals A_1B_1, A_2B_2, and A_3B_3 in Fig. 4a, but not in the intervals C_2D_2 and C_3D_3. As mentioned earlier, higher power input may be required to destabilize the system for the latter intervals.

5 Conclusions

In this chapter, thermoacoustic instability phenomenon in a Rijke tube is studied. First, it is shown that the mathematical model of the Rijke tube falls under the linear time-invariant neutral-type multiple time-delay systems class. Then utilizing the

cluster treatment of characteristic roots (CTCR) paradigm, operating conditions leading to thermoacoustic instability are determined exhaustively and precisely. The results are then verified on an experimental Rijke tube setup. The analytical development in this study is expected to contribute to futuristic designs of gas turbine combustors, where thermoacoustic instability is avoided.

Acknowledgements The authors would like to express their appreciation to the National Science Foundation grant CMMI-1462301 and UCONN (University of Connecticut) research excellence program for financial support.

References

1. Breda, D., Maset, S., Vermiglio, R.: Pseudospectral differencing methods for characteristic roots of delay differential equations. SIAM J. Sci. Comput. **27**, 482–495 (2005)
2. Dowling, A.P.: Nonlinear self-excited oscillations of a ducted flame. J. Fluid Mech. **346**, 271–290 (1997)
3. Dowling, A.P., Morgans, A.S.: Feedback control of combustion oscillations. Annu. Rev. Fluid Mech. **37**, 151–182 (2005)
4. Engelborghs, K., Luzyanina, T., Roose, D.: Numerical bifurcation analysis of delay differential equations using DDE-BIFTOOL. ACM Trans. Math. Softw. **28**, 1–21 (2002)
5. Fazelinia, H., Sipahi, R., Olgac, N.: Stability robustness analysis of multiple time delayed systems using "Building Block" concept. IEEE Trans. Autom. Control **52**, 799–810 (2007)
6. Gao, Q., Zalluhoglu, U., Olgac, N.: Investigation of local stability transitions in the spectral delay space and delay space. ASME J. Dyn. Syst. Meas. Control **136**, 051011-1 (2014)
7. Gelbert, G., Moeck, J.P., Paschereit, C.O., King, R.: Feedback control of unstable thermoacoustic modes in an annular Rijke tube. Control Eng. Pract. **20**, 770–782 (2012)
8. Gu, K., Niculescu, S.I.: Stability analysis of time-delay systems: a Lyapunov approach. In: Advanced Topics in Control Systems Theory, vol. 4, pp. 139–170. Springer, London (2006)
9. Hale, J.K., Verduyn Lunel, S.M.: Strong stabilization of neutral functional differential equations. IMA J. Math. Control Inf. **19**, 5–23 (2002)
10. Insperger, T., Stépán, G.: Semi-discretization method for delayed systems. Int. J. Numer. Methods Eng. **55**(5), 503–518 (2002)
11. Kolmanovskii, V.B., Nosov, V.R.: Stability of Functional Differential Equations. Mathematics in Science and Engineering, p. 180. Academic, New York (1986)
12. Matveev, K.I.: Thermoacoustic instabilities in the Rijke tube: experiments and modeling. Ph. D. thesis, California Institute of Technology, Pasadena, CA (2003)
13. Michiels, W., Niculescu, S.: Stability and Stabilization of Time-Delay Systems: An Eigenvalue-based Approach. SIAM, Philadelphia (2007)
14. Olgac, N., Sipahi, R.: The cluster treatment of characteristic roots and the neutral type time-delayed systems. ASME J. Dyn. Syst. Meas. Control **127**, 88–97 (2005)
15. Olgac, N., Vyhlídal, T., Sipahi, R.: A new perspective in the stability assessment of neutral systems with multiple and cross-talking delays. SIAM J. Control Optim. **47**(1), 327–344 (2008)
16. Olgac, N., Zalluhoglu, U., Kammer, A.S.: Predicting thermoacoustic instability; a novel analytical approach and its experimental validation. J. Propul. Power **30**(4), 1005–1015 (2014)
17. Olgac, N., Zalluhoglu, U., Kammer, A.S.: A new perspective in designing delayed feedback control for thermo-acoustic instabilities (TAI). Combust. Sci. Technol. **187**(5), 697–720 (2015)

18. Olgac, N., Cepeda-Gomez, R., Zalluhoglu, U., Kammer, A.S.: Parametric investigation of thermoacoustic instability (TAI) in a Rijke tube: a time-delay perspective. Int. J. Spray Combust. Dyn. **7**(1), 39–68 (2015b)
19. Raun, R.L., Beckstead, M.W., Finlinson, J.C., Brooks, K.P.: A review of Rijke tubes, Rijke burners and related devices. Prog. Energy Combust. Sci. **19**, 313–364 (1993)
20. Richard, J.P.: Time-delay systems: an overview of some recent advances and open problems. Automatica **39**, 1667–1694 (2003)
21. Rijke, P.L.: Notice of a new method of causing a new vibration of the air contained in a tube open at both ends. Philos. Mag. Ser. **4**(17), 419–422 (1859)
22. Sipahi, R., Olgac, N.: A unique methodology for the stability robustness of multiple time delay systems. Sys. Control Lett. **55**, 819–825 (2006)
23. Vyhlídal, T., Zítek, P.: Mapping based algorithm for large-scale computation of quasi-polynomial zeros. IEEE Trans. Autom. Control **54**, 171–177 (2009)
24. Zalluhoglu, U., Olgac, N.: Thermo-acoustic instability: theory and experiments. IFAC-PapersOnLine **48**(12), 75–80 (2015)
25. Zalluhoglu, U., Olgac, N.: Deployment of time delayed integral control for suppressing thermoacoustic instabilities. J. Guid. Control Dyn. **39**(10), 2284–2296 (2016)
26. Zalluhoglu, U., Kammer, A.S., Olgac, N.: Delayed feedback control laws for Rijke tube thermo-acoustic instability, synthesis and experimental validation. IEEE Trans. Control Syst. Technol. **34**(5), 1861–1868 (2016)
27. Zalluhoglu, U., Olgac, N.: A study of Helmholtz resonators to stabilize thermoacoustically driven pressure oscillations. J. Acoust. Soc. Am. **139**(4), 1962–1973 (2016)